Universidad de Granada

Master Métodos y Técnicas Avanzadas en Física

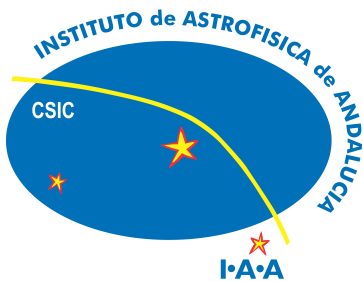# Study of Trans-Neptunian Objects using photometric techniques and numerical simulations

Dissertation presented by:
Audrey Thirouin

Supervisors: Dr. José Luis Ortiz Moreno (Instituto de Astrofísica de Andalucía, CSIC)

Dr. Adriano Campo Bagatin (Universidad de Alicante)

Granada, 2013

Los directores de la tesis **Dr ORTIZ MORENO José Luis**, investigador científico del CSIC en el Instituto de Astrofísica de Andalucía (IAA-CSIC), y **Dr CAMPO BAGATIN Adriano**, profesor titular de la Universidad de Alicante,

CERTIFICAN:

que a presente memoria titulada "Study of Trans-Neptunian Objects using photometric techniques and numerical simulations", se ha realizado bajo nuestra dirección por Audrey THIROUIN, en el Instituto de Astrofísica de Andalucía (IAA-CSIC) y constituye su Tesis para optar al grado de Doctor. Y para que así conste, en cumplimiento de la legislación vigente, presentamos ante la Comisión de Doctorado de la Universidad de Granada la referida Tesis.
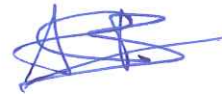
Granada, a 20 de Mayo de 2013

Directores de la Tesis:

Dr José Luis Ortiz Moreno

Dr Adriano Campo Bagatin

La doctoranda **Audrey THIROUIN** y los directores de la tesis **Dr ORTIZ MORENO José Luis** y **Dr CAMPO BAGATIN Adriano** garantizamos, al firmar esta tesis doctoral, que el trabajo ha sido realizado por el doctorando bajo la dirección de los directores de la tesis y hasta donde nuestro conocimiento alcanza, en la realización del trabajo, se han respetado los derechos de otros autores a ser citados, cuando se han utilizado sus resultados o publicaciones.

Granada, a 20 de Mayo de 2013

Directores de la Tesis:

Dr José Luis Ortiz Moreno   Dr Adriano Campo Bagatin

Doctoranda:

Audrey Thirouin

Dissertation Committee:

Dr Antonio Molina Cuevas	-	Universidad de Granada, Spain
Dra Inmaculada Foyo Moreno	-	Universidad de Granada, Spain
Dr Alain B. Doressoundiram	-	Laboratoire d'études spatiales et d'instrumentation en astrophysique (LESIA), Observatoire de Paris, site de Meudon, France
Dr Daniel Hestroffer	-	Institut de mécanique céleste et de calcul des éphémérides (IMCCE), Observatoire de Paris, site de Paris, France
Dr Fernando Moreno Danvila	-	Instituto de Astrofísica de Andalucía Consejo Superior de Investigaciones Científicas (IAA-CSIC), Spain

Reviewers:

Dr Derek C. Richardson	-	University of Maryland, USA
Dr Paolo Tanga	-	Observatoire de Nice, France

To Edmond and Josiane

Acknowledgments

It is not a fair task to acknowledge all the people who made this Ph.D. thesis possible with a few words. However, I will try to do my best to extend my great appreciation to everyone who helped me scientifically and emotionally throughout this study.
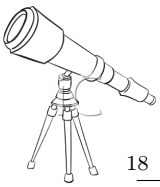
Contents

List of Figures

List of Tables

Chapter I

Introduction and Motivation

$\mathcal{I}$ n the eighties, our Solar System was composed by nine planets with their satellites, an asteroid belt between the orbit of Mars and Jupiter, the Trojan asteroids at the Jupiter's Lagrange points, and the comets. Comets and asteroids were classified as "minor planets". Nevertheless, the existence of a belt composed by planetesimals beyond Neptune's orbit was suspected. The observational confirmation of the existence of a reservoir of small bodies (the Trans-Neptunian Objects (TNOs)) at the edges of the Solar System needed more than sixty years after the discovery of Pluto in 1930. In around twenty years since the discovery of 1992 QB_1 by Jewitt and Luu (1993), the Trans-Neptunian belt moved from a speculation or a theoretical postulate (Leonard, 1930; Edgeworth, 1943; Edgeworth, 1949; Kuiper, 1951; Whipple, 1964; Fernandez, 1980) to be the most populated region of the Solar System. Currently, it is estimated that the Trans-Neptunian belt within the distance 30-50 AU from the Sun comprises approximately 100,000 objects with diameters of $\sim$100 km (Trujillo, Jewitt and Luu, 2001).

The discovery of a multitude of objects with very similar orbits to Pluto's orbit and also the fact that a mixture of ice/rock seems common to the majority of TNOs, implied that Pluto appeared to be not unique but one object of many more. Then, with the discovery of some TNOs with similar size to that of Pluto (Brown et al., 2006a; Sicardy et al., 2011), the definition of the term "planet" needed to be reviewed. The General Assembly of the International Astronomical Union (IAU) in 2006 changed the definition of planet and introduced a new type of bodies: the dwarf planets. According to the IAU definition:

- A **planet** is a celestial body that:

    - is in orbit around the Sun.
    - has sufficient mass for its self-gravity to overcome rigid body forces so that it assumes a hydrostatic equilibrium shape.
    - has cleared the neighborhood around its orbit.

- A **dwarf planet** is a celestial body that:

    - is in orbit around the Sun.
    - has sufficient mass for its self-gravity to overcome rigid body forces so that it assumes a hydrostatic equilibrium shape.
    - has not cleared the neighborhood around its orbit.
    - and is not a satellite.

- All other objects, except satellites, orbiting the Sun shall be referred to collectively as **small Solar System bodies**.

1
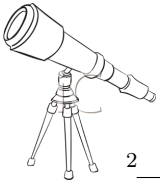
In conclusion, currently Pluto is not a planet but a dwarf planet and there are already three more bodies in the Trans-Neptunian region that have been officially recognized as dwarf planets by the IAU. To date, around 1400 TNOs have been discovered and can be classified in different dynamical groups: the classical objects, the scattered disk objects, the detached disk objects, and the resonant objects. The main dynamical classes in the Trans-Neptunian belt are well known but their definitions can vary. To date, mostly two main classifications are used: i) the Deep Ecliptic Survey (DES) classification from Elliot et al. (2005), and ii) the Gladman, Marsden and Vanlaerhoven (2008) classification. There are several populations that do not qualify as trans-Neptunian objects mainly because their orbits are not beyond Neptune's orbit, but they are associated with the TNOs. This includes the centaurs, the short-period comets, and even the irregular satellites of the giant planets.

However, our knowledge about the Trans-Neptunian belt is very limited. The general idea about TNOs is that they are composed by a mixture of rock and ice very similar to the comets composition. Spectroscopically, ices of water, methane, nitrogen, carbon monoxide, etc have been detected (Licandro et al., 2006a; Licandro et al., 2006b; Licandro et al., 2006c; Trujillo et al., 2005; Trujillo et al., 2007; Carry et al., 2011; Barucci et al., 2011; Brown, Burgasser and Fraser, 2011). Most of the TNOs are inactive; in other words, the ice on their surface is not sublimated, mainly because of their distances to the Sun. Some objects have been sent between the orbits of Jupiter and Neptune because of collisions, close encounters in the belt, or planetary encounters. Such objects, that are dynamically evolved and on unstable orbits, are called centaurs (Gladman, Marsden and Vanlaerhoven, 2008). Therefore, the centaurs are not Trans-Neptunian Objects because their orbits are not beyond Neptune's orbit, but they are an associated population to the TNOs. Centaurs can be ejected to very large perihelia or sent to the inner parts of the Solar System as short-period comets.

Due to their distances from the Sun, the TNOs are considered the least evolved bodies of the Solar System and therefore, their studies provide us with information about the composition and properties of the primitive solar nebula. The study of these bodies provide us clues about the origin and the evolution of the early Solar System. In addition, the Trans-Neptunian belt provides a natural connection to the study of the protoplanetary disks observed around some stars.

The main objective of this thesis was to determine and analyze, for a large sample of objects, the ranges of variability, their rotational periods, as well as other physical parameters that can be derived from short-term variability. The aim was to derive physical parameters such as axis ratios, phase coefficients, albedos, density, porosity, etc., for a good sample of TNOs and centaurs because only few studies were published prior to this thesis. Short-term variability studies allow us to determine the rotational, dynamical and physical evolution of these objects. But a lot of observing time is required to provide reliable short-term variability studies. In addition, it is thought that large objects are less colisionally evolved, so they probably retain the distribution of the primitive angular momentum of the early stages of the Solar System (Davis and Farinella, 1997).

At the beginning of this PhD, the sample of objects with measured rotational periods and lightcurve amplitudes was very limited. Only ∼50 objects with short-term variability were reported and many published rotational periods were uncertain or erroneous. In addition, Sheppard, Lacerda and Ortiz (2008) noticed an observational bias towards large amplitudes and short rotational periods. Increasing the sample size, improving rotational periods, lightcurves, and trying to overcome some observational biases were some of the objectives of this study. On the other hand, binary objects required a special treatment, with the objective to derive relevant physical parameters, some of them from the tidal effects in such systems.

Another motivation to carry out photometry observations was the support to the Herschel Space Observatory (HSO) key project "TNOs are cool!". HSO is a mission of the European Space Agency (ESA) and of the National Aeronautics and Space Administration (NASA). "TNOs are cool!" is a key-project of HSO dedicated to the observations of thermal emission from 130 TNOs and centaurs in ∼400h of observing time (Müller et al., 2009). This key project was the largest key-project of HSO and required a large international effort with more than 40 team members,
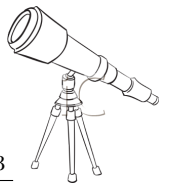
which include several researchers from IAA's solar system department. For the analysis and interpretation of the thermal data from HSO, thermal models or thermophysical models (Müller et al., 2009; Vilenius et al., 2012; Mommert et al., 2012) are required. To derive diameters and albedos, all these models require input parameters such as absolute magnitudes and spin periods or constraints on them, all of which require ground based photometry.

As a result of early findings during the project, a new model from a numerical point of view to explain the formation of the Haumea system is developed. By extension, this model is also able to explain the formation of some binary/multiple systems, and even the formation of unbound pairs of TNOs that was not considered as a possibility in the Trans-Neptunian belt. Haumea is a large object with very peculiar characteristics. Several models have been proposed by different authors to explain the formation of this object and its "family" as well as the peculiar characteristics of Haumea, but all of them have some inconsistencies.

This PhD thesis is divided into six parts:

- **Part I** provides general background to the reader and discusses some basic issues. The Trans-Neptunians Objects and the associated populations are described (**Chapters I and II**).

- **Part II** is dedicated to data calibration and reduction, the lightcurve physics and the description of the observational runs and instrumentation used (**Chapters III, IV, and V**).

- In **part III**, an exhaustive summary about short-term variability for all objects studied during this investigation is presented. For each object, lightcurve, rotational period and amplitude variation are reported. Some physical properties are derived from the lightcurves and exhaustive statistical studies are reported (**Chapters VI and VII**).

- In **part IV**, several physical properties of binary systems based on their short-term variability studies are presented. An exhaustive study based on a search of correlations/anti-correlations between orbital and physical parameters is proposed. (**Chapter VIII**).

- **Part V** presents a new formation model of Haumea system. A presentation of Haumea and its family characteristics, as well as a description of all formation models proposed to date, is presented. A summary about numerical simulations of a new model is reported. Such numerical simulations give us alternatives to explain the creation of the Haumea system (**Chapter IX**).

- Finally, in **part VI**, the conclusions of this thesis are summarized (**Chapter X**).

Most of the initial objectives have been achieved during this thesis and even some unforeseen discoveries resulted in other interesting scientific results. Most of the work presented in this manuscript has been published in international scientific journals. Here is reported some of the research of these papers as well as unpublished material.
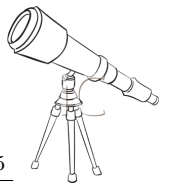
$\mathcal{E}$ n los años ochenta, nuestro Sistema Solar estaba compuesto por 9 planetas con sus satélites naturales, un cinturón de asteroides entre la órbita de Marte y la de Júpiter, los cometas y los asteroides llamados troyanos en los puntos de Lagrange de Júpiter. Cometas y asteroides eran considerados "planetas menores". Pero se sospechaba de la existencia de un cinturón de planetesimales más allá de la órbita de Neptuno. Tras el hallazgo de Plutón en 1930, hubo que esperar más de sesenta años para confirmar observationalmente la existencia de más objetos más allá de la órbita de Neptuno, los objetos Trans-Neptunianos (TNOs). En apenas veinte años desde el hallazgo de 1992 QB$_1$ por Jewitt and Luu (1993), el cinturón Trans-Neptuniano ha pasado de considerarse una conjetura o un postulado teórico (Leonard, 1930; Edgeworth, 1943; Edgeworth, 1949; Kuiper, 1951; Whipple, 1964; Fernandez, 1980) a ser la región más poblada del Sistema Solar. Actualmente, se estima que en la región entre 30 y 50 UA del Sol residen, aproximadamente 100,000 objetos con diámetros de ~100 km (Trujillo, Jewitt and Luu, 2001).

El descubrimiento de muchos objetos cuyas órbitas son muy similares a la de Plutón y también el hecho de que la mezcla de hielo/roca parece común a la mayoría de los TNOs, implicó que Plutón no era un planeta singular sino un objeto más de muchos. Luego, con el descubrimiento de algunos TNOs de tamaño similar al de Plutón (Brown et al., 2006a; Sicardy et al., 2011), se replanteó la definición del término "planeta". La Asamblea General de la International Astronomical Union (IAU, Unión Astronómica Internacional) en 2006 modificó la definición de planeta e introdujo un nuevo tipo de cuerpos: los planetas enanos. La resolución de la IAU es la siguiente:

- Un **planeta** es un cuerpo celeste que:

  - orbita alrededor del Sol.
  - tiene la suficiente masa para generar fuerzas capaces de vencer la rigidez del material, por autogravedad, de modo que alcance un equilibrio hidrostático.
  - ha limpiado la vecindad de su órbita de otros cuerpos.

- Un **planeta enano** es un cuerpo celeste que:

  - orbita alrededor del Sol.
  - tiene la suficiente masa para generar fuerzas capaces de vencer la rigidez del material, por autogravedad, de modo que alcance un equilibrio hidrostático.
  - no ha limpiado la vecindad de su órbita de otros cuerpos.
  - no es un satélite.

- Todos los otros objetos, excepto los satélites, que orbitan alrededor del Sol son los **cuerpos pequeños del Sistema Solar**. Esta categoría incluye a la mayoría de los asteroides, muchos TNOs, cometas y otros cuerpos pequeños que pueblan el Sistema Solar.

En conclusión, ahora Plutón no es un planeta, sino un planeta enano y ya hay otros tres cuerpos en la región Trans-Neptuniana que han sido reconocidos oficialmente como planetas enanos por la IAU. Al día de hoy, se han descubierto unos 1400 TNOs que se pueden classificar en diferentes grupos dinámicos: objetos clásicos, objetos del disco disperso, objetos desligados, y objetos resonantes. Los diferentes grupos dinámicos son conocidos, pero sus definiciones puedes variar. Se utilizan sobre todo dos clasificaciones: i) la clasificación llamada Deep Ecliptic Survey (DES) de Elliot et al. (2005), and ii) la clasificación de Gladman, Marsden and Vanlaerhoven (2008). Existen varias poblaciones que no se pueden calificar como objetos trans-neptunianos ya que no tienen una órbita tras la de Neptuno pero son asociados a los TNOs. Se pueden citar los centauros, los cometas de corto periodo, y los satélites irregulares de los planetas gigantes.

Nuestro conocimiento sobre la región trans-neptuniana del Sistema Solar es muy limitado. La idea general sobre los TNOs es que se trata de cuerpos compuestos fundamentalmente por mezclas de rocas y hielos muy similares a los de los cometas. Espectroscópicamente, se han detectado hielos de agua, de metano, de nitrógeno, de monóxido de carbono (Licandro et al., 2006a; Licandro et al., 2006b; Licandro et al., 2006c; Trujillo et al., 2005; Trujillo et al., 2007; Carry et al.,
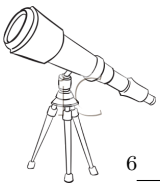
2011; Barucci et al., 2011; Brown, Burgasser and Fraser, 2011). La mayor parte de los TNOs son inactivos, es decir que el hielo de su superficie no se sublima, debido a su lejanía del Sol. Algunos objetos han sufrido colisiones o encuentros en el interior del cinturón, o encuentros planetarios que han podido transformar sus órbitas con perihelio y afelio entre las órbitas de Júpiter y de Neptuno. Estos objetos dinámicamente evolucionados y en órbitas inestables son los Centauros (Gladman, Marsden and Vanlaerhoven, 2008). Por lo tanto, los Centauros no son objetos Trans-Neptunianos ya que sus órbitas no está más allá de la de Neptuno pero son una población associada a los TNOs. Los centauros acaban siendo eyectados o enviados hacia el interior del Sistema Solar convirtiéndose en cometas de corto periodo.

Los TNOs, debido a su lejanía al Sol, son considerados los cuerpos menos evolucionados del Sistema Solar y por lo tanto su estudio nos da información clave sobre la materia que constituía la nebulosa solar primitiva. El estudio de estos cuerpos nos proporciona información sobre el origen y la evolución del Sistema Solar en sus fases iniciales. Además, el cinturón Trans-Neptuniano proporciona una conexión natural con el estudio de discos protoplanetarios que se observan alrededor de algunas estrellas.

El objetivo principal de esta tesis doctoral era determinar y analizar los rangos de variabilidad, los periodos de rotación y otra serie de parámetros físicos que se pueden derivar de la fotometría relativa de series temporales para una gran muestra de objetos. Se pretendía derivar parámetros físicos como razones de ejes, coeficientes de fase, albedo, cohesión interna, densidad, porosidad, etc. para una buena muestra de TNOs y centauros ya que hasta la fecha había pocos estudios. Dichos estudios permiten determinar la evolución rotacional, dinámica y física de estos objetos. Además, se piensa que los objetos grandes no están apenas evolucionados colisionalmente, por lo que posiblemente conservan la distribución de momento angular primitiva en las primeras fases de formación del Sistema Solar (Davis and Farinella, 1997).

Al empezar esta tesis doctoral, la muestra de periodos de rotación y de rangos de variabilidad era muy limitada. Se habían reportado ∼50 objetos con estudios de fotometría relativa de series temporales y muchos de los periodos de rotación determinados eran muy inciertos e incluso erróneos. Además, se había notado un fuerte sesgo hacia periodos cortos y grandes amplitudes (Sheppard, Lacerda and Ortiz, 2008). Aumentar la muestra, mejorar periodos de rotación, curvas de luz, y vencer algunos de los sesgos observacionales eran algunos de los objetivos de este trabajo de investigación. Por otro lado, los cuerpos binarios merecían un trato especial, con objeto de determinar parámetros físicos relevantes y las posibles evoluciones de las órbitas por fuerzas de marea.

Otra motivación para llevar a cabo observaciones de fotometría fue el apoyo para el key-project (proyecto-clave) "TNOs are Cool!" del Observatorio Espacial Herschel (Herschel Space Observatory, HSO). es una misión de la Agencia Espacial Europea (ESA) y de la NASA. "TNOs are Cool!" es un proyecto-clave del HSO dedicado a las observaciones de la emisión térmica de 130 TNOs y centauros en ∼400 h de tiempo de observación (Müller et al., 2009). Este proyecto-clave fue el proyecto clave del HSO más grande y requiere un gran esfuerzo internacional con un equipo de más de 40 miembros, que incluyen varios investigadores del Departamento de Sistema Solar de la IAA. Para el análisis y la interpretación de los datos térmicos del HSO, unos modelos térmicos o termofésicos (Müller et al., 2009; Vilenius et al., 2012; Mommert et al., 2012) son necesarios. Para derivar los diámetros y los albedos, todos estos modelos requieren parámetros de entrada como las magnitudes absolutas y los períodos de rotación o restricciones sobre ellos, y todo esto requiere observaciones desde Tierra dedicadas a la fotometría.

Como consecuencia de algunos hallazgos a lo largo de la tesis, se decidió hacer también un estudio desde un punto de vista numérico de un nuevo modelo para explicar la formación de la familia de Haumea, y por extensión un modelo de formación de sistemas binarios, múltiples e incluso formación de pares no ligados de TNOs que no se había considerado como posibilidad en el cinturón Trans-Neptuniano. Haumea es un objeto Trans-Neptuniano de grandes dimensiones que presenta caracteríticas muy peculiares. Varios modelos han sido propuestos para explicar la formación de la familia y las características peculiares de Haumea, pero todos ellos presentan algunas incoherencias.
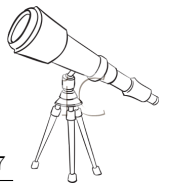
Esta memoria de tesis doctoral está dividida en seis partes:

- En la **Parte I**, se introduce el tema de esta investigación dando un bagaje general al lector, así como algunas cuestiones básicas acerca de los objetos Trans-Neptunianos y las poblaciones asociadas (**Capítulos I y II**).

- La **Parte II** está dedicada a la calibración y reducción de los datos usados en esta tesis, a la física de las curvas de luz y finalmente a la descripción de las campañas de observación y a la instrumentación utilizada (**Capítulos III, IV y V**).

- En la **Parte III**, se presenta un resumen exhaustivo de fotometría relativa de series temporales para todos los objetos estudiados durante esta investigación. Por lo tanto, curvas de luz, períodos de rotación y variaciones de amplitud son presentados para todos los objectos. También, se derivan algunas propiedades físicas de las curvas de luz y se presenta un estudio estadístico (**Capítulos VI and VII**).

- En la **Parte IV**, se derivan varias propiedades físicas de los sistemas binarios a partir de su fotometría de series temporales. También, se propone un estudio de correlaciones/anti-correlaciones entre parámetros orbitales y físicos (**Capítulo VIII**).

- La **Parte V** está dedicada a un modelo de formación de Haumea y su familia. Después de una presentación de Haumea y de su familia, así como una presentación de los posibles modelos de formación que existian, se presenta un resumen de simulaciones numéricas del nuevo escenario. Las simulaciones numéricas muestran que el escenario es factible y dan lugar a alternativas o variaciones interesantes para explicar la creación de la familia de Haumea (**Capítulo IX**).

- Finalmente, en la **Parte VI** se presentan las conclusiones generales de este trabajo (**Capítulo X**).

Una gran parte de los objetivos iniciales se han logrado a lo largo de la tesis, y a lo largo de la tesis fueron surgiendo algunos temas no previstos inicialmente que han dado lugar a interesantes resultados científicos. Gran parte del material de esta tesis ha ido dando lugar a publicaciones en revistas científicas internacionales. Aquí, se reúnen una gran parte de estas aportaciones y algunas más que se espera den lugar a otras publicaciones futuras.

Chapter II

Trans-Neptunian Objects and Centaurs

$\mathcal{T}$he observational confirmation of the existence of a reservoir of small bodies at the edges of the Solar System needed more than sixty years (Jewitt and Luu, 1993) after the discovery of Pluto in 1930. More than 1400 Trans-Neptunian Objects have been detected since the discovery of (15760) 1992 QB$_1$. The Kuiper Belt or Edgeworth-Kuiper Belt or Trans-Neptunian Belt (terminology discussed below) is the largest and relatively stable reservoir of small bodies in the Solar System.

In this chapter, we will summarize the first works about the existence of a small bodies reservoir beyond Neptune's orbit. Then, we will present the dynamical structure of this reservoir as well as its formation and evolution according to the Nice Model (Gomes et al., 2005; Morbidelli et al., 2005; Tsiganis et al., 2005). Finally, some other generalities will be introduced.

II.1 Discovery of the Trans-Neptunian Belt

II.1.1 A little bit of history ...

The first mention of a reservoir of objects beyond Neptune's orbit is in Leonard (1930). He suggested, after the discovery of Pluto, that Pluto might be the first of a series of Ultra-Neptunian planets. Edgeworth (1943); Edgeworth (1949) suggested that in the outer Solar System (beyond Neptune orbit), the material of the primordial solar nebula could not condense into large planets. And so, this material condensed into a sea of small bodies. Edgeworth's work is based on a qualitative and intuitive idea rather than on a theory based on understanding. Kuiper (1951) presented a more quantitative study. Based on the same approach as in Edgeworth (1943), he proposed that comet-like objects (called Pluto comets, in his terminology) must have been formed beyond Neptune's orbit. He thought that Pluto comets between 30 and 50 AU would have been ejected because of the gravitational influence of Pluto toward the Oort cloud (at that time, astronomers believed that Pluto's size was similar to Earth's size). But he said that beyond 50 AU, where Pluto's gravitational effect is negligible, the remnants of a circular comet ring are still present. Whipple (1964) described the comets as aggregates of volatile and solid material (and popularized the term "dirty snowball" to refer to comets). He also suggested the existence of a very massive comet belt which affects the orbit of some planets. Finally, in the 1980's, Fernandez (1980) published the most detailed and quantitative work about the Trans-Neptunian Belt. He determined that a reservoir of small bodies with low inclinations just beyond Neptune's orbit would be a good source for short-period comets.

Usually, this reservoir of small bodies beyond Neptune's orbit is called "Kuiper Belt", or "Edgeworth-Kuiper Belt", and sometimes "Edgeworth-Kuiper-Whipple Belt". In some cases, "Kuiper Disk" or "Edgeworth-Kuiper Disk" are used. The term "Disk" instead of "Belt" is a little more precise because "Belt" gives the impression of a ring of objects while objects are distributed at a range of distances. In this dissertation, we will use the neutral term "Trans-Neptunian Objects (TNOs)" to refer to objects with orbits beyond Neptune (Trans-Neptunian Belt).
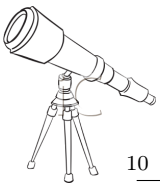
II.1.2 Discovery of the first Trans-Neptunian Object and planet definition revisited

Before the 1980s and the development of the Charge Coupled Devices (CCDs) [1], the surveys to search for small and faint objects beyond Neptune were not possible. However, it is necessary to point out that several photographic surveys have been done (Kowal, 1989). For example, Kowal, Liller and Chaisson (1977) used the blink technique and reported the discovery of a faint object with a very slow apparent motion on his photographic plates. This object received the provisional designation of 1997 UB, and then received the name of Chiron.

In 1987, David C. Jewitt and Jane X. Luu started their search for Trans-Neptunian Objects (TNOs) using CCD cameras. From 1988, Jewitt and Luu program was carried out with the 2.2 m University of Hawaii telescope (Mauna Kea, Hawaii). And finally, after five years of searching, they discovered the first object beyond Neptune orbit (Jewitt and Luu, 1993), not counting Pluto.
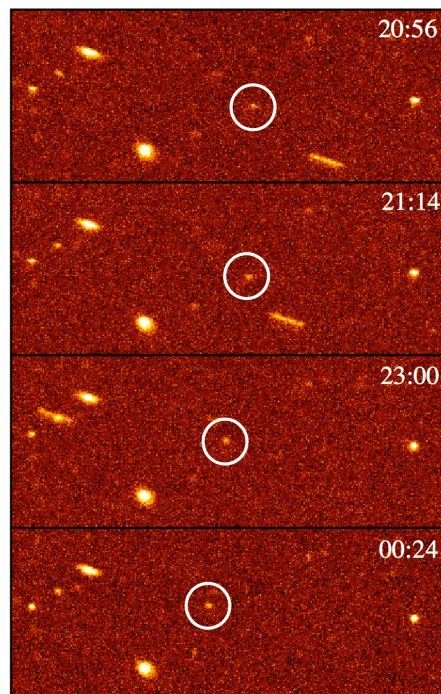
Figure 1: Discovery images of (15760) 1992 QB$_1$ recorded on August, 30th, 1992. The object is circled. The times at which the four images were taken is indicated in the top of each image. Figure from David C. Jewitt webpage: `http://www2.ess.ucla.edu/~jewitt/kb.html`.

Figure 1 is a montage of the first TNO discovery images. The stars and galaxies remain in the same place in each image while solar system objects have moved. The trail in images 1 to 3, is an asteroid. Due to the long exposure time and the high motion of the object, the asteroid appears elongated. But there is another moving object which appears point-like (in the circles in each image). One can note a very slow motion, around $3''$/h. This object is the first TNO discovered (after Pluto) and received the name of (15760) 1992 QB$_1$.

The discovery of a multitude of objects with very similar orbits as Pluto's orbit, and then, with the discovery of some TNOs with similar size to that of Pluto (Brown et al., 2006a; Sicardy et al., 2011), the definition of the term "planet" needed to be reviewed.

Before the 1990s, the definition of a "planet" was based on three criteria:

---

[1] See Section IV.1.1 for the CCD definition/explanation.
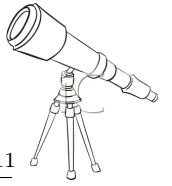
- a planet emits no radiation of its own

- a planet orbits a star

- a planet is larger than an asteroid

Our Solar System was composed by: i) nine planets: Mercury, Venus, Earth, Mars, Jupiter, Saturn, Uranus, Neptune, and Pluto, ii) various natural satellites orbiting such planets, and iii) small Solar System bodies also known as minor planets at that time.

The debate about the status of Pluto came in early 1999, mainly because, around a hundred of TNOs had been discovered and it was noticed that Pluto's orbit was not different from the Plutino's orbits (a plutino is an object in the 3:2 mean motion resonance with Neptune, see Section II.2.2 for more details.). The situation changed in 2005, with the discovery of a TNO potentially larger than Pluto, named Eris. Then, the third criterion of the planet definition was questioned (Bertoldi et al., 2006; Brown et al., 2006a) and a definition of the term "planet" was needed. Finally, in August 2006, the International Astronomical Union (IAU) resolved that planets and other bodies on our Solar System, except satellites, can be defined into three categories as follows:

- A "planet" is a celestial body that (a) is in orbit around the Sun, (b) has sufficient mass for its self-gravity to overcome rigid body forces so that it assumes a hydrostatic equilibrium shape, and (c) has cleared the neighborhood around its orbit.

- A "dwarf planet" is a celestial body that (a) is in orbit around the Sun, (b) has sufficient mass for its self-gravity to overcome rigid body forces so that it assumes a hydrostatic equilibrium shape, (c) has not cleared the neighborhood around its orbit, and (d) is not a satellite.

- All other objects, except satellites, orbiting the Sun shall be referred to collectively as "small Solar System bodies".

And so, Pluto is a dwarf planet according to this new definition and is recognized as the first one of a new category of objects.

II.2 Dynamical structure of the Trans-Neptunian Belt

Trujillo, Jewitt and Luu (2001) estimated that the Trans-Neptunian Belt (between 30-50 AU from the Sun) contains about 100,000 objects with a radii greater than 100 km. However, to date nearly 1400 TNOs and around 200 centaurs (object with an orbit not beyond Neptune's orbit, see Section II.2.4 for more details about centaurs) have been discovered. In Figure 2 are plotted the distributions of Trans-Neptunian Objects (distribution updated in November 2012) as a function of absolute visual magnitude (H). The Minor Planet Center (MPC) database has been used to plot the following distributions.

The Trans-Neptunian belt is dynamically structured into four main dynamical classes: i) classical objects, ii) resonant objects, iii) scattered disk objects and iv) detached objects. There are also some associated populations, like the Trojans, or the Centaurs (Figure 3).

The main dynamical classes in the Trans-Neptunian belt are well known but their definitions can vary. To date, mostly two main classifications are used: i) the Deep Ecliptic Survey (DES) classification from Elliot et al. (2005), and ii) the Gladman, Marsden and Vanlaerhoven (2008) classification. The DES classification [2] is based on the mean orbital parameters and the Tisserand parameter [3]. Whereas the Gladman, Marsden and Vanlaerhoven (2008) classification uses 10 mil-

---

[2]The Deep Ecliptic Survey classification can be found at: `http://www.boulder.swri.edu/~buie/kbo/desclass.html`

[3]The Tisserand parameter with Neptune is

$$T_{Neptune} = \frac{a_{Neptune}}{a} + 2\sqrt{\frac{a}{a_{Neptune}}(1 - e^2)} \cos i \qquad \text{(Equation II.1)}$$

where a, e, i are the orbital semi-major axis, eccentricity, and inclination of the object (respectively) and $a_{Neptune}$ is the semi-major axis of Neptune.
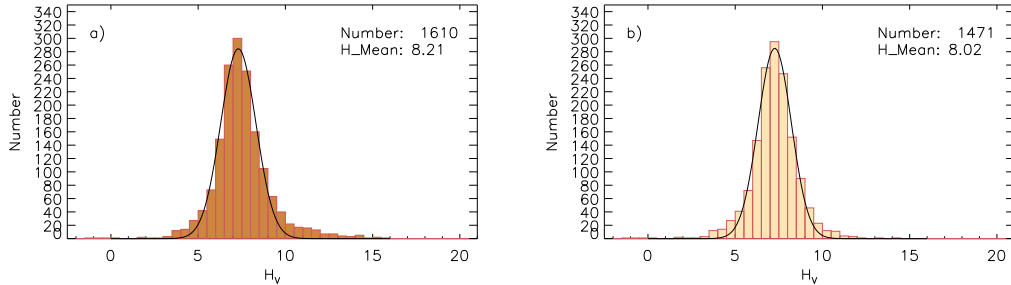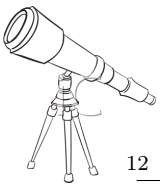
Figure 2: *Number of objects versus absolute visual magnitude for Trans-Neptunian Objects (right) and for Trans-Neptunian Objects with the Centaur population (left)*: Plot a) is the distribution of the Trans-Neptunian Objects with the Centaur population). Plot b) is the distribution of Trans-Neptunian Objects. A Gaussian fit is also plotted for each distribution. Number of objects ("Number"), and mean absolute magnitude ("H_Mean") are indicated.
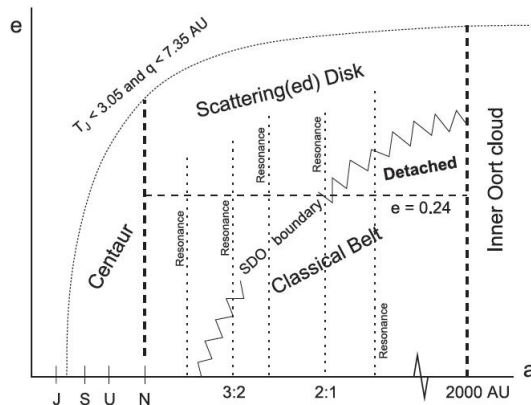
Figure 3: *Gladman, Marsden and Vanlaerhoven dynamical classification*: Gladman, Marsden and Vanlaerhoven (2008) proposed a schematic view (not in scale) of the Trans-Neptunian Belt by plotting the eccentricity (e) versus the semi-major axis (a). Positions of Jupiter (J), Saturn (S), Uranus (U), and Neptune (N) are indicated. Some resonances are also plotted: 3:2 and 2:1 indicate the locations of the corresponding mean motion resonances with Neptune. T_J is the Tisserand parameter with respect to Jupiter.

lion years orbit integration.

We must point out that there is an exhaustive survey whose main purpose is the discovery as well as the follow-up and dynamical classification of TNOs. The Canada-France Ecliptic Plane Survey (CFEPS) is a TNO survey based on observations carried out with the very wide CCD MegaPrime of the Canada-France-Hawaii Telescope Legacy Survey [4]. The TNO discovery phase ran from 2003 to 2007 and the follow-up observations was extended until 2009. The CFEPS minimized observational biases inherent in how the survey was conducted, and they also used a survey simulator. Such a simulator returns a sample of objects that would have been detected by the survey in a given size and orbital distributions (Jones et al., 2006). In conclusion, this survey is lowly biased and proposed a high-precision dynamical classification of the TNOs (Kavelaars et al.,

---

[4]A complete description of this survey can be found at `http://www.cfeps.net/`. Description of the Canada-France-Hawaii Telescope (CFHT) and instrumentation is at `http://www.cfht.hawaii.edu/en/`.
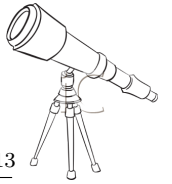
2009; Petit et al., 2011; Gladman et al., 2012; Shankman et al., 2012). Based on the dynamical classification of 169 TNOs, Petit et al. (2011) proposed an orbital structure of the Trans-Neptunian belt and draw some conclusions that we will present below.

In this work, we will use the Gladman, Marsden and Vanlaerhoven (2008) dynamical classification. Figure 3 is a schematic view of the Trans-Neptunian Belt according to this classification. Neptune defines the internal limit of the Trans-Neptunian belt. The majority of the TNOs have a semi-major axis between 30 and 60 AU and are forming a dynamical structure. In Figure 4 are plotted all known TNOs (on November 2012), with a semi-major axis between 30 and 60 AU, according to the Gladman, Marsden and Vanlaerhoven (2008) dynamical classification.

II.2.1 Classical Objects

About 60% of the known Trans-Neptunian Objects (TNOs) belong to the classical (or cubewano) population [5]. Classical TNOs have semi-major axes between 40 and 50 AU. But the majority of the classical objects are located between the 3:2 and the 2:1 mean motion resonances with Neptune [6] (i.e between 42 and 48 AU). However, they are not trapped into any mean motion resonance with Neptune. Their orbits are relatively circular with low eccentricities (typically, e<0.3) and have moderate inclinations. The classical group is the population originally predicted by Fernandez (1980), hence they received the name of "classical". They have higher eccentricities and inclinations than expected (Jewitt, Luu and Trujillo, 1998). This means that they have been highly modified through the evolution of the Solar System.

Brown (2001), and Levison and Stern (2001) suggested the existence of two different subpopulations in the classical population based on orbital inclination and on color trend: a first sub-population primordial and dynamically "cold", and a second one excited and dynamically "hot". Hereafter, we will use the terms "hot/cold" instead of "dynamically hot/cold", but we must keep in mind that it is a "dynamical" characteristic.

Hot classical objects are more dynamically excited and present higher orbital inclination ($i \geq 5°$) whereas the cold objects are more primordial, present a lower orbital inclination ($i < 5°$), and are redder. We used a cut-off limit of $i_{cut} = 5°$, but this limit is not completely secure. Some authors preferred to used a cut at 4°, others at 4.5°, and finally Peixinho, Lacerda and Jewitt (2008) suggested a threshold around 12°. The hot population represents a 44% of the classical objects, so, the cold population is dominating with 56% (Figure 5). These two sub-populations suggest different formation regions or different evolution. Then, through migration and scattering of the planets, the two populations came to reside where we see them now (Gomes, 2003; Levison and Morbidelli, 2003; Batygin, Brown and Fraser, 2011).

Levison and Stern (2001) identified a trend in the classical population distribution: the hot population tends to be brighter (larger) than the cold population. In Figure 5 are plotted the hot and cold population distributions and the trend noted by Levison and Stern (2001) is confirmed. The cold objects seem smaller ($H_{mean}=7.27$) than the hot ones ($H_{mean}=7.18$).

---

[5]The first TNO discovered, after Pluto, 1992 QB$_1$ belongs to this category (Jewitt and Luu, 1993). The term "cubewano" comes from the designation for this object ("QB1-o's"). In this dissertation, we prefer the term "classical".

[6]A mean motion resonance occurs when two bodies have periods of revolution that are a simple integer ratio of each other. For example, a TNO in the mean motion resonance 3:2 with Neptune means that it completes 2 orbits around the sun in the time it takes Neptune to complete 3 orbits.
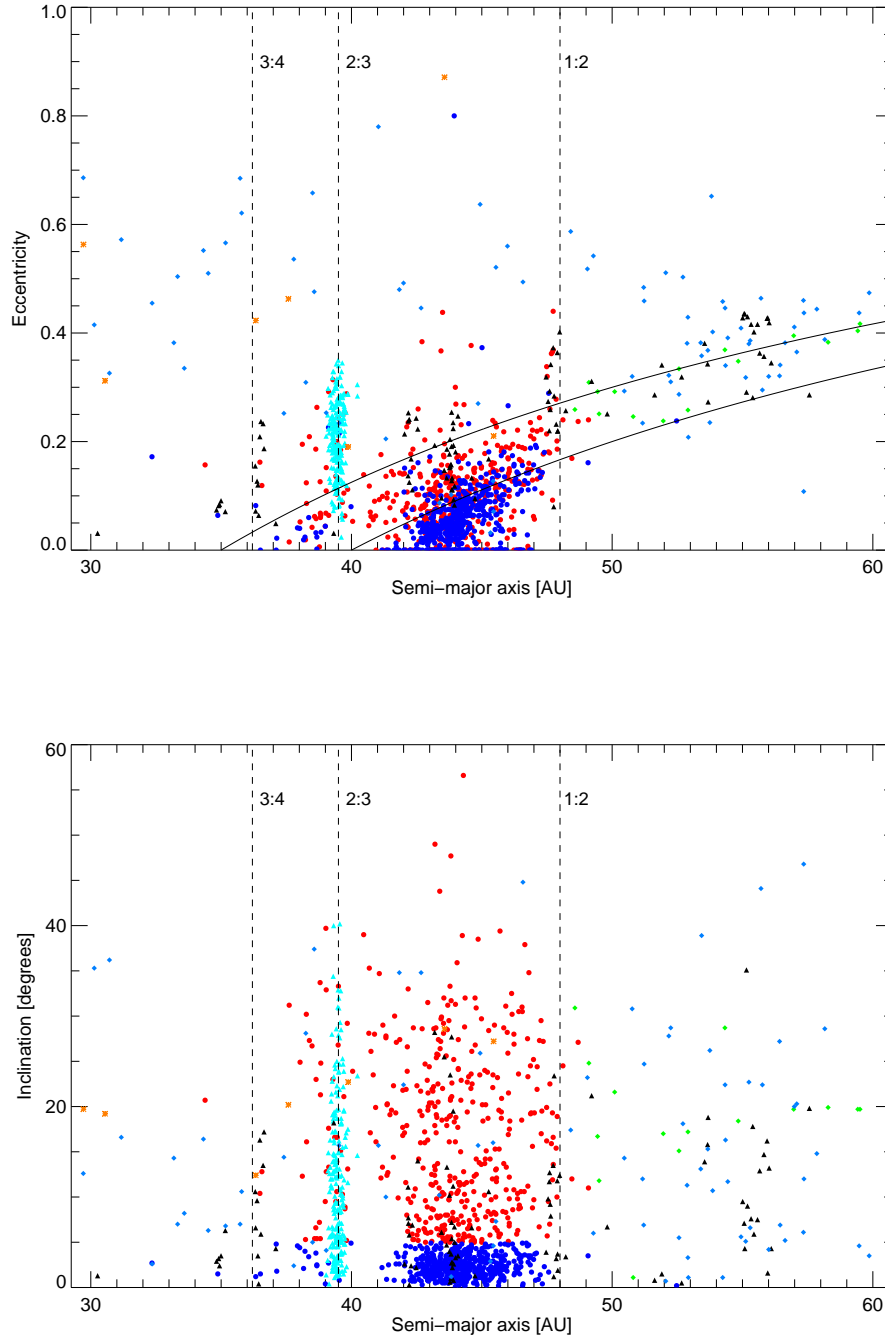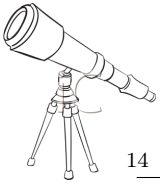
Figure 4: *Eccentricity (upper plot) and Inclination (lower plot) versus semi-major axis*: Legend is as follow: blue circles for the dynamically cold classical objects, red circles for the dynamically hot classical objects (see Section II.2.1 for more details), orange asterisks for the centaur population, cyan triangles for the plutinos, black triangles for the resonant population (without the Plutino one) (see Section II.2.2), blue diamonds for the detached objects and finally, green diamonds for the scattered disk objects (see II.2.3). Three mean motion resonances with Neptune are also plotted (dash lines), the 3:4, the 2:3 and the 1:2 with Neptune. Both plots are limited to objects with a semi-major axis between 30 and 60 AU for clarity. In the plot *Eccentricity versus semi-major axis*, two curves (continuous lines) correspond to perihelion distances of 35 and 40 AU. Orbital data obtained from the Minor Planet Center (MPC) database. We must point out that in several cases, the orbits estimated by the MPC are not well constraint, especially in case of no multi-opposition observations. Plots updated on November 2012.
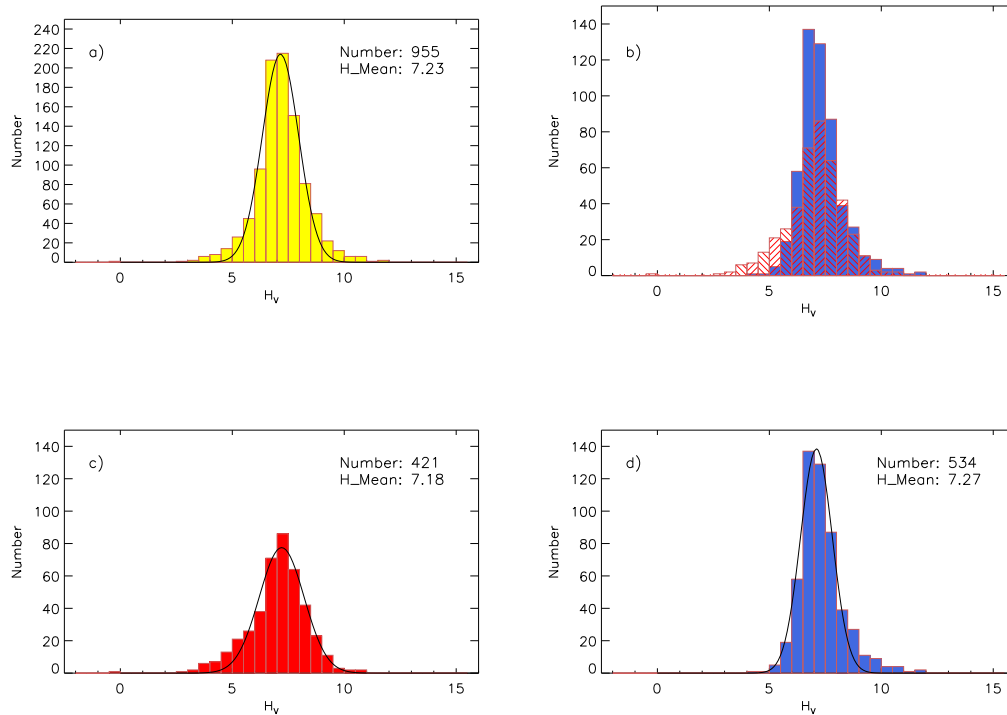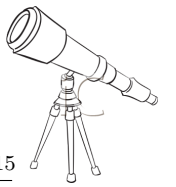
Figure 5: *Number of objects versus absolute visual magnitude for the classical population*: Plot a): the classical objects distribution; Plot b) are the distributions of dynamically cold classical objects (in blue) and of dynamically hot classical objects (in red). Plot c) and Plot d) are, respectively the hot and cold distributions. A Gaussian fit is also plotted. Number of objects ("Number"), and mean absolute magnitude ("H_Mean") are indicated for each distribution.

Based on the CFEPS database, Petit et al. (2011) found that the classical belt is a complex region that needs to be modeled with at least three populations: i) the dynamically hot population and, ii) two dynamically cold populations. The hot population presents perihelion distances between 35 to 40 AU and presents a wide inclination distribution. On the other hand, the cold population is divided into (at least) two sub-populations: i) the *stirred* component has orbits with semi-major axes between 42.5 and $\sim$47 AU, has a narrow inclination distribution and presents larger eccentricities at larger semi-major axes and, ii) there is a high TNOs number at low inclination and moderate eccentricity located at semi-major axes between 44-45 AU identified as the *kernel* component. Petit et al. (2011) estimated that the classical belt is composed by 8000^{+1800}_{-1600} objects with $H_g \leq 8.0$: 50% belongs to the hot population, 40% are from the stirred component and, 10% from the kernel component.

II.2.2   Resonant Objects

Any object captured in a mean motion resonance with Neptune is a "resonant object".

There are various mean motion resonances with Neptune, and one of the most densely populated is the 3:2 resonance (at a$\sim$39.4 AU) (Chiang and Jordan, 2002; Jewitt, Luu and Trujillo, 1998). Pluto is a 3:2 resonant object and leads to the denomination of Plutinos to all objects in this resonance. All objects trapped in this resonance have a Pluto-like orbit. Some plutinos cross the orbit of Neptune, but they are protected from close encounters with this planet (Malhotra, 1995). However, depending on their eccentricities, some plutinos may be pushed out of a reso-
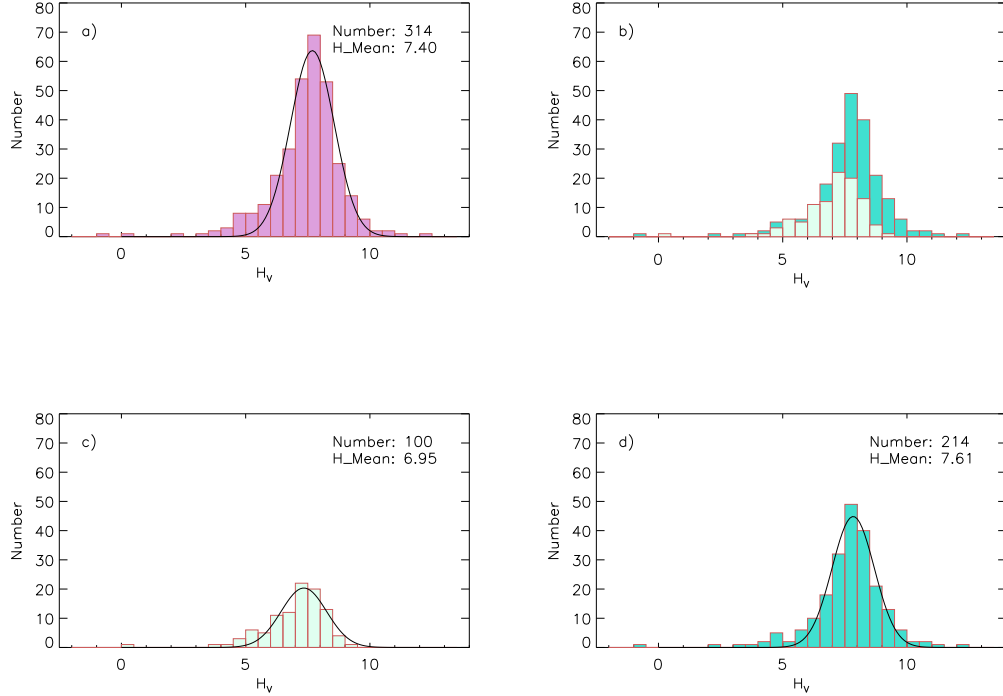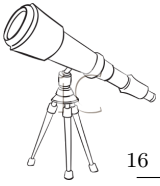
Figure 6: *Number of objects versus absolute visual magnitude for the resonant population*: Plot a): the resonant objects distribution; Plot b) are the distributions of the plutinos (in cyan) and of the resonant objects (without the plutino population) (in turquoise). Plot c) and Plot d) are, respectively, the plutino and the resonant (without plutino population) distributions. A Gaussian distribution fit is also plotted. Number of objects ("Number"), and mean absolute magnitude ("H_Mean") are indicated for each distribution.

nance by Pluto into a close encounter with Neptune (Yu and Tremaine, 1999). This mechanism is probably a source for the short-period comets in the inner Solar System. Overabundance of plutinos is probably due to the Neptune migration (Malhotra, 1993; Malhotra, 1995). Neptune could have been formed closer to the Sun and migrated outward to its current location, due to angular momentum exchange with surrounding planetesimals (Fernandez and Ip, 1984). With the migration of Neptune, its mean motion resonances moved through the Trans-Neptunian belt region and planetesimals were captured by such resonances. A migration of $\sim$8 AU over 10^7 yr reproduced the observed distribution of plutinos (Gomes, 2000). Resonant objects were captured into their resonances from the migration and circularization of Neptune orbit (Levison et al., 2008a; Malhotra, 1995).

The 2:1 resonance is the second most populated resonance with around 20% of all resonant objects. The objects in such a resonance have been called twotinos (Chiang and Jordan, 2002). Resonant objects, generally, have higher eccentricities and inclinations than the classical objects. Around 20% of the known TNOs belong to a mean motion resonance with Neptune (Figure 6). More than 30% of the resonant objects are plutinos. The plutino group appears brighter (H_{mean}=6.95) than the other resonant objects (H_{mean}=7.61). Assuming that they all have the same albedo, this would mean that plutinos are larger than the other resonants.

II.2.3 Scattered Disk Objects (SDOs) and Extended Scattered Disk Objects (ESDOs)

Scattered Disk Objects (SDOs) have large eccentricities and inclinations, and perihelia distances near the orbit of Neptune (q ∼30-45 AU). Due to their extended orbits, they are difficult to detect and their number may be underestimated (to date, there are <200 SDOs discovered (Figure 7)). The SDO population probably has been moved to their current orbit through interactions with Neptune (Gomes et al., 2008). Their orbits are still under the influence of Neptune gravitational field, so, are relatively unstable (Duncan and Levison, 1997).
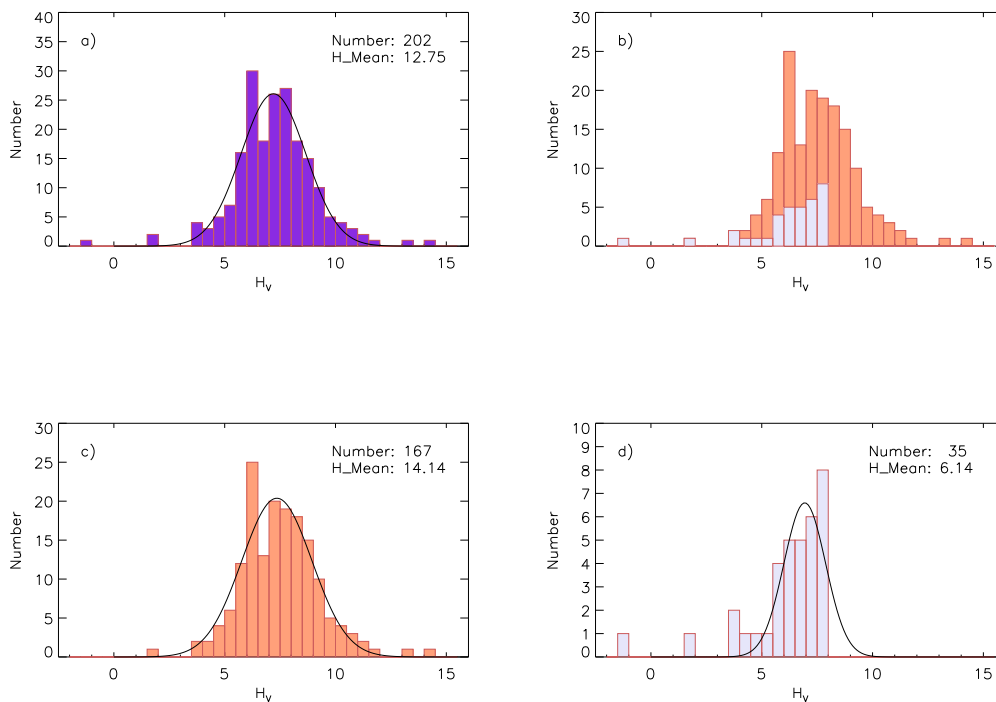
Figure 7: *Number of objects versus absolute visual magnitude for the scattered disk and extended scattered disk populations*: Plot a): the SDOs and ESDOs distributions; Plot b) are the distributions of the SDOs (in salmon) and of the ESDOs (in lavender). Plot c) and Plot d) are, respectively the SDOs and the ESDOs distributions. A Gaussian distribution fit is also plotted. Number of objects ("Number"), and mean absolute magnitude ("H_Mean") are indicated for each distribution.

Some objects with highly eccentric orbits, initially classified as SDOs, present perihelion distances beyond the Neptune gravitational influence. The existence of such objects led to consider the existence of another dynamical population (Gladman et al., 2002). This new class of objects received the name of Extended Scattered Disk Objects (ESDOs) also known as Detached Objects (DOs). Such objects are considered as transitional objects between the scattered disk and the inner Oort cloud. ESDOs have perihelia q>45 AU which cannot be produced by Neptune scattering (alone). Various models have been proposed to explain the existence of such objects. Currently, it is thought that these objects may have obtained their orbits from a stellar passage near the Trans-Neptunian Belt (Morbidelli and Levison, 2004), but there are other possible mechanisms.

Less than 15% of the known TNOs belong to the scattered and detached disks. But, as already mentioned, their number may be underestimated.

II.2.4   Centaurs

Centaurs are not considered TNOs by definition. The main reason is because their orbits are not beyond Neptune's orbit. Centaurs are an associated population and they are located on chaotic orbits between those of Jupiter and Neptune.
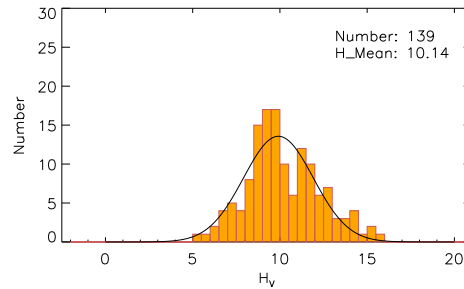
Figure 8: *Number of objects versus absolute visual magnitude for the centaur population*: Distribution of the centaur population is plotted. A Gaussian distribution fit is also plotted. Number of objects ("Number"), and mean absolute magnitude ("H_Mean") are indicated for each distribution.

According to the Minor Planet Center, a centaur is an object with a semi-major axis less than the semi-major axis of Neptune and a perihelion distance larger than Jupiter semi-major axis. Gladman, Marsden and Vanlaerhoven (2008) classifies the centaurs as having a perihelia halfway between the orbits of Jupiter and Saturn and a Tisserand parameter $T_{Jupiter}$>3.05. The centaur population has a short lifetime, less than 10^7 years (Hahn and Bailey, 1990). After this time, they can be ejected from the Solar System or become Jupiter Family Comets (JFCs). In fact, Levison and Duncan (1997) suggested that centaurs could be a transition population from SDOs towards the JFCs.

Peixinho et al. (2003), and Tegler and Romanishin (2003) suggested a bimodality in the centaur population. They proposed the existence of two different groups of centaurs: i) the very red centaurs and ii) the blue centaurs. Very red centaurs appear to have older surfaces which suffered irradiation while blue centaurs have younger surfaces rejuvenated by collisions and/or cometary-like activity. Such bimodality has been recently detected in the small TNOs population (Peixinho et al., 2012).

Centaurs are small with a mean absolute magnitude near 10. (Figure 8). Currently, less than 200 centaurs have been detected.

II.2.5   Other associated populations

Apart from the centaurs, there are various other populations associated to the Trans-Neptunian Belt. In Figure 9 are summarized dynamical interrelations between populations associated to the Trans-Neptunian belt.

II.2.5.1   Neptune Trojans

Trojans are minor bodies located in the Lagrange points L_4 and L_5 of a planet (Lagrangian points of gravitational equilibrium). In other words, they are located at 60° "ahead or behind" the planet's orbital longitude. The Neptune Trojan population occupies a thick disk (Sheppard and Trujillo, 2006).
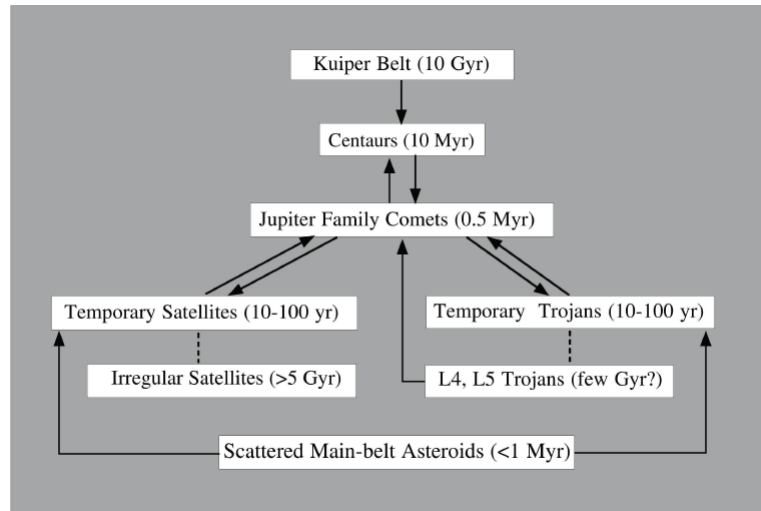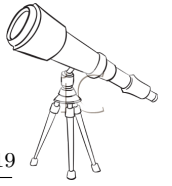
Figure 9: This figure summarizes the interrelations among the populations associated to the Trans-Neptunian Belt. Solid arrows (dash lines) denote established (no established) dynamical pathways. Numbers in parentheses indicate the approximate dynamical lifetimes of the different populations. Figure from Jewitt, Sheppard and Porco (2004).

To date, eight Neptune Trojans have been discovered. Six of them are located in the L_4 point whereas two are in the L_5 point of Neptune. The inclination of the known Neptune Trojans varies between $\sim 1°$ to $\sim 30°$. Such a high inclination is a clue for a freeze-in capture instead of in-situ or collisional formation (Sheppard and Trujillo, 2006). Sheppard and Trujillo (2006) also shown that Neptune Trojans have an indistinguishable slightly red colors. This means a common formation and evolutionary history. Neptune Trojan colors are consistent with Jupiter Trojans, irregular satellites and blue centaurs colors. Sheppard and Trujillo (2006) suggested that these populations may have been dispersed, then transported, and finally trapped in their current locations during or just after the planetary migration phase (see Section II.5 for a definition of planetary migration).

II.2.5.2 Short period comets and Jupiter Family Comets

Initially, the comet population was divided into two groups: the long-period comets also called nearly isotropic comets (P>200 yr), and the short-period comets also called ecliptic comets (P<200 yr). Then, the short-period comet population was divided into two sub-groups: the Jupiter Family Comets (or JFCs with P<20 yr) and the Halley-type comets (P>20 yr) [7].

JFCs have a very low orbital inclination, around $10°$ on average, whereas the Halley-type family has higher inclination, around $40°$ in average. Based on numerical simulations of planetesimals crossing Neptune orbit, Levison and Duncan (1997) confirmed that 30% of the initial planetesimal population ended as JFCs on a time scale of 100 Myr. Whereas, the Halley-type family was not produced. So, there is a dynamical relation between the Trans-Neptunian belt and short-period comets, in particular JFCs. However, comets suffer strong surface alteration when they get closer to the Sun. So, their surfaces are different to those of TNOs.

II.2.5.3 Irregular satellites

Outer satellites of the planet have distant, eccentric and stable orbits. Such orbits can be highly inclined or retrograde. These irregular orbits cannot have been formed by circumplanetary accre-

---

[7]The classification/nomenclature of the comets is more complicated, but as this is not the main topic of this work, we will keep the definition as simple as possible.
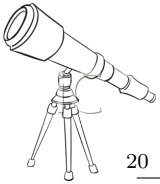
tion, so, irregular satellites are the results of early capture from heliocentric orbit.

When an object in heliocentric orbit is captured, some loss of energy is needed to make this capture permanent. Several mechanisms have been proposed: i) the capture by gas drag: an object (with the right size) passing through the gas and dust of a primordial circumplanetary nebulae would have experienced just enough gas drag to be captured (Pollack, Burns and Tauber, 1979), ii) the pull-down capture implies an increase of the Hill sphere of the planet making the object escape impossible (Heppenheimer and Porco, 1977), iii) the capture through collisional or collisionless interactions of two small bodies within the Hill sphere of a planet (Agnor and Hamilton, 2006).

Irregular satellites present a large set of colors. They are gray to slightly red which seems to indicate different regions of formation (Grav et al., 2003; Grav, Holman and Fraser, 2004). Gray irregular satellites have been probably formed in the Trans-Neptunian belt region whereas reddish ones may belong to inner parts of the Solar System. For example, Triton (irregular Neptune satellite) and Phoebe (irregular Saturn satellite) are most likely captured TNOs and confirm the contribution of the Trans-Neptunian belt in the irregular satellite population (Agnor and Hamilton, 2006; Johnson and Lunine, 2005).

II.3   Introduction to binarity/multiplicity in the Trans-Neptunian belt

II.3.1   Detection of binary/multiple systems
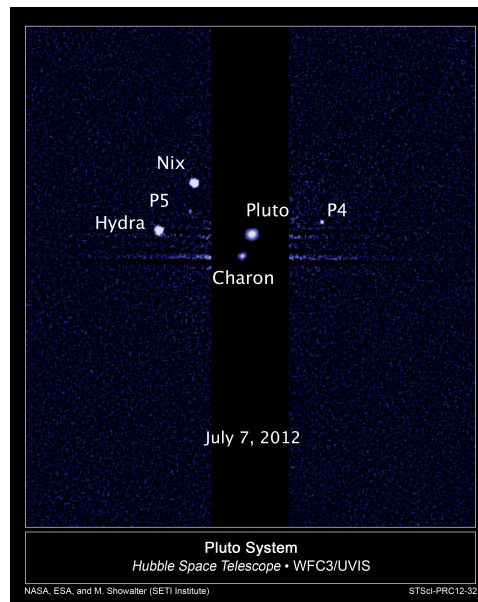
Figure 10: *Pluto and its five satellites: Charon, Nix, Hydra, P4, and P5.* This image, taken by NASA's Hubble Space Telescope with the Wide Field Camera 3, shows five moons orbiting Pluto. *Credits: NASA*

As of April 2013, 78 binary/multiple systems [8] have been identified in the Trans-Neptunian belt. The majority of such systems have only one satellite, but two systems are known to have

---

[8]The exact definition of binarity is: a binary TNO is a system of two TNOs orbiting their common center of mass or barycenter which lies outside either body. This is the case of the Pluto-Charon system. For most of the binary/multiple systems in the Trans-Neptunian belt we have no information about their barycenter, so the use of the term binary/multiple systems has be to be considered carefully. Often, in the literature, the term binary/multiple is used to refer to system with one or more companions despite the definition mentioned here.
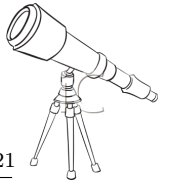
two companions, Haumea and 1999 TC_{36}, while the Pluto system (Figure 10) consists of the Pluto/Charon binary accompanied by four relatively small satellites. This means that $\sim$5% of the known TNOs have at least one companion. However, some estimations indicate that the proportion of such systems must be up to 20-25% (Noll et al., 2008a).

The discovery of binary/multiple systems in the Trans-Neptunian belt is subject to observational limitations. In fact, large telescopes, typically, 4-m class telescopes are required to detect companions. The first binary TNO (BTNO) (apart from Charon) was the companion of 1998 WW_{31} (Veillet et al., 2002). This detection was a "chance" discovery using the 3.6 m Canada-France Hawaii Telescope (CFHT) under excellent weather and seeing conditions. At the time of discovery, the apparent separation between both components of the 1998 WW_{31} system was around $1''$, so both components were easily resolved. We have to point out that this system is composed by near equal-sized objects with a low apparent magnitude difference of 0.4 mag that favored the detection from the ground.

II.3.2   Surveys to discover binaries

Several large ground-based surveys dedicated to the discovery of TNOs had some sensitivity to detect (or not) binaries (mainly wide separation binaries):

- The *Deep Ecliptic Survey (DES)* used the facilities of the Cerro Tololo Inter-American Observatory (CTIO), and the Kitt Peak National Observatory (KPNO) to carry out a survey of 550 deg^2 (Millis et al., 2002; Elliot et al., 2005). These observations were made with 4-m class telescopes using wide-field mosaic camera with pixel scale of $0.5''$. The Magellan telescope with the Magellan Instant Camera (MagIC, Osip et al. (2004)) (pixel scale of $0.069''$ and a field of view of $2.36'$ square) at Las Campanas Observatory was also used to complete such a survey. Both surveys reached 22.5 mag (Millis et al., 2002; Elliot et al., 2005; Kern, 2006). In total, around 400 TNOs and centaurs were discovered and only four binaries reported (Osip, Kern and Elliot, 2003; Kern and Elliot, 2005; Kern and Elliot, 2006a; Kern and Elliot, 2006b) between 1998 through the end of 2003.

- The *Deep Keck Search for Binary Kuiper Belt Objects* by Schaller and Brown (2003) observed over 150 TNOs to determine if any of these bodies have satellite. No new binary reported. Unfortunately, the observational limits as well as the list of surveyed objects have not been published.

- The *Canada France Ecliptic Plane Survey (CFEPS)* has surveyed approximately 500 deg^2 using the Canada-France-Hawaii Telescope equipped with the MegaCam camera with a $1° \times 1°$ field of view. The detection limit was about 24.3 magnitudes in g'. They reported three binary systems (Petit et al., 2008; Lin et al., 2010) during the TNO discovery phase from 2003 to 2007.

In conclusion, ground-based surveys have detected few binaries, and especially near-equal size systems (see Section II.3.3) with a separation higher than $1''$. The most prolific tool to detect binary/multiple systems is the *Hubble Space Telescope (HST)*. Several surveys with the HST have been realized:

- Trujillo and Brown (2002a); Brown and Trujillo (2002) reported the first search for satellites of TNOs using the Space Telescope Imaging Spectrograph instrument (STIS with a pixel scale of 50 milliarsec) between August 2000 and August 2002. From August 2001 to August 2002, they looked for companion around 25 TNOs and found two binaries: 1998 SM_{165} and 1999 TC_{36}.
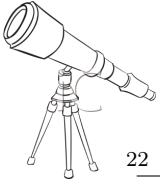
- Stephens et al. (2003) observed 72 TNOs with the instrument NICMOS (pixel scale of 75 milliarcsec) from August 2002 through June 2003 and reported 9 new binary systems.

- From July 2005 through January 2007, more than 100 TNOs were searched for binarity with the High Resolution Channel (HRC). With the clear filter, it was possible to reach a limiting magnitude of 27 mag. A significant number of new binaries were reported by Noll et al. (2006a); Noll et al. (2006b); Noll et al. (2006c); Noll et al. (2006d); Noll et al. (2006e); Noll et al. (2006f).

- Currently, Noll et al. team are carrying out a large survey dedicated to binary detection. Several new binaries have been reported: Noll et al. (2007a); Noll et al. (2007b); Noll et al. (2007c); Noll et al. (2007d); Noll et al. (2007e); Noll et al. (2008b); Noll et al. (2008c); Noll et al. (2009a); Noll et al. (2009b); Noll et al. (2009c); Noll, Benecchi and Grundy (2009); Noll et al. (2012), etc.

II.3.3 Physical parameters

II.3.3.1 Apparent magnitude difference

The relative sizes of the primary and secondary components are important physical parameters. The apparent magnitude difference or component magnitude difference is the difference of magnitudes (Δ_{mag}) between the satellite and the primary body. The magnitude difference can be used as a proxy of size (Noll et al., 2008a), as:

$$\frac{R_{primary}}{R_{satellite}} = \sqrt{\frac{A_{primary}}{A_{satellite}}} = \sqrt{\frac{p_{satellite}}{p_{primary}}}10^{-0.2\Delta_{mag}} \qquad \text{(Equation II.2)}$$

where $R_{primary}$ and $R_{satellite}$ are, respectively, the primary and secondary radius, $A_{primary}$ ($A_{satellite}$) is the primary surface area (the satellite surface area), and $p_{primary}$, $p_{satellite}$ are, respectively the primary and secondary albedos. A simplifying assumption is to consider that both components have the same albedo, so, Equation II.2 becomes:

$$R_{primary} = R_{satellite}10^{-0.2\Delta_{mag}} \qquad \text{(Equation II.3)}$$

Based on colors measurements, Benecchi et al. (2009) demonstrated that binary systems have identically colored components, so assuming that both components have similar albedo is a good approximation. However, we must point out that, in the case of Pluto/Charon where separate albedos have been measured, it has been shown that both components have different albedos (Buie and Tholen, 1989; Buie et al., 2010). Pluto has an active surface and an atmosphere so such a difference is not unexpected. The albedos of the satellited of large bodies can thus be very different to those of the primaries

In Figure 11, we plotted the apparent magnitude difference versus the primary absolute magnitude of all BTNOs, known to date in the Trans-Neptunian belt. One can appreciate an overabundance of nearly equal-sized systems with a $\Delta_{mag} \leq 1$ mag, and especially in the dynamically cold classical population.

II.3.3.2 Spatial distribution and binary frequency

In Figure 12 and Figure 13, all the TNOs known to date with semi-major axes between 30 to 60 AU are plotted [9]. Binary/multiple systems are highlighted: i) equal-sized binaries (with $\Delta_{mag} \leq 1$ mag) are shown with big red filled circles, and ii) systems with a large primary and a small satellite are shown with big green filled circles.

---

[9]All binary/multiple systems have been plotted even those with a not well constrained orbit.
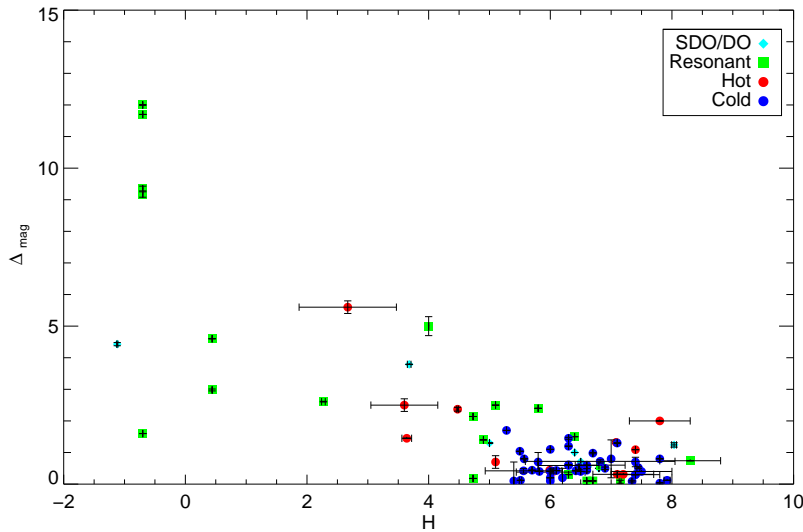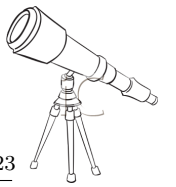
Figure 11: *Apparent magnitude difference versus absolute magnitude* In this plot, we focus on the apparent magnitude difference versus the primary absolute magnitude. We chose to distinguish each dynamical population. "SDO/DO" stands for Scattered Disk Object and Detached Object, "Hot/Cold" stand for objects dynamically hot/cold, and finally "Resonant" is for the resonant objects. We used an inclination (i) cut-off limit of $i_{cut} = 5°$ to distinguish dynamically cold ($i < 5°$) and dynamically hot ($i \geq 5°$) objects. Absolute magnitudes are from the Minor Planet Center. Apparent magnitude difference in the V-band.

Dynamical classification of the binary/multiple systems gives us reliable information about the formation and evolution of such dynamical classes. On one hand, there are objects on unstable, planet-crossing orbits having several close encounters with giant planets during their lifetimes, and so, such encounters can disrupt weakly bound binaries (Petit and Mousis, 2004). On the other hand, binaries in the classical disk may have suffered less alteration, and so the survival of the multiple systems is favored. Stephens and Noll (2006) reported a higher fraction of binary/multiple systems on stable orbits. They found that $22^{+10}_{-5}\%$ of dynamically cold classical TNOs are binaries, whereas for all other dynamical classes combined, only $5.5^{+4}_{-2}\%$ are binaries.

However, Petit and Mousis (2004) suggested that the fraction of binary/multiple systems must have been higher in order to explain the current distribution. Based on the case of binaries with a large separation, they estimated that such systems must have been initially an order of magnitude more numerous. They suggested three different ways of eliminating a binary system: i) the shattering of the satellite by a collision followed by the dispersing of the resultant fragments, ii) a small collision on the satellite able to give enough angular momentum to unbind the satellite from the primary, and iii) a gravitational perturbation from an encounter with a third body that will transfer enough energy to the satellite to unbind it. Finally, they concluded that binary systems are primordial. In fact, no scenario could explain a contemporary formation in the current rarefied environment.

In addition to the higher frequency of multiple systems in the dynamically cold classical population, the relative size distribution in such dynamical class is different. In fact, the dynamically cold classical objects seem smaller than the other populations members (see Section II.2.1 for more details or Levison and Stern (2001)), and mostly nearly equal-sized binaries are reported in this dynamical class (Noll et al., 2008a). One can appreciate in Figure 12 and Figure 13, that majority of the nearly equal-sized systems are at low eccentricity and low inclination, and so the dynamically cold classical population is the main reservoir of these binaries which seem to have been formed in-situ (Parker and Kavelaars, 2012). However, few nearly equal-sized binaries are located in mean
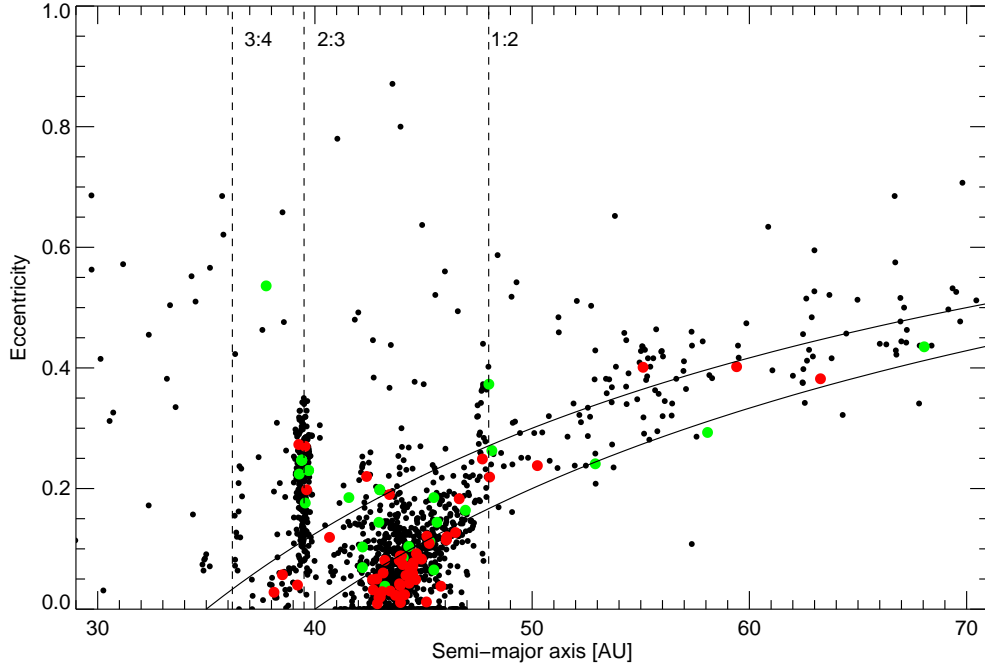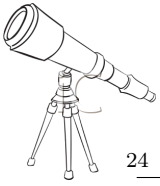
Figure 12: *Eccentricity versus semi-major axis: Binary population.* In this figure are plotted all known non-binary TNOs (black circles), equal-size binaries (red circles), and non-equal-size binaries (green circles). For clarity, this plot is limited to objects with a semi-major axes between 30 to 60 AU. Mean motion resonances 3:4, 2:3, and 1:2 with Neptune are indicated with dash lines. The two continuous curves correspond to perihelion distances of 35 and 40 AU. Orbital data obtained from the Minor Planet Center (MPC) database.

motion resonances, and in the scattered population.

II.4   Size distribution and total mass

II.4.1   Size Distribution

Size distribution of TNOs, so the total mass of the Trans-Neptunian belt is deduced from observational surveys. Various surveys have been performed and published. Here are some of them: Jewitt and Luu (1995), Chiang and Brown (1999), Sheppard et al. (2000), Gladman et al. (2001), Trujillo, Jewitt and Luu (2001), Larsen et al. (2001), Allen, Bernstein and Malhotra (2002), Bernstein et al. (2004), Petit et al. (2006), Fraser et al. (2008), Fuentes and Holman (2008), Sheppard et al. (2011), Rabinowitz et al. (2012).

The number of TNOs per square degree (also called sky density of TNOs) is obtained from the Cumulative Luminosity Function (CLF). The CLF is defined as:

$$\sum(< m) = 10^{\alpha(m-m_0)} \qquad \text{(Equation II.4)}$$

where $\sum(< m)$ is the number of TNOs per square degree brighter than the magnitude m. The magnitude m_0 is the magnitude at which the surface density $\sum(<m_0)=1$ object per square degree (or constant reference magnitude), and α is a power law coefficient.
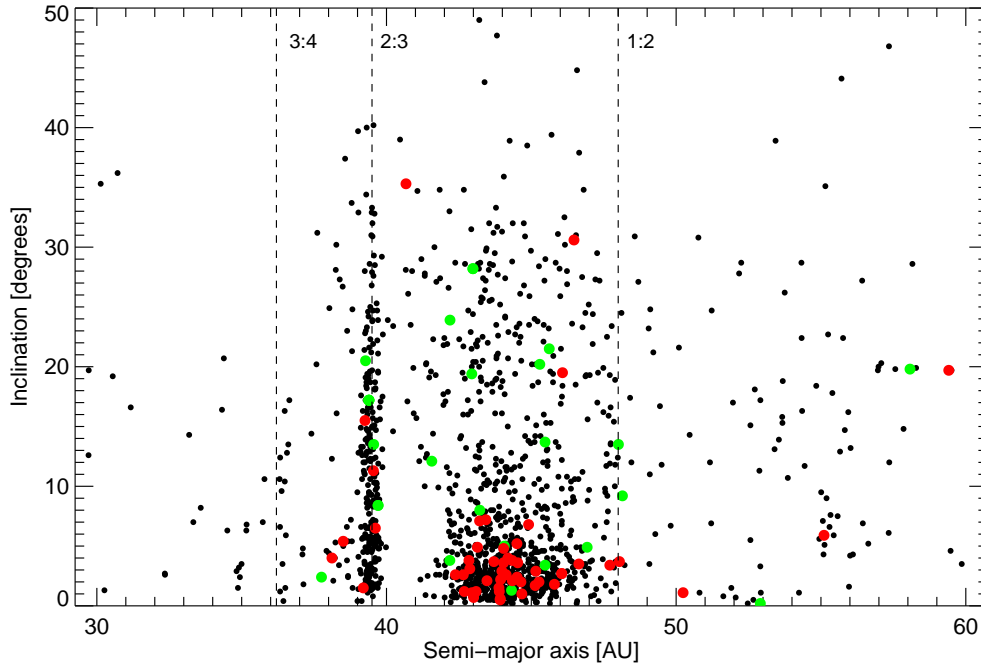
Figure 13: *Inclination versus semi-major axis: Binary population.* In this figure are plotted all known non-binary TNOs (black circles), equal-size binaries (red circles), and non-equal-size binaries (green circles). For clarity, this plot is limited to objects with a semi-major axes between 30 to 60 AU. Mean motion resonances 3:4, 2:3, and 1:2 with Neptune are indicated with dash lines. Orbital data obtained from the Minor Planet Center (MPC) database.

For example, in Figure 14, a CLF based on several surveys is proposed (Fuentes and Holman, 2008).

Equation II.4 can be expressed as:

$$log \sum (< m) = \alpha(m - m_0) \qquad \text{(Equation II.5)}$$

This means that from a CLF lineal fit, the α coefficient is estimated.

The size distribution of TNOs is assumed to follow a power-law distribution as:

$$N(r)dr \propto r^{-q}dr \qquad \text{(Equation II.6)}$$

where N(r) is the number of objects with radius between r and r+dr, and q is a constant. The constant q is determined from the CLF with the relation q = 1 + 5α (Gladman et al., 2001). Due to the TNOs faintness, the size distribution is only well determined observationally for objects with radii greater than 50 km. Trujillo, Jewitt and Luu (2001); Petit et al. (2006) estimated a constant q between 4.0 and 4.8. However, this value must change at a certain break radius to avoid a divergence in the mass (Kenyon and Windhorst, 2001). In fact, Bernstein et al. (2004) confirmed a deficit in small TNOs which indicates a break in the size distribution estimated by Trujillo, Jewitt and Luu (2001). Bernstein et al. (2004) proposed two different values for the α coefficient. For the brightest objects (visual magnitude <24), they found $\alpha\sim0.8$ and $\alpha\sim0.3$ for the faintest objects. Later, Fuentes and Holman (2008); Fraser and Kavelaars (2008); Fraser and Kavelaars (2009) confirm the broken power-law size distribution. Fraser and Kavelaars (2008) proposed a
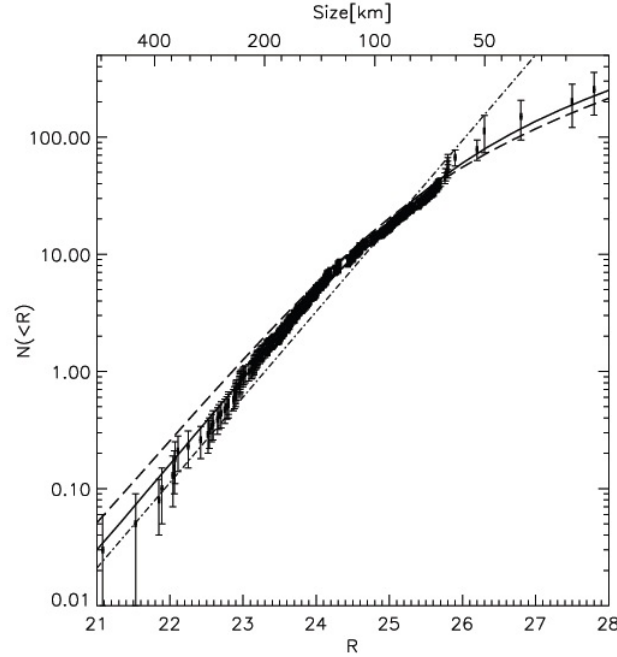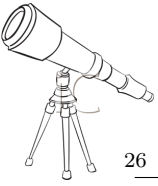
Figure 14: *Cumulative Luminosity Function of the Trans-Neptunian Belt based on several surveys*: Example of a cumulative number density based on several surveys. In some cases, surveys are dedicated to a certain dynamical class of TNOs, so, here Fuentes and Holman (2008) proposed a mix of severals surveys that can be biased toward a dynamical class. The dash dotted line is a lineal fit, from which the α coefficient is estimated. "N(<R)" is the number of objects with a red magnitude lower than "R". Figure from Fuentes and Holman (2008).

CLF for objects with visual magnitudes between 21 and 28 mag with a break at ∼26 mag. They proposed $\alpha \sim 0.69$ for objects with a visual magnitude between 21 and 26 mag and $\alpha \sim -0.4$ for object with a visual magnitude higher than 26 mag.

II.4.2   Total Mass

Bernstein et al. (2004) expressed the total mass of the TNO population as:

$$M_{tot} = \sum_{TNOs} M_i \qquad \text{(Equation II.7a)}$$

$$= M_{23} \Omega \int_{14}^{31} dR \sum (R) 10^{-0.6(R-23)} f^{-1}$$

$$\left\langle \left(\frac{p}{0.04} \right)^{-3/2} \left(\frac{d}{42\,AU} \right)^{6} \left(\frac{\rho}{1000\,kg\,m^{-3}} \right) \right\rangle \qquad \text{(Equation II.7b)}$$

$$M_{23} = 7.8 \times 10^{18}\,kg$$

where the surface density $\sum$ is the mean over solid angle Ω of the sky, and f is the fraction of the TNO sample at magnitude R that lies within the area Ω. The density is ρ, the albedo is p, and the heliocentric distance is d. The mass of a TNO that has a R=23 with the given canonical albedo, density and, distance is M_{23}. The angle brackets indicate an average over the TNOs at the given magnitude. Bernstein et al. (2004) calculated a M_{23}=7.8×10^{18} kg.

Bernstein et al. (2004) also derived the formula to compute the total mass of the classical belt, $M_{classical}$, as:

$$M_{classical} = (5.3 \pm 0.9) \times 10^{22}\,kg \times \left(\frac{p}{0.04} \right)^{-3/2} \left(\frac{d}{42\,AU} \right)^{6} \left(\frac{\rho}{1000\,kg\,m^{-3}} \right) \quad \text{(Equation II.8)}$$
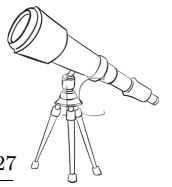
They computed a total mass of 0.010 M$_\oplus$ for the classical belt. Such an estimation is smaller than the values reported by Gladman et al. (2001) and Trujillo, Jewitt and Luu (2001). Bernstein et al. (2004) tried to derive a total mass formula for the "excited TNOs", i.e. the resonant and high-excitation nonresonant orbits. Unfortunately, the mean distance appears as d^6 (see Equation II.7) and is highly uncertain for the scattered disk and detached disk objects, but it is sensibly bounded for the plutino group. An upper bound on the plutino mass (M$_{plutino}$) is expressed as:

$$M_{plutino} \lesssim 1.3 \times 10^{23} \, kg \times \left(\frac{p}{0.04} \right)^{-3/2} \left(\frac{d}{39 \, AU} \right)^6 \left(\frac{\rho}{1000 \, kg \, m^{-3}} \right) \left(\frac{f}{0.5} \right)^{-1} \quad \text{(Equation II.9)}$$

Assuming a mean distance of 42 AU, and f=0.5, Bernstein et al. (2004) computed an excited class mass of 1.3×10^{23} kg.

Total mass (M) of the centaur population is estimated by integrating over the size distribution N(r), between a minimum radius (r$_{min}$) and a maximum radius (r$_{max}$). Assuming a q=4 size distribution, Sheppard et al. (2000) expressed the total mass of the centaurs as:

$$M(r_{min}, r_{max}) = \frac{4 \times 10^9 \pi \rho \Gamma}{3} \left(\frac{0.04}{p} \right)^{3/2} ln \left(\frac{r_{max}}{r_{min}} \right) \quad \text{(Equation II.10)}$$

where ρ is the bulk density of the objects, p is the albedo and Γ is a constant. Assuming an albedo of 0.04, a distribution of objects with radii between 1 and 200 km, and a density of 1000 kg m^{-3}, the total mass of the centaurs is:

$$M(1 \, km, 200 \, km) \sim 8 \times 10^{20} \, kg \sim 10^{-4} \, M_\oplus \quad \text{(Equation II.11)}$$

Bernstein et al. (2004) estimations are clearly lower than previous estimates and raise a problem. In fact, the minimal initial mass required to facilitate the accretion of the largest objects is 10 M$_\oplus$ (Hahn and Malhotra, 1999). This means that the mass in the Trans-Neptunian region must have been larger in the past to favor the accretion and to support the planetary migration (Stern, 1996; Hahn and Malhotra, 1999).

Various ideas to explain such a loss of mass have been proposed. Ida, Larwood and Burkert (2000) proposed an early stellar encounter. In such a case, a star passed through the primitive Trans-Neptunian belt and ejected the TNOs in hyperbolic orbits or in orbits with close encounters with Jupiter. Morbidelli and Valsecchi (1997); Petit, Morbidelli and Valsecchi (1999) considered a dynamical depletion caused by Neptune. Some large planetesimals scattered by Neptune could have dynamically excited some smaller TNOs. Such TNOs, on excited orbits, could have suffered encounters with Neptune which ejected them in the inner or outer parts of the Solar System. The Nice model (see next section) suggested that during the planetary migration, 99% of the Trans-Neptunian belt mass was removed. And finally, Brunini and Melita (2002); Lykawka and Mukai (2008) proposed the existence of a massive body at a distance >50 AU. According to Lykawka and Mukai (2008), one of the giant planets scattered this massive body (usually called Planet X) and the disk of TNOs to 40-50 AU and truncated the disk around 50 AU [10]. Then, the massive body acquired a stable highly inclined orbit at a distance ≥100 AU .

II.4.3 Extension of the Trans-Neptunian belt

The inner limit of the Trans-Neptunian belt is delimited by Neptune's orbit, unfortunately, the outer limit is not so well constraint. Scattered disk and extended disk objects have orbits that can be extended beyond 200 AU. This means, that SDO and ESDO are the most distant objects in the Trans-Neptunian belt. However, there is not a clearly limit to the end of the Trans-Neptunian belt.

Only two objects, Sedna and 2004 XR$_{190}$ have been detected with a perihelion above 50 AU. Sedna presents a very eccentric orbit (e=0.86) and has a perihelion at 76 AU, and so, it is classified as extended scattered disk object (Brown, Trujillo and Rabinowitz, 2004). On the other

---

[10]See the next sub-section for the cut-off definition.
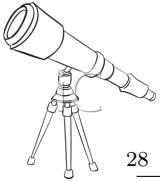
hand, 2004 XR_{190} is the only object with a perihelion above 50 AU (according to the MPC, the perihelion of 2004 XR_{190} is 51.603 AU) and a low eccentricity (e=0.107). Like Sedna, this object is classified as extended scattered disk object. Gomes et al. (2008); Gomes (2011) concluded that 2004 XR_{190} was scattered by a close encounter into the 3:8 mean motion resonance with Neptune. Then, 2004 XR_{190} escaped to the resonance while Neptune was still migrating outward and stayed in its current position. Sheppard et al. (2011) did not find a different composition for this object which seems to have a similar color to the scattered and the plutino objects. According to Gomes (2011), more objects dynamically similar to 2004 XR_{190} have to be found. Unfortunately, to date, none of them have been detected.

Jewitt, Luu and Trujillo (1998) already pointed out a cut-off in the Trans-Neptunian belt. In fact, based on surveys, they concluded that there is a sharp truncation at 50 AU. But this cut-off (also known as Kuiper cliff) could be an observational bias and in such case it is not real. Also, the cliff might end at ~76 AU. In fact Trujillo, Jewitt and Luu (2001) showed that the detection of objects at heliocentric distances higher than 76 AU is difficult. For example, if Varuna were moved to a heliocentric distance of 76 AU, it would have a visual magnitude around 22.6, well within the range of most surveys.

Various hypotheses that could explain this cut-off have been proposed:

- Jewitt, Luu and Trujillo (1998) considered that the size of the TNOs decreased rapidly beyond 50 AU, making them harder to detect. In fact, the planetesimal sizes formed by accretion depends on the material density presented in the nebula during the accretion phase. This density varies like R^{-2} (R is the heliocentric distance) whereas the accretion rate for the largest object is $R^{-3.5}$ (Luu and Jewitt, 2002). In this case, the cut-off is not real and we are in presence of an observational bias.

- As already mentioned, Brunini and Melita (2002); Lykawka and Mukai (2008) suggested the existence of a Mars- (or Earth)-sized object on an eccentric orbit at a distance >50 AU. This massive body would have scattered its neighboring objects into Neptune crossing orbits. This would have created a lake of objects beyond 50 AU. A similar possibility is shown in Ortiz et al. (2007a).

- Ida, Larwood and Burkert (2000) proposed that a passing star would have been able to create this truncation in the disk. However, Morbidelli and Levison (2003) indicated that the star must have passed in the Trans-Neptunian belt at a particular moment of the Solar System formation, so, the probability of such event is low.

- Levison and Morbidelli (2003) argued that the initial proto-planetary disk was truncated at ~30 AU (Neptune current position). Thanks to the planetary migration, the truncation migrated too to its current position (at ~50 AU). In this scenario, the truncation is a natural consequence of the dynamical evolution of the Solar System, but the initial limit at ~30 AU is also rather ad-hoc.

To date, the existence of such cut-off at ~50 AU is not secure. One of the main scientific topic of the 8.4 m Large Synoptic Survey Telescope (LSST) program will be to confirm or rule out the reality of this cut-off.

II.5 Nice Model: formation and evolution of the Trans-Neptunian belt

The Nice Model is a scenario for the dynamical evolution of the Solar System. This model has been published in three Nature papers in 2005: Gomes et al. (2005); Morbidelli et al. (2005); Tsiganis et al. (2005). In the next sub-sections, we will summarize this paper trilogy presenting the most important steps for the formation and evolution of the Trans-Neptunian belt.
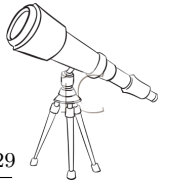
II.5.1   Description of the Nice Model

In this trilogy paper, they proposed that after the gas and dust dissipation of the primordial Solar System disk, the four giant planets (Jupiter, Saturn, Uranus and Neptune) were on near-circular orbits between ∼6 and ∼17 AU. So, the initial Solar System was much more closely spaced and more compact than in the present. The position of the four giant planets was different than the current one: Jupiter and Saturn were near the 2:1 mean motion resonance whereas Neptune was "before" Uranus. They suggested that a large and dense disk composed by small planetesimals (rocky and icy objects) was extended between 20 AU and around 35 AU. The total mass of this disk was estimated to about 30 $M_\oplus$.

Due to interactions with the planetesimal disk, Saturn, Neptune and Uranus migrated outwards whereas Jupiter migrated inwards. The planets scatter inwards the majority of the small bodies that they encounter.

After 600 to 800 Myr of migration, Jupiter and Saturn cross their mutual 2:1 resonance. This resonance increases their orbital eccentricities, destabilizing the entire planetary system. Jupiter shifts Saturn out towards its present position, and this relocation causes mutual gravitational encounters between Saturn, Neptune and Uranus. Neptune and Uranus orbits became more eccentric and injected some planetesimals in the inner Solar System and ejected some in the outer Solar System. Objects thrown in the outer part formed the Trans-Neptunian belt, whereas the ones ejected in the inner part produced the well known Late Heavy Bombardment [11] (LHB). In this model, Uranus and Neptune switched positions about a billion years into the life of the Solar System. In Figure 15 are represented some steps of the Nice Model.
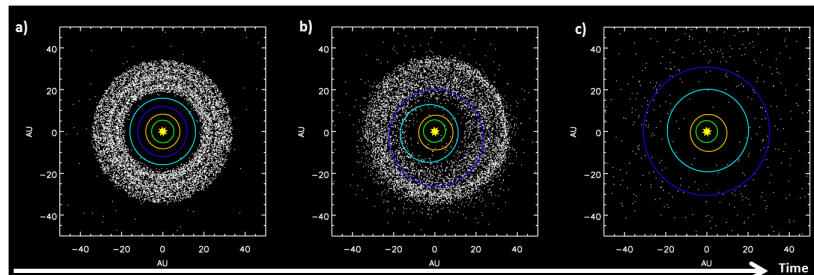
Figure 15: Here, are represented: yellow star is the Sun, green orbit for Jupiter, orange orbit for Saturn, blue orbit for Neptune, cyan orbit for Uranus, and white points are planetesimals. In plot a), initially, the giant planets are in a compact configuration and are surrounded by a disk of planetesimals extending to a distance of ∼34 AU. As a result of interaction with the disk of planetesimals, Neptune migrated outwards and "pushes out" the disk. When Saturn reaches the 2:1 mean motion resonance with Jupiter, a chaotic phase is triggered and all the planet's orbits are elongated. Neptune moves much further inot the disk of planetesimals and destabilizes it (plot b)), Neptune and Uranus exchanged their position and planetesimals are injected in the inner and ejected to the outer parts of the Solar System. However, we must point out that such exchange between Uranus and Neptune position only occurred in 50% of the simulations. In plot c), the Solar System is in a configuration more stable. An animation of the Nice Model can be found at http://media.skyandtelescope.com/video/Solar_System_Sim.mov

II.5.2   Formation and evolution of the Trans-Neptunian belt

Originally, the Trans-Neptunian belt was really different to the current one. The Trans-Neptunian belt was denser, closer to the Sun and extended to 30 AU.

---

[11]The LHB is a period with an abrupt increase in the rate of bombardment of the Moon. LHB happened approximately 4.1 to 3.8 billion years ago. The Nice Model showed that the Lunar seas can be explained by such bombardment.
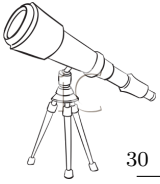
Some objects became gravitationally locked to Neptune orbit, and so, were trapped in the mean motion resonance with this planet (resonant objects). On the other hand, some objects have been sent into chaotic orbits by interactions with the migration of Neptune (scattered and detached disk objects).

In the case of classical objects, the Nice Model predicts a higher eccentricity, in average, than the current observed. Classical objects can be divided into two sub-groups: the dynamically hot and the dynamically cold objects. The two sub-groups possess different orbits, different colors, and different size distributions suggesting diverse composition and also not the same region of formation. As shown in Figure 16, the hot population has been probably formed in a large range of distances (starting from 20 AU) and then, ejected outward. On the other hand, the cold population seems to have been formed more or less in its current position (formation in-situ, Batygin, Brown and Fraser (2011)) and are known to be redder and smaller than the dynamically hot classical objects. According to the Nice Model, the color variation between the hot and the cold populations is explained by their proximity to the Sun. The hot objects may have been formed in a large range of distances from the Sun, and so present a large color variation (Trujillo and Brown, 2002b; Doressoundiram et al., 2002). However, Levison et al. (2008b) proposed that the color diversity may arise in part from surface evolution rather than completely from the primordial composition. Nevertheless, simulations realized by Thébault and Doressoundiram (2003) disagree with the resurfacing as the only cause of the color variations.
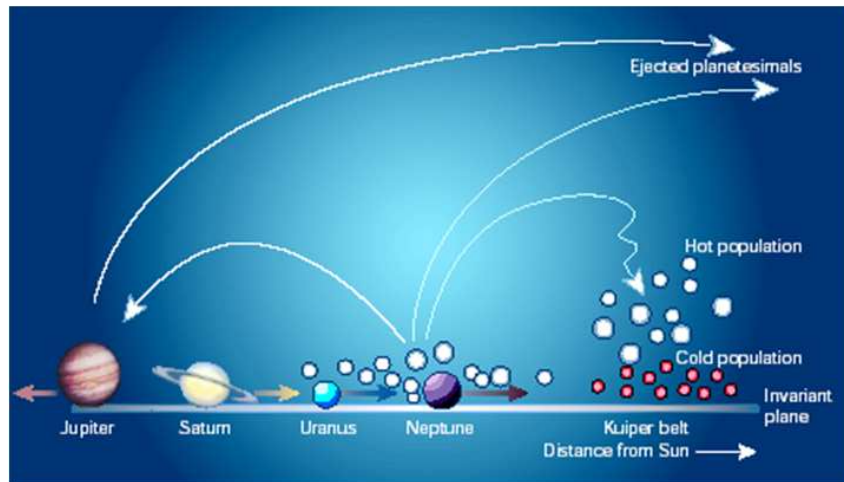
Figure 16: The cold classical objects seem to have been formed in-situ. Whereas the hot classical objects have been ejected from a more inner part of the Solar System to their current positions. Figure from Morbidelli and Levison (2003)

Chapter III

Observing runs and Instrumentation

$\mathcal{V}$ arious observational approaches to study the physical properties of the Trans-Neptunian Objects (TNOs) have been performed within the scientific community, including spectroscopic, photometric and binarity studies. Our own approach to study these objects is to detect the periodic variation of their brightness as a function of time, resulting from their rotation. We analyze their rotational periods, surfaces, shapes and their internal structure studying their lightcurves. Two different programs to study the short-term variability of TNOs were carried out: i) a program of TNOs lightcurves, and ii) our first attempt of coordinated campaign between Spain and Chile.

In this chapter, we will describe the telescopes, and the instrumentation used to achieve our main goal, as well as the observational strategy.

III.1 Observation Campaigns: Observatories, Telescopes and Instruments

In 2001, a team in the Instituto de Astrofísica de Andalucía-Consejo Superior de Investigaciones Científicas (hereafter IAA-CSIC) started a long-term program whose main goal was to study the short-term variability of the TNOs. Usually, this program is carried out at the Sierra Nevada Observatory. In this work, we present results based on observational runs carried out between January 2003 and February 2013. The 2001/2002 observational runs obtained at the Sierra Nevada Observatory with a different CCD camera, were not studied and they were discarded to analyze a homogeneous data set. During the past years, we also requested observing time in several facilities; Calar Alto, Roque de los Muchachos, La Silla, San Pedro de Atacama, and El Leoncito observatories.

In the following subsections, observatories, telescopes, and instruments required for our long-term program and for our coordinated campaign will be introduced.

III.1.1 Sierra Nevada Observatory

The Observatory of Sierra Nevada (hereinafter OSN) is located at Loma de Dilar in the National Park of Sierra Nevada (Granada, Spain) (Figure 17). It is operated and maintained by the IAA-CSIC. Four telescopes are currently located at the OSN: a 0.35 m, a 0.6 m, a 0.9 m, and a 1.5 m telescope. For our purpose, only the 1.5 m telescope has been used.

III.1.1.1 The 1.5 m telescope

Briefly, the 1.5 m telescope is a Ritchey-Chrétien telescope with a fork mount and with two Nasmyth foci. The East focus is equipped with a CCD detector whereas the Albireo Spectrograph

31
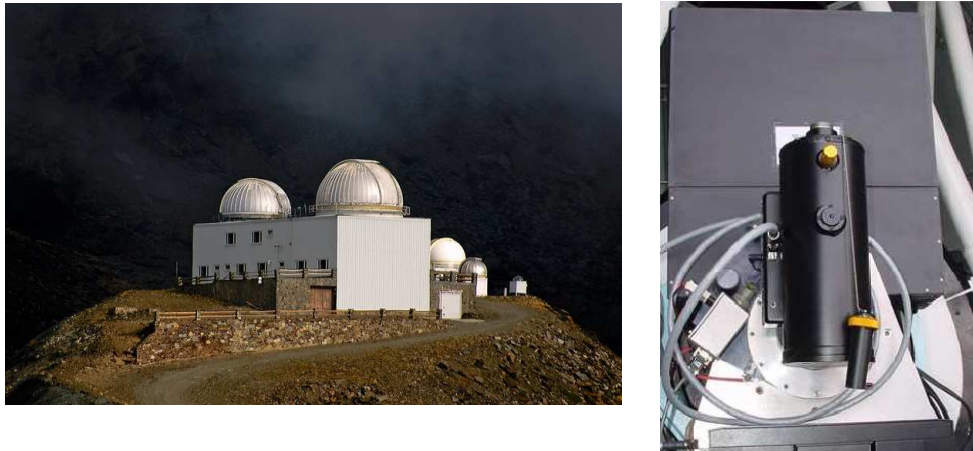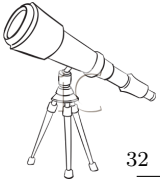
Figure 17: *Observatory of Sierra Nevada*: Principal building with the 1.5 m and the 0.9 m telescopes (left panel). The Roper Camera (right panel) has been used for all observational runs presented in this work. *Credits: OSN webpage*

is in the West focus. For this thesis, we used the CCD detector. Before March 2003, the telescope was equipped with a fast readout CCD Camera called Apogee (or APGE). This detector was based on a Kodak KAF1001E chip with a $7' \times 7'$ field of view ($0.413''$/pixel) and an image size of 1024×1024 pixels. In March 2003, Apogee was substituted by a Roper VersArray CCD camera, usually called Roper for short (Figure 17). Roper is a Back Illuminated CCD camera based on a chip Marconi EEV CCD 42-40 of 2048×2048 pixels. The total field of view is $7.8' \times 7.8'$ with a resolution of $0.232''$/pixel (pixel scale for a 1×1 binning).

Most of the observational runs, after 2003, were operated in service mode by: Francisco J. Aceituno Castro, Victor M. Casanova Escurín or Alfredo Sota Ballano.

III.1.2 Calar Alto Observatory

The German-Spanish Astronomical Center at Calar Alto (CAHA) is located in the Sierra de Los Filabres (Almería, Spain) (Figure 18). Since 2005, this observatory is operated jointly by the Max-Planck-Institut für Astronomie (MPIA, Heidelberg, Germany) and by the IAA-CSIC. CAHA provides three telescopes: the 1.23 m, the 2.2 m, and the 3.5 m telescopes. All of them have been used in this thesis. There are also a 1.5 m telescope operated by the National Astronomical Observatory of Spain, a 0.5 m robotic telescope from the Center of AstroBiology (CAB, Madrid, Spain), and a 0.8 m Schmidt telescope.

III.1.2.1 The 1.23 m telescope

Briefly, the 1.23 m telescope, built in 1975, is a Ritchey-Chrétien telescope with a german mount and a Cassegrain focus (Figure 19). Before September 2011, observations were carried out by means of the CCD SITE#2b camera, a 4k×4k CCD with a total field of view of $17'$. Observations were obtained with the R Johnson filter in a 2×2 binning mode. After September 2011, observations were carried out by means of the CCD DLR-MKIII camera, a 4k×4k CCD. The total field of view is $21.5' \times 21.5'$ with a 1×1 binning. The pixel scale is 15 μm. Observations were obtained with the R Johnson filter in a 2×2 binning mode. Most of the observational runs were carried out remotely by Nicolás F. Morales Palomino.

III.1.2.2 The 2.2 m telescope

Briefly, this telescope is a Ritchey-Chrétien telescope with a fork equatorial mount, and a Cassegrain focus (Figure 20). The primary mirror has a diameter of 2.2 m and a focal length of 17037 mm
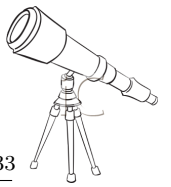
Figure 18: Calar Alto Observatory *Credits: Calar Alto webpage.*
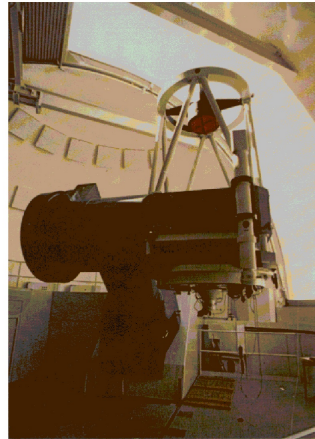
Figure 19: The 1.23 m telescope is a Ritchey-Chrétien telescope built in the 70's. *Credits: Calar Alto webpage.*

with the corrector (or 17611 mm without the corrector). The 2.2 m telescope is equipped with five instruments:

- **Bonn University Simultaneous CAmera (BUSCA)** is a CCD camera which allows simultaneous direct imaging of the same sky area in four colors.

- **AstraLux** is a lucky image instrument developed at the MPIA-Heidelberg.

- **Calar Alto Fiber-fed Echelle spectrograph (CAFE)** provides high resolution spectra over 3900-9600Å.

- **MPI fur Astronomie General-Purpose Infrared Camera (MAGIC)** is for observations in the near infrared.

- **Calar Alto Faint Object Spectrograph (CAFOS)** is a focal-reducer designed to work with a CCD detector.

For our observations at the 2.2 m Calar Alto telescope, we used the CAFOS instrument located at the Cassegrain focus of the telescope. CAFOS is equipped with a 2048×2048 pixels CCD and the image scale is $0.53''$/pixel (pixel scale for a 1×1 binning).
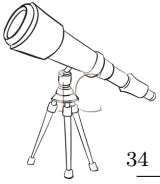
The majority of our observational runs were in-situ and operated by one/various member(s) of
our team. However, some observations were carried out in service mode.
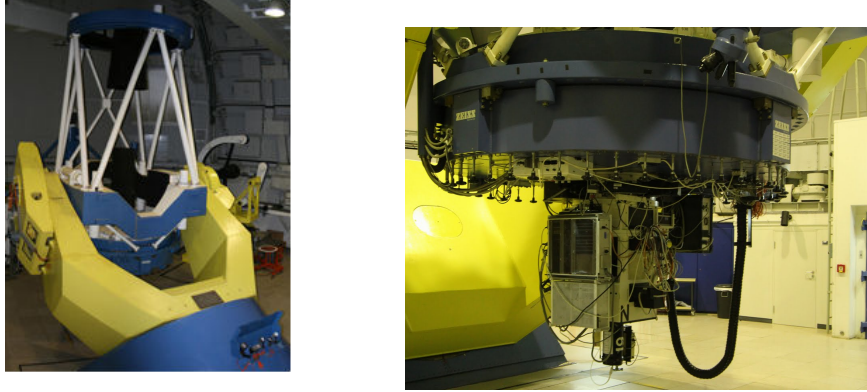
Figure 20: The 2.2 m telescope in the left panel and the CAFOS instrument in the right panel. *Credits:
Calar Alto webpage.*

III.1.2.3   The 3.5 m telescope

Briefly, the 3.5 m telescope (Figure 21) has a horse-shoe equatorial mount and is equipped with
five instruments installed at the prime focus of the telescope:

- **Large Area Imager for Calar Alto (LAICA)** is a mosaic CCD camera installed at the
  prime focus of the telescope.

- **Multi Object Spectroscopy Calar Alto (MOSCA)** is a focal-reducer designed to work
  with a CCD detector for imaging and spectroscopy.

- **Potsdam MultiAperture Spectrophotometer (PMAS)** is an integral field spectropho-
  tometer optimized to cover the optical wavelength regime.

- **TWIN** has been designed for spectroscopic observations of point sources or extended objects
  at intermediate spectral resolution (typically 20 to 150 Å per mm) in the wavelength range
  from 3200 to 11000 Å.

- **Omega 2000** is a prime focus near infrared wide field camera.

For our observations, we used LAICA (Figure 21) and MOSCA. LAICA is equipped with a 2×2
mosaic of 4k$\times$4k CCDs. The total field of view of is $44.36'\times44.36'$. The pixel scale is $0.225''$/pixel
(pixel scale for a 1×1 binning). Observations were carried out with the r' Sloan filter in a 2×2
binning mode. MOSCA has a total field of view of $11'\times11'$. The pixel scale is $0.3208''$/pixel (pixel
scale for a 1×1 binning). Observations were carried out with the R Johnson filter in a 2×2 binning
mode.

III.1.3   Roque de los Muchachos Observatory

The Observatorio del Roque de los Muchachos (hereinafter ORM) is situated on the edge of the
Caldera de Taburiente National Park, in the municipality of Garafía (La Palma, Canary Islands,
Spain). The observatory site is operated by the Instituto de Astrofísica de Canarias (hereinafter
IAC), and is part of the European Northern Observatory (Figure 22).

The ORM has a large set of telescopes (and instruments): the Gran Telescopio Canarias (GTC),
the William Herschel Telescope (WHT), the Telescopio Nazionale Galileo (TNG), the Nordic Op-
tical Telescope (NOT), the Isaac Newton Telescope (INT), the Liverpool telescope, the Mercator,
the Swedish 1-m solar telescope, the Dutch Open Telescope (DOT), the MAGIC telescopes and
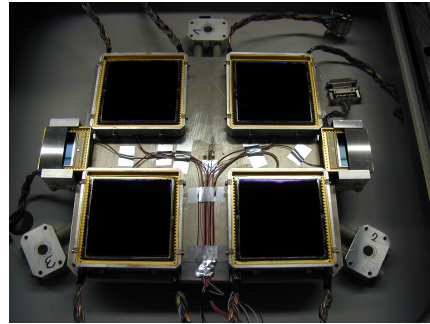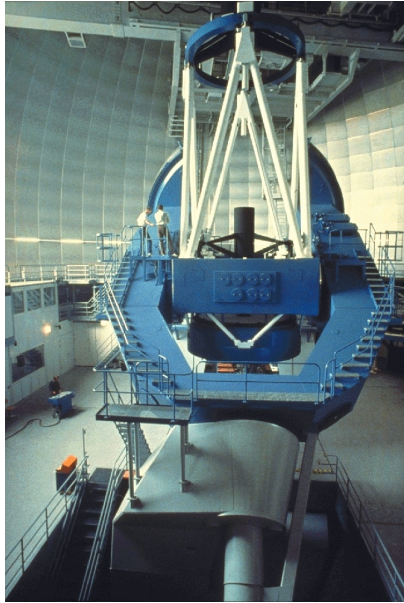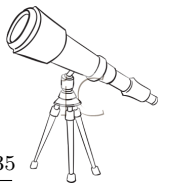
Figure 21: The 3.5 m telescope in the left panel and the LAICA instrument in the right panel. *Credits: Calar Alto webpage.*

the SuperWASP.

All our observational runs at the ORM were in-situ and operated by one/various member(s) of our team.
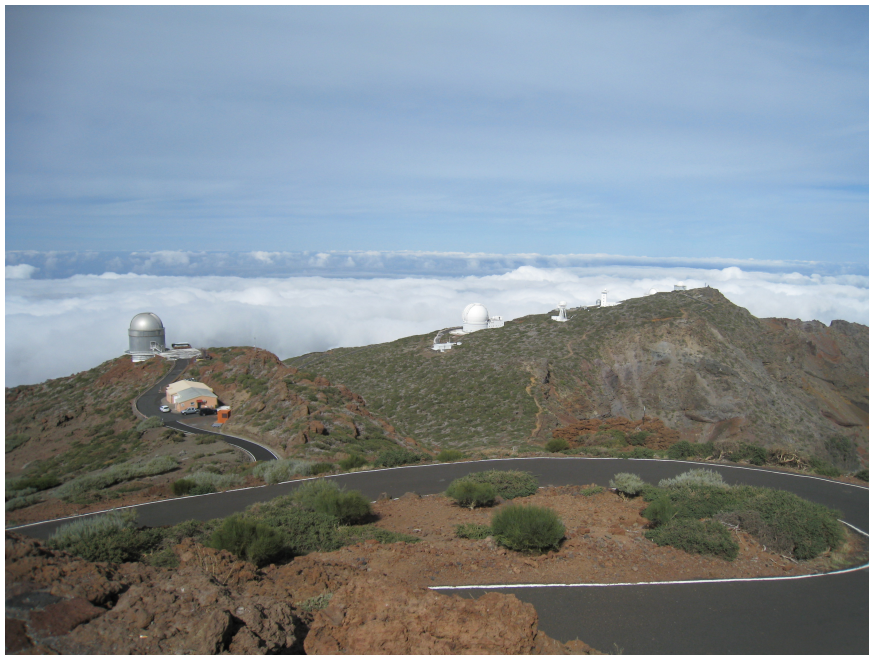
Figure 22: Part of the Roque de los Muchachos Observatory: the Nordic Optical Telescope (NOT, on the left) and the William Herschel Telescope (WHT, in the center of the image). *Credits: Nicolás F. Morales Palomino.*
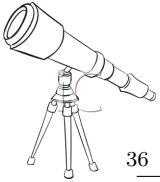
III.1.3.1   Isaac Newton Telescope (INT)

Briefly, the Isaac Newton Telescope (hereinafter INT) belongs to the Isaac Newton Group of Telescopes (ING). This telescope is owned and operated jointly by the Particle Physics and Astronomy Research Council (PPARC, United Kingdom), the Nederlandse Organisatie voor Wetenschappelijk Onderzoek (NWO, Netherlands) and the IAC (Spain).

The INT has a 2.54 m primary mirror with a focal ratio of f/2.94 (Figure 23). The INT is now mainly used with one instrument: the **Wide Field Camera (WFC)** at the prime focus. This camera consists of 4 thinned EEV 2154×4200 CCDs, for a total field of view of $34' \times 34'$ (Figure 23). The pixel scale is $0.33''$/pixel (pixel scale for a 1×1 binning). All observations reported here were performed with the R Harris filter.
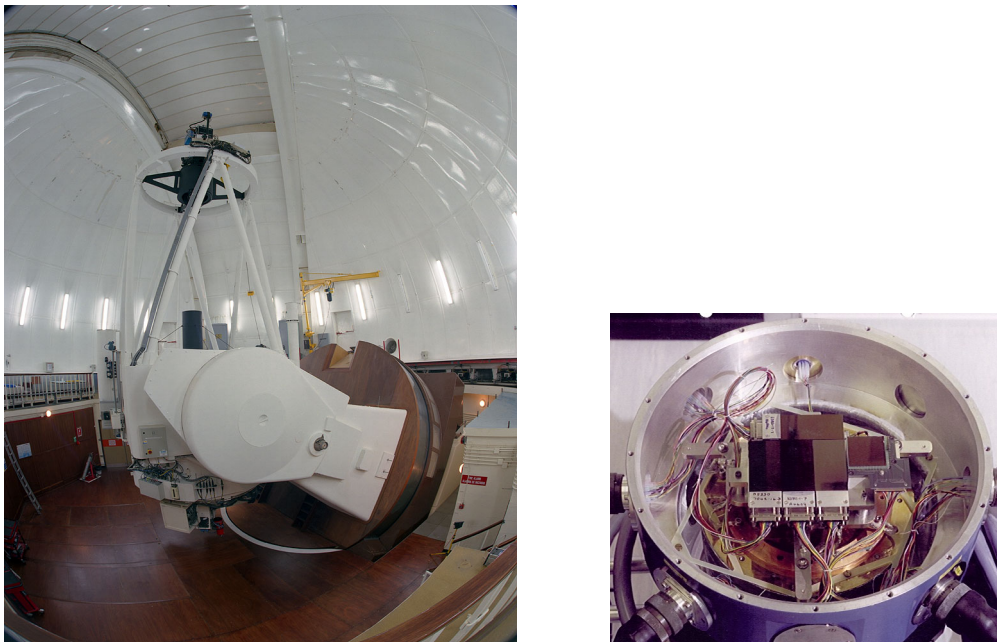
Figure 23: Isaac Newton Telescope (INT) (left panel) and the Wide Field Camera (WFC) (right panel) used for observational runs presented in this work. *Credits: INT webpage*

III.1.3.2   Nordic Optical Telescope (NOT)

Briefly, the Nordic Optical Telescope (hereinafter NOT) is a 2.6 m optical and infrared telescope (Figure 24) equipped with various instruments:

- **Nordic Optical Telescope near-infrared Camera and spectrograph (NOTCam)** is capable of high resolution imaging, low to medium-resolution spectroscopy, and wide field imaging.

- **Andalucia Faint Object Spectrograph and Camera (ALFOSC)** offers a wide and flexible set of observing modes. Direct imaging as well as multi-object spectroscopy are available simultaneously or not.

- **FIbre-fed Echelle Spectrograph (FIES)** is a high-resolution spectrograph.

We used the ALFOSC instrument built at the Astronomical Observatory (AO) at the Niels Bohr Institute for Astronomy, Physics and Geophysics (NBIfAFG), and property of the IAA-CSIC. ALFOSC has a field of view of $6.4' \times 6.4'$ and a pixel scale of $0.19''$/pixel (pixel scale for a 1×1 binning) (Figure 24). All our observations were carried out with the R Bessel filter.
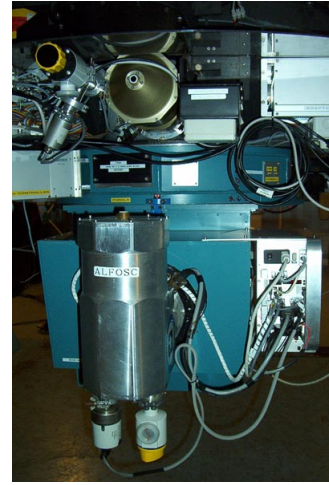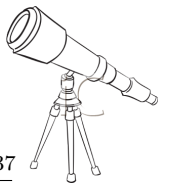
Figure 24: Nordic Optical Telescope (NOT) (left panel) and the ALFOSC instrument (right panel) used for observational runs presented in this work. *Credits: NOT webpage*

III.1.3.3 Telescopio Nazionale Galileo (TNG)

Briefly, the Telescopio Nazionale Galileo (hereinafter TNG) is a Ritchey-Chrétien telescope with an alt-azimuthal mount (Figure 25). The primary mirror has a diameter of 3.58 m and a focal ratio of f/11. The TNG is equipped with five instruments installed permanently in its two Nasmyth foci.

- In the Nasmyth A:
  - **Optical Imager Galileo (OIG)** is a CCD camera for direct imaging at optical wavelengths.
  - **Near Infrared Camera Spectrometer (NICS)** is an infrared camera/spectrometer.
  - **AdOpt** is a module of adaptive optics.

- In the Nasmyth B:
  - **Device Optimized for the LOw RESolution (DoLoRes or LRS)** is a low resolution spectrograph and camera.
  - **Spettografo Alta Risoluzione Galileo (SARG)** is a high resolution spectrograph.

For our observational runs at the TNG, we used the Device Optimized for the LOw RESolution instrument (DOLORES or LRS). We observed in image mode with the R Johnson filter and a 2×2 binning mode. The camera is equipped with a 2048x2048 CCD. The field of view is $8.6' \times 8.6'$ with a $0.252''$/pixel scale (pixel scale for a 1×1 binning).

III.1.4 Teide Observatory

The Teide Observatory is in Tenerife (Canary Islands, Spain) and is operated by the IAC (Figure 26). Opened in the early 1960s, this observatory is composed by nine nocturnal telescopes: the Carlos Sanchez infrared Telescope (TCS), the Mons reflecting telescope, the Optical Ground Station (OGS) telescope, the STellar Astrophysics and Research on Exoplanets (STARE) telescope, the Bradford Robotic telescope, the STELLar Activity (STELLA) 1 and 2 robotic telescopes, the SLOOH, and the IAC-80 telescope.

III.1.4.1 IAC-80 telescope

Briefly, the IAC-80 telescope (Figure 27) has an equatorial German mount, with an effective focal ratio of f/11.3 and a primary mirror of diameter 82 cm. The instrumentation is installed at the Cassegrain primary focus. Since 2005, the IAC-80 telescope is equipped with a 2048x2048 pixels CCD camera each of them with a 13.5x13.5 μm/pixel size. The total field of view is $10.6' \times 10.6'$.
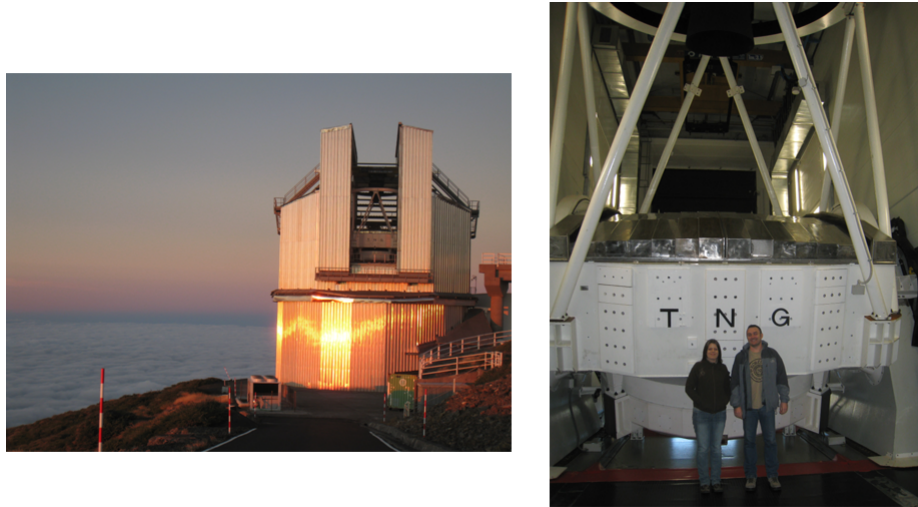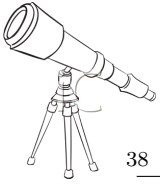
Figure 25: Building of the Telescopio Nazionale Galileo (left panel) and the Telescopio Nazionale Galileo (right panel). *Credits: Nicolás F. Morales Palomino.*

III.1.5   La Silla Observatory

La Silla Observatory is located in the southern part of the Atacama desert in Chile (Figure 28), 600 km north of Santiago de Chile and at an altitude of 2400 m. On March, 25th 1969, La Silla Observatory was formally inaugurated. In the 1970s and 1980s, three major telescopes were built and to date, the European Southern Observatory (hereinafter ESO) operates these three telescopes: the 3.6 m ESO telescope, the New Technology Telescope, and the 2.2-m Max-Planck-ESO telescope. There are also several telescopes located in this site and partly maintained by ESO, like the 1.54 m Danish Telescope, the 1.2 m Leonhard Euler Telescope, the Rapid Eye Mount Telescope, the TAROT (Télescope à Action Rapide pour les Objets Transitoires - Rapid Action Telescope for Transient Objects) telescope, the TRAPPIST telescope (TRAnsiting Planets and PlanetesImals Small Telescope), and the ESO 1-m Schmidt telescope.

III.1.5.1   New Technology Telescope (NTT)

Briefly, the 3.58 m New Technology Telescope (hereinafter NTT) is a Ritchey-Chrétien telescope with an alt-azimuthal mount (Figure 29). It was inaugurated in 1989 and was the precursor of a new telescope generation. The NTT proposes two instruments:

- **Son of ISAAC (SofI)** is a infrared spectrograph and imaging camera.

- **ESO Faint Spectograph and Camera version 2 (hereinafter EFOSC2)** has a multi mode capability including normal/polarimetric imaging/spectroscopy, multi-object spectroscopy and coronography.

For our observations, we used the EFOSC2 mounted in the Nasmyth B focus of the NTT (Figure 29). We observed in image mode with R Bessel filter and a 2×2 binning mode. The camera is equipped with a 2048×2048 CCD with a pixel size of 15x15μm (pixel scale for a 1×1 binning). The field of view is $5.2' \times 5.2'$.

III.1.6   Complejo Astronómico el Leoncito

The Leoncito Astronomical Complex (Complejo Astronómico El Leoncito, CASLEO) is an astronomical observatory in the San Juan Province of Argentina (Figure 30). CASLEO's telescope are located in two separate areas within the El Leoncito Park. The 2.15 m Jorge Sahade Telescope, and the 1.5 m Solar Submillimeter Telescope (SST) are at the main site on the edge of the Pampa de la Ciénaga del Medio. The 0.61 m Helen Sawyer Hogg telescope, the 0.41 m Horacio Ghielmetti
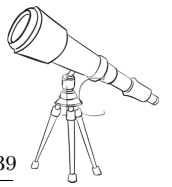
Figure 26: Teide Observatory in Tenerife, Canary Islands, Spain. *Credits: IAC webpage.*

Figure 27: Building of the IAC-80 telescope. *Credits: IAC webpage.*

Figure 28: La Silla Observatory is located in the southern part of the Atacama desert in Chile. *Credits: ESO webpage.*
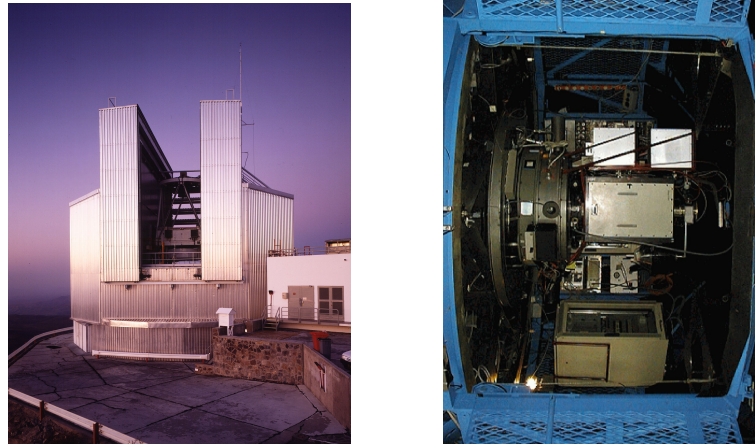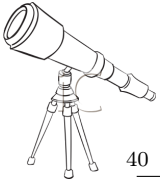
Figure 29: New Technology Telescope (NTT, left panel) and the EFOSC2 instrument in the Nasmyth B of the telescope (right panel). *Credits: NTT and ESO webpages.*

telescope, and the 0.45 m Astrograph for the Southern Hemisphere (ASH) are located on the Cerro Burek.

Figure 30: The 2.15 m Jorge Sahade telescope and the 1.5 m Solar Submillimeter telescope are on the image foreground. The 0.61 m Helen Sawyer Hogg telescope, the 0.41 m Horacio Ghielmetti telescope, and the 0.45 m Astrograph for the Southern Hemisphere (ASH) are located on the Cerro Burek mountain in the background. *Credits: Nicolás F. Morales Palomino.*

III.1.6.1 Astrograph for the Southern Hemisphere: ASH

The Astrograph for the Southern Hemisphere, also called ASH, is under an agreement between the IAA-CSIC and CASLEO. ASH is a Newtonian reflector with a Fork-type mount (Figure 31). It is a 0.45 m (f/2.8) remotely controlled telescope. ASH is equipped with a 11000M CCD SBIG detector, in the primary focus, with a 4008×2672 pixels matrix. The pixel scale is 1.47 $''$/pixel and the total field of view of the instrument is 97.8 $'$×65.2 $'$. All our observations were performed with a Luminance filter [1] and were carried out remotely by Nicolás F. Morales Palomino.

III.1.7 San Pedro de Atacama Observatory

San Pedro de Atacama Observatory (Figure 32) is a private observatory located in the Atacama Desert (Chile). Very dry climatic conditions and the little light pollution make this place unique for astronomers. Since 2005, the number of small telescopes in this area has been increasing every year.

---

[1]The Luminance filter is a very broad-band filter. This filter is centered at 550 nm and is 300 nm wide. The Luminance filter transmission curve can be found in Ortiz et al. (2011) Figure 1.
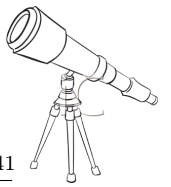
Figure 31: ASH is a 0.45 m (f/2.8) diameter remotely controlled telescope. *Credits: Nicolás F. Morales Palomino.*

Figure 32: Various small telescopes are installed in San Pedro de Atacama Observatory. ASH2 is on the left in this picture. *Credits: Nicolás F. Morales Palomino.*

III.1.7.1 Astrograph for the Southern Hemisphere 2: ASH2

In July 2009, a new telescope was installed in San Pedro de Atacama Observatory (Figure 33). This telescope belongs to our team at the IAA-CSIC and to the private company Astroimagen. The Astrograph for the Southern Hemisphere 2, usually called ASH2, is a 407 mm diameter telescope, with a focal of 1510 mm (or f3.7). ASH2 is equipped with a CCD camera STL11000M. The total field of view is 64 $'\times$82 $'$with a pixel scale of 1.23 $''$/pixel (pixel scale for a 1$\times$1 binning). All our observations were performed with a Luminance filter and were carried out remotely by Nicolás F. Morales Palomino.

Figure 33: ASH2 is a 0.40 m (f/3.7) diameter remotely controlled telescope. *Credits: Nicolás F. Morales Palomino.*

IV

Data calibration, Photometry, and Observing strategy

$\mathcal{A}$ ll data presented in this work were obtained thanks to Charge-Coupled Devices, also called CCDs. Such instruments generate several effects that need to be corrected or removed from the raw data. The processed images will then be, used for measuring the photon flux of our target a process called photometry.

Part of this chapter will be dedicated to the observing strategy used during this thesis, as well as the presentation of the data obtained during the past years. This chapter will also describe the standard calibration of the CCD images as well as several cosmetic effects that may affect the data reduction.

IV.1   Data calibration

IV.1.1   Charge-Coupled Devices or CCDs

The Charge-Coupled Device (hereinafter CCD) was invented in 1969 by Boyle and Smith (1970) of the Bell Laboratory. CCD detectors were first used in astronomy in 1976 to obtained images of the giant planets and were rapidly adopted in the astronomy field (Smith, 1976).

A CCD detector is a two-dimensional array of small independent units called pixels. Pixels are usually made of silicon. The main purpose of this kind of detector is to convert ultra-violet, visible and infrared radiations consisting of photons into electrons stored into the pixels. When an exposure ends, the CCD is read-out which means that the analogue signal of each pixel is converted into a digital signal by a computer and we obtain the final image.

IV.1.2   Calibration

For this work, the CCD detectors were used in direct imaging mode at visible and near infrared (nIR) wavelengths. In the following, we will only present the systematic and cosmetic corrections that are typical in imaging mode.

IV.1.2.1   Bias

The bias, also called offset by other researchers, shows the electronic noise of the detector. A bias exposure is an image with the shutter closed and the shortest possible exposure time. To subtract a single bias frame (frame or image) would introduce an electronic noise from that frame, so a serie of biases (typically 10 to 15 bias frames) are combined into a median bias frame (Figure 34). During this averaging process the highest and the lowest values for each pixel are discarded. The more
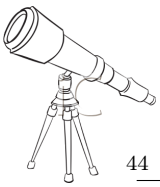
bias exposures are used for the median bias, the less noise will be introduced into the corrected images. Bias frames are usually taken at the beginning and/or at the end of the night.

IV.1.2.2   Flat-field

CCD detectors are non-uniformly illuminated and retain pixel-to-pixel variations in sensitivity. Flat-field frames are necessary to correct these effects. On the other hand, such flat-fields will allow us to correct any pattern of the detector and/or filters like those caused by dust which usually have a donut-like shape. A flat-field can be obtained by observing a screen on the inside of the dome of the telescope, which is illuminated by lights. In this case, we obtain a dome flat-field. The main advantage of dome flat-fields is that it is easy to obtain a good signal-to-noise image during the day, however, the direction of light entry in the telescope is different from that during the night, and there are other problems.

Usually, flat-fields are obtained by observing the sky during evening and/or morning twilight because during this time the sky better approximates uniform illumination and light enters the telescope in much the same way as during the night. In case of observations with filter(s), flat-field frames have to be carried out in each filter(s) that will be used during the night. Typically, a series of 10 to 15 flat-filed frames is carried out and then during the averaging process pixels with counts deviating more than 3σ from the mean are eliminated (Figure 34). We can use the normalized median of the flat-fields or the sigma-clipping process whose purpose is to eliminate pixels above the mean. In all cases, the final result has to be inspected for possible residuals from very bright saturated stars.

IV.1.2.3   Dark current

Because the detector has a non-zero temperature, some thermal electrons are generated and this effect is known as thermal noise. The thermal noise from the detector as well as from its surroundings adds a few counts to the frame and these extra counts have to be subtracted frame-by-frame. For this, we have to carry out images with close shutter and with the same exposure time as for the science images. Several dark current frames have to be obtained and averaged into one final dark frame. If dark frames are used, the bias level is present in them as well, and so, separate bias frames are unnecessary. For liquid N_2 cooled CCDs dark frames are usually unnecessary.

IV.1.2.4   Corrected image

To correct an image for known systematic effects, we have to apply the following procedure:

- Create a median bias frame which is a median or sigma-clipped over several bias frames obtained during the night.

- Subtract the median bias frame to the flat-field frames.

- Create a normalized median flat-field frame which is a normalized average over the flat-filed frames corrected from median bias frame.

- The corrected image is median bias subtracted and divided by the normalized median flat-field frame.

Such process can be summarized as:

$$Corrected\,Image = \frac{I - \overline{B}}{Norm(\overline{FF - \overline{B}})} \qquad \text{(Equation IV.1)}$$

where I is the raw image, B is the bias frame, FF is the flat filed image $\overline{X}$ indicates an average over several frames X, and Norm is a normalization factor. An example is shown in Figure 34. In Equation IV.1, one can realize that the corrected image is a 2 dimensional array or a matrix. So, the arithmetic operations are performed on matrices.
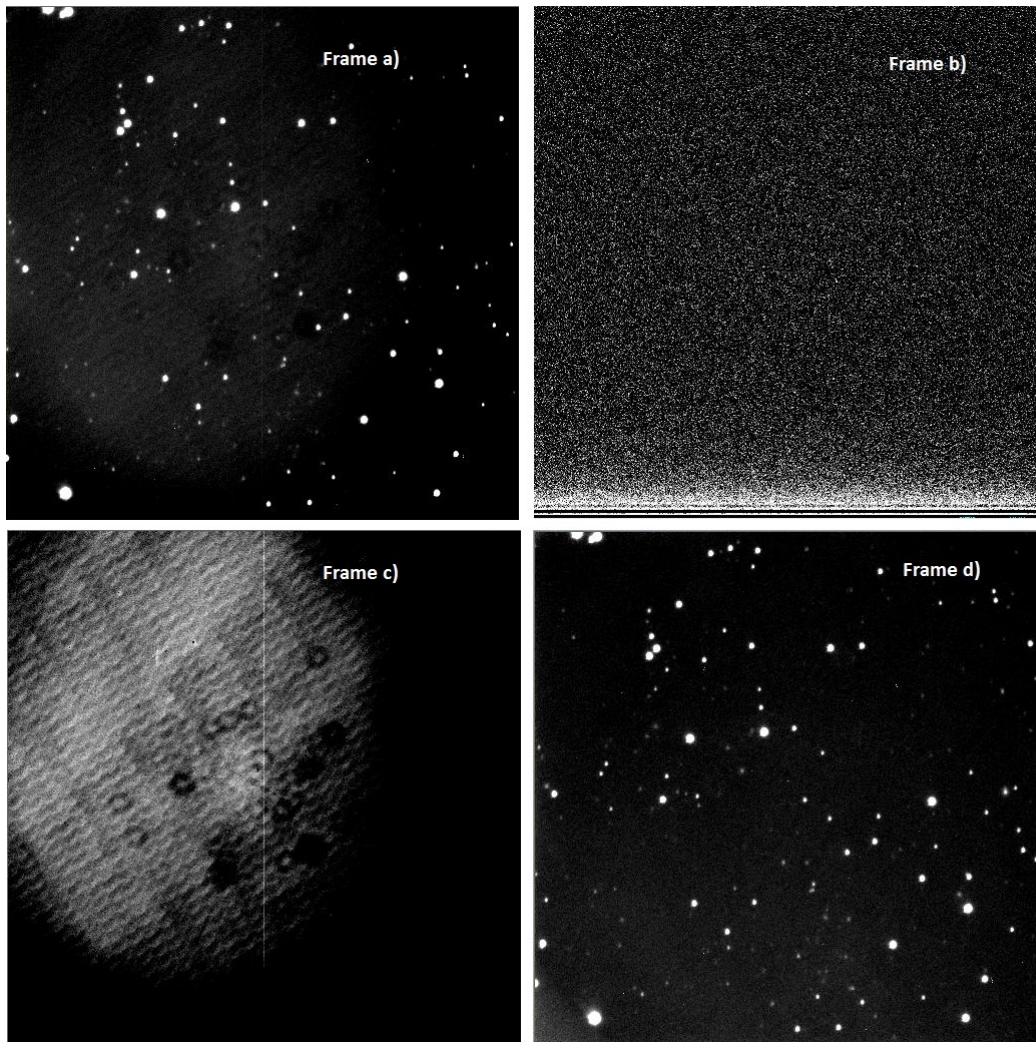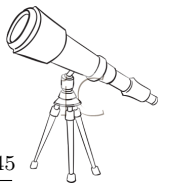
Figure 34: Examples of CCD images of 1024×1024 pixels. This snapshot is composed of: frame a): a raw image carried out with the 1.5 m OSN telescope; frame b): median bias image; frame c): median flat-field; frame d): the corrected image from systematic effects.

IV.1.2.5   Fringing

A pattern of fringes, also called "fringing" can occur during the observations due to interferences between the light reflected within the CCD and light that passes through the array and reflects back into it (Figure 35). One of the major cause of the fringing is the night sky emission lines that occur in the Earth's upper atmosphere, but this is only seen in nIR wavelengths.

Since the flat-fields are obtained with white light, they cannot correct these fringes. So, the fringes are an additive pattern and should be subtracted, not divided. To remove the fringes, the fringing pattern must be extracted from the scientific images themselves. Several steps exist to correct for fringing pattern:

- Obtain the observations with dithering (to shift the image by a few pixels in random directions)

- Subtract the median-bias from all frames

- Normalize the sky level of all the exposures to the average sky level. Store the normalization factor for further use
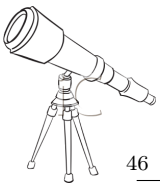
- Median average all the exposures. The result should contain no objects, just the fringes and the flat-field structure

- Divide the result by the median flat-field.

- Get the average sky level of this image and subtract it.

- Multiply the result by the median flat-field: this is the master fringe template.

- For each image, multiply the master fringe template by the normalization factor

- Subtract the result from the original image

- Divide the frames without the fringes by the median flat-field.
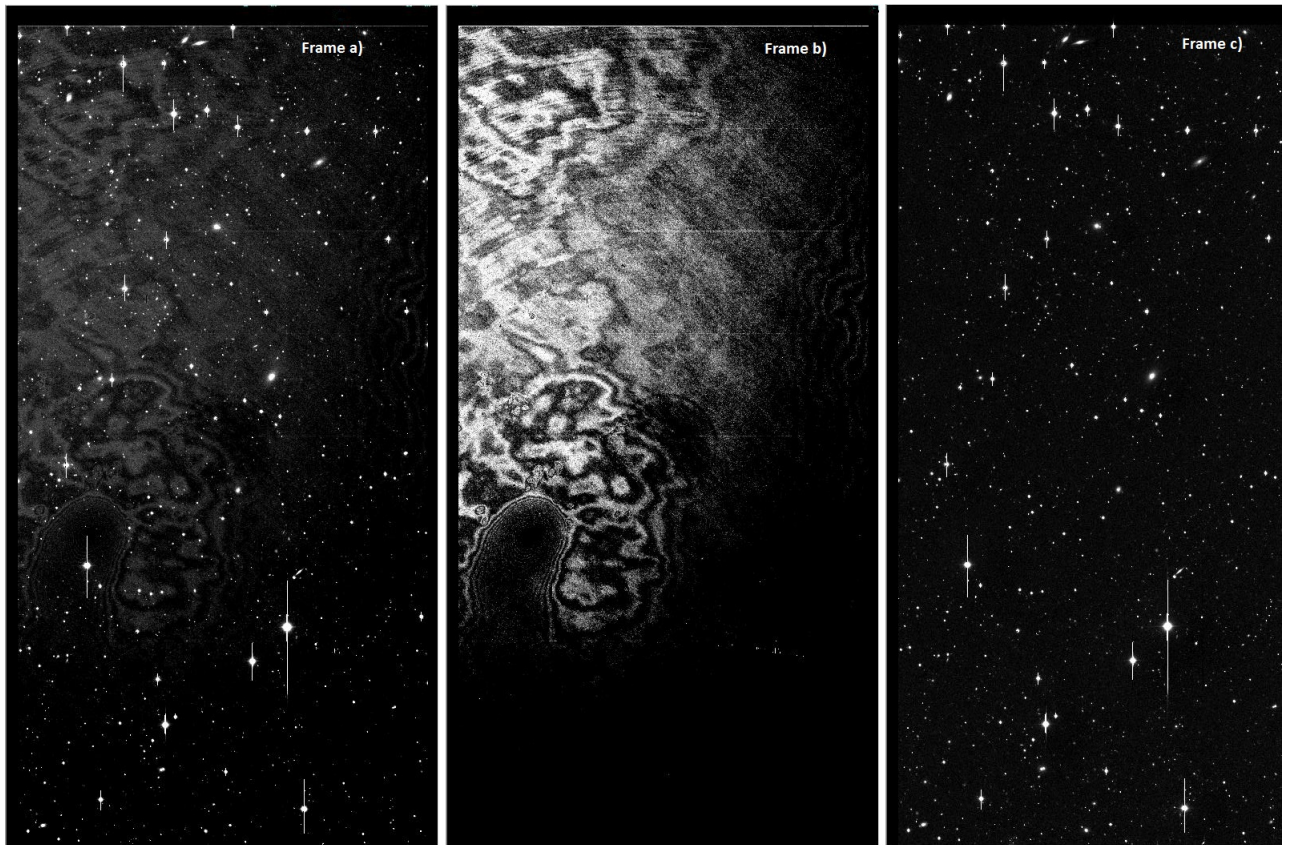
Figure 35: Examples of CCD images of 4200×2154 pixels. This snapshot is composed of: frame a): a raw image obtained with the Wide Field Camera (WFC) at the Isaac Newton Telescope (INT) presents a pattern of fringes; frame b): fringing pattern; frame c): the final image corrected from the fringing pattern. Note that the bias and flat-field corrections have not been applied. Some bright stars are saturated and present blooming effects (Section IV.1.2.8).

IV.1.2.6   Cosmic rays removal

Cosmic rays are very high energy particles that impact the detector and can affect the image, especially in case of long exposures. Such events produce an intensity increase on some pixels. Several automated routines exist for a global removal of the cosmic rays. Generally, pixels whose counts are above 5 times the standard deviation of the sky area are candidate for pixels affected by cosmic rays. The flux of the candidates is compared with the flux of its neighboring pixels, and if the neighbors flux sum is inferior to 6-8% of the candidate's flux, the pixel contaminated has to
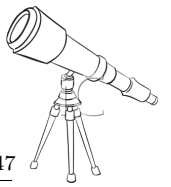
be replaced by interpolation.

In this work, no cosmic ray removal algorithms were used, and we rejected images in which the target is affected by a cosmic ray hit.

IV.1.2.7   Bad pixels and bad columns

Often isolated pixels (or group of pixels) present dark currents superior to its neighbors or are not sensitive to light because of manufacturing limitations or problems or damage. Pixels with too high counts are called hot pixels, whereas pixels with zero (or almost zero) sensitivity are named cold pixels. There are several methods to correct the bad pixels : i) create a global bad pixel mask or, ii) replace the pixel counts by the average value of its neighbors like in the cosmic ray removal case. Sometimes, a full column or row of bad pixels has to be corrected by interpolating the values of the neighboring columns or rows.

In this work, we opted to uncorrect the images from this effect, and we rejected images where the target was near/on a bad pixel or a bad column.

IV.1.2.8   Blooming

During long exposures, bright stars in the field can exceed the full well capacity of the pixels on which they are being recorded. As a light-gathering pixel exceeds its capacity to hold captured photons, the excess energy spills over into the adjacent pixels along a row. This spillover, called blooming produces a spike of light on every bright star in the image (Figure 35).

If the studied object passed near/in an area contaminated by blooming effect, the object photometric study is affected. In such cases, a rotation of the CCD detector is required, prior to obtaining the images.

IV.2   Photometry

Photometry is the method to measure the flux of an object or star. In other words, we want to determine the quantity and the temporal nature of the flux emitted or reflected by a source as a function of wavelength. In the image obtained by a detector, the source "occupies" several pixels and produces a two dimensional bell-shaped intensity distribution called Point-Spread-Function (PSF). Photometry consists in measuring the flux of all the pixels that contain the source's light and then, subtract the sky contribution to get the final source flux.

IV.2.1   Aperture photometry

Aperture photometry is a method to estimate the flux (and so the magnitude) of a source by picking an aperture or diaphragm. Usually, the aperture is defined as a circle around a source [1]. The flux from this aperture is then subtracted from the flux of an annulus around it which is called the sky annulus. In Figure 36, one can see various concentric regions centered on a source (here a star as example). The inner circle is the measuring aperture also called aperture that we will used to estimate all (or almost) the star flux. The next region is a "dead zone" (also known as no man's land) in which pixels are ignored. This zone prevents to take into account twice several pixels as well as avoid stars near the object from being measured. All these regions are shown in Figure 36. There are several softwares and packages to perform data reduction and photometry. But in this work, all the data reduction was performed with a common Interactive Data Language (IDL) reduction software based on the Daophot routines (Stetson, 1987).

Several issues have to be considered for perform a reliable photometric study:

---

[1]The aperture shape has to be adapted according to the form of the studied source. For example, an elliptical aperture is desirable in case of trailed object.
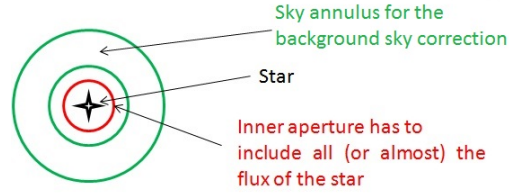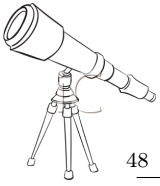
Figure 36: *Schematic figure of a photometry aperture*: The inner aperture has to measure all (or almost) the star's flux. The outer sky aperture is used to normalize the star's flux to the background sky.

- *How do we find the center of the source?* We are considering circular aperture centered on the source, in other words the center of the aperture is the center of the source (also called centroid). Several IDL routines have been elaborated to compute automatically the centroid position. One can cite the routines [2]: *cntrd* which computes the centroid using a derivative search or *gcntrd* which compute the centroid by Gaussian fits.

- *How do we estimate the aperture size?* We have to choose an aperture as small as possible to obtain the highest signal-to-noise ratio (S/N or SNR) by minimizing the contribution from the sky, but large enough to include most of the flux of the source. Knowing the PSF, we can quantify the flux collected and lost for a certain aperture. However, mathematically it is difficult to express the PSF function which is, typically a combination of three different functions indicated bellow:

  - Gaussian function: $G(r) \propto e^{\frac{-r^2}{2a^2}}$
  - Modified Lorentzian function: $L(r) \propto \dfrac{1}{1+\left(\frac{r^2}{a^2}\right)^b}$
  - Moffat function: $M(r) \propto \dfrac{1}{\left(1+\frac{r^2}{a^2}\right)^b}$

  where a and b are the fitting parameters, and r is the radius from the centroid of the point source. The Craig Markward's IDL routine *mpfit2dpeak* [3] can be used to fit a Gaussian, Lorentzian or Moffat model to data to select an appropriate aperture for the photometry. Usually, the PSF is described in terms of its Full Width at Half Maximum (FWHM) on its profile and we used the Gaussian function as approximation:

  $$FWHM \approx 1.67\sigma \qquad \text{(Equation IV.2)}$$

- *How do we estimate the sky aperture size?* We have to estimate the sky flux to subtract to the source's flux. Care has to be taken not to introduce spurious results due to faint background stars or galaxies in the sky aperture. The IDL routine *aper*, adapted from the daophot routine (Stetson, 1987), computes the photometry in concentric apertures [4].

- *What can we do in case of crowded field of view?* The main problem in case of crowded field of view is that our photometry will probably be affected by stars in the aperture and/or in the sky annulus, so our photometry will be "contaminated". On the other hand, we have to point out that to identify a moving target in such a field of view can be difficult. Several programs of optimal image subtraction can be used. In this work, we tested two different programs: i) the ISIS code (Alard and Lupton, 1999; Alard, 2000), and ii) the Yuan and Akerlof (2008) code. The Yuan and Akerlof (2008) code is based on the cross-convolution: two convolution kernels are generated to make a test image and a reference image separately transform to

---

[2]A complete description of these routines can be found at `http://idlastro.gsfc.nasa.gov/ftp/pro/idlphot/cntrd.pro` and at `http://idlastro.gsfc.nasa.gov/ftp/pro/idlphot/gcntrd.pro`.

[3]The routine can be found at: `http://www.physics.wisc.edu/~craigm/idl/down/mpfit2dpeak.pro`

[4]The routine *aper* can be found at: `http://idlastro.gsfc.nasa.gov/ftp/pro/idlphot/aper.pro`
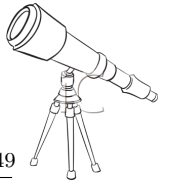
match as closely as possible. This code has been developed for the reliable identification of objects, so it is useful to identify a moving target in a crowded field of view. However, this code has not been developed to obtain a high precision photometry. The ISIS code can be explained in several steps: once we have a good reference image by stacking some of the best images of our dataset, one can use the image subtraction code to adjust the reference image to the seeing of each individual images. ISIS has two levels of rejection for variable object: i) checking that each individual star does not show flux variations, and ii) checking the chi-square for each individual star. The final output of the code will a subtracted image of the flux variation between the individual image and the reference frame.

IV.2.1.1 Aperture radius

The choice of the aperture radius is important. We had to choose an aperture as small as possible to obtain the highest S/N by minimizing the contribution from the sky, but large enough to include most of the flux of the source. Typically, we repeated the measurement using a set of apertures with radii around the FWHM, and also adaptable aperture radius (aperture radius is varying according to the seeing conditions of each image, and so, the aperture radius is different for each image).

IV.2.1.2 Sky background contribution

Sky background is estimated on a ring around the source where there is no significant signal from the source. Care has to be taken not to introduce spurious results due to faint background stars or galaxies in the sky aperture. Generally, we used an inner aperture radius of 3 times the source aperture radius and a width of 5 pixels (Howell, 2001).

In the perfect case, the sky background has a Gaussian distribution, and so an appropriate value for the sky background is the mean of the distribution. However, in the reality, the distribution is not symmetrical due to a possible faint stars or galaxies contribution. In case of asymmetrical distribution, the mean, mode and median are not equal and the best estimate of the sky background signal is the mode (Howell, 2001):

$$mode = 3 \times median - 2 \times mean \qquad \text{(Equation IV.3)}$$

IV.2.1.3 Magnitude and associated error

The total flux (F) from the source is the sum of all counts (C) from the corrected pixels from the estimated sky background (S) in the aperture divided by the exposure time (t_{exp}). Mathematically, the flux is:

$$F = \frac{C - A_{aperture} * S}{t_{exp}} \qquad \text{(Equation IV.4)}$$

where $A_{aperture}$ is the aperture area. Then, the source flux is converted in magnitude, m, as:

$$m = -10^{0.4} \log(F) \approx -2.5 \log(F) \qquad \text{(Equation IV.5)}$$

The flux measurement is affected by several errors, for example: i) error in the estimated flux of the source in the aperture, ii) error in the sky background estimation, and iii) contamination of the sky background in the aperture. Poisson statistics are used with photon-counting devices with the S/N being given by $\sqrt{N}$, where N is the total photons from the source. If the source and background noise contributions are negligible, the error is given by $\sqrt{N}$. However, noise sources are significant and in this case, the S/N is:

$$S/N = \frac{N_{source}}{\sqrt{N_{source} + n_{pixels}(N_{sky} + N_{dark} + N_{read}^2)}} \qquad \text{(Equation IV.6)}$$

where N_{source} is the total number of photons from the source after the sky subtraction, n_{pixels} is the number of pixels contained within the aperture, N_{sky} is the total number of sky photons per
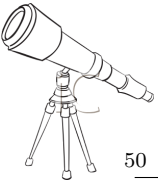
pixel, N_{dark} is the dark current in photons per pixel, and N_{read} is the read noise of the detector in electrons per pixel ([Howell, 1989](#)). The flux error ($Error_{flux}$) is given by:

$$Error_{flux} = \frac{F}{S/N} = \frac{\sqrt{N_{source} + n_{pixels}(N_{sky} + N_{dark} + N_{read}^2)}}{t_{exp}} \qquad \text{(Equation IV.7)}$$

For most of the CCD detectors, the term N_{dark} is negligible.

One can convert flux into magnitude, and the magnitude error ($Error_{magnitude}$) is:

$$Error_{magnitude} = \frac{2.5}{\ln(10)} \times \frac{Error_{flux}}{F} \approx 1.0857 \times \frac{Error_{flux}}{F} \qquad \text{(Equation IV.8)}$$

IV.2.2   Relative photometry

Relative photometry, also called differential photometry gives us a way to measure the relative magnitude of a source. With relative photometry, the apparent magnitudes of a source over time are determined without considering the conversion to absolute magnitudes. For example, by measuring the relative magnitude of a star and of an object, we have:

$$\Delta_m = m_{object} - m_{star} = -2.5 \log \frac{F_{object}}{F_{star}} \qquad \text{(Equation IV.9)}$$

where m_{object} and m_{star} are, respectively, the magnitudes of the object and of the star, and Δ_m is the difference between an object's magnitude and that of a reference (or comparison) star. In other words, we are measuring the difference in brightness between the reference and the target. Obviously, this can only be done when both, the object and the reference stars are in the same image or close enough. Relative photometry presents several advantages such as: i) it is easier than absolute photometry, mainly because the effects of the atmosphere effectively cancel out because the reference is seen through the same veil of sky as the target, and ii) provides the best accuracy when measuring small variations.

IV.2.3   Absolute photometric calibration

The absolute photometric calibration has been used in this work to obtain the solar phase curves of several objects, as well as their absolute magnitudes.

Previously, the steps required to obtain the instrumental magnitude have been presented. Now, we will introduce the photometric calibration that we have to apply in order to obtain the final photometry.

Standard stars are observed during the night to allow an absolute calibration. In fact, we need to correct for the atmospheric extinction and the zero-point that we will introduce below. As we are dealing with visible photometry, we use Landolt standard stars ([Landolt, 1992](#)), which are valid for the UBVRI photometric system.

IV.2.3.1   Airmass and Atmospheric extinction

The atmospheric extinction is the diminution of a source's light caused by going through the Earth's atmosphere. The intensity of atmospheric extinction depends on the atmosphere columns length crossed, the wavelength, and the atmospheric conditions. The quantification of the atmosphere column crossed by the source's light is called airmass and, usually expressed by the letter X:

$$X = \sec(z) - 0.0018167(\sec(z)-1) - 0.02875(\sec(z)-1)^2 - 0.0008083(\sec(z)-1)^3 \quad \text{(Equation IV.10)}$$

where z is the apparent zenith distance. Generally, Equation IV.10 is approximated by:

$$X \approx \sec(z)(1 - 0.0012(\sec^2 z - 1)) \qquad \text{(Equation IV.11)}$$
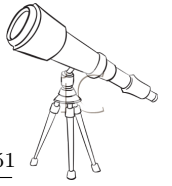
To calculate the apparent zenith distance, one can use:

$$\sec(z) = (\sin(\phi)\sin(\delta) + \cos(\phi)\cos(\delta)\cos(H))^{-1} \qquad \text{(Equation IV.12)}$$

where H is the hour angle (local sidereal time - right ascension), ϕ is the observer's latitude, and δ is the declination of source.

The atmospheric extinction by airmass unit is called extinction coefficient (k_λ). Extinction depends on the wavelength (λ), in other words, it depends on the filter used. The magnitude corrected by atmospheric effect (also called extra-atmosphere magnitude, $m_0(\lambda)$) is expressed as follows:

$$m_0(\lambda) = m(\lambda) - k_\lambda X \qquad \text{(Equation IV.13)}$$

where $m(\lambda)$ is the instrumental magnitude obtained at a λ wavelength. The atmospheric extinction coefficient, k_λ, can be determined by observing the same object (or star) through an appropriate filter at several times during the night at varying zenith angles. When the observed magnitudes of the object (or star) are plotted against computed airmass, they should lie on a straight line with a slope equal to k_λ.

IV.2.3.2 Photometric systems

Following, we will introduce some photometric systems. A lot of photometric systems can be used, but here we will only focused on some of them.

IV.2.3.2.1 Visual magnitudes The first estimates of stellar magnitudes were made either using the unaided eye or later by direct observation through a telescope. Magnitudes estimated in this way are referred to as visual magnitudes. The sensitivity of the human eye peaks at a wavelength of around 5500Å.

IV.2.3.2.2 Photographic magnitudes Photographic magnitudes were determined from the brightness of star images recorded on photographic plates and thus are determined by the wavelength sensitivity of the photographic plate. Early photographic plates were relatively more sensitive to blue than to red light and the effective wavelength of photographic magnitudes is about 4200Å. Such photographic magnitudes refer to early plates exposed without a filter.

IV.2.3.2.3 Johnson-Morgan photometric system (UBV) The Johnson-Morgan system, also known as the UBV photometric system is the first known standardized photoelectric photometric system (Johnson and Morgan, 1953). It is a wide band (system having bands at least 300Å wide) photometric system for classifying stars according to their colors. The letters U, B, and V stand for, respectively, ultraviolet, blue, and visual magnitudes. The mean wavelengths of such filters are 364 nm for U, 442 nm for B, and 540 nm for V.

IV.2.3.2.4 Johnson-Kron-Cousins photometric system (UBVRI) This photometric system is an extension of the Johnson-Morgan system. With the advent of CCD, as well as because CCDs were sensitive in the red and near-infrared, a new photometric system was needed. Cousins (1973) improved the Johnson-Morgan system to such wavelengths. Such a new photometric system is the Johnson-Kron-Cousins (UBVRI) system. The transmittance maximum is obtained at a wavelength of 360 nm in the U-band, at 440 nm in the B-band, at 550 nm in the V-band, at 650 nm in the R-band, and at 800 nm in the I-band.

IV.2.3.2.5 Bessell photometric system The UBVRI of the Johnson-Kron-Cousins system have been reanalyzed using standard-star photometry and synthetic photometry from spectrophotometry of a large range of stars by Bessell (1990). Small adjustments have been made for a better photometry and calibration. More improvements can be found in Bessell (2005).
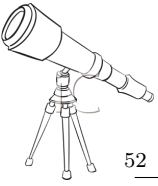
IV.2.3.3   Standard calibration

The first step for a standard calibration is to compute the zero-point. For each filter, we have to find the zero of the scale and shift our extra-atmospheric magnitude according to the zero-point. The second step is to add a color index term. In fact, there may be slightly mismatches between the standard system and our instrumental system. In other words, we have to determine the magnitude difference between the source's magnitude in the filter in question and in an adjacent filter. For BVRI photometry, instrumental magnitudes for each filter (m_B, m_V, m_R, and m_I) are calibrated into the corresponding standard magnitudes (B, V, R, and I) by using:

$$m_B = B + ZP_B + k_B X_B + C_{B,V}(B - V) \qquad \text{(Equation IV.14a)}$$
$$m_V = V + ZP_V + k_V X_V + C_{B,V}(B - V) \qquad \text{(Equation IV.14b)}$$
$$m_R = R + ZP_R + k_R X_R + C_{V,R}(V - R) \qquad \text{(Equation IV.14c)}$$
$$m_I = I + ZP_I + k_I X_I + C_{V,I}(V - I) \qquad \text{(Equation IV.14d)}$$

where ZP_1 is the zero-point in the filter 1, k_1 is the extinction coefficient in the filter 1, $C_{1,2}$ is the different color term between the filter 1 and the filter 2, and X_1 is the airmass in the filter 1.

Generally, standard stars magnitudes are expressed as a function of the following unknowns V, (B-V), (V-R), and (V-I):

$$m_B = [(B - V) + V] + ZP_B + k_B X_B + C_{B,V}(B - V) \qquad \text{(Equation IV.15a)}$$
$$m_V = V + ZP_V + k_V X_V + C_{B,V}(B - V) \qquad \text{(Equation IV.15b)}$$
$$m_R = [V - (V - R)] + ZP_R + k_R X_R + C_{V,R}(V - R) \qquad \text{(Equation IV.15c)}$$
$$m_I = [V - (V - I)] + ZP_I + k_I X_I + C_{V,I}(V - I) \qquad \text{(Equation IV.15d)}$$

IV.2.3.4   Final photometric errors

Final photometric errors for each calibrated magnitude and color index are based on:

- the photometric uncertainty: $\text{Error}_{magnitude}$ expressed in Equation IV.8.

- the uncertainty on the aperture correction is the root-mean-square residual of the fit to the stars profiles: $\text{Error}_{ApertureCorrection}$.

- the calibration uncertainty is the root-mean-square residual of the calibration equations to the standard stars: $\text{Error}_{Calibration}$.

Final uncertainty is:

$$FinalError = \sqrt{Error_{magnitude}^2 + Error_{ApertureCorrection}^2 + Error_{Calibration}^2}$$
$$\text{(Equation IV.16)}$$

IV.2.4   Aperture correction

As we already mentioned, the aperture has to be large enough to collect all the source flux, but at the same time has to be as small as possible to minimize the sky contribution. In fact, in Equation IV.8, we shown that the S/N is the collected flux divided by its error. So, we have to expect a higher S/N if the flux is high and if the aperture radius is small.

In order to improve the S/N for faint sources, Howell (1989) and Stetson (1990) developed a technique called: aperture correction or growth curve correction. A growth curve is obtained by estimated the flux variation with increasing aperture. However, as shown in Figure 37, growth curves are different for bright and faint sources.
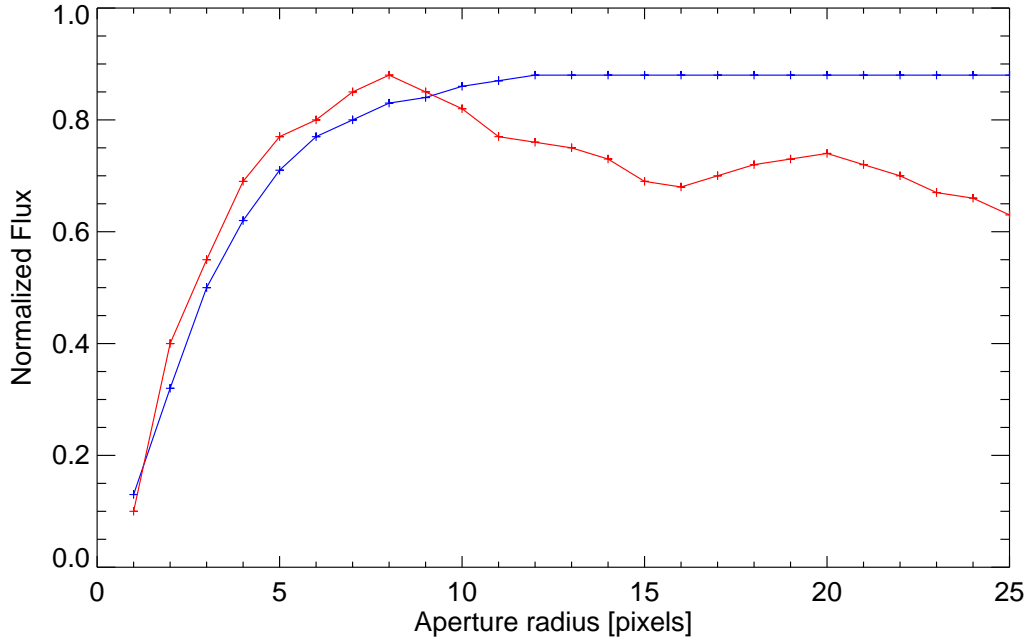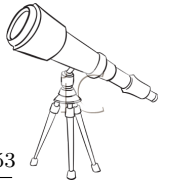
Figure 37: *Normalized flux versus aperture radius*: Examples of curves of growth for two sources with V-magnitude of 18 mag (blue curve) and of 22 mag (red curve) based on TNG data. The brightest source reaches a plateau of stability with increasing aperture, whereas the flux of the faintest source gets unstable beyond a certain aperture radius.

For bright sources, when we reach the aperture for which all the source flux is evaluated, the growth curve becomes stable and increasing the aperture radius does not change the flux estimation. On the other hand, the growth curve for faint object is unstable beyond a certain aperture radius when the sky background effects are non-negligible. In conclusion, if we are measuring a faint object's flux with a small aperture, we are minimizing the sky effect, but we are not collecting all the source's flux. The flux loss between a small aperture and the aperture that collect all the flux, can be estimated from the growth curve of a bright source.

In term of magnitudes, the magnitude loss (Δ_m) when we are using a small aperture is expressed as:

$$\Delta_m = m_{total} - m_{smallapert} \qquad \text{(Equation IV.17)}$$

where m$_{total}$ is the total source's magnitude, and $m_{smallapert}$ is the magnitude evaluated with a small aperture.

A faint object's magnitude measured with a small aperture can be corrected adding the equivalent magnitude loss from a bright source in the field (generally a bright star). In fact, since the
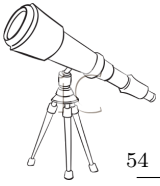
normalized growth curves must be equal, we obtain:

$$\frac{F^*_{smallAper}}{F^*_{total}} = \frac{F^{obj}_{smallAper}}{F^{obj}_{total}} \qquad \text{(Equation IV.18a)}$$

$$\Rightarrow m_{total} - m_{smallApert} = m^*_{total} - m^*_{smallApert} \qquad \text{(Equation IV.18b)}$$

$$\Rightarrow m_{total} - m_{smallApert} = \Delta^*_m \qquad \text{(Equation IV.18c)}$$

$$\Rightarrow m_{total} = m_{smallApert} + \Delta^*_m \qquad \text{(Equation IV.18d)}$$

where $\mathrm{F}^*_{smallAper}$ is the flux estimated in a small aperture of a star, F^*_{total} is the star's total flux, $\mathrm{F}^{*obj}_{smallAper}$ is the flux estimated in a small aperture of a faint object, and, F^{obj}_{total} is the object's total flux.

IV.3   Observing strategy

Once observational time is scheduled, we have to define an observing strategy or observational planning. The first step is to select the targets. Targets have to be selected according to: i) their visibilities, and ii) their brightnesses. First of all, we have to check the visibility (or observability) of each target from the observatory. An example of visibility curves is shown in Figure 38. Such visibility curves have been plotted for an observing run with the 1.5 m OSN telescope in February 2013. Several programs that show the observability of objects can be used, for example: http://catserver.ing.iac.es/staralt/. Target coordinates (right ascension (α) and declination (δ)) are generated thanks to ephemeris generator, such as: Minor Planet & Comet Ephemeris Service available at http://www.minorplanetcenter.net/iau/MPEph/MPEph.html, or the Jet Propulsion Laboratory HORIZONS Web-Interface at http://ssd.jpl.nasa.gov/horizons.cgi, or the Institut de Mécanique Céleste et de Calcul des Ephémérides (IMCCE, Institute of Celestial Mechanics and Ephemeris Calculator) ephemeris generator at http://www.imcce.fr/en/ephemerides/formulaire/form_ephepos.php. It is recommended to select targets visible during several hours per night, typically more than 4 h. Obviously, the perfect approach is to select targets visible over the entire night. We also have to check the target altitude along the night. In fact, it is not recommended to observe below 30° of altitude or at air masses higher than 2, because the signal-to-noise ratio (S/N) of the target and of the reference stars are too low to obtain valuable results.

The second criterion of the targets selection is their brightnesses. In fact, we are mostly using the 1.5 m OSN telescope. So, very faint objects cannot be observed with such a class of telescopes with the needed S/N, thus we restricted our target list to objects brighter than 21 mag in the V-band. In conclusion, we are limited to objects with a visual magnitude of 21 mag in the V-band for the 2 m class telescope. For the smallest telescope (ASH2), we are limited to ∼18 mag in the V-band. With a 4 m class telescope, we can observe up to 22.5 mag in the V-band.

In this work, we studied TNO temporal variability, and so one have to compare the magnitude variations of the target with star references. Preferentially, reference stars have to be the same during an entire observational run. Generally, the observational runs were over one week (or near), and so we had to keep as long as possible the target in the same filed of view to use the same reference stars. The drift rate of TNOs are typically low, ∼2″/h, but the drift rate of centaurs is higher than that of TNOs, typically ∼10″/h. For example, the 1.5 m OSN telescope has a field of view of $7.8'\times7.8'$. As the drift rate of TNOs is low, to keep the target in the same field of view over a week is possible. However, in the case of centaurs with a higher drift rate, it is impossible to keep the target in the same field of view over a week. In that case, we try to keep the target during at least two consecutive nights, then, if more data are required, the field of view has to be moved to re-observe the target and keep few reference stars in both fields of view. In fact, it is better to keep few reference stars in common in both field of view instead of having two different fields of view and, so two different sets of reference stars. It is convenient to check the field of view
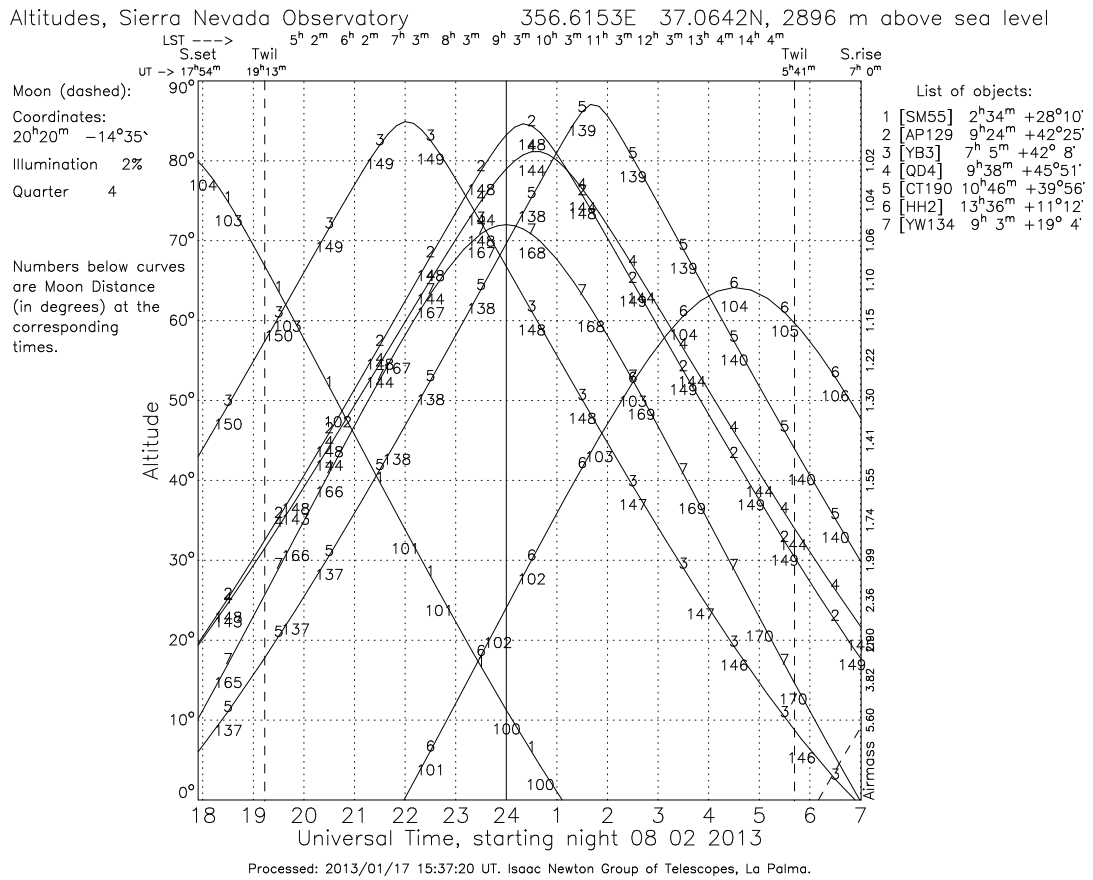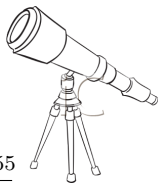
Figure 38: Example of visibility curves for an observational run plan with the 1.5 m OSN telescope. Here are the visibility curves for February, 8th 2013. For example, the first object indicated with the number "1" on the visibility curves is only visible during few hours at the beginning of the night. On the other hand, the second object, with the number "2" is visible the entire night. The curves indicate the altitude above the horizon versus universal time on February 8th, 2013.

of each target along an observational run. In fact, if the target will be near a galaxy, nebula, very bright star(s), or in an area crowded of stars, estimated flux of the target as well as the reference stars fluxes will be contaminated and so we prefer to observe another target. One can check the field of view over an observational run using, for example the Space Telescope Science Institute (STScI) Digitized Sky Survey at http://archive.stsci.edu/cgi-bin/dss_form or the Aladin Sky Atlas at http://aladin.u-strasbg.fr/.

Once the observable targets are selected, we have to estimate the exposure time required. Exposure times were chosen by considering two main factors. On one hand, it had to be long enough to achieve a S/N sufficient to study the observed object (typically, S/N>20). On the other hand, exposure time had to be short enough to avoid elongated images of the target (when the telescope was tracked at sidereal speed) or elongated field stars (if the telescope was tracked at the TNO rate of motion). The first step to estimate the exposure time is to check the visual magnitude of the target. For this, one can use the ephemeris generators introduced previously. Unfortunately, one must point that visual magnitudes proposed by such generators are only estimations and only in the V-band. If we want to observe with filter(s), we have to convert the V-band magnitude (m_V), such as: m_B-m_V = 0.99±0.17, m_V-m_R = 0.63±0.12, and m_V-m_I = 1.19±0.24 (Hainaut and Delsanti, 2002). When an absolute calibration is needed, the use of filter is not optional. For example, solar phase curve or color variation studies need an absolute calibration. As our main
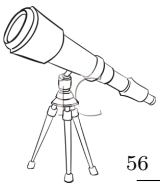
goal is to study the short-term variability of TNOs via relative photometry, the use of unfiltered images without absolute calibration is not a problem for our work. That is why the majority of our observations were performed without filter. The main interest of using no filter is to maximize the S/N. In some cases, we had to use filters. We performed some observations with R, and near-infrared blocking filters (nIR-Block hereinafter). These filters were chosen to maximize the S/N on TNOs while minimizing the fringing that appears at longer wavelengths on images from certain instruments. Sometimes, several filters are mounted by default in the filter wheel and there is not a "clear" position to observe without filter. In that case, we use the R filter. Once we know the magnitude of the target in the filter(s) that we plan to use, we can use the time exposure calculator corresponding of the detector and telescope that we will use. For example, the CAHA exposure time calculator is at `http://www.caha.es/prada/tcl/index.html`, the TNG exposure time calculator is at `http://www.tng.iac.es/observing/expcalc/imaging/`, the ESO exposure time calculator is at `http://www.eso.org/observing/etc/`, or the INT exposure time calculator is at `http://catserver.ing.iac.es/signal/`. Apart from the filter used, the exposure time varies according to the seeing, the airmass, and the brightness of the sky.

There are two options for the telescope tracking: i) the sideral tracking or ii) the non-sideral tracking, i.e. tracking at the TNO rate of motion. For this work, we always chose to track the telescope at sidereal speed.

As our main goal is to study the short-term variability of TNOs via relative photometry, we need dark night with a moon illumination <30 %. We generally, selected 2 (during summer night) to 3 (during winter night) objects per night. Typically, after the calibration data acquisition a block of 5 to 10 images of a first target is carried out, then a block of 5 to 10 images of a second target. This sequence of observations is repeated over the night. After the data reduction of the data carried out during the night, various decisions have to be made. We have to check the data quality, the data quantity and finally, to decide if more data are required in the following night.

In this work, we tried two different approaches to study the short-term variability of TNOs: i) regular observing run using just one telescope, and ii) coordinated campaign with two telescopes. In the next section, we will describe both approaches.

IV.4 Observing runs

IV.4.1 Regular observing runs

Our group at the Instituto de Astrofísica de Andalucía (IAA, CSIC) started a vast program on lightcurves (light intensity of an object as a function of time. See next chapter for more details) of the TNOs in 2001 in Spain.

Normally, observational campaigns are carried out with only one telescope. Under perfect conditions and if the selected target is visible the entire night, we can observe it during ∼5 h (summer nights) to ∼10 h (winter nights). Preferentially, we selected for observing runs presented in this work, targets visible during most of the night. Unfortunately, sometimes it was only possible to observe selected targets during few hours per night. On the other hand, the mean rotational period of the TNOs is around 8 h (see VII.2.1), and so during one summer night, we are not covering an entire target rotation. We must also point out that lots of TNOs have a nearly flat lightcurve (lightcurve with low peak-to-peak amplitude), and so lots of observations during several nights are needed to propose a reliable study.

IV.4.2 Our first coordinated campaign

A coordinated campaign is based on the coordination of observational runs with various telescopes all around the world. Using telescopes with similar characteristics in different continents, allows us to observe a target "continuously". In other words, if we can monitor our targets during a long time, we can detect long rotation periods and we can minimize the 24 h-aliases effect (see
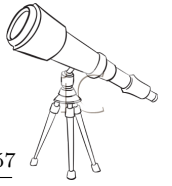
Section V.2.6). This had never been done for TNO time series studies.

In July 2009, we carried out the first coordinated campaign involving Europe and South America. Typically, an observational night of July in Europe starts around 22 h UT and finishes at 5 h UT, whereas an observational night in South America starts around 0 h UT and finishes at 10 h UT. Under perfect conditions and if the target is visible in both sites during the entire night, we have five extra hours of observational time. By using this approach, we have a continuous time coverage of about 15 h, thereby addressing some of the biases against long periods.

For our coordinated campaign, we used two similar telescopes: the Telescopio Nazionale Galileo (TNG) and the New Techonology Telescope (NTT) (see III.1.3.3 and III.1.5.1). Both telescopes have the same diameter and present the same design. In fact, the TNG was thought with the same design and the same optical innovations than the NTT.

For this coordinated campaign, our main concern was to observe objects visible from both sites. We carefully coordinated the observations, to match the field of view of both telescopes, and during all the campaign (Figure 39). The main goal to match exactly (or same similar as possible) the field of view was to use the same star references in both sites for the data reduction.
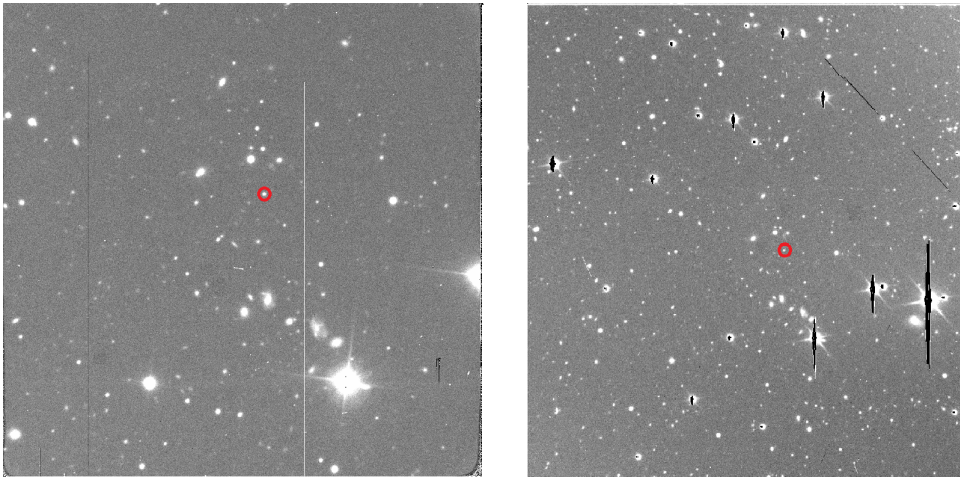
Figure 39: Example of fields of view obtained during our coordinated campaign. The target (145480) 2005 TB$_{190}$ is indicated by a red circle in the field of view obtained with the NTT (left panel) and with the TNG (right panel).

IV.4.3 Purposes of a coordinated campaign

Less than 5% of the known TNOs have a well determined rotational period. Sheppard, Lacerda and Ortiz (2008) and Thirouin et al. (2010) pointed out that the sample of studied objects is highly biased towards bright objects, large variability amplitudes and short rotational periods. Just 10 % of the rotational periods published are larger than 10 h. The majority of lightcurve amplitudes and rotational periods are published with large uncertainties or, sometimes, they are just estimations or limiting values. The sample of studied TNOs is essentially composed of bright (visual magnitude <22 mag) and large objects.

We can enumerate various reasons in order to explain some of these biases. First, we must point out observational limitations. A reliable study of TNO rotational properties requires a lot of observational time on medium to large telescope. This causes a bias toward brighter objects, but also short period and large amplitude. Another class of limitations is due to reduction problems. A reliable photometric study needs an effective data reduction. Determining low amplitude lightcurves and/or detecting long rotation periods are very time consuming and require lots of
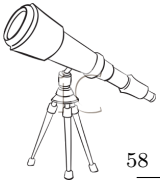
observing time. Furthermore, 24-h aliases frequently complicate the analysis of time series pho-
tometry. To help debias the sample of studied objects, and minimize the 24-h aliases effect, longer
term monitoring is needed.

IV.5   Observing log

Relevant geometric information about the observed objects at the dates of observations, the number
of images and filters used are summarized in Table 1.

Table 1: In this table, we summarize all observational runs analyzed and presented in this work. For each
observed target, the dates of observations (format MM/DD/YYYY), the number of images (#images)
carried out, the heliocentric (r_h) and geocentric (Δ) distances of the object and the corresponding phase
angle (α), what filter was used and the site of observations are indicated. Distances are expressed in
Astronomical Units [AU], and phase angle in degrees. The Institut de Mécanique Céleste et de Calcul des
Ephémérides (IMCCE, Institute of Celestial Mechanics and Ephemeris Calculator) ephemeris generator
has been used for the geometric data. For targets with various designations or official name, all possibilities
to name the target are proposed. "OSN" stands for Observatory of Sierra Nevada, "NTT" stands for New
Technology Telescope, and "TNG" for Telescopio Nazionale Galileo.

Object	Date	#images	r_h[AU]	Δ [AU]	α[°]	Filter	Telescope
(24835) 1995 SM$_{55}$							
	09/12/2012	9	38.437	37.892	1.27	Clear	OSN
	09/13/2012	20	38.436	37.878	1.26	Clear	OSN
	09/15/2012	23	38.436	37.851	1.23	Clear	OSN
	09/16/2012	22	38.436	37.837	1.21	Clear	OSN
	10/15/2012	10	38.430	37.545	0.69	Clear	OSN
	10/16/2012	61	38.430	37.538	0.67	Clear	OSN
(15874) 1996 TL$_{66}$							
	12/15/2004	16	35.140	34.343	0.95	Clear	OSN
	12/16/2004	16	35.141	34.354	0.98	Clear	OSN
	12/17/2004	30	35.141	34.365	1.00	Clear	OSN
	12/18/2004	14	35.141	34.376	1.02	Clear	OSN
(52872) 1998 SG$_{35}$ (Okyrhoe)							
	12/05/2007	26	5.804	5.626	9.73	Clear	OSN
	12/06/2007	33	5.804	5.610	9.71	Clear	OSN
	12/07/2007	19	5.804	5.594	9.69	Clear	OSN
	12/08/2007	14	5.803	5.578	9.67	Clear	OSN
	12/10/2007	40	5.803	5.546	9.61	Clear	OSN
	12/11/2007	33	5.803	5.530	9.58	Clear	OSN
	12/12/2007	35	5.803	5.517	9.54	Clear	OSN
	12/13/2007	33	5.803	5.500	9.51	Clear	OSN
	12/14/2007	38	5.803	5.483	9.47	Clear	OSN
	12/15/2007	38	5.803	5.468	9.42	Clear	OSN
(26375) 1999 DE$_9$							
	04/22/2009	20	36.079	35.320	1.06	Clear	OSN
	04/23/2009	5	36.080	35.332	1.08	Clear	OSN
(40314) 1999 KR$_{16}$							
	07/26/2009	16	36.034	35.913	1.61	R	NTT
	07/27/2009	12	36.034	35.929	1.61	R	NTT
(44594) 1999 OX$_3$							
	07/25/2009	18	22.433	21.545	1.29	R	NTT
	07/26/2009	23	22.431	21.536	1.25	R	NTT
	07/27/2009	19	22.430	21.527	1.21	R	NTT
(38628) 2000 EB$_{173}$ (Huya)							
	06/07/2010	21	28.676	27.852	1.20	Clear	OSN
	06/10/2010	9	28.676	27.880	1.28	Clear	OSN
	06/11/2010	19	28.676	27.890	1.30	Clear	OSN
	05/25/2012	43	28.578	27.632	0.74	R	1.23 m Calar Alto telescope
	05/26/2012	8	28.578	27.637	0.77	R	1.23 m Calar Alto telescope
	05/29/2012	39	28.578	27.651	0.84	R	1.23 m Calar Alto telescope
	06/12/2012	15	28.576	27.752	1.21	Clear	OSN
	06/14/2012	19	28.576	27.771	1.26	Clear	OSN
(20000) 2000 WR$_{106}$ (Varuna)							
	01/05/2005	22	43.248	42.266	0.06	R	OSN
	01/07/2005	13	43.249	42.267	0.09	R	OSN
	01/31/2005	27	43.252	42.378	0.61	R	OSN
	02/01/2005	5	43.252	42.387	0.63	R	OSN
	02/09/2005	10	43.253	42.462	0.79	R	OSN
	02/10/2005	11	43.253	42.473	0.81	R	OSN
	10/13/2009	10	43.483	43.494	1.31	Clear	OSN
	10/14/2009	10	43.483	43.477	1.31	Clear	OSN
	10/15/2009	16	43.483	43.460	1.31	Clear	OSN
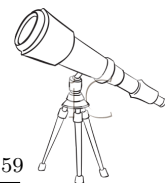
Object	Date	#images	r_h[AU]	Δ [AU]	α[°]	Filter	Telescope
	10/16/2009	15	43.483	43.443	1.31	Clear	OSN
	10/15/2009	6	43.483	43.426	1.31	R	2.2 m Calar Alto telescope
	10/17/2009	11	43.484	43.409	1.31	R	2.2 m Calar Alto telescope
	10/18/2009	14	43.484	43.392	1.31	R	2.2 m Calar Alto telescope
	04/07/2010	10	43.507	43.462	1.32	R	2.2 m Calar Alto telescope
	04/08/2010	13	43.508	43.479	1.32	Clear	2.2 m Calar Alto telescope
	04/09/2009	6	43.508	43.496	1.32	Clear	OSN
	04/10/2009	4	43.508	43.513	1.32	Clear	OSN
	01/31/2011	21	43.550	42.624	0.45	Clear	OSN
	02/02/2011	34	43.550	42.636	0.49	Clear	OSN
	01/29/2012	64	43.601	42.663	0.40	Clear	OSN
2001 QF$_{298}$							
	07/26/2009	15	43.057	42.440	1.08	R	NTT
	07/27/2009	12	43.057	42.426	1.07	R	NTT
(275809) 2001 QY$_{297}$							
	07/24/2009	5	43.142	42.168	0.39	R	TNG
	07/24/2009	22	43.142	42.168	0.38	R	NTT
	07/25/2009	10	43.143	42.166	0.36	R	NTT
	08/05/2010	10	43.223	42.215	0.15	R	NTT
	08/13/2010	7	43.225	42.212	0.04	R	NTT
	08/14/2010	6	43.225	42.213	0.06	R	NTT
(148975) 2001 XA$_{255}$							
	02/24/2009	39	9.352	8.583	3.98	Clear	OSN
	02/25/2009	31	9.352	8.573	3.90	Clear	OSN
(126154) 2001 YH$_{140}$							
	12/15/2004	7	36.437	35.572	0.75	Clear	OSN
	12/16/2004	10	36.437	35.564	0.72	Clear	OSN
	12/17/2004	12	36.437	35.556	0.70	Clear	OSN
	12/18/2004	6	36.437	35.548	0.67	Clear	OSN
	12/19/2004	10	36.438	35.541	0.65	Clear	OSN
(55565) 2002 AW$_{197}$							
	02/01/2003	100	47.272	46.295	0.16	Clear	OSN
	02/02/2003	66	47.272	46.294	0.15	Clear	OSN
	01/19/2004	20	47.158	46.221	0.37	Clear	OSN
	01/21/2004	50	47.158	46.211	0.33	Clear	OSN
	01/22/2004	30	47.157	46.207	0.31	Clear	OSN
	01/23/2004	45	47.157	46.202	0.29	Clear	OSN
	01/24/2004	30	47.157	46.199	0.28	Clear	OSN
	01/25/2004	30	47.156	46.195	0.26	Clear	OSN
(42355) 2002 CR$_{46}$ (Typhon)							
	01/28/2003	109	17.892	16.909	0.18	Clear	OSN
	02/02/2003	69	17.889	16.905	0.16	Clear	OSN
	03/04/2003	91	17.871	17.039	1.77	Clear	OSN
	03/06/2003	87	17.870	17.057	1.87	Clear	OSN
	03/09/2003	51	17.869	17.086	2.00	Clear	OSN
(55576) 2002 GB$_{10}$ (Amycus)							
	03/08/2003	67	15.188	14.328	1.93	Clear	OSN
	03/09/2003	64	15.188	14.320	1.87	Clear	OSN
(307251) 2002 KW$_{14}$							
	07/24/2009	3	40.655	40.149	1.25	R	TNG
	07/25/2009	16	40.656	40.167	1.26	R	NTT
	07/26/2009	18	40.656	40.182	1.27	R	NTT
	07/27/2009	16	40.657	40.197	1.28	R	NTT
(50000) 2002 LM$_{60}$ (Quaoar)							
	05/21/2003	30	43.406	42.421	0.31	Clear	OSN
	05/22/2003	77	43.406	42.418	0.29	Clear	OSN
	05/23/2003	98	43.406	42.415	0.27	Clear	OSN
	06/17/2003	18	43.404	42.430	0.38	Clear	OSN
	06/18/2003	38	43.404	42.434	0.40	Clear	OSN
	06/19/2003	62	43.404	42.438	0.42	Clear	OSN
	06/20/2003	65	43.404	42.443	0.44	Clear	OSN
	06/21/2003	45	43.404	42.448	0.46	Clear	OSN
	06/22/2003	12	43.404	42.454	0.48	Clear	OSN
	07/01/2011	34	43.123	42.165	0.46	R	TNG
	07/02/2011	26	43.123	42.170	0.48	R	TNG
	07/04/2011	6	43.123	46.182	0.52	R	TNG
(307261) 2002 MS$_4$							
	08/05/2005	15	47.420	46.747	0.92	Clear	OSN
	08/06/2005	15	47.420	46.759	0.94	Clear	OSN
	06/30/2011	39	47.120	42.143	0.35	R	TNG
	07/01/2011	15	47.120	42.145	0.35	R	TNG
	07/02/2011	27	47.119	42.146	0.36	R	TNG
	07/04/2011	6	47.119	46.151	0.38	R	TNG
(84522) 2002 TC$_{302}$							
	10/15/2009	15	46.552	45.589	0.32	nIR-Block	2.2 m Calar Alto telescope
	10/17/2009	21	46.551	45.582	0.28	nIR-Block	2.2 m Calar Alto telescope
	09/09/2010	23	46.331	45.684	0.96	Clear	OSN
	09/11/2010	11	46.329	45.656	0.93	Clear	OSN
	12/01/2010	6	46.275	45.463	0.70	Clear	IAC-80
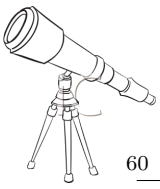
Object	Date	#images	r_h[AU]	Δ [AU]	α[°]	Filter	Telescope
(55636) 2002 TX$_{300}$							
	08/07/2003	127	40.824	40.305	1.23	Clear	OSN
	08/08/2003	177	40.825	40.292	1.22	Clear	OSN
	08/09/2003	173	40.825	40.279	1.21	Clear	OSN
	10/18/2009	19	41.534	40.615	0.54	Clear	2.2 m Calar Alto telescope
	09/06/2010	14	41.639	40.901	0.95	Clear	OSN
	09/07/2010	7	41.639	40.891	0.94	Clear	OSN
	09/08/2010	25	41.639	40.884	0.92	Clear	OSN
	09/09/2010	19	41.640	40.875	0.91	Clear	OSN
	09/10/2010	36	41.640	40.867	0.90	Clear	OSN
	09/11/2010	5	41.640	40.857	0.88	Clear	OSN
(55637) 2002 UX$_{25}$							
	01/05/2008	20	41.964	41.712	1.30	Clear	2.2 m Calar Alto telescope
	01/06/2008	22	41.963	41.728	1.31	Clear	2.2 m Calar Alto telescope
	01/07/2008	21	41.963	41.745	1.31	Clear	2.2 m Calar Alto telescope
(55638) 2002 VE$_{95}$							
	01/19/2004	10	28.016	27.651	1.88	Clear	OSN
	12/14/2004	5	28.050	27.202	1.04	Clear	OSN
	12/15/2004	10	28.050	27.211	1.07	Clear	OSN
	12/16/2004	15	28.050	27.220	1.10	Clear	OSN
	12/17/2004	18	28.050	27.228	1.12	Clear	OSN
	12/18/2004	5	28.051	27.239	1.15	Clear	OSN
	12/19/2004	50	28.051	27.248	1.18	Clear	OSN
2002 VT$_{130}$							
	11/01/2011	31	42.926	42.090	0.72	R	TNG
(1199791) 2002 WC$_{19}$							
	01/20/2004	15	43.908	43.315	1.03	Clear	OSN
	01/24/2004	30	43.906	43.369	1.08	Clear	OSN
	01/25/2004	50	43.905	43.382	1.10	Clear	OSN
(208996) 2003 AZ$_{84}$							
	12/29/2003	28	45.833	44.879	0.30	Clear	OSN
	12/31/2003	18	45.833	44.873	0.28	Clear	OSN
	01/19/2004	15	45.829	44.871	0.28	Clear	OSN
	12/14/2004	5	45.765	44.892	0.57	Clear	OSN
	12/15/2004	19	45.765	44.884	0.55	Clear	OSN
	12/16/2004	20	45.765	44.877	0.54	Clear	OSN
	12/17/2004	25	45.765	44.870	0.52	Clear	OSN
	12/18/2004	4	45.764	44.863	0.50	Clear	OSN
	12/19/2004	20	45.764	44.856	0.48	Clear	OSN
	02/04/2011	34	45.270	44.357	0.48	Clear	2.2 m Calar Alto telescope
	02/05/2011	34	45.270	44.362	0.49	Clear	2.2 m Calar Alto telescope
(120061) 2003 CO$_1$							
	01/19/2004	5	11.445	10.811	3.87	Clear	OSN
	01/21/2004	15	11.444	10.798	3.82	Clear	OSN
	01/22/2004	20	11.443	10.785	3.77	Clear	OSN
	01/23/2004	13	11.442	10.773	3.72	Clear	OSN
	01/24/2004	30	11.441	10.760	3.67	Clear	OSN
	01/25/2004	23	11.440	10.748	3.62	Clear	OSN
	04/19/2004	71	11.354	10.692	3.93	Clear	OSN
	04/23/2004	52	11.351	10.735	4.13	Clear	OSN
	04/25/2004	60	11.349	10.758	4.23	Clear	OSN
	04/26/2004	53	11.348	10.769	4.27	Clear	OSN
	04/27/2004	10	11.347	10.780	4.31	Clear	OSN
(136108) 2003 EL$_{61}$ (Haumea)							
	01/12/2007	6	51.175	51.050	1.09	R	2.2 m Calar Alto telescope
	01/13/2007	7	51.175	51.032	1.09	R	2.2 m Calar Alto telescope
	01/14/2007	8	51.175	51.017	1.09	R	2.2 m Calar Alto telescope
	01/15/2007	11	51.175	51.002	1.09	R	2.2 m Calar Alto telescope
	01/16/2007	4	51.175	50.986	1.08	R	2.2 m Calar Alto telescope
	01/17/2007	4	51.175	50.971	1.08	R	2.2 m Calar Alto telescope
	01/20/2010	10	51.024	50.809	1.08	Luminance	ASH2
	01/21/2010	10	51.023	50.793	1.08	Luminance	ASH2
	01/23/2010	10	51.023	50.763	1.07	Luminance	ASH2
	01/26/2010	10	51.023	50.718	1.05	Luminance	ASH2
	01/28/2010	36	51.023	50.693	1.05	R	1.23 m Calar Alto telescope
	01/30/2010	17	51.022	50.663	1.03	R	1.23 m Calar Alto telescope
	01/31/2010	34	51.022	50.650	1.03	R	1.23 m Calar Alto telescope
	04/30/2012	32	50.896	50.074	0.66	R	1.23 m Calar Alto telescope
	05/01/2012	69	50.896	50.079	0.67	R	1.23 m Calar Alto telescope
	05/02/2012	68	50.896	50.085	0.68	R	1.23 m Calar Alto telescope
	05/03/2012	33	50.896	50.091	0.69	R	1.23 m Calar Alto telescope
(120132) 2003 FY$_{128}$							
	02/09/2005	19	38.063	37.366	1.06	Clear	OSN
	02/10/2005	28	38.063	37.354	1.04	Clear	OSN
	02/11/2005	44	38.063	37.342	1.03	Clear	OSN
	02/12/2005	44	38.064	37.331	1.01	Clear	OSN
	03/09/2005	13	38.071	37.124	0.45	Clear	OSN
(174567) 2003 MW$_{12}$							
	05/27/2006	13	48.189	47.234	0.40	Clear	OSN
	05/28/2006	14	48.186	47.233	0.41	Clear	OSN
	06/05/2006	11	48.186	47.240	0.44	Clear	OSN
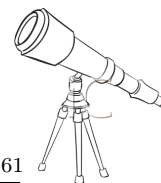
Object	Date	#images	r_h[AU]	Δ [AU]	α[°]	Filter	Telescope
	06/06/2006	29	48.185	47.242	0.45	Clear	OSN
	06/07/2006	22	48.185	47.245	0.46	Clear	OSN
	06/23/2006	5	48.180	47.319	0.65	Clear	OSN
	06/24/2006	10	48.180	47.326	0.66	Clear	OSN
	04/12/2008	10	47.968	47.307	0.92	Clear	OSN
	04/13/2008	17	47.967	47.295	0.89	Clear	OSN
	04/14/2008	10	47.967	47.284	0.88	Clear	OSN
	04/26/2008	36	47.963	47.158	0.73	Clear	OSN
	04/27/2008	27	47.963	47.150	0.71	Clear	OSN
	07/24/2009	6	47.812	47.235	1.01	R	TNG
	07/25/2009	12	47.812	47.247	1.02	R	TNG
	07/27/2009	7	47.812	47.260	1.03	R	TNG
	07/03/2011	27	47.573	46.746	0.72	R	TNG
	07/04/2011	29	47.573	46.754	0.73	R	TNG
	07/28/2011	26	47.565	47.002	1.03	Clear	OSN
	07/29/2011	30	47.564	47.015	1.04	Clear	OSN
	07/30/2011	9	47.564	47.029	1.05	Clear	OSN
	06/13/2012	8	47.456	46.519	0.48	Clear	OSN
	06/14/2012	6	47.456	46.522	0.49	Clear	OSN
	06/15/2012	32	47.455	46.524	0.50	Clear	OSN
(120178) 2003 OP$_{32}$							
	08/05/2005	15	41.059	40.111	0.51	Clear	OSN
	08/06/2005	10	41.059	40.109	0.50	Clear	OSN
	08/07/2005	15	41.060	40.107	0.49	Clear	OSN
	08/10/2005	15	41.060	40.103	0.47	Clear	OSN
	10/03/2005	10	41.074	40.440	1.09	Clear	OSN
	10/04/2005	21	41.075	40.452	1.10	Clear	OSN
	10/05/2005	24	41.075	40.465	1.11	Clear	OSN
	09/16/2007	12	41.265	40.418	0.76	Clear	OSN
	09/17/2007	10	41.266	40.427	0.78	Clear	OSN
	08/29/2011	10	41.652	40.682	0.39	Schott KG1 [5]	2.2 m Calar Alto telescope
	08/30/2011	15	41.652	40.684	0.40	Schott KG1	2.2 m Calar Alto telescope
	08/31/2011	5	41.652	40.866	0.41	Schott KG1	2.2 m Calar Alto telescope
(84922) 2003 VS$_2$							
	12/22/2003	34	36.431	35.654	0.96	Clear	OSN
	12/26/2003	21	36.431	35.696	1.04	Clear	OSN
	12/28/2003	26	36.431	35.718	1.08	Clear	OSN
	01/04/2004	109	36.431	35.803	1.20	Clear	OSN
	01/19/2004	19	36.431	36.015	1.41	Clear	OSN
	01/20/2004	30	36.431	36.030	1.42	Clear	OSN
	01/21/2004	40	36.431	36.046	1.43	Clear	OSN
	01/22/2004	50	36.431	36.061	1.44	Clear	OSN
	09/04/2010	16	36.477	36.401	1.58	Clear	OSN
	09/05/2010	12	36.477	36.385	1.58	Clear	OSN
	09/06/2010	12	36.477	36.367	1.58	Clear	OSN
	09/07/2010	10	36.478	36.351	1.57	Clear	OSN
	09/07/2010	10	36.478	36.354	1.57	R	NOT
	09/08/2010	17	36.478	36.335	1.57	Clear	OSN
	09/08/2010	8	36.478	36.338	1.57	R	NOT
(136204) 2003 WL$_7$							
	12/05/2007	51	15.201	14.300	1.55	Clear	OSN
	12/06/2007	32	15.201	14.307	1.61	Clear	OSN
	12/07/2007	20	15.200	14.313	1.67	Clear	OSN
	12/08/2007	40	15.200	14.321	1.72	Clear	OSN
	12/10/2007	35	15.199	14.336	1.84	Clear	OSN
	12/11/2007	44	15.199	14.343	1.90	Clear	OSN
	12/13/2007	40	15.198	14.360	2.01	Clear	OSN
	12/14/2007	41	15.198	14.369	2.06	Clear	OSN
(90482) 2004 DW (Orcus)							
	03/08/2004	34	47.612	46.746	0.59	R	OSN
	03/09/2004	24	47.612	46.752	0.60	R	OSN
	03/10/2004	32	47.612	46.759	0.62	R	OSN
	03/11/2004	16	47.612	46.768	0.63	R	OSN
	03/23/2004	23	47.614	46.874	0.81	R	OSN
	04/22/2004	39	47.619	47.267	1.14	R	OSN
	04/23/2004	53	47.619	47.282	1.15	R	OSN
	04/25/2004	48	47.619	47.313	1.16	R	OSN
	04/26/2004	42	47.620	47.329	1.16	R	OSN
	04/27/2004	37	47.620	47.345	1.17	R	OSN
	12/15/2009	10	47.525	47.883	1.10	Luminance	ASH
	12/17/2009	10	47.495	47.883	1.09	Luminance	ASH
	12/18/2009	10	47.480	47.884	1.08	Luminance	ASH
	12/20/2009	10	47.450	47.884	1.06	Luminance	ASH
	12/22/2009	10	47.421	47.884	1.04	Luminance	ASH
	12/23/2009	10	47.407	47.884	1.03	Luminance	ASH
	12/24/2009	10	47.393	47.884	1.02	Luminance	ASH
	12/25/2009	10	47.379	47.884	1.01	Luminance	ASH
	12/27/2009	10	47.352	47.885	0.99	Luminance	ASH
	01/08/2010	10	47.203	47.886	0.85	Luminance	ASH

---

[5] The Schott KG1 filter is a near-infrared blocking filter.
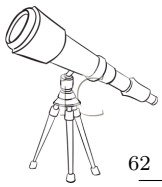
Object	Date	#images	r_h[AU]	Δ [AU]	$\alpha[°]$	Filter	Telescope
	01/09/2010	10	47.191	47.886	0.84	Luminance	ASH
	01/10/2010	10	47.180	47.886	0.83	Luminance	ASH
	01/11/2010	10	47.170	47.886	0.81	Luminance	ASH
2004 NT$_{33}$							
	07/25/2009	14	38.164	37.327	0.87	R	TNG
	07/26/2009	11	38.164	37.234	0.87	R	TNG
	07/27/2009	21	38.164	37.321	0.86	R	TNG
	10/13/2009	15	38.185	37.783	1.38	Clear	OSN
	10/14/2009	20	38.185	37.796	1.39	Clear	OSN
	10/15/2009	15	38.185	37.810	1.39	Clear	OSN
	10/16/2009	15	38.186	37.824	1.40	Clear	OSN
	10/17/2009	10	38.186	37.837	1.41	Clear	OSN
	10/18/2009	20	38.186	37.851	1.41	Clear	OSN
(307982) 2004 PG$_{115}$							
	09/08/2010	11	36.880	36.005	0.78	Clear	OSN
	09/09/2010	6	36.881	36.013	0.80	Clear	OSN
	09/10/2010	10	36.881	36.020	0.82	Clear	OSN
	09/11/2010	20	36.881	36.029	0.84	Clear	OSN
(120347) 2004 SB$_{60}$ (Salacia)							
	06/30/2011	4	44.234	43.991	1.28	R	TNG
	07/01/2011	22	44.235	43.975	1.28	R	TNG
	07/03/2011	27	44.235	43.946	1.27	R	TNG
	07/04/2011	20	44.235	43.932	1.26	R	TNG
	11/31/2011	42	44.263	43.617	0.98	R	TNG
	09/13/2012	26	44.335	43.414	0.53	Clear	OSN
	09/15/2012	37	44.336	43.413	0.52	Clear	OSN
	10/12/2012	15	44.342	43.514	0.73	Clear	OSN
	10/15/2012	40	44.342	43.537	0.77	Clear	OSN
(144897) 2004 UX$_{10}$							
	09/14/2007	10	38.824	38.016	0.89	Clear	OSN
	09/17/2007	12	38.835	37.988	0.83	Clear	OSN
	11/30/2007	52	38.834	38.103	0.99	Clear	OSN
(230965) 2004 XA$_{192}$							
	10/13/2009	12	35.799	35.507	1.53	Clear	OSN
	10/14/2009	10	35.799	35.494	1.52	Clear	OSN
	10/15/2009	10	35.799	35.481	1.52	Clear	OSN
	10/16/2009	10	35.799	35.467	1.51	Clear	OSN
	10/17/2009	24	35.799	35.454	1.50	Clear	OSN
	10/18/2009	13	35.798	35.439	1.49	Clear	OSN
	12/17/2009	33	35.787	34.978	0.91	R	3.5 m Calar Alto telescope
(308193) 2005 CB$_{79}$							
	01/06/2008	22	40.171	39.337	0.75	Clear	2.2 m Calar Alto telescope
	01/07/2008	15	40.171	39.328	0.73	Clear	2.2 m Calar Alto telescope
	05/01/2008	14	40.131	40.073	1.44	Clear	OSN
	05/04/2008	18	40.130	40.122	1.44	Clear	OSN
	12/26/2008	38	40.048	39.333	0.97	Clear	OSN
	02/24/2009	29	40.032	39.122	0.57	Clear	OSN
	02/25/2009	90	40.031	39.128	0.59	Clear	OSN
(136472) 2005 FY$_9$ (Makemake)							
	03/01/2006	21	51.926	51.076	0.57	R	OSN
	03/02/2006	9	51.926	51.073	0.56	R	OSN
	04/07/2006	145	51.932	51.150	0.69	R	OSN
	04/08/2006	23	51.933	51.157	0.70	R	OSN
	04/10/2006	84	51.933	51.171	0.72	R	OSN
	04/12/2006	55	51.933	51.188	0.75	R	OSN
	05/27/2006	15	51.941	51.716	1.09	R	OSN
	05/28/2006	20	51.941	51.731	1.10	R	OSN
	05/29/2006	5	51.941	51.744	1.10	R	OSN
	06/05/2006	5	51.942	51.846	1.12	R	OSN
	06/06/2006	10	51.942	51.863	1.12	R	OSN
	06/07/2006	35	51.942	51.877	1.12	R	OSN
	06/10/2006	10	51.943	51.922	1.12	R	OSN
	12/14/2006	31	51.973	51.974	1.08	R	OSN
	12/15/2006	36	51.974	51.960	1.08	R	OSN
	12/16/2006	30	51.974	51.945	1.08	R	OSN
	12/17/2006	18	51.974	51.930	1.08	R	OSN
	12/18/2006	5	51.974	51.915	1.08	R	OSN
	01/11/2007	9	51.978	51.570	0.99	R	2.2 m Calar Alto telescope
	01/12/2007	10	51.978	51.557	0.98	R	2.2 m Calar Alto telescope
	01/13/2007	7	51.978	51.544	0.98	R	2.2 m Calar Alto telescope
	01/14/2007	9	51.978	51.531	0.97	R	2.2 m Calar Alto telescope
	01/15/2007	4	51.978	51.518	0.96	R	2.2 m Calar Alto telescope
	01/16/2007	5	51.979	51.505	0.95	R	2.2 m Calar Alto telescope
	03/09/2007	10	51.987	51.122	0.54	R	OSN
	03/10/2007	20	51.987	51.121	0.54	R	OSN
	03/11/2007	32	51.987	51.121	0.54	R	OSN
	03/12/2007	25	51.987	51.120	0.54	R	OSN
	03/21/2012	94	52.257	51.388	0.54	V	OSN
	03/22/2012	74	52.257	51.389	0.54	V	OSN
(145451) 2005 RM$_{43}$							
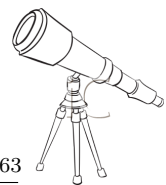
Object	Date	#images	r_h[AU]	Δ [AU]	α[°]	Filter	Telescope
	10/13/2006	19	35.139	34.322	0.94	Clear	OSN
	10/14/2006	12	35.139	34.314	0.92	Clear	OSN
	10/15/2006	18	35.146	34.356	0.97	Clear	OSN
	10/17/2006	12	35.146	34.375	1.01	Clear	OSN
	10/18/2006	27	35.146	34.385	1.03	Clear	OSN
	01/11/2007	4	35.149	34.687	1.43	Clear	2.2 m Calar Alto telescope
	01/12/2007	5	35.149	34.702	1.44	Clear	2.2 m Calar Alto telescope
	01/13/2007	5	35.149	34.716	1.45	Clear	2.2 m Calar Alto telescope
	01/14/2007	8	35.149	34.731	1.46	Clear	2.2 m Calar Alto telescope
	01/15/2007	3	35.149	34.747	1.47	Clear	2.2 m Calar Alto telescope
(145452) 2005 RN$_{43}$							
	09/14/2007	7	40.714	39.807	0.62	Clear	OSN
	09/16/2007	10	40.714	39.821	0.66	Clear	OSN
	09/17/2007	10	40.714	39.828	0.68	Clear	OSN
	09/19/2007	6	40.714	39.843	0.71	Clear	OSN
	08/03/2008	15	40.706	39.767	0.55	Clear	OSN
	08/04/2008	15	40.706	39.761	0.53	Clear	OSN
	08/05/2008	30	40.706	39.756	0.51	Clear	OSN
	08/07/2008	25	40.706	39.747	0.47	Clear	OSN
	08/08/2008	37	40.706	39.743	0.45	Clear	OSN
(145453) 2005 RR$_{43}$							
	10/22/2006	10	38.410	37.527	0.69	R	INT
	10/23/2006	6	38.410	37.522	0.68	R	INT
	10/26/2006	7	38.411	37.507	0.62	R	INT
	12/15/2006	17	38.423	37.639	0.90	Clear	OSN
	12/16/2006	18	38.423	37.648	0.91	Clear	OSN
	12/17/2006	12	38.424	37.658	0.93	Clear	OSN
	12/18/2006	26	38.424	37.668	0.95	Clear	OSN
	01/11/2007	4	38.430	37.974	1.31	Clear	2.2 m Calar Alto telescope
	01/12/2007	5	38.430	37.989	1.32	Clear	2.2 m Calar Alto telescope
	01/13/2007	1	38.430	38.004	1.33	Clear	2.2 m Calar Alto telescope
	01/14/2007	6	38.430	38.019	1.34	Clear	2.2 m Calar Alto telescope
	01/15/2007	5	38.431	38.034	1.35	Clear	2.2 m Calar Alto telescope
	01/16/2007	5	38.431	38.050	1.36	Clear	2.2 m Calar Alto telescope
	09/14/2007	5	38.491	38.025	1.33	Clear	OSN
	09/15/2007	10	38.491	38.011	1.32	Clear	OSN
	09/17/2007	15	38.492	37.984	1.30	Clear	OSN
(145480) 2005 TB$_{190}$							
	07/24/2009	6	46.396	45.650	0.86	R	TNG
	07/24/2009	24	46.396	45.650	0.86	R	NTT
	07/25/2009	11	46.396	45.638	0.84	R	TNG
	07/25/2009	8	46.396	45.638	0.84	R	NTT
	07/26/2009	8	46.396	45.627	0.82	R	TNG
	07/27/2009	12	46.396	45.616	0.81	R	TNG
(145486) 2005 UJ$_{438}$							
	01/11/2007	4	9.837	9.345	5.10	Clear	2.2 m Calar Alto telescope
	01/12/2007	4	9.834	9.358	5.14	Clear	2.2 m Calar Alto telescope
	01/13/2007	5	9.832	9.371	5.19	Clear	2.2 m Calar Alto telescope
	01/15/2007	3	9.828	9.398	5.28	Clear	2.2 m Calar Alto telescope
	01/16/2007	7	9.826	9.411	5.32	Clear	2.2 m Calar Alto telescope
	11/30/2007	39	9.190	8.205	0.27	Clear	OSN
	01/06/2008	23	9.123	8.372	4.16	Clear	2.2 m Calar Alto telescope
	01/07/2008	29	9.122	8.381	4.24	Clear	2.2 m Calar Alto telescope
	12/26/2008	15	8.594	7.634	0.29	Clear	OSN
(202421) 2005 UQ$_{513}$							
	08/02/2008	10	48.806	48.389	1.09	Clear	OSN
	08/03/2008	13	48.806	48.376	1.08	Clear	OSN
	08/04/2008	15	48.806	48.362	1.07	Clear	OSN
	08/09/2008	25	48.805	48.294	1.03	Clear	OSN
	09/20/2009	18	48.735	47.859	0.58	Clear	OSN
	09/21/2009	41	48.735	47.855	0.57	Clear	OSN
	09/23/2009	19	48.735	47.847	0.55	Clear	OSN
	10/13/2009	35	48.731	47.826	0.50	Clear	OSN
	10/14/2009	35	48.731	47.828	0.50	Clear	OSN
	10/15/2009	30	48.731	47.830	0.51	Clear	OSN
	10/16/2009	25	48.731	47.832	0.51	Clear	OSN
	10/17/2009	35	48.731	47.834	0.52	Clear	OSN
	10/18/2009	14	48.731	47.837	0.52	Clear	OSN
(229762) 2007 UK$_{126}$							
	10/28/2011	54	44.515	43.688	0.72	R	TNG
	10/30/2011	42	44.513	43.673	0.69	R	TNG
	10/31/2011	26	44.512	43.665	0.67	R	TNG
(250112) 2007 UL$_{126}$ (or 2002 KY$_{14}$)							
	08/01/2008	15	8.665	7.793	3.62	Clear	OSN
	08/02/2008	15	8.665	7.787	3.55	Clear	OSN
	08/03/2008	30	8.664	7.781	3.48	Clear	OSN
	08/04/2008	25	8.664	7.775	3.40	Clear	OSN
	08/05/2008	5	8.663	7.769	3.34	Clear	OSN
(341520) 2007 TY$_{430}$							
	10/28/2011	18	29.041	28.057	0.28	R	TNG
	10/29/2011	19	29.041	28.059	0.31	R	TNG
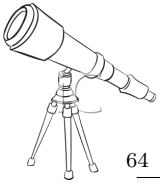
Object	Date	#images	r_h[AU]	Δ [AU]	α[°]	Filter	Telescope
	10/31/2011	17	29.040	28.066	0.38	R	TNG
	11/01/2011	36	29.040	28.069	0.41	R	TNG
(315530) 2008 AP_{129}							
	01/25/2012	25	37.814	36.928	0.66	Clear	OSN
	01/26/2012	30	37.814	36.928	0.66	Clear	OSN
	01/30/2012	15	37.815	36.929	0.66	Clear	OSN
	02/08/2013	20	37.930	37.051	0.69	r'	TNG
	02/09/2013	37	37.930	37.054	0.69	Clear	OSN
	02/13/2013	27	37.932	37.068	0.73	Clear	OSN
	02/14/2013	63	37.932	37.073	0.74	Clear	OSN
(281371) 2008 FC_{76}							
	10/15/2009	16	11.209	10.639	4.29	nIR-Block	2.2 m Calar Alto telescope
	10/17/2009	22	11.207	10.660	4.37	nIR-Block	2.2 m Calar Alto telescope
	10/19/2009	15	11.205	10.682	4.44	Clear	OSN
	10/11/2012	28	10.295	9.384	2.38	Clear	OSN
	10/16/2012	15	10.293	9.395	2.52	Clear	OSN
(315898) 2008 QD_4							
	01/26/2012	9	5.880	5.199	7.37	Clear	OSN
(342842) 2008 YB_3							
	01/26/2012	16	6.654	5.736	3.32	Clear	OSN
	01/28/2012	60	6.656	5.735	3.65	Clear	OSN
2010 BK_{118}							
	09/10/2012	33	6.174	5.222	3.30	Luminance	ASH2
	09/11/2012	39	6.176	5.218	3.14	Luminance	ASH2

IV.6 Optimal reduction

In relative photometry, we can also use multiple reference stars. For instance, with two reference stars, we can measure the difference between the target and one of the references, and then between the two references. If the reference stars are stable, the difference over a period of observation will be constant. For increased confidence, several reference stars can be used. In this work, we used between 6 and 25 field stars. As previously mentioned, care has to be taken not to introduce spurious results due to faint background stars or galaxies in the aperture for the photometry.

For all apertures used, we chose the results giving the lowest scatter in the photometry of both targets and stars. Several sets of reference stars were used to establish the relative photometry of all the targets. In many cases, several stars had to be rejected from the analysis because they showed some variability. Finally, the set that gave the lowest scatter was used for the final result. The final photometry of our targets was computed by taking the median of all the lightcurves obtained with respect to each reference star. By applying this technique, spurious results were eliminated and the dispersion of photometry was improved.

During the observational campaigns, we tried to stick to the same field of view, and therefore to the same reference stars, for each observed target. In some cases, due to the drift of the observed object, the field changed completely or partially. If the field changed completely, we used different reference stars for two or three subsets of nights in the entire run. If the field changed partially, we tried to keep the greatest number of common reference stars during the whole campaign. In the case of the coordinated campaign, we tried to observe the same field of view with both telescopes for any given target. In this way, we can use the same reference stars and do a better job in image processing and analysis.

The absolute photometry has been done only in few cases reported in this thesis. For example, absolute photometry techniques have been done to obtain the solar phase curves of two objects: 1999 KR_{16} (Figure 121), and 1999 OX_3 (Figure 124). As this thesis is not dedicated to color studies, and as most of our data were obtained without filter, the use of absolute photometry is limited.

As already mentioned, all the data reduction presented in this work has been performed with a common Interactive Data Language (IDL) reduction software based on the Daophot routines (Stetson, 1987) and developed by our team at the IAA-CSIC. This photometric code is semi-automatic, and can be presented in several steps:

- *The aperture radius choice*: Once each image is bias subtracted and flat-fielded using the me-

dian bias and median flat field, we have to select the aperture radius in order to maximize the S/N. The code allow us a set of apertures with radii around the full width at half-maximum (FWHM), and also adaptable aperture radius (aperture radius is varying according to the seeing conditions of each image, and so, the aperture radius is different for each image). Then, for all apertures used, we have to choose the results giving the lowest scatter in the photometry of both targets and stars.
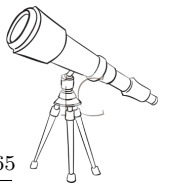
- *The reference stars choice*: Several sets of reference stars are generally used to establish the relative photometry of all the targets. In many cases, several stars have to be rejected from the analysis because they show some variability. Finally, the set that gives the lowest scatter has to be used for the final result.

- *Semi-automatic code*: Generally, we obtained several images of an object during a night. The code allow us to select manually the target (TNO or centaur) and the references stars on one of the images obtained during the night. Then, we generate a TIFF image within which all the reference stars, as well as the object are marked. Once the target and reference stars are selected on this first image, it is not necessary to repeat this process for all the images of the night. In fact, the code computes the drift of the object for each image, in other words we are able to follow and pinpoint the position of the object along the night and so the flux of the object and the reference stars is computed automatically for all the images of the night. During an observational campaign, we tried to keep the same field and therefore the same reference stars, so for the program it is easy to follow the same reference stars and the object. However, in some cases, owing to the drift of the observed object, the field changed completely or partially. If the field changed completely, we used different reference stars for two or three subsets of nights in the entire run. If the field changed partially, we tried to keep the greatest number of reference stars in common during the whole campaign. In some cases, due to tracking or drift problem, there is an important offset between the images, so the field are only partially matching. In such a case, it is interesting to align the images. A sub-routine called *hastrom* [6] has been implemented to align the images. However, in case of densely populated field of view, it is better to use the program Registar [7].

- *Photometric results*: some of the outputs of this program are the files which contain the object fluxes, the reference stars fluxes, and the Julian dates. Obviously, there are several files depending of the aperture radii used to estimate the fluxes.

- *Data combination*: When we combined several observing runs, we had to normalize the photometry data to its average because we did not have absolute photometry that would allow us to link one run with the other; in several instances, we did experiment with trying to link several runs by using absolute photometry, and the errors involved were generally much larger than what we can achieve by normalizing the photometry to the mean or median value. Furthermore, the small jumps in the photometry caused by the inevitable absolute photometry offsets cause spurious frequencies in the periodogram analysis (see next chapter for more details about the Lomb periodogram). This is especially true for very low variability objects, which are numerous. By normalizing the means of several runs, we assume that a similar number of data points are in the upper part and lower part of the curves. This may not be true if the runs are only two or three nights long, but this is not usually the case. We emphasize that we normalized the mean of each run not the mean of each night. We must point out that when we combined several observing runs obtained at different epochs, (for example runs separated by years), the light time correction of the data is required. The light time correction is needed during the observation of any moving object. The light time is calculated by dividing the object's geometric distance from Earth by the speed of light.

---

[6]The hastrom routine can be found at http://idlastro.gsfc.nasa.gov/ftp/pro/astrom/hastrom.pro.
[7]Registar can be found at: http://www.aurigaimaging.com/
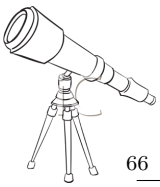
Such a light time is then converted in Julian date and subtracted from the Julian day of the observations. When we combined observing runs separated by several years, we assume that the orientation of the rotation axis of the object has not substantially changed with respect to the observer. In case of significant change in the spin axis orientation, lightcurves are not in phase and there is a shift between the maxima and minima of the curves as well as a change in the lightcurve amplitude (Farnham, 2001a; Tegler et al., 2005; Lacerda, 2011). If a change is noticed in the lightcurve due to spin axis orientation variations, one can use the epoch method and the amplitude method to estimate the ecliptic latitude and longitude of the spin axis as well as the sense of the object rotation (Gehrels, 1967; Zappala, 1981; Kaasalainen and Torppa, 2001; Kaasalainen, Torppa and Muinonen, 2001).

- *Search for periodicity*: To search for any periodic signal in the data, we applied different techniques such as: i) the Lomb periodogram; ii) the Phase Dispersion Minimization (PDM); iii) the CLEAN technique and iv) the Pravec-Harris method. All theses techniques have been developed for asteroid lightcurves, but they are perfectly applicable to TNO/centaur lightcurves. All these techniques will be presented in the next chapter. Some of them are implemented in the IDL code previously mentioned.

Chapter V

Rotational period and lightcurve amplitude

$\mathcal{A}$n object in rotation will in general produce brightness variations that can be measured giving rise to what we call lightcurves. Such lightcurves are produced by various mechanisms: i) albedo variations on the body surface, ii) non spherical shape, and/or iii) contact or eclipsing binary. Short-term photometric lightcurves allow us to study the spins, shapes, surfaces, angular momentum, internal structure and densities of the Trans-Neptunian Objects and centaurs.

Part of this chapter is dedicated to the physics of lightcurves and their importance for understanding the Trans-Neptunian belt. This is a necessary background to understand the results shown in Chapter VI. We also introduce some physical properties that can be derived or constrained from a lightcurve. Various methods to determine the rotational period from the lightcurve datasets, such as Lomb periodogram, the Pravec-Harris method, the CLEAN algorithm, and the Phase Dispersion Minimization (PDM) are also reviewed.

V.1 Lightcurve introduction

The rotational brightness variations or lightcurve of an object is determined by the periodic variation of the body brightness as a function of time, resulting from its rotation. In other words, we measure the light intensity of an object as a function of time. The time separation of repeated brightness peaks in the lightcurve gives the spin period of the object.

V.1.1 Physics of lightcurves

Sheppard and Jewitt (2004) proposed a "classification" of the lightcurves according to their amplitude variations, and rotational periods. Three regions in the amplitude-period space are shown in Figure 40.

V.1.1.1 Causes of the brightness variations

The apparent magnitude (m_R in the R-band) of a body is determined by its geometrical position relative to the Sun and Earth as:

$$m_R = m_{sun} - 2.5 \times log \left[\frac{p_R r^2 \phi(\alpha)}{2.25} \times 10^{16} R^2 \Delta^2 \right] \qquad \text{(Equation V.1)}$$

where m_{sun} is the apparent red magnitude of the Sun (m_{sun}=-27.10), p_R is the geometric albedo in the R-band of the object, R and Δ are the heliocentric and geocentric distances (respectively) expressed in AU, r is the equal-area equivalent radius of the object in km, and $\phi(\alpha)$ is the phase
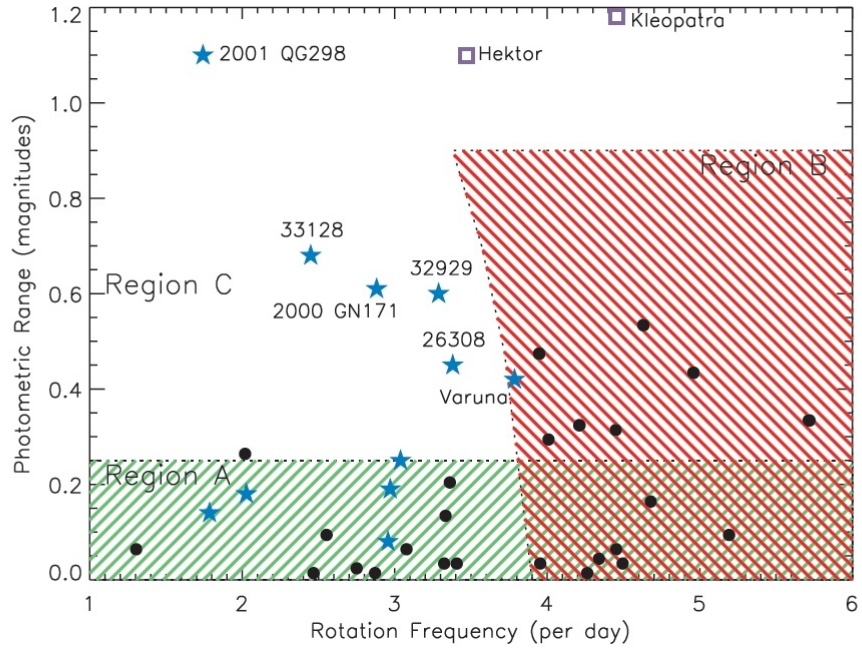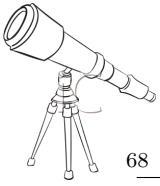
Figure 40: *Photometric range versus rotation frequency*: In this plot, three regions are defined as: i) Region A: the lightcurve amplitude could be equally well caused by albedo, elongation, or binarity, ii) Region B: the lightcurve amplitude is most likely caused by rotational elongation, iii) Region C: the lightcurve amplitude is most likely caused by binarity of the object. Stars are for TNOs, circles for main-belt asteroids (radii $\geq$100 km), and squares denote the Trojan Hektor and the main-belt asteroid Kleopatra. The name or designation of some objects is also indicated. Figure from Sheppard and Jewitt (2004).

function. In the case of TNOs, the phase function can be approximated by:

$$\phi(\alpha) = 10^{-0.4\beta\alpha} \qquad \text{(Equation V.2)}$$

where α is the phase angle (in degrees) and β is the linear phase coefficient in magnitudes per degree at phase angles $<2°$. Objects present magnitude variations as a function of their phase angle such as the brightness increases with decreasing phase angle. By plotting the magnitude versus the phase angle, we have the so-called solar phase curve also known as phase effect curve. Examples are presented in Figure 121, and Figure 124.

In order to remove the brightness variations caused by the differing positional geometry of an object, one can use the reduced magnitude instead of the apparent magnitude:

$$m_R(1,1,\alpha) = m_R - 5log(R\Delta) \qquad \text{(Equation V.3)}$$

The absolute magnitude (H_R) is the object magnitude if the object was at 1 AU from the Sun and Earth and at a phase angle of $0°$ and is expressed as:

$$H_R = m_R(1,1,\alpha = 0°) = m_R - 5log(R\Delta) - \beta\alpha \qquad \text{(Equation V.4)}$$

V.1.1.2   Elongation from material strength

An elongated triaxial object will show a double-peaked rotational period. In others words, each of its two long and short axes will be observed during one full rotation (Figure 44). Assuming objects as triaxial ellipsoids, with axes a>b>c and rotating along c, the lightcurve amplitude, Δm, varies
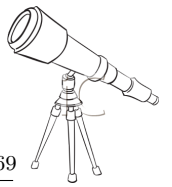
as a function of the observational angle ξ [1] according to Binzel et al. (1989):

$$\Delta m = 2.5 \, log\left(\frac{a}{b}\right) - 1.25 \, log\left(\frac{a^2 \cos^2 \xi + c^2 \sin^2 \xi}{b^2 \cos^2 \xi + c^2 \sin^2 \xi}\right) \qquad \text{(Equation V.5)}$$

The lower limit for the object elongation (a/b), assuming an equatorial view ($\xi = 90°$) is:

$$\Delta m = 2.5 \, log\left(\frac{a}{b}\right) \Rightarrow \left(\frac{a}{b}\right) = 10^{0.4\Delta m} \qquad \text{(Equation V.6)}$$

The smaller TNOs are expected to not be dominated by self-gravity. So, they may be structurally elongated. This idea seems in agreement with the large amplitude lightcurves of small TNOs (Table 7), unfortunately, to date, there are only few lightcurves of such objects.

V.1.1.3 Surface albedo variations

The albedo is the ratio of reflected radiation from the body surface to incident radiation from it. There are several definitions of albedo: i) the geometric albedo is the ratio of the object backscattered energy at $\alpha=0°$ to that scattered by a perfect white disk of the same cross section, ii) the Bond albedo is the ratio between the energy refracted and reflected by the object in all directions to the energy incident on the geometric cross section. The Bond albedo (A) is related to the geometric albedo (p):

$$A = pq \qquad \text{(Equation V.7)}$$

where q is the so called phase integral and is calculated as:

$$q = 2 \int_0^\pi \frac{I(\alpha)}{I(0)} \sin \alpha \, d\alpha. \qquad \text{(Equation V.8)}$$

where $I(\alpha)$ is the scattered flux into the phase angle α. Surface albedo variations can sometimes be associated to color variations.

Surface albedo variations on TNOs are not expected to create large amplitude lightcurves. For the asteroids, albedo variations are usually responsible for lightcurves amplitude between 0.10 mag and 0.20 mag (Magnusson and Lagerkvist, 1991). The high amplitude lightcurves of large objects which we can clearly attribute to an aspherical shape can help to determine typical magnitude of hemispheric albedo changes if we compare the two maxima or two minima in the double-peaked lightcurves. Such differences in the cases of 2003 VS$_2$ and Haumea are around 0.04 mag, whereas for Varuna the greatest difference is 0.1 mag. Hence, this means that the hemispherically averaged albedo typically has variations around 4 to 10% (Thirouin et al., 2010). So, we expect that the variability induced by surface features is on the order of 0.1 mag. or slightly higher.

In this work (see Section VII.2.1 for more details), we test what is the lightcurve amplitude limit to distinguish between shape- and albedo-dominated lighcurves (i.e. to distinguish between single- and double-peaked lighcurves [2]). We test three lightcurve amplitude (Δm) limits: i) a threshold at Δm=0.10 mag, ii) at Δm=0.15 mag, and iii) at Δm=0.20 mag, to distinguish between single- and double-peaked lightcurves. The entire study can be found in Section VII.2.1. Based on such a study, we adopt a threshold of 0.15 mag to distinguish between shape- and albedo- dominated lightcurves. This value has been used by several investigators as the transition from low variability to medium-large variability (e.g. Sheppard, Lacerda and Ortiz (2008)), but the exact transition limit has been quantitatively investigated in this thesis and in Thirouin et al. (2010); Duffard et al. (2009). Lightcurves with very little variations are usually called flat lightcurves.

---

[1] The observational angle, ξ, is the angle between the rotation axis and the line of sight, also known as aspect angle

[2] The double peak rotational period is twice the single peak rotational period.
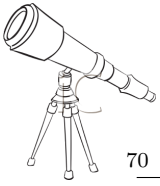
V.1.1.4 Rotational elongation

An object with no internal cohesion will adopt an equilibrium figure depending on its rotation rate and will break if it reaches its critical rotational period, P_{crit} when the centrifugal acceleration (a_c) equals the gravitational acceleration (a_g):

$$a_c = a_g \qquad\qquad \text{(Equation V.9a)}$$

$$\left(\frac{2\pi}{P_{crit}}\right)^2 r = \frac{Gm}{r^2} \qquad\qquad \text{(Equation V.9b)}$$

$$\Rightarrow P_{crit} = \left(\frac{3\pi}{G\rho}\right)^{1/2} \qquad\qquad \text{(Equation V.9c)}$$

where G is the gravitational constant, ρ the density of the object, and r the object radius. Equation V.9 can be expressed depending only on the body density. The critical period in hours for a spherical bodies is:

$$P_{crit} = \frac{3.3}{\sqrt{\rho}} \qquad\qquad \text{(Equation V.10)}$$

For a prolate spheroid, the critical period in hours is, according to Pravec and Harris (2000), approximately:

$$P_{crit} \approx \frac{3.3}{\sqrt{\rho}}\sqrt{\frac{a}{b}} \qquad\qquad \text{(Equation V.11a)}$$

$$\Rightarrow P_{crit} \approx 3.3\sqrt{\frac{1+\Delta m}{\rho}} \qquad\qquad \text{(Equation V.11b)}$$

where Δm is the lightcurve amplitude.

Davidsson (1999); Davidsson (2001) took into account internal cohesion and defined the critical period as:

$$P_{crit} = \frac{\pi}{\sqrt{\frac{1}{3}\pi\rho G + \frac{T}{\rho r^2}}} \qquad\qquad \text{(Equation V.12)}$$

where T is the tensile strength. This formula is valid for spherical bodies. But Davidsson (1999); Davidsson (2001) also derived expressions for non-spherical bodies.

All TNOs, even those with a long rotational period are believed to be rotationally deformed. In fact, the rotational elongation depends on the structure and on the strength of a body. Haumea and Varuna present peculiar lightcurves (see Section VI.2.22 and Section VI.3.8) due to rotational deformation because of their fast rotations (Rabinowitz et al., 2006; Jewitt and Sheppard, 2002).

V.1.1.5 Eclipsing or contact binary

Another mechanism able to produce a lightcurve is the binarity, and in particular, in case of eclipsing or contact binaries. Leone et al. (1984) showed that very close binary components should be elongated by mutual tidal forces and should generate a large amplitude lightcurve. Leone et al. (1984) suggested that the maximum amplitude for a tidally distorted contact binary (or nearly contact binary) is ~1.2 mag.

In the Trans-Neptunian belt, there is a well known case of a contact binary: (139775) 2001 QG_{298}. Sheppard and Jewitt (2004) observed this object in 2002-2003 and proposed a double-peaked rotational period of 13.7744±0.0004 h and a lightcurve amplitude of 1.14±0.04 mag. In August 2010, Lacerda (2011) re-observed this object and found a lower lightcurve amplitude, 0.7±0.1 mag, but both lightcurves have the same rotational period and appear aligned on rotational phase (Figure 41).
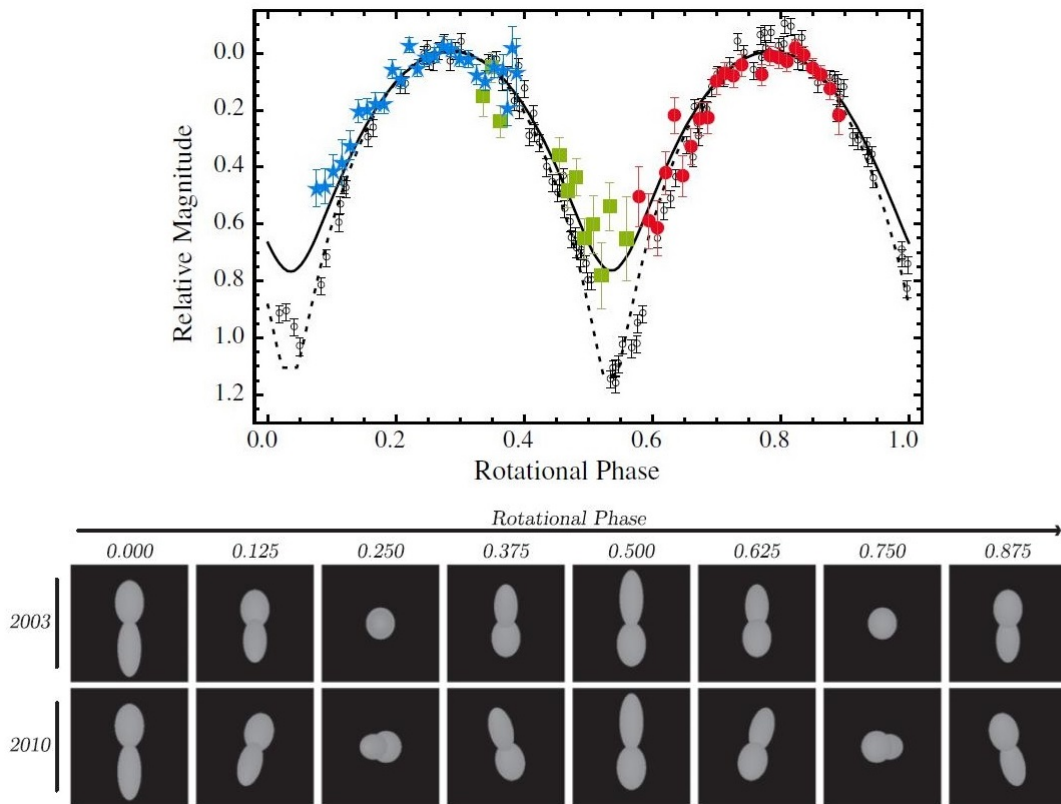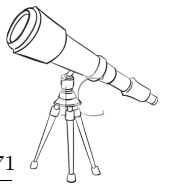
Figure 41: *A change in the lightcurve of 2001 QG$_{298}$*: Upper plot: lightcurves of 2001 QG$_{298}$ in 2003 (open circles, data from Sheppard and Jewitt (2004)) and in 2010 (filled symbols). The lightcurve amplitude has decreased from Δm^{2003}= 1.14±0.04 mag in 2003 to Δm^{2010}= 0.7±0.1 mag in 2010. Bottom plot: system configuration has seen from Earth in 2003 and in 2010, assuming that 2001 QG$_{298}$ has an obliquity (or axial tilt which is the angle between an object's rotational axis and its orbital axis) of ϵ=90°. Figure adapted from Lacerda (2011).

Such a variation in the lightcurve amplitude is due to the change of the observational circumstances. In fact, 2001 QG$_{298}$ was observed equator-on in 2003 whereas it was observed at ∼16° off the equator in 2010 (Figure 41). In others words, 2001 QG$_{298}$ has traveled an angular distance of ∼16° in its heliocentric orbit between 2003 and 2010, and the spin axis has changed the same angle with respect to the Earth.

Sheppard and Jewitt (2004) estimated that the fraction of similar objects is at least 10% to 20% in the Trans-Neptunian belt. But based on the high obliquity of 2001 QG$_{298}$ (obliquity, usually designed with ϵ, is the angle between an object's rotational axis and its orbital axis. Based on the 2010 lightcurve of 2001 QG$_{298}$, the obliquity has been estimated to be $(90\pm30)°)$ and assuming that most of the contact binaries have similar obliquity, their abundance may be larger than the one estimated by Sheppard and Jewitt (2004) (Lacerda, 2011). However, to date, only one contact binary (2001 QG$_{298}$) has been found in the Trans-Neptunian belt, despite their high abundance estimate. The main reason is that such objects are identified only in certain geometric circumstances (i.e. nearly equator-on). Lacerda (2011) estimated that 85% of contact binaries are not detected due to unfavorable observing geometry. These values may depend on object sizes and dynamical classes.
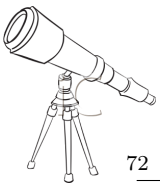
V.1.1.6   Phase effect on the rotation lightcurves

Belskaya, Barucci and Shkuratov (2003); Belskaya et al. (2006) pointed out that phase angle may affect the lightcurve amplitudes. In fact, based on lightcurves of Varuna obtained between 2001 to 2005, Belskaya et al. (2006) suggested that observations at low phase angle (typically, $\alpha \leq 0.1°$) can have an increase in the lightcurve amplitude. In Figure 42 this effect is illustrated. One can note that at low phase angle, the lightcurve amplitude of Varuna is higher and there is also a shift of the extrema. Observations carried out at very low phase angle, $\alpha < 0.1$-$0.2°$ are affected by a strong non-linear opposition effect. For phase angles such as $\alpha > 0.2°$, the phase angle coefficient β varies linearly between ~ 0.01 to 0.20 mag/$°$ and is likely associated with albedo. For observations largely spread out in time or near the opposition, care has to be taken for a possible phase effect.
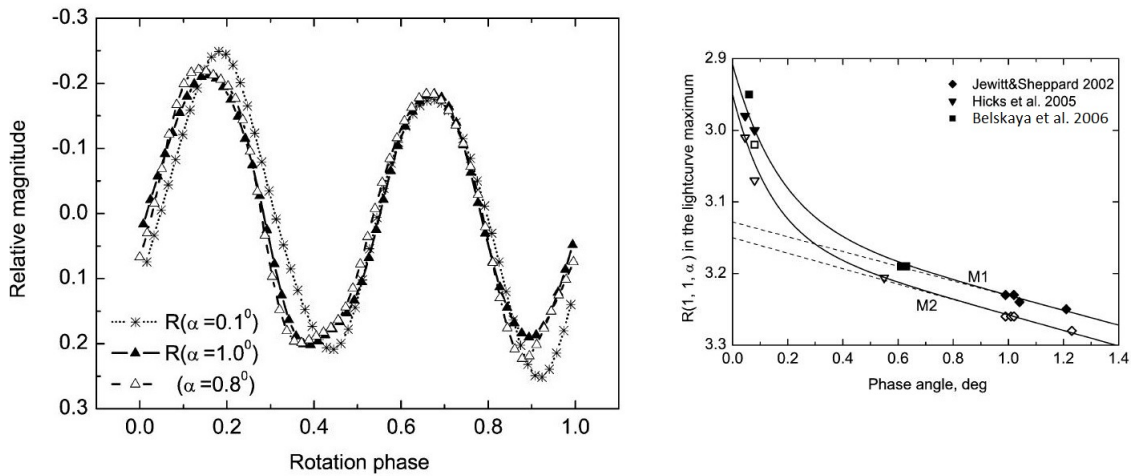
Figure 42: *Opposition effect*: Composite lightcurves of Varuna at different phase angles (left plot). The lightcurve amplitude is increasing toward small phase angles and extrema position are shifted. On the right, are plotted the magnitude phase curves of Varuna calculated for the primary (M1) and secondary (M2) maxima of the lightcurves. There is a non-linear increase in Varuna's magnitude at very low phase angles. Figure adapted from Belskaya et al. (2006).

V.1.1.7   Variable lightcurves

A TNO or centaur lightcurve may be variable for several reasons: i) non-periodic variations due to a recent impact, ii) complex rotational state, iii) cometary activity, and iv) change in the object pole orientation.

- *Impact*: Currently, the probability of collisions in the Trans-Neptunian belt is very low, so we can discard such an effect.

- *Complex rotational state*: According to Burns and Safronov (1973), the time required ($t_{complex}$) for an object to damp a complex rotational state to a rotation along its principal axis is:

$$t_{damp} = \frac{\mu Q}{\rho r^2 \omega^3 K^2} \qquad \text{(Equation V.13)}$$

where μ is the body rigidity, Q is the ratio of energy contained in the oscillation to the energy lost per cycle, ρ is the object density, r the radius, and K is the irregularity of the object (K$\sim$0.01 for spherical object and K$\sim$0.1 for highly elongated object). Using reasonable assumptions, one can calculate that the time necessary to damp a complex rotational state to a principal axis rotation is much less than the age of the Solar System, and so we have to expect that most TNOs and centaurs are not in complex rotational state.
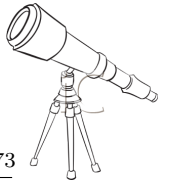
- *Cometary activity*: TNO cometary activity is not expected at these larges distance from the Sun because the solar radiation cannot cause sublimation of water ices. However, in the case of the centaurs whose orbits have perihelion distances ≥5 AU, cometary activity can be detected. For example, the coma of (2060) Chiron has been detected by Meech and Belton (1989), cometary activity has been reported by Choi and Weissman (2006) for the Centaur (60558) Echeclus, and Jewitt (2009) observed a sample of twenty-three centaurs and found nine to be active. Some TNOs have been reported to have possible variability like (19308) 1996 TO_{66} (Hainaut et al., 2000), and (24835) 1995 SM_{55} (Sheppard and Jewitt, 2003), perhaps associated to some degree sublimation, but this is was not proven.

- *Change in the pole orientation*: Centaurs have relatively short orbital periods and so, their pole orientation to our line of sight may change over few years. Thanks to the lightcurve amplitude variability over the years, it is possible to constrain the object pole orientation. Farnham (2001a) and Tegler et al. (2005) determined the pole orientation of Pholus. The case of the TNOs is different because these objects have longer orbital periods than the centaurs and so we are not expecting lightcurve amplitude changes from year to year. To date, only 2001 QG_{298} has been observed for pole variation effect (Sheppard and Jewitt, 2004; Lacerda, 2011)

V.1.2 Physical properties derived from lightcurves

Lightcurves are important to understand the Trans-Neptunian belt formation and evolution. Short-term variability studies not only provide the lightcurve amplitude and the rotational periodicity of an object, they also give us information about the object shape and deformation, the surface homogeneity or heterogeneity, the object density, and in case of binary systems, we can estimate the albedo. Following, we will introduce the physical properties derived from lightcurve.

V.1.2.1 Shape

Chandrasekhar (1987) studied the figures of equilibrium for fluid bodies. This work is useful to derive various essential properties about TNOs/centaurs in our case, assuming that they are in hydrostatic equilibrium or are gravitational aggregates (rubble-piles with no cohesion between the fragments).

Assuming a triaxial object with axis a>b>c (along the directions x,y, and z respectively), we can define the volume (V) as:

$$V = \int dV = \frac{4}{3}\pi abc \qquad \text{(Equation V.14)}$$

Considering that the object is rotating uniformly along the c-axis with a fixed angular velocity (Ω), the moment of inertia about the c-axis is:

$$I = \frac{1}{5}M(a^2 + b^2) \qquad \text{(Equation V.15)}$$

where M is the object mass. The fluid pressure (p) within the object is:

$$p = p_0 - \rho\left(\psi - \frac{1}{2}\Omega^2(x^2 + y^2)\right) \qquad \text{(Equation V.16)}$$

where p_0 is a constant, ψ is the gravitational potential, ρ is the density (the density is constant, ρ = M/V) The gravitational potential inside a homogeneous self-gravitating ellipsoidal object is:

$$\psi = \frac{-3}{4}GM\left(\alpha_0 - \sum_{i=1,3}\alpha_i x_i^2\right) \qquad \text{(Equation V.17)}$$

where G is the gravitational constant, x_i are the axes, and

$$\alpha_0 = \int_0^\infty \frac{du}{\Delta} \qquad \text{(Equation V.18)}$$
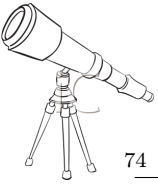
$$\alpha_i = \int_0^\infty \frac{\mathrm{d}u}{(a_i^2 + u)\Delta} \qquad \text{(Equation V.19)}$$

$$\Delta = (a^2 + u)^{1/2}(b^2 + u)^{1/2}(c^2 + u)^{1/2} \qquad \text{(Equation V.20)}$$

where a$_i$ are the axes (a,b, and c), and u $= c^2 \tan^2\theta$ (with θ the angle subtended between the radius vector and the z-axis in spherical coordinates). Finally, assuming p=0, Equation V.16 can be written as:

$$p_0 = \frac{1}{2}\rho \left(\left(\frac{3}{2}GM\alpha_1 - \Omega^2 \right) x^2 + \left(\frac{3}{2}GM\alpha_2 - \Omega^2 \right) y^2 + \left(\frac{3}{2}GM\alpha_3 - \Omega^2 \right) z^2 \right) \qquad \text{(Equation V.21)}$$

Since

$$\frac{x^2}{a^2} + \frac{y^2}{b^2} + \frac{y^2}{c^2} = 1 \qquad \text{(Equation V.22)}$$

Equation V.21 can be expressed as:

$$\left(\alpha_1 - \frac{\Omega^2}{(3/2)GM} \right) a^2 = \left(\alpha_2 - \frac{\Omega^2}{(3/2)GM} \right) b^2 = \alpha_3 c^2 \qquad \text{(Equation V.23)}$$

Equation V.23 can also be written as:

$$\frac{\Omega^2}{2\pi G\rho} = abc \int_0^\infty \frac{u\mathrm{d}u}{(a^2 + u)(b^2 + u)\Delta} \qquad \text{(Equation V.24)}$$

In the case of an elongated object (triaxial object or Jacobi ellipsoid), the axes are a>b>c. In other words, the object is flattened along its axis of rotation (c-axis). The degree of flattening is measured by the eccentricity (e):

$$e = \left(1 - \frac{c^2}{a^2} \right)^{1/2} \qquad \text{(Equation V.25)}$$

Thus if e=0 then there is no flattening, and the object is spherical. Assuming a spheroid (a=b) and:

$$u = a^2\lambda \qquad \text{(Equation V.26)}$$

$$\lambda = \frac{e^2}{z^2 - 1} \qquad \text{(Equation V.27)}$$

Equation V.21 can be expressed as:

$$\begin{aligned}
\frac{\Omega^2}{2\pi G\rho} &= (1 - e^2)^{1/2}e^2 \int_0^\infty \frac{\lambda\mathrm{d}\lambda}{(1 + \lambda)^2(1 + \lambda - e^2)^{3/2}} \\
&= \frac{2(1 - e^2)^{1/2}}{e^3} \left(\int_0^e \frac{z^2\mathrm{d}z}{(1 - z^2)^{1/2}} - (1 - e^2) \int_0^e \frac{z^2\mathrm{d}z}{(1 - z^2)^{3/2}} \right) \\
&= \frac{3 - 2e^2}{e^3}(1 - e^2)^{1/2} \sin^{-1} e - \left(\frac{3}{e^2} \right)(1 - e^2) \qquad \text{(Equation V.28)}
\end{aligned}$$

Finally and in order to match the equation proposed by Chandrasekhar (1987), Equation V.28 is usually expressed:

$$\bar{\Omega}^2 = \frac{\Omega^2}{\pi G\rho} = \frac{2\sqrt{1 - e^2}}{e^3}(3 - 2e^2) \sin^{-1} e - \frac{6}{e^2}(1 - e^2) \qquad \text{(Equation V.29)}$$

Triaxial ellipsoid (a>b>c) are defined by two eccentricities:

$$e_1 = \sqrt{1 - (b/a)^2} \qquad \text{(Equation V.30)}$$

$$e_2 = \sqrt{1 - (c/a)^2} \qquad \text{(Equation V.31)}$$
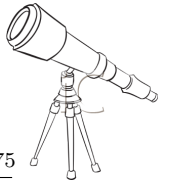
Table 2: $\bar{\Omega}^2$ as a function of the eccentricity (e) for the MacLaurin sequence. Table adapted from Chandrasekhar (1987).

e	$\bar{\Omega}^2$	e	$\bar{\Omega}^2$	e	$\bar{\Omega}^2$
0	0	0.75	0.31947	0.91	0.44507
0.10	0.00534	0.80	0.36316	0.92	0.44816
0.15	0.01204	0.81	0.37190	0.93	0.44933
0.20	0.02146	0.81267	0.37423	0.94	0.44785
0.25	0.03363	0.82	0.38059	0.95	0.44264
0.30	0.04862	0.83	0.38917	0.95289	0.44022
0.35	0.06647	0.84	0.39761	0.96	0.43193
0.40	0.08727	0.85	0.40583	0.97	0.41257
0.45	0.11108	0.86	0.41378	0.98	0.37802
0.50	0.13799	0.87	0.42136	0.99	0.31030
0.55	0.16807	0.88	0.42845	0.995	0.24371
0.60	0.20135	0.89	0.43490	0.999	0.12540
0.65	0.23783	0.90	0.44053	0.9999	0.04286

The parameter $\bar{\Omega}^2$ is expressed as:

$$\bar{\Omega}^2 = \frac{\Omega^2}{\pi G \rho} = 2abc \int_0^\infty \frac{u\,\mathrm{d}u}{(a^2+u)(b^2+u)\Delta} \qquad \text{(Equation V.32)}$$

And we have purely geometric relations between the axes ratio such as:

$$a^2 b^2 \int_0^\infty \frac{\mathrm{d}u}{(a^2+u)(b^2+u)\Delta} = c^2 \int_0^\infty \frac{\mathrm{d}u}{(c^2+u)\Delta} \qquad \text{(Equation V.33)}$$

V.1.2.1.1 MacLaurin spheroid In Table 2, the relation between $\bar{\Omega}^2$ and the eccentricity e for a MacLaurin spheroid is shown for several eccentricities. The eccentricity e, is:

$$e^2 = 1 - \frac{c^2}{a^2} \qquad \text{(Equation V.34)}$$

In Figure 43 the MacLaurin sequence is plotted. The eccentricity varies between 0 (spheroid) and 1 (ellipsoid). The MacLaurin sequence reaches its maximum for e∼0.93 and $\bar{\Omega}^2$∼0.45. However, the MacLaurin sequence becomes unstable after the MacLaurin/Jacobi bifurcation point (see below for bifurcation point definition). In other words, only the MacLaurin sequence before the bifurcation point has to be considered.

V.1.2.1.2 Jacobi ellipsoid In Table 3, the relation between $\bar{\Omega}^2$ and the axes ratio a/c and b/a for a Jacobi ellipsoid is listed for a sample of axial ratios. In Figure 43 is also plotted the Jacobi sequence. This sequence starts at the MacLaurin/Jacobi bifurcation point, at e= 0.81267.

V.1.2.1.3 Bifurcation point A bifurcation is a qualitative shift in the character of the solutions to an equation. One of the best examples of a bifurcation is the transition from spheroidal to ellipsoidal shapes. Using previous equations, we can demonstrate that for e = 0.81267 and $\Omega^2/\pi G\rho$ = 0.37423, there is a transition between the spheroidal and the ellipsoidal shape. In other words, a MacLaurin spheroid is deformed into a triaxial Jacobi ellipsoid.

V.1.2.2 Elongation and density

If we assume TNOs as triaxial ellipsoids, with axes a>b>c (rotating along c), the lightcurve amplitude, Δm, varies as a function of the observational angle ξ according to Binzel et al. (1989):

$$\Delta m = 2.5\,log\left(\frac{a}{b}\right) - 1.25\,log\left(\frac{a^2 \cos^2\xi + c^2 \sin^2\xi}{b^2 \cos^2\xi + c^2 \sin^2\xi}\right) \qquad \text{(Equation V.35)}$$
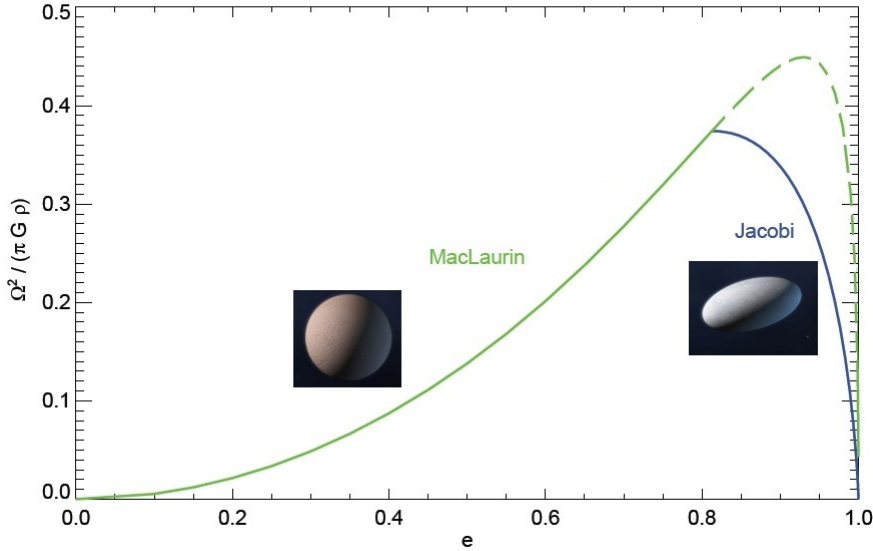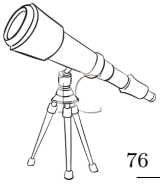
Figure 43: *MacLaurin and Jacobi sequences*: this plot summarizes Chandrasekhar (1987). The bifurcation point is located at the transition between both sequences, at e = 0.81267 and $\Omega^2/\pi G\rho = 0.37423$. As mentioned, only the MacLaurin sequence before the bifurcation point has to be considered.

The lower limit for the object elongation (a/b) is obtained, assuming an equatorial view ($\xi = 90°$):

$$\Delta m = 2.5 \, log \left(\frac{a}{b}\right) \qquad \text{(Equation V.36)}$$

To date, only a few TNOs have a pole orientation estimation. Assuming a random distribution of spin vectors, the probability of viewing an object in the angle range $[\xi, \xi + d\xi]$ is proportional to $\sin(\xi)d\xi$. The average viewing angle is $\xi=60°$ (Sheppard, 2004; Sheppard, Lacerda and Ortiz, 2008). In this dissertation, we will also use a viewing angle of $\xi=60°$ and so a more likely estimate for the object elongation is:

$$\frac{a}{b} = \frac{10^{\Delta m/2.5}}{\sin 60°} \approx \frac{10^{\Delta m/2.5}}{0.87} \qquad \text{(Equation V.37)}$$

From the a/b ratio, it is also possible to estimate the a/c ratio (see Table 3).

Considering that the object is a rubble pile and thus fluid-like and a Jacobi ellipsoid in hydrostatic equilibrium, we can compute a lower limit to the density (ρ) using the study of the figures of equilibrium for fluid bodies by Chandrasekhar (1987). As already mentioned:

$$\bar{\Omega}^2 = \frac{\Omega^2}{\pi G\rho} \longrightarrow \rho = \frac{\Omega^2}{\pi G\bar{\Omega}^2} \qquad \text{(Equation V.38)}$$

where $\Omega = 2\pi/P$ and P is the rotational period. Such a density is only a lower limit density from the minimum a/b, but it can give us an idea of the body composition (icy or rocky body).

V.1.2.3 Geometric albedo

In case of binary systems, it is possible to estimate the system albedo thanks, in part, to the system lightcurve.

Based on the lower limit of the density, ρ, one can define the volume of the system as V_{system} = M_{system}/ρ, where M_{system} is the mass of the system derived from the orbit. We assume that
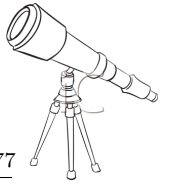
Table 3: $\bar{\Omega}^2$ as a function of b/a and c/a for the Jacobi sequence. Table adapted from Chandrasekhar (1987).

b/a	c/a	$\bar{\Omega}^2$	b/a	c/a	$\bar{\Omega}^2$
1.00	0.582724	0.374230	0.48	0.372384	0.302642
0.96	0.570801	0.373987	0.44	0.349632	0.287267
0.92	0.558330	0.373190	0.40	0.325609	0.269678
0.88	0.544526	0.371785	0.36	0.300232	0.249693
0.84	0.531574	0.369697	0.32	0.273419	0.227153
0.80	0.517216	0.366837	0.28	0.245083	0.201946
0.76	0.502147	0.363114	0.24	0.215143	0.174052
0.72	0.486322	0.358424	0.20	0.183524	0.143610
0.68	0.469689	0.352649	0.16	0.150166	0.111044
0.64	0.452194	0.345665	0.12	0.115038	0.077281
0.60	0.433781	0.337330	0.08	0.078166	0.044168
0.56	0.414386	0.327493	0.04	0.039688	0.015415
0.52	0.393944	0.315989	0	0	0

both components have the same density which is the system density. If both components of the system have the same albedo, the primary radius ($R_{primary}$) can be expressed as:

$$R_{primary} = \left(\frac{3V_{system}}{4\pi \left(1 + 10^{-0.6\Delta_{mag}} \right)} \right)^{1/3} \qquad \text{(Equation V.39)}$$

where Δ_{mag} is the component magnitude difference [3]. Assuming that both components have the same albedo, the satellite radius ($R_{satellite}$) is:

$$R_{satellite} = R_{primary} 10^{-0.2\Delta_{mag}} \qquad \text{(Equation V.40)}$$

The effective radius of the system, $R_{effective}$, is:

$$R_{effective} = \sqrt{R_{primary}^2 + R_{satellite}^2} \qquad \text{(Equation V.41)}$$

We can derive the geometric albedo, p_λ, given by the equation:

$$p_\lambda = \left(\frac{C_\lambda}{R_{effective}} \right)^2 10^{-0.4H_\lambda} \qquad \text{(Equation V.42)}$$

where C_λ is a constant depending on the wavelength (Harris, 1998), and H_λ the absolute magnitude in the λ band. For observations in the V band, $C_V = 664.5$ km.

V.1.3   Other considerations

V.1.3.1   Single or double-peaked lightcurve

One important point is to distinguish between single- and double-peaked lightcurve. Assuming a triaxial object, we expect a lightcurve with two maxima and two minima, corresponding to a full rotation (Figure 44). In such a case, we expect a double-peaked lightcurve. However, if the object is spherical or an oblate spheroid, we expect a lightcurve with one minimum and one maximum per rotation cycle if there are spots on their surfaces.

Basically, we can say that a double-peaked lightcurve is due to the shape of the body whereas a single-peaked lightcurve is due to albedo variations on the surface. In practice sometimes, it is not easy to distinguish between the two possibilities from the observations. In Thirouin et al. (2010) and Duffard et al. (2009), we proposed a threshold of 0.15 mag in order to separate if the lightcurve is due to albedo or due to the target shape (see Section VII.2.1 for more details).

---

[3] The apparent magnitude difference or component magnitude difference is the difference of magnitudes (Δ_{mag}) between the magnitude of satellite and the primary magnitude.
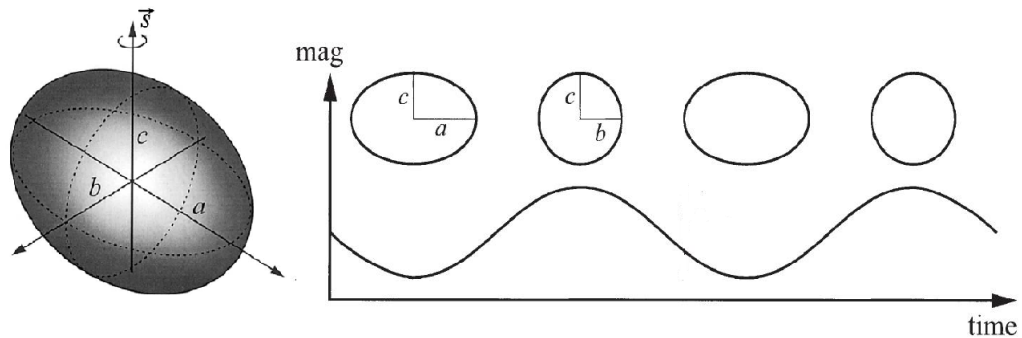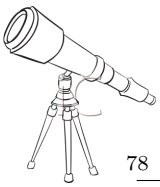
Figure 44: *Magnitude versus time*: Assuming TNOs as triaxial ellipsoids, with axes a>b>c (rotating along c), we have to consider the double peaked periodicity as the true rotational period. Figure adapted from Lacerda and Luu (2003).

V.1.3.2   Lightcurve of binary and multiple systems. Mutual events

For this dissertation, we observed various binary [4] or multiple systems (no eclipsing nor contact binaries). As we are studying systems, we have to keep in mind a possible contribution of the satellite in the photometry (so in the lightcurve). Both components of the system are not resolved in our data, so, we are measuring the magnitude of the pair.

In case of a wide system, with a long orbital period and large separation between both components, the satellite contribution to the lightcurve is negligible. In case of very faint satellite, its lightcurve contribution is also negligible. But, the case of systems with a short orbital period (typically a few days) and a small separation between both components requires more attention. Various systems in our sample have an orbital period around 5 days. Our observational runs are, generally, over one week, and so, an entire (or nearly entire) orbital period is covered. In fact, depending on the geometry of the system, mutual events between the primary and the satellite can be observed. Care was taken to check each observational night for possible mutual events between the primary and the satellite. No mutual event has been detected during our short-term variability runs.

A mutual event is produced when the two components alternate in passing in front of one another, eclipse and occultation between the primary and its satellite. Observations of mutual events between components of a binary/multiple system have been used to constrain binary/multiple asteroid mutual orbits, shapes, and densities (Descamps et al., 2007). Observations of mutual events in the Trans-Neptunian belt is very challenging. Before 2012, mutual events have been observed only for three systems in the Trans-Neptunian belt: 2001 QG$_{298}$ (special case of contact binary previously introduced) (Lacerda, 2011), Haumea (Ragozzine and Brown, 2010), and Pluto-Charon (Binzel and Hubbard, 1997). Detection and analysis of mutual events is not trivial and require a considerable observational and coordinated effort. Several observational campaigns have been planned to observe mutual events in the Sila-Nunam (formerly (79360) 1997 CS$_{29}$) system and are partially reported in Grundy et al. (2012). In fact, thanks to exhaustive observational runs with the *Hubble Space Telescope* during the last ten years, the orbit of this system is

---

[4]The exact definition of binarity is: a binary TNO is a system of two TNOs orbiting their common center of mass or barycenter which lies outside either body. This is the case of the Pluto-Charon system. For most of the binary/multiple systems in the Trans-Neptunian belt we have no information about their barycenter, so the use of the term binary/multiple systems has be to be considered carefully. Often, in the literature, the term binary/multiple is used to refer to system with one or more companions despite the definition mentioned here.

well known (Grundy et al., 2012): an orbital period of 12.50995±0.00036 days, semimajor axis of (2777±19) km, eccentricity of 0.020±0.015, inclination of (103.51±0.39)°, longitude of ascending node of (140.76±0.66)°. During the next few years (usually called a season), the two components of this system will alternate in passing in front of one another, and so, mutual events (eclipse and occultation) between the primary and its satellite will be observable (Figure 45, left panel). In Figure 45 (right panel), is shown the first mutual event reported for the Sila-Nunam system (Grundy et al., 2012).
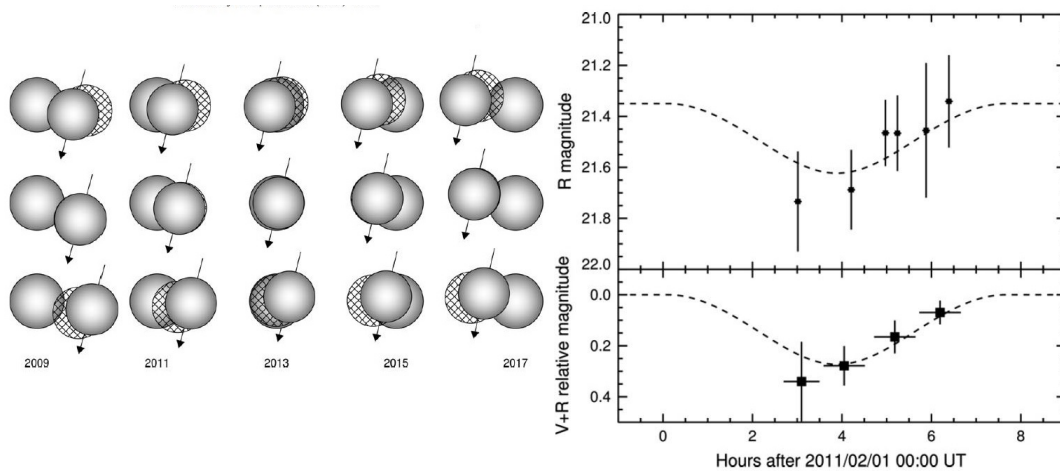
Figure 45: *Mutual event in the Sila-Nunam system*: On the left: Schematic views of mutual events as seen from Earth on the instantaneous sky plane between 2009 and 2017. North is up and East is to the left. All events shown here are inferior events in which Nunam passes in front of (occults) and/or casts a shadow on (eclipses) Sila. The Nunam direction of motion relative to Sila is indicated by arrows. Because the orbit is circular (or nearly so) and the two bodies are the same size (or nearly so), superior events look much the same except that the body in the foreground is Sila instead of Nunam. The Nunam shadow at the distance of Sila is indicated by the hatched region. The middle row shows an event near opposition for each of the years indicated along the bottom. The top row shows events near western quadrature (early in the apparition) and the bottom row shows events near eastern quadrature (late in the apparition). On the right: Photometric observations of the 2011 February 1st mutual event. The top panel shows absolutely calibrated data from SMARTS. The bottom panel shows relative V + R photometry from the Perkins telescope. The dashed curve is a model lightcurve computed for the mutual orbital elements by assuming Sila and Nunam are spherical bodies with radii of 125 and 118 km (respectively), and equal albedos. Figure adapted from Grundy et al. (2012).

On the other hand, we have to take care with a possible periodic signature of the satellite. In fact, the satellite is rotating, so the rotational period of the satellite may "interfere" in the pair rotational period estimation. And finally, we have to take into account the orbital period of the satellite. Thanks to a mid-term photometric and astrometric study of the system Orcus-Vanth, Ortiz et al. (2011) based on observations carried out during a period of 33 days, a high-precision relative astrometry and photometry revealed a periodicity of 9.7±0.3 days induced by the known Orcus satellite, Vanth. Ortiz et al. (2011) have showed that the periodicity in the astromerty residuals is coincident with the orbital period and such values of the residuals are correlated with the theoretical positions of the satellite with respect to the primary. The photometric study of the system revealed a periodicity of 9.7±0.3 days which is also coincident with the orbital period and may attributed to the satellite. In other words, the satellite rotation is synchronous.
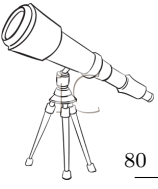
V.2   Periodicity estimation

To search for periodic signals in the photometry, we applied different techniques such as: i) the Lomb periodogram; ii) the Phase Dispersion Minimization (PDM); iii) the CLEAN technique and iv) the Pravec-Harris method. All theses techniques have been developed for asteroid lightcurves, but they are perfectly applicable to TNO/centaur lightcurves.

V.2.1   The Lomb periodogram

The Lomb method (Lomb, 1976) as implemented in Press et al. (1992) has been used. This method is a modified version of the Fourier spectral analysis. The main difference with the Fourier spectral analysis is the fact that this method takes into account irregularly spaced data. This method gives a weight to each data point instead of considering an interval time. In such a case, the spectral power is normalized and usually called Lomb-normalized spectral power ($P_N(\omega)$) as:

$$P_N(\omega) = \frac{1}{2\sigma^2} \frac{\left(\sum_j (h_j - \bar{h}) \cos \omega(t_j - \tau)\right)^2}{\sum_j \cos^2 \omega(t_j - \tau)} + \frac{\left(\sum_j (h_j - \bar{h}) \sin \omega(t_j - \tau)\right)^2}{\sum_j \sin^2 \omega(t_j - \tau)} \qquad \text{(Equation V.43)}$$

where ω is an angular frequency ($\omega = 2\pi/P$ with P as rotational period), and σ^2 is the variance of the data. The mean of the measurements is $\bar{h}$ whereas h_j are the measurements at their times t_j. The parameter τ is defined by:

$$\tan(2\omega\tau) = \frac{\sum_j \sin 2\omega\tau_j}{\sum_j \cos 2\omega\tau_j} \qquad \text{(Equation V.44)}$$

The best period is the one that maximizes the Lomb-normalized spectral power. Hereafter, the term "Lomb periodogram"will be used instead of "Lomb-normalized periodogram" because this term is used in the literature. In Figure 46, a Lomb periodogram is plotted. The highest peak (the maximum of the Lomb-normalized spectral power) is reached at the best rotational frequency. The rotational frequency (Ω) is given in cycles/day (or number of rotations per day) and is related to the rotational period (P) by: $\Omega = 24/P$ where 24 is in hours.

V.2.2   The Pravec-Harris technique

This method was developed for asteroid lightcurves by Harris et al. (1989). But as already mentioned it is perfectly adaptable to the TNO/centaur case. This method consists in fitting the data to a Fourier series. Such Fourier fits can be at any degree and it is expressed as:

$$H(\alpha, t) = \bar{H}(\alpha) + \sum_{l=1}^{m} A_l \sin \frac{2\pi l}{P}(t - t_0) + B_1 \cos \frac{2\pi l}{P}(t - t_0) \qquad \text{(Equation V.45)}$$

where $H(\alpha,t)$ is the computed absolute magnitude at a solar phase angle α and at a time t. $\bar{H}(\alpha)$ is the mean absolute magnitude at phase angle α. A_l and B_l are Fourier coefficients. The rotational period is P and t_0 is the zero-point time chosen at (or nearly) the middle of the time span of the observations (i.e. time reference). The residual between the observations and the fit for the ith observation is $V_i(\alpha_j)$:

$$\frac{\delta_i}{\epsilon_i} = \frac{V_i(\alpha_j) - H(\alpha_j, t_j)}{\epsilon_i} \qquad \text{(Equation V.46)}$$

where α_j is the reference phase angle on the jth night and the time of the ith observation is t_i. The error estimates of the measurements are ϵ_i.

We perform a least-squares fit of the data by finding the minimum of the bias-corrected variance:

$$s^2 = \frac{1}{n - (2m + p + 1)} \sum_{i=1}^{n} \left(\frac{\delta_i}{\epsilon_i}\right)^2 = minimum \qquad \text{(Equation V.47)}$$
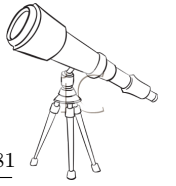
where δ_i is the deviation from the observations to the model as: $\delta_i = V_i(\alpha_j) - H(\alpha_j, t_j)$ with α_j the solar phase angle of the night j. The constants m and p are, respectively, the degree of the Fourier series and the number of days of data. Generally, the variance s^2 is computed for a range of periods and degrees to find the best fit. The standard error (SE) of the Fourier coefficients is given by:

$$SE = \left(\frac{s^2}{\sum\limits_{i=1}^{n} \frac{1}{\epsilon_i^2}} \right)^{1/2} \qquad \text{(Equation V.48)}$$

Some improvements of this method have been proposed in Pravec, Sarounova and Wolf (1996). The analysis of the lightcurves was performed in the way previously presented. But they also computed the amplitude ($Ampl_l$) and the argument ($\phi_l = 2\pi l/P$):

$$Ampl_l = \sqrt{A_l^2 + B_l^2} \; for \; l \; = \; 1 \; to \; n,$$
$$\cos \phi_l = \frac{A_l}{Ampl_l} ; \sin \phi_l = \frac{B_l}{Ampl_l} \; for \; l \; = \; 1 \; to \; n \qquad \text{(Equation V.49)}$$

Hereafter, the term "Pravec-Harris method" to refer to this technique will be used.

V.2.3 The CLEAN method

The CLEAN algorithm has its origin in radio astronomy (Högbom, 1974). This algorithm has been adapted to the optical domain to clean up the spectral window pattern for frequency analysis (Roberts, Lehar and Dreher, 1987). The first step of this method is to construct the dirty spectrum which is the Fourier transform of the data. For a continuous lightcurve (g(t)), the power at the frequency f is $|G(f)|^2$,

$$G(f) = FT[g(t)] = \int_{-\infty}^{+\infty} g(t) e^{-2\pi i f t} \mathrm{d}t \qquad \text{(Equation V.50)}$$

where FT[g(t)] is the Fourier transform of g(t). Assuming that we observe g(t) at certain times t_j specified by the sampling function s(t). The observed data are given by the function d(t)=g(t)s(t). So, the power spectrum ($|D(f)|^2$) is

$$D(f) = FT[d(t)] = G(f) \star FT[s(t)] \qquad \text{(Equation V.51)}$$

where FT[s(t)] is the spectral window function and $\star$ is the convolution operator. And so, the second step of this method is to deconvolve the observed spectrum with the window function shifted to the highest peak of the dirty spectrum. Then, one subtracts the scaled spectral window from the dirty spectrum to produce a residual spectrum. This deconvolution process is repeated until the strongest residual peak is below a specific cut-off level or for a chosen number of iterations. Finally, the CLEAN algorithm restores the removed frequency to the spectrum by convolving it with the cleaned residual spectrum. Foster (1995) developed the CLEANest frequency spectrum which is the sum of a discrete amplitude spectrum and the residual spectrum. The discrete spectrum is derived from a model fit of the best M frequencies to the data according to:

$$x(t_i) = \sum\nolimits_{k=1}^{M} a_k \cos\left(2\pi\nu_k(t_i - \tau)\right) + b_k \sin\left(2\pi\nu_k(t_i - \tau)\right) + c + \epsilon_i \qquad \text{(Equation V.52)}$$

where $x(t_i)$ describes the variations due to M oscillation modes with frequencies μ_k, a_k, b_k and c are free fitting parameters, ϵ_i is the measurement errors, and τ is an arbitrary reference epoch. Such a process is done for one frequency at a time until finding the best frequency

V.2.4 The Phase Dispersion Minimization (PDM)

The Phase Dispersion Minimization (hereafter PDM) was developed by Stellingwerf (1978). It is useful for data sets with gaps, non-sinusoidal variations, or poor time coverage and it is specially
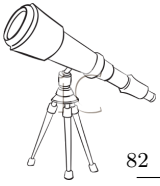
suited to detect periodic signals regardless of the lightcurve shape.

The PDM method searches for the best period that minimizes the Θ parameter. The Θ parameter is :

$$\Theta = \frac{s^2}{\sigma^2} \qquad \text{(Equation V.53)}$$

where the data dispersion (s^2) assuming a rotational period is :

$$s^2 = \frac{\sum_{j=1}^{M}(n_j-1)s_j^2}{\sum_{j=1}^{M}(n_j-M)} \qquad \text{(Equation V.54)}$$

and the variance σ^2 of the data is expressed as:

$$\sigma^2 = \sum_{i=1}^{N} \frac{(x_i-\bar{x})^2}{(N-1)} \qquad \text{(Equation V.55)}$$

s_j are the variances of M distinct samples, N is the number of observations, x_i are the measurements and $\bar{x}$ is the mean of the measurements. In other words, the Θ parameter measures the dispersion of the data phased to a specific rotational period divided by the variance of the non-phased data (i.e. non-phased to a rotational period). The samples, M, are taken in order to all members have a similar phase (ϕ_i) corresponding to a rotational period used as a test. Usually the phase interval is [0,1] and it is divided into bins of fixed size.

V.2.5   Confidence levels

When a possible rotational period is identified, it is useful to know how confident that estimation is. In the Lomb periodogram case, the confidence level is given by:

$$P(> z) = 1 - (1 - e^{-z})^M \qquad \text{(Equation V.56)}$$

where M is the number of independent frequencies and z is the maximum spectral power (Scargle, 1982). Each method, previously presented, has its own formula to compute the confidence level. Here, we only mention the confidence level estimation for the Lomb periodogram because it is the easiest one and the most used.

However, the best approach to compute such confidence level is probably based on Monte Carlo simulations in which one can generate random photometric data taking into account non-random photometry errors (systematic or non-systematic errors) (Gutiérrez et al., 2001). In Figure 46 is plotted a Lomb periodogram in which two different confidence levels based on Monte Carlo simulations are plotted: i) simulations in which random Gaussian errors are assumed and, ii) simulations in which night-to-night random offsets are added.

V.2.6   Alias problems

During an observational run, the data obtained are not randomly spaced in time, not evenly spaced in time. In fact, there are regular (or not) gaps in data acquisition. Thus, there are lots of frequencies in the data that interfere with the true periodic variability of the object. For example, there are frequencies not randomly spaced in time such as: i) the read-out time of the instrument, ii) the exposure time, iii) the fact to observe an object at the same (or nearly) moment, and during the same time each night. But there are also frequencies caused by changes in the observing plan (e.g. changes for weather conditions or technical problems or voluntary changes in the observational planning). However, the main aliases are associated with the night-to-night observing. In fact, observing each 24 h provokes a serious gap in the data and generates a lot of difficulties to estimate the true rotational period of the observed object.

The 24-h alias because of daylight is:

$$P_{alias}^{-1} = 1.0027k \pm P_{real}^{-1} \qquad \text{(Equation V.57)}$$
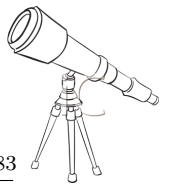
where $(1.0027)^{-1}$ is the length of the sidereal day and k is an integer. The main alias is seen for k=1. Other minor aliases are seen at k>1. The aliases are easily identified in a Lomb periodogram expressed in the frequency domain. In Figure 46, a Lomb periodogram is plotted. The main peak (i.e. the highest peak) is located near 2 cycles/day. Whereas the other peaks are aliases and are at nearly 1 cycle/day spacing.
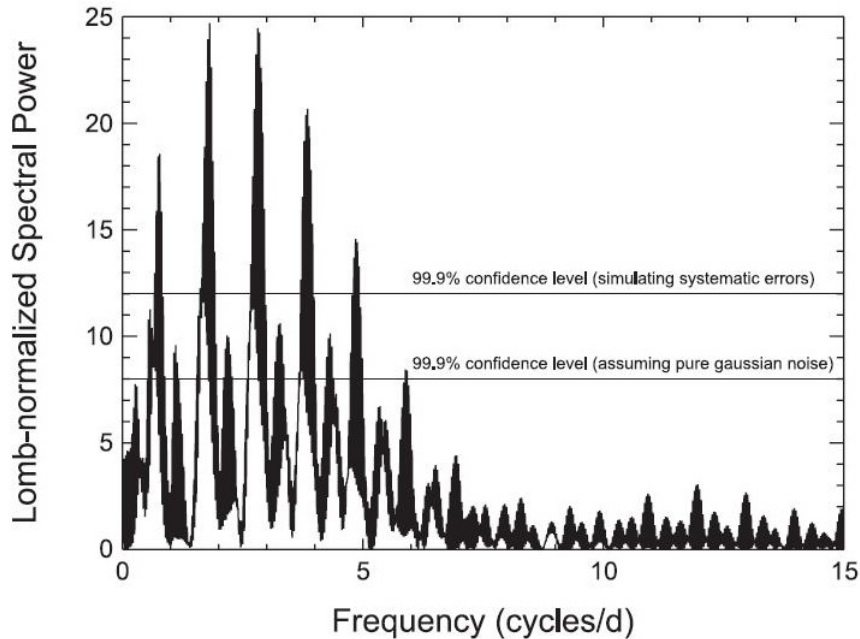
Figure 46: *Example of Lomb periodogram*: The main peak corresponds to Elatus rotational period whereas the other peaks at nearly 1 cycle/day spacing are aliases. Two horizontal lines are the significance levels assuming systematic errors and assuming gaussian noise. Figure from Sheppard, Lacerda and Ortiz (2008).

Most of the photometric studies about TNOs/centaurs reported are based on "short" observational runs carried out in few days and so, we only detect the short-term variability of the object. The best option to minimize the 24-h alias effect is to observe continuously through coordinated campaigns using several telescopes around the world (see Section IV.4.2). However, the long-term monitoring of objects is difficult because it is hard to schedule time on several medium to large telescopes around the world, for long time spans.

One the other hand, and especially in the case of an object with a nearly flat lightcurve, a very large dataset is required in order to favor or discard a rotational periodicity. So, for this work, we always mix our data with available data from other sources. Such approach is also useful to complete a partial lightcurve.

V.2.7   Peak-to-peak lightcurve amplitude

We call peak-to-peak lightcurve amplitude or full lightcurve amplitude, to the amplitude between the maximum and the minimum of the lightcurve.

A lightcurve can be fitted by a sinusoidal fit or a Fourier series (1st or 2nd order generally) fit, depending if we are considering a single- or double-peaked rotational periodicity. Such fits are respectively:

$$Fit_{sinusoidal} = a\sin(2\pi\phi_{rot} + b) + c \qquad \text{(Equation V.58)}$$

$$Fit_{Fourier1} = a + b\cos(2\pi\phi_{rot}) + c\sin(2\pi\phi_{rot}) \qquad \text{(Equation V.59)}$$
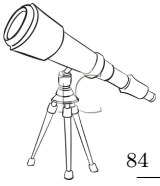
$$Fit_{Fourier2} = a + b\cos(2\pi\phi_{rot}) + c\sin(2\pi\phi_{rot})$$
$$+ d\cos(4\pi\phi_{rot}) + e\sin(4\pi\phi_{rot}) \quad \text{(Equation V.60)}$$

where a, b, c, d, and e are constants and ϕ_{rot} is the rotational phase. Each constant of such fits has its own error bar that can be computed by a non-linear least squares method (see Bevington and Robinson (2003) for more details). Thanks to such fits, we are able to estimate the lightcurve amplitude and the associated error. In this dissertation, we used Fourier Series fits for all lightcurves (see Chapter VI).

Chapter VI

Results on short-term variability of Trans-Neptunian Objects and Centaurs

$\mathcal{O}$ ne of the goals of this thesis was to try to increase the number of Trans-Neptunian Objects and centaurs whose short-term variability has been studied and to compile a high quality database with the least possible biases, which may be used to perform statistical analyses. More than 10,000 images obtained between 2003 and 2013 using several telescopes around the world have been reduced and analyzed. In this chapter, lightcurves, possible rotation periods and photometric amplitudes for 45 objects are reported. For 9 more objects, an estimation of the amplitude and only a very crude spin period are proposed. For several objects, a new analysis of data previously used in Ortiz et al. (2003a); Ortiz et al. (2003b); Ortiz et al. (2006); Ortiz et al. (2007b); Belskaya et al. (2006) has been done and, in some cases additional data have been included. Part of the results of this short-term variability study have been summarized in several papers: Thirouin et al. (2010); Thirouin et al. (2012); Thirouin et al. (2013a); Thirouin et al. (2013b). We present here all the results in their full extent. The short-term variability of several objects is presented here for the first time.

VI.1 Introduction

In the next sub-sections, short-term variability information for 54 Trans-Neptunian Objects (TNOs) and centaurs is reported. All lightcurves are plotted over two cycles (rotational phase from 0 to 2) for a better visualization of the cyclical variation. For each lightcurve, a Fourier series is used to fit the photometric data.

Error bars for the measurements are not shown on the plots for clarity but one-sigma error bars on the relative magnitudes are reported in the material online of Thirouin et al. (2010); Thirouin et al. (2012); Thirouin et al. (2013b); Thirouin et al. (2013a). An example of this online material can be found in the Appendix A. In such a table, we report the name of the object, and for each image we specify the Julian date, the relative magnitude and the 1-σ error associated, the filter used during the observational run, the phase angle, the topocentric and heliocentric distances. The full table is available in .pdf or ascii format upon request. The typical error bars of the individual integrations are $\sim$0.01 mag for the brightest targets, and 0.06 mag for the faintest objects (in the poorest observing conditions).

Relevant geometric information about the observed objects at the dates of observations, the number of images and filters used are summarized in Table 1 in Section IV.5. The following sub-sections are dedicated to discuss the short-term variability of each object and are organized according to the Gladman, Marsden and Vanlaerhoven (2008) dynamical classification (see Section II.2). In Table 4, one can find the orbital elements of all the objects studied during this thesis.
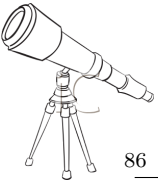
Table 4: Orbital elements of the TNOs and centaurs studied in this thesis: in this table are reported the object name, the perihelion distance (q in AU), the aphelion distance (Q in AU), the absolute magnitude (H), the argument of perihelion (M in °), longitude of the ascending node (Node in °), the inclination (Incli in °), the orbital eccentricity (e), and the semimajor axis (a in AU). Orbital elements extracted from the Minor Planet Center (MPC) database updated on May, 18th 2013.

Object	q	Q	H	M	Peri.	Node	Incli.	e	a
(24835) 1995 SM$_{55}$	37.442	46.641	4.8	326.3	70.1	21	27	0.109	42.041
(15874) 1996 TL$_{66}$	35.053	134	5.4	5.4	184.9	217.7	24	0.586	84.732
(52872) 1998 SG$_{35}$ Okyrhoe	5.781	10.891	10.9	78.4	337.4	173.1	15.7	0.307	8.336
(26375) 1999 DE$_9$	32.228	79.031	5.1	23.5	159.4	322.9	7.6	0.421	55.629
(44594) 1999 OX$_3$	17.576	47.072	7.3	338.8	144.3	259.3	2.6	0.456	32.324
(40314) 1999 KR$_{16}$	33.956	63.236	5.8	342	58.8	205.7	24.8	0.301	48.596
(20000) 2000 WR$_{106}$ Varuna	40.881	45.497	3.6	98.8	273.3	97.3	17.1	0.053	43.189
(38628) 2000 EB$_{173}$ Huya	28.532	50.063	4.9	357.5	67.7	169.3	15.5	0.274	39.297
(148975) 2001 XA$_{255}$	9.332	48.404	11.1	6.6	90.3	105.9	12.6	0.677	28.868
2001 QF$_{298}$	35.118	43.699	5.1	150.6	41.3	164.2	22.4	0.109	39.408
(275809) 2001 QY$_{297}$	40.21	47.299	5.6	80.1	124.9	108.8	1.5	0.081	43.754
(126154) 2001 YH$_{140}$	36.384	48.806	5.4	16.8	355.4	108.8	11.1	0.146	42.595
(55576) 2002 GB$_{10}$ Amycus	15.166	34.749	7.8	29.6	238.8	315.5	13.4	0.392	24.958
(42355) 2002 CR$_{46}$ Typhon	17.514	58.35	7.5	10.7	158.9	351.9	2.4	0.538	37.932
(84522) 2002 TC$_{302}$	39.107	72.282	3.8	320.7	86.1	23.8	35	0.298	55.695
(250112) 2007 UL$_{126}$ or 2002 KY$_{14}$	8.634	16.579	9.5	31.4	99.9	245.4	19.5	0.315	12.607
(50000) 2002 LM$_{60}$ Quaoar	41.607	44.752	2.4	276.5	163	189	8	0.036	43.179
(55565) 2002 AW$_{197}$	41.312	53.382	3.4	289.5	294.3	297.4	24.3	0.127	47.347
(307251) 2002 KW$_{14}$	37.17	55.849	5	46.4	121.9	59.9	9.8	0.201	46.509
(307261) 2002 MS$_4$	35.436	47.788	3.7	213.2	215	216.2	17.7	0.148	41.612
(55636) 2002 TX$_{300}$	38.102	48.72	3.2	67.2	342.2	324.7	25.9	0.122	43.411
(55637) 2002 UX$_{25}$	36.686	49.105	3.7	293.5	275.8	204.6	19.4	0.145	42.896
(55638) 2002 VE$_{95}$	28.001	51.242	5.6	16.4	207.6	199.8	16.3	0.293	39.621
2002 VT$_{130}$	41.399	43.983	5.8	100.7	354.3	334.2	1.2	0.03	42.691
(1199791) 2002 WC$_{19}$	35.464	60.985	4.9	313.9	43.2	109.8	9.2	0.265	48.225
(120061) 2003 CO$_1$	10.906	30.453	8.9	25.4	116.1	78.5	19.8	0.473	20.68
(136204) 2003 WL$_7$	14.957	25.598	8.6	7.8	70.8	4.7	11.2	0.262	20.278
(136108) 2003 EL$_{61}$ Haumea	34.65	51.465	0.1	206.5	240.7	121.8	28.2	0.195	43.058
(84922) 2003 VS$_2$	36.445	42.895	4.1	11.7	113.9	302.8	14.8	0.081	39.67
(120132) 2003 FY$_{128}$	36.981	61.844	4.9	26.5	174	341.7	11.8	0.252	49.412
(120178) 2003 OP$_{32}$	38.65	47.6	3.6	67.2	68.5	183	27.2	0.104	43.125
(174567) 2003 MW$_{12}$	39.052	52.113	3.4	262.2	184.6	184.1	21.5	0.143	45.583
(208996) 2003 AZ$_{84}$	32.73	46.552	3.7	224.4	14.6	251.9	13.5	0.174	39.641
(307982) 2004 PG$_{115}$	36.415	143	4.9	4.2	75.8	230.5	16.3	0.595	89.859
(90482) 2004 DW Orcus	30.649	48.087	2.2	169.7	73.7	268.4	20.5	0.221	39.368
(120347) 2004 SB$_{60}$ Salacia	37.688	46.465	4.2	116.6	309.6	280.2	23.9	0.104	42.076
2004 NT$_{33}$	36.928	49.804	4.4	35.8	38	241.1	31.2	0.148	43.366
(144897) 2004 UX$_{10}$	37.601	40.733	4.5	84.1	158.8	148	9.5	0.04	39.167
(230965) 2004 XA$_{192}$	35.479	59.49	4	353.8	131.9	328.7	38.1	0.253	47.485
(145451) 2005 RM$_{43}$	35.123	149	4.4	3.4	318.5	84.7	28.7	0.618	92.038
(145480) 2005 TB$_{190}$	46.191	105	4.7	357.9	171.9	180.5	26.5	0.39	75.768
(145486) 2005 UJ$_{438}$	8.262	27.231	10.8	13.5	208.3	262.9	3.8	0.534	17.747
(136472) 2005 FY$_9$ Makemake	38.269	52.842	-0.4	154.6	297.1	79.3	29	0.16	45.555
(145453) 2005 RR$_{43}$	37.318	49.609	4	38.5	281.1	85.9	28.5	0.141	43.463
(145452) 2005 RN$_{43}$	40.536	42.446	3.9	331.8	177.9	187	19.3	0.023	41.491
(308193) 2005 CB$_{79}$	37.284	49.687	4.7	315.8	90.2	112.8	28.6	0.143	43.485
(202421) 2005 UQ$_{513}$	37.151	49.778	3.4	222.3	220.1	307.9	25.7	0.145	43.464
(229762) 2007 UK$_{126}$	37.6	111	3.4	341.6	345.9	131.3	23.3	0.494	74.377
(341520) 2007 TY$_{430}$	28.842	50.082	6.8	354	205.6	196.7	11.3	0.269	39.462
(281371) 2008 FC$_{76}$	10.175	19.352	9.1	354.2	142	245.7	27.1	0.311	14.763
(315898) 2008 QD$_4$	5.445	11.427	11.4	38.8	69.2	344.7	42	0.355	8.436
(342842) 2008 YB$_3$	6.49	16.791	9.3	19.3	330.6	112.5	105	0.442	11.64
(315530) 2008 AP$_{129}$	35.999	48.067	4.7	41.4	59.1	14.9	27.4	0.144	42.033
2010 BK$_{118}$	6.106	931	10.2	0	179.1	176	143.9	0.987	468

VI.2   Classical objects

VI.2.1   (275809) 2001 QY$_{297}$

Using *Hubble Space Telescope* images, Noll et al. (2008a) reported the discovery of a satellite with
an apparent magnitude difference [1] of around 0.42 mag [2] and a separation [3] at the discovery of
0.091″. As already pointed out in Section V.1.3.2, we have to keep in mind a possible contribution
of the satellite in the photometry (in the lightcurve) and care has to be taken with the study of
this systems.

For this thesis, 2001 QY$_{297}$ was observed during our coordinated campaign in 2009 and during
three more nights in 2010 with the 3.58 m NTT. In 2009, we obtained around 10.2 h split in two
nights and around 2.3 h in three nights of observations in 2010. The Lomb periodogram (Figure 47)
of our two data sets shows three groups of peaks: the first one, with the highest spectral power,
suggests a spin period around 5.84 h, the second one around 4.61 h and the last one around
7.25 h. The CLEAN technique confirms a periodic signature at 5.84±0.34 h. However, PDM
presents a single peak period of 7.21±0.39 h, and the Pravec-Harris technique a period around
14.4±0.6 h and also a possible spin period of 5.84±0.34 h. The best-fit lightcurve is obtained for a
period of 5.84 h (Figure 48) because the alternative fits show more scatter. The amplitude of the
lightcurve is large, 0.49±0.03 mag assuming a 5.84 h periodicity. Assuming that large amplitudes
(>0.15 mag) are mainly due to shape effects, we must consider the double-peaked lightcurve (see
Section V.1.3.1). Then, if 5.84 h is our preferred photometric period, a preferred rotational period
of 11.68 h (2×5.84) is deduced.
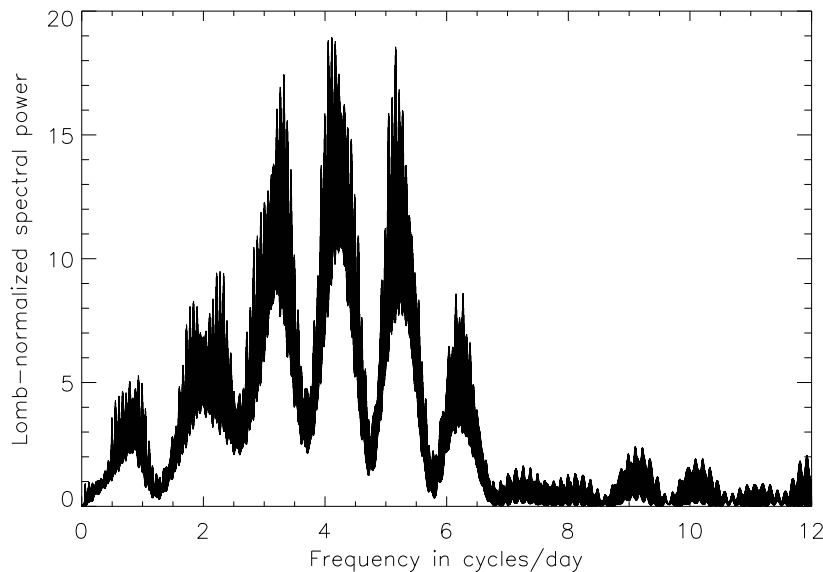
Figure 47: *Lomb-normalized spectral power versus frequency in cycles/day for 2001 QY$_{297}$*: The Lomb
periodogram of our data set shows three groups of peaks: the first one, with the highest spectral power,
suggested a rotational period around 5.84 h, the second one around 4.61 h and the last one around 7.25 h.

A previous study of this target, based on 13 images obtained in around 5 h of observations was
done by Kern (2006) who got some constraints on the spin period of 12.2±4.3 h with an amplitude
of 0.66±0.38 mag. This is consistent with our results. In conclusion, 2001 QY$_{297}$ has a moderately

---

[1] The apparent magnitude difference or component magnitude difference is the difference of magnitudes (Δ_{mag})
between the magnitude of satellite and the primary magnitude.

[2] Magnitude difference in the F606W band that is approximately the same as the V-band.

[3] The separation is the distance between the primary and the secondary, also called semi-major axis.
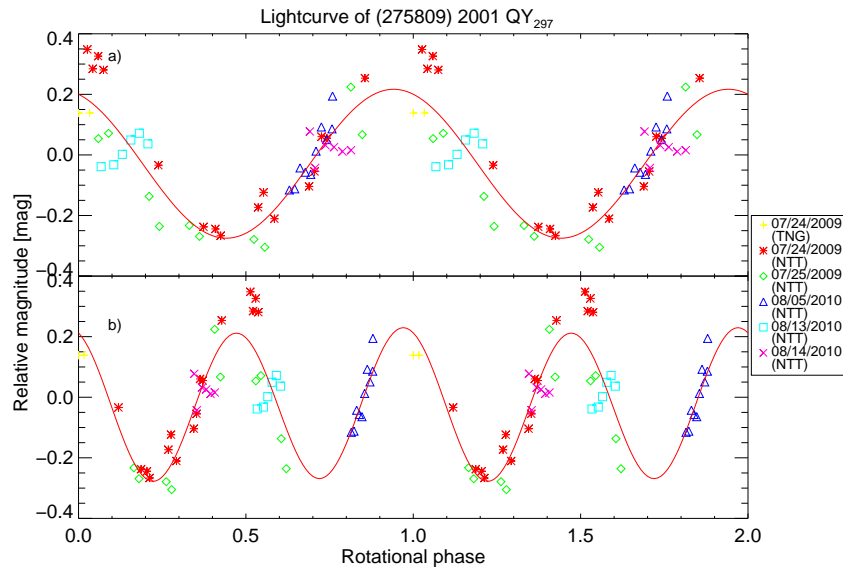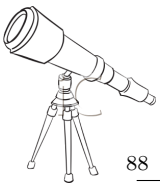
Figure 48: *Relative magnitude versus rotational phase for 2001 QY$_{297}$*: Plot a) is the single-peaked lightcurve obtained for a rotational period of 5.84 h. Plot b) is the double-peaked lightcurve obtained for a rotational period of 11.68 h (2×5.84). Continuous lines are a Fourier Series fits of the photometric data. Different symbols correspond to different dates.

long rotational period and a very high amplitude, which is consistent with the constraints by Kern (2006).

As already mentioned, 2001 QY$_{297}$ has a satellite. This system turned out to be an asynchronous binary system because the primary has a much smaller rotational period than the orbital one. Both components of the system are not resolved in our data, so, we are measuring the magnitude of the pair. The satellite has a long orbital period: 138.11±0.02 days and it is orbiting at a distance of 9960±30 km from the primary (Grundy et al., 2011c). The magnitude difference between 2001 QY$_{297}$ and its satellite is 0.42±0.07 mag (Noll et al., 2008a). Due to the orbital and physical characteristics of the system with a small satellite, the satellite contribution to the lightcurve is negligible.

VI.2.2 (55565) 2002 AW$_{197}$

Ortiz et al. (2006) published a possible lightcurve for 2002 AW$_{197}$, based on observations carried out on November and December 2002, on February 2003 and on January 2004 with the 1.5 m OSN telescope. Ortiz et al. (2006) presented a Lomb periodogram with several peaks (peaks with a spectral power higher than 99%). The highest peak was located at 8.86 h and was accompanied by two aliases, with lower spectral power than the first peak, at 13.94 h and at 6.94 h. Another peak with a high confidence was identified at 15.82 h. They favored a single-peaked rotational period of 8.86 h (with a reliable code of 2 according to Lagerkvist, Magnusson and Rickman (1989)).

In December 2003, R-band observations were carried out by Sheppard (2007) with the University of Hawaii 2.2 m telescope. They presented a very flat lightcurve (amplitude <0.03 mag) based on 27 images and concluded that 2002 AW$_{197}$ has no significant short-term variability.

The data sets of February 2003 and of January 2004 have been already published in Ortiz et al. (2006), but were re-reduced and re-analyzed in Thirouin et al. (2010). The Lomb periodogram (Figure 49) presents several peaks above the 99% confidence level. The highest peak is located at
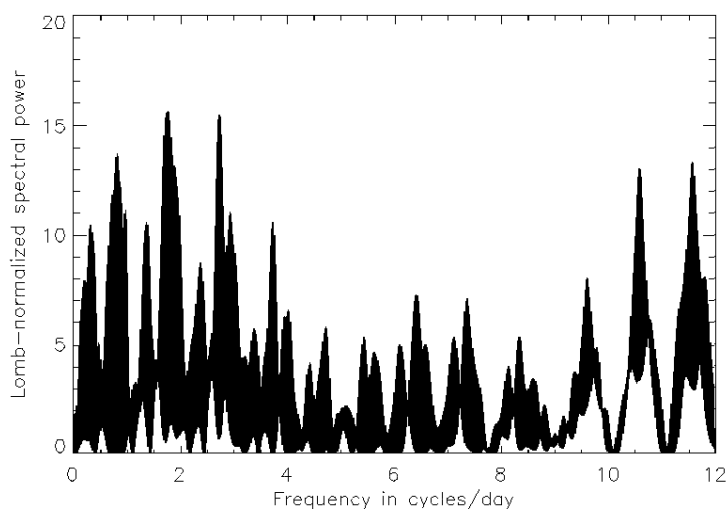
Figure 49: *Lomb-normalized spectral power versus frequency in cycles/day for 2002 AW$_{197}$*: The Lomb periodogram of our 2003 and 2004 data sets shows several peaks. The main peak is located at 1.75 cycles/day (13.71 h) and several aliases are located at 2.74 cycles/day (8.78 h), at 3.73 cycles/day (6.94 h, and at 0.79 cycles/day (30.38 h).

Figure 50: *Relative magnitude versus rotational phase for 2002 AW$_{197}$*: Single-peaked lightcurve for 2002 AW$_{197}$ obtained by using a spin period of 8.78 h. The continuous line is a Fourier Series fit of the photometric data. Different symbols correspond to different dates.

13.71 h (1.75 cycles/day) and several aliases are located at 8.78 h and 6.94 h. Peaks at 13.71 h and 8.78 h have a similar spectral power. The PDM, CLEAN and Pravec-Harris techniques favored a spin period of 8.78 h or 13.71 h with a similar spectral power. However, from visual inspection, the best-fit lightcurve is obtained for a period of 8.78 h because the alternative fits exhibit more
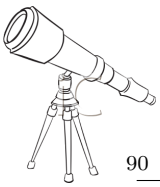
scatter. In Figure 50, the corresponding lightcurve with a spin period of 8.78 h, and a small amplitude of only 0.02±0.02 mag is plotted.

In conclusion, 2002 AW$_{197}$ has a nearly flat lightcurve and most likely a 8.78 h rotational period, but spin periods of 13.71 h and 6.94 h are also possible. For very low amplitude lightcurves it is often difficult to determine which is the true rotational period and which are the aliases in the periodograms.

VI.2.3   (307251) 2002 KW$_{14}$

Figure 51: *Lomb-normalized spectral power versus frequency in cycles/day for 2002 KW$_{14}$*: The Lomb periodogram shows one peak located at 4.29 h (5.59 cycles/day) and two aliases, with a lower spectral power, at 5.25 h (4.57 cycles/day) and at 3.69 h (6.49 cycles/day).

This target was observed along ∼10 h during 3 nights with the 3.58 m NTT and 0.2 h with the 3.58 m TNG. The Lomb peridogram (Figure 51) shows a peak with a high spectral power at 4.29 h (5.59 cycles/day) and two main aliases, with a lower spectral power, at 5.25 h (4.57 cycles/day) and at 3.69 h (6.49 cycles/day). All the techniques used confirmed a photometric spin period of 4.29 h or 5.25 h with a similar spectral power. In Figure 52, both options (plots a) and c)) are plotted.

According to our assumption that high amplitude lightcurve is due to the shape of the object, one has to consider the double-peaked lightcurve. In this case, the rotational period of this body should be 8.58 h or 10.5 h. The preferred period is 8.58 h, corresponding to an amplitude of 0.21±0.03 mag (Plot b) in Figure 52). However, also a lightcurve fit assuming a rotational period of 10.5 h with an amplitude of 0.26±0.03 mag is possible (plots d) in Figure 52).

Benecchi and Sheppard (2013) also studied 2002 KW$_{14}$ and reported 5 nights of observations (only 40 data points) with the Irénée du Pont 2.5 m telescope at Las Campanas Observatory (Chile). They proposed a single-peaked rotational period of 6.63 h or a double-peaked rotational period of 13.25 h. In both cases, the lightcurve amplitude is 0.25±0.03 mag. However, our rotational periodicity of 5.25 h is also reported by Benecchi and Sheppard (2013) as an alias with a spectral power higher than 99.9%. The rotational period favored by Benecchi and Sheppard (2013) is also an alias in our study. Unfortunately, Benecchi and Sheppard (2013) photometric
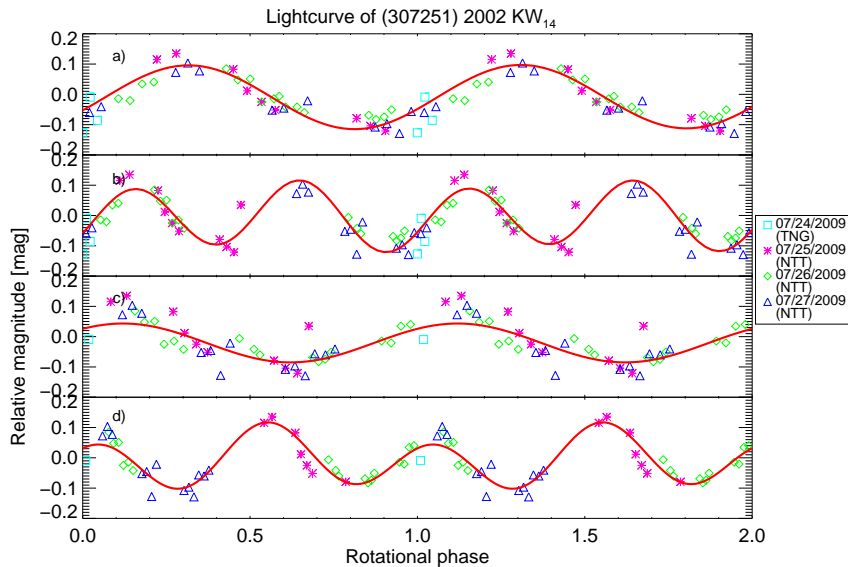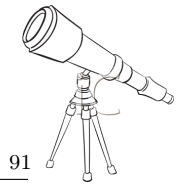
Figure 52: *Relative magnitude versus rotational phase for 2002 KW_{14}*: Plot a) is the single-peaked
lightcurve obtained with a rotational period of 4.29 h. Plot b) is the double-peaked lightcurve obtained
with a rotational period of 8.58 h. Plot c) is the single-peaked lightcurve obtained with a rotational period
of 5.25 h. Plot d) is the double-peaked lightcurve obtained with a rotational period of 10.5 h. Continuous
lines are a Fourier Series fits of the photometric data. Different symbols correspond to different dates.

results are not available and so, it is not possible to mix both data sets in order to favor or discard
a rotational period. Both studies agreed that 2002 KW_{14} shows a high lightcurve amplitude.

VI.2.4   (50000) 2002 LM_{60} or Quaoar

Using *Hubble Space Telescope* images, Brown and Suer (2007) reported the discovery of a faint
satellite (with 5.6 mag difference with respect to the primary in the F606W band) on February
22nd, 2007. In November 2009, the satellite received the name of Weywot.

2002 LM_{60} (hereinafter Quaoar) was observed during two observational runs in May and June
2003 and results are published in Ortiz et al. (2003b), who inferred a 17.67883 h double-peaked
periodicity and an amplitude of 0.133 mag. But also the single-peaked periodicity of 8.84 h was
possible.

Rabinowitz, Schaefer and Tourtellotte (2007) presented BVI band observations obtained using
the 1.3 m SMARTS telescope. They suggested a 8.84 h single-peaked rotational lightcurve with
an amplitude of 0.18 mag, which is consistent with the single-peaked lightcurve proposed by Ortiz et al. (2003b).

Lin, Wu and Ip (2007) presented R band results based on the analysis of 57 images acquired
in June 2003 using the Lulin 1 m Telescope. They proposed a 9.42 h single-peaked rotational
lightcurve with a spectral power higher than 99.9% and a ∼0.3 mag amplitude. Such a high amplitude is inconsistent with previous results, which were obtained using larger telescopes and data sets.

As part of this thesis, in Thirouin et al. (2010) we re-reduced and re-analyzed the May and
June 2003 data published in Ortiz et al. (2003b). In Thirouin et al. (2010), we concluded that the
Lomb periodogram and the CLEAN technique showed one peak with a high spectral power corresponding to a periodicity at 8.84 h (2.72 cycles/day). But a double-peaked lightcurve at 17.68 h
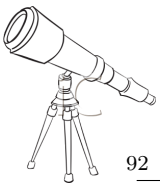
was also an option to consider. In fact, both the PDM and the Pravec-Harris method suggested the double-peaked periodicity. The lightcurve amplitude was 0.15 ± 0.04 mag. A slight preference for the single-peaked period was noticed in Thirouin et al. (2010).
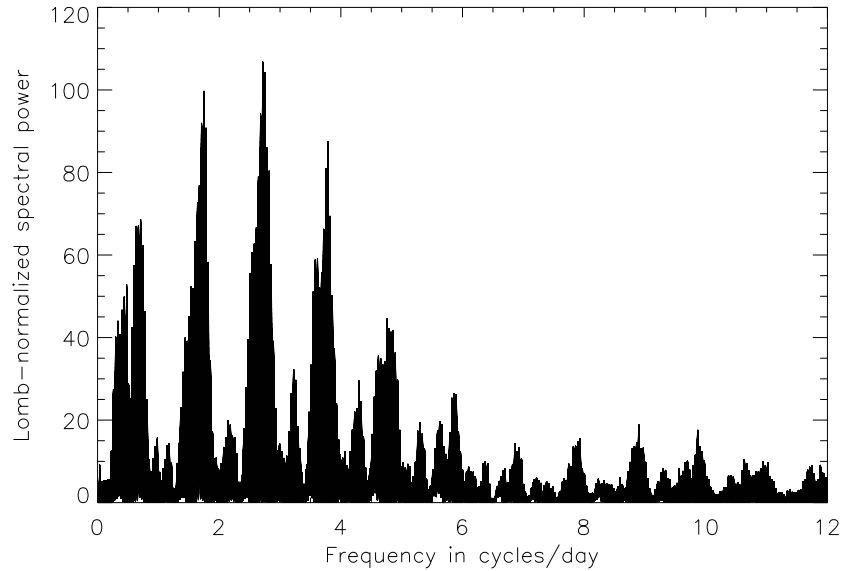
Figure 53: *Lomb-normalized spectral power versus frequency in cycles/day for Quaoar*: The Lomb periodogram of our 2003, 2011 data sets as well as V-band data from Rabinowitz, Schaefer and Tourtellotte (2007) shows one main peak located at 8.84 h and several aliases located at 1.74 cycles/day (13.79), and 3.74 cycles/day (6.42 h).

Quaoar was re-observed in July 2011 with the 3.58 m TNG. With just few data, the single-peaked periodicity is confirmed with an amplitude of 0.13 ± 0.02 mag. By merging the 2003, 2011 data sets and Rabinowitz, Schaefer and Tourtellotte (2007) V-band observations, an accurate spin period of 8.83898 h is obtained (Figure 53). In Figure 54, the three lightcurves obtained during the past few years are plotted. The final lightcurve amplitude is 0.112 ± 0.011 mag. However, we must point that there are four other peaks with a very similar spectral power (Figure 55) located at: 8.84232 h (P1 peak indicated in Figure 55), at 8.84118 h (P2), at 8.83910 h (P3), and at 8.83887 h (P4).

In conclusion, we prefer a single-peaked rotational period of 8.841 ± 0.002 h for Quaoar.

VI.2.5   (307261) 2002 MS$_4$

The study of 2002 MS$_4$ is really difficult because it is crossing a crowded stars field. In other words, the TNO moves in a part of the sky with many background stars that sometimes get blended with the TNO pint spread function. However, we decided to observe it in two occasions. The first one was in August, 2005 at the OSN. The second one was in June-July, 2011 with the 3.58 m TNG, taking advantage that the object traversed a dark cloud inside the milky way.

In 2005, 15 images were obtained in around 2 h in the first observing night, and 5 images in 20 minutes during the second night. With only 20 images, a reliable rotational period estimation is not possible.
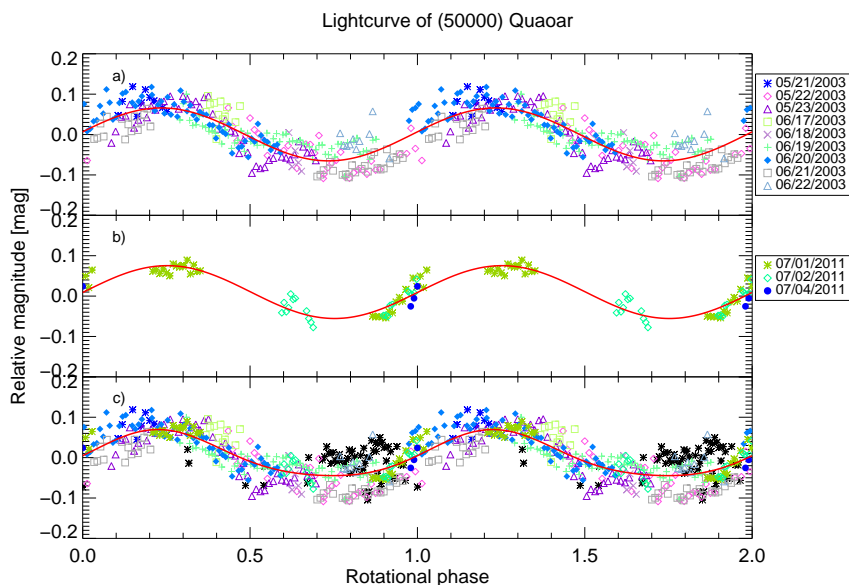
Figure 54: *Relative magnitude versus rotational phase for Quaoar*: Plot a) is the single-peaked lightcurve
obtained in 2003. Plot b) is the single-peaked lightcurve obtained in 2011. Plot c) is the single-peaked
lightcurve obtained by merging the 2003 and 2011 data sets with V-band data of Rabinowitz, Schaefer and
Tourtellotte (2007). Rabinowitz, Schaefer and Tourtellotte (2007) data are in indicated in the plot c) with
a black asterisk. The same symbols as mentioned previously in the plot a) and plot b) legends have been
used for the plot c). Only the V-band data of Rabinowitz, Schaefer and Tourtellotte (2007) are plotted
here. Continuous lines are a Fourier Series fits of the photometric data. Different symbols correspond to
different dates.
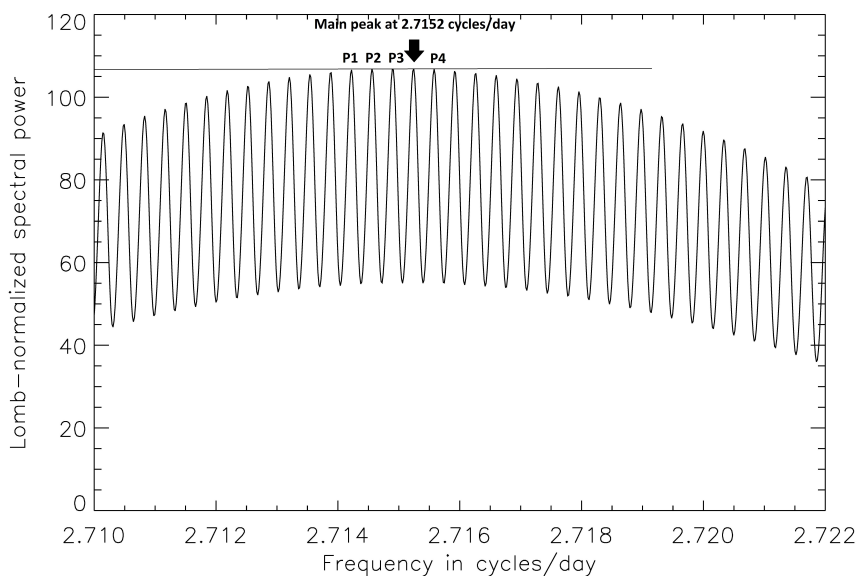
Figure 55: Enlargement of the Lomb periodogram of our 2003, 2011 data sets as well as V-band data
from Rabinowitz, Schaefer and Tourtellotte (2007) presented in Figure 53. The main peak is located at
2.71524 cycles/day and four other peaks with a very similar spectral power (P1 to P4) are noted.

Figure 56: *Lomb-normalized spectral power versus frequency in cycles/day for 2002 MS$_4$*: The Lomb periodogram of our 2005 and 2011 data sets shows two peaks with a similar spectral power located at 3.27 cycles/day and at 2.30 cycles/day.

Figure 57: *Relative magnitude versus rotational phase for 2002 MS$_4$*: Single-peaked lightcurve for 2002 MS$_4$ obtained by using a spin period of 7.33 h (Plot a)) and using a spin period of 10.44 h (Plot b)). Continuous lines are a Fourier Series fits of the photometric data. Different symbols correspond to different dates.

The Lomb periodogram of our two data sets (2005 and 2011) shows two main peaks with a high spectral power (Figure 56) and several aliases. The highest peak is located at 7.33 h (3.27 cycles/day) and the second one is located at 10.44 h (2.30 cycles/day). The second peak is an alias of the first one. The PDM and CLEAN techniques and the Pravec-Harris method confirmed these two options. However, Pravec-Harris method seems to favor the double-peaked periodicities cor-

responding.

In Figure 57, both single-peaked lightcurves are proposed. The first lightcurve assuming a spin
period of 7.33 h exhibits an amplitude of 0.05±0.01 mag. The second lightcurve with a rotational
period of 10.44 h has an amplitude of 0.05±0.01 mag. We present here the only short-term vari-
ability study for this object. No literature on this object is available.

VI.2.6   (55636) 2002 TX$_{300}$

Based on data obtained between October and December 2002 with the 1.5 m OSN telecope
as well as with the Nordic Optical Telescope (NOT), and the Canada-France-Hawaii Telescope
(CFHT), Ortiz et al. (2004) published a rotational period of 7.89±0.03 and a lightcurve amplitude
of 0.09±0.08 mag.

Sheppard and Jewitt (2003) presented a 8.12 h or a 12.1 h single-peaked rotational R-band
lightcurve with an amplitude peak-to-peak of 0.08±0.02 mag (they only reported photometric am-
plitude estimated from apparent maximum and minimum, and not lightcurve amplitude obtained
from a Fourier fit as it has been done it this work).

2002 TX$_{300}$ was observed during two observational runs: one in August 2003, and one in
September 2010 but also during one isolated night in October 2009. The 2003 data set is al-
ready published in Thirouin et al. (2010) where we concluded that the spin period of this object
should be 8.14±0.02 h. But a possible rotational period around 12 h was not completely discarded.

Figure 58: *Lomb-normalized spectral power versus frequency in cycles/day for 2002 TX$_{300}$*: The Lomb
periodogram of our 2003, 2009 and 2010 data sets shows several peaks with a main peak at 4.08 h (5.89 cy-
cles/day).

The Lomb periodogram based on all our data sets (2003, 2009, and 2010) indicates a main
peak at 4.08 h (5.89 cycles/day) (Figure 58). All used techniques confirmed this period, except
the Pravec-Harris method which favored a double-peaked period at 8.15 h (2.94 cycles/day). A
double-peaked lightcurve seems to be the best option (Figure 59). The corresponding amplitude
is 0.05±0.01 mag (Thirouin et al., 2012). However, the possibility of a rotational period around 12
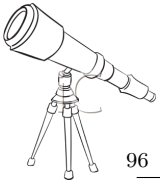
h cannot be excluded (Figure 59). In such a case, the lightcurve amplitude is lower, 0.01±0.01 mag.
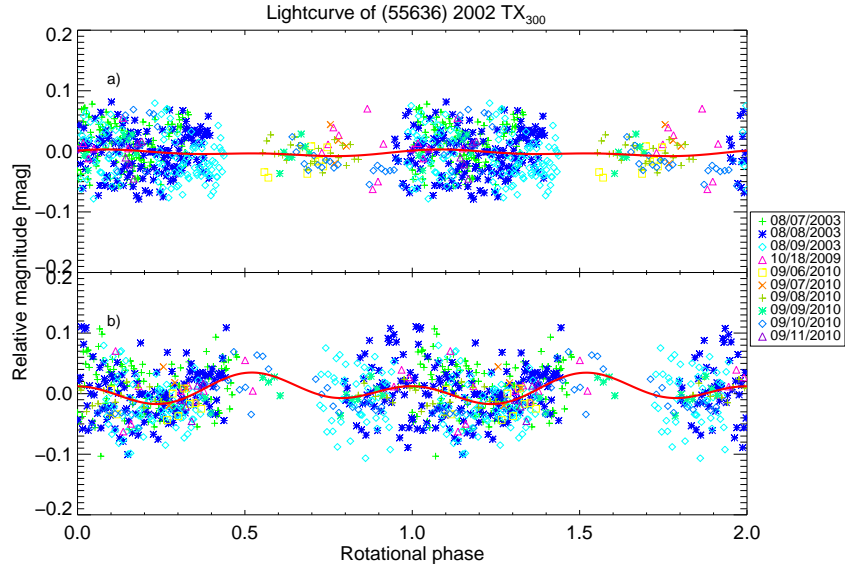
Figure 59: *Relative magnitude versus rotational phase for 2002 TX$_{300}$:* Single-peaked lightcurve for 2002 TX$_{300}$ obtained by using a spin period of 11.7 h (Plot a)) and a spin period of 8.15 h (Plot b)). The continuous lines are a Fourier Series fit of the photometric data. Different symbols correspond to different dates.

In conclusion, a rotational period around 8.15 h seems to be the best option for 2002 TX$_{300}$.

VI.2.7   (55637) 2002 UX$_{25}$

Using *Hubble Space Telescope* images, Brown and Suer (2007) reported the discovery of a satellite with an apparent magnitude difference of 2.5±0.2 mag in the F606W band.

Sheppard and Jewitt (2003) observed this object during two nights at the 2.2 m University of Hawaii telescope. They concluded that 2002 UX$_{25}$ has a flat lightcurve with an amplitude peak-to-peak <0.06 mag.

Rabinowitz, Schaefer and Tourtellotte (2007) presented data obtained between July 2003 and December 2003 with the 1.3 m SMARTS telescope. They did not provide a spin period estimation but they suggested an amplitude of 0.13±0.09 mag. As Rabinowitz, Schaefer and Tourtellotte (2007) study was carried for solar phase curve and not short-term variability, we have to be careful with their result.

Rousselot et al. (2005b) presented a vast study of this object at different phase angles. They carried out two different observing runs in October and December 2003 with a 2 m telescope located at the Pik Terskol observatory (Russia). They found two possible rotational period: 14.382±0.001 h or 16.782±0.003 h. Using a double-peaked lightcurve with a rotationalk period of 16.782 h, the amplitude is 0.21±0.06 mag (in the R-band). Such a high amplitude is ruled out by Sheppard and Jewitt (2003) and our own results shown below.

For this thesis, 2002 UX$_{25}$ was observed during a run in January 2008 at Calar Alto Observatory. The Lomb periodogram (Figure 60) shows several peaks with a low spectral power. The main peak, with the highest spectral power, is located at 6.55 h (3.66 cycles/day). Two aliases of
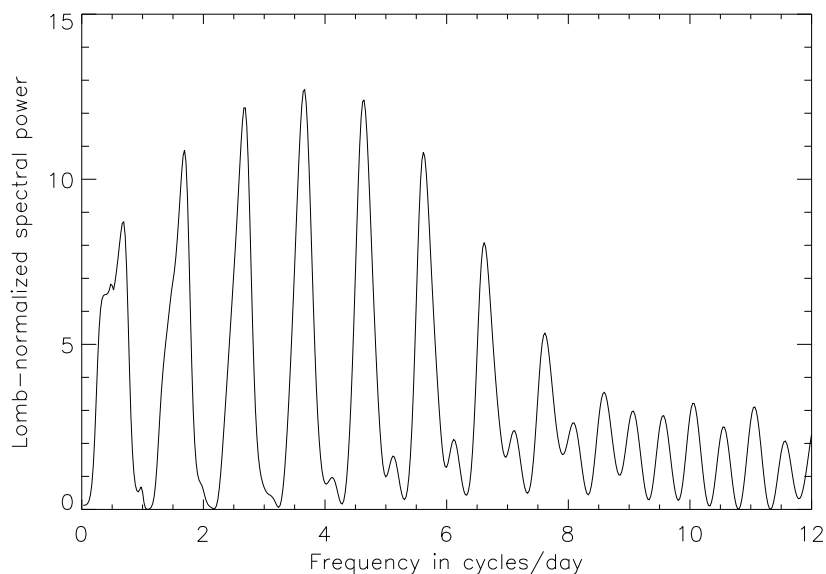
Figure 60: *Lomb-normalized spectral power versus frequency in cycles/day for 2002 UX$_{25}$*: The Lomb
periodogram shows several peaks located at 6.55 h, at 9.02 h and at 5.15 h

the main peaks are at 9.02 h and 5.15 h. All techniques confirmed the possible rotational periods
already mentioned. As the main peak is favored by all methods used, in Figure 61 the correspond-
ing lightcurve is plotted. The lighturve amplitude is 0.09±0.03 mag. Our study also ruled out the
high amplitude noticed by Rousselot et al. (2005b).
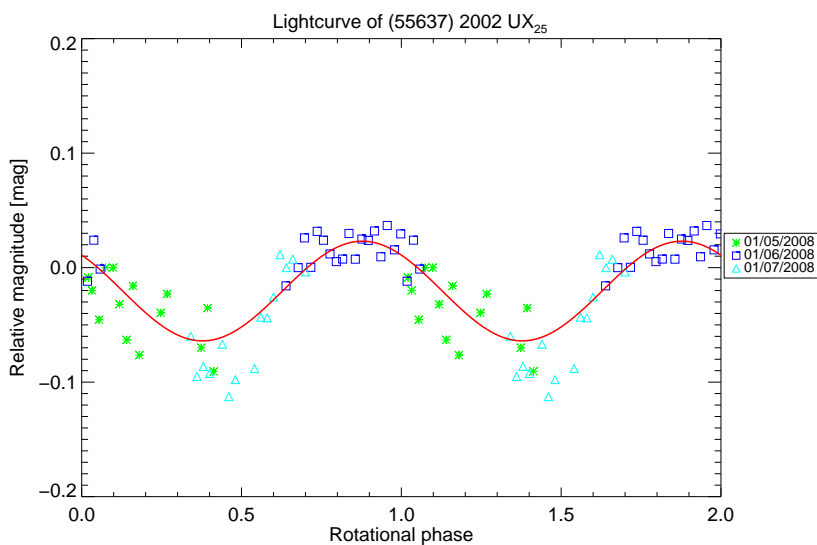
Figure 61: *Relative magnitude versus rotational phase for 2002 UX$_{25}$*: Single-peaked lightcurve for
2002 UX$_{25}$ obtained by using a spin period of 6.55 h. The continuous line is a Fourier Series fit of
the photometric data. Different symbols correspond to different dates.
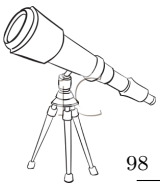
VI.2.8   2002 VT$_{130}$

Using *Hubble Space Telescope* images, Noll et al. (2009b) announced on September 24th, 2009 the discovery of a satellite with an apparent magnitude difference of 0.44 mag in the F606W band.

2002 VT$_{130}$ was observed during one night in 2011 at the 3.58 m TNG. In around 4 h of observations, an amplitude variation of 0.21 mag is reported. Unfortunately, with just few observational hours a reliable rotational period cannot be determined.

VI.2.9   (120132) 2003 FY$_{128}$

Sheppard (2007) observed 2003 FY$_{128}$ on March 2005 with the Dupont 2.5 m telescope in Las Campanas (Chile). He presented a flat lightcurve (amplitude <0.08 mag) based on only 17 data points and concluded that this object has no significant short-term variability.

Dotto et al. (2008) also observed this object. They reported more than 13 h of observations carried out in April 2007, in the R-band at the 3.58 m NTT. They could not determine a rotational period and suggested a short-term variability longer than 7 h for this object.
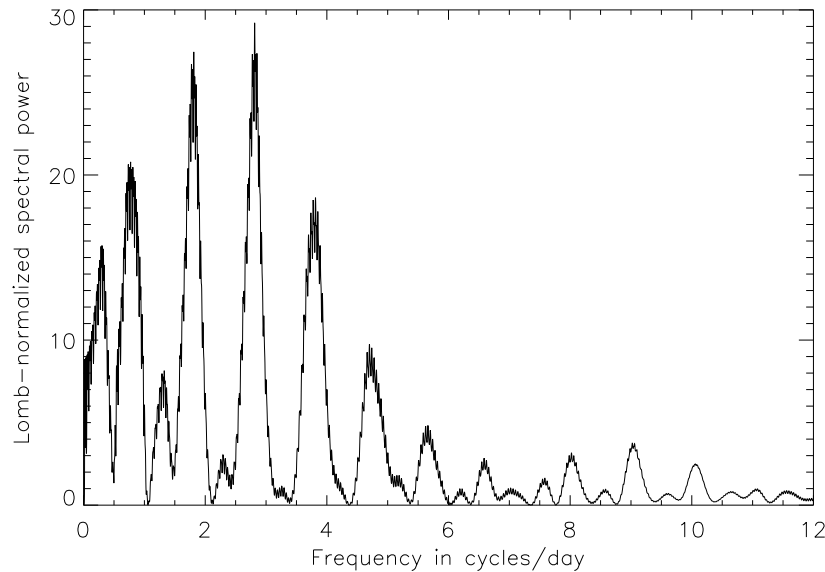
Figure 62: *Lomb-normalized spectral power versus frequency in cycles/day for 2003 FY$_{128}$*: The Lomb periodogram of our data and of Sheppard (2007) data shows two peaks located at 1.76 cycles/day, and at 2.81 cycles/day (with a higher spectral power than the previous peak).

During this thesis, we also studied this object. 2003 FY$_{128}$ was observed in February and March 2005. The Lomb periodogram of our data and Sheppard (2007) data, (Figure 62) indicates one clear peak with a high spectral power (>99%) located at 8.54 h (2.81 cycles/day) and an alias at 1.76 cycles/day (13.64 h). All techniques confirmed such a periodicity. In Figure 63, the corresponding single-peaked lightcurve with an amplitude of 0.12±0.02 mag is plotted. However, a double-peaked periodicity of 17.08 h might be more appropriate because the fit to a Fourier series shows minima and maxima of different values, but neither PDM nor the Harris method, which are less sensitive to the exact shape of the lightcurve, proposed a periodicity 17.08 h, so the single-peaked spin period seems the best option (Thirouin et al., 2010).

In conclusion, a period of 8.54 h appears reasonable and is consistent with Dotto et al. (2008) results. On the other hand, our data and Sheppard (2007) data are matching.
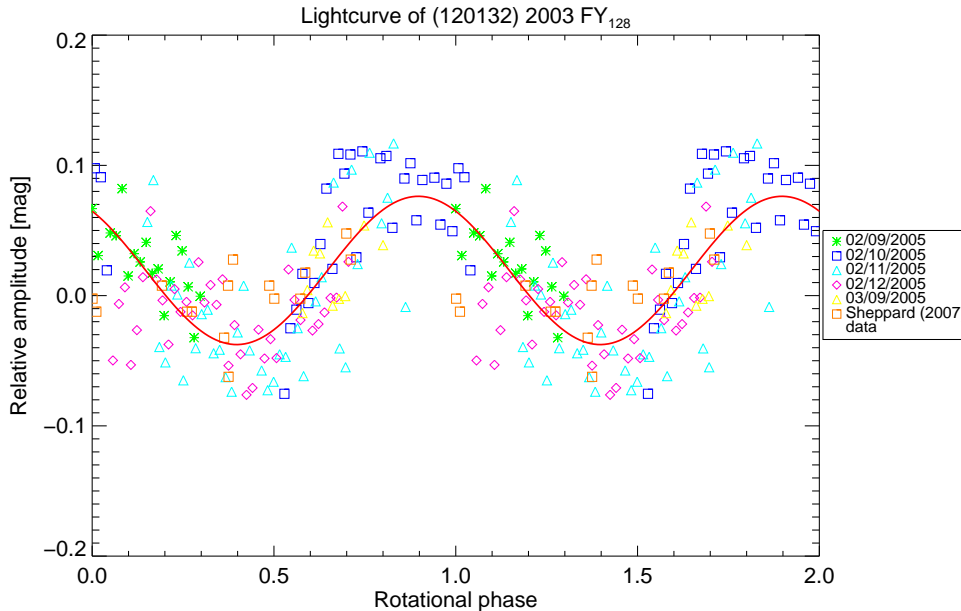
Figure 63: *Relative magnitude versus rotational phase for 2003 FY$_{128}$*: Single-peaked lightcurve for 2003 FY$_{128}$ obtained by using a spin period of 8.54 h. The continuous line is a Fourier Series fit of the photometric data. Different symbols correspond to different dates.

VI.2.10 (174567) 2003 MW$_{12}$

Using *Hubble Space Telescope* images obtained in April 26st 2009, the discovery of a satellite was reported in 2011 (Grundy et al., 2011a). The satellite is faint, with an apparent magnitude difference of ∼1.45 mag in the F606W band.

2003 MW$_{12}$ has been studied during this thesis. Thirouin et al. (2010) published a lightcurve for this object based on data obtained in 2006 and in 2008 and suggested two possible rotational periods: 5.9 h or 7.87 h.

2003 MW$_{12}$ was also re-observed in July 2009 and 2011 with the 3.58 m TNG, and in June 2012 at the OSN. The Lomb periodogram of the 2005, 2008, 2009, 2011, and 2012 data sets (Figure 64) shows several peaks. The highest peak is located at 5.91 h (4.06 cycles/day) and the two main aliases are at 7.87 h (3.04 cycles/day) and at 4.76 h (5.04 cycles/day). All techniques (PDM, CLEAN, and Pravec-Harris method) inferred a spin period of 5.91 h or 7.87 h. A 5.91 h rotational period is favored with a higher spectral power and, so, appears to be the best option. In Figure 65, the corresponding single-peaked lightcurve with an amplitude of 0.02±0.01 mag is plotted. For very low amplitude objects, it is difficult to estimate a secure rotational period. In fact, small variations in the photometry from night to night can transmit more power to/from a 24 h-alias from/to the main peak. So, it is not possible to completely discard the 7.87 h or the 4.76 h single-peaked rotational period.

Only Benecchi and Sheppard (2013) studied 2003 MW$_{12}$ too. They presented 4 nights of observations with the Irénée du Pont 2.5 m telescope at Las Campanas Observatory (Chile) and reported a flat lighturve with an amplitude <0.04 mag which is in agreement with our result. They did not report any rotational period estimation.
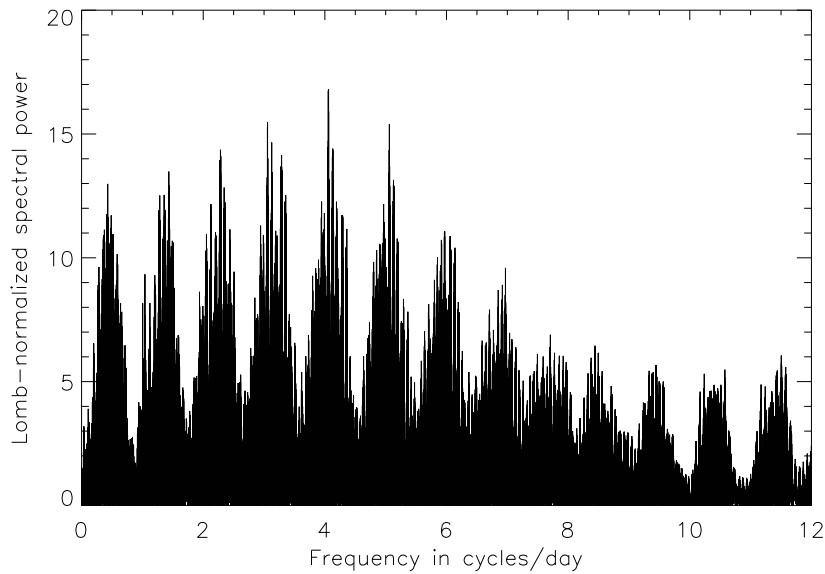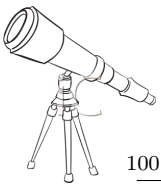
Figure 64: *Lomb-normalized spectral power versus frequency in cycles/day for 2003 MW$_{12}$*: The Lomb periodogram of our 2005 to 2012 data sets shows one highest peak is located at 5.91 h (4.06 cycles/day) and the two largest aliases are at 7.87 h (3.04 cycles/day) and at 4.76 h (5.04 cycles/day).
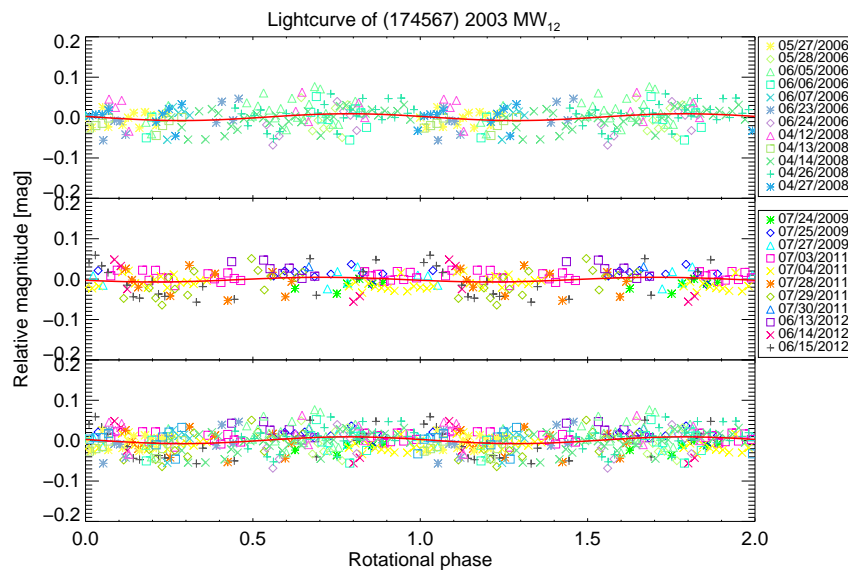
Figure 65: *Relative magnitude versus rotational phase for 2003 MW$_{12}$*: Single-peaked lightcurve for 2003 MW$_{12}$ obtained by using a spin period of 5.91 h. Plot a) is the first lightcurve obtained in 2006 and 2008. Plot b) is the lightcurve obtained between 2009 and 2012. By merging all the data, we obtained the single-peaked lightcurve shown in the Plot c). The continuous lines are a Fourier Series fits of the photometric data. Legends of plot a) and plot b) were used for the plot c).

VI.2.11   (120178) 2003 OP$_{32}$

Rabinowitz et al. (2008) presented 78 R-band observations of 2003 OP$_{32}$ obtained in 2006 at the
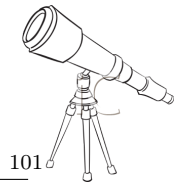
1.3 m SMARTS telescope. They proposed a single-peaked lightcurve with a periodicity of 4.845 h
and an amplitude of 0.26 mag.

We also observed 2003 OP$_{32}$ during several runs between 2005 and 2007. In Thirouin et al.
(2010), we proposed a single-peaked lightcurve with a spin period of 4.05 h and an amplitude
peak-to-peak of 0.13±0.01 mag.

We re-observed this object in August 2011. The Lomb periodogram of our 2005, 2007 and 2011
data sets altogether shows one peak located at 5.90 cycles/day (4.07 h) and two aliases located at
4.95 cycles/day (4.85 h) and at 6.91 cycles/day (3.47 h) (Figure 66). All techniques used confirm
a periodic signature at 4.07 h. In Figure 67, the corresponding single-peaked lightcurve with an
amplitude of 0.12±0.01 mag is plotted. In conclusion, our data completely ruled out the possibility
of a large amplitude lightcurve noted by Rabinowitz et al. (2008).
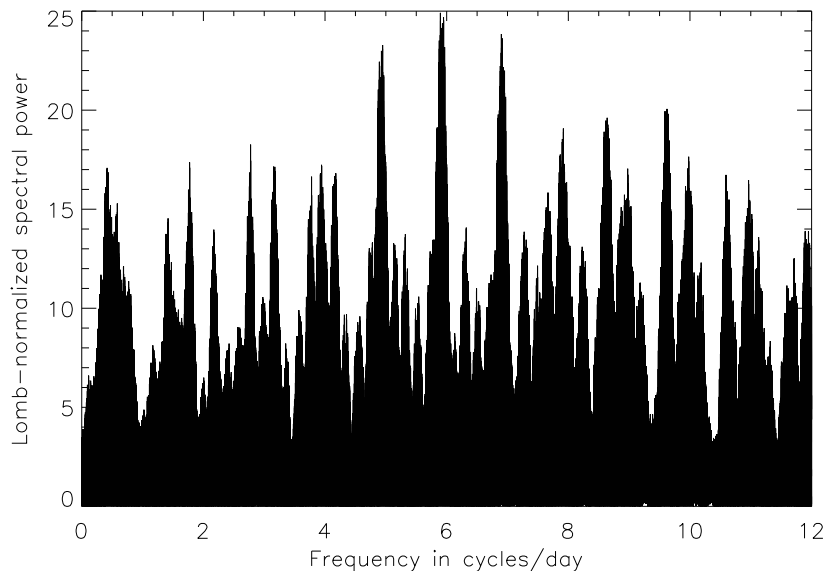
Figure 66: *Lomb-normalized spectral power versus frequency in cycles/day for 2003 OP$_{32}$*: The Lomb
periodogram of our 2005, 2007 and 2011 data sets shows three peaks located at 4.95 cycles/day, at 5.90 cy-
cles/day (main peak), and at 6.91 cycles/day.

Benecchi and Sheppard (2013) observed 2003 OP$_{32}$, during 6 nights with the Irénée du Pont
2.5 m telescope at Las Campanas Observatory (Chile). They favored a single-peaked rotational
period of 4.85 h or a double-peaked rotational period of 9.71 h. Their peak-to-peak lightcurve
amplitude is 0.18±0.01 mag. However, Benecchi and Sheppard (2013) reported more than 7
peaks with a spectral power higher than 99.9%, including the 4.07 h rotational period obtained in
Thirouin et al. (2010); Thirouin et al. (2013a). Also, the Benecchi and Sheppard (2013) period is
one of the peaks in the Figure 66. As the Benecchi and Sheppard (2013) photometric data are not
available, a mix of all the data sets to favor or discard the 4.07 h or the 4.85 h rotational period is
not possible. On the other hand, Benecchi and Sheppard (2013) obtained a lightcurve amplitude
slightly higher than our 0.12 mag lightcurve amplitude reported. However, Benecchi and Sheppard
(2013) only reported photometric amplitude estimated from apparent maximum and minimum,
and not lightcurve amplitude obtained from a lightcurve fit as it has been done in this thesis.
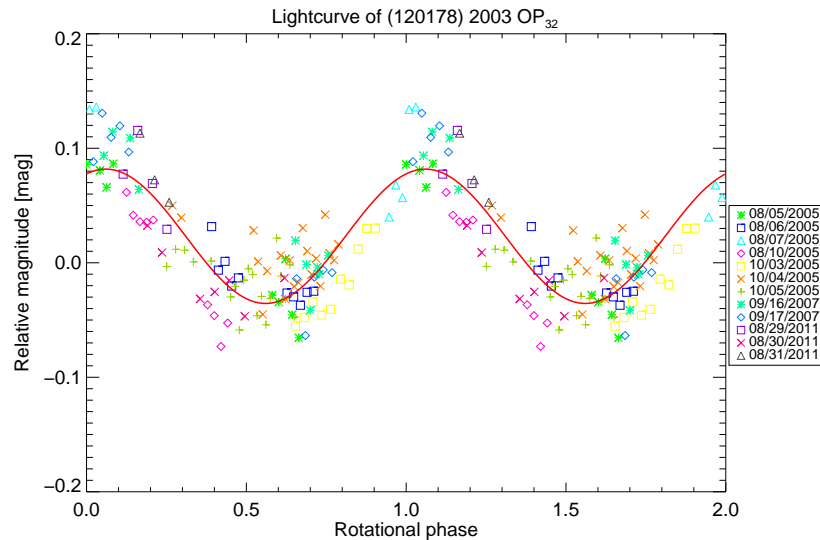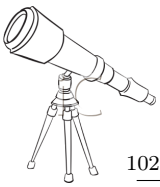
Figure 67: *Relative magnitude versus rotational phase for 2003 OP$_{32}$*: Single-peaked lightcurve for 2003 OP$_{32}$ obtained by using a spin period of 4.07 h. The continuous line is a Fourier Series fit of the photometric data. Different symbols correspond to different dates.

VI.2.12   2004 NT$_{33}$

We observed 2004 NT$_{33}$ during two runs in July and October 2009. The Lomb peridogram (Figure 68) shows a peak with a high spectral power at 7.87 h (3.05 cycles/day) and two aliases with a lower spectral power at 11.76 h (2.04 cycles/day) and at 5.91 h (4.06 cycles/day). The PDM, and CLEAN techniques confirmed the highest peak around 7.8 h. The Pravec-Harris technique suggested a spin period of 7.87 h, a double peak period of 23.52 h, and a possible rotational period of 3.1 h. The best-fit lightcurve is obtained for a period of 7.87 h and a corresponding amplitude of 0.04±0.01 mag (Figure 69) (Thirouin et al., 2012).

VI.2.13   (120347) 2004 SB$_{60}$ or Salacia

Using *Hubble Space Telescope* images, Noll et al. (2006e) reported the discovery of a satellite (named Actaea) with an apparent magnitude difference of 2.36 mag in the F606W band.

Thirouin et al. (2010) published a possible lightcurve for the Salacia-Actaea system based on data obtained out with the 1.5m OSN telescope in August 2005 and in August 2008. They favored a 6.09 h spin period, however, an alias at 8.1 h was not completely discarded. In both cases, the lightcurve amplitude was very low, 0.03±0.01 mag.

Salacia was re-observed on July and October 2011 with the 3.58 m TNG, and in September and October 2012 at the OSN. The Lomb periodogram based on all the data sets, (Figure 70) shows several peaks. The highest peak is located at 3.63 cycles/day (6.61 h) and the two aliases with a lower spectral power are located at 2.59 cycles/day (9.27 h) and at 4.58 cycles/day (5.24 h). All techniques inferred the spin period of 6.61 h with the highest spectral power. In Figure 71, the corresponding single-peaked lightcurve with a peak-to-peak amplitude of 0.04±0.02 mag is plotted. Only the 2011-2012 data set is presented here because it exhibits a lowest dispersion in comparison with the 2005-2008 data set.
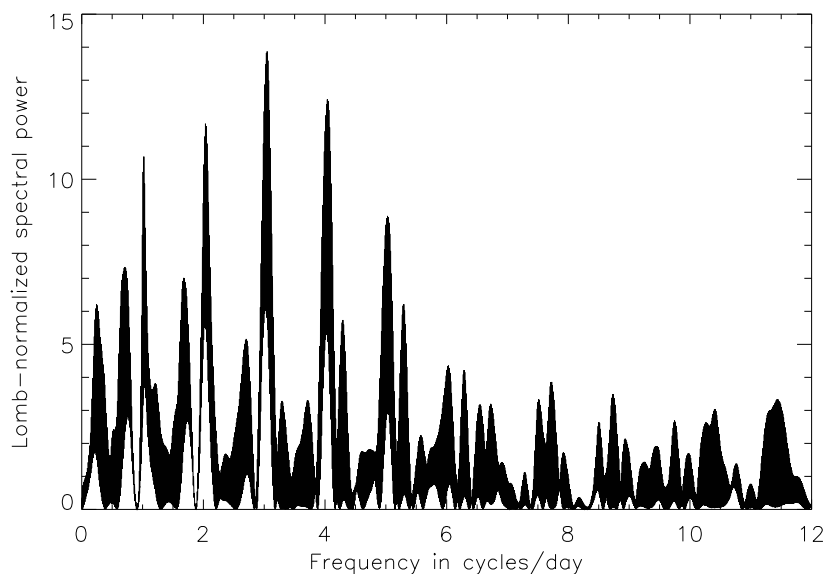
Figure 68: *Lomb-normalized spectral power versus frequency in cycles/day for 2004 NT$_{33}$:* The Lomb periodogram shows a peak with a high spectral power at 3.05 cycles/day and two aliases with a lower spectral power at 2.04 cycles/day and at 4.06 cycles/day.
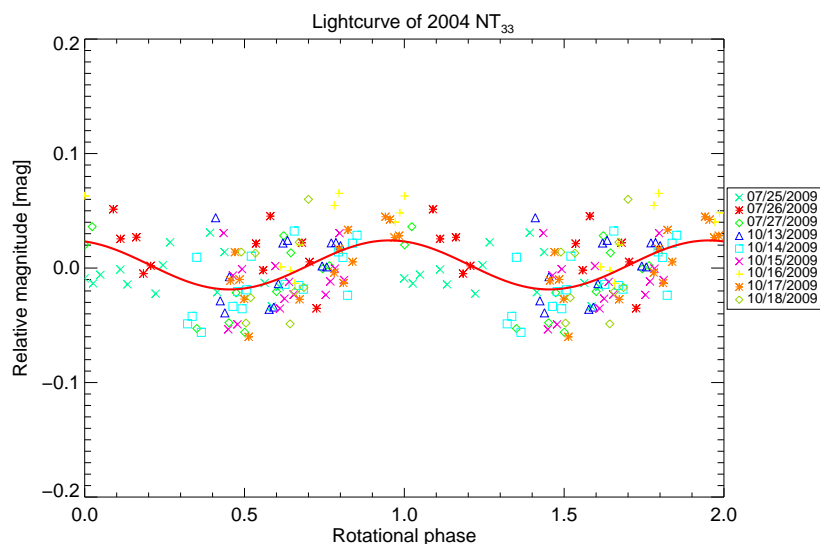
Figure 69: *Relative magnitude versus rotational phase for 2004 NT$_{33}$:* Single-peaked lightcurve for 2004 NT$_{33}$ obtained by using a spin period of 7.87 h. The continuous line is a Fourier Series fit of the photometric data. Different symbols correspond to different dates.

The alias located at 8.1 h, and reported in Thirouin et al. (2010), is discarded thanks to our new study. The possibility of a rotational period between 6 and 7 h remains and appears the best option.

Only Benecchi and Sheppard (2013) studied the short-term variability of Salacia. Based on four nights of observations with the Irénée du Pont 2.5 m telescope at Las Campanas Observatory
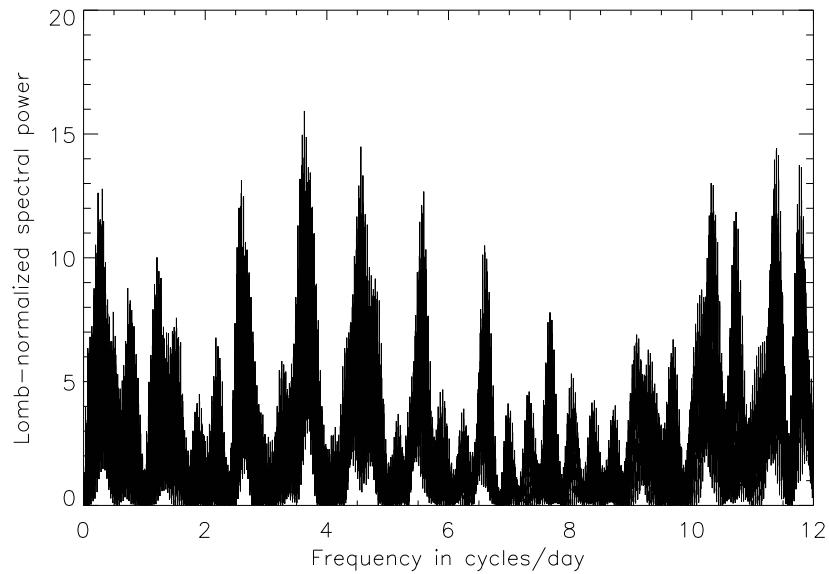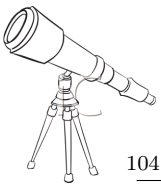
Figure 70: *Lomb-normalized spectral power versus frequency in cycles/day for Salacia*: The Lomb periodogram based on all the data sets shows a peak with a high spectral power at 3.63 cycles/day (6.61 h) and the two aliases with a lower spectral power are located at 2.59 cycles/day (9.27 h) and at 4.58 cycles/day (5.24 h).
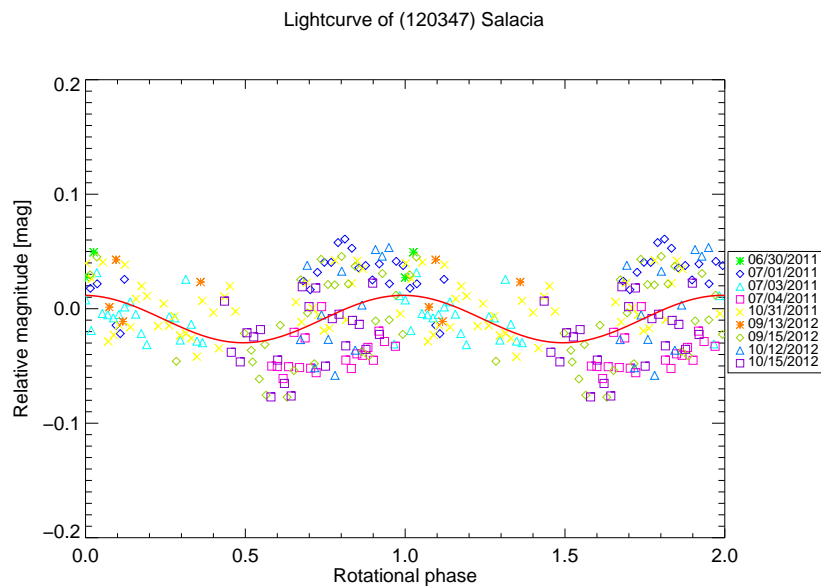
Figure 71: *Relative magnitude versus rotational phase for Salacia*: Single-peaked lightcurve for Salacia obtained by using a spin period of 6.61 h. The continuous line is a Fourier Series fit of the photometric data. Different symbols correspond to different dates.

(Chile), they reported a flat lightcurve with an upper limit on the lightcurve amplitude of 0.04 mag. They did not present any rotational period estimation.
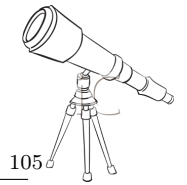
VI.2.14 (230965) 2004 XA$_{192}$
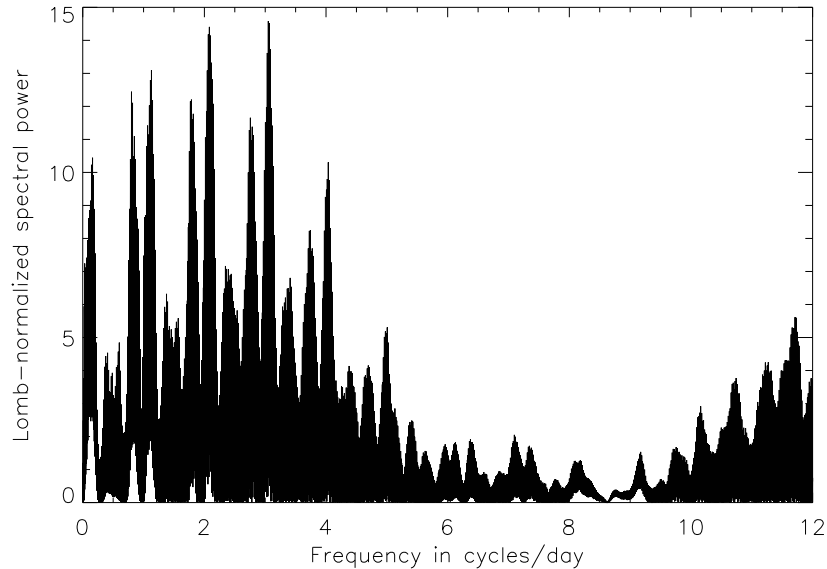
Figure 72: *Lomb-normalized spectral power versus frequency in cycles/day for 2004 XA$_{192}$*: The Lomb periodogram shows two peaks located at 3.05 cycles/day, and at 2.09 cycles/day.

We observed 2004 XA$_{192}$ during one run in October 2009 and during one isolated night in December 2009. The Lomb periodogram (Figure 72) shows two peaks with a similar spectral power. The second peak at 7.88 h (3.05 cycles/day) seems to be a little bit higher than the first one at 11.49 h (2.09 cycles/day). The PDM and CLEAN techniques confirmed the second peak at 7.88 h, but a period around 11 h is still present with a high spectral power. The Pravec-Harris technique presented a double peak period at 15.76 h. In all cases, the amplitude of the curve is 0.07±0.02 mag. A spin period of 7.88 h appears to be the best option for this object (Figure 73). The alternative fit of 11.49 h exhibits more scatter and is not preferred (Thirouin et al., 2012).

VI.2.15 (308193) 2005 CB$_{79}$

2005 CB$_{79}$ was observed in January and May 2008, and during one isolated night in December 2008. The Lomb periodogram (Figure 74) shows one main peak located at 6.76 h (3.55 cycles/day) and two aliases at 2.52 cycles/day and at 4.47 cycles/day. The single-peaked lightcurve, using a rotational period of 6.76 h, has an amplitude of 0.05±0.02 mag (Figure 75). All techniques confirmed this single-peaked rotational period.

VI.2.16 (136472) 2005 FY$_9$ or Makemake

Makemake was inspected for binarity, but, no satellite [4] was reported by Brown et al. (2006b).

Photometric observations in R-band on 21 nights spanning several months (February 2006 - January 2007) were obtained using the 1.5 m OSN telescope and the 2.2 m CAHA telescope and analyzed in Ortiz et al. (2007b). They proposed the first short-term variability study of Makemake. They favored a single-peaked rotational period of 11.24 h or a double-peaked rotational period of

---

[4]Makemake does not have a satellite detectable within 0.4″ with a brightness of more than 1% of the primary
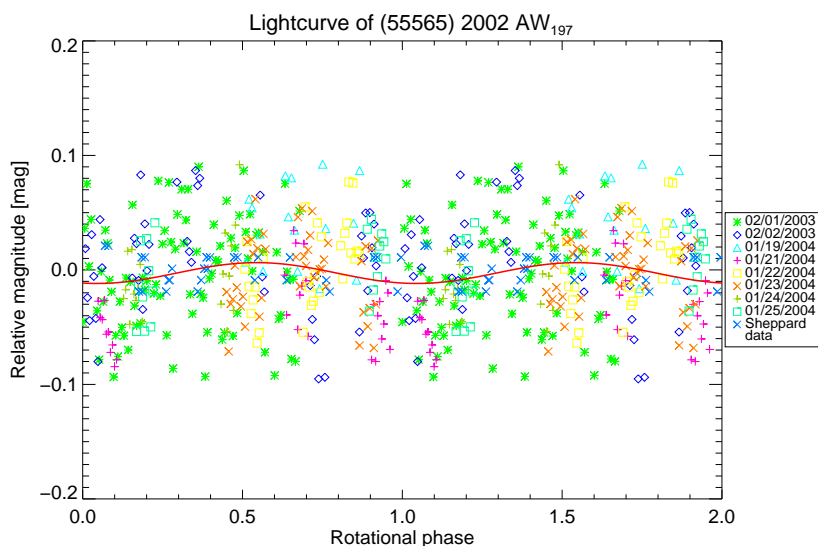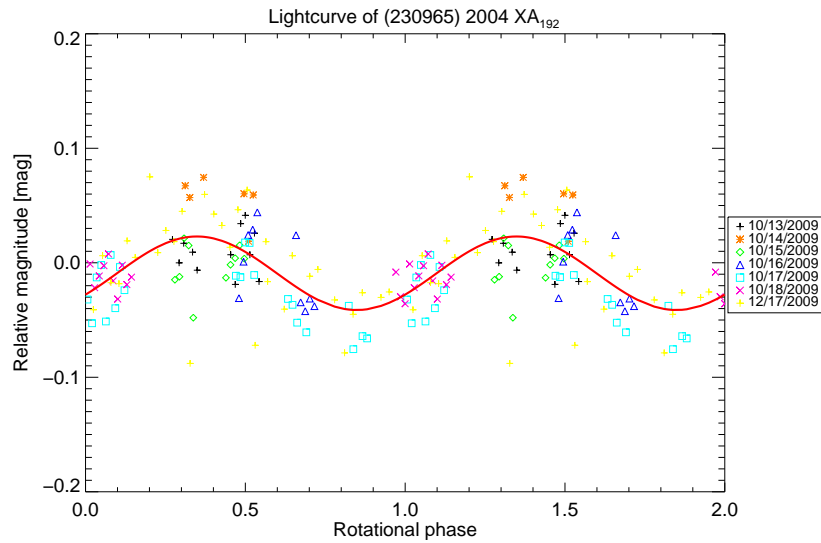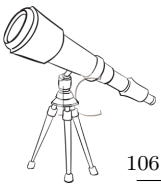
Figure 73: *Relative magnitude versus rotational phase for 2004 XA$_{192}$*: Single-peaked lightcurve for 2004 XA$_{192}$ obtained by using a spin period of 7.88 h. The continuous line is a Fourier Series fit of the photometric data. Different symbols correspond to different dates.
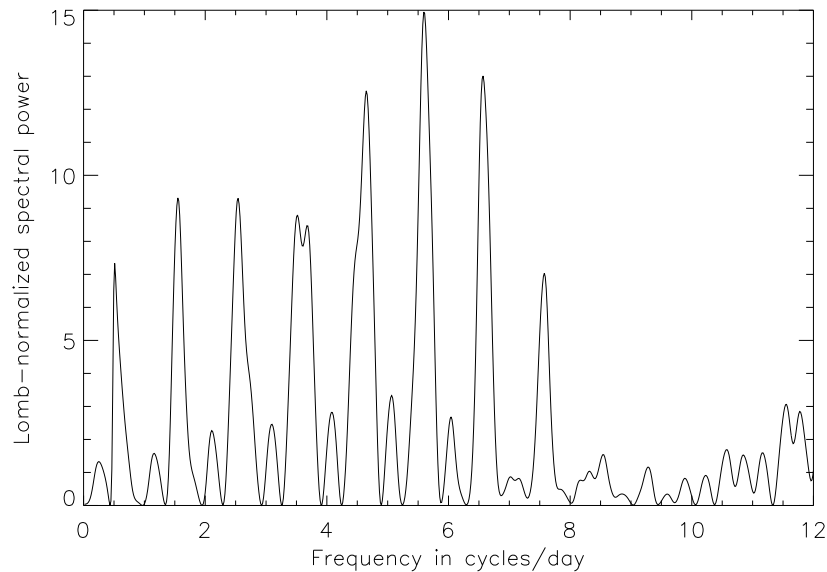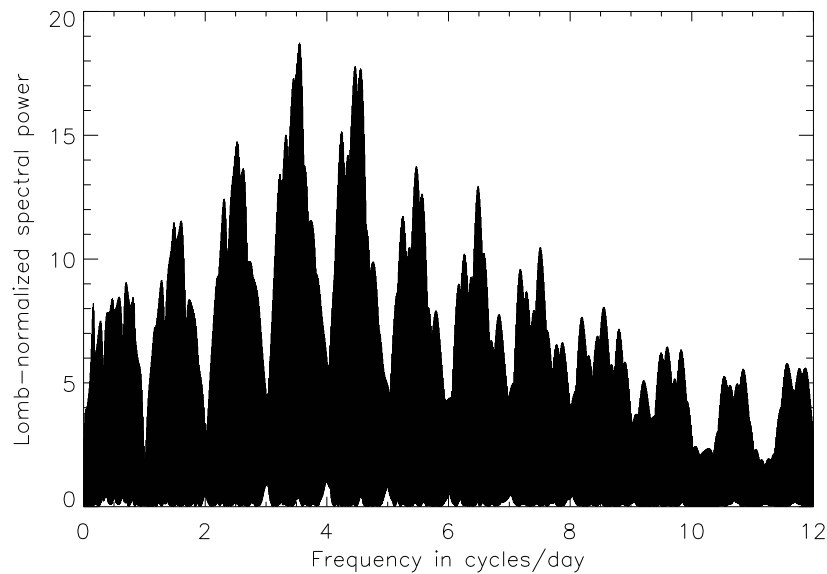

Figure 74: *Lomb-normalized spectral power versus frequency in cycles/day for 2005 CB$_{79}$*: The Lomb periodogram shows three peaks located at 3.55 cycles/day (main peak), at 4.47 cycles/day, and at 2.52 cycles/day

22.48 h, and an extremely low variability.

Heinze and de Lahunta (2009) carried out an extensive photometric program for Makemake in 2007 with the University of Arizona's 1.54 m Kuiper Telescope on Mt. Bigelow (Tucson, Arizona, USA). They concluded that Makemake rotational period is 7.7710±0.0030 h and the lightcurve
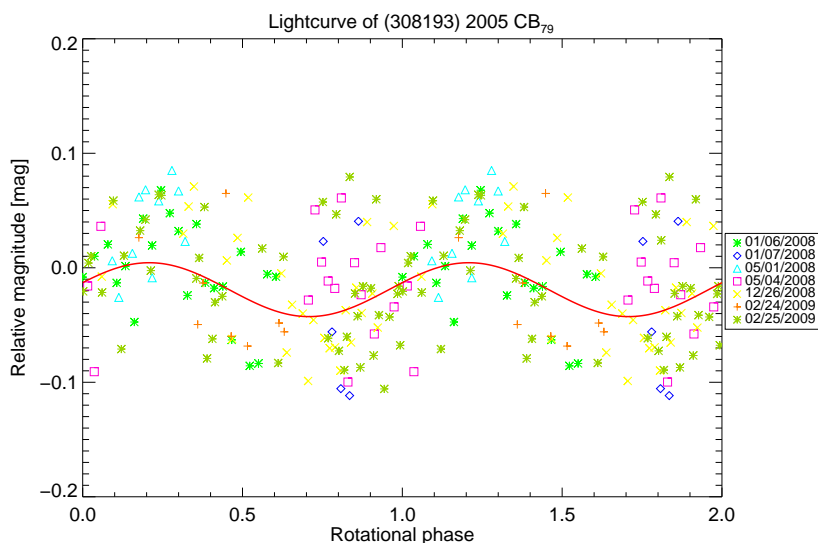
Figure 75: *Relative magnitude versus rotational phase for 2005 CB$_{79}$*: Single-peaked lightcurve for
2005 CB$_{79}$ obtained by using a spin period of 6.76 h. The continuous line is a Fourier Series fit of
the photometric data. Different symbols correspond to different dates.

amplitude is 0.0286±0.0016 mag in the V-band. This period was a peak in Ortiz et al. (2007b)
periodogram, but was interpreted as an alias.
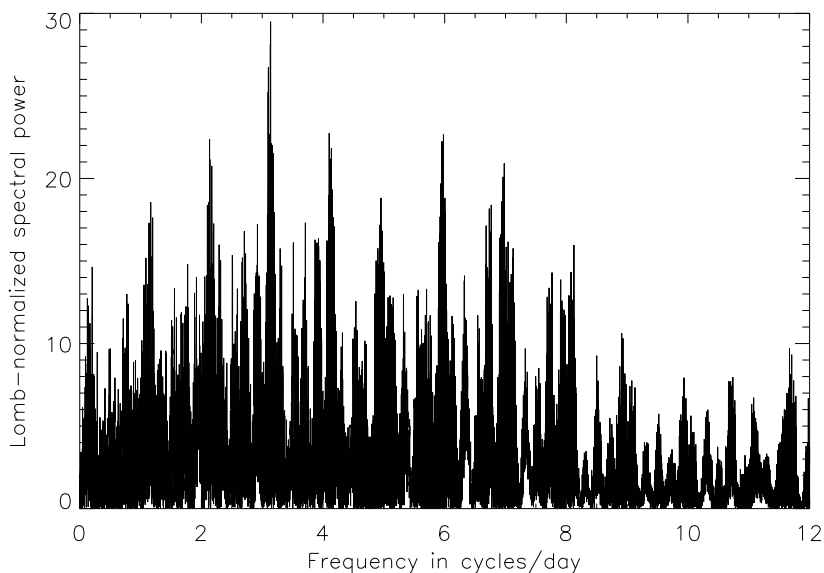
Figure 76: *Lomb-normalized spectral power versus frequency in cycles/day for Makemake*: The Lomb
periodogram of our 2006 and 2007 data sets shows several peaks. The main peak is located at 7.65 h
(3.13 cycles/day).

In Thirouin et al. (2010), we re-reduced and re-analyzed part of the data presented in Or-

tiz et al. (2007b) and we included more data obtained in May and June 2006 and March 2007. In Thirouin et al. (2010), we concluded that a spin period of 7.65 h seems to be the best option. In fact, the Lomb periodogram (Figure 76) shows one peak at around 7.7 h with a high spectral power. In Figure 77, the 2006 and 2007 lightcurves, and finally the mix of all the data sets are plotted. In all cases, the amplitude of the curve is very low, 0.014±0.002 mag.
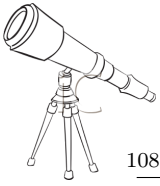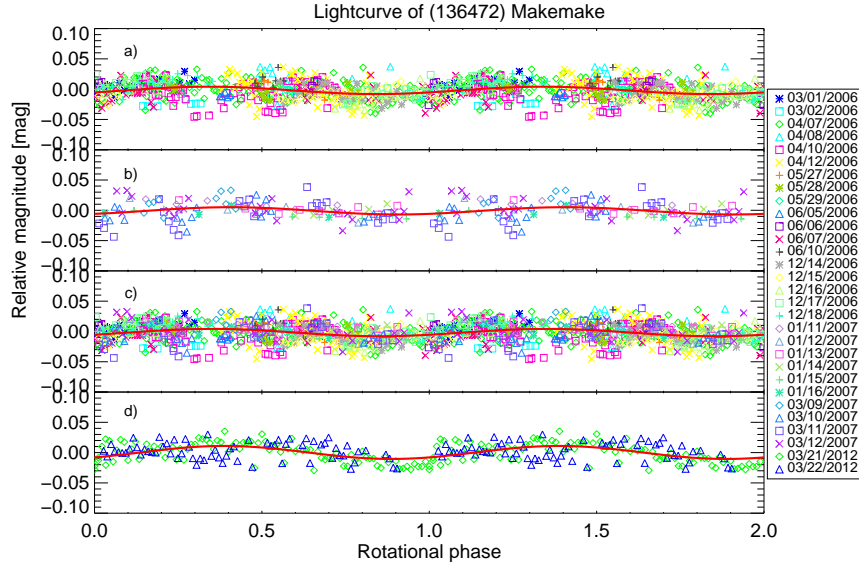
Figure 77: *Relative magnitude versus rotational phase for Makemake*: Plot a) is the single peak lightcurve obtained in 2006. Plot b) is the single-peaked lightcurve obtained in 2007. Plot c) is the single-peaked lightcurve obtained by merging the 2006 and 2007 data sets. Plot d) is the single-peaked lightcurve obtained in 2012 in the V-band. Continuous lines are a Fourier Series fits of the photometric data. Different symbols correspond to different dates.

In conclusion, the rotational period obtained is in agreement with Heinze and de Lahunta (2009). Regarding the lightcurve amplitude, there is a difference between our estimation and Heinze and de Lahunta (2009) one. Our observations were carried out in the R-band, whereas Heinze and de Lahunta (2009) ones were carried out in the V-band.

In March 2012, Makemake was re-observed, but this time in the V-band using the 1.5 m OSN telescope. Two nights of data were obtained when the object was at low phase angle. Thanks to this new campaign, the rotational periodicity around 7.7 h is confirmed, and the lightcurve amplitude is 0.022±0.001 mag in the V-band. So, a higher lightcurve amplitude in the V-band than in the R-band is confirmed. However it does not completely match the Heinze and de Lahunta (2009) value of 0.0286 mag.

A rotational period of 7.7 h has been derived and we noticed a very low lightcurve amplitude. Such a low lightcurve amplitude suggests that Makemake is a spheroidal object. The lightcurve amplitude in the R-band is 0.014±0.002 mag whereas in the V-band, the amplitude is 0.022±0.001 mag. Such a variable lightcurve amplitude according to the filter in which the data were obtained has been noticed by Heinze and de Lahunta (2009).

Makemake is not the only body that presents a variable lightcurve amplitude according to the filter used. In fact, the amplitude of Pluto's lightcurve is 0.30 mag in the B-band, 0.26 mag in the V-band and 0.21 mag in the R-band (Buratti et al., 2003). Pluto and Makemake also share a similar spectra and very similar red color. The explanation for the red color and the large lightcurve

amplitude of Pluto is that there are different regions covered with dark red tholins [5] (Buratti et al., 2003). The tholins are less dark relative to the surrounding bright ice in the R-band than in the B-band and so, we have to expect a lower lightcurve amplitude at red wavelengths. Because of Makemake's and Pluto's spectral and color resemblances, one can expect that the lightcurve amplitude of Makemake would be similar to Pluto's one. However, this work and Heinze and de Lahunta (2009) study have shown that Makemake lightcurve amplitude is very low. Such a low amplitude suggests that Makemake's surface is very uniform or that we see it with a nearly pole-on orientation.

On the other hand, Stansberry et al. (2008) based on *NASA Spitzer Space Telescope* thermal data and Lim et al. (2010) based on data from the *Herschel Space Observatory* noted that Makemake is too bright at 24 microns to allow any simple thermal model. In fact, only considering two different terrains it is possible to explain Makemake thermal observations. One of the terrains in the thermal models must be very dark to explain Makemake's thermal output at 24 microns and another very bright terrain. However, such a dark terrain would not cause strong lightcurve variations, because it covers just a small fraction of the surface.

VI.2.17 (145452) 2005 RN$_{43}$
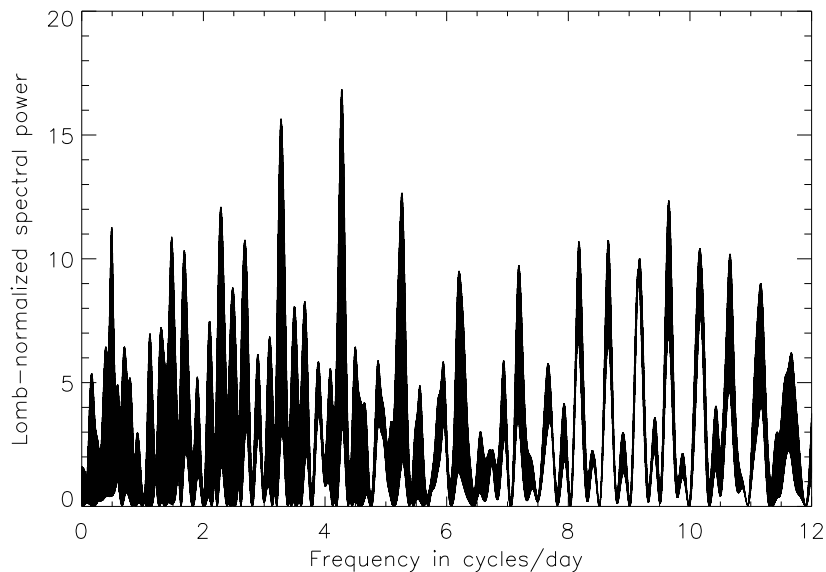
Figure 78: *Lomb-normalized spectral power versus frequency in cycles/day for 2005 RN$_{43}$*: The Lomb periodogram of our 2007 and 2008 data sets shows one main peak located at 5.62 h (4.28 cycles/day) and one largest alias located at 7.32 h (3.28 cycles/day).

This object was observed during four nights in September 2007 and, during five nights in August 2008. The Lomb periodogram (Figure 78) exhibits a peak with a spectral power higher than 99% at 5.62 h (4.28 cycles/day) and a second peak with a lower spectral power at 7.32 h (3.28 cycles/day). The PDM, CLEAN and Pravec-Harris methods confirm these two peaks but seem to favor the second peak at 7.32 h. The lightcurve amplitude is low, 0.04±0.01 mag (Figure 79). Due to the low variability of 2005 RN$_{43}$, it is difficult to favor one period over the other. But 7.32 h seems to be the best option (Thirouin et al., 2010).

---

[5]Tholins are molecules formed by solar ultraviolet irradiation of simple organic compounds such as methane or ethane.
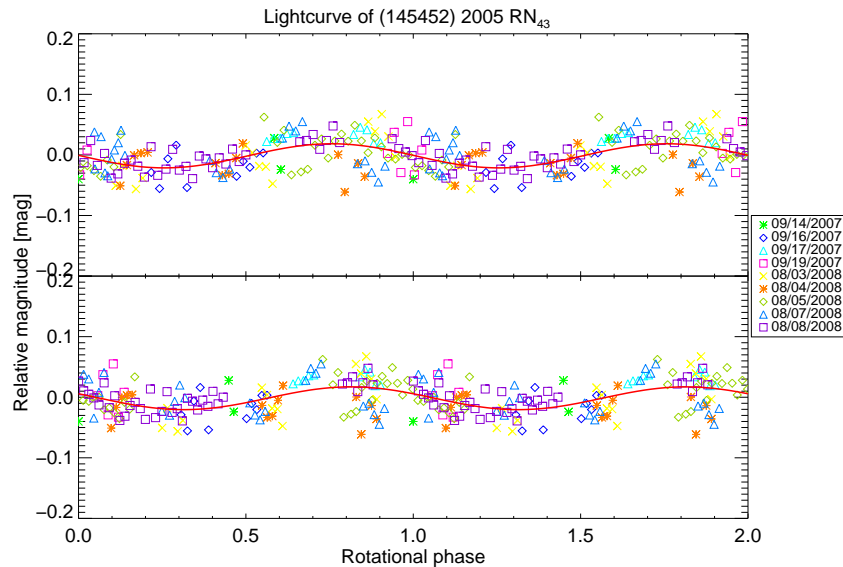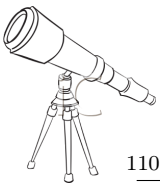
Figure 79: *Relative magnitude versus rotational phase for 2005 RN$_{43}$*: Plot a) is a single-peaked lightcurve using a spin period of 5.62 h. Plot b) is a single-peaked lightcurve using a rotational period of 7.32 h. The continuous lines are a Fourier Series fit of the photometric data. Different symbols correspond to different dates.

Benecchi and Sheppard (2013) also studied the short-term variability of 2005 RN$_{43}$. Based on four nights of observations with the Irénée du Pont 2.5 m telescope at Las Campaas Observatory (Chile), they reported a single-peaked rotational period of 6.95 h or a double-peaked rotational period of 13.89 h. The lightcurve amplitude is 0.06±0.01 mag. Benecchi and Sheppard (2013) photometric data are not available, and so a mix of all the data to favor or discard a rotational period is not possible. However, by fitting the 2007-2008 data sets to the rotational period estimated by Benecchi and Sheppard (2013), the obtained lightcurve clearly show that the 2007-2008 data sets are not consistent with such a rotational period. Thus it appears that either our work or Benecchi and Sheppard (2013) work are mistaken.

VI.2.18   (145453) 2005 RR$_{43}$

2005 RR$_{43}$ was observed during several runs between October 2006 and September 2007. The Lomb periodogram (Figure 80) shows several peaks. The most significant peak is located at 7.87 h (3.05 cycles/day). There is a second and third peak with lower significance levels located at 6.59 h and at 5.99 h. PDM identified the same peaks at the same values and a third peak at 4.1 cycles/day. Other techniques confirmed the peaks detected in the Lomb periodogram. A lightcurve with a single peak periodicity of 7.87 h is plotted in Figure 81. The lightcurve has an amplitude of 0.06±0.01 mag (Thirouin et al., 2010).

Perna et al. (2009) proposed a double-peaked periodicity of 5.08±0.04 h which is an alias in our study. This result is based on 15 h of observations split in three nights at the 3.58 m NTT. The amplitude is 0.12±0.03 mag. Such an amplitude is completely ruled out in our result. And, also ruled out by Benecchi and Sheppard (2013) results. In fact, they reported an upper limit on the lightcurve amplitude of 0.06 mag based on five observational nights with the Irénée du Pont 2.5 m telescope at Las Campanas Observatory (Chile). Benecchi and Sheppard (2013) did not provide information about rotational periodicity. In conclusion, a 7.87 h rotational period seems the best option.
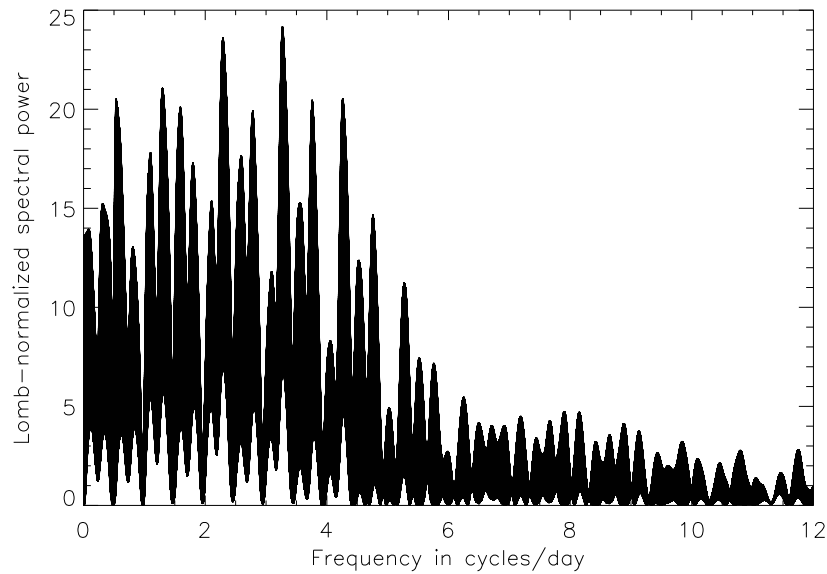
Figure 80: *Lomb-normalized spectral power versus frequency in cycles/day for 2005 RR$_{43}$*: The Lomb periodogram of our 2006 and 2007 data sets shows several peaks located at 7.87 h (3.05 cycles/day), at 6.59 h (3.64 cycles/day), and at 5.99 h (4.01 cycles/day).
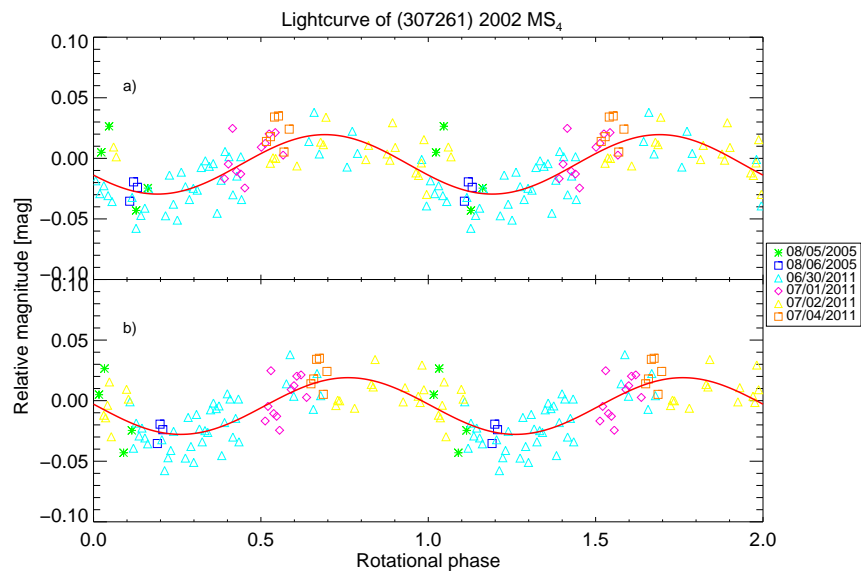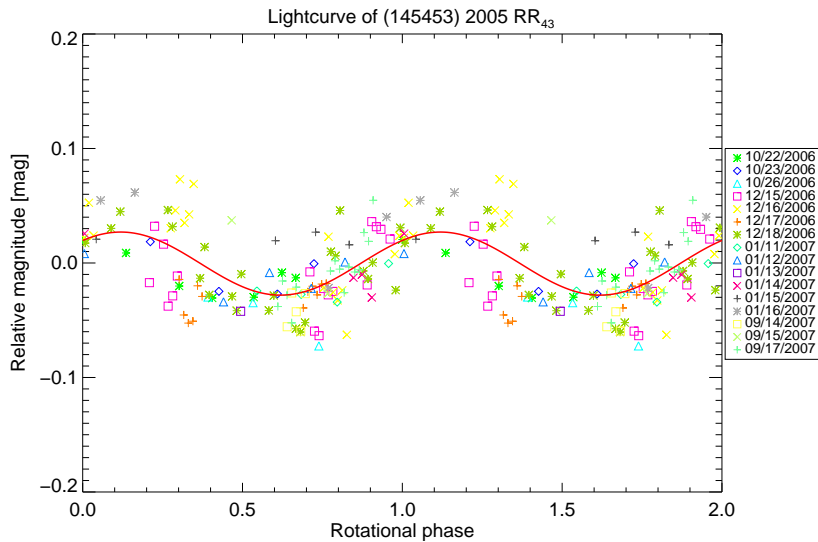

Figure 81: *Relative magnitude versus rotational phase for 2005 RR$_{43}$*: Single-peaked lightcurve for 2005 RR$_{43}$ obtained by using a spin period of 7.88 h. The continuous line is a Fourier Series fit of the photometric data. Different symbols correspond to different dates.

VI.2.19   (202421) 2005 UQ$_{513}$

For this object, we have a time base of around 10 h obtained in August 2008. In September 2009, the time base is 8 h split in 3 nights and in October 2009, it is around 45 h in 6 nights.

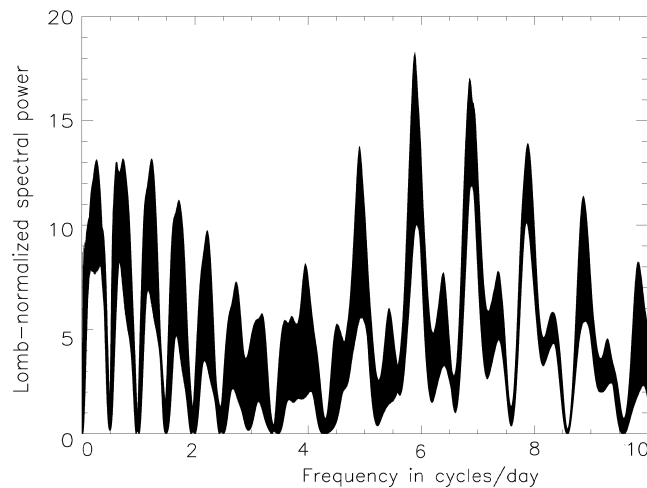Figure 82: *Lomb-normalized spectral power versus frequency in cycles/day for 2005 UQ$_{513}$*: The Lomb periodogram of our 2008 and 2009 data sets shows one main peak located at 7.03 h (3.41 cycles/day) and aliases at 10.01 h (2.40 cycles/day) and at 5.43 h (4.42 cycles/day).

The Lomb periodogram (Figure 82) shows one clear peak and two possible 24h-aliases. The highest peak is located at 7.03 h (3.41 cycles/day) and the aliases are located at 10.01 h (2.40 cycles/day) and at 5.43 h (4.42 cycles/day). The PDM, CLEAN, Pravec-Harris techniques confirmed these peaks. In Figure 83, single-peaked lightcurves assuming a rotational period of 10.01 h and 7.03 h are plotted. In all cases, the amplitude of the curve is 0.05±0.02 mag (Thirouin et al., 2012). The alternative spin period of 5.43 h exhibits more scatter and appears less favorable. In conclusion, a spin period of 7.03 h seems the best option. No literature on this object is available.

VI.2.20   (315530) 2008 AP$_{129}$

2008 AP$_{129}$ was observed during a run in January 2011, in poor atmospheric conditions, and during one more run in February 2013 with the 3.58 m TNG and the 1.5 m OSN telescope. The Lomb periodogram of our 2011 and 2013 data sets (Figure 84) shows one clear peak located at 9.04 h (2.65 cycles/day) and the second one with a smaller spectral power is located at 3.84 cycles/day (6.25 h). PDM, CLEAN, and Pravec-Harris techniques confirmed these two peaks with an higher spectral power for the 9.04 h spin period. In Figure 85, the corresponding lightcurve using a rotational periodicity of 9.04 h is plotted. The amplitude of the curve is 0.12±0.02 mag. In summary, 9.04 h is preferred but 6.25 h is also a possible period. No literature on this object is available.

VI.2.21   (24835) 1995 SM$_{55}$

Sheppard and Jewitt (2003) observed this object for several nights in October and November 2001 with the University of Hawaii 2.2 m telescope. Based on the October data set, they reported a
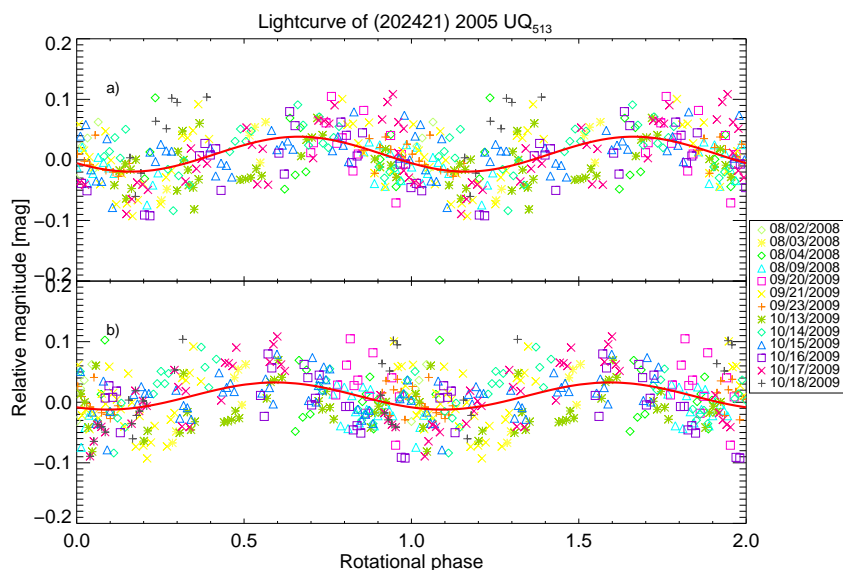
Figure 83: *Relative magnitude versus rotational phase for 2005 UQ_{513}*: Plot a) is our single-peaked
lightcurve obtained for a rotational period of 7.03 h. Plot b) is our single-peaked lightcurve obtained
for a rotational period of 10.01 h. Continuous lines are a Fourier Series fits of the photometric data.
Different symbols correspond to different dates. The legend is the same for both plots.
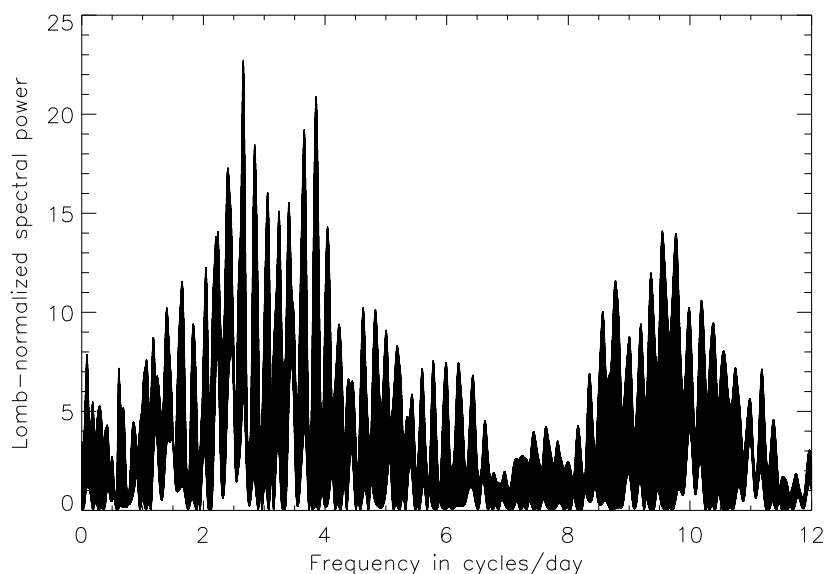
Figure 84: *Lomb-normalized spectral power versus frequency in cycles/day for 2008 AP_{129}*: The Lomb
periodogram of our 2012 and 2013 data sets shows one clear peak located at 2.65 cycles/day and several
aliases. The largest alias is located at 3.84 cycles/day.

scattered photometry and no spin period estimation. With the additional November data set, they
suggested a single-peaked rotational period of 4.04 h or a double-peaked periodicity of 8.08 h and
an average peak-to-peak amplitude of 0.19±0.05 mag (they only reported photometric amplitude
estimated from apparent maximum and minimum, and not lightcurve amplitude obtained thanks
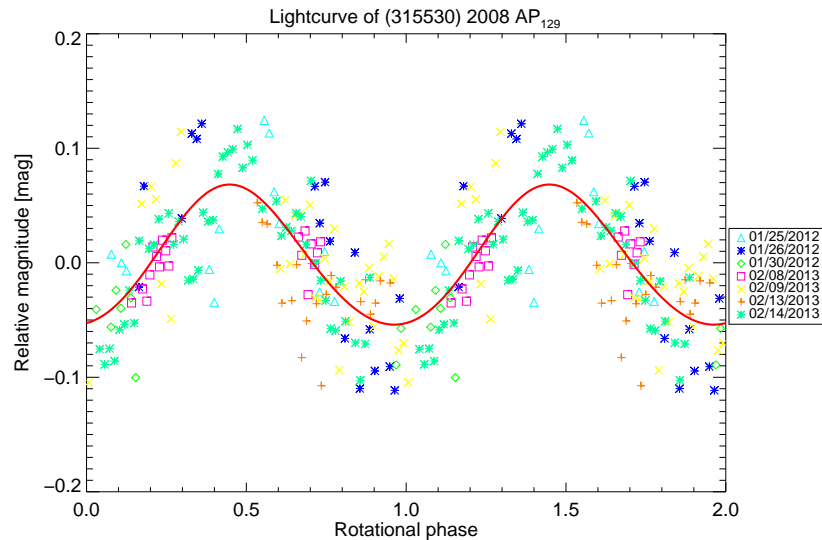
Figure 85: *Relative magnitude versus rotational phase for 2008 AP$_{129}$*: Single-peaked lightcurve for 2008 AP$_{129}$ obtained by using a spin period of 9.04 h. The continuous line is a Fourier Series fit of the photometric data. Different symbols correspond to different dates.

to a lightcurve fit as it has been done it this work). Unfortunately, in both cases, the curves were too noisy given the photometric uncertainties. Sheppard and Jewitt (2003) concluded that the amplitude of the lightcurve may be variable from night to night. Such variations could be due to: i) the presence of a companion, ii) cometary activity, or iii) complex rotational state. Sheppard and Jewitt (2003) pointed out that this object has been investigated for binarity with the *Hubble Space Telescope* and that no satellite with a separation $\geq 0.1''$ and having a magnitude difference ≤ 2.5 was found. 1995 SM$_{55}$ is one of the bluest TNOs which could be attributed to a recent exposition (due to a collision, for example) of its volatile-rich interior (Hainaut and Delsanti, 2002). On the other hand, the lightcurve amplitude may be due to freshly exposed material by cometary activity (Hainaut and Delsanti, 2002).

This object was observed in 2012 to look for a possible change in the lightcurve. A four-night observing run in September 2012 was carried out and also data on two consecutive nights in October 2012 with the 1.5 m OSN telescope were obtained. The Lomb periodogram (Figure 86) based on this data set presents a main peak located at 6.34 cycles/day (3.79 h) and two other peaks with a lower spectral power located at 5.35 cycles/day (4.49 h) and at 7.33 cycles/day (3.27 h). The Pravec-Harris method and PDM technique favor a double-peaked rotational period of 7.57 h (double-peaked rotational period of 3.79 h). On the other hand, the double-peaked lightcurve seems asymmetric with a first peak taller than the second one. Despite the low lightcurve amplitude (0.06±0.01 mag), the double-peaked lightcurve with a rotational period of 7.57 h seems the best option (Figure 87).

By merging our data with Sheppard and Jewitt (2003) data, the Lomb periodogram plotted in Figure 88 is obtained. The main peak is located at 5.94 cycles/day (4.04 h), and there are two other peaks with a lower spectral power located at 4.07 cycles/day, and at 5.07 cycles/day. The lightcurve is asymmetric with a first peak taller than the second one. As previously, the double-peaked lightcurve with a rotational period of 8.08 h seems the best option. In Figure 89 are plotted: the double-peaked lightcurve obtained by Sheppard and Jewitt (2003), the double-peaked lightcurve obtained in September-October 2012 and the double-peaked lightcurve obtained by merging all the data about 1995 SM$_{55}$. In all cases, a spin period of 8.08 h. Based on the Fourier
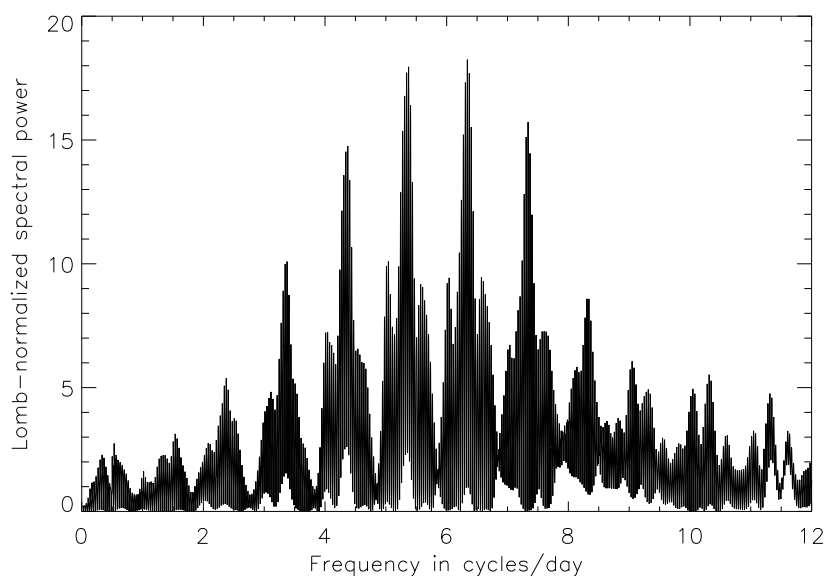
Figure 86: *Lomb-normalized spectral power versus frequency in cycles/day for 1995 SM$_{55}$*: The Lomb periodogram shows several main peaks: the first one, with the highest spectral power, is located at 6.34 cycles/day (3.79 h), the second and third one are located at 5.35 cycles/day (4.49 h) and at 7.33 cycles/day (3.27 h).
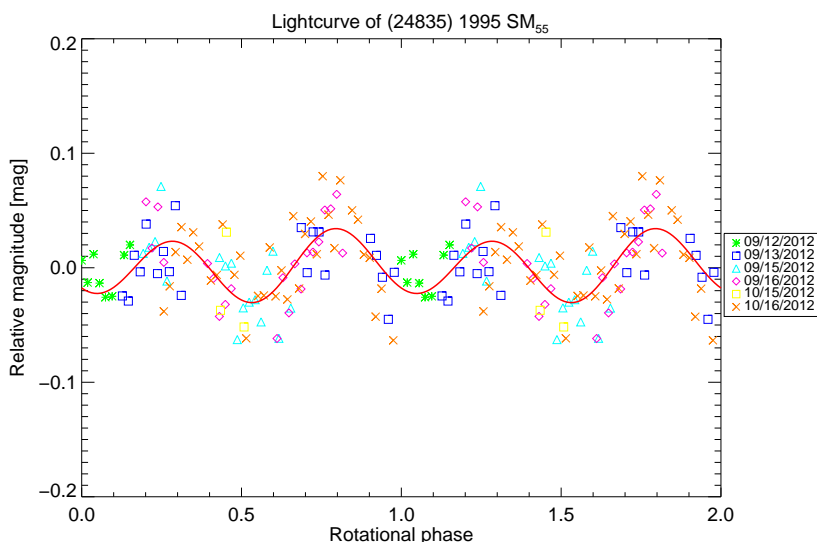
Figure 87: *Relative magnitude versus rotational phase for 1995 SM$_{55}$*: Double-peaked lightcurve obtained for a spin period of 7.57 h. Continuous line is Fourier Series fit of the photometric data. Different symbols correspond to different dates.

series fits, the lightcurve amplitude is 0.06±0.01 mag for Sheppard and Jewitt (2003) lightcurve, and a lightcurve amplitude of 0.07±0.02 mag for the 2012 lightcurve of 1995 SM$_{55}$. The lightcurve obtained by merging all the data sets has an amplitude of 0.05±0.02 mag.

In conclusion, a double-peaked spin period between 7.5 and 8.1 h remains the best option. However, we must point out that both data sets are not matching perfectly. In fact, when we merging several data sets, we assumed that the spin axis orientation of the object has not changed. In the case of 1995 SM_{55}, the data sets are separated by eleven years, and a significant change in the spin axis orientation may have happened and there could be a shift between both lightcurves. This possibility has to be considered and care has to be taken to merge all the data. Such s study will be carried out in the future by using the epoch method of Gehrels (1967).
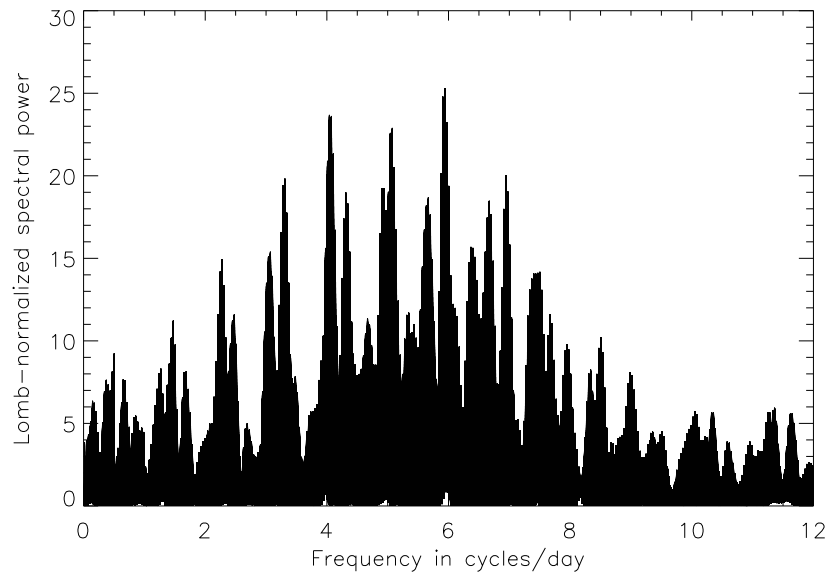
Figure 88: *Lomb-normalized spectral power versus frequency in cycles/day for 1995 SM_{55}*: The Lomb periodogram shows main three peaks: the first one, with the highest spectral power, is located at 5.94 cycles/day, the second and third one are located at 4.07 cycles/day and at 5.07 cycles/day.

VI.2.22   (20000) 2000 WR_{106} or Varuna

Varuna is one of the best known objects and has been investigated for short-term variability several times. Farnham (2001) proposed a double-peaked rotational lightcurve with an amplitude of 0.50 mag based on observations carried out in January, March and September 2001. Jewitt and Sheppard (2002) used R-observations made in February and April 2001 at the 2.2 m University of Hawaii telescope. They suggested a 6.3436±0.0002 h double-peaked rotational lightcurve with a 0.42±0.02 mag amplitude. Ortiz et al. (2003a) presented results based on data obtained in February 2002 with the 1.5 m OSN telescope. They favored a period of 6.3436 h and an amplitude of 0.41 mag. Hicks, Simonelli and Buratti (2005) presented results based on data obtained in December 2002 and January 2003 with the California Institute of Technology 60-in (P60) and 200-in (P200) telescopes located on Palomar Mountain. They favored a rotational periodicity of 6.344±0.001 h and an amplitude of 0.47±0.04 mag. Belskaya et al. (2006) presented R-observations carried out in November and December 2004 and on January and February 2005 with the 1.5 m OSN telescope. They obtained a rotational periodicity of 6.34358 h. They noted an amplitude variation according to the observational phase angle. At large phase angle (typically, larger than 0.8°), the amplitude was 0.42 mag, whereas very near the opposition (phase angle around 0°), the amplitude reached 0.47 mag. Rabinowitz, Schaefer and Tourtellotte (2007) presented photometric results based on 78 images carried out in December 2004 and April 2005 with the 1.3 m telescope of the Small and Moderate Aperture Research Telescope System (SMARTS). They suggested a 6.344 h double-peaked rotational lightcurve with an amplitude of 0.49 mag. Varuna was observed in January and February 2005 by our team. In Thirouin et al. (2010), we published a double-
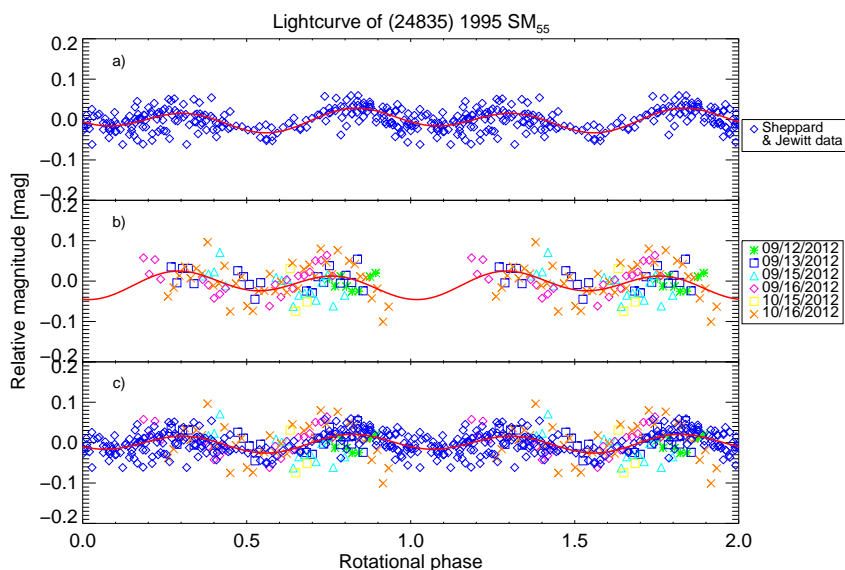
Figure 89: *Relative magnitude versus rotational phase for 1995 SM₅₅*: Plot a) is the double-peaked lightcurve obtained by Sheppard and Jewitt (2003). Plot b) is the double-peaked lightcurve obtained for a rotational period of 8.08 h. Plot c) is the final lightcurve obtained by merging our data and Sheppard and Jewitt (2003) data. The same legend has used in Plot c), as Plot a) and Plot b). Continuous lines are Fourier Series fits of the photometric data. Different symbols correspond to different dates.

peaked lightcurve with a spin period of 6.3418 h and an amplitude of 0.43±0.01 mag.
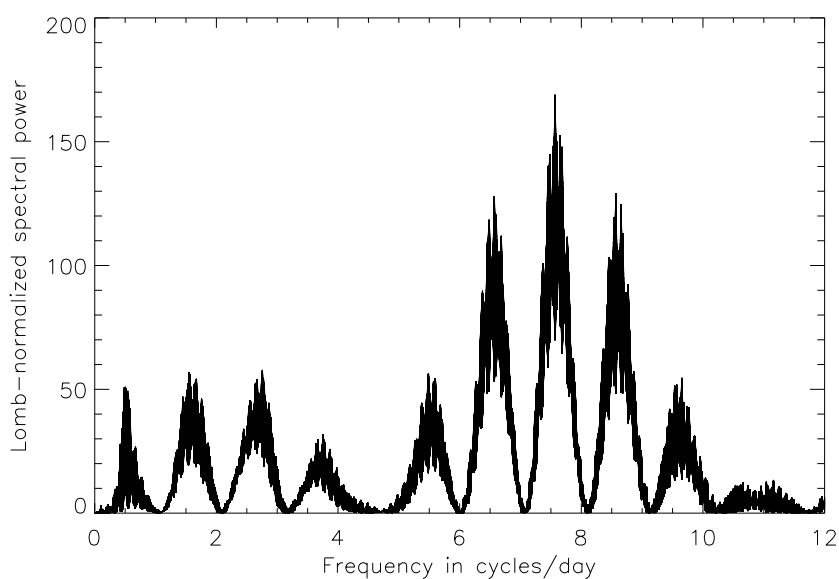
Figure 90: *Lomb-normalized spectral power versus frequency in cycles/day for Varuna*: The Lomb periodogram shows one clear peak located 7.57 cycles/day or 3.17 h.

By merging all our data sets (2002 to 2013) and Jewitt and Sheppard (2002) data [6], a very high precision rotational period is reported. The Lomb periodogram (Figure 90) shows one clear peak at 3.1717837 h (7.5667203 cycles/day). The amplitude variation is caused by the shape of the object and so, we prefer the double-peaked rotational period, as the true rotational period for Varuna (double-peaked rotational period of 6.3435674 h). In Figure 91 and Figure 92 all the lightcurves obtained between 2002 and 2013, as well as Jewitt and Sheppard (2002) Varuna lightcurve are plotted, separately.

In conclusion, there is an agreement about Varuna double-peaked rotational period. The only "divergent" issue is the amplitude. In fact, near the opposition, Varuna seems to have a larger amplitude. We included Varuna as a regular target in our short-term variability, and several observational runs were performed between 2009 and 2013 to check, in particular, a possible amplitude variation. In Table 5, are summarized the phase angle and the amplitude recorded in the literature and in our own database.
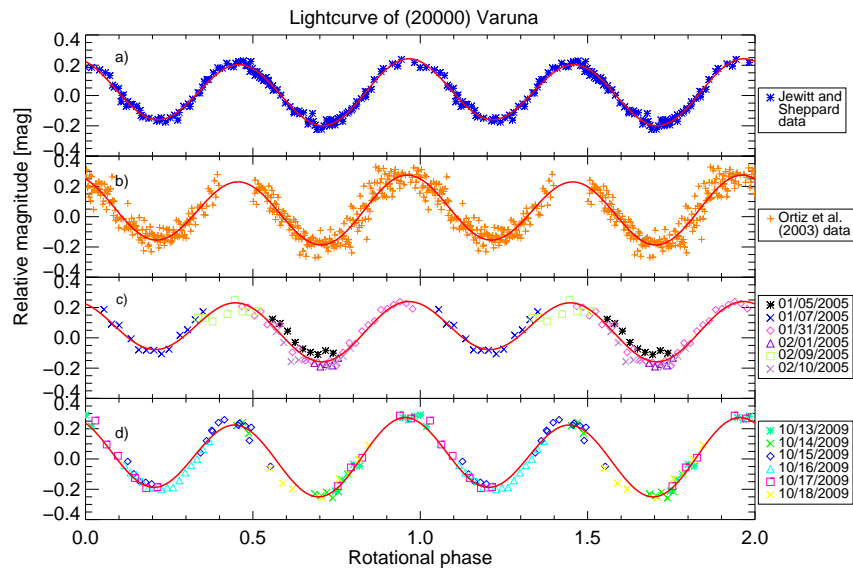
Figure 91: *Relative magnitude versus rotational phase for Varuna*: Plot a) is Jewitt and Sheppard (2002) double-peaked lightcurve based on data obtained in 2001. Plot b) is Ortiz et al. (2003a) double-peaked lightcurve obtained thanks to data obtained in 2002. Plot c) is Thirouin et al. (2010) double-peaked lightcurve based on data obtained in 2005. Plot d) is the double-peaked lightcurve based on data obtained in 2009. Figure 92 is a continuation of this figure for different dates.

In Figure 93, all Fourier fits obtained between 2001 and 2013 (8 different epochs spanning 12 years) are plotted. One can appreciate the variation in the lightcuves amplitudes, as well as a possible slight shifts in the position of the maxima (and minima) from year-to-year. In fact, the 2001 lightcurve presents an amplitude of 0.42±0.02 mag whereas the 2012-2013 lightcurve has an amplitude of 0.50±0.02 mag. We also noted a trend of increasing lightcurve amplitude above the error bars, despite the phase angle effect noticed by Belskaya et al. (2006). Such a variation can be an indication of change in the spin axis orientation of Varuna with respect to the observer. To date, only for centaurs (for example Pholus), such a change in the axis orientation variations have been reported and studied. Once we have noticed such a change, one can proceed to a lightcurve inversion based on the epoch and amplitude methods Magnusson (1986) to derive the ecliptic latitude and longitude of the spin axis, as well as the sense of the object rotation. On the other hand, using constraints derived from two stellar occultations by Varuna on February 9th 2010 and on

---

[6]We only used such data set because it present the lowest dispersion among all the other sources.
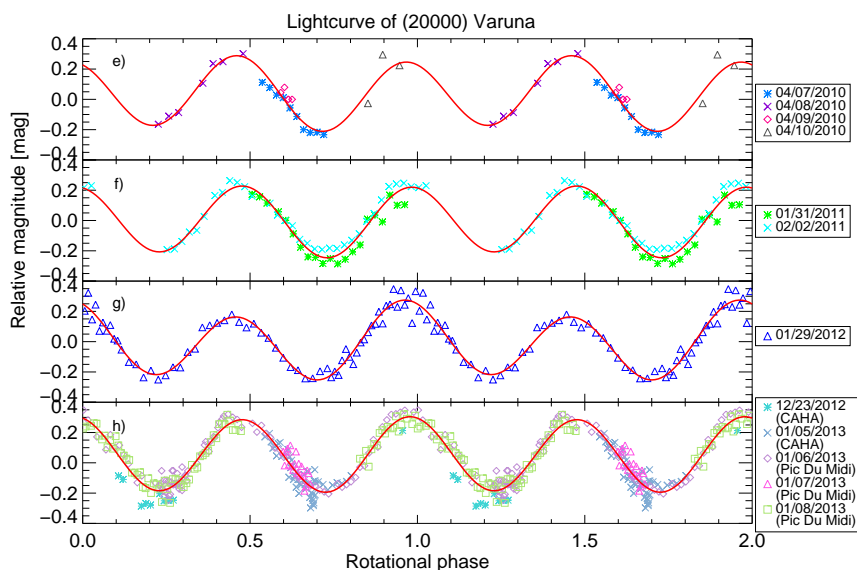
Figure 92: *Relative magnitude versus rotational phase for Varuna*: Plot e) is the double-peaked lightcurve based on data obtained in 2010. Plot f) is the double-peaked lightcurve obtained in 2011. Plot g) is the 2012 double-peaked lightcurve. Plot h) is the 2012-2013 double-peaked lightcurve.
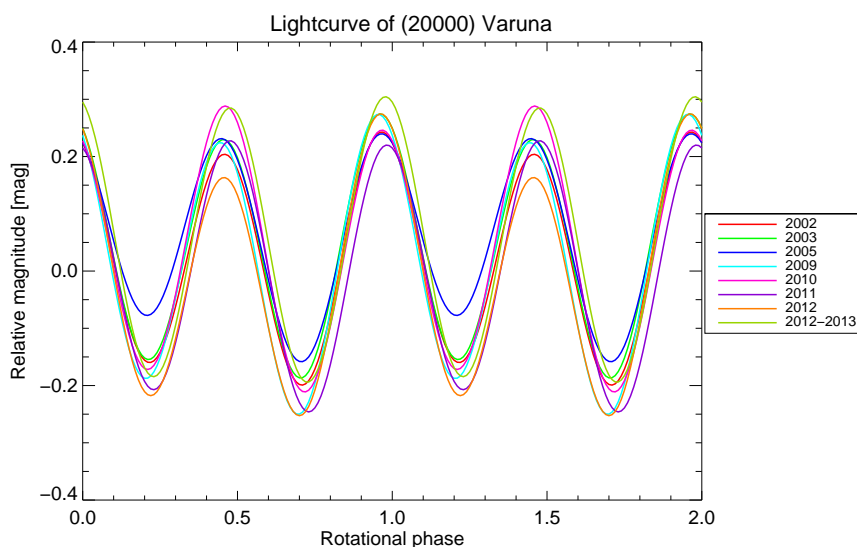
Figure 93: *Relative amplitude versus rotational phase for Varuna*: In this figure are plotted the double-peaked fits of all Varuna lightcurves presented previously. One can appreciate the lightcurve amplitude changes as well as possible shifts of the maxima/minima positions.

January 8th 2013, we will be able to derive the spin axis orientation of Varuna, its size, albedo, shape (axis ratios), and density. This study is beyond the scope of this thesis and will be carried out in the future.

Due to its fast rotation, and its double-peaked nature, Varuna may be elongated from its high
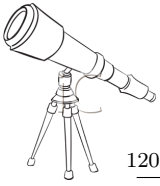
Table 5: In this table are summarized the phase angle of each Varuna observational runs and the peak-to-peak amplitude obtained.

Data	Phase angle [°]	Amplitude [mag.]
Farnham (2001)	0.57 to 0.63	0.50[a]
Jewitt and Sheppard (2002)	1 to 1.2	0.42±0.02
Ortiz et al. (2003a)	0.81 to 0.83	0.41±0.02
Hicks, Simonelli and Buratti (2005)	0.036 to 0.553	0.47±0.04
Belskaya et al. (2006)	0.056 to 0.92	0.47 to 0.42
Rabinowitz, Schaefer and Tourtellotte (2007)	0.06 to 1.3	0.49±0.17
Thirouin et al. (2010)	0.05 to 0.79	0.43±0.01[b]
2009 data	1.31	0.52±0.02
2010 data	1.32	0.50±0.02
2011 data	0.43 to 0.48	0.47±0.01
2012 data	0.36	0.53±0.02
2012-2013 data	0.19 to 0.52	0.50±0.02

Notes:

[a]: Results from in a Division For Planetary Science (DPS) abstract. Data are not available and no error bars are reported.

[b]: The 2005 lightcurve reported in Thirouin et al. (2010) has a lower amplitude than expected. Such a difference may be due to the fact that the lightcurve has been obtained a different phase angle and based on three different sets of data (separated by several nights) that have been merged (whereas the other lightcurves have been obtained during consecutive nights).

angular momentum. We must point out that Varuna presents a peak taller than the second one of around 0.1 mag.

Using Chandrasekhar (1987), and assuming that Varuna is a Jacobi ellipsoid, we computed a lower limit to the density of 1.03 g cm^{-3} (equatorial view) or a density of 1.08 g cm^{-3} assuming a viewing angle of 60°. The axes ratios are b/a=0.67 and c/a=0.47 assuming an equatorial view and are b/a=0.59 and c/a=0.43 assuming a viewing angle of 60°. Such a low bulk density requires significant porosity (see Chapter VII).

VI.3   Resonant objects

VI.3.1   (26375) 1999 DE$_9$

Sheppard and Jewitt (2003) observed 1999 DE$_9$ between April 2000 and April 2001 with the University of Hawaii 2.2 m diameter telescope (Mauna Kea, Hawaii, USA). They concluded that this object may have a long-period lightcurve, >12 h, and a very low variability ($\sim$ 0.1 mag).

During this thesis, 1999 DE$_9$ was observed on April 22th, and 23th, 2009. We spent $\sim$2 h, $\sim$0.5 h (respectively) of observing time for this target. Unfortunately, due to the very low amplitude ($<$ 0.1 mag) and the few data obtained, we are not able to propose a satisfactory study. We can just conclude that 1999 DE$_9$ has a very low amplitude lightcurve ($<$0.1 mag) and maybe a long rotational period.

By merging our data and Sheppard and Jewitt (2003) data, a possible rotational period of 12.33 h (1.95 cycles/day), which is consistent with Sheppard and Jewitt (2003) constraint is obtained (Figure 94). Unfortunately, the Lomb periodogram presents several peaks with a high spectral power, at 0.91 cycles/day and at 2.73 cycles/day. Both peaks appear to be aliases of the
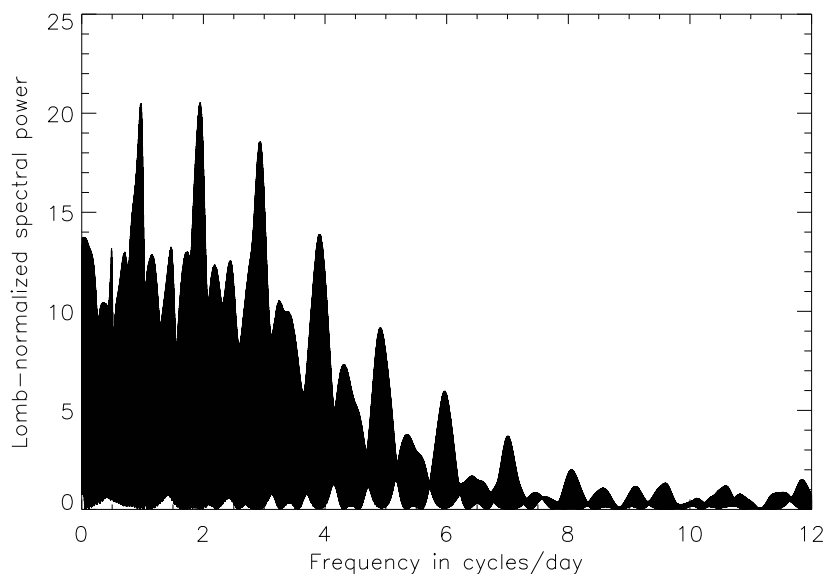
Figure 94: *Lomb-normalized spectral power versus frequency in cycles/day for 1999 DE9*: The Lomb periodogram of our data and Sheppard and Jewitt (2003) data suggests a main peak at 12.33 h.
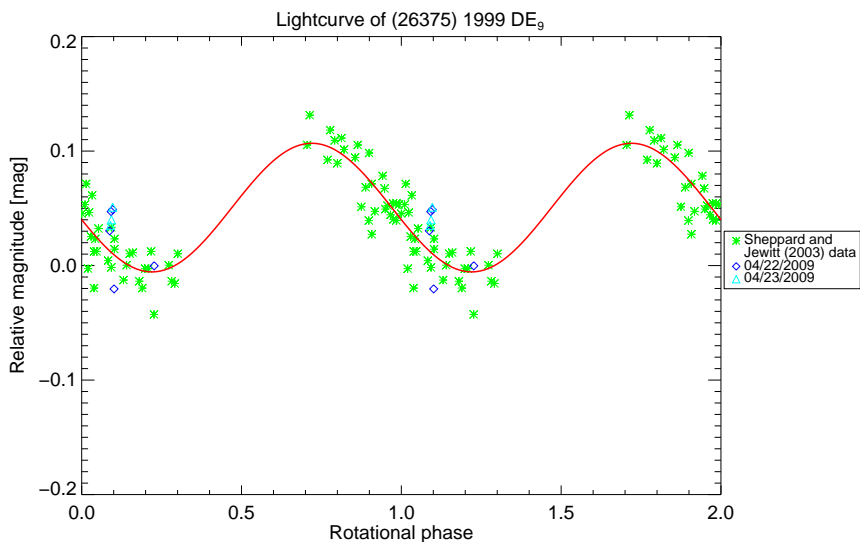
Figure 95: *Relative magnitude versus rotational phase for 1999 DE9*: Rotational phase curve for 1999 DE9 obtained by using a spin period of 12.33 h. The continuous line is a Fourier Series fit of the photometric data. Different symbols correspond to different dates.

main peak. All techniques confirmed all these peaks but seem to favored the one at 12.33 h. In Figure 95, the corresponding single-peaked lightcurve with an amplitude of 0.09±0.03 mag is plotted. Due to the few data points and due to the low lightcurve amplitude, other possible rotational periods cannot be discarded.

In conclusion, 1999 DE$_9$ presents a flat light curve and probably a long spin period, around 12.33 h.

VI.3.2   (38628) 2000 EB$_{173}$ or Huya
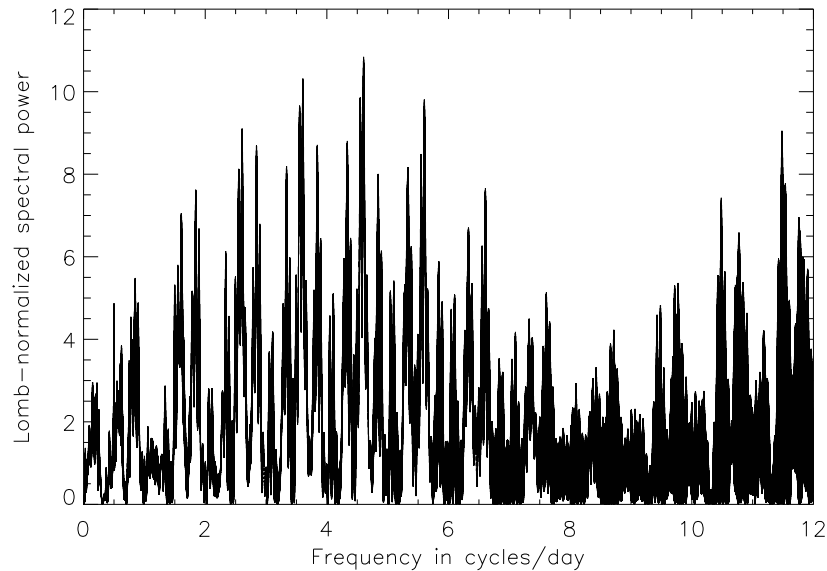
Figure 96: *Lomb-normalized spectral power versus frequency in cycles/day for Huya*: The Lomb periodogram presents one peak located at 4.61 cycles/day, and two aliases located at 3.52 cycles/day and at 5.51 cycles/day.

Thanks to data acquired with the *Hubble Space Telescope*, Noll et al. (2012) confirmed the discovery of a satellite with an apparent magnitude difference around 1.4 mag in the F606W band.

Sheppard and Jewitt (2002) observed Huya during three nights with the University of Hawaii 2.2 m telescope. They concluded that Huya has a very flat lightcurve with an amplitude < 0.06 mag. They did not provide a spin period estimation.

Lacerda and Luu (2006) also reported a flat lightcurve (amplitude < 0.04 mag) based on three observational nights with the 2.5 m Isaac Newton Telescope (INT). They did not provide a rotational period estimation.

Based on two runs carried out in February and March 2002, Ortiz et al. (2003a) proposed a single-peaked rotational period of (6.75 or 6.68 or 6.82)±0.01 h and an amplitude peak-to-peak <0.1 mag.

Huya was re-observed in 2010 and 2012 with the 1.5 m OSN telescope and with the 1.23 m Calar Alto telescope in 2012. The Lomb periodogram (Figure 96) shows one peak located at 5.21 h (4.61 cycles/day), and two aliases located at 6.82 h (3.52 cycles/day) and at 4.36 h (5.51 cycles/day). However, in all cases, such peaks have a low spectral power. All techniques confirm the highest peak at 5.21 h, and the two aliases with a lowest spectral power. In Figure 97, the corresponding single-peaked lightcurve with an amplitude of 0.02±0.01 mag is plotted. We must point out that the rotational period around 6.8 h noted by Ortiz et al. (2003a) is also a possibility in the newest data set but as an alias. As already mentioned, for very low amplitude objects, it is difficult to estimate a secure rotational period estimation. In fact, small variations in the photometry can transmit more power to/from a 24 h-alias from/to the main peak. So, we cannot

discard the alias as true period
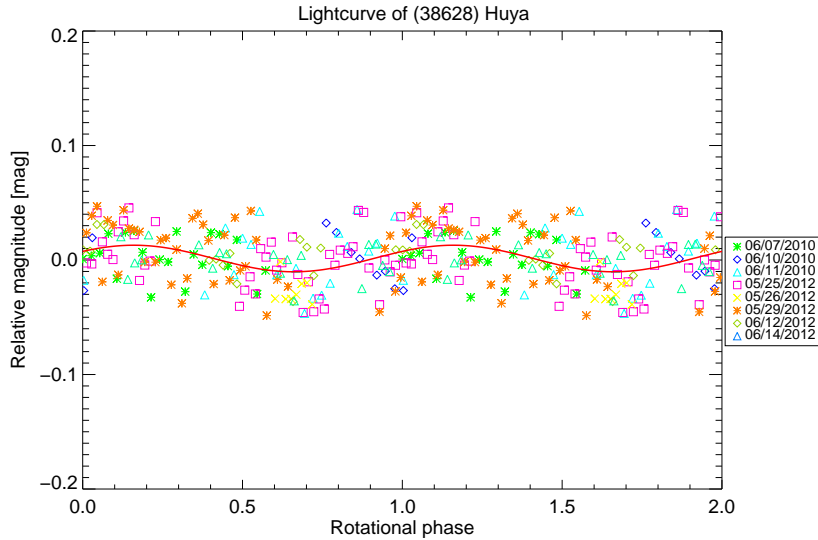
Figure 97: *Relative magnitude versus rotational phase for Huya*: Rotational phase curve for Huya obtained
by using a spin period of 5.21 h. The continuous line is a Fourier Series fit of the photometric data. Different
symbols correspond to different dates.

An attempt to merge all data sets (data from Ortiz et al. (2003a), Sheppard and Jewitt (2002)
and our 2010-2012 data sets) has been carried out. Unfortunately, the combination is not satisfac-
tory, maybe because of a change in the spin axis orientation.

VI.3.3 2001 QF$_{298}$

Sheppard and Jewitt (2003) observed this object during 4 nights and concluded that the amplitude
variation was about 0.1 mag.

2001 QF$_{298}$ was observed during only one run in 2009 at the 3.58 m NTT. During the first
night, in less than 4 h of observations, a 0.11 mag amplitude variation is reported. During an even
shorter observation time ($\sim$2 h) in the second night, a 0.07 mag amplitude variation is estimated.

As in Sheppard and Jewitt (2003), a search for rotational periodicity have been done but nei-
ther of both studies proposed a reliable rotational period. This body presents a low amplitude
lightcurve ($\lesssim$0.1 mag) and will require more data.

VI.3.4 (126154) 2001 YH$_{140}$

The first short-term variability study of 2001 YH$_{140}$ was presented by Ortiz et al. (2006). Using
data from December 15th-20th, 2004, Ortiz et al. (2006) favored a periodicity of 8.45 h but pre-
sented two aliases located at 6.22 h and at 12.99 h.

Sheppard (2007), from R-band observations taken on December 2003 at the University of
Hawaii 2.2 m telescope, suggested a single peak periodicity of 13.25$\pm$0.20 h with an amplitude

of 0.21±0.04 mag.
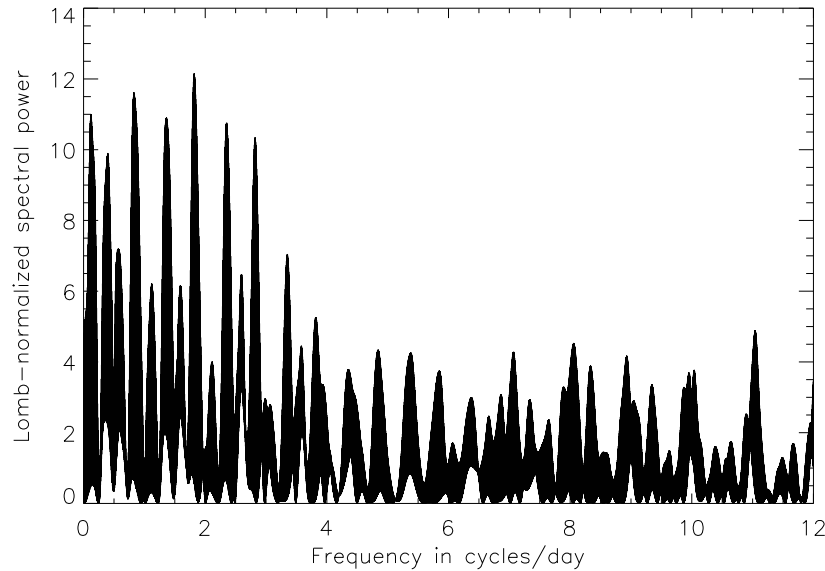
Figure 98: *Lomb-normalized spectral power versus frequency in cycles/day for 2001 YH$_{140}$*: The Lomb periodogram shows several peaks located at 13.2 h (1.82 cycles/day), at 8.40 h (2.86 cycles/day) and at 6.19 h (3.88 cycles/day).

In Thirouin et al. (2010), we re-reduced and re-analyzed the December 2004 run already studied by Ortiz et al. (2006). The Lomb periodogram showed three peaks of low spectral power located at 13.2 h (1.82 cycles/day), at 8.40 h (2.86 cycles/day) and at 6.19 h (3.88 cycles/day). The best-fit lightcurve was obtained for a spin period of 13.2 h. The amplitude of the lightcurve was 0.13±0.05 mag. All techniques confirmed this rotational period (Thirouin et al., 2010).

The Lomb periodogram, obtained by merging the 2004 data set with Sheppard (2007) data set, (Figure 98) shows several peaks with a high spectral power. The main peak, with the highest spectral power, is located at 1.82 cycles/day (13.19 h). All techniques confirm such a peak. In Figure 99, the corresponding single-peaked lightcurve with an amplitude of 0.15±0.03 mag is plotted.

In conclusion, there is agreement about the rotation period of this body, bearing in mind that 13.20 h is very close to the 12.99 h possible alias reported in Ortiz et al. (2006). However, the amplitude that we report is somewhat different, although consistent within their error bars. We propose a single-peaked lightcurve with a rotational periodicity of 13.19 h and an amplitude of 0.15±0.03 mag, consistent with Sheppard (2007) one.

VI.3.5   (84522) 2002 TC$_{302}$

2002 TC$_{302}$ was observed during two runs in 2009 and 2010, and during one isolated night in 2010. The Lomb periodogram (Figure 100) presents three peaks with similar spectral power. The highest peak is located at 5.41 h (4.44 cycles/day) and two aliases are located at 4.87 h (4.93 cycles/day) and at 6.08 h (3.95 cycles/day). The PDM and Pravec-Harris techniques confirm the highest peak at 5.41 h, but, CLEAN favors a spin period of 6.08 h. The best-fit lightcurve is obtained for a single-peaked rotational period of 5.41 h (Figure 101). The amplitude of the curve is 0.04±0.01 mag (Thirouin et al., 2012).

Figure 99: *Relative magnitude versus rotational phase for 2001 YH$_{140}$:* Rotational phase curve for
2001 YH$_{140}$ obtained by using a spin period of 13.19 h. The continuous line is a Fourier Series fit of
the photometric data. Different symbols correspond to different dates.
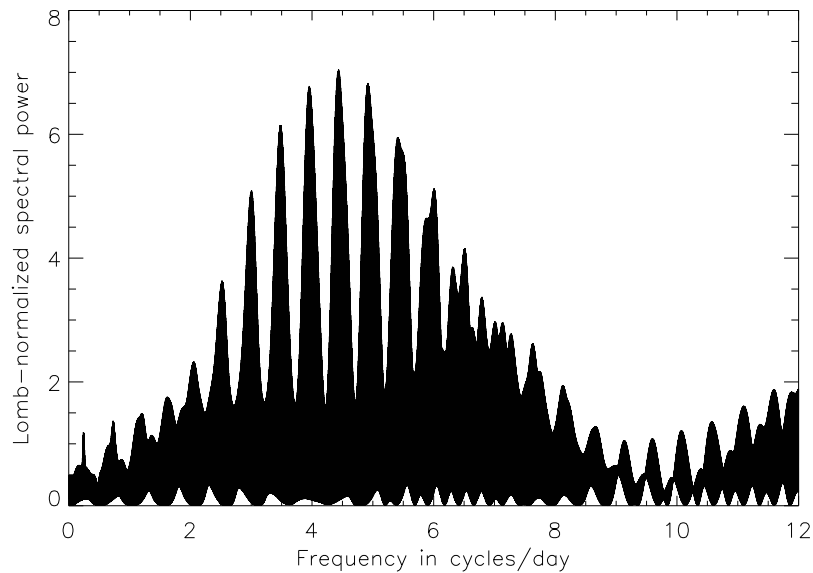
Figure 100: *Lomb-normalized spectral power versus frequency in cycles/day for 2002 TC$_{302}$:* The Lomb
periodogram shows several peaks. The highest peaks are located at 5.41 h, at 4.87 h and at 6.08 h.

VI.3.6   (55638) 2002 VE$_{95}$

Sheppard and Jewitt (2003) observed 2002 VE$_{95}$. They reported one night of observations carried
out at the University of Hawaii 2.2 m telescope. They could not determine a periodicity. An
amplitude variation of <0.06 mag was derived during their observations.
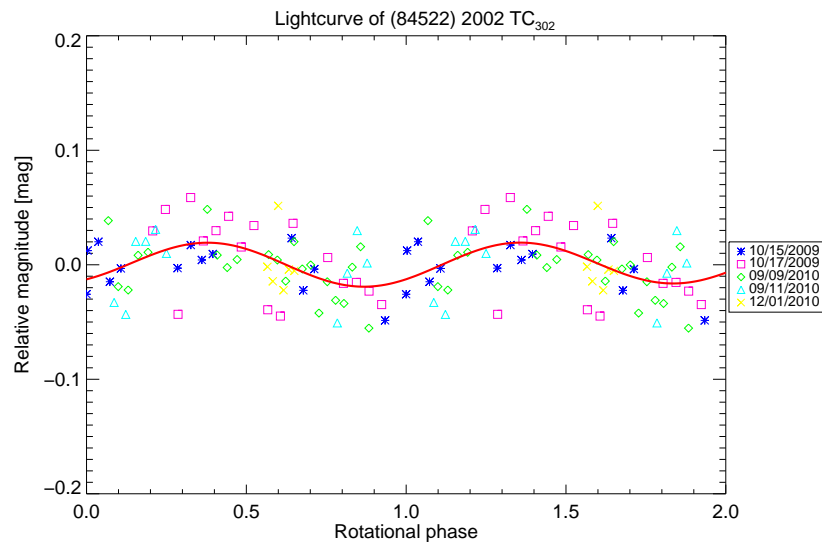
Figure 101: *Relative magnitude versus rotational phase for 2002 TC₃₀₂*: Rotational phase curve for 2002 TC$_{302}$ obtained by using a spin period of 5.41 h. The continuous line is a Fourier Series fit of the photometric data. Different symbols correspond to different dates.

Ortiz et al. (2006) presented observations carried out in November and December 2002, and December 2004 with the 1.5 m OSN telescope. They did not favor or discard any periodicity between 6.76 h, 7.36 h and 9.47 h. In all cases, the amplitude of the lightcurve was below 0.08 mag.
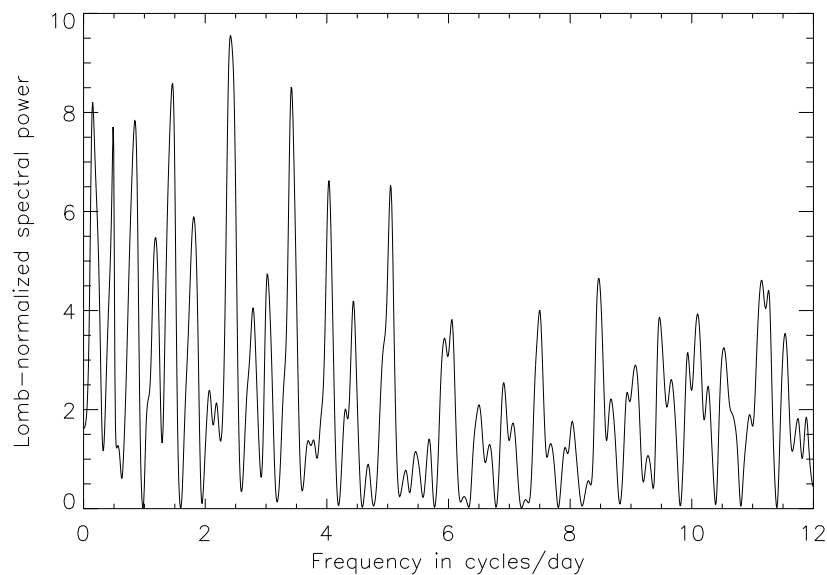
Figure 102: *Lomb-normalized spectral power versus frequency in cycles/day for 2002 VE₉₅*: The Lomb periodogram of the January and December 2004 data sets shows several peaks with low spectral powers located at 9.97 h (2.41 cycles/day), 17.32 h (1.39 cycles/day), 6.18 h (3.88 cycles/day) and at 4.90 h (4.90 cycles/day).
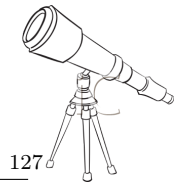
In Thirouin et al. (2010), we re-reduced and re-analyzed the December 2004 data set analyzed
in Ortiz et al. (2006), and we added one isolated night of observations carried out in January 2004.
The Lomb periodogram (Figure 102) of the January and December 2004 data sets shows several
peaks. The highest peak is located at 9.97 h (2.41 cycles/day) and three aliases are at 17.32 h
(1.39 cycles/day), 6.18 h (3.88 cycles/day) and 4.90 h (4.90 cycles/day). All techniques suggested
the same peaks. In Figure 103, the single-peaked lightcurve with a rotational period of 9.97 h and
an amplitude of 0.04±0.02 mag is plotted (Thirouin et al., 2010).

One should keep in mind that 2002 VE$_{95}$ has very low amplitude variations and the overall
scatter of our data is greater than for other low variability objects that we have studied in more
detail. Since Ortiz et al. (2006) did not identify any clear periodicity and Sheppard and Jewitt
(2003) could not determine a period, our derivation is only tentative and more observation data
with smaller scatter will be necessary to derive a rotation period completely reliable.

Figure 103: *Relative magnitude versus rotational phase for 2002 VE$_{95}$*: Rotational phase curve for
2002 VE$_{95}$ obtained by using a spin period of 9.97 h. The continuous line is a Fourier Series fit of
the photometric data. Different symbols correspond to different dates.

VI.3.7   (119979) 2002 WC$_{19}$

Using *Hubble Space Telescope* images, Noll et al. (2007a) reported the discovery of a satellite with
an apparent magnitude difference around 2.5 mag in the F606W band.

Sheppard (2007) observed this object during four nights in December 2004. He did not provide
any rotational period value nor estimation. He reported a flat lightcurve with an amplitude varia-
tion <0.05 mag.

In this thesis, we present observations carried out during three nights in January 2004 with the
1.5 m telescope of Sierra Nevada Observatory. We spent ~2 h, ~5 h, and ~5 h (respectively) of
observing time for this target. Unfortunately, with just few hours, a reliable spin period cannot be
determined. An amplitude variation of <0.1 mag is reported.

A mix of the 2004 data set and Sheppard (2007) data has been done, but the data sets were not enough for a rotational period study. In conclusion, 2002 WC$_{19}$ presents a nearly flat lightcurve with an amplitude variation <0.1 mag.

VI.3.8   (208996) 2003 AZ$_{84}$

Using *Hubble Space Telescope* images, Brown and Suer (2007) reported the discovery of a satellite with a separation of 0.22$''$ and an apparent magnitude difference of 5.0±0.3 mag in the F606W band.

Sheppard and Jewitt (2003) observed 2003 AZ$_{84}$ for three nights in February 2003, with the University of Hawaii 2.2 m telescope. They favored a 6.72±0.05 h single-peaked rotational lightcurve with an amplitude of 0.14±0.03 mag (they only reported photometric amplitude estimated from apparent maximum and minimum, and not lightcurve amplitude obtained thanks to a lightcurve fit as it has been done it this work).

Ortiz et al. (2006) presented data obtained in January and December 2004. According to this study, the highest peak was located at 5.28 h and there were two aliases of similar spectral power located at 4.32 h and at 6.76 h. Both aliases could also be the rotational period, and one of them agreed with the period reported by Sheppard and Jewitt (2003).
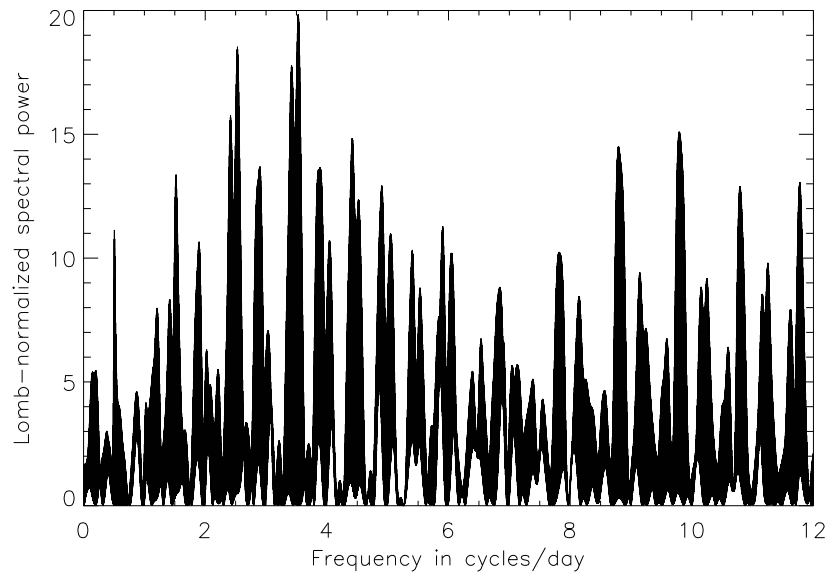
Figure 104: *Lomb-normalized spectral power versus frequency in cycles/day for 2003 AZ$_{84}$*: The Lomb periodogram of our 2004 and 2011 data sets shows several peaks. The main peak is located at 3.53 cycles/day, but there are several aliases. The alias with the highest spectral power is at 2.53 cycles/day.

In Thirouin et al. (2010), we re-reduced and re-analyzed the January and December 2004 data sets published in Ortiz et al. (2006). We concluded that this object has a single-peaked lightcurve with a rotational period of 6.79 h and an amplitude of 0.07±0.01 mag.

This object was re-observed in February 2011. By merging all the data (January and December 2004 and February 2011 data sets), a rotational period of 6.79±0.03 h was derived (Figure 104). This period is also derived from the PDM analysis and both the CLEAN and Pravec-Harris methods. In Figure 105, a 6.79 h single-peaked lightcurve with an amplitude of 0.07±0.01 mag is plotted.
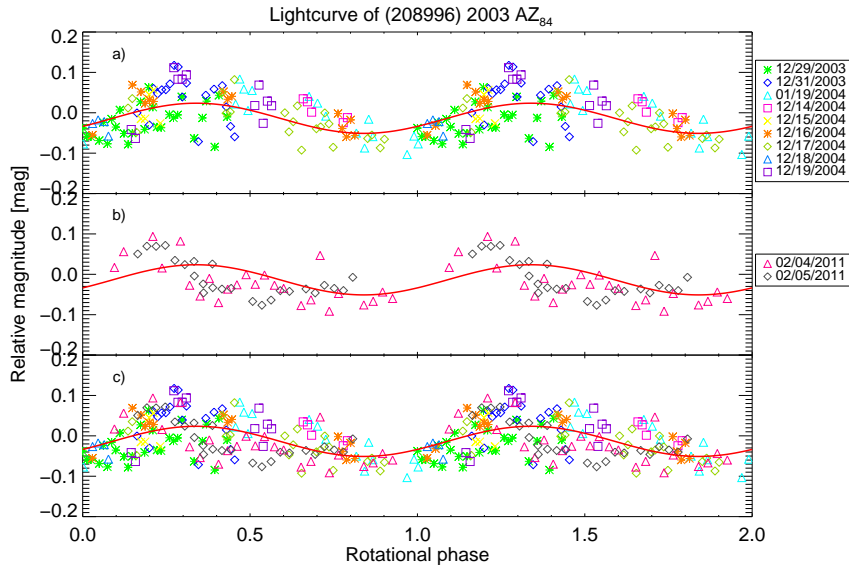
Figure 105: *Relative magnitude versus rotational phase for 2003 AZ$_{84}$:* Rotational phase curve for
2003 AZ$_{84}$ obtained by using a spin period of 6.79 h. The continuous line is a Fourier Series fit of
the photometric data. Different symbols correspond to different dates.

In summary, there is an agreement about the rotation period of this body. A 6.79±0.04 h
single-peaked lightcurve seems to be the best option.

VI.3.9 (136108) 2003 EL$_{61}$ or Haumea

Using the Keck telescope (Mauna Kea, Hawaii, USA), two satellites were observed around Haumea.
The largest satellite was found on January 26th, 2005 by Brown (2005a). The second one was dis-
covered on June 30th, 2005 by Brown (2005b). On September 17th, 2008, both satellites received
their permanent designations and were named Hi'iaka and Namaka, respectively. The magnitude
differences between Haumea and its satellites Hi'iaka and Namaka, are 2.98±0.03 mag and 4.6 mag
(respectively) in the K' band.

Rabinowitz et al. (2006) presented R-observations acquired between January and July 2005
using the 1.3 m SMARTS telescope, the 5.1 m Hale telescope at the Palomar Mountain Obser-
vatory, and the 0.8 m telescope at the Tenagra Observatory. They derived a 3.9154±0.0002 h
double-peaked rotational lightcurve with an amplitude of 0.28±0.02 mag for Haumea.

Lacerda, Jewitt and Peixinho (2008) used observations carried out in June and July 2007 at
the 2.2 m University of Hawaii telescope. Observations were performed using the R, B, and J
filters. They obtained a 3.9155±0.0001 h double-peaked rotational lightcurve with an amplitude
of 0.29±0.02 mag. In Lacerda, Jewitt and Peixinho (2008), the existence of a dark red spot on the
surface of Haumea was suggested to explain the asymmetric lightcurve and the color variations
reported along its rotation.

Haumea was observed several times during the last few years by our team. Three different
observational runs in January 2007, January 2010 and April 2012 were carried out. The 2007 data
set is published in Thirouin et al. (2010) where we favored a double-peaked lightcurve with a se-
cure periodicity of 3.9153 h and an amplitude of 0.28±0.02 mag. In 2010 and 2012, we re-observed
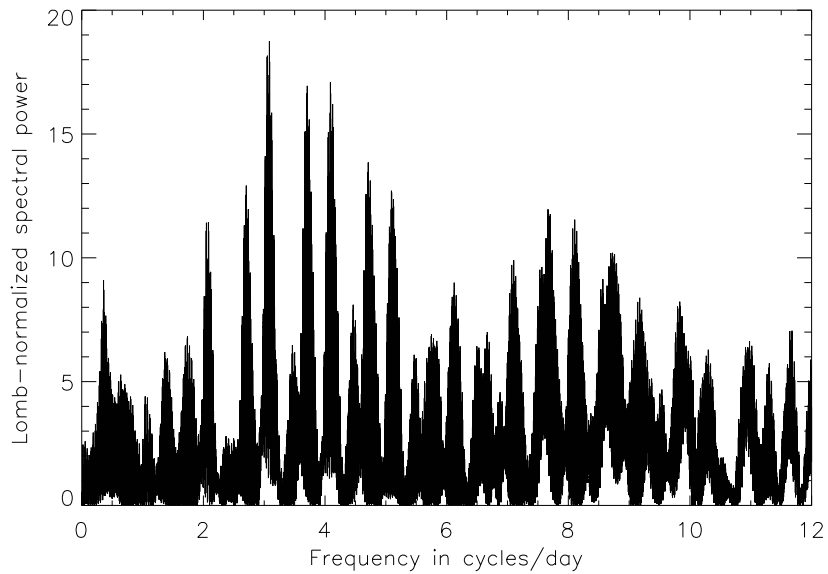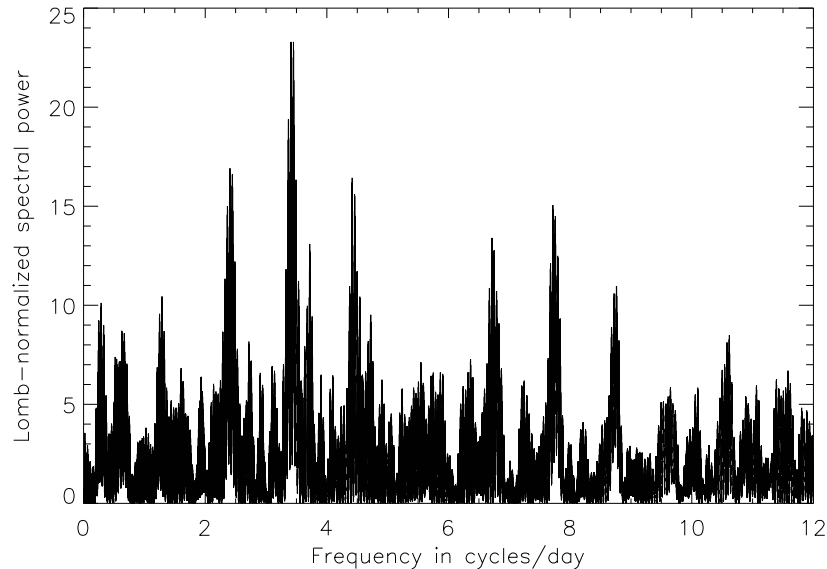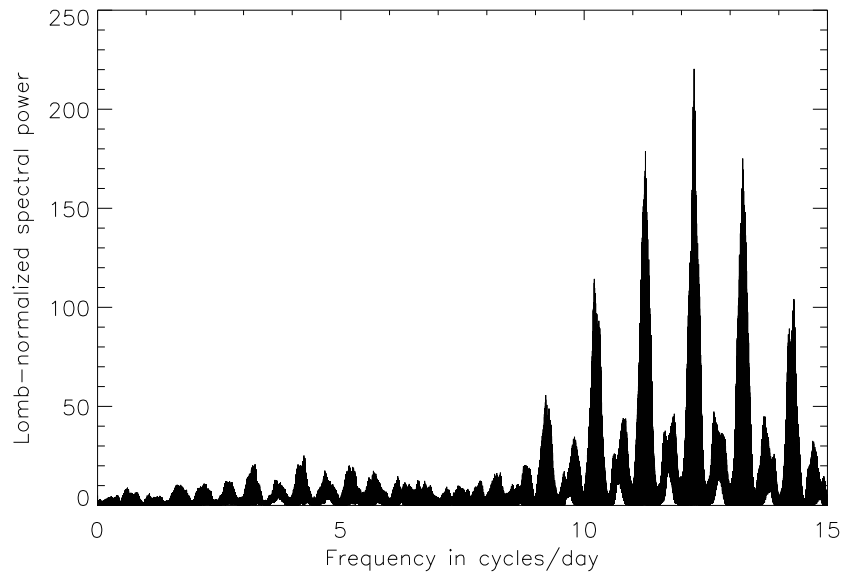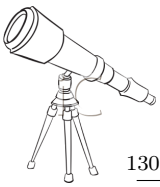
Figure 106: *Lomb-normalized spectral power versus frequency in cycles/day for Haumea*: The Lomb periodogram of our 2007, 2010, and 2012 data sets as well as R-filter Lacerda, Jewitt and Peixinho (2008) data shows one clear peak located at 12.2595 cycles/day (1.95767 h).

Haumea to check for any changes in the lightcurve, and found a very similar spin period and a consistent peak-to-peak lightcurve amplitude.

Due to its fast rotation, and its double-peaked nature, Haumea may be elongated from its high angular momentum. As already pointed out Haumea presents a peak taller than the second one of around 0.04 mag.

Using Chandrasekhar (1987), and assuming that Haumea is a Jacobi ellipsoid, we computed a lower limit to the density of 2.59 g cm^{-3} (equatorial view) or a density of 2.69 g cm^{-3} assuming a viewing angle of 60°. The axes ratios are b/a=0.77 and c/a=0.51 assuming an equatorial view and are b/a=0.67 and c/a=0.47 assuming a viewing angle of 60° (see Chapter VII).

Haumea also presents surface variations. In fact, Lacerda, Jewitt and Peixinho (2008) suggested that the asymmetric lightcurve of Haumea is due to a dark spot. Such an asymmetric lightcurve is also reported in this work, Section VI.3.8.

In Figure 107, adapted from Lacerda, Jewitt and Peixinho (2008) are shown different models able to explain the Haumea asymmetric lightcurve to a dark spot. Such surface albedo variations are also detectable through a thermal lightcurve and allow us to distinguish between the single- and double-peaked rotational period. A positive correlation between the thermal and the optical lightcurves indicates that the main cause of the brightness variation is due to the body shape, and so we have to consider a double peaked rotational lightcurve. An anti-correlation indicates that surface albedo variations are the main cause of the brightness variations and only cause a single-peaked lightcurve.

Lellouch et al. (2010), based on *Herschel Space Observatory* data, presented the first thermal lightcurve of Haumea and confirmed the elongated shape of this object and so, the double-peaked rotational period. Unfortunately, due to the data quality, they were not also able to confirm the presence of a dark spot on the surface of Haumea.
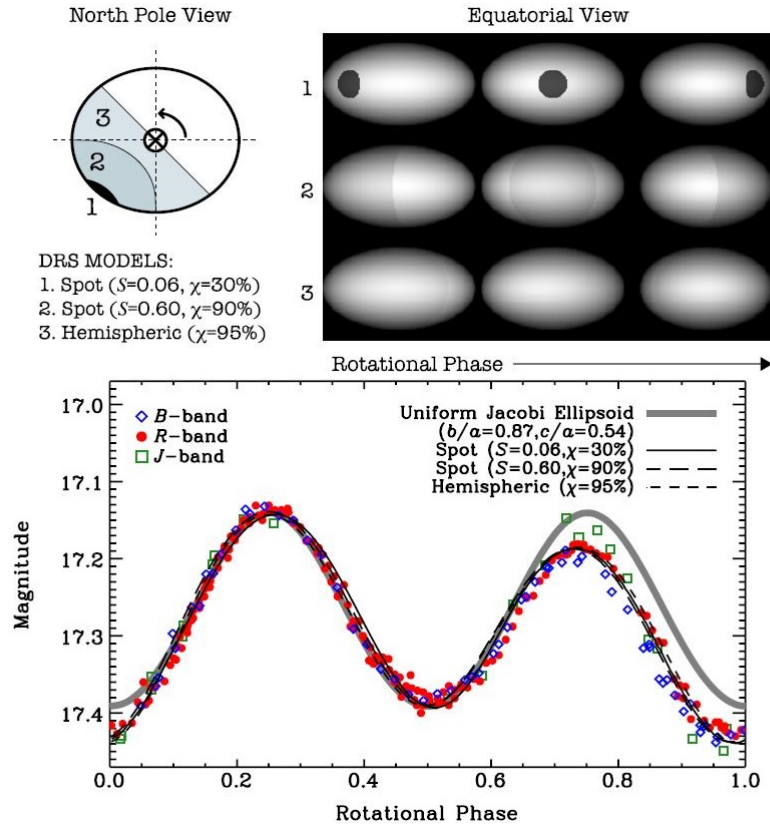
Figure 107: *Lightcurve of Haumea with its elongation and dark spot*: Upper plot: three models of the dark spot on Haumea's surface. The north pole and three equatorial views of the ellipsoid (from left to right: flank-on, spot-on, and tip-on, or rotational phases ∼0.750, ∼0.875, and ∼1.000). The spot in each model is characterized by a surface area S (expressed as a fraction of the maximum equatorial cross-sectional area of Haumea) and an albedo, χ, normalized to the albedo of the surface outside the spot. The spots are assumed to be located on the equator of Haumea. "Hemispheric" is a model in which a whole hemisphere of Haumea has a darker albedo (similar to Iapetus, satellite of Saturn). Bottom plot: Haumea lightcurve based on images carried out in the B, R and J bands. The thick gray line corresponds to a Jacobi equilibrium ellipsoid model, assumed to have uniform surface optical properties. The three thin black lines correspond to models with non-uniform surfaces. "Spot" models have darker circular regions located on the equator of the Jacobi ellipsoid presented in the upper plot. Figure adapted from Lacerda, Jewitt and Peixinho (2008).

In this work, we reported several lightcurves of Haumea on 4 epochs spanning 2007 to 2011 that allowed us to derive a precise rotational period.

In order to obtain an even more accurate rotational period for Haumea, a mix of the 2007, 2010 and 2012 data sets as well as the R-filter Lacerda, Jewitt and Peixinho (2008) data has been done. Only the R-band of Lacerda, Jewitt and Peixinho (2008) has been used because of the high quality and quantity of such data. Haumea lightcurve from Rabinowitz et al. (2006) presents a higher dispersion and they were not used. By merging all the data sets and Lacerda, Jewitt and Peixinho (2008) data, an accurate rotation period of 3.91534±0.00002 h (Figure 106) and a relative amplitude of 0.28±0.01 mag are obtained. In Figure 108, all lightcurves obtained from our differents data sets and Lacerda, Jewitt and Peixinho (2008) data are plotted. Based on several lightcurves obtained between 2007 and 2012, no significant change in the amplitude variation is reported.
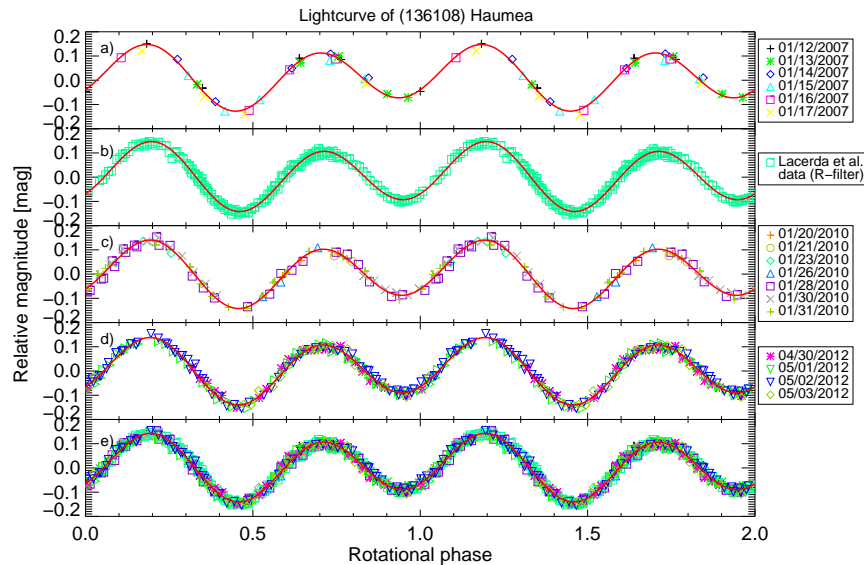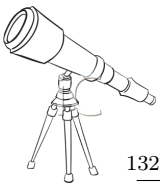
Figure 108: *Relative magnitude versus rotational phase for Haumea*: Plot a) is the lightcurve obtained in 2007 thanks to data obtained with the 2.2 m Calar Alto telescope. Plot b) is based on R-filter observations by Lacerda, Jewitt and Peixinho (2008). Lacerda, Jewitt and Peixinho (2008) plotted the apparent magnitude of Haumea versus the rotational phase. Here, the relative magnitude of Haumea versus the rotational phase has been plotted. Plot c) is the 2010 lightcurve based on ASH2 and 1.23 m CAHA telescopes observations. Plot d) is the 2012 lightcurve based on 1.23 m CAHA telescope images. Plot e), is a mix of all the data sets and Lacerda, Jewitt and Peixinho (2008) data. Continuous lines are a Fourier Series fits of the photometric data. Different symbols correspond to different dates.

VI.3.10   (84922) 2003 VS$_2$

Ortiz et al. (2006) observed 2003 VS$_2$ in December 2003 and in January 2004 with the 1.5 m OSN telescope. They obtained two possible rotational periods: 3.71 h or 4.39 h. The second value is an alias of the first one. The lightcurve amplitude was estimated as 0.23±0.07 mag.

Sheppard (2007) presented a short-term variability study dedicated to 2003 VS$_2$ based on R-filter observations carried out on December 2003 at the University of Hawaii 2.2 m telescope. He proposed a lightcurve with a double peak periodicity of 7.41±0.02 h and a lightcurve amplitude of 0.21±0.02 mag. This period is twice one of the values reported in Ortiz et al. (2006) and makes sense because the lightcurve is double-peaked.

In Thirouin et al. (2010), we re-reduced and re-analyzed the December 2003 and January 2004 data sets already studied by Ortiz et al. (2006). We concluded that the Lomb periodogram as well as all techniques used showed a clear main peak, with a spectral power >99 %, located at 3.71 h (6.47 cycles/day). However, due to the high amplitude of this lightcurve, 0.21±0.03 mag, we have to consider the double-peaked lightcurve. So, a spin period of 7.42 h is indeed the correct one for this object.

2003 VS$_2$ was re-observed in October 2010 by our team. Thanks to this new data set, the previous periodicity of 7.42 h and the lightcurve amplitude of 0.22±0.01 mag are confirmed.

By merging our data sets (December 2003, January 2004, and October 2010) with Sheppard (2007) data, an accurate rotational is estimated. The Lomb periodogram (Figure 109) shows a clear peak at 7.4208 h. In Figure 110, all this study is summarized by plotting all the lightcurves obtained during the last years. The final lightcurve has a peak-to-peak amplitude of 0.224±0.013 mag.
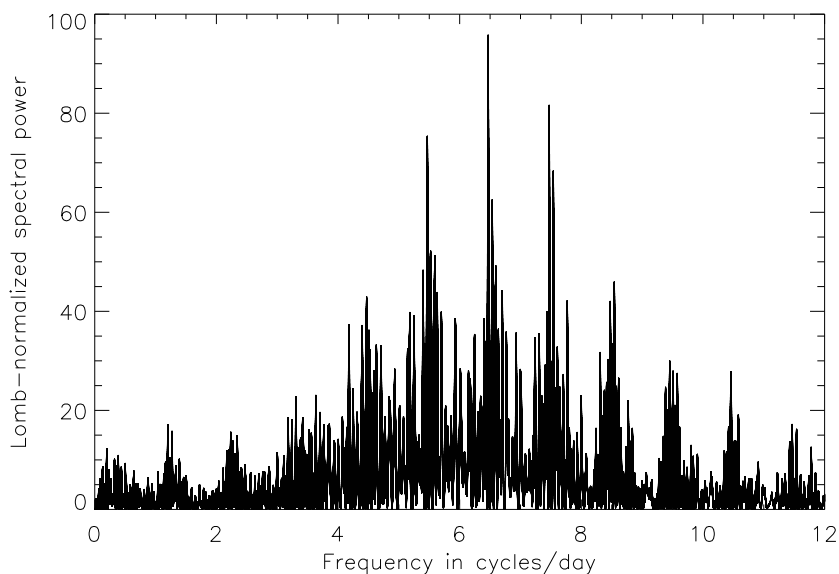
Figure 109: *Lomb-normalized spectral power versus frequency in cycles/day for 2003 VS$_2$*: The Lomb
periodogram of our 2003, 2004, and 2010 data sets and Sheppard (2007) data shows one clear peak located
at 6.47 cycles/day, and two aliases located at 5.47 cycles/day, and at 7.47 cycles/day.
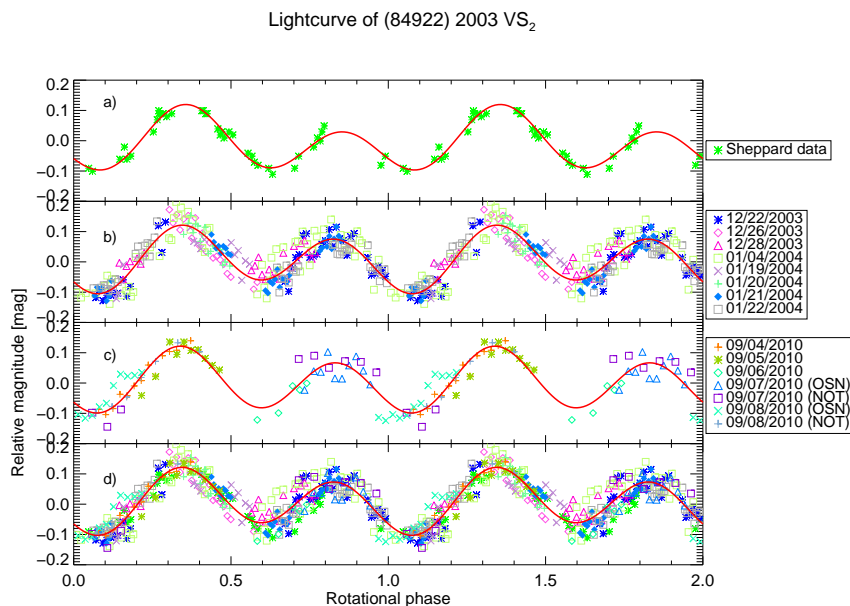
Figure 110: *Relative magnitude versus rotational period for 2003 VS$_2$*: Plot a) is based on R-filter obser-
vations obtained by Sheppard (2007). Sheppard (2007) plotted the R-magnitude of 2003 VS$_2$ versus the
rotational phase. Here, are plotted the relative magnitude versus the rotational phase and the light-time
correction has been applied. Plot b) is the 2003/2004 lightcurve based on observations obtained with the
1.5 m OSN telescope. Plot c) is the 2010 lightcurve obtained thanks to the 1.5 m OSN telescope. Plot d)
is a mix of the data sets and Sheppard (2007) data. Plot d) legend is not shown for clarity but the same
symbols and colors than in the previous plots were used. Continuous lines are a Fourier Series fits of the
photometric data. Different symbols correspond to different dates.
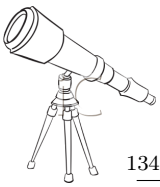
As already noticed by Sheppard (2007), we confirm that 2003 VS$_2$ lightcurve is asymmetric. The first peak is taller than the second one (of ∼0.05 mag). This object is probably elongated (large amplitude lightcurve) and presents two different maxima which seems to indicate a complex shape. The second option is to consider the possibility of strong color variations of the surface, like it is the case for Haumea (Lacerda, Jewitt and Peixinho, 2008). As there is no study about the color variation during one entire rotational period for this object, we cannot discard such an idea. However, due to its fast rotation, and its double-peaked nature, the most reasonable option is to consider that 2003 VS$_2$ may be elongated from its high angular momentum.

Using Chandrasekhar (1987), and assuming that 2003 VS$_2$ is a Jacobi ellipsoid, we computed a lower limit to the density of 0.72 g cm^{-3} (equatorial view) or a density of 0.74 g cm^{-3} with a viewing angle of 60°. The axes ratios are b/a=0.82 and c/a=0.52 assuming an equatorial view and are b/a=0.71 and c/a=0.48 assuming a viewing angle of 60° (see Chapter VII).

In this thesis, we reported data obtained in December 2003-January 2004 and in September 2010. In around 7 years, we did not notice any significant change in the lightcurve amplitude, and all lightcurves are in phase.

As already pointed out several objects present a peak taller than the second one. Such differences in the cases of 2003 VS$_2$ and Haumea are around 0.04/0.05 mag, whereas for Varuna the greatest difference is 0.1 mag. Hence, this means that the hemispherically averaged albedo typically has variations around 4 to 10% (Thirouin et al., 2010). So, we expect that the variability induced by surface features is on the order of 0.1 mag. This is agreement with the threshold of 0.15 mag used in this work to select between shape- and albedo-dominated lightcurves.

VI.3.11 (90482) 2004 DW or Orcus

Using observations with the *Hubble Space Telescope* from November 13th, 2005, Brown and Suer (2007) reported the discovery of a satellite around Orcus. The apparent magnitude difference is 2.54±0.01 mag in the F606W filter (Brown et al., 2010). In April 2010, this satellite received the name Vanth.

Ortiz et al. (2006) proposed the first study about the short-term variability of Orcus. Based on observations carried out in March and April 2004, they concluded that a rotation period of 10.08 h appeared most likely but they point out the presence of two aliases with an high spectral power located at 7.09 h and at 17.43 h. Finally, they favored the value of 10.08 h and a lightcurve amplitude of 0.04±0.02 mag.

Sheppard (2007) obtained R-filter observations at the Dupont 2.5 m telescope (Las Campanas, Chile) in February and March 2005. Based on 43 images, he did not notice a significant short-term variability and suggested a flat lightcurve with an amplitude < 0.03 mag.

Rabinowitz, Schaefer and Tourtellotte (2007) presented the result of 143 images obtained between February and July 2004 at the 1.3 m SMARTS telescope. They suggested a 13.19 h single-peaked rotational lightcurve with an amplitude of 0.18 mag. This is obviously inconsistent with both Sheppard (2007) and Ortiz et al. (2006), in terms of period and amplitude.

Part of the data used in Ortiz et al. (2006) have been re-reduced and re-analyzed. Results are published in Thirouin et al. (2010) in which a single-peaked rotational period of 10.47 h (2.29 cycles/day) was favored. The amplitude of the curve was 0.04±0.01 mag.

Orcus was also observed in December 2009 and January 2010 with the 0.45 m ASH telescope by our team. Results are published in Ortiz et al. (2011) where a mid-term astrometric and photometric study was carried out. Here we will only use the photometric data.
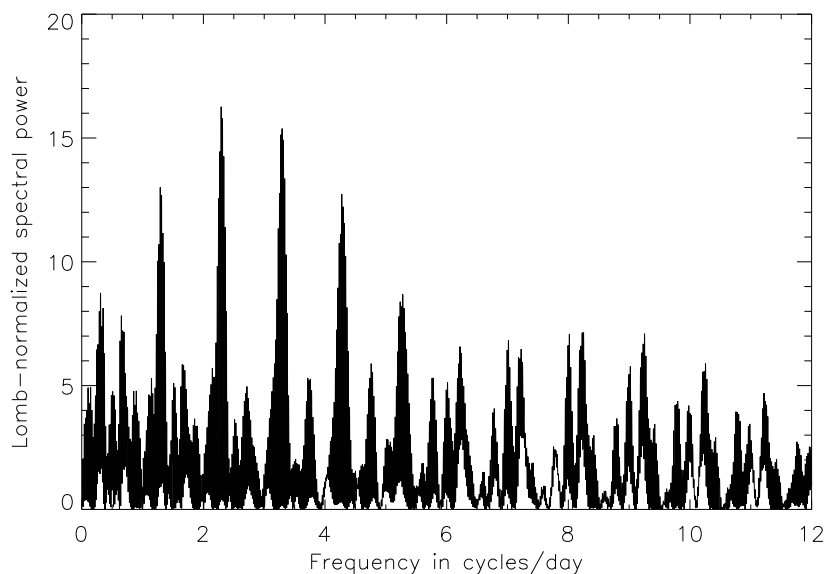
Figure 111: *Lomb-normalized spectral power versus frequency in cycles/day for Orcus*: The Lomb periodogram of the 2004 data sets shows one peak with a high significance level (>99%) located at 10.47 h (2.29 cycles/day).
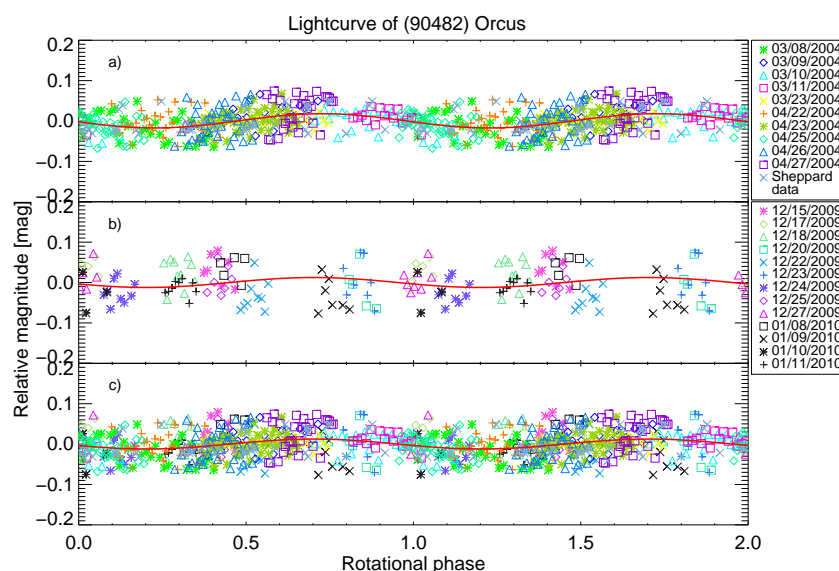
Figure 112: *Relative magnitude versus rotational period for Orcus*: Plot a) is the 2004 lightcurve based on observations obtained with the 1.5 m OSN telescope and with data from Sheppard (2007). Plot b) is the 2009-2010 lightcurve obtained thanks to the ASH2 telescope phased to the 10.47 h single peak periodicity. Plot c) is a mix of our data sets and Sheppard (2007) data. The legend of the plot c) is the same as previous legends. Continuous lines are a Fourier Series fits of the photometric data. Different symbols correspond to different dates.

Here we report the short-term variability of Orcus. Ortiz et al. (2006) data were not used, be-

cause part of these data were re-reduced and re-analyzed (Thirouin et al., 2010), nor Rabinowitz, Schaefer and Tourtellotte (2007) data due to their inconsistency. The Lomb periodogram (Figure 111) and all techniques used show one clear peak with a high significance level (>99%) located at 10.47 h (2.29 cycles/day). In Figure 112, a lightcurve with an amplitude of 0.04±0.01 mag and a rotational period of 10.47 h is proposed.
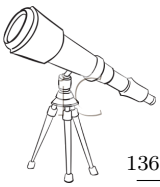
VI.3.12 (144897) 2004 UX$_{10}$

This body was observed in September and in November 2007. The Lomb periodogram (Figure 113) shows three peaks with a high an very similar spectral power located at 4.23 cycles/day (5.68 h), at 3.88 cycles/day, and at 4.58 cycles/day. The highest peak is at 5.68 h and the other values are aliases. However, all of them have very similar spectral power. The PDM technique determines a periodicity of 5.30 h, which is consistent with the Lomb one. In Figure 114, the lightcurve with a spin period of 5.68 h and an amplitude of 0.09±0.02 mag is plotted (Thirouin et al., 2010). From our results, a periodicity of 5.68 h is possible.
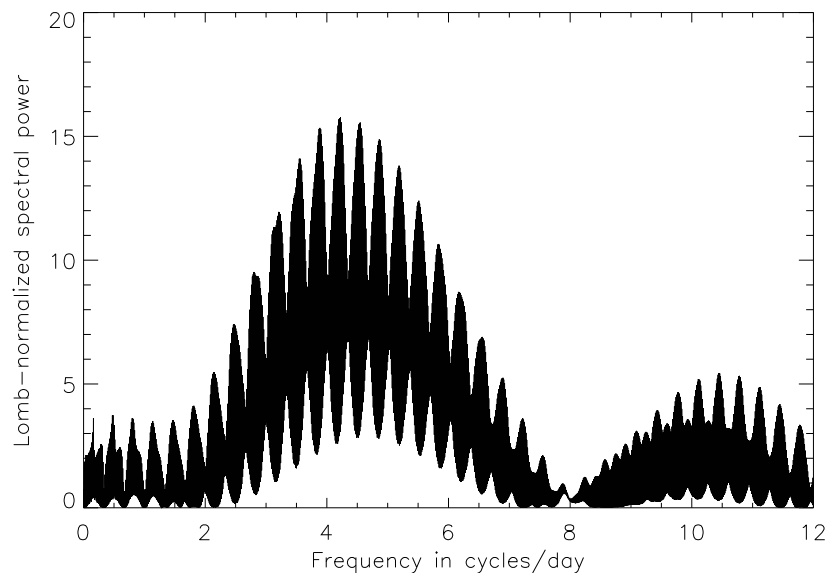
Figure 113: *Lomb-normalized spectral power versus frequency in cycles/day for 2004 UX$_{10}$*: The Lomb periodogram shows three peaks with a high spectral power located at 4.23 cycles/day (5.68 h), at 3.88 cycles/day, and at 4.58 cycles/day

Perna et al. (2009) observed this target during three nights (around 12 h of observations). They suggested a double-peaked lightcurve with a double-peaked rotational period of 7.58±0.05 h. As there is no information about possible aliases in Perna et al. (2009) nor Lomb periodograms (or other methods to estimate the periodicity), one cannot check if the 5.68 h rotational period is an alias or not. On the other hand, they obtained a lightcurve amplitude of 0.14±0.04 mag which is ruled out in our data set. The rotational period of 7.58 h is an alias in our study, so both values seem reasonable.

VI.3.13 (341520) 2007 TY$_{430}$

Thanks to data acquired at the 8.1 m Gemini telescope (Hawaii, USA), Sheppard and Trujillo (2008) confirmed, on August 1st, 2008, the discovery of a satellite around 2007 TY$_{430}$. The appar-
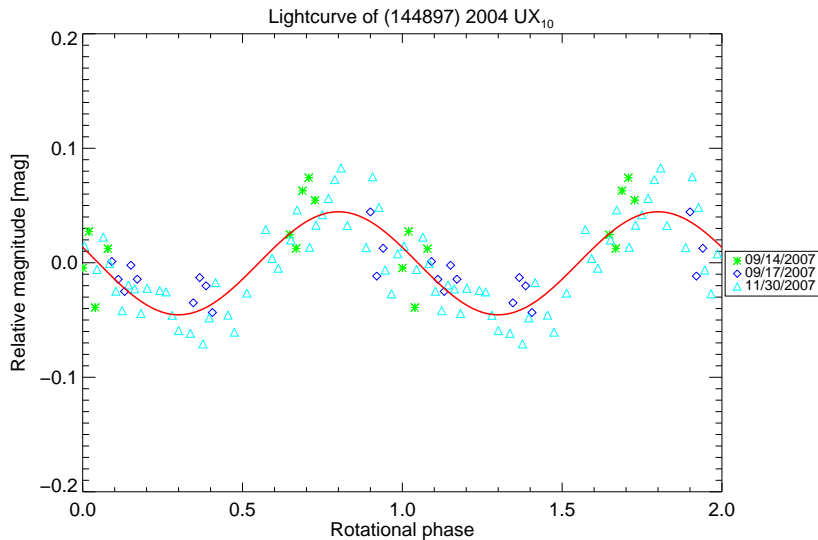
Figure 114: *Relative magnitude versus rotational period for 2004 UX$_{10}$*: Rotational phase curve for
2004 UX$_{10}$ obtained by using a spin period of 5.68 h. The continuous line is a Fourier Series fit of
the photometric data. Different symbols correspond to different dates.

ent magnitude difference is very low, ∼0.1 mag in the V-band. According to Sheppard, Ragozzine
and Trujillo (2012), this system has equal-size components. In other words, both components of
this system have a similar size.

2007 TY$_{430}$ was observed during around 14 h, split in 4 nights, at the 3.58 m TNG in 2011.
The Lomb periodogram (Figure 115) shows one peak with a high spectral power (>99%), located
at 4.64 h (5.17 cycles/day). All techniques confirmed this periodicity. In Figure 116, the single-
peaked lightcurve with a spin period of 4.64 h and an amplitude of 0.20±0.03 mag is plotted. The
lightcurve amplitude is large, so, according to our definition, one has to consider the double-peaked
period, 9.28 h (Thirouin et al., 2013b). The first maximum is a little bit taller than the second one
(∼0.05 mag). This difference confirms the complex shape of 2007 TY$_{430}$ and clearly favors the
double-peaked lightcurve.

However, we do not know if the variation comes from the primary or the satellite because
both objects are apparently of very similar size so their contributions to the lightcurve cannot be
disentangled.

VI.4   Scattered and Detached disk objects

VI.4.1   (15874) 1996 TL$_{66}$

Luu and Jewitt (1998) used the 6.5 m Multiple Mirror Telescope (MMT) on Mount Hopkins (Ari-
zona, USA) to observe this object in the R-filter. Observations were made during one night (over
6 h) on October, 15th, 1996. They noted an amplitude <0.06 mag but they could not determine
a periodicity.

1996 TL$_{66}$ was also observed by Romanishin and Tegler (1999) with the 2.3 m telescope on Kitt
Peak (Arizona, USA). Observations were made in October 1997 in the V-band. Results were based
on only 25 images. They could not identify a short-term periodicity, but they noted an amplitude
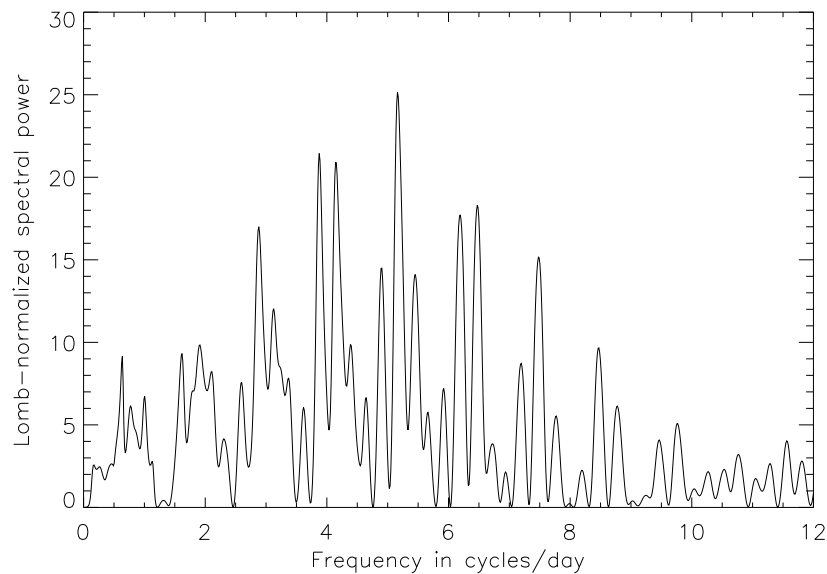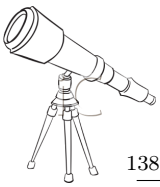
Figure 115: *Lomb-normalized spectral power versus frequency in cycles/day for 2007 TY$_{430}$*: The Lomb periodogram shows one peak located at 5.17 cycles/day and several aliases with lower spectral powers.
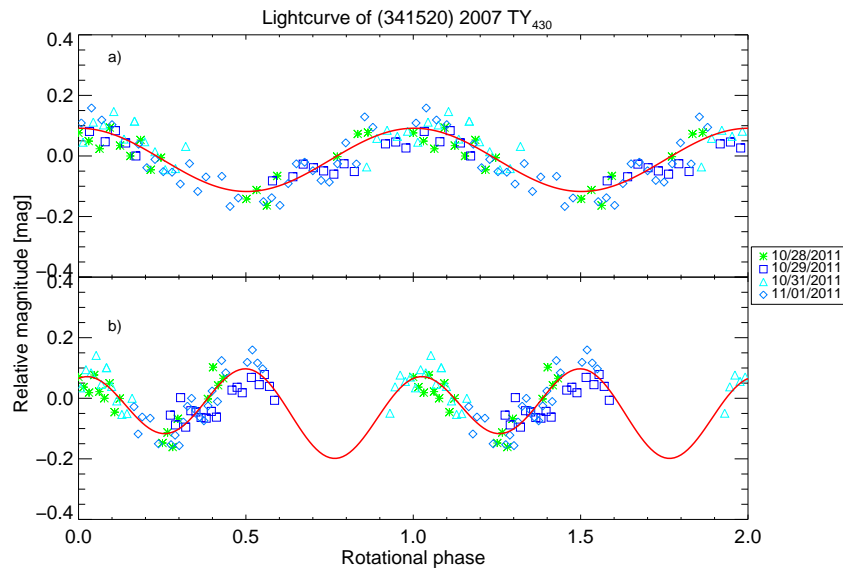
Figure 116: *Relative magnitude versus rotational period for 2007 TY$_{430}$*: Rotational phase curves for 2007 TY$_{430}$ obtained by using a spin period of 4.64 h (single-peaked lightcurve Plot a)) and using a spin period of 9.28 h (double-peaked lightcurve Plot b)). The continuous lines are a Fourier Series fits of the photometric data. Different symbols correspond to different dates.

<0.06 mag.

Using data obtained on December 2004 with the 1.5 m OSN telescope, Ortiz et al. (2006) presented a 12.1 h single-peaked rotational lightcurve with a <0.12 mag lightcurve amplitude. But according to the reliability code assigned to this value by Ortiz et al. (2006) this period is clearly

uncertain.

In Thirouin et al. (2010), we re-reduced and re-analyzed the data obtained on December 2004
and already published in Ortiz et al. (2006). The Lomb periodogram (Figure 117) shows several
peaks all of equally low confidence. We cannot reliably determine a periodicity. We are only able
to identify the peak with the highest spectral power at 8.04 h (2.99 cycles/day) and two aliases
located at 12 h and 6 h. The lightcurve presented in Figure 118 is a single peak periodicity of
12 h with an amplitude of 0.07±0.02 mag. The CLEAN and the Pravec-Harris analysis suggest a
period of 5.1 h and PDM proposes 10.2 h (Thirouin et al., 2010).
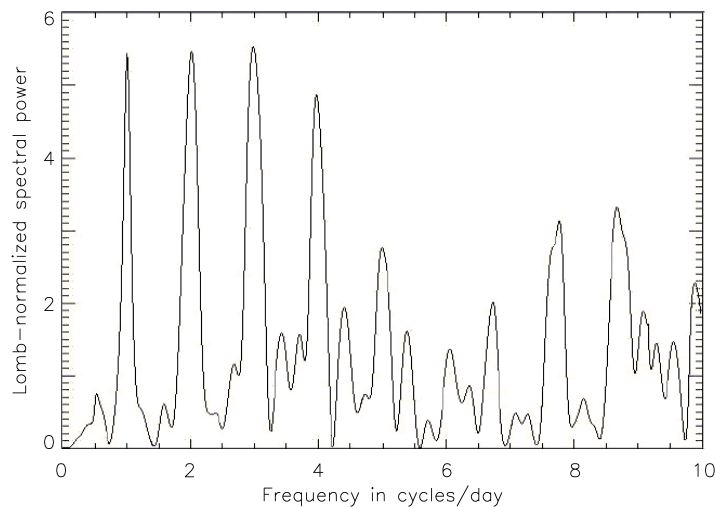
Figure 117: *Lomb-normalized spectral power versus frequency in cycles/day for 1999 TL_{66}:* The Lomb
periodogram shows several peaks located at 8.04 h (2.99 cycles/day) and two aliases located at 12 h and
6 h.

In conclusion, the periodicity of this object is uncertain, and with more observations, a more
reliable period might be derived.

VI.4.2   (40314) 1999 KR_{16}

1999 KR_{16} was observed during two nights in 2009 at the 3.58 m NTT. We report an ampli-
tude variation around 0.22 mag in 3.4 h of observations (Thirouin et al., 2012). Obviously, with
less than 4 h of observations we are not able to present a satisfactory study based only our data set.

This object has been already observed by Sheppard and Jewitt (2002). Using their 2001 data
set, Sheppard and Jewitt (2002) obtained two best-fit periods of 5.840 h and 5.929 h, but they
did not discard the possibility of a double-peaked period. They obtained a peak-to-peak range
of the lightcurve of 0.18±0.04 mag (amplitude estimation not based on apparent maximum and
minimum of the lightcurve).

The Lomb periodogram of our data merged with Sheppard and Jewitt (2002) ones (Figure 119)
shows one peak with a high spectral power, located at 5.80 h (4.14 cycles/day) and two aliases at
7.73 h (3.10 cycles/day) and at 4.73 h (5.08 cycles/day). PDM and CLEAN techniques confirmed
the rotational period of 5.8 h. Pravec-Harris method suggested the double-peaked period. In Fig-
ure 120, we present the single-peaked lightcurve. The amplitude of the curve is 0.12±0.06 mag,
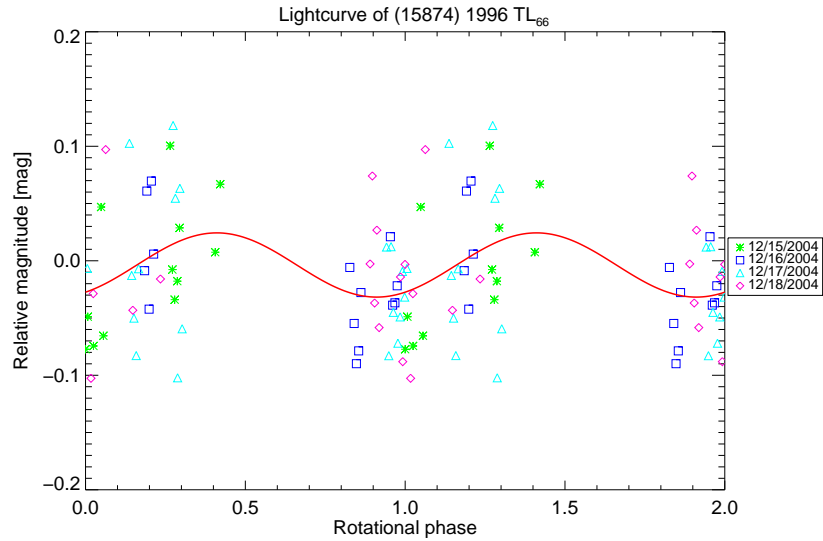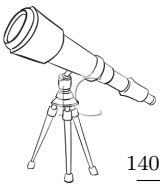
Figure 118: *Relative magnitude versus rotational phase for 1996 TL$_{66}$*: Single-peaked lightcurve using a spin period of 12.1 h. The continuous line is a Fourier Series fit of the photometric data. Different symbols correspond to different dates.

which is not at odds with Sheppard and Jewitt (2002), within uncertainty limits, even if slight differences can be seen, maybe due to the fact that usually, they perform sinusoidal fits instead of the Fourier series fit used in this work.

In conclusion, we suggest a rotational period estimation of 5.8 h, close to the one estimated by Sheppard and Jewitt (2002) for this object (Thirouin et al., 2012).

Our data, as Sheppard and Jewitt (2002) data, were obtained with a R-filter, So, we are able to provide an absolute calibration of these data. In Figure 121, we plot the solar phase curve of 1999 KR$_{16}$. To merge Sheppard and Jewitt (2002) data and data reported in this work, we obtain a phase angle range of around 1.5°, and we estimated a H$_R$ = 5.41±0.03 mag and β = 0.12±0.03 mag·deg^{-1}. These results are consistent with Sheppard and Jewitt (2002), who found H$_R$ = 5.37±0.02 mag and β = 0.14±0.02 mag·deg^{-1}.

VI.4.3 (44594) 1999 OX$_3$

1999 OX$_3$ was observed in 2009 at the 3.58 m NTT. Around 14 h over 3 nights of observations were obtained. The Lomb periodogram (Figure 122) shows several peaks. The highest one is found at 15.45 h (1.55 cycles/day), and two aliases are located at 9.26 h (2.59 cycles/day) and at 36.92 h (0.65 cycles/day). In all cases, the spectral power of these peaks is low. The PDM technique favored the peak around 9 h. CLEAN showed two peaks with a similar spectral power around 9 h and 15 h. Pravec-Harris method favored three possible rotational periods: 9.26 h, 13.4 h, and 15.45 h. In Figure 123, all lightcurves are plotted. The amplitude of the curves is 0.11±0.02 mag (Thirouin et al., 2012). Unfortunately, the spectral power of all the peaks is not very high so the significance level is not as high as in most other cases. There is no published photometry for this object to compare with.

Figure 124 shows the solar phase curve of 1999 OX$_3$, based on Bauer et al. (2003) and on our data. We get H$_R$ = 6.65±0.03 mag and β = 0.30±0.03 mag·deg^{-1} from all data. Bauer et al. (2003) reported H$_R$(1,α) = 7.1 mag, uncorrected for phase angle and for possible rotation.
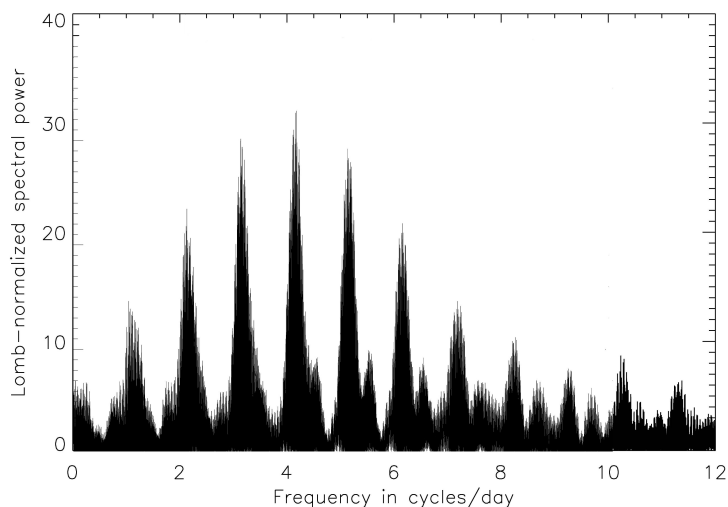
Figure 119: *Lomb-normalized spectral power versus frequency in cycles/day for 1999 KR₁₆*: The Lomb
periodogram of our data merged with Sheppard and Jewitt (2002) ones shows one peak with a high
spectral power, located at 5.80 h (4.14 cycles/day) and two aliases at 7.73 h (3.10 cycles/day) and at
4.73 h (5.08 cycles/day).
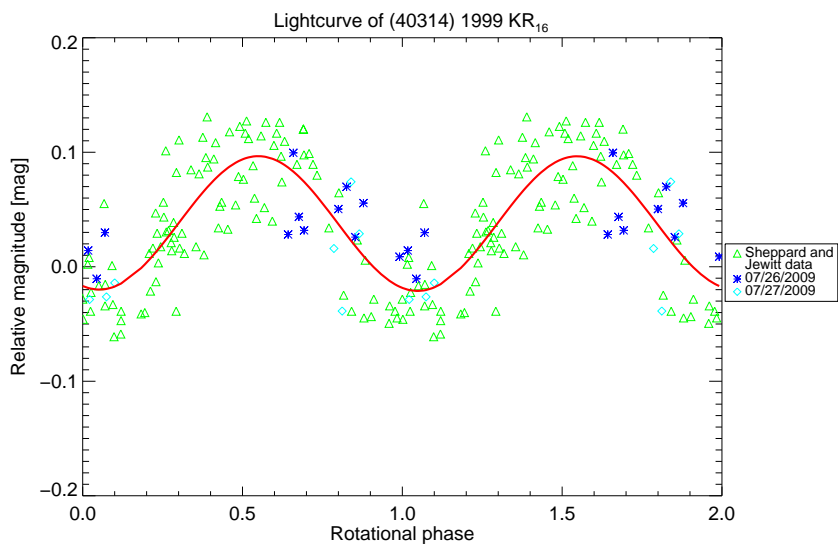
Figure 120: *Relative magnitude versus rotational phase for (40314) 1999 KR₁₆*: we merge our data with
Sheppard and Jewitt (2002) data and we obtained a spin period of 5.8 h for this object. The continuous
line is a Fourier Series fit of the photometric data. Different symbols correspond to different dates.
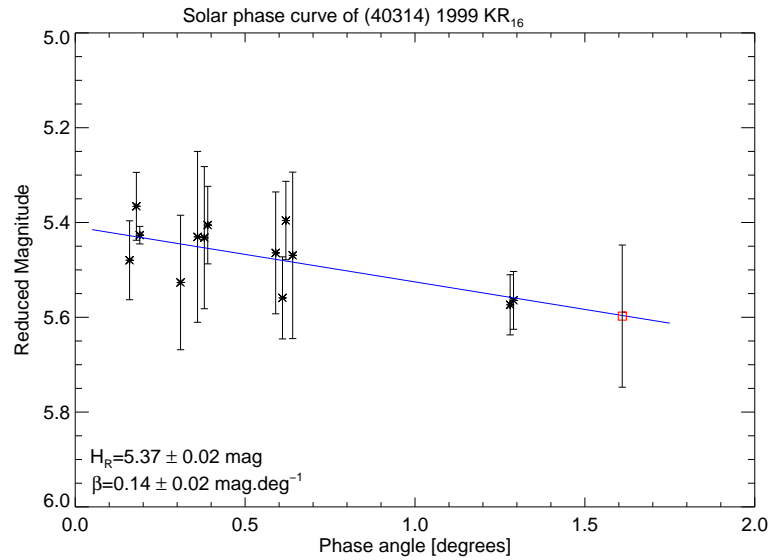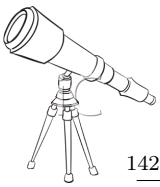
Figure 121: *Reduced magnitude versus phase angle for (40314) 1999 KR₁₆: we plot data published in* Sheppard and Jewitt (2002) *with a black asterisk symbol and data reported in this work with a red square symbol. Continuous blue line is a linear fit of all data. We also report on this plot the corrected R-band magnitudes (H$_R$) and the phase coefficient in magnitudes per degree (β)*
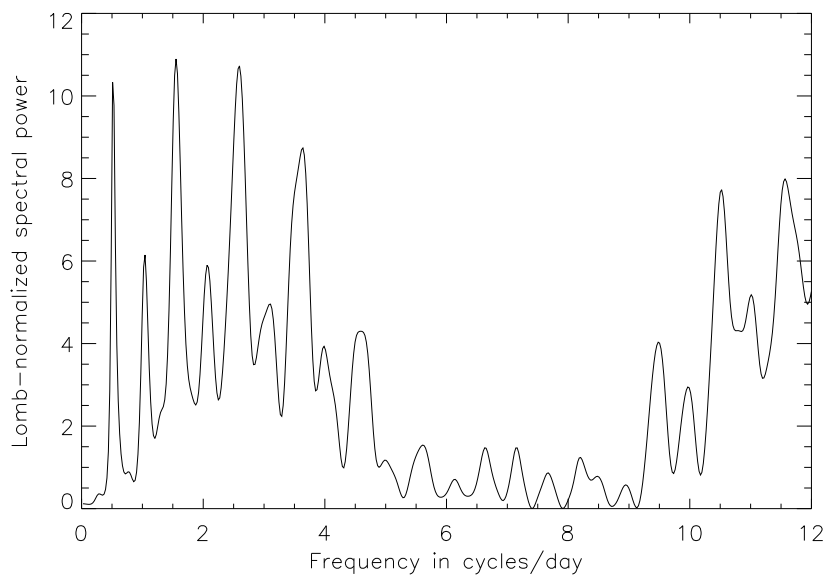
Figure 122: *Lomb-normalized spectral power versus frequency in cycles/day for 1999 OX₃: The Lomb periodogram shows several peaks located at 15.45 h, at 9.26 h and at 36.92 h.*

VI.4.4   (42355) 2002 CR₄₆ or Typhon

Using observations with the *Hubble Space Telescope* from January 20th, 2006, Noll et al. (2006d) detected a satellite around Typhon. The apparent magnitude difference is 1.30±0.06 mag in the
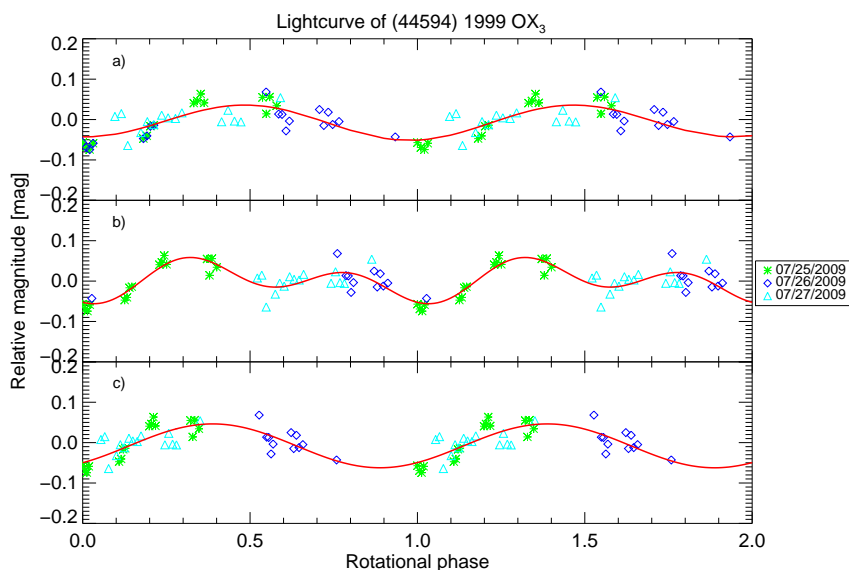
Figure 123: *Relative magnitude versus rotational phase for 1999 OX₃*: possible lightcurves obtained by using different spin periods; 9.26 h (plot a)), 13.4 h (plot b)) and 15.45 h (plot c)). Continuous lines are a Fourier Series fits of the photometric data. Different symbols correspond to different dates.
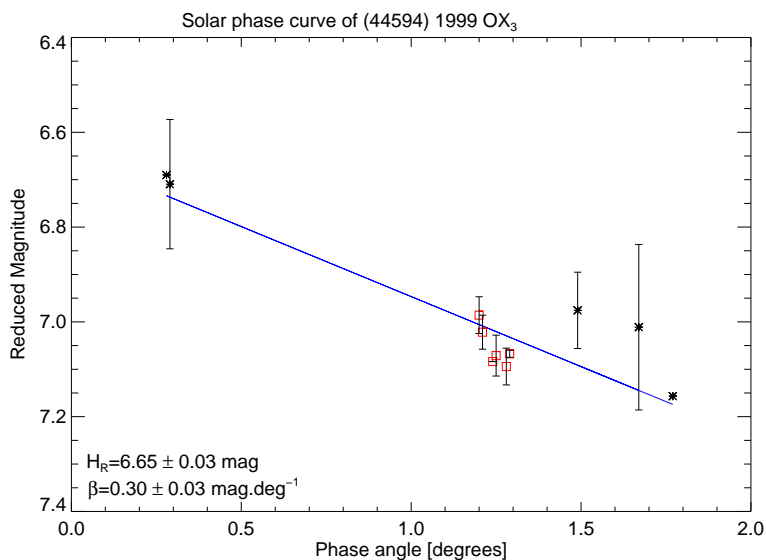
Figure 124: *Reduced magnitude versus phase angle for (44594) 1999 OX₃*: we plot data published in Bauer et al. (2003) with a black asterisk symbol and data reported in this work with a red square symbol. Continuous blue line is a linear fit of all data. We also report on this plot the corrected R-band magnitudes (H_R) and the phase coefficient in magnitudes per degree (β)

F606W band (Grundy et al., 2008). In November 2006, the satellite was named Echidna.
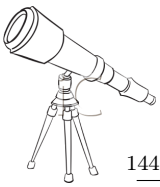
Sheppard and Jewitt (2002) observed Typhon during 4 nights using the University of Hawaii 2.2 m telescope, but their study could not estimate a periodicity. They presented a flat lightcurve with an amplitude <0.05 mag, which is consistent with our result.

Ortiz et al. (2003a) presented observations carried out in March 2002 with the 1.5 m OSN telescope. They proposed two possible spin period of 3.66 h and 4.35 h. Unfortunately, with a spectral power below a 50% confidence level, no period was favored. The amplitude was reported to be <0.15 mag.

Typhon was observed again in January and March 2003. The Lomb periodogram (Figure 125) shows several peaks, but one of them has a much higher spectral power. Thus, we present a lightcurve corresponding to this periodicity in Figure 126 that has a 9.67 h (2.48 cycles/day) single peak period, and a very small amplitude of 0.07±0.02 mag. However, the 24 h-aliases are also present and in all cases the spectral power is low (Thirouin et al., 2010).
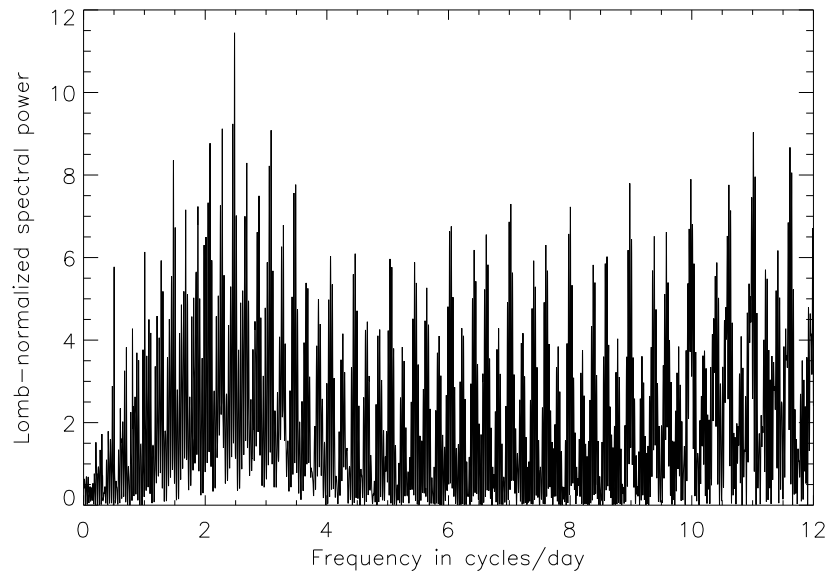
Figure 125: *Lomb-normalized spectral power versus frequency in cycles/day for Typhon*: The Lomb periodogram shows several peaks. The main peak is located at 9.67 h (2.48 cycles/day).

In conclusion, Typhon presents a nearly flat lightcurve, according to our result and published articles. The period proposed in the present work is tentative as we know that low variability objects are easily affected by small night-to-night instrumental/observation changes that can artificially boost the power of some spurious frequencies.

VI.4.5 (307982) 2004 PG$_{115}$

2004 PG$_{115}$ was observed during two nights with the 1.5 m OSN telescope in September 2010. During the first night, an amplitude variation of 0.08 mag during ~1 h, and a variation of 0.07 mag in <1 h during the second night are reported.

Unfortunately, with only few observational hours, a reliable rotational period cannot be estimated.
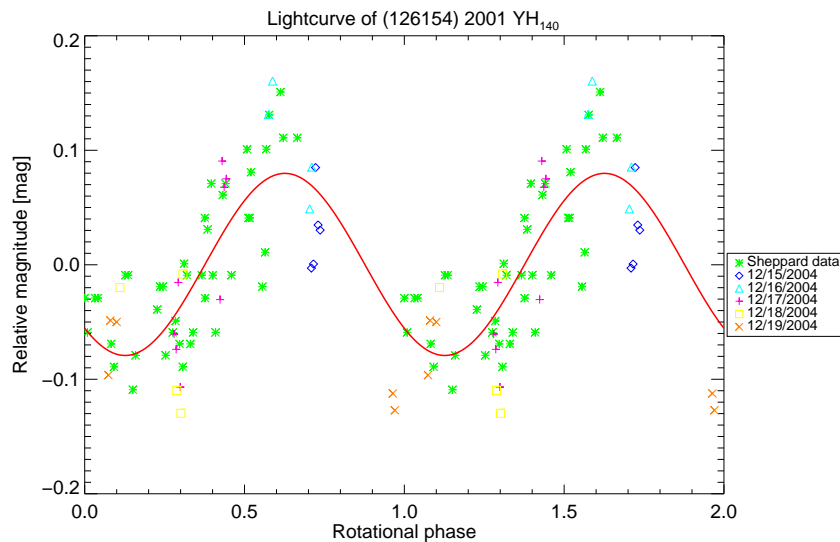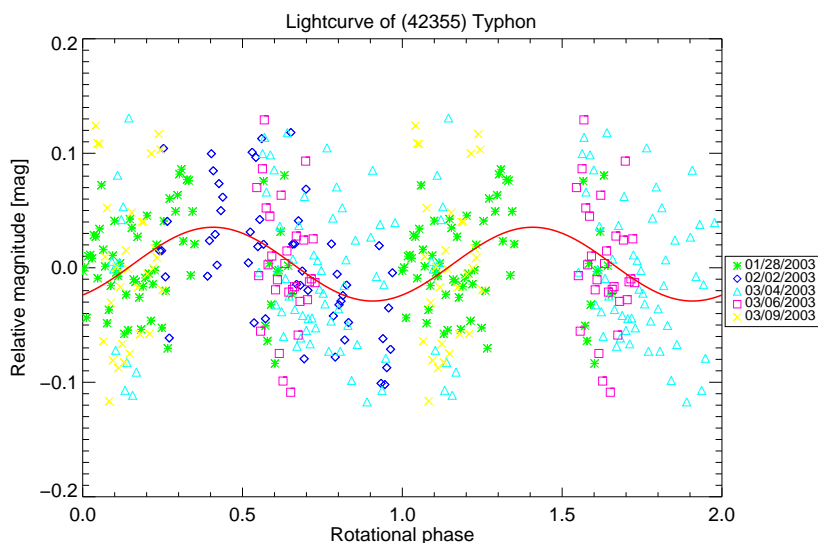
Figure 126: *Relative magnitude versus rotational phase for Typhon*: Rotational phase curve obtained by using a spin period of 9.67 h. The continuous line is a Fourier Series fit of the photometric data. Different symbols correspond to different dates.

VI.4.6 (145451) 2005 RM$_{43}$

2005 RM$_{43}$ was observed in October and November 2006, and in January 2007 with the 1.5 m OSN telescope. The Lomb periodogram (Figure 127) exhibits a very high peak at 3.58 cycles/day (6.71 h) and two main aliases located at 2.58 and 3.80 cycles/day. The lightcurve (Figure 128) has an amplitude of 0.05±0.01 mag. All methods confirmed a rotational periodicity around 6.7 h with a significant enough spectral power (Thirouin et al., 2010).

Perna et al. (2009) collected an observing time of about 17 h during three nights of observations. They suggested a double-peaked lightcurve with a spin period of 9.00±0.06 h and an amplitude of 0.12±0.05 mag. As there is no information about possible aliases in Perna et al. (2009) nor Lomb periodograms (or other methods to estimate the periodicity), it is not possible to check if the 6.71 h rotational period is an alias or not in their work. However, the 9 h rotational period found be Perna et al. (2009) is an alias in our study. On the other hand, they obtained a lightcurve amplitude of 0.12±0.05 mag which is ruled out in our data set, so we can suggest an observational, instrumental or reduction problem that affected their photometry.

VI.4.7 (145480) 2005 TB$_{190}$

This object was one of our target during our coordinated campaign between Chile and Spain, in 2009 involving the 3.58 m NTT and the 3.58 m TNG. The Lomb periodogram (Figure 129) shows one peak with a high spectral power and two aliases with a lower spectral power. The highest peak is located at 12.68 h (1.89 cycles/day) and two aliases are located at 28.57 h (0.84 cycles/day) and at 8.16 h (2.94 cycles/day). All techniques confirm a rotational period of 12.68 h for this target. The Pravec-Harris technique favored two possible rotational periods: 12.68 h and 16.32 h (2×8.16 h). Our first estimation of 12.68 h seems to be the best option. The amplitude of the curve is 0.12±0.01 mag (Figure 130) (Thirouin et al., 2012). There is no bibliographic reference to compare our results with.
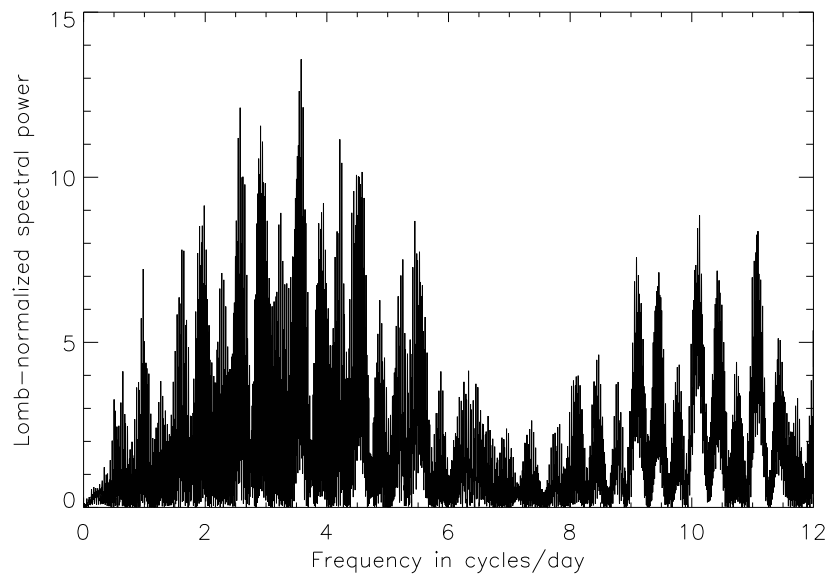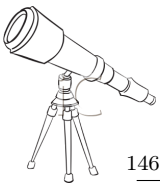
Figure 127: *Lomb-normalized spectral power versus frequency in cycles/day for 2005 RM$_{43}$*: The Lomb periodogram suggests one main peak at 3.58 cycles/day (6.71 h) and two aliases located at 2.58 and 3.80 cycles/day.
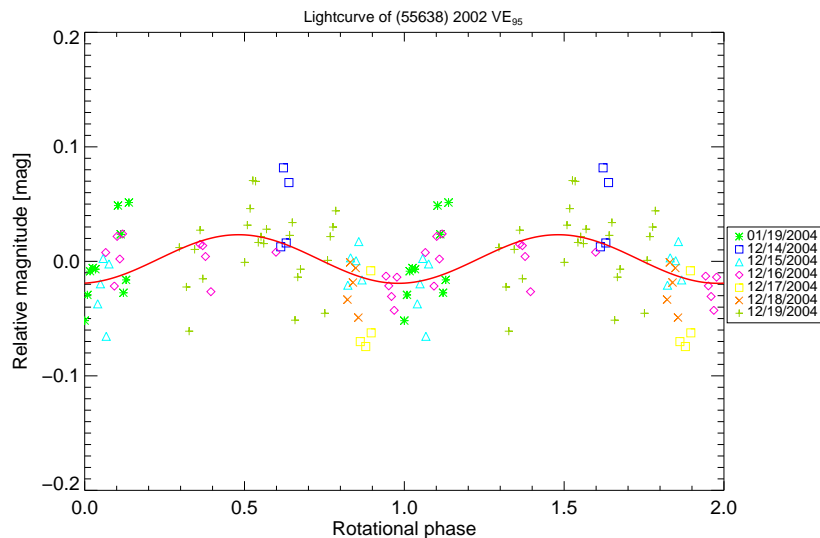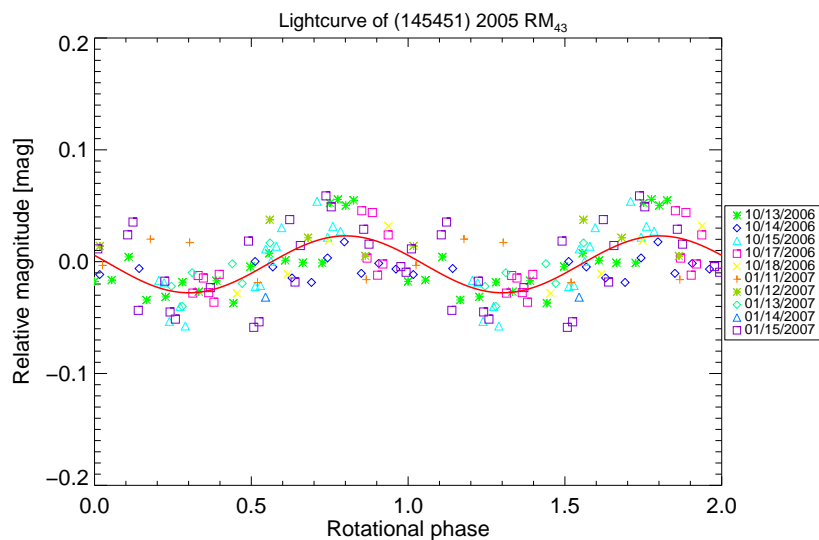

Figure 128: *Relative magnitude versus rotational phase for 2005 RM$_{43}$*: Rotational phase curve obtained by using a spin period of 6.71 h. The continuous line is a Fourier Series fit of the photometric data. Different symbols correspond to different dates.

VI.4.8   (229762) 2007 UK$_{126}$

Grundy et al. (2011b) reported the discovery of a faint moon, with a magnitude difference of 3.79 mag in the F606W band.
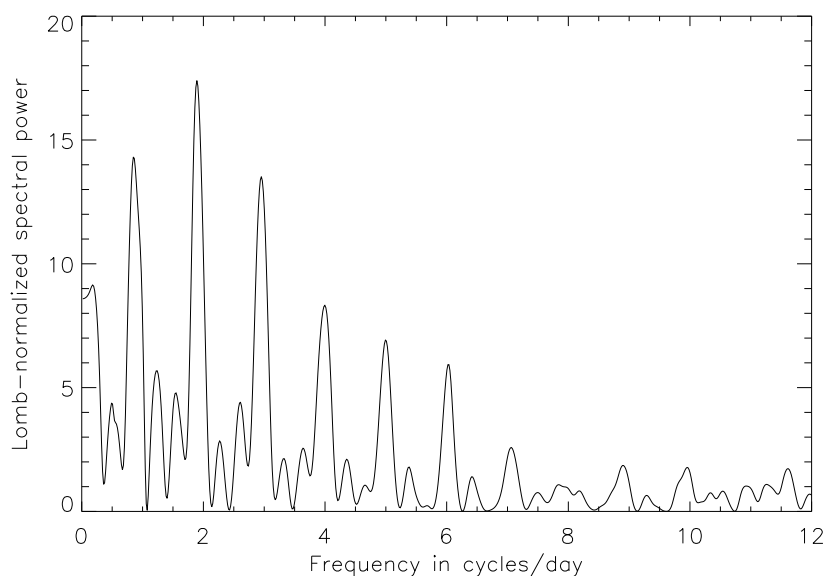
Figure 129: *Lomb-normalized spectral power versus frequency in cycles/day for 2005 TB$_{190}$*: The Lomb periodogram shows one peak located at 12.68 h (1.89 cycles/day).
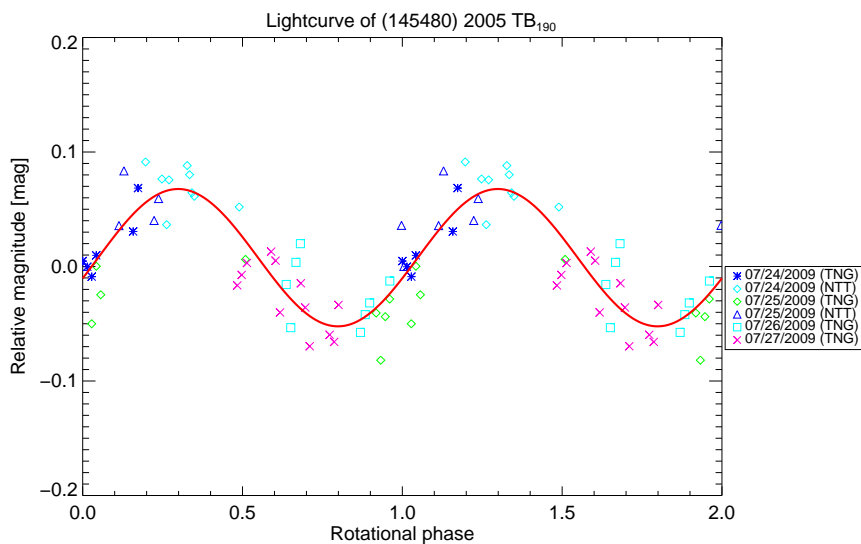
Figure 130: *Relative magnitude versus rotational phase for 2005 TB$_{190}$*: Rotational phase curve obtained by using a spin period of 12.68 h. The continuous line is a Fourier Series fit of the photometric data. Different symbols correspond to different dates.

2007 UK$_{126}$ has been observed on October 2011 with the 3.58 m TNG. We report three observation nights with a time base (time coverage between the first and the last image of the night) of, ~4 h, ~4 h, and ~2 h, respectively.

The Lomb periodogram (Figure 131) shows one main peak located at 11.05 h (2.17 cycles/day),
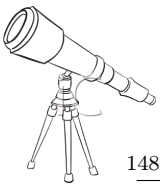
and several aliases located at 14.30 h (1.68 cycles/day), at 20.25 h (1.19 cycles/day), etc. All techniques confirmed such peaks, with a slightly preference for the peak at 11.05 h. 2007 UK$_{126}$ presents a flat lightcurve with a photometric variation of 0.03±0.01 mag (Figure 132). We must point out that the presence of numerous aliases with significant spectral power in the Lomb periodogram complicates the study and we are not able to propose a secure rotational period based on our data. We can only conclude that this object has probably a long rotational period (>10 h). There is no bibliographic reference to compare our results with. More observations are needed to complete this study.
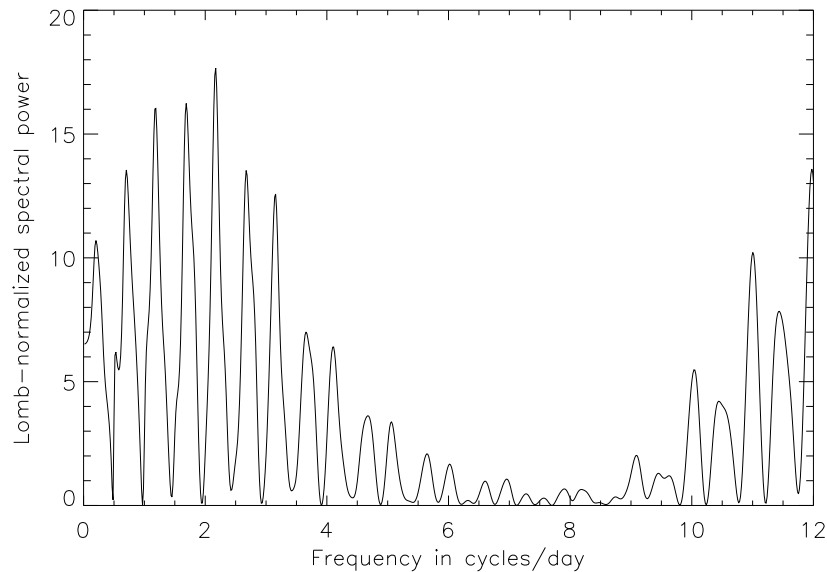
Figure 131: *Lomb-normalized spectral power versus frequency in cycles/day for 2007 UK$_{126}$: the Lomb periodogram shows one peak with the highest spectral power located at 11.04 h (2.17 cycles/day), and several aliases located at 14.30 h (1.68 cycles/day) and at 20.25 h (1.19 cycles/day).*

VI.5   Centaurs

VI.5.1   (52872) 1998 SG$_{35}$ or Okyrhoe

Bauer et al. (2003) observed Okyrhoe at the University of Hawaii 2.2 m telescope. Observations were performed during three consecutive nights in September 1999, in R band. They proposed a 16.6 h double-peaked rotational lightcurve with an amplitude of 0.2 mag.

Okyrhoe was observed during one run in December 2006 by our team. The Lomb periodogram Figure 133 suggests a single-peaked periodicity of 6.08 h (3.95 cycles/day) or 4.86 h (4.94 cycles/day). The Pravec-Harris method and PDM suggested a spin period of 4.86 h, whereas the CLEAN method favored a 6.08 h rotational period. In Figure 134 are plotted both lightcurves with an amplitude of 0.07±0.01 mag in both cases (Thirouin et al., 2010).

Bauer et al. (2003) mentioned a lightcurve amplitude of 0.2 mag. However, such a high amplitude is ruled out by our data, and so we can only suggest an observational, instrumental or reduction problem that affected their photometry. In conclusion, 4.86 h and 6.08 h appear as possible rotational periods for Okyrhoe.
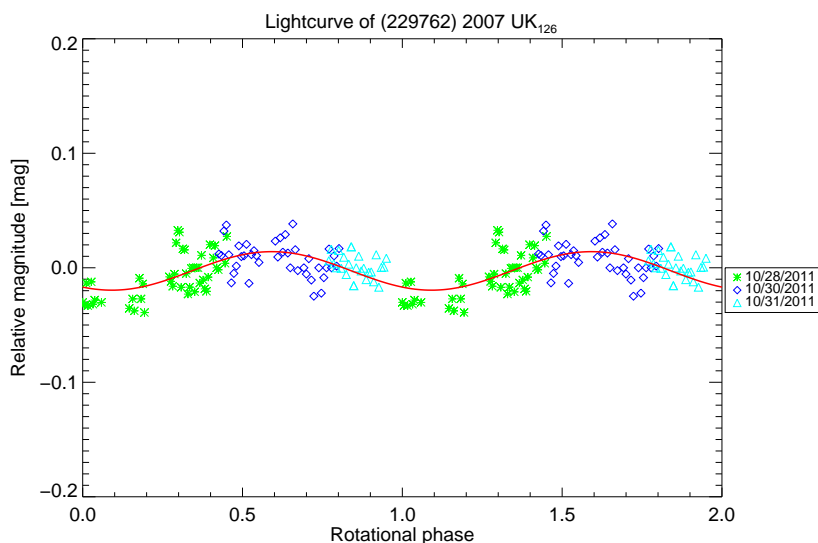
Figure 132: *Relative magnitude versus rotational phase for 2007 UK$_{126}$*: Rotational phase curve for 2007 UK$_{126}$ obtained by using a spin period of 11.05 h. The continuous line is a Fourier Series fit of the photometric data. Different symbols correspond to different dates.
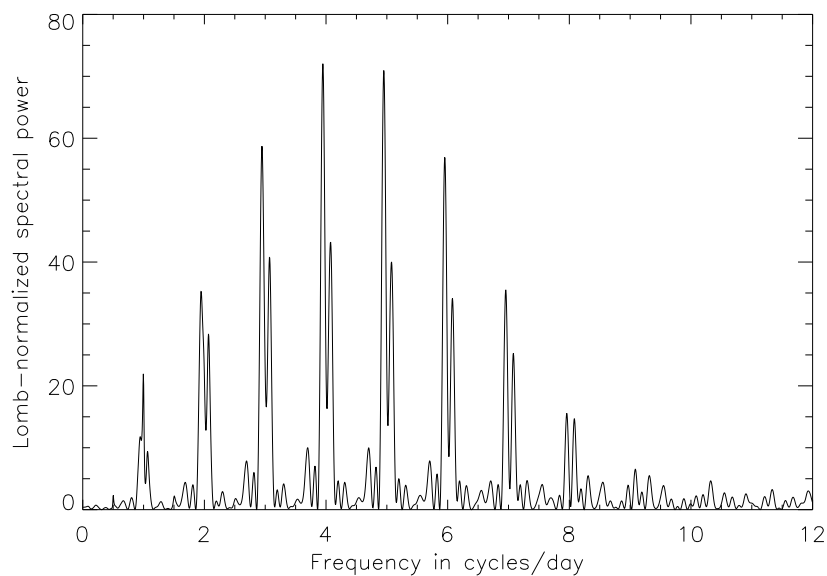
Figure 133: *Lomb-normalized spectral power versus frequency in cycles/day for Okyrhoe*: The Lomb periodogram suggests two possible rotational period: 6.08 h (3.95 cycles/day) or 4.86 h (4.94 cycles/day).

VI.5.2 (148975) 2001 XA$_{255}$

2001 XA$_{255}$ was observed during $\sim$5 h on April, 24th, 2009 and less than 2 h on April, 25th, 2009 with the 1.5 m OSN telescope. With just few data, a reliable rotational study cannot be proposed. An amplitude of variability of $\sim$ 0.13 mag is guessed.
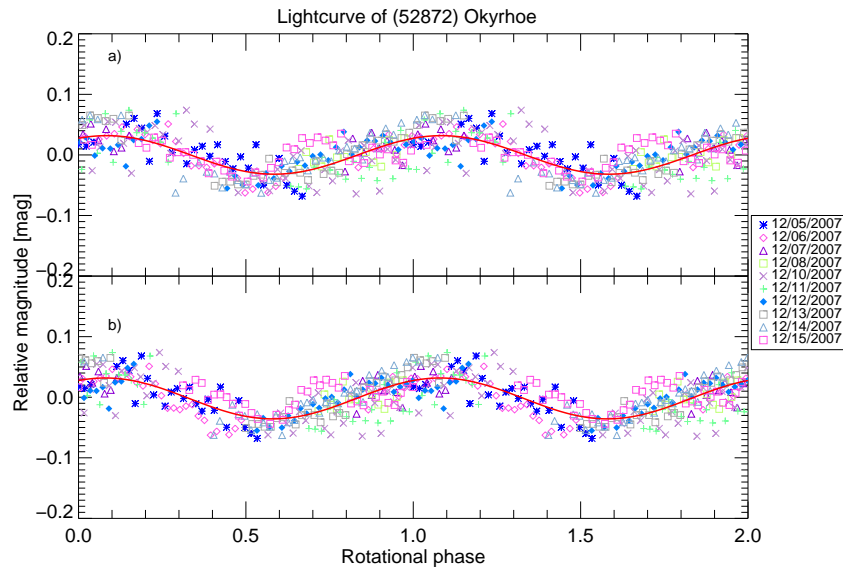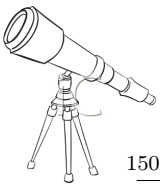
Figure 134: *Relative magnitude versus rotational phase for Okyrhoe*: Rotational phase curve obtained by using a spin period of 4.86 h (Plot a)) and using a spin period of 6.08 h (Plot b)). The continuous lines are a Fourier Series fit of the photometric data. Different symbols correspond to different dates.

There is no other study about 2001 XA_{255} to compare with.

VI.5.3 (55567) 2002 GB_{10} or Amycus

Amycus was observed during two consecutive nights in March 2003 by our team with the 1.5 m OSN telescope. The short-term variability of Amycus is already published in Thirouin et al. (2010). The Lomb periodogram (Figure 135) shows two peaks with a high spectral power at 2.46 and 1.48 cycles/day. All techniques confirmed such peaks. The main peak at 9.76 h (2.46 cycles/day) is only slightly favored and the single-peaked corresponding lightcurve with an amplitude of 0.16±0.01 mag is proposed in Figure 136.

As there is no more time series analysis for Amycus in the literature, this study cannot be improved. A spin period of 9.76 h is favored, but more observations are necessary to determine a more precise rotational period.

VI.5.4 (120061) 2003 CO_1

Ortiz et al. (2006) proposed the first short-term variability study of this object. Based on observations carried out on January and April 2004 with the 1.5 m OSN telescope. They proposed several rotational periods: 3.53 h, 4.13 h, 4.99 h or 6.30 h. The authors favored a 4.99 h single-peaked rotational lightcurve with an amplitude of 0.10±0.05 mag.

In Thirouin et al. (2010), we re-reduced and re-analyzed the January and April 2004 data sets published in Ortiz et al. (2006), and we included more observational data (January 19th-24th, 2004 and April, 27th, 2004). The Lomb periodogram (Figure 137) presents a main peak located at 5.31 cycles/day, and two main aliases at 6.3 cycles/day and at 4.3 cycles/day. All methods confirm that the 4.51 h rotational period is the most likely choice. In Figure 138, the lightcurve with a single peak periodicity of 4.51 h (5.31 cycles/day) and an amplitude of 0.06±0.01 mag is plotted (Thirouin et al., 2010).
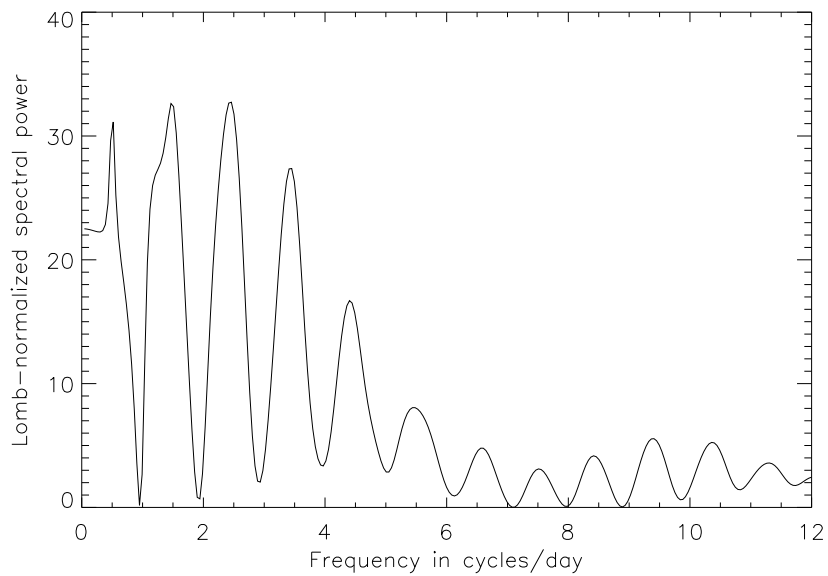
Figure 135: *Lomb-normalized spectral power versus frequency in cycles/day for Amycus*: The Lomb periodogram shows two peaks with a high spectral power at 2.46 and 1.48 cycles/day.
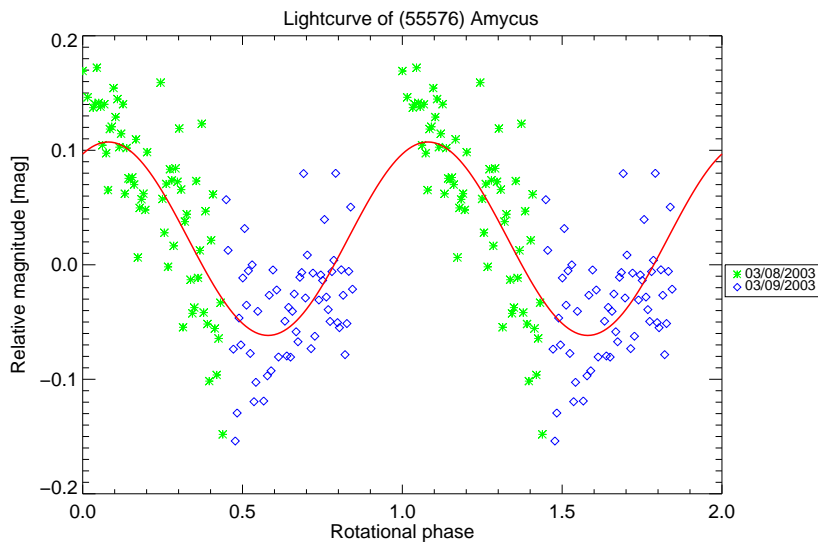
Figure 136: *Relative magnitude versus rotational phase for Amycus*: Rotational phase curve obtained by using a spin period of 9.76 h. The continuous line is a Fourier Series fit of the photometric data. Different symbols correspond to different dates.

In conclusion, the closest agreement between both studies seems to be around the 5 h range.
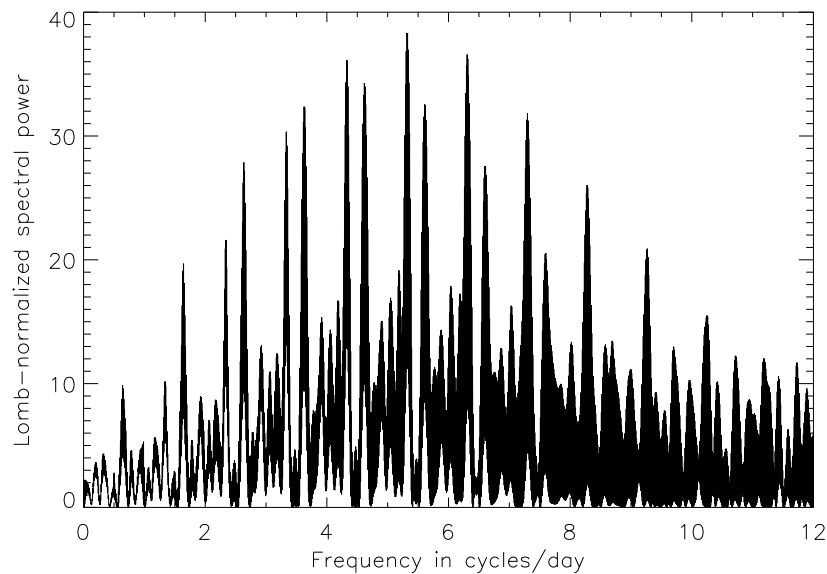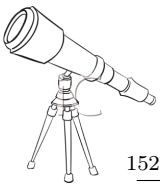
Figure 137: *Lomb-normalized spectral power versus frequency in cycles/day for 2003 CO_1*: The Lomb periodogram shows one main peak located at 5.31 cycles/day, and its two aliases at 6.3 cycles/day and at 4.3 cycles/day.
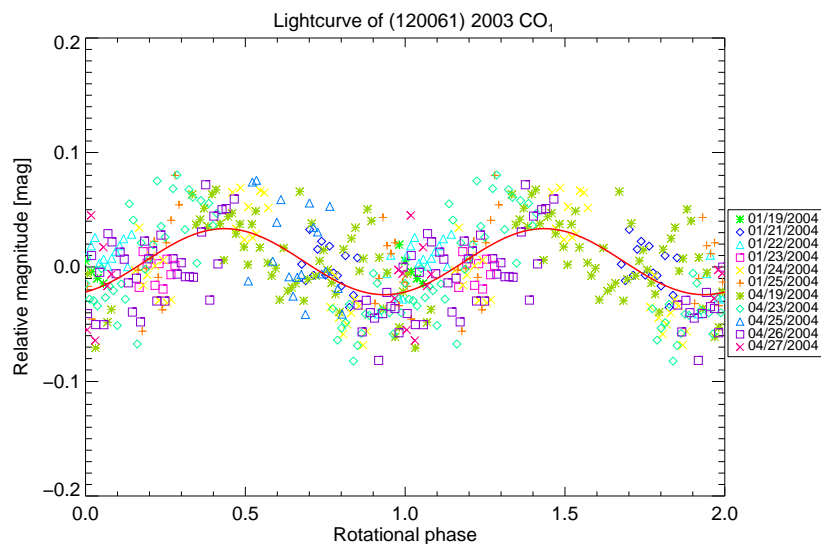
Figure 138: *Relative magnitude versus rotational phase for 2003 CO_1*: Rotational phase curve obtained by using a spin period of 4.51 h. The continuous line is a Fourier Series fit of the photometric data. Different symbols correspond to different dates.

VI.5.5   (136204) 2003 WL_7

2003 WL_7 was observed in December, 2007 with the 1.5 m OSN telescope. The Lomb periodogram (Figure 139), PDM, CLEAN, and the Pravec-Harris techniques suggest one main periodicity located at 8.22 h (2.92 cycles/day). However, the spectral power of the main peak is not very
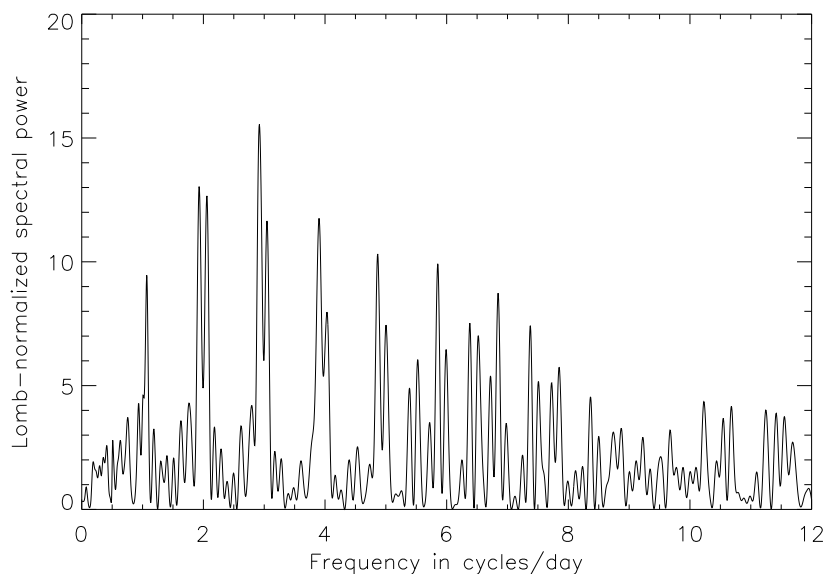
Figure 139: *Lomb-normalized spectral power versus frequency in cycles/day for 2003 WL₇*: The Lomb periodogram shows one main peak located at 8.22 h (2.92 cycles/day).

high. In Figure 140, the single-peaked rotational lightcurve with an amplitude peak-to-peak of 0.04±0.01 mag is plotted (Thirouin et al., 2010). There is no bibliographic reference of photometric results for this object to compare with.
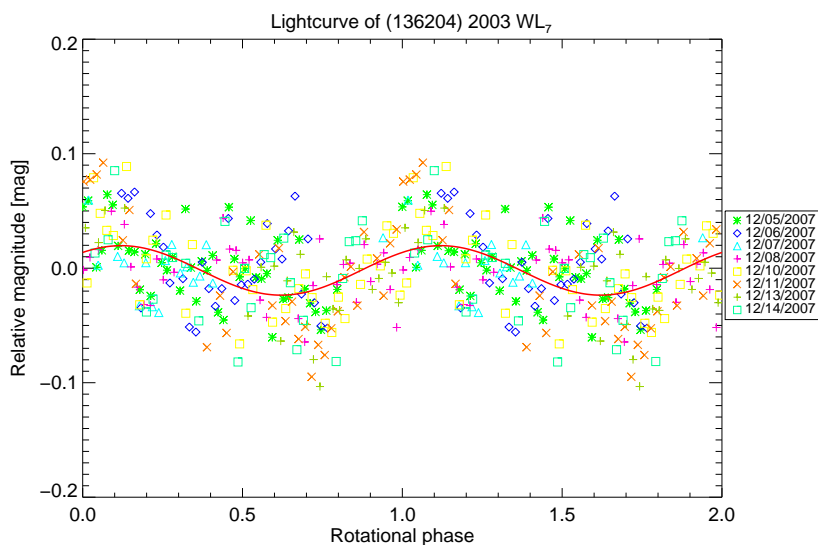
Figure 140: *Relative magnitude versus rotational phase for 2003 WL₇*: Rotational phase curve obtained by using a spin period of 8.22 h. The continuous line is a Fourier Series fit of the photometric data. Different symbols correspond to different dates.
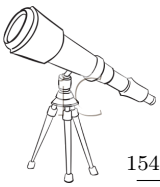
VI.5.6 (145486) 2005 UJ$_{438}$
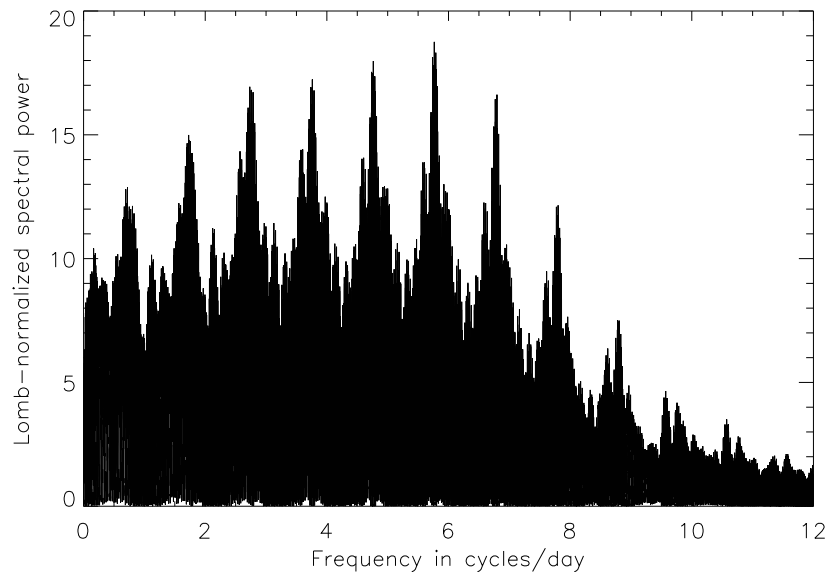
Figure 141: *Lomb-normalized spectral power versus frequency in cycles/day for 2005 UJ$_{438}$*: The Lomb periodogram shows several peaks. The main peak is located at 4.16 h (5.77 cycles/day)

2005 UJ$_{438}$ was observed during two observing runs in January 2007 and 2008, and during one isolated night in December 2008. The Lomb periodogram (Figure 141) shows several peaks. The main peak, with the highest spectral power, is located at 4.16 h (5.77 cycles/day), but there are important diurnal aliases. The CLEAN, Pravec-Harris, and PDM techniques determine a spin period around 4.2 h. However, a double-peaked periodicity of 8.32 h might be more appropriate because the fit to a Fourier series shows minima and maxima of different values, but neither PDM nor the Harris method, which are less sensitive to the exact shape of the lightcurve, proposed a periodicity of 8.32 h. In Figure 142 are plotted the single-peaked and the double-peaked lightcurve. The lightcurve amplitude is 0.11±0.01 mag in both cases. There is no literature reference on photometric results for this body that we are aware of. Thus we cannot compare our results with others and our preliminary conclusion is that 8.32 h seems a reasonable value with the caveats that the apparent 24-h aliases can be the true periodicity, and also the low amplitude would favor the single-peaked version of the lightcurve, which correspond to a period of 4.16 h.

VI.5.7 (25012) 2007 UL$_{126}$ or 2002 KY$_{14}$

2007 UL$_{126}$ was observed on August 2008. The Lomb periodogram (Figure 143) and the PDM technique show two peaks with a high spectral power located at 3.56 h (6.74 cycles/day) and at 4.2 h (5.71 cycles/day). In both cases, the lightcurve amplitude is 0.11±0.01 mag. The CLEAN, PDM, and Pravec-Harris methods suggest a 4.2 h spin period. The double-peaked lightcurves of the two mentioned periodicities do look slightly more likely, in both cases the lightcurve amplitude is 0.12±0.01 mag which favors the single-peaked lightcurve. To our knowledge, there is no literature reference on photometric results for this body.

VI.5.8 (281371) 2008 FC$_{76}$

2008 FC$_{76}$ was observed during three nights, in 2009 with the 1.5 m OSN and the 2.2 m CAHA telescopes. Unfortunately, it was impossible to take long observational sequences. Only few hours
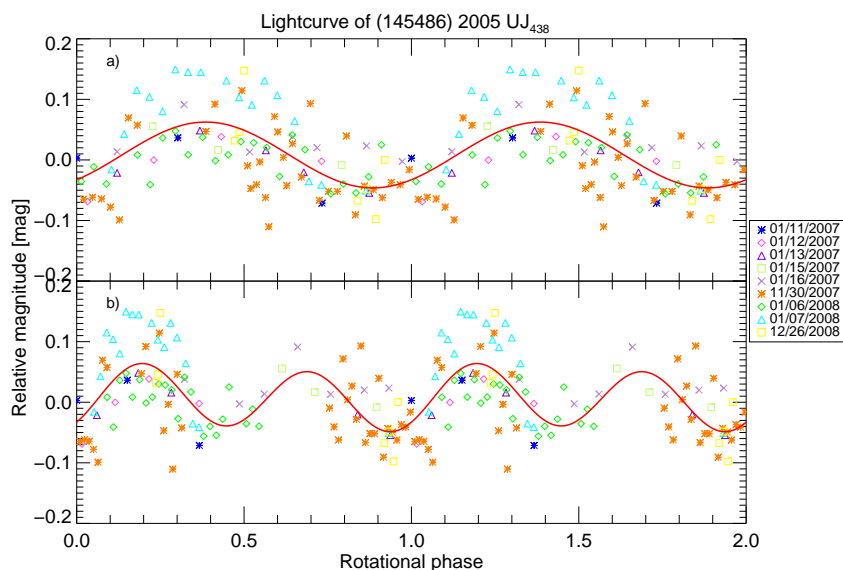
Figure 142: *Relative magnitude versus rotational phase for 2005 UJ$_{438}$*: Rotational phase curve obtained by using a spin period of 4.16 h (plot a)) and 8.32 h (Plot b)). The continuous lines are a Fourier Series fits of the photometric data. Different symbols correspond to different dates.
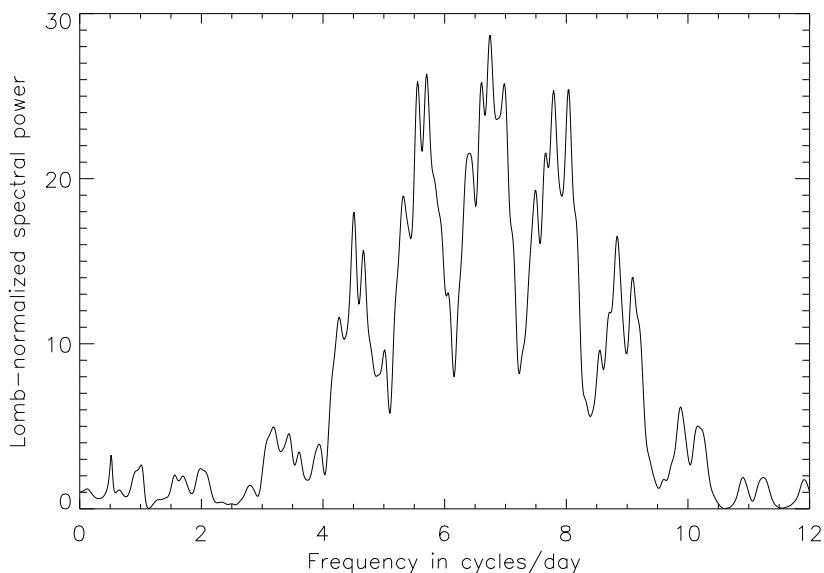
Figure 143: *Lomb-normalized spectral power versus frequency in cycles/day for 2007 UL$_{126}$ or 2002 KY$_{14}$*: The Lomb periodogram shows several peaks located at 3.56 h (6.74 cycles/day) and at 4.2 h (5.71 cycles/day)

of observations per night, respectively, ∼2 h (16 images), ∼4 h (22 images), and ∼1 h (15 images) are reported. With just a few hours, a reliable rotational period estimation is not possible. An amplitude variation of ∼0.04 mag during the first night, ∼0.1 mag in the second night and, ∼0.06 mag during the last night are reported. In 2012, this centaur was re-observed during two nights with the 1.5 m OSN telescope. An amplitude variation of ∼0.13 mag in less than 2 h of observations
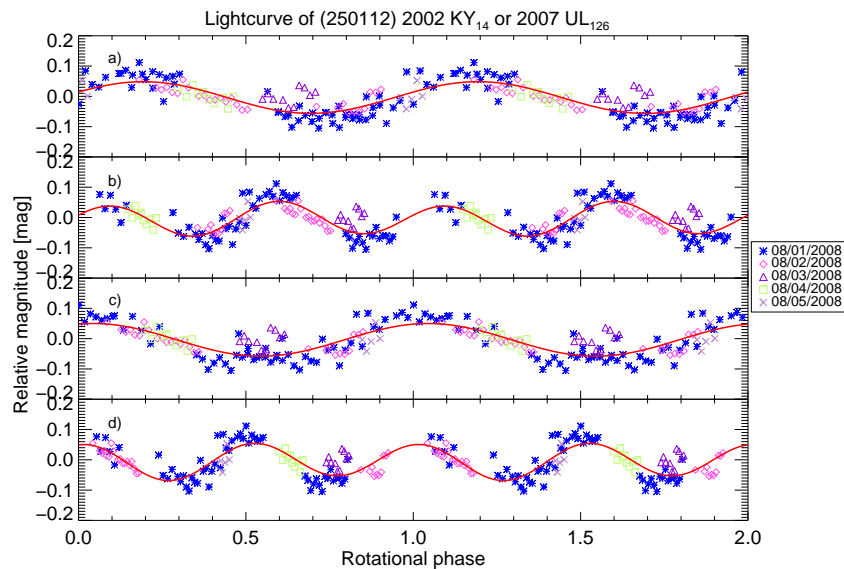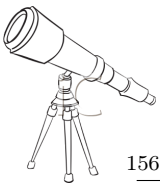
Figure 144: *Relative magnitude versus rotational phase for 2007 UL$_{126}$ or 2002 KY$_{14}$*: Rotational phase curve obtained by using a spin period of 3.56 h (Plot a)), 7.12 h (Plot b)), 4.2 h (5.71 cycles/day) (Plot c)), and 8.4 h (Plot d)). The continuous lines are a Fourier Series fits of the photometric data. Different symbols correspond to different dates.

during the first night and an amplitude variation of 0.11 mag in 1 h of observing in the second night are estimated. A preliminary rotational study seems to favor a periodogram period around 6 h. There is no data available for this object in the literature.

VI.5.9 (315898) 2008 QD$_4$

2008 QD$_4$ was observed during one night, in 2012 with the 1.5 m OSN. Unfortunately, only few hours of observations, ∼4 h were obtained. With just few hours of data, a reliable rotational period study is not possible. An amplitude variation around 0.09 mag is reported.

VI.5.10 (342842) 2008 YB$_3$

2008 YB$_3$ is one of the few minor bodies (with 2008 KV$_{42}$, and 2010 BK$_{118}$) found to have a retrograde orbit. 2008 YB$_3$ was observed during 2 nights, in 2012, at the OSN. The first night, this centaur has been observed during ∼2.5 h, and during 3 h the second night. The amplitude variations were 0.17 mag and 0.19 mag during the first and the second night, respectively. With just few hours of observational, a reliable spin period study is not possible. But a very preliminary study seems to favor a rotational period around 8 h.

VI.5.11 2010 BK$_{118}$

2010 BK$_{118}$ was discovered on January 30th, 2010, by the NASA's WISE observatory [7]. This object is classified as centaur, but it is a record-breaker. This object has the second most eccentric orbit (e=0.986), a perihelion distance of just 6.105 AU, whereas the semi-major axis is 451 AU [8]. Perihelion was reached during May 2012 and the post-perihelic opposition (the object was closest to the Sun with a visual magnitude of 17.9) arrived in 2012 September.

---

[7]Wide-field Infrared Survey Explorer (WISE) observatory is a NASA-funded Explorer mission. A complete description can be found at: http://wise.ssl.berkeley.edu/index.html.

[8]Eccentricity, perihelion distance, and semi-major axis from the Minor Planet Center database.
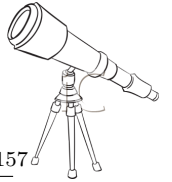
On September, 10th and 11th, we observed this object with the ASH2 telescope. During the
first night, an amplitude variation around 0.12 mag has been reported in ∼3 h of observations. In
around 3.5 h observing time during the second night, the amplitude variation was ∼0.15 mag. A
preliminary rotational study seems to favor a rotational period of 7.1 h. Unfortunately, with only
few hours, this study remains uncertain.

VI.6   Results summary

In Table 6 are summarized some of the results obtained in this work.
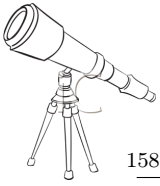
Table 6: Summary of results from this work. In this table, we present the name of the object, the preferred period (Pref. phot. per. in hour) and lightcurve amplitude (Amp. in magnitude), the preferred photometric period (Pref. rot. per. in hour), the preferred photometric period (Pref. phot. per. in magnitude), the Julian Date (φ_0) for which the phase is zero in our lightcurves (without light time correction), and the absolute magnitudes (Abs. mag.). The Julian date for which the phase is zero (the zero phase) is the date of the object's first image used for the short-term variability study. The relative magnitude (Δ^0_m) at the zero phase from the fit is indicated in the fifth column. Absolute magnitudes are from the Minor Planet Center database. The preferred photometric period is the periodicity obtained thanks to the data reduction. In some cases, as mentioned in the Section V.1.3.1, the double rotational periodicity is preferred due to the high amplitude lightcurve (the preferred period). For each object, its dynamical classification according to Gladman, Marsden and Vanlaerhoven (2008) is also indicated.

Object	Dynamical classification	Pref. phot. per. [h]	Pref. rot. per. [h]	Amp. [mag]	φ_0 [JD]	Δ^0_m [mag]	Abs mag	Binary/Multiple?
(55567) 2002 GB_{10} Amycus	Centaur	9.76	9.76	0.16±0.01	2452707.45519	0.097	7.8	
(136108) 2003 EL_{61} Haumea	Resonant	1.95767	3.91534	0.28±0.01	2454112.62040	-0.065	0.2	Yes
(38628) 2000 EB_{173} Huya	Resonant	5.21	5.21	0.02±0.01	2455355.38744	0.008	4.9	Yes
(136472) 2005 FY_9 Makemake	Classical-Hot	7.65	7.65	0.014±0.002	2453796.63861	-0.005	-0.3	
(52872) 1998 SG_{35} Okyrhoe	Centaur	4.86 or 6.08	4.86 or 6.08	0.07±0.01	2454440.62025	0.027 or 0.028	11.3	
(90482) 2004 DW Orcus	Resonant	10.47	10.47	0.04±0.01	2453073.36884	-0.003	2.3	Yes
(50000) 2002 LM_{60} Quaoar	Classical-Hot	8.8399	8.8399	0.112±0.001	2452781.58625	0.005	2.6	Yes
(120347) 2004 SB_{60} Salacia	Classical-Hot	6.61	6.61	0.04±0.02	2453588.43205	0.012	4.4	Yes
(42355) 2002 CR_{46} Typhon	Scattered Disk	9.67	9.67	0.07±0.02	2452668.46043	-0.024	7.2	Yes
(20000) 2000 WR_{106} Varuna	Classical-Hot	3.1717837	6.3435674	(0.43 to 0.53)±0.02	2451957.49983[9]	0.224	3.6	
(24835) 1995 SM_{55}	Classical-Hot	4.04	8.08	0.05±0.02	2452193.902488[10]	-0.015	4.8	
(15874) 1996 TL_{66}	Scattered Disk	12.1	12.1	0.07±0.02	2453355.37197	-0.027	5.4	
(26375) 1999 DE_9	Resonant	12.33	12.33	0.09±0.03	2451662.7686[11]	0.040	5.1	
(40314) 1999 KR_{16}	Scattered Disk	5.8	5.8	0.12±0.06	2451662.9409[12]	-0.017	5.8	
(44594) 1999 OX_3	Detached	9.26 or 13.4 or 15.45	9.26 or 13.4 or 15.45	0.11±0.02	2455038.69404	-0.043 or -0.029 or -0.050	7.4	
2001 QF_{298}	Resonant	-	-	~0.11	2455039.71221	-	5.1	
(275809) 2001 QY_{297}	Classical-Hot	5.84	11.68	0.49±0.03	2455037.61147	0.213	5.7	Yes
(148975) 2001 XA_{255}	Centaur	-	-	~0.13	2454887.48840	-	11.2	
(126154) 2001 YH_{140}	Resonant	13.19	13.19	0.15±0.03	2452992.92900[13]	-0.055	5.4	
(55565) 2002 AW_{197}	Classical-Hot	8.78	8.78	0.02±0.02	2452672.42954	-0.011	3.3	
(307251) 2002 KW_{14}	Classical-Hot	4.29 or 5.25	8.58 or 10.5	(0.21 or 0.26)±0.03	2455037.40786	-	5.0	
(307261) 2002 MS_4	Resonant	7.33 or 10.44	7.33 or 10.44	0.05±0.01	2455743.42317	-0.014 or -0.003	3.7	
(84522) 2002 TC_{302}	Classical-Hot	5.41	5.41	0.04±0.01	2455120.41362	-0.012	3.8	
(55636) 2002 TX_{300}	Classical-Hot	8.15 or 11.7	8.15 or 11.7	(0.01 or 0.05)±0.01	2452859.51500	0.001 or 0.012	3.3	
(55637) 2002 UX_{25}	Resonant	6.55	6.55	0.09±0.03	2454471.26576	0.011	3.7	Yes
(55638) 2002 VE_{95}	Resonant	9.97	9.97	0.04±0.02	2453024.42248	-0.019	5.3	
2002 VT_{130}	Classical-Cold	-	-	~0.21	2455867.59285	-	5.8	Yes
(55638) 2002 WC_{19}	Resonant	-	-	<0.1	2453025.37946	-	5.0	Yes
(208996) 2003 AZ_{84}	Resonant	6.79	6.79	0.07±0.01	2453026.54640	-0.034	3.6	Yes
(120061) 2003 CO_1	Centaur	4.51	4.51	0.06±0.01	2453024.70117	-0.022	8.9	
(120132) 2003 FY_{128}	Hot-Classical	8.54	8.54	0.12±0.02	2453411.64303	0.065	5.0	
(174567) 2003 MW_{12}	Hot-Classical	5.91	5.91	0.02±0.01	2453884.58013	0.003	3.6	
(120178) 2003 OP_{32}	Hot-Classical	4.07	4.07	0.13±0.01	2453588.39312	0.078	4.1	Yes
(84922) 2003 VS_2	Resonant	3.7104	7.4208	0.224±0.013	2452992.768380[14]	-0.031	4.2	
(136204) 2003 WL_7	Centaur	8.24	8.24	0.04±0.01	2454440.28625	0.014	8.7	
(307982) 2004 PG_{115}	Scattered disk	-	-	~0.07	2455448.34345	-	3.9	
2004 NT_{33}	Classical-Hot	7.87	7.87	0.04±0.01	2455038.48984	0.023	4.4	
(144897) 2004 UX_{10}	Resonant	5.68	5.68	0.09±0.02	2454358.47542	0.013	4.7	
(230965) 2004 XA_{192}	Classical-Hot	7.88	7.88	0.07±0.02	2455118.50584	-0.031	4.0	
(308193) 2005 CB_{79}	Classical-Hot	6.76	6.76	0.05±0.02	2454472.56600	-0.013	5.0	
(145451) 2005 RM_{43}	Scattered Disk	6.71	6.71	0.05±0.01	2454022.46809	0.006	4.4	
(145452) 2005 RN_{43}	Classical-Hot	5.62 or 7.32	5.62 or 7.32	0.04±0.01	2454358.44257	-0.001 or 0.006	3.9	

[9] Zero phase of Varuna from Jewitt and Sheppard (2002)
[10] Zero phase of Varuna from Sheppard and Jewitt (2003)
[11] Zero phase of (26375) 1999 DE_9 from Sheppard (2004)
[12] Zero phase of (40314) 1999 KR_{16} from Sheppard and Jewitt (2002)
[13] Zero phase of (126154) 2001 YH_{140} from Sheppard (2007)
[14] Zero phase of (84922) 2003 VS_2 from Sheppard (2007)

Table 6: continued.

Object	Dynamical classification	Pref. phot. per. [h]	Pref. rot. per. [h]	Amp. [mag]	φ_0 [JD]	Δm_r^0 [mag]	Abs mag	Binary/Multiple?
(145453) 2005 RR$_{43}$	Classical-Hot	7.87	7.87	0.06±0.01	2454031.46931	0.020	4.0	
(145480) 2005 TB$_{190}$	Detached	12.68	12.68	0.12±0.01	2455037.62904	-0.010	4.7	
(145486) 2005 UJ$_{438}$	Centaur	8.32	8.32	0.11±0.01	2454112.31250	-0.033	10.5	
(202421) 2005 UQ$_{513}$	Classical-Hot	7.03 or 10.01	7.03 or 10.01	0.05±0.02	2455118.32179	-0.002 or -0.009	3.4	
(341520) 2007 TY$_{430}$	Resonant	4.64	9.28	0.24±0.05	2455863.49277	0.065	6.9	Yes
(25012) 2007 UL$_{126}$ or 2002 KY$_{14}$	Centaur	3.56 or 4.2	7.12 or 8.4	0.11±0.01	2454680.38646	0.008 or 0.049	9.4	
(229762) 2007 UK$_{126}$	Detached	11.05	11.05	0.03±0.01	2455863.54538	-0.017	3.4	Yes
(315530) 2008 AP$_{129}$	Classical-Hot	9.04	9.04	0.12±0.02	2455952.41458	-0.053	4.7	
(281371) 2008 FC$_{76}$	Centaur	-	-	< 0.1	2455120.37177	-	9.1	
(315898) 2008 QD$_4$	Centaur	-	-	~0.09	2455953.33477	-	11.3	
(342842) 2008 YB$_3$	Centaur	-	-	~0.18	2455953.29841	-	9.4	
2010 BK$_{118}$	Centaur	-	-	< 0.15	2456181.55350	-	10.2	

Physical properties from lightcurves and interpretation

$\mathcal{T}$ he rotational properties of asteroids provide information about important physical proper-
ties, such as shape, density, cohesion etc (Pravec and Harris, 2000; Holsapple, 2001; Holsapple,
2004). As for asteroids, the rotational properties of the Trans-Neptunian Objects (TNOs) and cen-
taurs provide a wealth of knowledge about the basic physical properties of these icy bodies. In
addition, rotational properties provide valuable clues about the primordial distribution of angular
momentum, as well as the degree of collisional evolution of the different dynamical groups in the
Trans-Neptunian belt.

Based on the short-term variability study presented in the previous chapter, some proper-
ties of the TNOs and centaurs from their lightcurves are derived in this chapter. The most ex-
haustive study, to date about lightcurve amplitudes, and spins is presented here. A search for
correlations/anti-correlations between physical and orbital parameters is reported as well.

VII.1 Inventory

VII.1.1 Current inventory of the short-term variability studies

Using the literature and the results presented in the previous chapter, a database of lightcurves
with rotational periods and/or lightcurve amplitudes has been created. This database, updated in
May 2013, is presented in Table 7.

The number of objects with a well determined rotational period is still limited and highly
biased. Less than 5% of the known TNOs have a well determined rotational period. Sheppard,
Lacerda and Ortiz (2008) and Thirouin et al. (2010) pointed out that the sample of studied objects
is highly biased towards bright objects, large variability amplitudes and short rotational periods.
The majority of lightcurve amplitudes and rotational periods are published with large uncertain-
ties or, sometimes, they are just estimations or limiting values. The sample of studied TNOs is
essentially composed of bright (typically, visual magnitude <22 mag) and large objects. Several
limitations, and especially observational, can be enumerated to explain such biases. A reliable
study of TNO rotational properties requires a lot of observational time on medium size telescopes
(typically 2-m class telescopes). The telescope time required for this type of program is difficult to
obtain, mainly because a lot of time is required, and also because blocks of at least four consecutive
nights are needed.

A reliable photometric study needs an effective data reduction as well. Determining low am-
plitude lightcurves and/or detecting long rotation periods is very time consuming and require lots
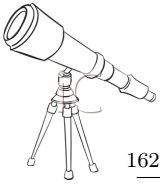
of observing time. Furthermore, 24-h aliases frequently complicate the analysis of time series photometry. To help debias the sample of studied objects, and minimize the 24-h aliases effect, longer term monitoring is needed, and this is why we devised a coordinated campaign (see Section IV.4.2 for more details).

When analyzing the current database about short-term variability of TNOs and centaurs, several features can be noticed. We note two special cases: Pluto-Charon and Sila-Numan. Both systems are tidally locked and synchronized (Buie, Tholen and Wasserman, 1997; Grundy et al., 2012). This means that the primary and the secondary rotations are synchronized with the orbital period.

The second noticeable characteristic is that the derived peak-to-peak lightcurve amplitudes are low, typically < 0.15 mag. Sheppard and Jewitt (2002) introduced the term of photometrically flat lightcurves for lightcurves with an amplitude lower than 0.15 mag. Such overabundance of nearly-flat lightcurves is probably due to a large abundance of spheroidal bodies with homogeneous surfaces, as we will see in this chapter.

The another characteristic is that just 10 % of the rotational periods published are larger than 10 h. The sample is highly biased towards short rotational periods. In fact, a large data set is required to estimate a long rotational period, but the most adequate approach is the coordinated campaign with several telescopes around the world. The detached disk object, 2005 TB_{190}, is a paradigmatic example of the efficiency of having coordinated campaigns (see Section VI.4.7). In fact, during the first two nights of our coordinated campaign, we managed to coordinate observations from the Canary Islands and Chile, observing this body on the first night during 2.2 h at the Telescopio Nazionale Galileo (Canary Islands, TNG), and around 4 h at the New Technology Telescope (Chile, NTT), allowing us to study close to a half period on one single coordinated run. Finally, with less than 50 images in four nights, we could reliably estimate the moderately long rotational period for this object. Detection and reliable estimations of long rotational periods was one of the goals of this coordinated campaign. One would have needed many more images and the detection of this long periodicity would have probably been difficult without a coordinated campaign. Thus, with several coordinated campaign in the future we may be able to determine the percentage of long periods and try to debias the sample in this regard.

VII.1.2   Database

In Table 7 are summarized the short-term variability studies of TNOs and centaurs reported in the literature and in this work.

Table 7: In this table, the short-term variability of all TNOs and centaurs from this work and the literature is listed. In case of multiple rotational periods, the preferred rotational period, according to the authors of each study, is indicated in bold. Absolute magnitudes reported here are from the Minor Planet Center (MPC) database. Dynamical classification used is the Gladman, Marsden and Vanlaerhoven (2008) classification. The complete reference list can be found after this table. Table updated in May, 2013.

Object	Class	Single peak periodicity [h]	Double peak periodicity [h]	Amplitude [mag]	Absolute magnitude	Ref
(134340) Pluto	Resonant	153.2	-	0.33	-0.7	B97
Charon	Resonant	153.6	-	0.08	0.9	B97
(2060) 1977 UB Chiron	Centaur	-	5.9180±0.0001	0.088±0.003	6.5	B89
(5145) 1992 AD Pholus	Centaur	-	9.98	0.15/0.60	7.0	B92,H92,F01a,T06
(7066) 1993 HA$_2$ Nessus	Centaur	-	-	0.15	...	RT99
		-		0.5	9.6	RT99
		5.68±0.19	-	<0.2	...	D98
			-	0.76±0.08	...	K06b
(15789) 1993 SC	Resonant	7.7	-	0.04	6.9	T97
(15820) 1994 TB	Resonant	3.0/3.5	6.0/7.0	<0.04	7.1	RT99
				0.26/0.34		RT99
(19255) 1994 VK$_8$	Classical-Cold	3.9/4.3/4.7/5.2	7.8/8.6/9.4/10.4	<0.04	...	SJ02
		4.75		0.42	7.0	RT99
(10370) 1995 DW$_2$ Hylonome	Centaur	-	-	-	8.0	CB99
(8405) 1995 GO Asbolus	Centaur	-	8.9351±0.003	<0.04	9.0	RT99
				0.55		D98,K00
				0.34	...	RT99
(24835) 1995 SM$_{55}$	Classical-Hot	4.04±0.03	8.08±0.03	0.14±0.10	4.8	R07
				0.19±0.05		SJ03
				0.05±0.02	...	TW
(32929) 1995 QY$_9$	Resonant	3.5	7.0	0.60	7.5	RT99
		Between 3.3 y 3.7		0.60	...	RT99
(26181) 1996 GQ$_{21}$	SDO	-	7.3±0.1	0.60±0.04	...	RT99,SJ02
(15874) 1996 TL$_{66}$	SDO	6/8/**12.1±0.01**	-	<0.10	5.2	SJ02
				<0.12	5.4	O06
				<0.06	...	LJ98,RT99
		12		0.07±0.02	...	T10
(19308) 1996 TO$_{66}$	Classical-Hot	**3.96±0.04** or 4.80±0.05	**7.92±0.04** or 5.90±0.05 or 9.6±0.1	0.26±0.03	4.5	SJ03
			11.9	0.25±0.05	...	B06
			6.25±0.03	0.12 to 0.33	...	H00
(15875) 1996 TP$_{66}$	Resonant	1.96	-	<0.10	...	RT99
				0.04	6.8	CB99
(118228) 1996 TQ$_{66}$	Resonant	-	-	0.12	7.1	RT99
1996 TS$_{66}$	Classical-Hot	-	-	0.14	6.5	LL06
				0.16	...	RT99
(58534) 1997 CQ$_{29}$ Logos	Classical-Cold	-	-	~0.8	6.6	N08
(79360) 1997 CS$_{29}$ Sila	Classical-Cold	-	-	<0.08	5.1	SJ02
				<0.22	...	RT99
(10199) 1997 CU$_{26}$ Chariklo	Centaur	-	-	0.14±0.07	...	G12, BS13
1997 CV$_{29}$	Classical-Hot	-	-	<0.1	6.4	D98
(33128) 1998 BU$_{48}$	Centaur	(4.9 or 6.3)±0.01	~16	~0.4±0.1	7.3	CK04
(91133) 1998 HK$_{151}$	Resonant	-	(9.8 or 12.6)±0.01	0.68±0.04	7.2	SJ02
(52872) 1998 SG$_{35}$ Okyrhoe	Centaur	4.68 or 6.08	16.6	<0.15	7.6	SJ02
				0.2	11.3	B03
(26308) 1998 SM$_{165}$	Resonant	3.983	7.1±0.01	0.07±0.01	...	T10
			7.966	0.45±0.03	5.8	SJ02
				0.56		R01
(35671) 1998 SN$_{165}$	Classical-Cold	5.03	8.84	0.16±0.01	5.8	LL06
			10.1±0.8	0.151±0.02		P02
(33340) 1998 VG$_{44}$	Resonant	-	-	<0.10	6.5	SJ02
(19521) 1998 WH$_{24}$ Chaos	Classical-Hot	-	-	<0.10	4.9	SJ02,LL06
1998 XY$_{95}$	SDO	1.31	-	~0.1	6.2	CB01
1999 CD$_{158}$	Resonant	>12?	-	0.6	5.1	S10
(26375) 1999 DE$_9$	Resonant	12.33	-	<0.10	4.7	SJ02
(79983) 1999 DF$_9$	Classical-Hot	(5.840 or 5.929)±0.001	**6.65**/9.2	0.09±0.03	6.1	TW
				0.40±0.02		LL06
(40314) 1999 KR$_{16}$	DO	5.8	(11.680 or 11.858)±0.002	0.18±0.04	5.8	SJ02
				0.12±0.06		T12
(44594) 1999 OX$_3$	SDO	9.26 or 13.4 or 15.45	-	0.11±0.02	7.4	T12
(66652) 1999 RZ$_{253}$ Borasisi	Classical-Cold	-	-	<0.05	5.9	LL06

Table 7: continued.

Object	Class	Single peak periodicity [h]	Double peak periodicity [h]	Amplitude [mag]	Absolute magnitude	Ref
(47171) 1999 TC$_{36}$	Resonant	6.4±1.0	-	0.08±0.02	...	K06b
		6.21±0.02	-	0.06	4.9	O03b
				<0.07	...	LL06
(29981) 1999 TD$_{10}$	SDO	7.71±0.02	15.42±0.02	0.65±0.05	8.8	O03b,R03
			15.45	0.65	...	C03
			15.382	0.41±0.08	...	M04
			15.3833	0.53±0.03	...	R05a
				0.65±0.05	...	C00
(31824) 1999 UG$_5$ Elatus	Centaur	5.8		0.24	10.1	G01
		13.25		0.102±0.005	...	B02
		13.41±0.04		0.45	6.5	S10
2000 CG$_{105}$	Classical-Hot			<0.14	6.3	LL06
(80806) 2000 CM$_{105}$	Classical-Cold			0.06	6.7	SS09
2000 CP$_{104}$	Classical-Hot			<0.1	4.7	O03b
(38628) 2000 EB$_{173}$ Huya	Resonant	(6.68/**6.75**/(6.82) ±0.01		<0.15	...	SJ02
				<0.097	...	S02
				<0.04	...	SJ03,LL06
(60558) 2000 EC$_{98}$ Echeclus	Centaur	5.21		0.02±0.01	9.0	T13
2000 FV$_{53}$	Resonant	13.401	26.802	0.24±0.06	8.2	R05b
(47932) 2000 GN$_{171}$	Resonant		7.5	0.07±0.02	6.0	TB06
			8.329±0.005	0.61±0.03		D08
				0.64±0.11		R07
(87555) 2000 QB$_{243}$	SDO	9.01±0.04		0.20±0.02	8.3	K06b
(54598) 2000 QC$_{243}$ Bienor	Centaur	4.57±0.02	9.14±0.04	0.75±0.09	7.6	O03b
			9.17	0.34±0.08		R07
				0.38±0.02		K06b
(20000) 2000 WR$_{106}$ Varuna	Classical-Hot	(4.723 or 4.594)±0.001	6.3436±0.0001	0.41±0.09	3.6	O03b
		3.1718	6.34±0.01	0.42±0.03		SJ02
			6.34	0.5		F01b
		3.17±0.01	6.34358±0.00002	0.42		B06
			6.344	0.49±0.17		R07
(82075) 2000 YW$_{134}$	SDO	6.3418		0.43±0.01		T10
(150642) 2001 CZ$_{31}$	Classical-Hot		**4.71**/5.23	<0.10	5.0	SJ03
				0.21±0.02	5.7	LL06
(82158) 2001 FP$_{185}$	SDO			<0.20	6.1	SJ02
(82155) 2001 FZ$_{173}$	SDO			<0.06	6.2	SJ03
2001 KA$_{77}$	Classical-Hot	>6		>0.14	5.0	SJ02
2001 KD$_{77}$	SDO	4.8±2.2		<0.07	5.8	SJ03
2001 KG$_{77}$	Resonant	3.38±0.39		0.80±0.26	8.1	K06b
(182294) 2001 KU$_{76}$	Resonant	5.27±0.02		0.34±0.06	6.8	K06b
(28978) 2001 KX$_{76}$ Ixion	Resonant			0.28±0.05	6.6	K06b
				<0.05	3.2	O03b,SJ03
(32532) 2001 PT$_{13}$ Thereus	Centaur	15.9±0.5	8.3091±0.0001	0.06±0.03	9.0	R10
		4.1546±0.0005	8.34	0.16±0.02		O03b
			8.34	0.16		FD03
			8.4	0.34±0.08		R07
2001 QC$_{298}$	Classical-Hot		~12	0.15		F01b
				0.4	6.1	S10
2001 QF$_{298}$	Resonant	3.89±0.24	7.78±0.48	0.30±0.04	4.7	K06b
				<0.12		SJ03
				~0.11		TW
(139775) 2001 QG$_{298}$	Resonant	6.8872±0.0002	13.7744±0.0004	1.14±0.04	7.0	SJ04
			13.7744±0.0004	0.07±0.01		L11
(88611) 2001 QT$_{297}$ Teharonhiawako	Classical-Cold	5.50±0.01 or 7.10±0.02	11.0±0.02 or 14.20±0.04	<0.15	5.5	Os03
				(0.32 or 0.30)±0.04		K06b
(88611B) 2001 QT$_{297}$ B Sawiskera	Classical-Cold	4.75		0.6	6.2	Os03
		4.749±0.001	9.498±0.02	0.48±0.05		Os03
(275809) 2001 QY$_{297}$	Classical-Cold	5.84	11.68	0.49±0.03	5.7	K06b
		12.2±4.3		0.66±0.38		T12
(148780) 2001 UQ$_{18}$ Altjira	Classical-Hot			<0.3	5.6	S07
(42301) 2001 UR$_{163}$	DO			<0.08	4.2	SJ03
(126154) 2001 YH$_{140}$	Resonant	6.22/**8.45±0.05**/12.99		0.19±0.04	5.4	O06
		13.25±0.2		0.21±0.04		S07
		13.19		0.15±0.03		TW
(148975) 2001 XA$_{255}$	Centaur		-	~0.13	11.2	TW

Table 7: continued.

Object	Class	Single peak periodicity [h]	Double peak periodicity [h]	Amplitude [mag]	Absolute magnitude	Ref
(55565) 2002 AW197	Classical-Hot	6.49/**8.86**±**0.01**/13.94/15.82	17.74	0.08±0.07	3.3	O06
		8.78	-	0.02±0.02	...	T10
(42355) 2002 CR46 *Typhon*	SDO	(3.66 or 4.35)±0.02	-	<0.15	7.2	O03b
		-	-	<0.05	...	SJ03
		>5	-	-	...	D08
(55567) 2002 GB10 Amycus	Centaur	9.67	-	0.07±0.01	7.8	T10
2002 GH32	Classical-Hot	9.76	-	0.16±0.01	5.5	T10
(83982) 2002 GO9 Crantor	Centaur	-	-	0.75	9.1	S10
		(6.97 or 9.67)±0.03	-	0.14±0.04		O03b
2002 GP32	Resonant	-	-	0.34		RT99
		~3.3	~6.6	>1	6.7	K06b
		-	-	<0.03		S07
2002 GW32	Resonant	4.0±0.1	-	0.18±0.04	7.4	K06b
(95626) 2002 GZ32	Centaur	>3	-	>1.0	6.8	K06b
(307251) 2002 KW14	Classical-Hot	4.29 or 5.25	5.80±0.03	0.15±0.03	5.0	D08
		6.63/5.23	8.58 or 10.5	0.21 or 0.26±0.03		T12
(119951) 2002 KX14	Classical-Cold	-	**13.25**/10.46	0.25±0.03	4.4	BS13
(50000) 2002 LM60 Quaoar	Classical-Hot	8.84	-	<0.05	2.6	O03a
		9.42	17.67788±0.0004	0.13±0.03		R07
		-	-	0.18±0.10		L07
		8.8399	-	~0.3		TW
(307261) 2002 MS4	Classical-Hot	7.33 or 10.44	18.84	0.112±0.001	3.7	TW
(73480) 2002 PN34	SDO	(4.23 or 5.11)±0.03	-	0.05±0.01	8.2	O03b
2002 TC302	Resonant	5.41	(8.45 or 10.22)±0.06	0.18±0.04	3.8	T12
(55636) 2002 TX300	Classical-Hot	(**8.12** or 12.101)±0.08	(**16.24** or 24.20)±0.08	0.04±0.01	3.3	SJ03
		7.89±0.03	15.78	0.08±0.02		O04
		-	8.16	0.09±0.08		T10
		-	-	0.04±0.01		T12
(55637) 2002 UX25	Classical-Hot	-	8.15 or 11.7	(0.01 or 0.05)±0.01		S12
		-	18.35	-	3.6	R05b
		-	14.382±0.001 or 16.782±0.003	0.21±0.06		SJ03
		-	-	<0.06		R07
		6.55	-	0.13±0.09		TW
(55638) 2002 VE95	Resonant	(6.76/6.88/7.36/9.47)±0.01	-	0.09±0.03	5.3	O06
		-	-	0.08±0.04		SJ03
2002 VT130	Classical-Cold	9.97	-	<0.06		T10
(119979) 2002 WC19	Resonant	-	-	0.05±0.01	5.8	TW
		-	-	~0.21	5.1	S07
		-	-	<0.05		TW
(208996) 2003 AZ84	Resonant	(4.32/5.28/6.72/**6.76**)±0.01	-	<0.01	3.6	O06
		6.72±0.05	-	0.10±0.04		SJ03
		6.79	-	0.14±0.03		T10
		6.78	-	0.07±0.01		TW
(120061) 2003 CO1	Centaur	3.53/4.13/**4.99**±**0.01**/6.30	-	0.10±0.05	8.9	O06
		4.51	-	0.06±0.01		T10
2003 BF91	Classical-Cold	**9.1**/7.3	-	1.09±0.25	11.7	TB06
2003 BG91	Classical-Cold	**4.2**/4.5/4.6/4.9	-	0.18±0.075	10.7	TB06
2003 BH91	Classical-Cold	2.8	-	0.42	11.9	TB06
(136108) 2003 EL61 Haumea	Resonant	-	3.9154±0.0002	0.28±0.02	0.2	R06
		-	3.9155±0.0001	0.29±0.02		LJ08
		-	3.92	0.28±0.02		T10
2003 FE128	Resonant	5.85±0.15	-	0.50±0.14	6.3	K06b
2003 FM127	Classical-Cold	6.22±0.02	-	0.46±0.04	7.1	K06b
(65489) 2003 FX128 Ceto	SDO	-	4.43±0.03	0.13±0.02	6.3	D08
(120132) 2003 FY128	DO	-	-	<0.08	5.0	S07
		>7	-	-		D08
(174567) 2003 MW12	Classical-Hot	8.54	-	0.12±0.02		T10
		5.90 or 7.87	-	0.06±0.01	3.6	T10
		-	-	<0.04		BS13
(120178) 2003 OP32	Classical-Hot	5.91	-	0.02±0.01		T13
		4.845±0.003	-	0.26±0.04	4.1	Ra08
		4.05	-	0.13±0.01		T10
		4.85/6.09	**9.71**/12.18	0.18±0.01		BS13
2003 QB112	Classical-Hot	4.07	-	0.13±0.01	7.0	TW
2003 QY90A	Classical-Cold	3.4±1.1	-	0.34±0.06	6.3	SS09
						K06a

Table 7: continued.

Object	Class	Single peak periodicity [h]	Double peak periodicity [h]	Amplitude [mag]	Absolute magnitude	Ref
2003 QY$_{90B}$	Classical-Cold	7.1±2.9	-	0.90±0.18	6.3	K06a
2003 QY$_{111}$	Classical-Cold	-	-	0.60	6.6	SS09
2003 SQ$_{317}$	Classical-Hot	3.7	7.5	1	6.3	S10
(136199) 2003 UB$_{313}$ Eris	DO	13.69/28.08/32.13	-	<0.1±0.01	-1.2	Du08
		3.55	-	~0.5	...	L07
		25.92	-	<0.01	...	R07,S07
2003 UZ$_{117}$	Classical-Hot	-	~6	0.1	...	R08
2003 UZ$_{413}$	Resonant	-	4.13±0.05	0.13±0.03	5.3	P09
(90377) 2003 VB$_{12}$ Sedna	SDO	10.273±0.003	-	0.02	4.3	P09
(84922) 2003 VS$_2$	Resonant	(3.71 or 4.39)±0.01	-	0.23±0.07	1.6	G05
			7.41±0.02	0.21±0.02	4.2	O06
			7.42	0.21±0.01	...	S07
			7.4208	0.224±0.013	...	T10
(136204) 2003 WL$_7$	Centaur	8.24	-	0.04±0.01	8.7	TW
(90482) 2004 DW Orcus	Resonant	7.09/**10.08±0.01**/17.43	**20.16**	0.04±0.02	2.3	T10
		13.19	-	0.18±0.08	...	O06
			-	<0.03	...	R07
(90568) 2004 GV$_9$	Classical-Hot	10.47	-	0.04±0.01	4.0	S07
			-	<0.08	...	T10
2004 NT$_{33}$	Classical-Hot	7.87	5.86±0.03	0.16±0.03	4.4	S07
(307982) 2004 PG$_{115}$	SDO	-	-	0.04±0.01	4.4	D08
2004 PT$_{107}$	Classical-Hot	-	~20	~0.07	3.9	T12
(120347) 2004 SB$_{60}$ Salacia	Classical-Hot	6.09 or 8.10	~17.5	0.05	6.0	TW
		6.61	-	0.2	4.4	S10
			-	0.03±0.01	...	T10
			-	0.04±0.02	...	T13
(120348) 2004 TY$_{364}$	Classical-Hot	5.85±0.01	11.70±0.01	<0.04	...	BS13
(144897) 2004 UX$_{10}$	Classical-Hot	-	7.58±0.05	0.22±0.02	4.5	S07
			-	0.14±0.04	4.7	P09
(230965) 2004 XA$_{192}$	Classical-Hot	5.68	-	0.09±0.02	4.0	T10
(308193) 2005 CB$_{79}$	Classical-Cold	6.76	-	0.05±0.02	5.0	T12
(136472) 2005 FY$_9$ Makemake	Classical-Hot	**4.82**/6.06	**9.65**/12.13	0.31±0.04	6.1	T10
		11.24±0.01	20.54/**22.48**	0.03±0.01	-0.3	BS13
		7.7710±0.0030	-	0.0286±0.0016	...	O07
			-	0.014±0.002	...	H09
2005 GE$_{187}$	Resonant	7.65	-	0.5	...	T10
(303712) 2005 PR$_{21}$	Classical-Cold	6.1	-	<0.28	7.1	S10
(303775) 2005 QU$_{182}$	DO	9.61	19.22	0.12±0.02	6.1	BS13
(145451) 2005 RM$_{43}$	SDO	-	9.00±0.06	0.12±0.05	3.5	BS13
		6.71	-	0.05±0.01	4.4	P09
(145452) 2005 RN$_{43}$	Classical-Hot	5.62 or 7.32	**13.89**/19.46	0.04±0.01	3.9	T10
(145453) 2005 RR$_{43}$	Classical-Hot	**6.95**/9.73	5.08±0.04	0.06±0.01	...	BS13
		7.87	-	0.12±0.03	4.0	P09
			-	0.06±0.01	...	T10
(145480) 2005 TB$_{190}$	DO	12.68	-	<0.06	...	BS13
(145486) 2005 UJ$_{438}$	Centaur	8.32	-	0.12±0.01	4.7	T12
(202421) 2005 UQ$_{513}$	Classical-Hot	-	-	0.11±0.01	10.5	T10
		7.03 or 10.01	-	0.3	3.4	S10
2006 HJ$_{123}$	Resonant	-	-	0.05±0.02	...	T12
2007 JF$_{43}$	Classical-Hot	**5.95**/4.75	**11.90**/9.50	<0.13	5.7	BS13
2007 JH$_{43}$	Resonant	6.04/4.83	**12.09**/9.66	0.22±0.02	5.6	BS13
(278361) 2007 JJ$_{43}$	Classical-Hot	-	-	<0.08	4.7	BS13
(225088) 2007 OR$_{10}$	SDO	-	-	0.13±0.02	3.9	BS13
2007 TY$_{430}$	Resonant	-	9.28	<0.09	2.0	BS13
(229762) 2007 UK$_{126}$	DO	11.05	-	0.24±0.05	6.9	T13
(25012) 2007 UL$_{126}$ or 2002 KY$_{14}$	Centaur	3.56 or 4.2	7.12 or 8.4	0.03±0.01	3.4	T13
(315530) 2008 AP$_{129}$	Classical-Hot	9.04	-	0.11±0.01	9.4	T10
(281371) 2008 FC$_{76}$	Centaur	-	-	0.12±0.02	4.7	TW
(315898) 2008 QD$_4$	Centaur	-	-	<0.1	9.1	TW
(305543) 2008 QY$_{40}$	SDO	-	-	~0.09	11.3	TW
(342842) 2008 YB$_3$	Centaur	-	-	~0.15	5.2	TW
2009 YE$_7$	Classical-Hot	-	-	~0.18	9.4	BS13
2010 BK$_{118}$	Centaur	-	-	<0.20	10.2	BS13
2010 EK$_{139}$	SDO	3.53	7.07	0.12±0.02	4.4	BS13

Table 7: continued.

Object	Class	Single peak periodicity [h]	Double peak periodicity [h]	Amplitude [mag]	Absolute magnitude	Ref
2010 EL$_{139}$	Classical-Hot	3.16	6.32	0.15±0.03	5.1	BS13
(312645) 2010 EP$_{65}$	Classical-Hot	**7.48**/5.77/8.45	**14.97**/11.54/16.90	0.17±0.03	5.5	BS13
2010 ER$_{65}$	SDO	-	-	<0.16	5.4	BS13
2010 ET$_{65}$	SDO	3.94	7.88	0.13±0.02	5.2	BS13
2010 FX$_{86}$	Classical-Hot	7.90	15.80	0.26±0.04	4.3	BS13
2010 HE$_{79}$	Classical-Hot	9.75	19.49	0.11±0.02	7.4	BS13
2010 KZ$_{39}$	SDO	-	-	<0.17	4.0	BS13
2010 PU$_{75}$	SDO	**6.19**/4.91	**12.39**/9.82	0.27±0.03	5.6	BS13
2010 RF$_{43}$	Classical-Hot	-	-	<0.08	4.1	BS13
2010 RO$_{64}$	Classical-Hot	-	-	<0.16	5.3	BS13
2010 TY$_{53}$	Centaur	-	-	<0.14	5.2	BS13
2010 VK$_{201}$	Classical-Hot	**3.79**/3.28	**7.59**/6.55	0.30±0.02	4.5	BS13
2010 VZ$_{98}$	SDO	4.86	9.72	<0.18	5.0	BS13
2010 WG$_9$	SDO	131.89±0.06	263.78±0.12	0.14	8.1	R13
2013 AZ$_{60}$	SDO	-	-	~0.2	10.1	TW

References list:

B89: Bus et al. (1989); B92: Buie and Bus (1992); H92: Hoffmann and et al. (1992); B97: Buie, Tholen and Wasserman (1997); T97: Tegler et al. (1997); D98: Davies et al. (1998); LJ98: Luu and Jewitt (1998); CB99: Collander-Brown et al. (1999); RT99: Romanishin and Tegler (1999); C00: Consolmagno et al. (2000); H00: Hainaut et al. (2000); K00: Kern et al. (2000); CB01: Collander-Brown et al. (2001); F01a: Farnham (2001a); F01b: Farnham (2001); G01: Gutiérrez et al. (2001); R01: Romanishin et al. (2001); B02: Bauer et al. (2002); P02: Peixinho, Doressoundiram and Romon-Martin (2002); SJ02: Sheppard and Jewitt (2002); S02: Schaefer and Rabinowitz (2002); B03: Bauer et al. (2003); C03: Choi, Brosch and Prialnik (2003); FD03: Farnham and Davies (2003); O03a: Ortiz et al. (2003a); O03b: Ortiz et al. (2003b); Os03: Osip, Kern and Elliot (2003); R03: Rousselot et al. (2003); SJ03: Sheppard and Jewitt (2003); CK04: Chorney and Kavelaars (2004); M04: Mueller et al. (2004); O04: Ortiz et al. (2004); SJ04: Sheppard and Jewitt (2004); G05: Gaudi et al. (2005); R05a: Rousselot et al. (2005a); R05b: Rousselot et al. (2005b); T05: Tegler et al. (2005); TB06: Trilling and Bernstein (2006); B06: Belskaya et al. (2006); K06a: Kern and Elliot (2006a); K06b: Kern (2006); LL06: Lacerda and Luu (2006); O06: Ortiz et al. (2006); R06: Rabinowitz et al. (2006); L07: Lin, Wu and Ip (2007); O07: Ortiz et al. (2007b); R07: Rabinowitz, Schaefer and Tourellotte (2007); S07: Sheppard (2007); D08: Dotto et al. (2008); Du08: Duffard et al. (2008); LJ08: Lacerda, Jewitt and Peixinho (2008); N08: Noll et al. (2008a); Ra08: Rabinowitz et al. (2008); R08: Roe, Pike and Brown (2008); H09: Heinze and de Lahunta (2009); P09: Perna et al. (2009); SS09: Santos-Sanz et al. (2009) S10: Snodgrass et al. (2010); R10: Rousselot and Petit (2010); T10: Thirouin et al. (2010); T12: Thirouin et al. (2012); L11: Lacerda (2011); G12: Grundy et al. (2012); S12: Sonnett, Meech and Sarid (2012); BS13: Benecchi and Sheppard (2013); R13: Rabinowitz et al. (2013); T13: Thirouin et al. (2013b); TW: Results are unpublished and are only reported in this work.
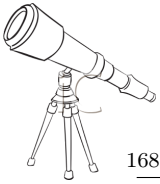
VII.2 Rotational period distributions

VII.2.1 Single- or double- peaked lightcurves ?

Using the literature and our results presented in this work (Table 7), one can study the rotational period distributions of the TNOs and centaurs. In this discussion about rotational period, Pluto-Charon and Sila-Numan systems have been removed from the sample, as both systems are tidally locked and synchronized (Buie, Tholen and Wasserman, 1997; Grundy et al., 2012). So they do not preserve their primordial angular momentum. In theory, all binary objects should be removed from the sample because they all may have some degree of tidal interaction and slowing down of the primary rotations (see chapter VIII). A recent study about 2010 WG$_9$ suggested a rotational period of 131.89±0.06 h or 263.78±0.12 h (Rabinowitz et al., 2013). Such long rotational periods have been observed only for tidally-evolved binary TNOs (see Chapter VIII), suggesting that this object may be such a system. As the case of 2010 WG$_9$ may be similar to the cases of Pluto-Charon and Sila-Numan systems, we will not take into account this object. For all considerations, only objects with a determined rotational period and lightcurve amplitude are taken into account. In other words, if only amplitudes are available but not rotational period, those data are not used. In case of multiple determination of rotational periods and/or lightcurve amplitudes, the preferred value by the author(s) who published the study is selected. If no preferred value is mentioned, we proceed to a random choice. In fact, in some cases several rotational periods are possible, and in such cases we have to choose randomly one of these rotational periods. For this purpose, we use a specific program which select randomly a rotational period for the object between all the possible rotational periods. Then, we build a histogram in the range [Ω, Ω+dΩ]. Such a process is repeated 100,000 times and for each time a new histogram is built. The final histogram is built by computing the mean of the frequencies in each bin. In other words, the final histogram keeps the information of the previous 100,000 previous histograms.

From the lightcurves alone, it is difficult to determine if the variability is caused by albedo variations on the body surface or due to the elongated shape of the body. Therefore, it is difficult to decide if we have to consider the single- or double-peaked rotational lightcurve. In fact, as mentioned in Section V.1.3.1, a double-peaked lightcurve is due to the shape of the body whereas a single-peaked lightcurve is due to albedo variations on the surface. However, often it is not that easy to distinguish a shape-dominated lightcurve from an albedo-dominated lightcurve. Thus, it is usually difficult to decide whether the true rotation period coincides with the photometric period or it is twice that value.

In this section, we test what is the lightcurve amplitude limit to distinguish between shape- and albedo-dominated lighcurves (i.e. to distinguish between single- and double-peaked lighcurves). In other words, we test three lightcurve amplitude (Δm) limits: i) a threshold at Δm=0.10 mag, ii) at Δm=0.15 mag, and iii) at Δm=0.20 mag, to distinguish between single- and double-peaked lightcurves. For example, considering the first threshold mentioned, we consider that lightcurves with an amplitude smaller than or equal to 0.10 mag are single-peaked (i.e. equivalent to assume that the lightcurve variation is due to albedo markings), and lighcurves with an amplitude higher than 0.10 mag are double-peaked (i.e. equivalent to assume that the lightcurve variation is due to the elongated shape of the body). This has a profound effect on the final spin period distribution.

First of all, we must point out that Binzel et al. (1989) studied the asteroid rotation rates distributions. They concluded that for asteroids with a diameter D>125 km, a Maxwellian is able to fit the observed rotation rate distributions implying that their rotation rates may be determined by collisional evolution. Whereas, for asteroids with a diameter D<125 km, there is an excess of slow rotators and their non-Maxwellian distributions suggests that their rotation rates are more strongly influenced by other process resulting from their formation in catastrophic disruption events etcetera. As the number of TNOs/centaurs whose short-term variability has been studied is still too limited, we do not divide the sample according to the object sizes. In the future, when more short-term variability studies will be known, an interesting point will be to check if the small objects are fitting or not a Maxwellian distribution.

Secondly, as pointed out in Binzel et al. (1989), there are several biases in the asteroid lightcurve database, mainly because it is easier to determine reliable and publishable parameters for an asteroid that have a short rotational period with a large lightcurve amplitude. Similar biases have been noted in the TNOs/centaurs lightcurve database (Sheppard, Lacerda and Ortiz, 2008; Thirouin et al., 2010). In the analysis carried out by Binzel et al. (1989), they tried to eliminate bias effects as much as possible by including all asteroids even those with a low reliability code (i.e. a low reliability code means that the rotational period estimated has a low confidence level and may be wrong). Binzel et al. (1989) stressed that excluding poor reliability objects results into overweighing asteroids with large amplitudes and short periods, so introducing a significant bias in the results of the statistical studies. Based on such a study, we decided to proceed in the same way, and we included all the TNOs/centaurs with a short-term variability study, even if the rotational period estimated is not unambiguously determined.

Thirdly, the bin size used here for the histograms is the same as that used in Binzel et al. (1989). On the other hand, the sample of TNOs/centaurs with a short-term variability study is still too limited to consider smaller bin sizes.
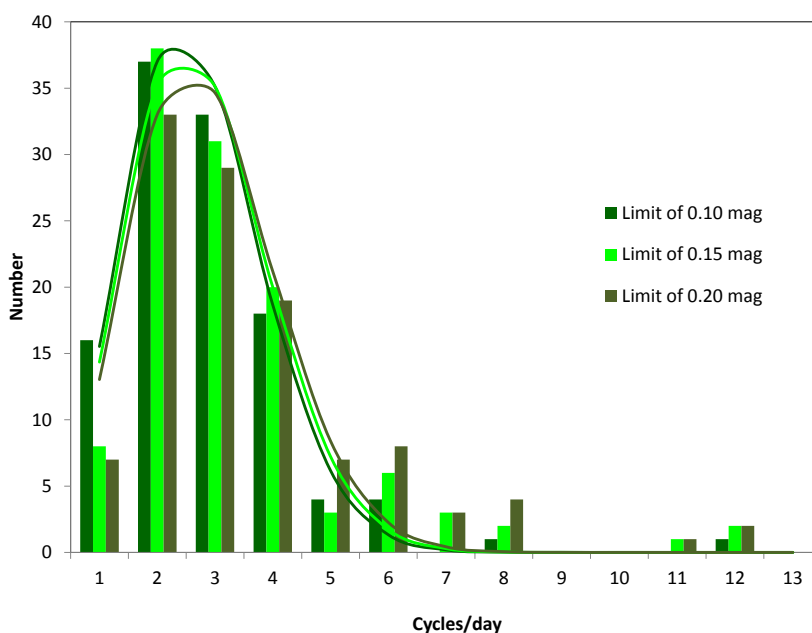
Figure 145: *Histogram in cycles/day for the whole sample (TNOs+centaurs)*: Several thresholds (0.10 mag, 0.15 mag, and 0.20 mag) have been used in order to distinguish between shape- and albedo-dominated lightcurves. Maxwellian fits to the whole sample give a mean rotational period of 8.84 h assuming a threshold of 0.10 mag, of 8.58 h assuming a threshold of 0.15 mag, and 8.30 h considering a threshold of 0.20 mag. Distributions updated in May, 2013.

In Figure 145, the histogram of rotation periods of the sample composed of TNOs and centaurs is plotted. Three different distributions according to the thresholds previously mentioned are shown. As in Binzel et al. (1989), the rotational frequency distribution is fitted to a Maxwellian distribution, expressed as:
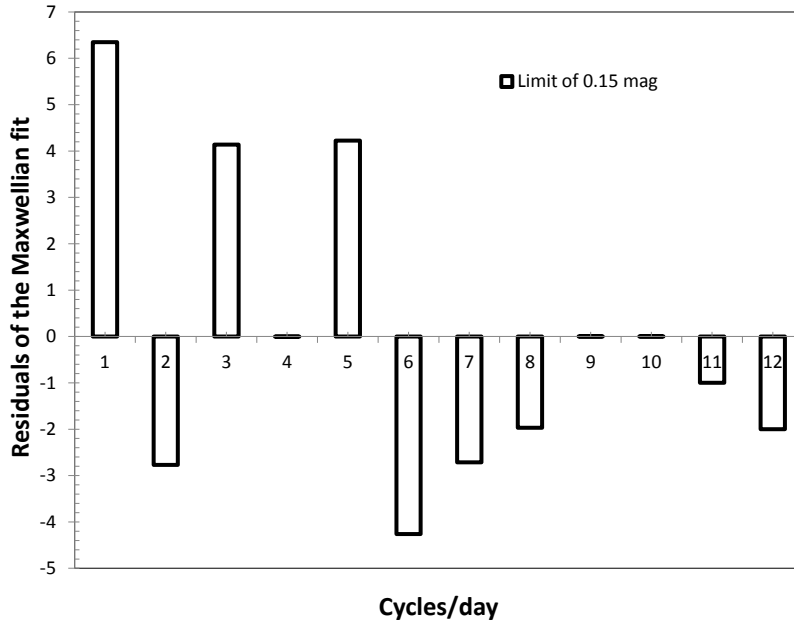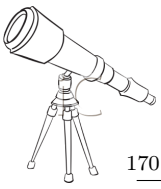
Figure 146: *Residuals versus rotational frequency for the whole sample (TNOs+centaurs)*: In this figure, the residuals between the Maxwellian fits and the whole sample observed distributions assuming a threshold of 0.15 mag are plotted.

$$f\left(\Omega\right) = \sqrt{\frac{2}{\pi}} \frac{N\Omega^2}{\sigma^3} exp\left(\frac{-\Omega^2}{2\sigma^2}\right) \qquad \text{(Equation VII.1)}$$

where N is the number of objects, Ω is the rotation rate in cycles/day, and σ is the width of the Maxwellian distribution. The mean value, Ω_{mean}, of this distribution is expressed as:

$$\Omega_{mean} = \sqrt{\frac{8}{\pi}}\sigma \qquad \text{(Equation VII.2)}$$

In Table 8 are summarized the lightcurve amplitude limits used, the number of objects in each sample, the σ parameter, the significance level of the Maxwellian distribution fits, and the mean rotational rates from the fits. To compute the goodness of the fits (or significance level of the fits), the chi-square (χ^2) test has been used. This test allows us to compute the probability that the observed distribution and the theoretical distribution are compatible. For example, if the significance level is 99%, this means that both distributions are compatible at the 99% level.

In Figure 147, and Figure 149 are plotted, respectively, the sample without the centaur population and the centaur population alone, and the Maxwellian fits information can be found in Table 8. In conclusion, for the whole sample (TNOs+centaurs), and for the sample without the centaur population, the best fits are obtained for a threshold of 0.15 mag. This means that lightcurves with an amplitude smaller than or equal to 0.15 mag are single-peaked (i.e. equivalent to assume that the lightcurve variation is due to albedo markings), and lighcurves with an amplitude higher than 0.15 mag are double-peaked (i.e. equivalent to assume that the lightcurve variation is due to the elongated shape of the body). Concerning the centaurs alone, the sample is very limited with less than 20 objects with short-term variability studies, so the significance levels of the fits are low in
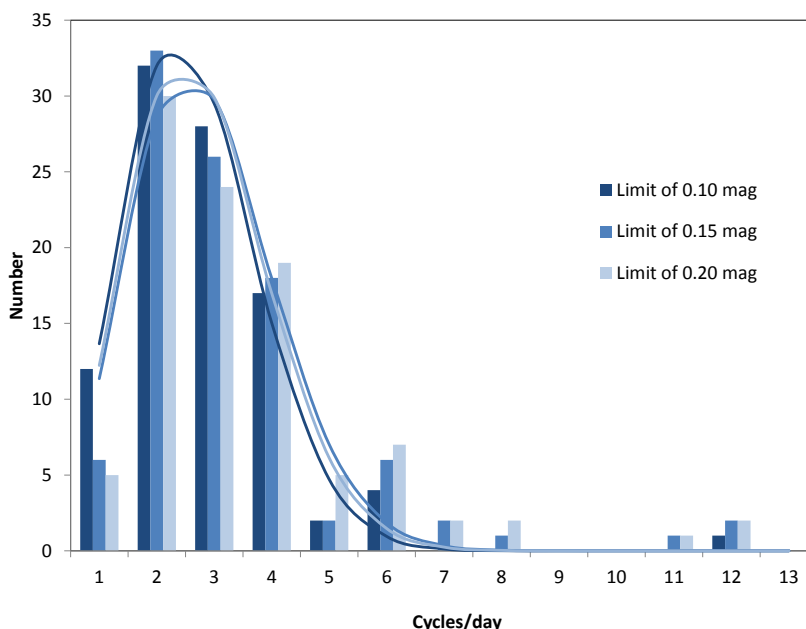
Figure 147: *Histogram in cycles/day for the TNO sample (no centaurs)*: Several thresholds (0.10 mag, 0.15 mag, and 0.20 mag) have been used in order to distinguish between shape- and albedo-dominated lightcurves. Maxwellian fits to the whole sample give a mean rotational period of 8.98 h assuming a threshold of 0.10 mag, of 8.35 h assuming a threshold of 0.15 mag, and 8.58 h considering a threshold of 0.20 mag. Distributions updated in May, 2013.

all cases. A threshold of 0.15 mag seems the best option and will be used in this work and for all the samples.

Based on the Maxwellian distribution fits and using a threshold of 0.15 mag, mean rotational periods of 8.58 h for the entire sample (TNOs+centaurs), of 8.35 h for the sample without the centaurs and of 8.56 h for the centaur population are calculated (Equation VII.2). The mean rotational periods computed in this work are slightly higher than previously reported by Duffard et al. (2009). Duffard et al. (2009) reported that from Maxwellian fits to the rotational frequencies distribution the mean rotation rates are 7.35 h for the entire sample, 7.71 h for the TNOs alone and 8.95 h for the centaurs. The mean values of the histograms (mean value not based on the Maxwellian fit as before) are respectively, 9.32 h, 9.11 h, and 10.47 h for the whole sample, the sample without the centaurs, and the centaur population. These estimates may be more appropriate to compare with the average of 8.5 h quoted in Sheppard, Lacerda and Ortiz (2008).

In Figure 146 and in Figure 148, the residuals between the Maxwellian distribution fits and the observed distributions are plotted for the whole sample (TNOs+centaurs), and for the sample without the centaurs, respectively. On can appreciate a lack of slow rotators and so confirm that the sample is highly biased towards short rotational periods.
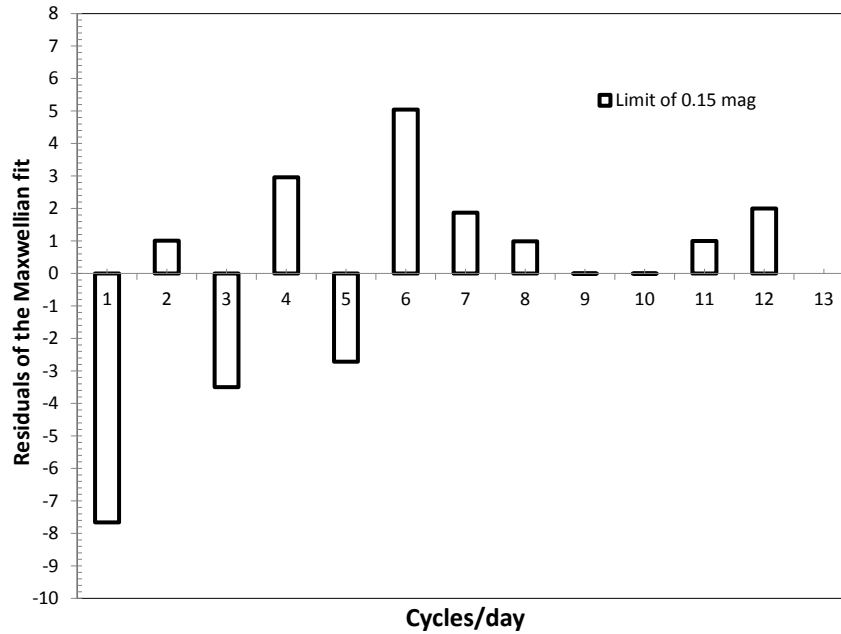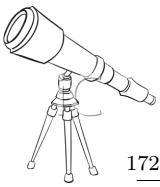
Figure 148: *Residuals versus rotational frequency for the whole sample (TNOs+centaurs)*: In this figure, the residuals between the Maxwellian fits and the TNOs sample distributions assuming a threshold of 0.15 mag are plotted.

VII.2.2   Filtered distributions

In Figure 145, Figure 147, and Figure 149, one can appreciate that there are several fast rotators with rotational periods around 2 h (11 cycles/day). The reason for this is that such objects have a lightcurve amplitude smaller than 0.15 mag and were considered to have single-peaked lightcurves whereas in reality, they likely have double-peaked lightcurves. However, in some cases the rotational periods estimated seem to be wrong due to reductions problems or wrong interpretation of the time series analysis.

In Figure 150 a more "realistic" distribution in which these outliers have been removed, is shown. Based on the Maxwellian distribution fits, mean rotational periods of 7.99 h for the entire sample (TNOs+centaurs), of 8.97 h for the sample without the centaurs and of 7.95 h for the centaur population are computed. The mean rotational periods of the distributions (mean rotational not obtained from the fit) are, respectively, 9.34 h, 9.07 h, and 10.23 h for the whole sample, the sample without the centaurs, and the centaur population.

In Figure 151, the residuals between the Maxwellian distribution fits and the filtered distributions are plotted for the whole sample (TNOs+centaurs), and for the sample without the centaurs, respectively. On can appreciate a lack of slow rotators and so confirm that the sample is highly biased towards short rotational periods.

One can compare the spin period distributions of the main-belt asteroids (MBAs) and of the TNOs. We show in Figure 152, that the rotational period distribution of the TNOs and the MBAs are different. Because the sample of TNOs with a small size and a large rotational period is very limited, and so in order to avoid bias in our comparison between both samples, only TNOs and
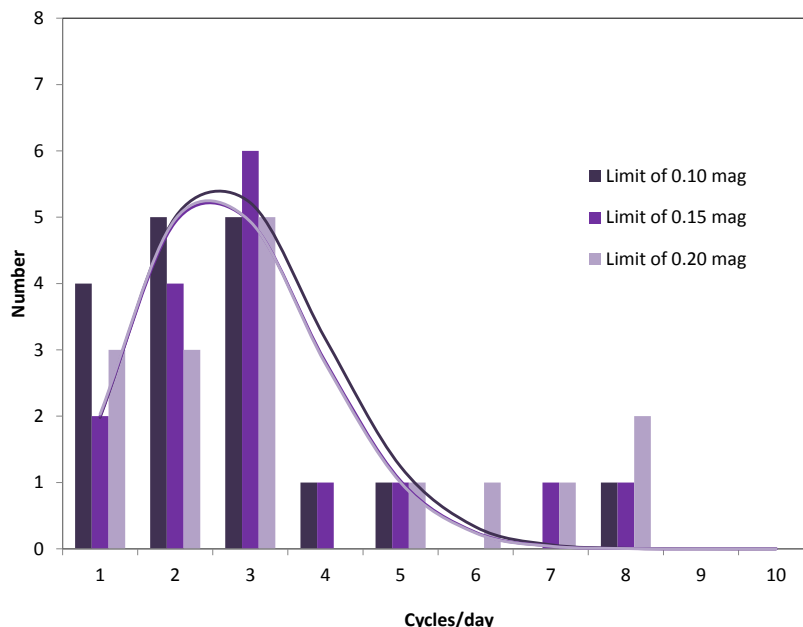
Figure 149: *Histogram in cycles/day for the Centaurs*: Several thresholds (0.10 mag, 0.15 mag, and
0.20 mag) have been used in order to distinguish between shape- and albedo-dominated lightcurves.
Maxwellian fits to the whole sample give a mean rotational period of 8.34 h assuming a threshold of
0.10 mag, of 8.56 h assuming a threshold of 0.15 mag, and 8.60 h considering a threshold of 0.20 mag.
Distributions updated in May, 2013.

MBAs with diameter $\geq$200 km and rotational period $\leq$20 h are considered. We do this because we
know that our sample is biased in that rotation rate. In Table 9, we listed the asteroids used for
this study. In such a range of parameters, the mean rotational period of the TNO sample is 7.88 h
whereas the MBA sample has a mean rotational period of 6.08 h. According to the Student's t-test,
both distributions are different at 99% (confidence level), and according to the Kolmogorov-Smirov
(also known as K-S) test, the probability that the rotational periods of the TNOs and of the MBAs
are drawn from the same parent distribution is 0.2%. In conclusion, it is clear that TNOs spin
slower than the asteroids, and a reason for this is not obvious.

VII.2.3 Rotational period distributions from our sub-sample

In this sub-section, the rotational period distributions based only on the data obtained during this
thesis is studied. Obviously, the sample is limited with only 6 centaurs, and 38 TNOs. In Figure 153, the rotational period distributions of the whole sample, the sample without the centaurs
and the centaurs alone are plotted.

We must emphasize that in our sample, not only objects with short rotational periods and large
amplitude lightcurves have been reported, but also objects with nearly flat lightcurves. Thus, our
database is probably less biased than other database reported in the literature. So, we did not
exclude poor reliability objects in order to not bias the statistical studies (Binzel et al., 1989).

Based on the Maxwellian distribution fits, mean rotational periods of 7.17 h for the entire
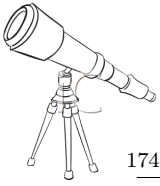
Table 8: In this table, some results based on the Maxwellian fits are summarized. Three different samples are considered: "TNOs+Centaurs", "TNOs" is limited to objects with an orbit beyond Neptune (centaurs are not included), and the "Centaurs". The number of objects in each sample, the σ and the significance level (SL) of the different fits according to the amplitude limit used are also reported. And finally, the median rotational period (P_{mean}) obtained thanks to the fit is indicated in the last column.

Samples	Amplitude limits [mag]	Number of objects	σ	SL [%]	P_{mean} [h]
TNOs+Centaurs	0.10	114	1.702	58	8.84
	0.15	**114**	**1.753**	**99**	**8.58**
	0.20	114	1.811	34	8.30
TNOs	0.10	97	1.674	12	8.98
	0.15	**97**	**1.801**	**98**	**8.35**
	0.20	97	1.752	97	8.58
Centaurs	0.10	17	1.535	<5	8.34
	0.15	17	1.542	24	8.56
	0.20	17	1.804	30	8.60

Table 9: In this table, the asteroids with a diameter larger than 200 km, and with rotational period below 20 h are reported. The Asteroid Lightcurve Database (LCDB) has been used to obtain information about asteroid short-term variability studies (http://www.minorplanet.info/lightcurvedatabase.html).

Object	Rotational period [h]	Diameter [km]
Themis	8.374	202.25
Thisbe	6.042	204
Hermione	5.55128	206.16
Eugenia	5.699	206.29
Egeria	7.045	207.64
Amphitrite	5.3921	212.22
Ursula	16.83	216.1
Camilla	4.844	219.38
Doris	11.89	221.8
Herculina	9.405	222.39
Fortuna	7.4432	223.19
Psyche	4.196	225
Patientia	9.727	225.31
Hektor	6.924	233.23
Cybele	6.0814	237.26
Juno	7.21	252
Eunomia	6.083	255.33
Sylvia	5.184	260.94
Euphrosyne	5.53	279.82
Europa	5.6304	293
Davida	5.131	300
Interamnia	8.727	316.62
Vesta	5.342	468.3
Pallas	7.8132	512.59
Ceres	9.07417	848.4
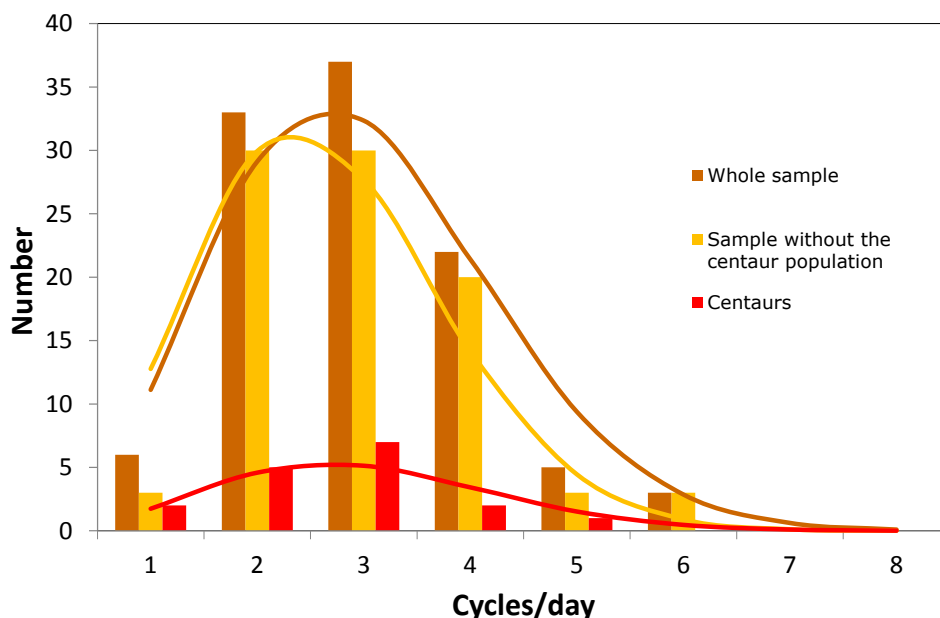
Figure 150: *Histogram in cycles/day for the three different samples: the whole sample (TNOs+Centaurs),
the sample without the centaur population and only the centaurs*: more realistic distributions for three
samples composed by: i) the whole sample, ii) the sample without the centaurs population, and iii) the
centaurs are plotted. Maxwellian fits to the whole sample give a mean rotational period of 7.99 h for
the whole sample, of 8.97 h for the sample without the centaur population, and 7.95 h for the centaur
population alone. Distributions updated in May, 2013.

sample (TNOs+centaurs), of 7.05 h for the sample without the centaurs and of 6.32 h for the
centaur population are calculated. The significance level of the different fits are low, 6% for the
whole sample, 7% for the TNO sample, and 5% for the centaurs. Such mean rotational periods are
slightly lower than previously reported by Sheppard, Lacerda and Ortiz (2008), but are consistent
with Duffard et al. (2009). For the rotation periods directly from the histograms, without fits, the
mean values are, respectively, 8.30 h, 8.45 h, and 7.40 h for the whole sample, the sample without
the centaurs, and the centaur population.

VII.2.4   Rotational period distribution of the Haumea family members

In the asteroid belt, several families have been identified, and one can enumerate the Koronis,
Vesta, Veritas, Flora families as examples. The members of the families are thought to be frag-
ments of past collisions. Paolicchi, Burns and Weidenschilling (2002) suggested that large collisions
influence the spin properties of the target as well as of the material ejected (the family members)
during the event. If one assumes that the Haumea family [1] is the result of a large collision, one
might expect that the rotational properties of the family are different from the other TNOs.

---

[1]The chapter IX is dedicated to the Haumea family, so all information about this family can be found in such a
chapter.
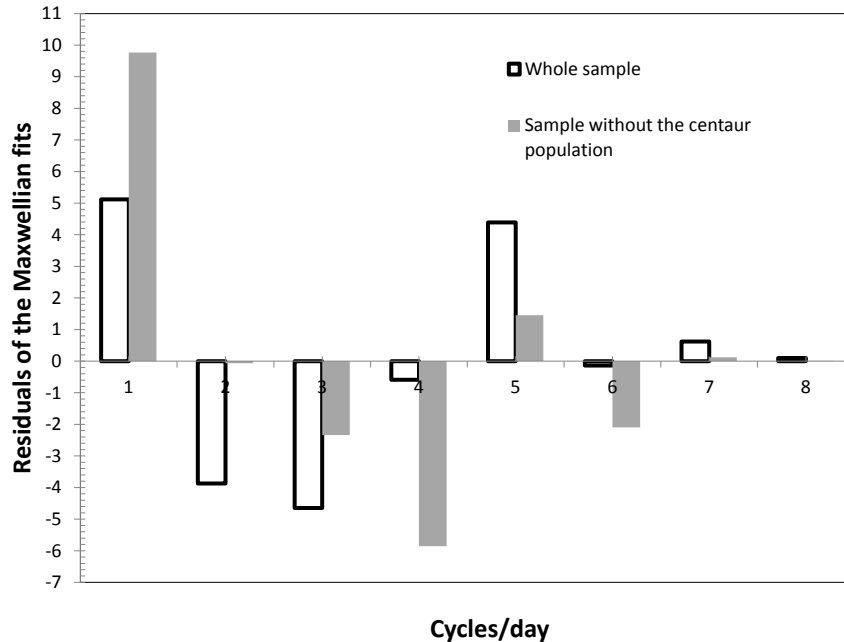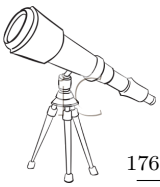
Figure 151: *Residuals versus rotational frequency for the "realistic" distribution*: in this figure, the residuals between the Maxwellian fits and the observed distributions shown in Figure 150 are plotted.

To date, 12 members of the Haumea family, plus Haumea itself, have been identified. As pointed out in the chapter IX, the membership of 2008 AP_{129} is not confirmed yet, so care has to be taken with this object. Unfortunately, short-term variability studies are not available for all the family members. Only 8 objects (7 family members, plus Haumea itself) have been studied for short-term variability. In this work, a short-term variability study has been presented for the non-confirmed family member, 2008 AP_{129} (see Section VI.2.20).

In Figure 154, the members of the family are plotted. Care was taken to consider two different samples: with and without 2008 AP_{129}. The Maxwellian fits to the sample with 2008 AP_{129} give a mean rotational period of 6.60 h and 6.78 h without 2008 AP_{129}. Obviously, the samples are still too limited to derive reliable conclusions. However, one can appreciate that the Haumea family members seem to rotate faster than the other TNOs. In fact, all members have a rotational period below 10 h and there are two fast rotators in this family: Haumea and 2003 OP_{32}. It is also interesting to point out that these two fast rotators are also the members with the highest lightcurve amplitude. So, it is reasonable to assume that both objects have elongated shapes mainly due to their fast rotation. The rest of the family has a low amplitude, the mean lightcurve amplitude is 0.12 mag. A lightcurve of 2003 SQ_{317} has been reported in Snodgrass et al. (2010), and they derived a large lightcurve amplitude of 1 mag. Such a high variation is suspicious, but taking it into account, a mean lightcurve amplitude of 0.22 mag for the family members is computed.

The poor Maxwellian fit is for the Haumea family may imply that the family is not the result of a collision (see Chapter IX). However, we must point out that the Haumea family does not necessarily have to follow a Maxwellian distribution. In fact, Binzel et al. (1989) studied the rotational period distribution of two families of asteroids in the main belt: Eos and Koronis fam-
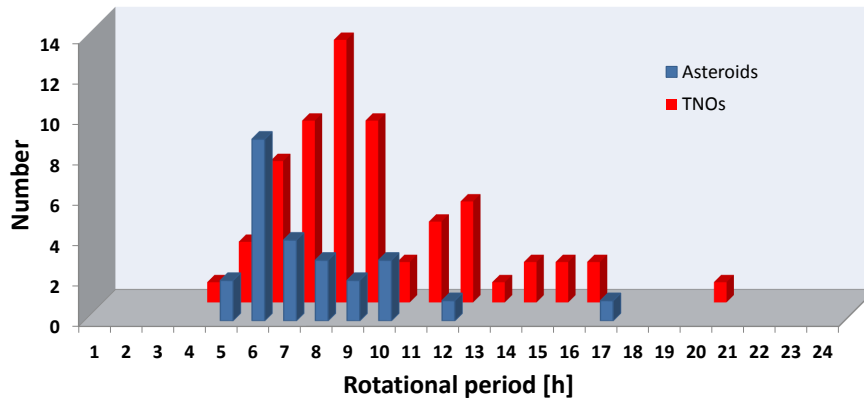
Figure 152: *Number of objects versus rotational period for asteroids and TNOs*: Distributions of two samples composed by: i) the asteroids with a diameter larger than 200 km, and with rotational period below 20 h, ii) the TNOs with a diameter larger than 200 km are plotted. In such range of parameters, the mean rotational period of the TNO sample is 7.88 h whereas the MBA sample has a mean rotational period of 6.08 h. Distributions updated in May, 2013.

ilies. They concluded that the Eos family asteroids display faster mean rotation rates and their distribution can be fit by a Maxwellian. While the Koronis family asteroids clearly display slower mean rotation rates and non-Maxwellian distribution. They suggested that the Eos family is an older family that has undergone a large degree of collisional evolution subsequent to its formation whereas the Koronis family may be relatively young and its members have not been significantly affected by subsequent collisional evolution. Based on the Haumea family distribution it is difficult to propose a clear conclusion, especially with only few members with a short-term variability study.

On the other hand, based on the Koronis and Eos family studies, Binzel et al. (1989) noted that the largest fragments of the families appear to have relatively similar rotation rates. In other words, it seems that the largest fragments may "remember" the spin rate of their parent body. The largest members of the family are 2003 OP$_{32}$, 2002 TX$_{300}$, and 2005 RR$_{43}$ with rotational periods between 4.07 h and 8.15 h. But we must point out that the Haumea family member sizes have large uncertainty (see Chapter IX). In conclusion, short-term variability studies of the family members are needed as well as size distribution of the fragments.

VII.2.5   Rotational period distribution of the binary/multiple systems

Several objects studied in this work, as well as in the literature are binary or multiple systems. Due to the presence of a companion (or several companions), tidal effects may have slow down the primaries rotational period, as well as the secondaries rotational rate. Two cases in the Trans-Neptunian belt are known to be tidally locked and synchronized: Pluto-Charon and Sila-Nunam.
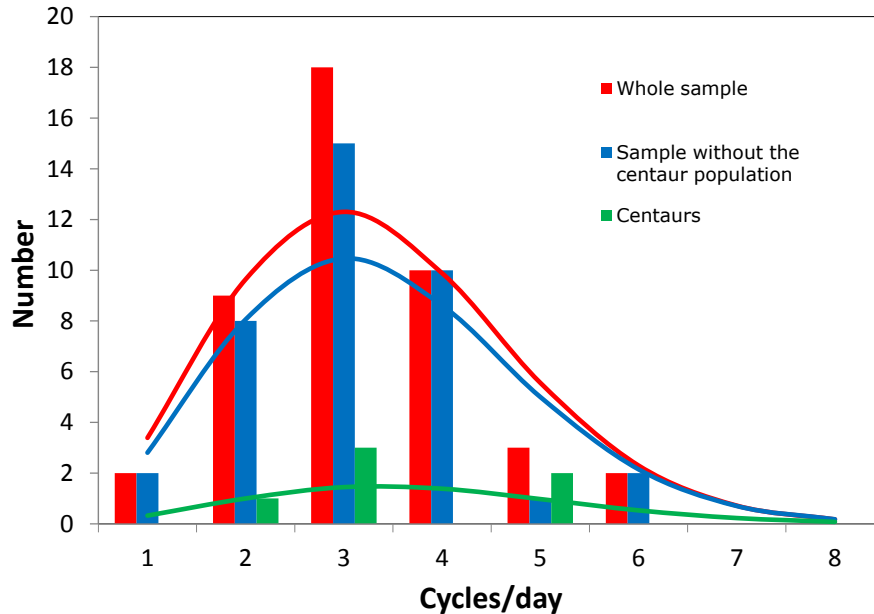
Figure 153: *Histogram in cycles/day for the three different samples: the whole sample (TNOs+centaurs), the sample without the centaur population and only the centaurs*: we plotted the distributions for three samples composed by: i) the whole sample, ii) the sample without the centaurs population, and iii) the centaurs. Only data obtained during this work are reported here. Maxwellian fits to the whole sample give a mean rotational period of 7.17 h for the whole sample, of 7.05 h for the sample without the centaur population, and 6.32 h for the centaur population alone. Distributions updated in May, 2013.

In other words, the rotational period distribution of the binary/multiple systems may be different to the others TNOs. A complete study will be dedicated to binaries in Section VIII.1.5.2.

VII.3   Spin barrier

VII.3.1   Spin barrier in the Trans-Neptunian belt

Two plots of rotational periods versus absolute magnitudes are shown in Figure 155 and Figure 156. The first plot compiles all the objects studied in this work whereas the second one shows a larger sample composed by the objects studied in this work as well as the literature data. Different symbols are used according to the dynamical classification of Gladman, Marsden and Vanlaerhoven (2008). As can be seen, no objects spin faster than 4 h. This is what we call the spin barrier.

According to Figure 155, there is only a very slight indication that objects with large absolute magnitude rotate faster. Because absolute magnitude is a proxy for size, this implies that the smaller objects rotate faster than the larger ones and that would be consistent with the usual collisional scenario in which the small objects are fragments and are more collisionally evolved than the large objects (Davis and Farinella, 1997). Since collisions tend to spin up the bodies, the faster rotation rates for the smaller objects seems to be consistent with this idea, but one should keep in mind that the small objects studied here are all centaurs and they might have suffered specific processes that could lead to spin up. Without taking into account the centaurs, the trend indicates
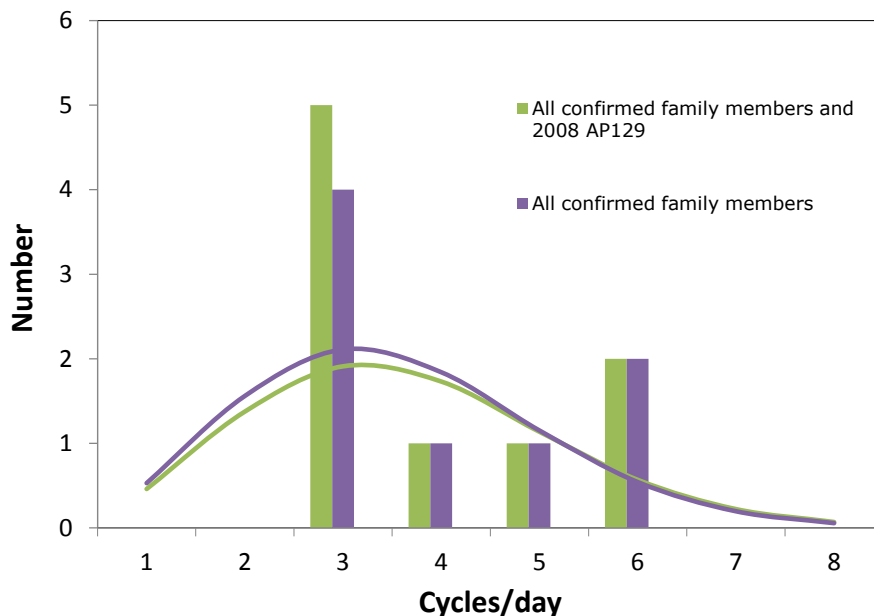
Figure 154: *Histogram in cycles/day of the Haumea family members*: The distribution of the confirmed
family members is plotted and the second distribution takes into account the non-confirmed member,
2008 AP$_{129}$. The Maxwellian distributions provide very poor fits. The Maxwellian fits to the sample com-
posed by all the confirmed members give a mean rotational period of 6.78 h, whereas including 2008 AP$_{129}$,
the mean rotational period is 6.60 h. Distributions updated in May, 2013.

that the smallest objects rotate slowly (linear fit in Figure 155). This trend is more evident in
Figure 156, where a larger sample is used.

VII.3.2   Critical rotational period and density of TNOs from the spin
barrier

Based on the sample of objects studied in this work, there is an apparent spin barrier between
3.9 h and 4 h. Based on the whole sample (literature and the sample studied in this work), such a
barrier is also confirmed. There are no objects spinning faster than this barrier. This may mean
that objects that reach this rotation rate get disrupted.

Assuming this spin barrier as the critical rotational period, one can compute the average density
of the sample. The critical period, P_c, is defined by equating the centrifugal acceleration to the
acceleration caused by gravity (see Section V.1.1.4). From that constraint, it follows that for a
spherical object without internal cohesion [2]:

$$P_c = \left(\frac{3\pi}{G\rho} \right)^{\frac{1}{2}}$$ (Equation VII.3)

---

[2]Here, we assumed that the object is a spheroidal body without internal cohesion, which is not a real case. So,
the computed density is only a crude estimation.
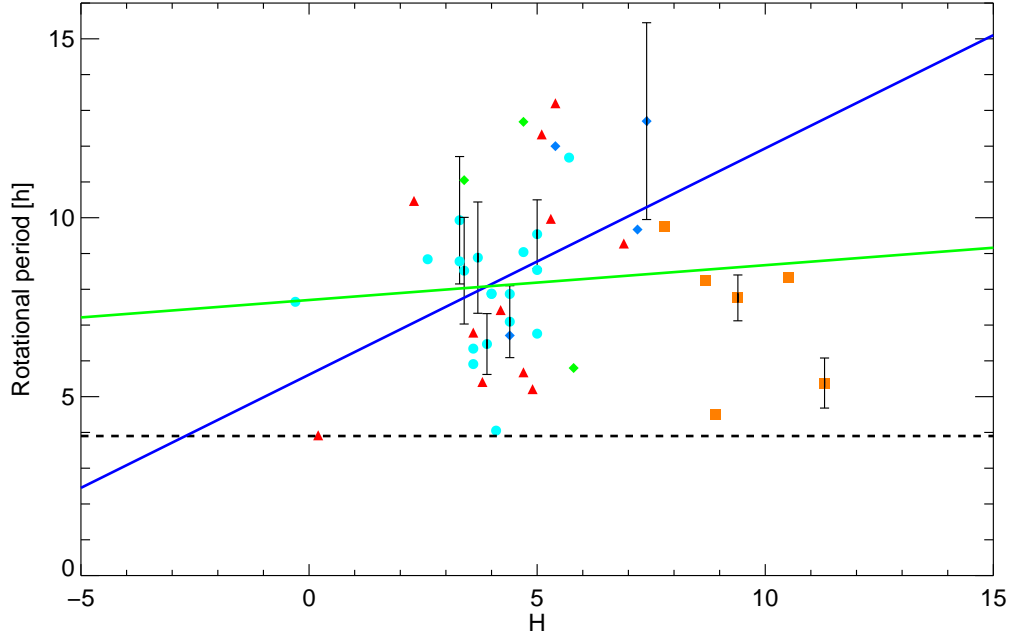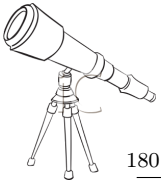
Figure 155: *Rotational period versus absolute magnitude*: In this figure are plotted all objects presented in this work. Different symbols correspond to different object classification as: orange squares for centaurs, green diamonds for detached objects, blue circles for classical objects, blue diamonds for SDOs, and red triangles for resonant objects. Dashed line defines a spin barrier. Continuous green line is a linear fit of the entire sample whereas the continuous blue line is a linear fit without taking into account the centaurs. Absolute magnitudes are from the Minor Planet Center database. Plot updated in May, 2013.

where G is the gravitational constant, and ρ is the density. Since a rotational period of 3.9 h is the critical rotational period, one can derive a density. A density of 0.72 g cm^{-3} is obtained.

Davidsson (1999); Davidsson (2001) pointed out that the critical period in Equation VII.3 is not a reliable estimate for true bodies and derived alternative expressions to Equation VII.3. According to Davidsson (1999); Davidsson (2001), the critical period (P_c^{sphere}) for a sphere with internal cohesion is:

$$P_c^{spheroidal} = \frac{\pi}{\sqrt{\frac{1}{3}\pi G\rho + \frac{S}{\rho R^2}}} \qquad \text{(Equation VII.4)}$$

where G is the gravitational constant, ρ is the density, R is the body radius, and S is the tensile strength (expressed in Pascal). Using Equation VII.4 with a tensile strength of 0.01 MPa and a body radius of 100 km, a density of 0.70 g cm^{-3} is obtained.

Davidsson (2001) also derived expressions of the critical period for oblate and prolate objects. In the case of oblate spheroid, the critical period (P_c^{oblate}) is:

$$P_c^{oblate} = \frac{\pi}{\sqrt{\frac{1}{4}G\rho A + \frac{S}{\rho R_0^2}}} \qquad \text{(Equation VII.5)}$$

where A is expressed as:

$$A = \frac{2\pi f}{(1+f^2)^{\frac{3}{2}}} \arctan\sqrt{\frac{1}{f^2} - 1} - \frac{2\pi f^2}{1 - f^2} \qquad \text{(Equation VII.6)}$$

where f is the axis ratio such that:

$$x^2 + y^2 + \left(\frac{z}{f}\right)^2 = R_0^2 \qquad \text{(Equation VII.7)}$$

where R_0 is the length of the semimajor axis, and x, y, z are the coordinated of the ellipsoid's surface. Using Equation VII.5 with a tensile strength of 0.01 MPa and a semimajor axis (R_o) of 100 km, and an axis ratio f=0.8, a density of 0.77 g cm^{-3} is calculated.

In the case of prolate spheroid, Davidsson (2001) expressed the critical period ($P_c^{prolate}$) as:

$$P_c^{prolate} = \frac{\pi}{\sqrt{\frac{1}{4}G\rho\epsilon + \frac{S}{\rho R_p^2 f^2}}} \qquad \text{(Equation VII.8)}$$

where ϵ is expressed as:

$$\epsilon = \frac{2\pi f}{(f^2 - 1)^{\frac{3}{2}}} \ln\left(\frac{f + \sqrt{f^2 - 1}}{f - \sqrt{f^2 - 1}}\right) - \frac{4\pi}{f^2 - 1} \qquad \text{(Equation VII.9)}$$

where f is the axis ratio such as:

$$x^2 + y^2 + \left(\frac{z}{f}\right)^2 = R_p^2 \qquad \text{(Equation VII.10)}$$

where R_p is the length of the semimajor axis, and x, y, z are the coordinated of the ellipsoid's surface. Using Equation VII.8 with a tensile strength of 0.01 MPa and a semimajor axis (R_p) of 100 km, and an axis ratio f=1.5, a density of 1.03 g cm^{-3} is obtained.

For a prolate spheroid, Pravec and Harris (2000) expressed the critical period (P_c) as:

$$P_c \approx 3.3\sqrt{\frac{1 + \Delta m}{\rho}} \qquad \text{(Equation VII.11)}$$

where ρ is the density, and Δm is the lightcurve amplitude, and P_c is the period in hours. Using Equation VII.11 with Δm=0.15 mag, a density of 0.82 g cm^{-3} is calculated.

VII.3.3 Spin barriers in the Trans-Neptunian and asteroid populations

In this sub-section, the spin barriers in the asteroid and TNO populations are studied. In Figure 157, all the asteroids and the TNOs with a rotational periods reported in the literature are plotted. It has been shown that asteroids with sizes from a few hundred meters up to about 10 km show a spin barrier at ∼2.2 h. In other words, such a spin barrier is interpreted as a critical spin limit for bodies in the gravity regime. Pravec and Harris (2000) showed that asteroids with a diameter (D) above 3 km are strengthless objects or are just cracked but coherent bodies, whereas a cohesionless structure is predominant for asteroids with a diameter between 0.2 to 3 km. The spin barrier disappears at diameters less than 0.2 km where most objects rotate too fast and so a cohesion is implied in the smaller asteroids (typically, in the Near Earth Asteroids (NEAs)).

At larger sizes (for D>50 km), the number of asteroids near the spin barrier at 2.2 h (blue dashed line in Figure 157) decreases and the larger asteroids seems to rotate slower. In Figure 157 are also shown the centaurs and the TNOs. One can appreciate that the largest TNOs are following a similar tendency as the asteroids. In Figure 157 is also plotted the spin barrier for the TNOs at
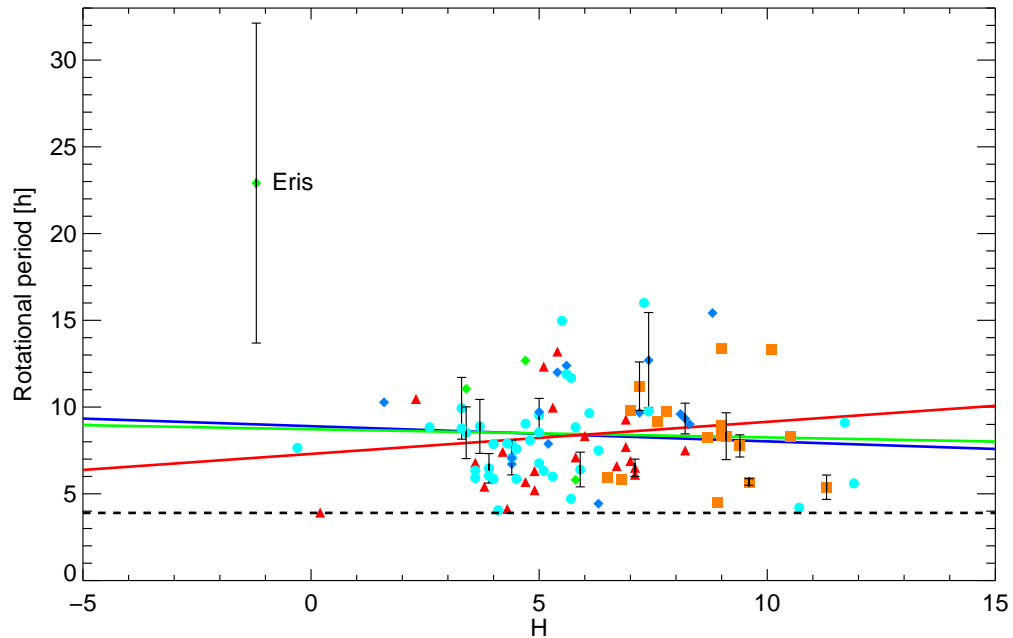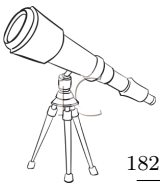
Figure 156: *Rotational period versus absolute magnitude*: In this figure are plotted all objects presented in this work as well as objects reported in the literature. Different symbols correspond to different object classification as: orange squares for centaurs, green diamonds for detached objects, blue circles for classical objects, blue diamonds for SDOs, and red triangles for resonant objects. Dashed line defines a spin barrier. Continuous green line is a linear fit of the entire sample whereas the continuous blue line is a linear fit without taking into account the centaurs. Continuous red line is a linear fit without taking into account the centaurs and Eris. Absolute magnitudes are from the Minor Planet Center database. Plot updated in May, 2013.

around 4 h (red dashed line in Figure 157).

In conclusion, the slower spin barrier of the TNOs probably indicated that the density of the TNOs is smaller that of the asteroids, which indeed should be the case of TNOs have more ices than rock.

VII.4 Density from other considerations

Density is an important parameter to understand the TNOs and centaurs. Unfortunately, densities are known for only a few objects and most of them are binary systems. In fact, when a TNO has a satellite, one can study the satellite orbit in order to measure the system mass, from the orbital period of the satellite, and if the size of the TNO is determined, one can derive the system density (see Chapter VIII). To date, only two non-binary TNOs have an "estimated" density: Varuna (Jewitt and Sheppard, 2002), and Makemake (Ortiz et al., 2012a), by other means.

Several models can be used to compute a lower limit to the density for particular objects: i) Chandrasekhar (1987) work about figures of equilibrium for fluid bodies, ii) Pravec and Harris (2000) work about prolate spheroid critical rotational period, iii) Davidsson (1999) and Davidsson (2001) work about rotational breakup of solid objects.
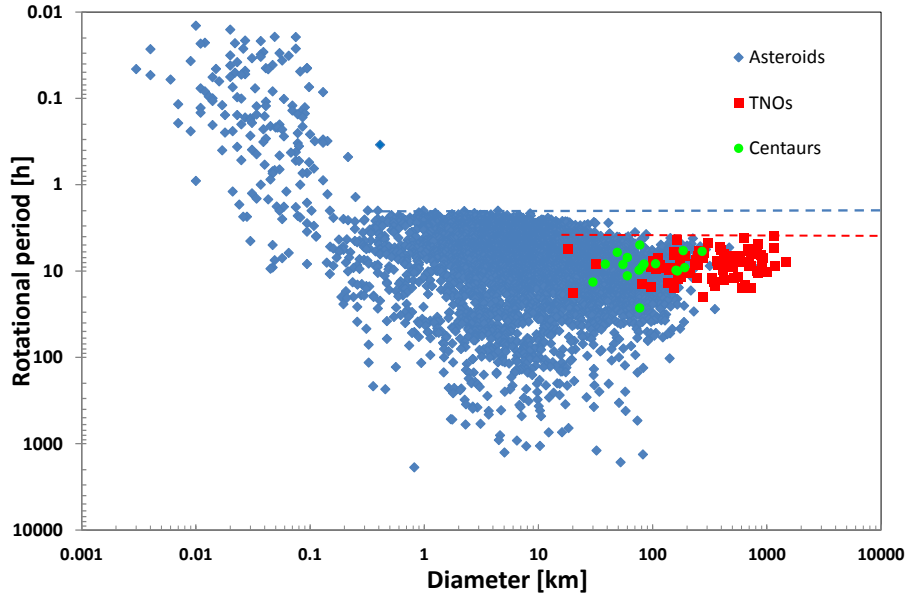
Figure 157: *Rotational period versus diameter for the asteroids, TNO and Centaur populations:* In this
figure are plotted the asteroids, centaurs, and TNOs whose short-term variability is known.The blue dashed
line is the spin barrier for the asteroid population at 2.2 h and the red dashed line is the spin barrier of the
TNO and centaur populations at 4 h presented in this work. Short-term variability of TNOs and centaurs is
reported in Table 7. The Asteroid Lightcurve Database (LCDB) has been used to obtain information about
asteroid short-term variability studies (`http://www.minorplanet.info/lightcurvedatabase.html`). Plot
updated in May, 2013.

VII.4.1   Pravec and Harris model

For a prolate spheroid, the critical period (P_{crit}) in hours is, according to Pravec and Harris (2000),
approximately:

$$P_{crit} \approx \frac{3.3}{\sqrt{\rho}} \sqrt{\frac{a}{b}} \qquad \text{(Equation VII.12a)}$$

$$\Rightarrow P_{crit} \approx 3.3 \sqrt{\frac{1 + \Delta m}{\rho}} \qquad \text{(Equation VII.12b)}$$

$$\Rightarrow \rho \approx 3.3^2 \times \frac{1 + \Delta m}{P_{crit}^2} \qquad \text{(Equation VII.12c)}$$

where Δm is the lightcurve amplitude, ρ is the density, and a/b is the axis ratio. So, this formula
takes into account two parameters obtained thanks to the lightcurve: the rotational period and
the peak-to-peak lightcurve amplitude.

The previous formula has been developed for prolate spheroids, i.e. for objects showing large
lightcurve amplitude variation. But here we will derive the density for each object studied in this
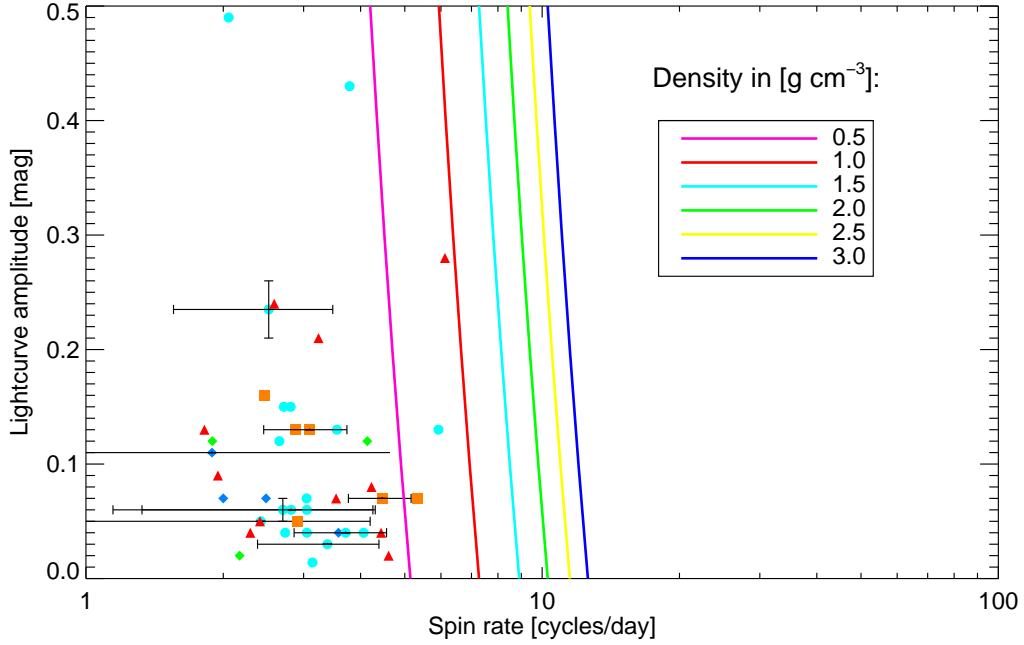
Figure 158: *Lightcurve amplitude versus rotational rate for all objects studied in this work.* All objects presented in this work are shown: turquoise circles are for classical objects, green/blue diamonds are for SDOs/DOs (respectively), red triangles are for resonant objects and orange squares are for centaurs. In the case of various rotational periods are found for the same target, we plot the average value and the corresponding error bars. Each vertical line defines a density value as indicated in the legend.

work. In Table 10 are summarized the name of the object, its rotational period and lightcurve amplitude as well as the density computed using the Equation VII.12. The mean lower limit to the density is 0.24 g cm^{-3}.

In Figure 158 the lightcurve amplitudes versus rotational frequency for all the TNOs and centaurs studied in this work are plotted. Several curves are also plotted representing the critical spin rate for bulk density of 0.5-3.0 g cm^{-3}. The majority of the objects studied in this work have a lower limits to the density of 0.5 g cm^{-3}. Only three objects, Haumea, 2003 CO$_1$, and 2003 OP$_{32}$ have a density between 0.5 and 1 g cm^{-3}. However, this is only a lower limit and thus the densities are likely higher.

VII.4.2   Davidsson model

According to Davidsson (2001), the critical period (P$_{crit}$) for an already shear fractured body can be expressed as:

$$P_{crit} = \sqrt{\frac{\pi^3}{2.8G\rho}} \qquad\qquad \text{(Equation VII.13a)}$$

$$\Rightarrow \rho = \frac{\pi^3}{2.8GP_{crit}^2} \qquad\qquad \text{(Equation VII.13b)}$$
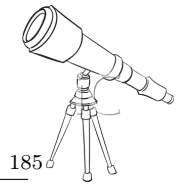
where G is the gravitational constant, and ρ is the density. This formula has been suggested by Davidsson (2001) to compute the lower limit to the density of the cometary nuclei, so it assumes a low internal cohesion for a spherical object. This formula only takes into account the rotational period of the object, and not the lightcurve amplitude as the Pravec and Harris (2000) formula.

Using the previous equation, the lower limit for the densities of all the objects studied in this work have been computed. The results are reported in Table 11. The mean lower limit to the density is 0.25 g cm^{-3}.

In conclusion, Davidsson (2001) and Pravec and Harris (2000) models supply similar values, and only allow us to derive a very crude lower limits to the densities.

Table 10: In this table, the name of the object, its rotational period and lightcurve amplitude are summarized. The lower limits to the densities have been computed based on Pravec and Harris (2000) work, for each object studied during this thesis.

Object	Rotational period [h]	Lightcurve amplitude [mag]	Density [g/cm^3]
Amycus	9.76	0.16±0.01	>0.13
Haumea	3.92	0.28±0.01	>0.91
Huya	5.21	0.02±0.01	>0.41
Makemake	7.65	0.014±0.002	>0.19
Okyrhoe	4.86 or 6.08	0.07±0.01	>0.49 or >0.32
Orcus	10.47	0.04±0.01	>0.10
Quaoar	8.839	0.112±0.001	>0.16
Salacia	6.61	0.04±0.02	>0.26
Typhon	9.67	0.07±0.01	>0.12
Varuna	6.34	0.43±0.02	>0.39
(24835) 1995 SM$_{55}$	8.08	0.05±0.02	>0.17
(15874) 1996 TL$_{66}$	12	0.07±0.02	>0.08
(26375) 1999 DE$_9$	12.33	0.09±0.03	>0.08
(40314) 1999 KR$_{16}$	5.8	0.12±0.06	>0.36
(44594) 1999 OX$_3$	9.26 or 13.4 or 15.45	0.11±0.02	>0.14 or> 0.07 or >0.05
(275809) 2001 QY$_{297}$	11.68	0.49±0.03	>0.12
(126154) 2001 YH$_{140}$	13.19	0.15±0.03	>0.07
(55565) 2002 AW$_{197}$	8.78	0.02±0.02	>0.14
(307251) 2002 KW$_{14}$	8.58 or 10.5	(0.21 or 0.26)±0.03	>0.18 or >0.12
(307261) 2002 MS$_4$	7.33 or 10.44	0.05±0.01	>0.21
(84522) 2002 TC$_{302}$	5.41	0.04±0.01	>0.39
(55636) 2002 TX$_{300}$	8.15	0.05±0.01	>0.17
(55637) 2002 UX$_{25}$	6.55	0.09±0.03	>0.28
(55638) 2002 VE$_{95}$	9.97	0.04±0.02	>0.12
(208996) 2003 AZ$_{84}$	6.78	0.07±0.01	>0.25
(120061) 2003 CO$_1$	4.51	0.06±0.01	>0.57
(120132) 2003 FY$_{128}$	8.54	0.12±0.02	>0.17
(174567) 2003 MW$_{12}$	5.91	0.02±0.01	>0.32
(120178) 2003 OP$_{32}$	4.07	0.13±0.01	>0.74
(84922) 2003 VS$_2$	7.4208	0.224±0.013	>0.24
(136204) 2003 WL$_7$	8.24	0.04±0.01	>0.17
2004 NT$_{33}$	7.87	0.04±0.01	>0.18
(144897) 2004 UX$_{10}$	5.68	0.09±0.02	>0.35
(230965) 2004 XA$_{192}$	7.88	0.07±0.02	>0.19
(308193) 2005 CB$_{79}$	6.76	0.05±0.02	>0.25
(145451) 2005 RM$_{43}$	6.71	0.05±0.01	>0.25
(145452) 2005 RN$_{43}$	5.62 or 7.32	0.04±0.01	>0.35 or >0.21
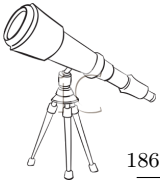
Table 10: continued.

Object	Rotational period [h]	Lightcurve amplitude [mag]	Density [g/cm^3]
(145453) 2005 RR$_{43}$	7.87	0.06±0.01	>0.19
(145480) 2005 TB$_{190}$	12.68	0.12±0.01	>0.08
(145486) 2005 UJ$_{438}$	8.32	0.11±0.01	>0.17
(202421) 2005 UQ$_{513}$	7.03 or 10.01	0.05±0.02	>0.23 or >0.11
(341520) 2007 TY$_{430}$	9.28	0.24±0.05	>0.16
(25012) 2007 UL$_{126}$ or 2002 KY$_{14}$	7.12 or 8.4	0.11±0.01	>0.24 or >0.17
(229762) 2007 UK$_{126}$	11.05	0.03±0.01	>0.09
(315530) 2008 AP$_{129}$	9.04	0.12±0.02	>0.15

Table 11: In this table, the name of the object, its rotational period and lightcurve amplitude are summarized. The crude lower limits to the density have been computed for each object reported here based on Davidsson (2001) formula for spheroidal objects.

Object	Rotational period [h]	Lightcurve amplitude [mag]	Density [g/cm^3]
Amycus	9.76	0.16±0.01	>0.13
Haumea	3.92	0.28±0.01	>0.83
Huya	5.21	0.02±0.01	>0.47
Makemake	7.65	0.014±0.002	>0.22
Okyrhoe	4.86 or 6.08	0.07±0.01	>0.54 or >0.35
Orcus	10.47	0.04±0.01	>0.12
Quaoar	8.839	0.112±0.001	>0.16
Salacia	6.61	0.04±0.02	>0.29
Typhon	9.67	0.07±0.02	>0.14
Varuna	6.34	0.43±0.02	>0.32
(24835) 1995 SM$_{55}$	8.08	0.05±0.02	>0.19
(15874) 1996 TL$_{66}$	12	0.07±0.02	>0.09
(26375) 1999 DE$_9$	12.33	0.09±0.03	>0.08
(40314) 1999 KR$_{16}$	5.8	0.12±0.06	>0.38
(44594) 1999 OX$_3$	9.26 or 13.4 or 15.45	0.11±0.02	>0.15 or >0.07 or >0.05
(275809) 2001 QY$_{297}$	11.68	0.49±0.03	>0.09
(126154) 2001 YH$_{140}$	13.19	0.15±0.03	>0.07
(55565) 2002 AW$_{197}$	8.78	0.02±0.02	>0.17
(307251) 2002 KW$_{14}$	8.58 or 10.5	(0.21 or 0.26)±0.03	>0.17 or >0.12
(307261) 2002 MS$_4$	7.33 or 10.44	0.05±0.01	>0.24 or >0.12
(84522) 2002 TC$_{302}$	5.41	0.04±0.01	>0.44
(55636) 2002 TX$_{300}$	8.15	0.05±0.01	>0.19
(55637) 2002 UX$_{25}$	6.55	0.09±0.03	>0.30
(55638) 2002 VE$_{95}$	9.97	0.04±0.02	>0.13
(208996) 2003 AZ$_{84}$	6.78	0.07±0.01	>0.28
(120061) 2003 CO$_1$	4.51	0.06±0.01	>0.63
(120132) 2003 FY$_{128}$	8.54	0.12±0.02	>0.18
(174567) 2003 MW$_{12}$	5.91	0.02±0.01	>0.37
(120178) 2003 OP$_{32}$	4.07	0.13±0.01	>0.77
(84922) 2003 VS$_2$	7.4208	0.224±0.013	>0.23
(136204) 2003 WL$_7$	8.24	0.04±0.01	>0.19
2004 NT$_{33}$	7.87	0.04±0.01	>0.21
(144897) 2004 UX$_{10}$	5.68	0.09±0.02	>0.40
(230965) 2004 XA$_{192}$	7.88	0.07±0.02	>0.21
(308193) 2005 CB$_{79}$	6.76	0.05±0.02	>0.28
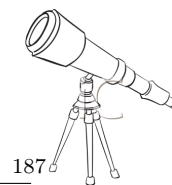
Table 11: continued.

Object	Rotational period [h]	Lightcurve amplitude [mag]	Density [g/cm^3]
(145451) 2005 RM$_{43}$	6.71	0.05±0.01	>0.28
(145452) 2005 RN$_{43}$	5.62 or 7.32	0.04±0.01	>0.41 or >0.24
(145453) 2005 RR$_{43}$	7.87	0.06±0.01	>0.21
(145480) 2005 TB$_{190}$	12.68	0.12±0.01	>0.08
(145486) 2005 UJ$_{438}$	8.32	0.11±0.01	>0.19
(202421) 2005 UQ$_{513}$	7.03 or 10.01	0.05±0.02	>0.26 or >0.13
(341520) 2007 TY$_{430}$	9.28	0.24±0.05	>0.15
(25012) 2007 UL$_{126}$ or 2002 KY$_{14}$	7.12 or 8.4	0.11±0.01	>0.25 or >0.18
(229762) 2007 UK$_{126}$	11.05	0.03±0.01	>0.10
(315530) 2008 AP$_{129}$	9.04	0.12±0.02	>0.16

VII.4.3 Densities of binary/multiple systems for more direct measurements

True densities are relatively well known for only a handful of TNOs, and in all those cases the densities were obtained because the TNO was binary or had a satellite that could be resolved and its orbital period measured. In case of binary systems it is possible to estimate the mass from the mutual orbit. The total mass (M_{sys}) of a binary system can be expressed as:

$$M_{sys} = \frac{4\pi^2 a^3}{GT^2}$$

(Equation VII.14)

where G is the gravitational constant, a is the semi-major axis, and T is the orbital period. For instance, densities are obtained using the mass divided by a guessed volume. The volume is guessed because the diameter is obtained assuming an average albedo that allows us to obtain the radius of the body from its brightness. In several cases the diameters are known to a good accuracy and those cases are shown in Figure 159. For these bodies the densities are reliable.

In Figure 159, we focused on the density estimation versus the primary diameter. Only the binary population has been considered in a first step. The binary sample has been divided into three groups according to their sizes: the biggest objects with an absolute magnitude lower than 2, the smallest objects with an absolute magnitude higher than 5, and finally the intermediate objects with an absolute magnitude between 2 and 5.

The sample composed by the largest objects: Pluto, Charon, Eris, and Haumea has a mean density of 2.29 g cm^{-3}. The sample of intermediate size objects is composed by: Salacia, and Orcus with a mean density of 1.46 g cm^{-3} for this group. The sample with the smallest objects is composed by: Sila, Altjira, Teharonhiawako, Typhon, Ceto, 2001 XR$_{254}$, 2001 QY$_{297}$, 1999 TC$_{36}$ and 1998 SM$_{165}$ has a mean density of 0.55 g cm^{-3} for this group.

There are only few binary systems with a density estimation but, a clear trend is identified. As previously noted in Sheppard, Lacerda and Ortiz (2008), we confirmed that biggest (smallest) objects have a higher (lower) density. To date, there are only two non-binary objects with a density estimation: Varuna (Jewitt and Sheppard, 2002), and Makemake (Ortiz et al., 2012a). These two objects seem to follow the trend previously mentioned. The mean densities, including the two non-binary objects, are 2.18 g cm^{-3} and 1.07 g cm^{-3} for sample with the largest objects and for the intermediate size objects group, respectively.
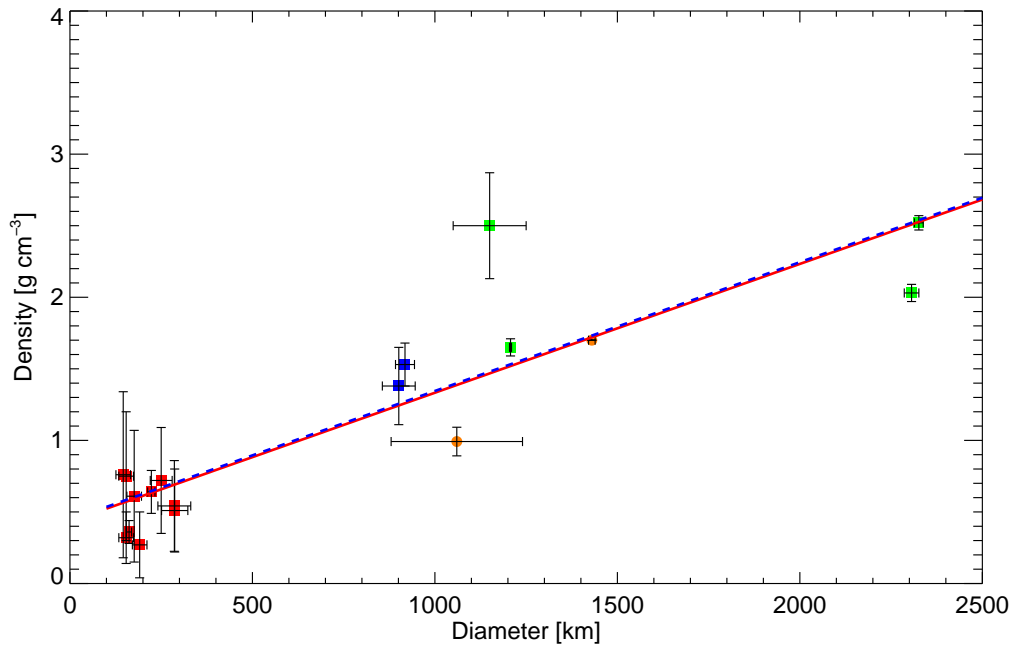
Figure 159: *Density versus diameter:* Green squares for binary/multiple objects with an absolute magnitude lower than ∼2, blue squares for objects with an absolute magnitude between ∼2 and 5, red squares for objects with an absolute magnitude higher than 5. Absolute magnitudes are from the Minor Planet Center (MPC) database. Quaoar/Weywot density estimated in Fraser and Brown (2010); Fraser et al. (2013) differs from the one derived by Braga-Ribas et al. (2013). We did not consider Quaoar in our study. The dashed blue line is a linear fit for the BTNOs. The orange circles are for two non-binary TNOs: Varuna and Makemake. The continuous red line is a linear fit considering the binary and not-binary populations, altogether. Density/diameter estimations are from this work and from: Fornasier et al. (2013), Vilenius et al. (2013), Vilenius et al. (2012), Santos-Sanz et al. (2012), Stansberry et al. (2012), Grundy et al. (2012), Sicardy et al. (2011), Benecchi et al. (2010), Brown et al. (2010), Buie et al. (2006), Rabinowitz et al. (2006), Spencer et al. (2006), Jewitt and Sheppard (2002), Ortiz et al. (2012a).

VII.4.4   Hydrostatic equilibrium. Jacobi ellipsoid and MacLaurin spheroid: Chandrasekhar's work

According to Chandrasekhar (1987) study of figures of equilibrium for fluid bodies, one can estimate lower limits for densities from rotational periods and the lower limits to the elongation of the objects. That is to say, assuming that a given TNO is a triaxial ellipsoid (also known as Jacobi ellipsoid) in hydrostatic equilibrium, one can compute a lower limit to the density. This study is summarized in Figure 160 where all objects presented in this work have been plotted. The vertical lines represent the locus of rotating ellipsoids in hydrostatic equilibrium with densities between 200 kg m^{-3} to 3000 kg m^{-3} (Chandrasekhar, 1987). We must emphasize that such a study is assuming that TNOs and centaurs are in hydrostatic equilibrium, but we do not know if such objects are in hydrostatic equilibrium.

In the sample of objects studied in this work, only seven bodies have a high amplitude lightcurve (>0.15 mag) and can be assumed to be Jacobi ellipsoids: 2001 QY$_{297}$, 2002 KW$_{14}$, 2003 VS$_2$, 2007 TY$_{430}$, Haumea, Amycus and, Varuna. 2001 QY$_{297}$ has a very low density if it is in hydrostatic equilibrium, 2003 VS$_2$, and 2002 KW$_{14}$ seem to have a density between 0.5 and 1 g cm^{-3}. Haumea has a high density higher than 2.5 g cm^{-3}, whereas Varuna has a density near 1 g cm^{-3}.
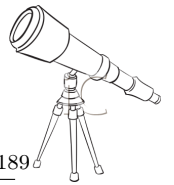
2007 TY$_{430}$ has a low density around 0.5 g cm^{-3}. The lower limit for the densities of these six bodies, assuming a viewing angle of 60°, and assuming an equatorial view have been computed using Equation V.37. The results are reported in Table 12.
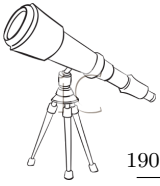
Table 12: In this table, the name of the object, its rotational period (Rot. per.) and lightcurve amplitude (Lightcurve ampl.) are summarized. The lower limit to the density has been computed for each object based on Chandrasekhar (1987) work, assuming a viewing angle of 60° and an equatorial view (viewing angle of 90°). As mentioned in the discussion, this model is assuming that object are in hydrostatic equilibrium and are triaxial (Jacobi). In this table, the lower limit density for the MacLaurin spheroids studied in this work is also reported but one has to keep in mind those densities based on assumption that do not hold.

Jacobi or MacLaurin	Object	Rot. per. [h]	Lightcurve ampl. [mag]	Density Eq. view [g cm^{-3}]	Density $\xi=60°$ [g cm^{-3}]
Jacobi	Amycus	9.76	0.16±0.01	>0.41	>0.42
	Haumea	3.92	0.28±0.01	>2.59	>2.69
	Varuna	6.34	0.43±0.02	>1.03	>1.08
	(275809) 2001 QY$_{297}$	11.68	0.49±0.03	>0.31	>0.33
	(307251) 2002 KW$_{14}$	8.58 or 10.5	(0.21 or 0.26)±0.03	>0.53 or >0.36	>0.55 or >0.37
	(341520) 2003 VS$_2$	7.42	0.224±0.013	>0.72	>0.74
	(341520) 2007 TY$_{430}$	9.28	0.24±0.05	>0.46	>0.47
MacLaurin	Huya	5.21	0.02±0.01	>1.43	>1.44
	Makemake	7.65	0.014±0.002	>0.66	>0.67
	Okyrhoe	4.86 or 6.08	0.07±0.01	>1.78 or >1.05	>1.80 or >1.07
	Orcus	10.47	0.04±0.01	0.35	>0.36
	Quaoar	8.839	0.112±0.001	0.50	>0.51
	Salacia	6.61	0.04±0.02	0.89	>0.90
	Typhon	9.67	0.07±0.02	0.42	>0.42
	(24835) 1995 SM$_{55}$	8.08	0.05±0.02	>0.60	>0.60
	(15874) 1996 TL$_{66}$	12	0.07±0.02	>0.27	>0.27
	(26375) 1999 DE$_9$	12.33	0.09±0.03	>0.26	>0.26
	(40314) 1999 KR$_{16}$	5.8	0.12±0.06	>1.16	>1.18
	(44594) 1999 OX$_3$	9.26 or 13.4 or 15.45	0.11±0.02	>0.45 or >0.22 or >0.16	>0.46 or >0.22 or >0.17
	(126154) 2001 YH$_{140}$	13.19	0.15±0.03	>0.22	>0.23
	(55565) 2002 AW$_{197}$	8.78	0.02±0.02	>0.50	>0.51
	(307261) 2002 MS$_4$	7.33 or 10.44	0.05±0.01	>0.72 or >0.36	>0.73 or >0.36
	(84522) 2002 TC$_{302}$	5.41	0.04±0.01	>1.33	>1.34
	(55636) 2002 TX$_{300}$	8.15 or 11.7	0.05±0.01	>0.59 or >0.28	>0.59 or >0.29
	(55637) 2002 UX$_{25}$	6.55	0.09±0.03	>0.91	>0.92
	(55638) 2002 VE$_{95}$	9.97	0.04±0.02	>0.39	>0.40
	(208996) 2003 AZ$_{84}$	6.78	0.07±0.01	>0.85	>0.86

Table 12: continued.

| Object | Rot. per. | Lightcurve ampl. | Density Eq. view | Density $\xi=60^o$ |
	[h]	[mag]	[g cm^{-3}]	[g cm^{-3}]
(120061) 2003 CO$_1$	4.51	0.06±0.01	>1.91	>1.94
(120132) 2003 FY$_{128}$	8.54	0.12±0.02	>0.53	> 0.55
(174567) 2003 MW$_{12}$	5.91	0.02±0.01	>1.11	>1.12
(120178) 2003 OP$_{32}$	4.07	0.13±0.01	>2.36	>2.41
(136204) 2003 WL$_7$	8.24	0.04±0.01	>0.57	>0.58
2004 NT$_{33}$	7.87	0.04±0.01	>0.63	>0.63
(144897) 2004 UX$_{10}$	5.68	0.09±0.02	>1.21	>1.23
(230965) 2004 XA$_{192}$	7.88	0.07±0.02	>0.63	>0.64
(308193) 2005 CB$_{79}$	6.76	0.05±0.02	>0.85	>0.86
(145451) 2005 RM$_{43}$	6.71	0.05±0.01	>0.86	>0.87
(145452) 2005 RN$_{43}$	5.62 or 7.32	0.04±0.01	>1.23 or >0.73	>1.24 or >0.73
(145453) 2005 RR$_{43}$	7.87	0.06±0.01	>0.63	>0.64
(145480) 2005 TB$_{190}$	12.68	0.12±0.01	>0.24	>0.25
(145486) 2005 UJ$_{438}$	8.32	0.11±0.01	>0.56	>0.57
(202421) 2005 UQ$_{513}$	7.03 or 10.01	0.05±0.02	>0.79 or >0.39	>0.80 or >0.39
(25012) 2007 UL$_{126}$	7.12 or 8.4	0.11±0.01	>0.77 or >0.55	>0.78 or >0.56
or 2002 KY$_{14}$				
(229762) 2007 UK$_{126}$	11.05	0.03±0.01	>0.32	>0.32
(315530) 2008 AP$_{129}$	9.04	0.12±0.02	>0.48	>0.49

Jacobi
or
MacLaurin
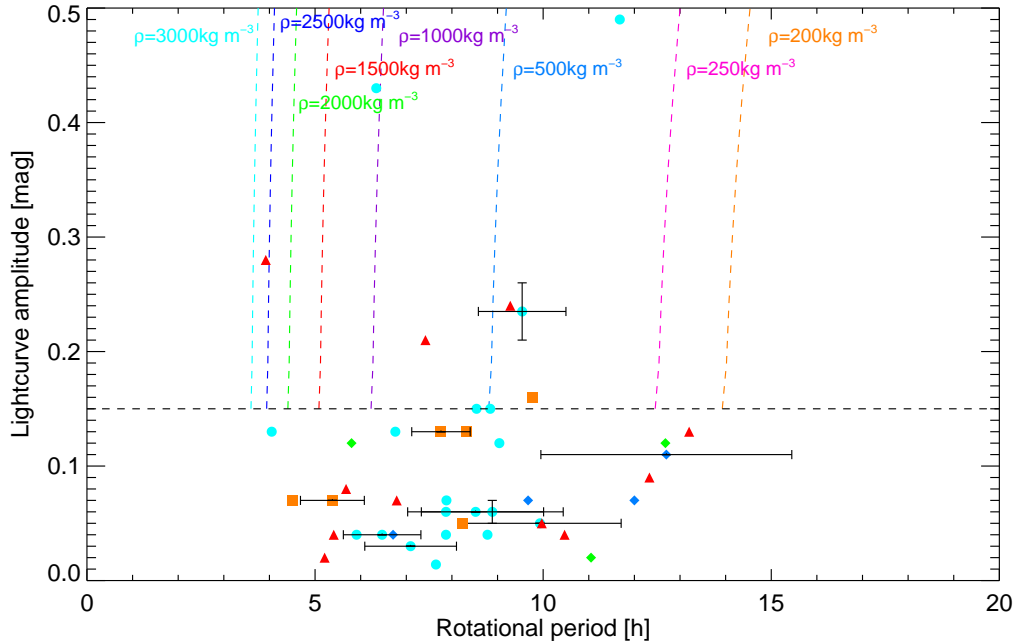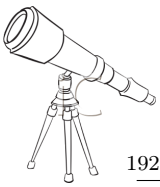
Figure 160: *Lightcurve amplitude versus rotational period for theoretical Jacobi ellipsoids of various densities compared with observations.* All objects presented in this work are shown: turquoise circles are for classical objects, green/blue diamonds are for SDOs/DOs (respectively), red triangles are for resonant objects and orange squares are for centaurs. In the case of various rotational periods are found for the same target, we plot the average value and the corresponding error bars. Horizontal line defines the separation between shape and albedo dominated lightcurves as in the previous plot. Each vertical dash line defines a density (ρ) value. Density values are indicated on the top of each line. This study assumes that TNOs are in hydrostatic equilibrium. The black dash line, at Δm=0.15 mag, is indicating the separation between the shape and albedo-dominated lightcurves.

Most of the targets studied in this work have low-amplitude lightcurves, probably due to albedo differences on their surface. So, they are probably MacLaurin spheroids and the previous study on lower limit densities cannot be applied. In fact, most objects are far from the theoretical curves for acceptable values for the density which indicates that those objects are likely MacLaurin spheroids or that the hydrostatic equilibrium assumption does not hold (Figure 160). The theoretical curves in Figure 160 have been obtained thanks to Chandrasekhar (1987) (see Section V.1.2.1).

However, in Table 12 are also reported the lower limits to the density for the MacLaurin spheroids. As already mentioned, such study is only for triaxial object in hydrostatic equilibrium, so one has to keep in mind that derived densities for MacLarin spheroids are mere academic calculations.

Lower limits to densities range from 0.22 g cm^{-3} for 2001 YH$_{140}$ to 2.59 g cm^{-3} for Haumea (considering an equatorial view in both cases). In other words, 2001 YH$_{140}$ would adopt a Jacobi shape if its density is at least 0.22 g cm^{-3}. The average lower limits to the density is 0.80 g cm^{-3}, and 0.83 g cm^{-3} for the Jacobi ellipsoids assuming an equatorial view and a viewing angle of 60° (respectively). The average density is 0.73 g cm^{-3}, and 0.74 g cm^{-3} for the MacLaurin spheroids assuming an equatorial view and a viewing angle of 60° (respectively). The average density is 0.74 g cm^{-3}, and 0.75 g cm^{-3} for the MacLaurin spheroids and Jacobi ellipsoids altogether assuming an equatorial view and a viewing angle of 60° (respectively). We must point out that the average
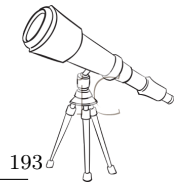
densities computed here are similar to the densities computed in Section VII.3 for the spin barrier.

In conclusion, Chandrasekhar (1987) model is probably the best option to estimate the lower limit of the density. However, such a model can only be applied to Jacobi objects in hydrostatic equilibrium.

VII.4.5   Comparison of densities derived from lightcurves with the well-known densities of binaries

From the spin barrier we derive a typical density for the TNOs of around 0.7 and 0.8 g cm^{-3} depending on various assumptions, but in all cases we assume little or no cohesion. This is what we expect for rubble pile objects or highly fractured objects, or even objects whose interiors are fluid-like.

These densities are similar to those directly obtained for binaries whose masses and volumes have been determined so accurate densities were obtained. These are summarized in Figure 159 where a plot of densities as a function of size is shown. Because the average diameter of the objects in our sample is around 500 to 700 km, and the density from the linear fit to that diameter in Figure 159 corresponds to densities of around 0.8 to 1 g cm^{-3}, it appears that the density determined from the spin barrier is not far from the reality, so the underlying assumptions on the internal structure of the TNOs, seem correct. In other words, the TNOs in general behave like rubble piles or fluid-like objects, so it appears that hydrostatic equilibrium is met, and therefore the figures of equilibrium formalism from Chandrasekhar (1987) should be valid. Here we have applied that formalism to the study of a few objects that could potentially be Jacobi objects, from which densities could be obtained, and the average densities were 0.9 g cm^{-3}.

However, the approach of studying just a few objects that seem to be Jacobi (only 7 objects) does not fully exploit the figures of equilibrium formalism, because we left the MacLaurin objects, that seem to be the most numerous. There is a way to take full advantage of our knowledge of hydrostatic equilibrium and the database on rotation properties. In Duffard et al. (2009) we presented a model that uses a Maxwellian rotational frequency distribution such as that obtained previously in this work. The model generates a set of 100,000 objects and each object is randomly assigned to a rotation period from the distribution. All objects are assumed to be in hydrostatic equilibrium with a fixed density. Lightcurve amplitude is only a result of the shape of the body and inclination of its rotation axis (randomly chosen). The body shapes are computed using Chandrasekhar (1987) equations. In other words, Jacobi ellipsoids produce a non-flat lightcurve whereas MacLaurin spheroids generate a flat lightcurve. One of the results of this model is that we have to expect for a fixed density of 1000 kg m^{-3}, 55.63% of MacLaurin spheroids and only 12.61% of Jacobi ellipsoids. The remaining 31.75% are non-equilibrium figures that were discarded from the sample. For a density of 1500 kg m^{-3}, only 11.92% are Jacobi ellipsoids and 72.31% are MacLaurin spheroids. When the density increases, the percentage of MacLaurin spheroids increases too. The percentage of Jacobi ellipsoids has a maximum close to densities of 1200-1300 kg m^{-3}.

With the new sample of amplitudes and rotation periods obtained in this thesis and the literature, the percentage of low amplitude lightcurves has increased compared to the values used in Duffard et al. (2009), which, according to Figure 6 of that work would mean that the average density of the TNOs would be slightly larger than 1.1 g cm^{-3}, but because the average spin rate has decreased compared to the values used in Duffard et al. (2009), the percentage of MacLaurin objects increases considerably. Taking both factors into account, an average density of around 1.0 g cm^{-3} seems more appropriate. This value is in agreement with the density obtained in the linear fit of Figure 159 for average objects of 700 km diameter.

In summary, the figures of equilibrium formalism is a good approximation for the shapes of the TNOs and reproduces all the rotational properties observed thus far. On the other hand, the resulting density is confirmed with independent methods.
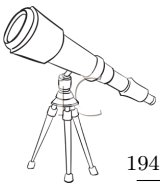
VII.5   Internal structure

VII.5.1   Porosity

The density of an object depends on its internal composition. In the previous section, lower limits to the density for all the objects studied during this work were presented. Only a few objects, and essentially binary systems, have a measured density (see Section VII.4.3). Several objects, like Varuna have a density around 1 g/cm^3 despite its relatively large size, but even lower densities are reported for other objects. To explain the very low densities, $\lesssim 1$ g/cm^3, it is helpful to consider the concept of porosity. For example, Jewitt and Sheppard (2002) suggested that the low density of Varuna is due to porosity. Some objects have a higher density $\gg 1$ g/cm^3, which suggests that they are primarily composed of rock and ice. Objects of a high density and large diameter might have a core of rock and a mantle of ice. Lacerda, Jewitt and Peixinho (2008) proposed that the high density of Haumea is consistent with this body being the core of a large differentiated body whose interior became exposed.
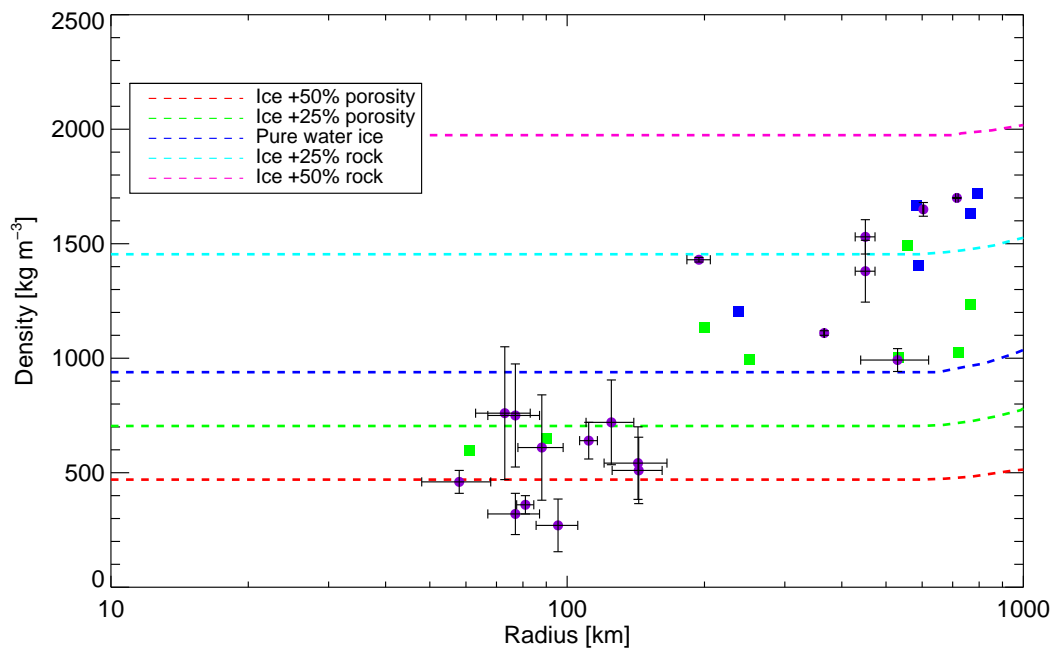
Figure 161: *Radius and densities of TNOs, Saturn and Uranus satellites*: purple circles are for TNOs, green squares for Uranus satellites, and blue squares for Saturn satellites. Several lines are overplotted to show the expected bulk density with size of a pure water ice sphere, and with porosity and rock (Lupo and Lewis, 1979). Density estimations are from: Thirouin et al. (2013b), Vilenius et al. (2013), Santos-Sanz et al. (2012), Stansberry et al. (2012), Grundy et al. (2012), Sicardy et al. (2011), Benecchi et al. (2010), Brown et al. (2010), Buie et al. (2006), Rabinowitz et al. (2006), Spencer et al. (2006), Jewitt and Sheppard (2002), Ortiz et al. (2012a). Figure updated from Sheppard and Jewitt (2002).

Figure 161 is an update of Figure 18 in Sheppard and Jewitt (2002). One can realize that the TNOs are following the same trend as outer icy bodies, like the Saturn and Uranus satellites. As previously noted in Sheppard and Jewitt (2002), we confirmed that biggest (smallest) objects

have a higher (lower) density (Figure 161). The biggest objects have a mean density above 2 g
cm^{-3} which implies a rock/water ice ratio of 70/30. The intermediate-sized objects have densi-
ties above 1 g cm^{-3}. This suggests that these objects are essentially composed by ice with some
denser material. The small objects have densities less than 1 g cm^{-3}, and likely have some internal
porosity/macro-porosity (Jewitt and Sheppard, 2002).

VII.5.2 Material strength

It is pertinent to assess whether the hydrostatic equilibrium assumption can be applicable to the
objects in our sample. Tancredi and Favre (2008) addressed the issue of the minimum diame-
ter needed for an object so that its mass can overcome the rigid body forces and thus adopt a
hydrostatic equilibrium shape to become a dwarf planet. The definition of "dwarf planet" was
introduced during the General Assembly of the International Astronomical Union (IAU) in 2006,
and the resolutions states that: *A planet is a celestial body that a) is in orbit around the Sun, b)
has sufficient mass for its self-gravity to overcome rigid body forces so that it assumes a hydrostatic
equilibrium (nearly round) shape, and c) has cleared the neighborhood around its orbit.*
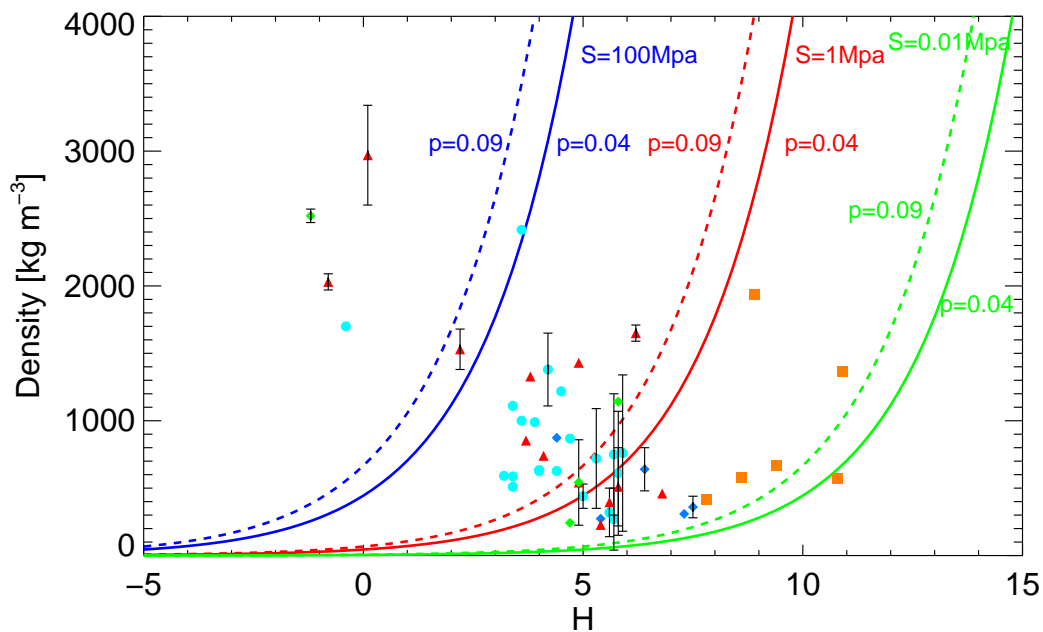
Figure 162: *Material strength of TNOs, and centaurs*: Density versus the absolute magnitude for several
objects whose densities, as well as lower limit of the density, have been estimated. The curves of density
above which hydrostatic equilibrium as function of absolute magnitude are overplotted. Data without error
bars are only a lower limit of the density (see Section VII.4.4). Density estimations with error bars are
from: Thirouin et al. (2013b), Vilenius et al. (2013), Santos-Sanz et al. (2012), Stansberry et al. (2012),
Grundy et al. (2012), Sicardy et al. (2011), Benecchi et al. (2010), Brown et al. (2010), Buie et al. (2006),
Rabinowitz et al. (2006), Spencer et al. (2006), Jewitt and Sheppard (2002), Ortiz et al. (2012a). Different
symbols correspond to different object classification as: orange squares for centaurs, green diamonds for
detached objects, blue circles for classical objects, blue diamonds for SDOs, and red triangles for resonant
objects.

As mentioned by Tancredi and Favre (2008), different criteria can be used to estimate the
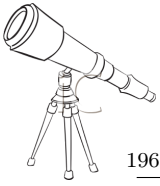
condition when a self-gravitating body overcomes the material strength, i.e.:

- Case A: the central pressure is higher than the material strength (Cole, 1984).

- Case B: the material strength is high enough to sustain the local gravitational stress caused by a topographic change (Johnson and McGetchin, 1973).

- Case C: the plastic deformation that transforms an irregular shape into an equilibrium ellipsoid occurs if the differential stress is higher than the yield strength of the material (Slyuta and Voropaev, 1997).

By integrating the hydrostatic differential equation with various assumptions one arrives at several expressions that relate the critical radius (R_{crit}) for a self-gravitating body, the density (ρ), and the material strength (S). These equations can be collectively expressed as in Tancredi and Favre (2008):

$$R_{crit}\,\rho = \sqrt{\frac{3\alpha^2 S}{2\pi G}} \qquad \text{(Equation VII.15)}$$

where α can take several values according to the different criteria used (and ranges from $\alpha=1$ in the most simplistic case (Case A), to $\alpha = 5^{\frac{1}{2}}$ for a spherical body in more realistic cases (Cases B and C)). The material strength (S) shows a wide range of values: 1-10 MPa for water ice at temperatures just below freezing (Petrovic, 2003), or 100-200 MPa for terrestrial rocks (Thomas, 1989). But there are estimated of much lower tensile strengths for comets.

On the other hand, one can express the size of a body using its V-band albedo (p_v), absolute magnitude (H_v) in the V-band, and the magnitude of the Sun (V_{sun}). The diameter (D) is expressed in Russell (1916) as:

$$D = 2\sqrt{\frac{2.24\ 10^{16}\ 10^{0.4(V_{sun}-H_v)}}{p_v}} \qquad \text{(Equation VII.16)}$$

Therefore, one can express the condition for hydrostatic equilibrium in terms of H, density, albedo and strength.

The density of all the objects as a function of the H parameter is shown in Figure 162. In this plot, all the binary/multiple systems with a reported density, as well as all the Jacobi ellipsoids and MacLaurin spheroids studied in this work are indicated. In Figure 162, the curves of density above which hydrostatic equilibrium is met, as a function of the absolute magnitude are plotted. We considered three values of material strength: 0.01, 1, and 100 MPa. We chose two albedos values: 0.04 and 0.09. Such curves have been plotted using the Equation VII.15. The first noticeable feature is that the centaurs require a much lower material strength to be in hydrostatic equilibrium while TNOs may have more internal cohesion. In other words, if the centaurs are in hydrostatic equilibrium (which may not be the case), they require a very low tensile strength. On the other hand, TNOs require a higher material strength to be in hydrostatic equilibrium. Largest objects, such as Pluto, Eris, are probably in hydrostatic equilibrium, and require high material strength, typically higher than 100 Mpa.

Assuming that TNOs and centaurs have been formed from similar materials, one can expect that both populations require a similar material strength.

VII.6   Lightcurve amplitudes

VII.6.1   Lightcurve amplitude versus absolute magnitude

Two plots of lightcurve amplitudes versus absolute magnitudes are shown in Figure 163 and Figure 164. The first plot compiles all the objects studied in this work whereas the second one shows a

larger sample composed by the objects studied in this work as well as the literature data. Different symbols are used according to the dynamical classification of Gladman, Marsden and Vanlaerhoven (2008).
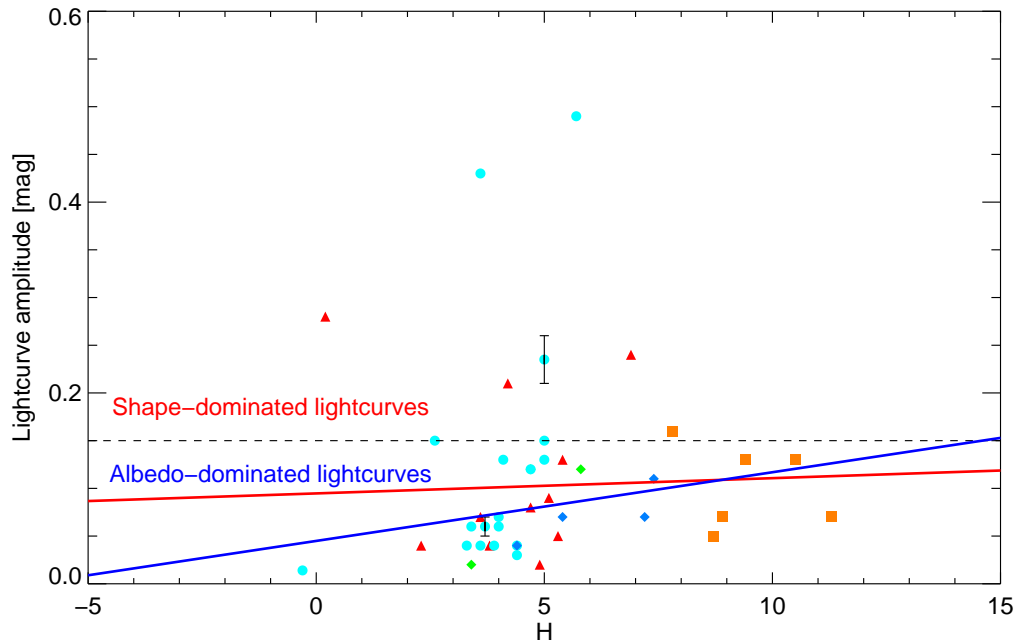
Figure 163: *Lightcurve amplitude versus absolute magnitude*: Amplitudes reported in this dissertation are plotted. Only amplitudes reported with a rotational period are taking into account. The legend of this plot is: orange squares are for centaurs, green diamonds for detached objects, blue circles for classical objects, blue diamonds for SDOs, and red triangles for resonant objects. The dash line, at Δm=0.15 mag, is indicating the likely separation between the shape and albedo-dominated lightcurves. The continuous red line is a linear fit considering the entire sample, whereas the continuous blue line is a linear fit of the entire sample without Haumea, Varuna and 2001 QY_{297}. Absolute magnitudes are from the Minor Planet Center database.

In Figure 163, the peak-to-peak lightcurve amplitudes versus the absolute magnitudes of only the objects of Chapter VI are plotted. One can appreciate that the majority of studied objects present a low amplitude, typically < 0.15 mag. In fact, except some cases like 2001 QY_{297}, Varuna, Haumea, 2003 VS_2, 2007 TY_{430}, and 2002 KW_{14}, most of the TNOs have a low amplitude. Average amplitudes of 0.06 mag, 0.12 mag, 0.11 mag and 0.10 mag for, respectively, the scattered/detached, the resonant are obtained, the classical and the centaur groups. So, there is not a dynamical group with a higher/smaller amplitude in our database. The scattered/detached group seems to have a lower mean lightcurve amplitude, however, the sample is limited (only three objects), and so more data are required to confirm such a tendency.

In this work (see Section VII.2.1), a threshold of 0.15 mag has been suggested in order to distinguish among lightcurve variations due to albedo or due to the shape of the target because the best fits to Maxwellian distributions were obtained with that assumption, but this is also consistent with the variability in the two maxima or two minima of the triaxial ellipsoids studied here such as Varuna, Haumea, etc. Low amplitudes can be explained by albedo heterogeneity on the surface of a MacLaurin spheroid, while large amplitudes of variability are probably due to the shape of
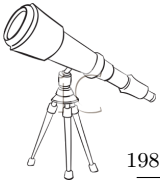
an elongated Jacobi body. According to this assumption, a high lightcurve amplitude of a large object may be attributed to a non spherical shape (typically a triaxial ellipsoid). In Figure 163 and Figure 164, the likely separation between shape- and albedo-dominated lightcurves is plotted.

In Figure 163, two linear fits are plotted. The continuous red line is a linear fit considering the entire sample, whereas the continuous blue line is a linear fit of the entire sample without Haumea, Varuna and 2001 QY$_{297}$. These three objects are showing the largest lightcurve amplitudes in our sample. One can appreciate a trend: smaller objects have larger lightcurve amplitudes.
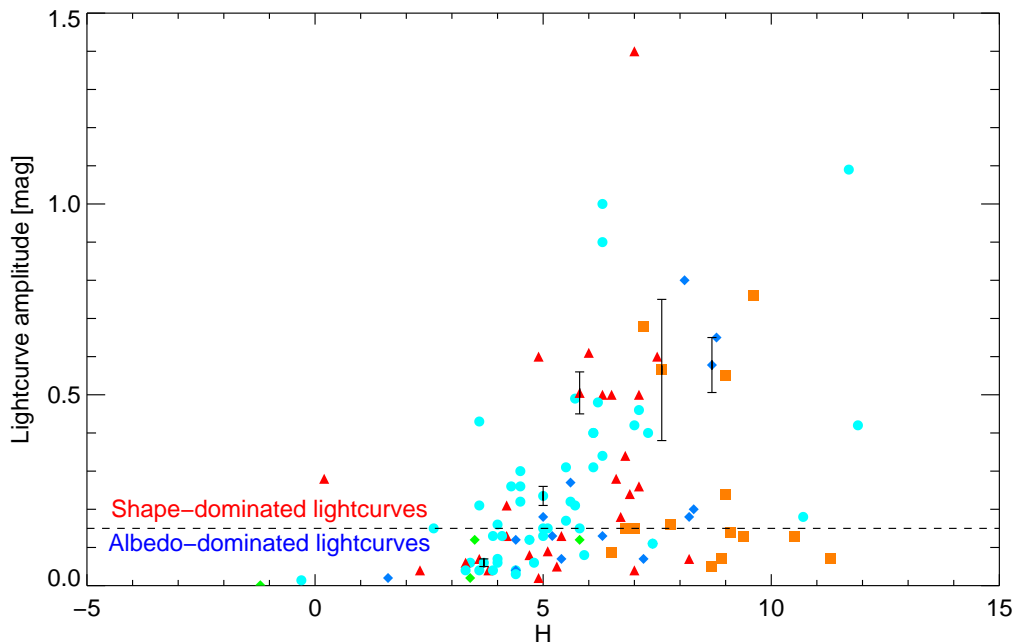
Figure 164: *Lightcurve amplitude versus absolute magnitude*: Amplitudes reported in this dissertation and from the literature (see Table 7) are plotted. The legend of this plot is: orange squares are for centaurs, green diamonds for detached objects, blue circles for classical objects, blue diamonds for SDOs, and red triangles for resonant objects. The dash line, at Δm=0.15 mag, is indicating the likely separation between the shape and albedo-dominated lightcurves. Absolute magnitudes are from the Minor Planet Center database.

In Figure 164 are reported all the results from this work as well as the results from the literature. One can appreciate an evident trend, previously reported in Sheppard, Lacerda and Ortiz (2008): smaller objects have larger lightcurve amplitudes. In other words, the smaller objects are more irregular in shape. This is probably because they are more collisionally evolved (Davis and Farinella, 1997).

VII.6.2   Lightcurve amplitude distributions

In Figure 165, the number of objects that have a lightcurve amplitude reported in Table 7 is showed. Nearly 60% of the objects (TNOs and Centaurs altogether) have a lightcurve amplitudes ≤0.2 mag. Such low lightcurve amplitudes maybe due to: i) the majority of the objects are spherical or MacLaurin spheroids with low albedo contrast on the surface or ii) the majority of the objects have a pole-on (or nearly) configuration. The most reasonable option to explain such a low
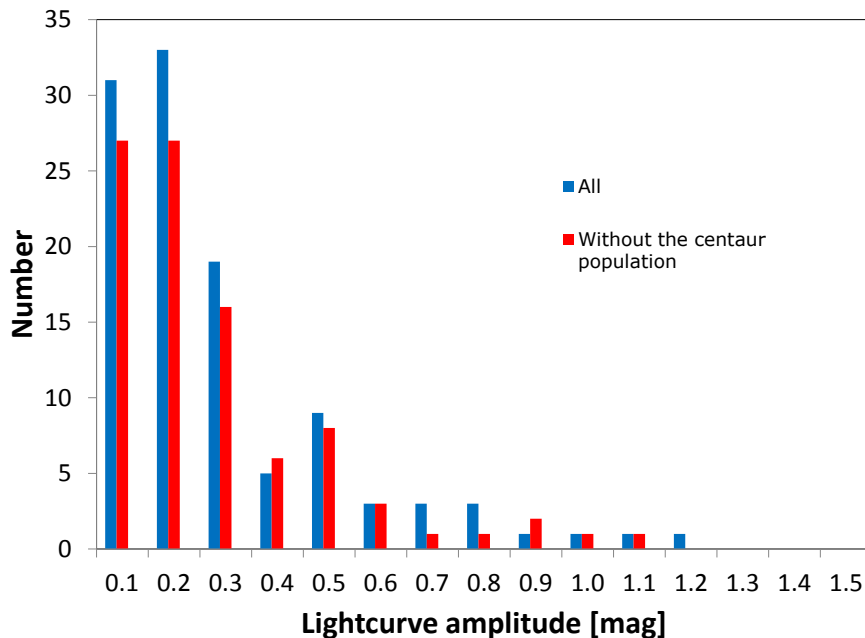
Figure 165: *Number of objects versus lightcurve amplitude*: Blue bars represent the whole sample, and red bars represent the sample without the centaur population. The large abundance of small amplitude is a hint that most of the TNOs are MacLaurin bodies. The MacLaurin objects (oblate spheroids) do not show large variability from rotation because they are symmetrical with respect to the spin axis.

lightcurve amplitude feature is that most of the objects are spheroids with a low albedo contrast. Assuming that most of the objects are oriented pole-on is less probable. Low amplitude lightcurves, also known as flat lightcurves, indicate objects that are less collisionally evolved. In fact, the centaurs, known to be more collisionally evolved, seem to have a higher lightcurve amplitude which indicates a higher elongation on the shape of the bodies (Davis and Farinella, 1997).

In fact, the majority of studied objects are the brightest ones and so, the sample is biased. We already mentioned a bias towards short rotational period and large lightcurve amplitude. Only few faint (and thus small) objects have been studied for short-term variability, such as 2003 BF_{91}, 2003 BG_{91}, 2003 BH_{91} by Trilling and Bernstein (2006), and some faint binary systems by Kern (2006). Based on such works, it seems that faint objects present higher variability, however care has to be taken between binary and non-binary objects (see Chapter VIII) .

VII.6.3   Lightcurve amplitude distributions of binary/multiple systems

Several objects studied in this work, as well as in the literature, are binary or multiple systems. Assuming that binaries have been formed by collisions [3], we have to expect primaries with irregular shapes, so high lightcurve amplitude. The sample of binaries whose short-term variability has been studied is limited. It seems that the binaries have also a low lightcurve amplitude. However, the few dynamically cold classical binaries studied, seem to have a larger amplitude. But such a larger lightcurve amplitude is probably of the dynamically cold classical objects and not of the dynamically cold classical binaries. A complete study will be dedicated to such systems in

---

[3]Many binaries might not be from collisions (see Chapter VIII)
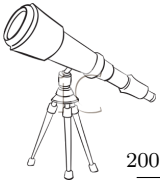
Section VIII.1.5.1

VII.6.4   Body elongation

Assuming TNOs in general as triaxial ellipsoids, with axes a>b>c (rotating along c), the lightcurve amplitude, Δm, varies as a function of the observational angle ξ (angle between the rotation axis and the line of sight) according to Binzel et al. (1989):

$$\Delta m = 2.5 \, log \left(\frac{a}{b} \right) - 1.25 \, log \left(\frac{a^2 \cos^2 \xi + c^2 \sin^2 \xi}{b^2 \cos^2 \xi + c^2 \sin^2 \xi} \right) \qquad \text{(Equation VII.17)}$$

A lower limit for the object elongation (a/b), assuming an equatorial view ($\xi = 90°$) is:

$$\Delta m = 2.5 \, log \left(\frac{a}{b} \right) \qquad \text{(Equation VII.18)}$$

The body elongation can be expressed as:

$$\frac{a}{b} = 10^{0.4 \Delta m} \qquad \text{(Equation VII.19)}$$

Assuming a viewing angle of ξ=60°, the lower limit for the object elongation is:

$$\frac{a}{b} = \frac{10^{\Delta m/2.5}}{\sin 60°} \approx \frac{10^{\Delta m/2.5}}{0.87} \qquad \text{(Equation VII.20)}$$

Once the object's elongation (a/b) is estimated, thanks to Chandrasekhar (1987) works about figures of equilibrium, one can compute the c/a ratio (see Section V.1.2.1 for more details). In Table 13 are reported the axes ratios (a/b and c/a) for each object whose short-term variability has been studied in this work. In order to propose a reliable study, two cases have been considered: i) the object is being viewed with an angle ξ=90°, i.e. equatorial view, and ii) the object is being viewed with an angle of ξ=60°.

Considering an equatorial viewing, an average of 0.90 and 0.55 for the axes ratios a/b and c/a, respectively, are calculated. The averages, assuming an observational angle of 60°, are lower with 0.79 for a/b and 0.51 for c/a.

In order to explain the large abundance of flat lightcurves and to estimate how many non-flat lightcurves are to be expected, Duffard et al. (2009) developed a Monte Carlo model (see Section VII.4.5).

Table 13: In this table, the name of the object, and its peak-to-peak lightcurve amplitude are summarized. The axis ratios have been computed for each object based on Chandrasekhar (1987) work and assuming a viewing angle of 60° and an equatorial view.

Object	Lightcurve amplitude [mag]	b/a eq. view	c/a eq. view	b/a ξ=60°	c/a ξ=60°
Amycus	0.16±0.01	0.86	0.54	0.75	0.50
Haumea	0.28±0.01	0.77	0.51	0.67	0.47
Huya	0.02±0.01	0.98	0.58	0.85	0.53
Makemake	0.014±0.002	0.99	0.58	0.86	0.54
Okyrhoe	0.07±0.01	0.94	0.56	0.82	0.52
Orcus	0.04±0.01	0.96	0.57	0.84	0.53
Quaoar	0.112±0.001	0.90	0.55	0.78	0.51
Salacia	0.04±0.02	0.96	0.57	0.84	0.53
Typhon	0.07±0.02	0.94	0.56	0.82	0.52
Varuna	0.43±0.02	0.67	0.47	0.59	0.43
(24835) 1995 SM$_{55}$	0.05±0.02	0.95	0.57	0.83	0.53
(15874) 1996 TL$_{66}$	0.07±0.02	0.94	0.56	0.82	0.52
(26375) 1999 DE$_9$	0.09±0.03	0.92	0.56	0.80	0.52
(40314) 1999 KR$_{16}$	0.12±0.06	0.89	0.55	0.78	0.51
(44594) 1999 OX$_3$	0.11±0.02	0.90	0.55	0.79	0.51
(275809) 2001 QY$_{297}$	0.49±0.03	0.64	0.45	0.55	0.41
(126154) 2001 YH$_{140}$	0.15±0.03	0.87	0.54	0.76	0.50
(55565) 2002 AW$_{197}$	0.02±0.02	0.98	0.58	0.85	0.53
(307251) 2002 KW$_{14}$	(0.21 or 0.26)±0.03	0.82 or 0.79	0.52 or 0.51	0.71 or 0.68	0.48 or 0.47
(307261) 2002 MS$_4$	0.05±0.01	0.95	0.57	0.83	0.53
(84522) 2002 TC$_{302}$	0.04±0.01	0.96	0.57	0.84	0.53
(55636) 2002 TX$_{300}$	0.05±0.01	0.95	0.57	0.83	0.53
(55637) 2002 UX$_{25}$	0.09±0.03	0.92	0.56	0.80	0.52
(55638) 2002 VE$_{95}$	0.04±0.02	0.96	0.57	0.84	0.53
(208996) 2003 AZ$_{84}$	0.07±0.01	0.94	0.56	0.82	0.52
(120061) 2003 CO$_1$	0.06±0.01	0.95	0.57	0.82	0.52
(120132) 2003 FY$_{128}$	0.12±0.02	0.89	0.55	0.78	0.51
(174567) 2003 MW$_{12}$	0.02±0.01	0.98	0.58	0.85	0.53
(120178) 2003 OP$_{32}$	0.13±0.01	0.89	0.55	0.77	0.51
(84922) 2003 VS$_2$	0.224±0.013	0.82	0.52	0.71	0.48
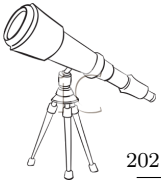
Table 13: continued.

Object	Lightcurve amplitude [mag]	b/a eq. view	c/a eq. view	b/a $\xi=60°$	c/a $\xi=60°$
(136204) 2003 WL$_7$	0.04±0.01	0.96	0.57	0.84	0.53
2004 NT$_{33}$	0.04±0.01	0.96	0.57	0.84	0.53
(144897) 2004 UX$_{10}$	0.09±0.02	0.92	0.56	0.80	0.52
(230965) 2004 XA$_{192}$	0.07±0.02	0.94	0.56	0.82	0.52
(308193) 2005 CB$_{79}$	0.05±0.02	0.95	0.57	0.83	0.53
(145451) 2005 RM$_{43}$	0.05±0.01	0.96	0.57	0.83	0.53
(145452) 2005 RN$_{43}$	0.04±0.01	0.96	0.57	0.84	0.53
(145453) 2005 RR$_{43}$	0.06±0.01	0.95	0.57	0.82	0.52
(145480) 2005 TB$_{190}$	0.12±0.01	0.89	0.55	0.78	0.51
(145486) 2005 UJ$_{438}$	0.11±0.01	0.90	0.55	0.79	0.51
(202421) 2005 UQ$_{513}$	0.05±0.02	0.96	0.57	0.83	0.53
(341520) 2007 TY$_{430}$	0.24±0.05	0.80	0.52	0.70	0.48
(25012) 2007 UL$_{126}$ or 2002 KY$_{14}$	0.11±0.01	0.90	0.55	0.79	0.51
(229762) 2007 UK$_{126}$	0.03±0.01	0.98	0.58	0.85	0.53
(315530) 2008 AP$_{129}$	0.12±0.02	0.89	0.55	0.78	0.51
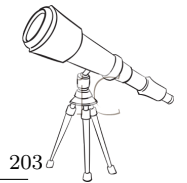
VII.7 Correlations of rotation parameters with orbital and physical parameters

A search for correlations between physical (albedo, rotational period, and lightcurve amplitude)[4] and orbital parameters (perihelion distance, aphelion distance, absolute magnitude, argument of perihelion, longitude of the ascending node, inclination, orbital eccentricity, and semimajor axis) has been done in this thesis. Only physical parameters derived from lightcurves have been considered in this study. The Spearman rank correlation (Spearman, 1904) has been used because this method is less sensitive to atypical/wrong values and does not assume any population probability distribution. The strength of the correlations has been obtained by computing the Spearman coefficient ρ and the significance level (SL). The ρ coefficient has values between -1 and 1. If $\rho > 0$, there is a possible correlation, whereas $\rho < 0$ indicates a possible anti-correlation and if $\rho = 0$, there is no correlation. A correlation is: i) strong if $|\rho| > 0.6$, ii) weak if $0.3 < |\rho| < 0.6$, and iii) inexistent if $|\rho| < 0.3$. The significance of the ρ parameter is measured by the SL: i) very strong evidence of correlation if SL>99%, ii) strong evidence of correlation if SL>97%, and iii) reasonably strong evidence of correlation if SL>95%. Such criteria have been used in several studies of correlations/anti-correlations between colors and orbital elements, for example in Hainaut, Boehnhardt and Protopapa (2012); Peixinho, Lacerda and Jewitt (2008); Peixinho et al. (2012).

Orbital parameters and albedo values are reported in Table 25 and Table 26, respectively. In case of several albedos values for one object, we proceed to a random choice as explained in Section VII.2.1.

In Table 24 (see Appendix B), correlations and anti-correlations are summarized. In a first step, the sample has been divided into five sub-groups: the entire sample, the binary sample, the sample without binary objects, the sample without the centaur population, and finally the sample without the binary nor the centaur populations. In order to provide a complete study, the sample has been also divided according to the dynamical classes (Gladman, Marsden and Vanlaerhoven (2008) dynamical classification) and according to the size. An absolute magnitude cut-off of 5 to distinguish small/large objects has been used. Pluto-Charon and Sila-Nunam systems have not been included because they are tidally locked (Grundy et al., 2012; Buie, Tholen and Wasserman, 1997), in the search for correlations with rotational period. Care was taken to select only objects with a rotational period and lightcurve amplitude estimations, and objects with only a constraint about the lightcurve amplitude were not included in our samples. 2010 WG$_9$ is also excluded from our sample because there are evidences that this object is a tidally-evolved binary TNO (Rabinowitz et al., 2013).

Our main purpose in this section is to report features of the non-binary population whereas the study of the binary population will be done in the Chapter VIII. First of all, we must point out that, as previously mentioned, there are several observational biases in the database, so care has to be taken with the correlation/anti-correlation interpretations.

1. *Lightcurve amplitude correlations/anti-correlations*:

   (a) *Lightcurve amplitude versus absolute magnitude*:

   A clear evidence of correlation with a very strong significance level between the lightcurve amplitude and the absolute magnitude in most of the samples studied in this work is noted. Such a correlation indicates that smaller objects have larger lightcurve amplitudes than the larger ones. So, small objects are probably more deformed than the

---

[4]We only looked for correlations with physical parameters derived from the lightcurves, and so, for example the correlations between colors and orbital parameters are not reported here. Several studies about this topic have been published already, for example: Hainaut, Boehnhardt and Protopapa (2012); Peixinho, Lacerda and Jewitt (2008); Peixinho et al. (2012)

larger ones. Such a fact seems in agreement with the collisional evolution (Davis and Farinella, 1997).

There is weak evidence of an anti-correlation between such parameters in the resonant group made of objects with an absolute magnitude lower than 5. A reason for such anti-correlation is not obvious. The sample is limited (only 11 objects), so care has to be taken and more data are required to confirm or not such tendency.

(b) *Lightcurve amplitude versus eccentricity and inclination*:

There are evidences of anti-correlation between the lightcurve amplitude and eccentricity in several sub-groups, as well as between lightcurve amplitude and inclination. Such anti-correlations indicates that objects with a small lightcurve amplitude (with less deformation) are in eccentric and inclined orbits whereas objects with a high lightcurve amplitude (deformed objects) are in circular orbits at low inclination.

Anti-correlation between lightcurve amplitude and eccentricity affects objects with an absolute magnitude (H) less than 5 (large objects). In the case of the classical population, all objects (independent of their sizes) follow such tendency.

(c) *Other correlations/anti-correlations*:

Several correlations and anti-correlations between lightcurve amplitude and ascending node, perihelion distance, and argument of the perihelion are also listed in Table 24. Reasons for such features are not obvious and may be attributed to observational biases. More observational informations are required to confirm or discard such features.

2. *Rotational period correlations/anti-correlations*:

Correlations/anti-correlations between rotational period and orbital parameters have been obtained. Correlations between spin period and the argument of the perihelion in some sub-groups have been noted, as well with the inclination. A possible reason for such correlations is not clear and may be attributed to an observational bias. More observations are required to confirm or discard such features.

3. *Albedo correlations/anti-correlations*:

(a) *Albedo versus eccentricity and inclination*:

There is an anti-correlation between the albedo and the inclination in several samples, as well as between the albedo and the eccentricity. These anti-correlations indicate that objects with a high albedo are at low inclination and low eccentricity. Such an idea has been already noted by Brucker et al. (2009), especially in the case of dynamically cold classical objects. However, the dynamically hot classical objects at higher inclination, also present an anti-correlation between the albedo and the inclination (based on a limited sample of objects) but only for object with H≥5. The case of the sample without the centaur population is interesting and indicates different characteristics according to the object size. In fact, the sample limited to objects with H<5 presents a correlation, whereas the sample composed by objects with H≥5 favors an anti-correlation.

(b) *Albedo versus absolute magnitude*:

There is an anti-correlation between the albedo and the absolute magnitude. This means that the large objects have higher albedos. Based on Haumea, Eris, or Makemake albedos such fact is confirmed (Lellouch et al., 2010; Sicardy et al., 2011; Ortiz et al., 2012b).

Only two samples, dynamically cold classical objects and dynamically hot classical objects with an absolute magnitude higher than 5, are showing a strong correlation between albedo and absolute magnitude.

(c) *Other correlations/anti-correlations*:

Several correlations and anti-correlations between albedo and ascending node, perihelion-aphelion distances, and argument of the perihelion are also listed in Table 24. Reasons for such features are not obvious and may be attributed to observational biases. More observations are required to confirm or discard such features.

VII.8   Summary

We found that the percentage of low amplitude rotators is higher than previously thought. In fact, only 7 of 45 objects ($\sim$16 per cent) in the sample (Amycus, Haumea, Varuna, 2002 KW$_{14}$, 2001 QY$_{297}$, 2003 VS$_2$, and 2007 TY$_{430}$) show a lightcurve with an amplitude $\Delta m >$0.15 mag. Eight of 45 objects ($\sim$18 per cent) in the sample (2001 QY$_{297}$, 2005 TB$_{190}$, Orcus, 1999 DE$_9$, 1996 TL$_{66}$, 1999 OX$_3$, 2001 YH$_{140}$, and 2007 UK$_{126}$,) have a rotational period P$_{rot}$ $\geq$10 h.

In the sample, more than 80 per cent of the studied objects have a low variability (less than 0.15 mag) and corresponding lightcurves could be explained by albedo variations. Such bodies are probably MacLaurin spheroids with a highly homogeneous surface. As mentioned, only a few objects present a large lightcurve amplitude and could be explained by the shape of rotationally elongated Jacobi ellipsoids. In this work, we estimated that 0.15 mag seems to be a good measure of the typical variability caused by albedo features. In other worlds, a lightcurve with a low amplitude is an albedo-dominated lightcurve whereas lightcurve with a large amplitude (larger than 0.15 mag) are shape-dominated lightcurve. As already pointed out several objects present a peak taller than the second one. Such differences in the cases of 2003 VS$_2$ and Haumea are around 0.04 mag, whereas for Varuna the greatest difference is 0.1 mag. Hence, this means that the hemispherically averaged albedo typically has variations around 4 to 10% (Thirouin et al., 2010). So, we expect that the variability induced by surface features is on the order of 0.1 mag. In fact, 0.15 mag is preferred from Maxwellian fits to the rotation periods distribution.

Based on our sample reported here, we noted that the rotation rates appear to be slightly higher (faster objects) than previously suggested Sheppard, Lacerda and Ortiz (2008). However, based on a larger sample (sample reported here+literature) it seems that the mean rotational periods are based on Maxwellian distribution fits, 7.99 h for the entire sample (TNOs+centaurs), 8.97 h for the sample without the centaurs, and 7.95 h for the centaur population. The plots of both amplitude versus size and rotation rate versus size seem to be compatible with the typical collisional evolution scenario in which larger objects have been only slightly affected by collisions, whereas the small fragments are highly collisionally evolved bodies with usually more rapid spins of larger amplitudes.

There appears to be a spin barrier that allows us to obtain a mean density that is also compatible with the average density derived based under hydrostatic equilibrium assumptions. Such a rotational spin barrier has been reported at $\sim$4 h for the TNOs and centaurs whereas such a spin barrier has been reported around 2 h for the asteroids. The result based on our sample suggests densities of around 0.7 g cm^{-3}. Several formulas have been used to derive such a lower limit to the density depending of the object shape (prolate, oblate, spherical object), but in all cases the lower limit to the density have similar values.

We also studied the rotational period distribution of the Haumea family members. We do not get a satisfactory Maxwellian fit which might imply that the family does not come from a collision as is the case for the families in the asteroid belt. However, we must point out that Binzel et al. (1989) suggested that the rotational periods of the asteroid family members may not always fit a Maxwellian distribution. We noted that the fragments of this family seem to rotate faster than the other TNOs.

The average density is low, with density lower than 1 g cm^{-3} which indicates that objects are porous. However, it is not secure that centaurs are in hydrostatic equilibrium. On the other hand, if we assume that TNOs and centaurs are formed with similar mixture of rock/ice, one has to expect that for both populations a similar tensile strength might be applicable. The tensile strength is much lower than for usual geophysical solids.

An exhaustive search for correlations/anti-correlations between physical and orbital parameters reveals several features according to the dynamical classes and according to the object sizes. However, several correlations/anti-correlations are weak and more data is required to confirm whether they are real or due to observation biases in the sample.

VIII

Binary/multiple systems in the Trans-Neptunian Belt

$\mathcal{T}$he first Trans-Neptunian binary to be discovered since Pluto, was 1998 WW$_{31}$ (Veillet et al., 2002). The study of binaries can supply mass, density, albedo, etc of each component of the system. Some approaches can be used to complement the binarity study, such as spectroscopy (Carry et al., 2011) or photometric studies of binary systems (Thirouin et al., 2013b). Here, we focus on the short-term variability study of the Binary Trans-Neptunian Objects (BTNOs) which allow us to retrieve rotational periods from the photometric periodicities and also provides constraints on several physical properties.

In the previous chapter, we studied the rotational properties of the non-binary population from which we derived and studied some properties such as the shapes, surfaces heterogeneity, density, internal structure etcetera. Here, we discuss the amplitude and rotational period distributions of the binary/multiple systems. The tidal interaction between the primary and satellite can alter the spin properties considerably. The main purpose of this chapter is to check if the binary and non-binary populations share the same rotational features and obtain important clues about formation and evolution of the Trans-Neptunian belt. In order to complete our portrait of the binary population, we present an exhaustive study based on a search for correlations/anti-correlations between orbital and physical parameters, as it has been done for the non-binary population. Finally, we derive several physical properties and propose possible formation models for several binaries whose short-term variability has been reported in this work.

This work has been done in collaboration with Dr Keith S. Noll during a stay at the NASA-Goddard Space Flight Center (NASA-GSFC) and will be published in Thirouin et al. (2013b).

VIII.1   Short-term variability of binary/multiple systems

VIII.1.1   Importance of lightcurves of binary/multiple systems

Apart from the physical parameters already derived from the lightcurves in Chapter VII, in the case of binaries it is also possible to derive several physical parameters about the system components, such as diameter of the components and the albedo under some assumptions. Study of short-term variability of binary and multiple systems also allow us to identify which systems are tidally locked or not. The study of the tidal interaction provides clues on the internal structure of these bodies, and orbital evolution.

In this Chapter, we want to check if the TNOs and the BTNOs are following the same trends, and obviously the natural question is whether the study of short-term variability of BTNOs can

be used to constrain their origin and/or evolution.

VIII.1.2 Inventory of the short-term variability for binary/multiple systems

VIII.1.2.1 Observations of binary/multiple systems

As previously mentioned, care has to be taken with the observations of binary/multiple systems (see Section V.1.3.2). In fact, a possible contribution of the satellite in the photometry (so in the lightcurve) may affect our study. In case of eclipsing binaries, one has to expect mutual events between the primary and the secondary (Grundy et al., 2012), while if the lightcurve presents a large amplitude (typically, $\sim$1.2 mag according to Leone et al. (1984)) one expects a tidally distorted contact binary (or nearly contact binary).

A binary/multiple system lightcurve can be: i) unresolved or ii) resolved. In case of unresolved lightcurves, both components of the system are not resolved, so one measures the magnitude of the pair. Resolved ground-based lightcurves of binaries are challenging and can only be obtained under excellent conditions with large telescopes, and only for systems with large separation between both components.

Several attempts of resolved ground-based lightcurves have been done. For example, we can cite the case of the 2001 QT_{297} system (Teharonhiawako-Sawiskera) or the case of the 2003 QY_{90} system. (Osip, Kern and Elliot, 2003; Kern and Elliot, 2006a). The primary, 2003 QY_{90}, and the satellite, 2003 QY_{90} B were observed to change by 0.34$\pm$0.06 mag and 0.90$\pm$0.18 mag, respectively, over 6 h of observation, whereas Teharonhiawako presents a low amplitude and its satellite, Sawiskera has a higher variability of 0.5-0.6 mag in 30 minutes of observations.

The best option to obtain resolved lightcurves is to carry out space-based observations from the *Hubble Space Telescope (HST)*. For example, the study of the system Pluto-Charon with the HST provided detailed lightcurve measurements of both components (Buie, Tholen and Wasserman, 1997).

VIII.1.2.2 Short-term variability studies obtained during this work

For this thesis, various binary or multiple systems (no eclipsing nor contact binaries) were observed. In all cases presented in this work, the lightcurves are based on unresolved images, so one is measuring the magnitude of the pair.

Here, we report unresolved lightcurves for eleven binary systems, for one triple system, and lightcurve amplitude estimation for two binaries (see Chapter VI). The sample contains six classical systems: (275809) 2001 QY_{297}, (55637) 2002 UX_{25}, (174567) 2003 MW_{12}, (120347) 2004 SB_{60} or Salacia, (50000) 2002 LM_{60} or Quaoar, 2002 VT_{130}, one detached disk system: (229762) 2007 UK_{126}, six resonant systems: (136108) 2003 EL_{61} or Haumea, (341520) 2007 TY_{430}, (90482) 2004 DW or Orcus, (38628) 2000 EB_{173} or Huya, (55638) 2002 WC_{19}, (208996) 2003 AZ_{84}, and one scattered disk system: (42355) 2002 CR_{46} or Typhon.

VIII.1.2.3 Short-term variability studies from the literature

Using the literature and the results presented in this work, we created a database of lightcurves with rotational periods and/or lightcurve amplitudes of binary/multiple systems. This database, updated on May 2013, is presented in Table 14. We compiled 32 primaries and 3 satellites with a rotational period and/or peak-to-peak amplitude or constraints.
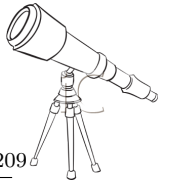
The number of binary/multiple systems with a well determined rotational period is still limited and highly biased. Like for the TNOs short-term variability database of the previous chapter, the sample of BTNOs is highly biased towards large variability amplitudes and short rotational periods. A reliable study of BTNO rotational properties requires a lot of observational time on large telescope (typically up to a 4-m class telescope) because most of the BTNOs are faint (typically, visual magnitude >22 mag). On the other hand, to obtain resolved lightcurve is very challenging and can only be obtained under excellent conditions of seeing and atmospheric conditions for systems with a separation higher than $1''$ between both components.
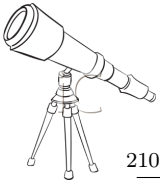
Table 14: In this table, we listed the short-term variability of BTNOs. In case of multiple rotational periods, the preferred rotational period, according to the authors of each study, is indicated in bold. The reference list can be found at the end of this table.

Object	Single peak periodicity [h]	Double peak periodicity [h]	Amplitude [mag]	Absolute magnitude	Ref
(134340) Pluto	153.2	-	0.33	-0.7	B97
Charon	153.6	-	0.08	0.9	B97
(148780) Altjira	-	-	<0.3	5.6	S07
(66652) Borasisi	6.4±1.0	-	<0.05	5.9	LL06
			0.08±0.02	...	K06b
(65489) Ceto	13.69/28.08/32.13	4.43±0.03	0.13±0.02	6.3	D08
(136199) Eris	3.55	-	<0.1±0.01	-1.2	Du08
			~0.5	...	L07
	25.92	-	<0.01	...	R07, S07
			0.1	...	R08
(136108) Haumea	-	3.9154±0.0002	0.28±0.02	0.2	R06
	-	3.9155±0.0001	0.29±0.02	...	L08
		3.92	0.28±0.02	...	T10
(38628) Huya	-	-	<0.1	4.7	O03b
			<0.15	...	SJ02
			<0.097	...	S02
	(6.68/**6.75**/6.82)±0.01	-	<0.04	...	SJ03,LL06
	5.21		0.02±0.01	...	T13
(58534) Logos	-	-	~0.8	6.6	N08
(90482) Orcus	7.09/**10.08±0.01**/17.43	**20.16**	0.04±0.02	2.3	O06
	13.19	-	0.18±0.08	...	R07
			<0.03	...	S07
	10.47	-	0.04±0.01	...	T10
(50000) Quaoar	-	17.6788±0.0004	0.13±0.03	2.6	O03a
			0.18±0.10	...	R07
	8.84	18.84	~0.3	...	L07
	9.42	17.68	0.15±0.04	...	T10
(120347) Salacia	8.84	~17.5	0.2	4.4	S10
	6.09 or 8.10	-	0.03±0.01	...	T10
	6.61	-	0.04±0.02	...	T13
(79360) Sila	-	-	<0.04	...	B13
			0.08	5.1	SJ02
	150.1194	-	0.22	...	RT99
(88611) Teharonhiawako	-	300.238	0.14±0.07	...	G12, B13
	5.50±0.01 or 7.10±0.02	11.0±0.02 or 14.20±0.04	(0.32 or 0.30)±0.04	5.5	Os03
(88611B) Sawiskera	4.7526±0.0007	9.505±0.001	~0.6	5.5	K06b
	4.749±0.001	9.498±0.02	0.48±0.05	...	Os03
(42355) Typhon	(3.66 or 4.35)±0.02	-	<0.15	7.2	K06b
	>5	-	<0.05	...	O03b
			-	...	SJ03
(26308) 1998 SM165	9.67	7.1±0.01	0.07±0.01	...	D08
			0.45±0.03	...	T10
	3.983	7.966	0.56	5.8	SJ02
			-	...	R01
(47171) 1999 TC36	-	8.40±0.05	0.06	...	S06
	6.21±0.02	-	<0.07	4.9	O03b
			<0.05	...	LL06
		-	-	...	SJ03

Table 14: continued.

Object	Single peak periodicity [h]	Double peak periodicity [h]	Amplitude [mag]	Absolute magnitude	Ref
(80806) 2000 CM$_{105}$	-	-	<0.14	6.3	LL06
2001 QC$_{298}$	-	~12	0.4	6.1	S10
(82075) 2000 YW$_{134}$	3.89±0.24	7.78±0.48	0.30±0.04	...	K06b
(139775) 2001 QG$_{298}$	-	-	<0.10	5.0	SJ03
	6.8872±0.0002	13.7744±0.0004	1.14±0.04	7.0	SJ04
	-	-	0.07±0.01	...	L11
(275809) 2001 QY$_{297}$	5.84	11.68	0.49±0.03	5.7	T12
(55637) 2002 UX$_{25}$	12.2±4.3	-	0.66±0.38	...	K06b
	-	14.382±0.001 or 16.782±0.003	0.21±0.06	3.6	R05b
	-	-	<0.06	...	SJ03
	6.55	-	0.13±0.09	...	R07
	-	-	0.06±0.03	...	TW
(119979) 2002 WC$_{19}$	-	-	<0.05	5.1	S07
2003 AZ$_{84}$	(4.32/5.28/6.72/**6.76**)±0.01	-	0.10±0.04	3.6	O06
	6.72±0.05	-	0.14±0.03	...	SJ03
	6.79	-	0.07±0.01	...	T10
2003 FE$_{128}$	5.85±0.15	-	0.50±0.14	6.3	K06b
(174567) 2003 MW$_{12}$	5.90 or 7.87	-	0.06±0.01	3.6	T10
	5.91	-	0.04±0.01	...	T13
2003 QY$_{90A}$	-	-	<0.04	...	B13
	3.4±1.1	-	0.34±0.06	6.3	K06a
2003 QY$_{90B}$	7.1±2.9	-	0.90±0.18	6.3	K06a
2005 EF$_{298}$	-	-	<0.13	6.1	B13
(303712) 2005 PR$_{21}$	-	-	<0.28	6.1	B13
2007 TY$_{430}$	-	9.28	0.24±0.05	6.9	T13
2007 UK$_{126}$	11.05	-	0.03±0.01	3.4	T13

References list:

B97: Buie, Tholen and Wasserman (1997); RT99: Romanishin and Tegler (1999); SJ02: Sheppard and Jewitt (2002); O03a: Ortiz et al. (2003a); O03b: Ortiz et al. (2003b); Os03: Osip, Kern and Elliot (2003); SJ03: Sheppard and Jewitt (2003); SJ04: Sheppard and Jewitt (2004); R05b: Rousselot et al. (2005b); K06a: Kern and Elliot (2006a); K06b: Kern (2006); LL06:Lacerda and Luu (2006); O06:Ortiz et al. (2006); R06: Rabinowitz et al. (2006); S06: Spencer et al. (2006); L07: Lin, Wu and Ip (2007); R07:Rabinowitz, Schaefer and Tourtellotte (2007); S07: Sheppard (2007); D08: Dotto et al. (2008); Du08: Duffard et al. (2008); L08: Lacerda, Jewitt and Peixinho (2008); N08: Noll et al. (2008a); R08: Roe, Pike and Brown (2008); S10: Snodgrass et al. (2010); T10: Thirouin et al. (2010); L11: Lacerda (2011); G12: Grundy et al. (2012); T12: Thirouin et al. (2012); B13: Benecchi and Sheppard (2013); T13: Thirouin et al. (2013b); TW: Results are not published yet and are only reported in this work.
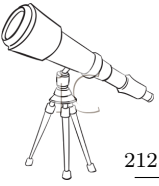
VIII.1.3   Derived properties from lightcurves of binary systems

As most of the properties from the lightcurves have already been analyzed, below, we only focus on the properties that one can derive in case of short-term variability of binary systems.

In this sub-section, we present the methodology to derive the albedo, and primary/secondary sizes from the lightcurve. The technique used to derive the density from the lightcurves has been already explained in Section V.1.2.2. Then, we will compare our results as well as our technique to derive such information from the lightcurve with other methods. In fact, the density, albedo and/or sizes of both components can also be obtained from other methods such as: i) thermal modeling based on data obtained, for example with the *Herschel Space Observatory* or the *Spitzer Space Telescope*, ii) from the mutual orbit of binary component, iii) from direct imaging, or from iv) stellar occultation by (B)TNOs and centaurs. However, such methods only provided some information that require the complement of other techniques. For example, thermal modeling which provides the albedo and effective diameter of the system requires the absolute magnitude as well as the rotational period of the object in order to derive a reliable study (Müller et al., 2010; Lellouch et al., 2010; Lim et al., 2010; Vilenius et al., 2012; Vilenius et al., 2013; Mommert et al., 2012). On the other hand, stellar occultations allow us to derive the size of the object with a high precision, but the system density can only be derived if the system mass is known (Sicardy et al., 2011). If the system mass is unknown (or if the object is not a binary), the lower limit of the density can be estimated from the lightcurve in this case (Ortiz et al., 2012a).

VIII.1.3.1   Size and Albedo from lightcurves: methodology

Assuming that TNOs are in hydrostatic equilibrium, one can estimate a lower limit of the bulk densities, ρ, according to Chandrasekhar (1987) (See Section V.1.2.2). Based on the lower limit to the density, ρ, one can define the volume of the system as $V_{system} = M_{system}/\rho$, where M_{system} is the mass of the system and is known from the orbit of the system. We assume that both components have the same density which is the system density. If both components of the system have the same albedo, the primary radius ($R_{primary}$) can be expressed as:

$$R_{primary} = \left(\frac{3V_{system}}{4\pi \left(1 + 10^{-0.6\Delta_{mag}} \right)} \right)^{1/3} \qquad \text{(Equation VIII.1)}$$

where Δ_{mag} is the component magnitude difference [1] (Noll et al., 2008a).

Assuming that both components have the same albedo, the satellite radius ($R_{satellite}$) is:

$$R_{satellite} = R_{primary} 10^{-0.2\Delta_{mag}} \qquad \text{(Equation VIII.2)}$$

The effective radius of the system, $R_{effective}$, is:

$$R_{effective} = \sqrt{R_{primary}^2 + R_{satellite}^2} \qquad \text{(Equation VIII.3)}$$

We can derive the geometric albedo in the λ band, p_λ, given by the equation:

$$p_\lambda = \left(\frac{C_\lambda}{R_{effective}} \right)^2 10^{-0.4H_\lambda} \qquad \text{(Equation VIII.4)}$$

where C_λ is a constant depending on the wavelength (Harris, 1998), and H_λ the absolute magnitude in the λ band.

It is important to remember that we derived lower limit of the density, so the derived sizes are upper limits and derived albedo is a lower limit.

---

[1] The apparent magnitude difference or component magnitude difference is the difference of magnitudes (Δ_{mag}) between the magnitude of satellite and the primary magnitude.
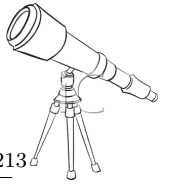
VIII.1.3.2   Size and Albedo from lightcurves: results

In Table 15, the density, primary and satellite sizes and albedo from lightcurves are summarized for each system studied in this thesis. In order to estimate the sizes and the albedos using previous equations, we need the system masses reported in Table 15.

From the lightcurves, we report albedo, primary/satellite sizes and lower limit of the density for 7 systems. In four cases, we are only able to derive the lower limit of the density. For the 2002 WC$_{19}$ and the 2002 VT$_{130}$ systems, as we have only constraints about their short-term variability, we are not able to derive such parameters.

As pointed out in the Chapter VII, low amplitudes lightcurves ($\leq$0.15 mag) can be explained by albedo heterogeneity on the surface of a MacLaurin spheroid, while large amplitude lightcurves ($>$0.15 mag) are probably due to the shape of an elongated Jacobi body. In Table 15, we reported a lower limit of the density computed thanks to Chandrasekhar (1987) study of figures of equilibrium for fluid bodies. To compute the lower limit of the density according to Chandrasekhar (1987), we have to assume that the object is a triaxial ellipsoid in hydrostatic equilibrium. So, according to our criterion, only objects with a large amplitude lightcurve have to be considered as Jacobi ellipsoids. In the case of low variability objects, the lower limit of the density computed should be regarded as a very rough estimation which is likely incorrect.

VIII.1.3.2.1   Jacobi ellipsoid   In our sample, only two binary systems have a large lightcurve amplitude: 2007 TY$_{430}$ and 2001 QY$_{297}$ and can be considered as Jacobi ellipsoids. We found that the 2001 QY$_{297}$ system has a very low lower limit of the density of 0.29 g cm^{-3}, we derived a primary radius of $<$129 km, a secondary radius of $<$107 km and a geometric albedo of $>$0.08 for both components. For the 2007 TY$_{430}$ system, we found that both components have similar radii of $<$58 km (primary) and $<$55 km (secondary), we derived a low density of 0.46 g cm^{-3}, and a geometric albedo of $>$0.12 for both components.

VIII.1.3.2.2   MacLaurin spheroid   Most of the lightcurves of binary systems studied in this thesis are more significantly affected by albedo effects, than shape effects. In such cases, the objects are MacLaurin most likely spheroids. As already pointed out the lower limit of the density, as well as other parameters are only very crude estimations. For example, the computed lower limit of Quaoar density is clearly off, because Braga-Ribas et al. (2013) obtained a density around 2 g cm^{-3}.

Table 15: Density, sizes and albedo from this work and from the literature: for each system whose short-term variability have been studied in this work, we present the name of the system, the system mass (M_{syst}), the lower limit of the density (ρ), upper limits of the primary and satellite sizes (R_p and R_s, respectively) and the lower limit of the geometric albedo (p_v). Several techniques can be used to estimate these parameters such as thermal modeling (thermal), determined from mutual orbit of binary components (orbit), direct imaging (direct), occultation or from the lightcurve. Only the values derived from the lightcurves have been obtained during this thesis. We must point out that when the density is derived from the lightcurve it is only the lower limit of the density. The last column of this table is dedicated to the references. As explained in Section VIII.1.3.3, the primary radius is an equivalent radius to that of a sphere in volume or in area.

System	M_{syst} $\times10^{18}$[kg]	ρ [g cm^{-3}]	R_p [km]	R_s [km]	p_v	Technique	Reference
Salacia-Actaea	438±16	$1.16^{+0.59}_{-0.36}$	453±52	152±18	$0.0357^{+0.0103}_{-0.0072}$	thermal	S12
	...	1.38±0.27	431±35	146±11	0.0439±0.0044	thermal	S12, V12
	...	$1.29^{+0.29}_{-0.23}$	427±23	143±12	0.044±0.004	thermal	S12, F13
	...	>0.9	<491	<165	>0.03	lightcurve	S12, T13
2003 MW$_{12}$	260±10	?	399±49	205±25	$0.077^{+0.025}_{-0.014}$	thermal	G11, V13[a]
	...	>1.11	<366	<188	>0.09	lightcurve	G11, T13
2007 TY$_{430}$	0.790±0.021	0.5	<60	<60	>0.17	estimation[b]	Sh12
	...	>0.46	<58	<55	>0.12	lightcurve	Sh12, T13
2001 QY$_{297}$	4.10±0.04	$0.32^{+0.18}_{-0.13}$	130±21	107±17	$0.075^{+0.037}_{-0.027}$	thermal	G11a, V12, V13
	...	>0.29	<129	<107	>0.08	lightcurve	G11a, T12
Huya		?	236±11	124±6	0.05±0.05	thermal	S08
		?	195±12	102±6	0.081±0.011	thermal	M12
		>1.43	?	?	?	lightcurve	T13
Orcus-Vanth	632±1	1.5±0.3	450±34	136±10	0.28±0.04	thermal+orbit	B10
	...		453±36	137±11	0.197±0.034	thermal	B10, S08
	...		416.5±22.5	126±8	0.25±0.03	thermal	B10, L10
	...	$1.53^{+0.15}_{-0.13}$	459±13	138±9	$0.231^{+0.018}_{-0.011}$	thermal	B10, F13
	...	>0.35	<749	<225	>0.09	lightcurve	B10, T10, TW
Typhon-Echidna	0.949±0.052	$0.44^{+0.44}_{-0.17}$	78±8	43±4	?	thermal+orbit	G08
	...	?	76±8	42±4	$0.051^{+0.012}_{-0.008}$	thermal	G08, S08
	...	?	61±4	34±3	0.08±0.01	thermal	G08,M10
	...	$0.36^{+0.08}_{-0.07}$	81±4	45±3	0.044±0.003	thermal	G08, SS12
	...	>0.42	<76	<42	>0.06	lightcurve	G08, T10, TW
Quaoar-Weywot		?	633±100	47±7	$0.092^{+0.036}_{-0.023}$	direct	B04
		?	425±99	33±8	$0.199^{+0.132}_{-0.070}$	thermal	S08
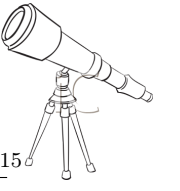
Table 15: continued.

System	M_{syst} $\times 10^{18}$ [kg]	ρ [g cm^{-3}]	R_p [km]	R_s [km]	p_v	Technique	Reference
	?	?	450±56	34±4	$0.172^{+0.055}_{-0.036}$	thermal	B09
	1600±300	4.2±1.3	445±35	34±3	?	orbit	F10
	(1300-1500)±100	2.7-5.0	?	?	?	orbit	Fr13
	1650±160	1.6±1.3 or 4.5±1.8	?	?	?	orbit^c	VBM12
	(1300-1500)±100	$2.18^{+0.43}_{-0.36}$	535±19	41±6	$0.137^{+0.011}_{-0.013}$	thermal	Fr13, F13
	(1300-1500)±100	1.99±0.46	569^{+24}_{-17}	41±6	0.109±0.007	occultation^d	Fr13, B13
	1600±300	>0.5	<914	<69	>0.06	lightcurve	F10, T10, TW
2003 AZ$_{84}$	?	?	446±28	45±3	0.065±0.008	thermal	M10
	?	?	362±32	36±32	0.065±0.008	thermal	M12
	?	>0.85	?	?	?	lightcurve	T10
2007 UK$_{126}$	?	?	295±38	52±7	$0.167^{+0.058}_{-0.038}$	thermal	SS12
	?	>0.32	?	?	?	lightcurve	T13
2002 UX$_{25}$	?	?	329±52	104±17	$0.12^{+0.05}_{-0.03}$	thermal	S08
	?	?	332±12	105±12	$0.107^{+0.005}_{-0.008}$	thermal	F13
	?	>0.91	?	?	?	lightcurve	TW

Notes:

a.: Vilenius et al. (2013) paper is in preparation and some values may differ with the final paper version.

b.: Sheppard, Ragozzine and Trujillo (2012) only assume a possible density in order to derive a size and albedo, none of these values have been computed.

c.: Two orbital solutions are suggested by Vachier, Berthier and Marchis (2012), and two different density estimations are derived depending on the orbital solution.

d.: Braga-Ribas et al. (2013) obtained the equatorial radius of Quaoar.

References list: B04: Brown and Trujillo (2004); G08: Grundy et al. (2008); S08: Stansberry et al. (2008); B09: Brucker et al. (2009); B10: Brown et al. (2010); F10: Fraser and Brown (2010); L10: Lim et al. (2010); M10: Müller et al. (2010); T10: Thirouin et al. (2010); G11: Grundy et al. (2011b); G11a: Grundy et al. (2011c); M12: Mommert et al. (2012); S12: Stansberry et al. (2012); SS12: Santos-Sanz et al. (2012); Sh12: Sheppard, Ragozzine and Trujillo (2012); T12: Thirouin et al. (2012); V12: Vilenius et al. (2012); VBM12: Vachier, Berthier and Marchis (2012); B13: Braga-Ribas et al. (2013); F13: Fornasier et al. (2013); Fr13: Fraser et al. (2013); T13: Thirouin et al. (2013b); V13: Vilenius et al. (2013); TW: Results are not published yet and are only reported in this work.

VIII.1.3.3   Size and Albedo from other methods

The component sizes and/or albedo can be estimated by other means. For example, thermal modeling can be used to estimate such parameters (Stansberry et al., 2008; Müller et al., 2010; Mommert et al., 2012; Vilenius et al., 2012; Vilenius et al., 2013; Fornasier et al., 2013), as well as direct imaging (Brown and Trujillo, 2004), from the mutual orbit (Grundy et al., 2008; Brown et al., 2010) or from stellar occultations (Sicardy et al., 2011; Braga-Ribas et al., 2013). So, it is possible to verify if the derived parameters from lightcurves and other methods are consistent or not, so to check the validity of our method.

In Table 15, the density, sizes of both components and/or albedo derived from other method(s) are summarized. As already mentioned, our method is only valid for Jacobi ellipsoids, so care has to be taken in the cases of objects with low variability which are presumably MacLaurin spheroids. We must point out that for non spherical bodies the concept of radius does not make sense and we need to talk about an equivalent radius to that of a sphere in volume or in area.

In the case of thermal modeling, we must emphasize that the radius obtained thanks to modeling of *Spitzer Space Telescope* or *Herschel Space Observatory* data are equivalent radius of the projected area, and not the "exact radius", so care has to be taken with this and as consequence the derived density, for example, present a high uncertainty. For example, assuming that an object is triaxial with semi-axes a>b>c, and viewed from its equator, the equivalent radius (R_{eq}) is:

$$R_{eq} = \sqrt{\frac{ca + cb}{2}} \qquad \text{(Equation VIII.5)}$$

Based on the lightcurve amplitude, and assuming that such an object is in hydrostatic equilibrium, one can derive the ratios b/c and a/c according to Chandrasekhar (1987). Using the equivalent radius estimated by thermal modeling, one can calculate the semi-axes, a, b, and c. Finally, the equivalent volume radius can be expressed as:

$$R_{eq}^v = \sqrt[3]{abc} \qquad \text{(Equation VIII.6)}$$

In conclusion, one must keep in mind that the radii proposed in Stansberry et al. (2008); Lellouch et al. (2010); Müller et al. (2010); Mommert et al. (2012); Vilenius et al. (2012); Vilenius et al. (2013); Fornasier et al. (2013) are equivalent radii of the projected area, so densities should not be computed using these values.

In the cases of Quaoar-Weywot and Orcus-Vanth systems, our values are clearly off, but this was expected as in both cases, we are studying MacLaurin spheroids. Based on the low amplitude lightcurves of Salacia-Actaea, 2003 MW_{12}, and Typhon-Echidna systems, we have to expect MacLaurin spheroids. For Salacia-Actaea, we derived a density >1 g cm^{-3}, a primary (secondary) radius of <491 km (<165 km), and a geometric albedo of >0.03 for both components. Our albedo estimation is lower than the albedo obtained with thermal modeling, and we derived higher radii. In the cases of 2003 MW_{12} and Typhon-Echidna systems, we derived higher albedos and lower radii for the components. However, we must point out that our estimations for these three systems are consistent with the thermal modeling within the error bars.

In the case of 2007 TY_{430}, there is no study able to confirm our estimations. Sheppard, Ragozzine and Trujillo (2012) concluded that assuming a minimum density of 0.5 g cm^{-3}, the system albedo is >0.17 and that both components radii are <60 km. This is similar to our own results but they assumed a density to start with. For the 2001 QY_{297} system, Vilenius et al. (2013) derived a very low density of $0.32^{+0.18}_{-0.13}$ g cm^{-3}, a geometric albedo of $0.075^{+0.037}_{-0.027}$, and primary/secondary radii around 130 km/107 km. Such results are in agreement with the parameters derived from the lightcurve of this system.

For Huya, 2003 AZ_{84}, 2007 UK_{126}, and 2002 UX_{25}, we only derived the lower limits to their densities. However, as all of these systems have a low lightcurve amplitude, our estimation is only

a crude value.

In this section, we have shown that deriving physical parameters such as albedo, sizes and density from the lightcurves of binary systems is a reliable technique for Jacobi ellipsoids.

VIII.1.4   Some correlations

We searched for correlations between physical (albedo, rotational period, and lightcurve amplitude) and orbital parameters (perihelion distance, aphelion distance, absolute magnitude, argument of perihelion, longitude of the ascending node, inclination, orbital eccentricity, and semimajor axis). Only physical parameters derived from lighturves have been considered in this study. We used the Spearman rank correlation (Spearman, 1904) because this method is less sensitive to atypical/wrong values and do not assume any population probability distribution. We computed the strength of the correlations by calculating the Spearman coefficient ρ and the significance level (SL). The ρ coefficient has values between -1 and 1. If $\rho > 0$, there is a possible correlation, whereas $\rho < 0$ indicated a possible anti-correlation and if $\rho = 0$, there is no correlation. We consider a correlation as: i) strong if $|\rho| > 0.6$, ii) weak if $0.3 < |\rho| < 0.6$, and iii) inexistent if $|\rho| < 0.3$. The significance of the ρ parameter is measured by the SL: i) very strong evidence of correlation if SL>99%, ii) strong evidence of correlation if SL>97%, and iii) reasonably strong evidence of correlation if SL>95%. Such criteria have been used in several studies of correlations/anti-correlations between colors and orbital elements, for example in Hainaut, Boehnhardt and Protopapa (2012); Peixinho, Lacerda and Jewitt (2008); Peixinho et al. (2012).

In Table 24 (see Appendix B), we summarize correlations and anti-correlations. In a first step, we divided our sample into five sub-groups: the entire sample, the binary sample, the sample without binary objects, the sample without the centaur population, and finally the sample without the binary and the centaur populations. In order to provide a complete study, we also divided the sample according to their dynamical classes (Gladman, Marsden and Vanlaerhoven (2008) dynamical classification) and according to their size. We chose an absolute magnitude cut-off of 5 to distinguish small/large objects. We did not include Pluto-Charon and Sila-Nunam systems, because they are tidally locked (Grundy et al., 2012; Buie, Tholen and Wasserman, 1997) so they do not preserve their original angular momentum, in the search for correlations with rotational period. 2010 WG$_9$ is not included in our sample because there are evidences that this object is a tidally-evolved binary TNO (Rabinowitz et al., 2013). Care was taken to select only objects with a rotational period and lightcurve amplitude estimations, and objects with only a constraint about the lightcurve amplitude were not included in our samples. Correlations/anti-correlations found in the non-binary sample have been presented in Chapter VII and will not be explained here.

Our main purpose in this section is to report features of the binary population not noticed in the non-binary population. First of all, we must point out that, as previously mentioned, there are several observational biases in the database, so care has to be taken with the correlation/anti-correlation interpretations.

1. *Lightcurve amplitude correlations/anti-correlations*:

    There are evidences of anti-correlation between lightcurve amplitude and eccentricity in several sub-groups, as well as between lightcurve amplitude and inclination. Such anti-correlations indicate that objects with a small lightcurve amplitude (with less deformation) are in eccentric and inclined orbits whereas objects with a high lightcurve amplitude (deformed objects) are in circular orbits at low inclination. Anti-correlation between lightcurve amplitude and eccentricity affects objects with an absolute magnitude (H) less than 5 (large objects). However, in the case of the binary population and the classical objects, this anti-correlation affects small objects and the all object sizes (respectively).

For the case of lightcurve amplitude versus absolute magnitude, values of the Spearman parameter (ρ) and significance level (SL) clearly indicate that the smaller objects are probably more deformed than the larger ones. Except in the case of resonants with H<5 and the sample of large objects without the binaries where lightcurve amplitude and absolute magnitude are anti-correlated. In the case of centaurs and dynamically cold classicals no correlation/anti-correlation between such parameters is reported. However, we must keep in mind that both samples are limited.

In conclusion, we are not showing any special different feature between the binary and the non-binary populations regarding the lightcurve amplitude.

2. *Albedo correlations/anti-correlations*:

There is an anti-correlation between the albedo and the inclination in several samples, as well as between the albedo and the eccentricity. These anti-correlations indicate that objects with a high albedo are at low inclination and low eccentricity. Such a possibility has been already noted by Brucker et al. (2009), especially in the case of dynamically cold classical objects. However, we must point out that dynamically hot classical objects at higher inclination, also present an anti-correlation between the albedo and the inclination but only for object with H≥5 (based on a limited sample of objects).

The case of the sample without the centaur population is interesting and indicates different characteristics according to the object size. In fact, the sample limited to objects with H<5 presents correlations between albedo-inclination and albedo-eccentricity, whereas the sample composed by objects with H≥5 favors anti-correlations between the same parameters. We must point out that not only the sample without the centaur population is presenting such fact according to the object size. In fact, there are some weak evidences in other samples. For example, there is a strong correlation between albedo and eccentricity in the binary population with H≥5, and a weak (the sample is composed by few objects, and so according to our criterion this anti-correlation give us a hint) anti-correlation in the binary population with H<5.

In conclusion, albedo correlations/anti-correlations of the binary and the non-binary population are similar, so the binary population is not showing different feature with the non-binary population.

3. *Spin period correlations/anti-correlations*:

We looked for correlations/anti-correlations between rotational period and orbital parameters. Correlations between rotational period and the argument of the perihelion in some sub-groups have been noted, as well with the inclination. A possible reason for such correlations is not clear and may be attributed to observational biases.

Several correlations and anti-correlations between physical parameters and ascending node, perihelion distance, and argument of the perihelion are also listed in Table 24. Reasons for such features are not obvious and may be attributed to observational biases. More observational information is required to confirm or discard such features. We must also point out several weak correlations/anti-correlations such as rotational period versus absolute magnitude in the dynamically cold classical and resonants groups, and rotational period versus eccentricity in the binary population, unfortunately, more short-term variability studies are needed. In fact, one must keep in mind that only 32 primaries and 3 satellites have a rotational period and/or peak-to-peak amplitude or constraints reported in the literature and in

this work.

In conclusion, the binary population is not showing different feature compared to the non-binary population. Thanks to these correlations, it is evident that each dynamical class has its own characteristics and so formation and evolution. We also point out the dependence of the object size. Largest and smallest objects present different features. However, in several cases the sample is still too limited and drawing reliable conclusions is not obvious.

VIII.1.5   Lightcurve amplitude and Rotational period distributions

VIII.1.5.1   Lightcurve amplitude distributions

In Figure 166 and Figure 167, we show the number of objects having a lightcurve amplitude value reported in the literature and in this work. Objects with only a constraint about their lightcurve amplitude were not taken into account.
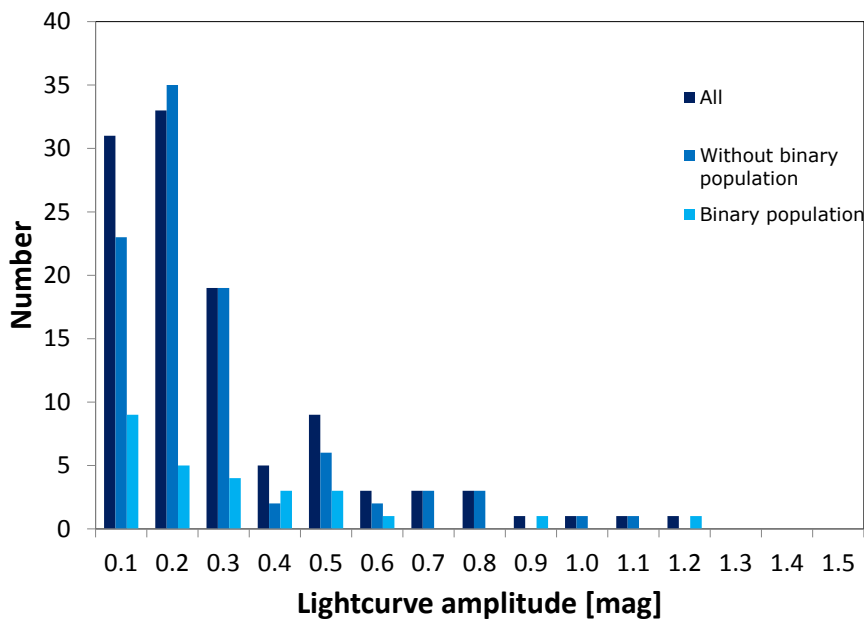
Figure 166: *Number of objects versus lightcurve amplitude:* we consider three different samples: the whole sample, the sample without binary objects, and the binary sample.

In the Figure 166, we focus on three samples: the entire sample, the binary population, and the sample without the binary population. First of all, we must point out that the majority of objects (in the three samples) have a low amplitude, <0.2 mag. Around 57% of the entire sample, 59% of the sample without the binary population and 54% of the binary sample have a low amplitude. The main reason for observing flat lightcurves would be due to a spherical object (or MacLaurin) with low albedo variations along the surface. The second option for such lightcurve amplitude would be due to the pole-on orientation of the object (rotational axis toward the observer). The most reasonable option is to consider that observed objects are mostly MacLaurin spheroids with

a very high homogeneity on their surfaces. As pointed out in Section VII.6.4, Duffard et al. (2009) estimated that for a fixed density of 1 g cm^{-3}, one expects 55.63% of MacLaurin spheroids and only 12.61% of Jacobi ellipsoids while for a fixed density of 1.5 g cm^{-3}, one expects 11.92% of Jacobi ellipsoids and 72.31% of MacLaurin spheroids. On the other hand, we must point out that the smallest objects, collisionally more evolved, have a higher peak-to-peak lightcurve amplitude (Duffard et al., 2009). For example, the centaur population seems to have a higher amplitude, unfortunately, to date, there are only 17 lightcurves reported for such a population.
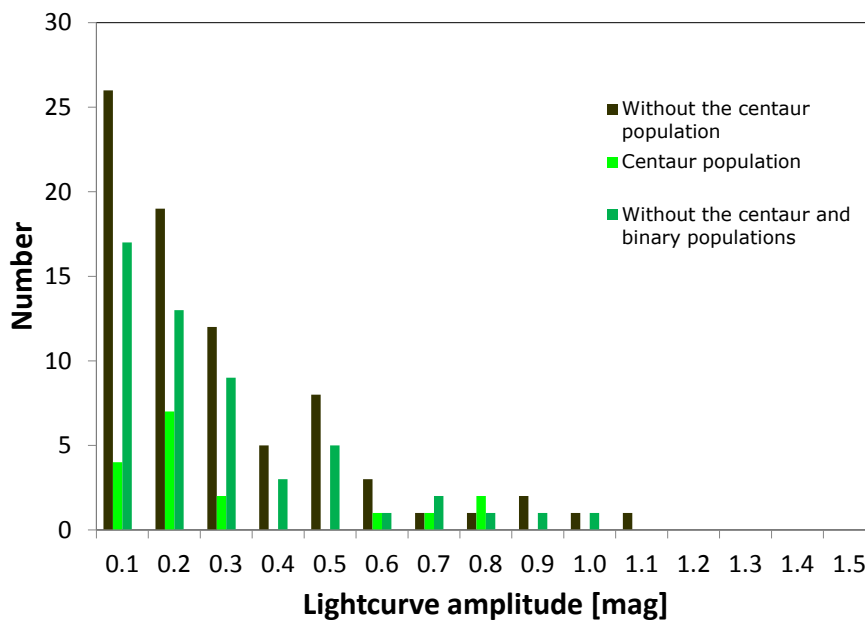
Figure 167: *Number of objects versus lightcurve amplitude:* we consider three different samples: the sample without the centaur population, the centaur population, and the sample without the centaur and the binary populations.

In Figure 167, we proposed a new distribution considering the centaur population. The sample without the binary and the centaur populations has mainly amplitudes between 0.1 and 0.2 mag. In conclusion, there are hints that the binary amplitudes may be slightly larger than the non-binary population, but overall the distributions are similar and only more studies about short-term variability of binary systems will allow us to confirm or not such a tendency. On the other hand, we must point out that the smallest objects seems to have a higher amplitude. In fact, in the previous chapter, we mentioned and studied the strong correlation between the lightcurve amplitude and the absolute magnitude.

VIII.1.5.2 Rotation period distributions

For our discussion about rotational periods, we removed Pluto-Charon and Sila-Numan systems from our sample. Both systems are tidally locked and synchronized (Buie, Tholen and Wasserman, 1997; Grundy et al., 2012). Because the primordial spin rate of the primary has been altered by the satellite, we excluded them from our study. A recent study about 2010 WG$_9$ suggested a rotational period of 131.89±0.06 h or 263.78±0.12 h (Rabinowitz et al., 2013). Such long rotational
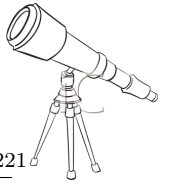
periods have been observed only for tidally-evolved binary TNOs (see Chapter VIII), suggesting that this object may be such a system. As the case of 2010 WG$_9$ may be similar to the cases of Pluto-Charon and Sila-Numan systems, we will not take into account this object in the discussion about rotational period.

For all considerations in this dissertation only objects with a well determined period and amplitude are taken into account. In case of multiple determinations of the period and/or amplitude, we selected the preferred value by the author(s) who published the study. If no preferred value is mentioned, we proceed to a random choice. In fact, in some cases several rotational periods are possibles, and in such cases we have to choose randomly one of these rotational periods. For this purpose, we use a specific program which randomly selects a rotation period for the object between all the possible rotational periods. Then, we build a histogram in the range [Ω, Ω+dΩ]. The process is repeated 100,000 times and for each time a new histogram is built. The final histogram is built by computing the mean of the frequencies in each bins. In other words, the final histogram keeps the information of the previous 100,000 previous histograms.

As in Binzel et al. (1989), we fitted the rotational frequency distribution to a Maxwellian distribution expressed as:

$$f\left(\Omega\right) = \sqrt{\frac{2}{\pi}} \frac{N\Omega^2}{\sigma^3} exp\left(\frac{-\Omega^2}{2\sigma^2}\right) \hspace{2cm} \text{(Equation VIII.7)}$$

where N is the number of objects, Ω is the rotation rate in cycles/day, σ is the width of the Maxwellian distribution. The mean value of this distribution is:

$$\Omega_{mean} = \sqrt{\frac{8}{\pi}}\sigma \hspace{2cm} \text{(Equation VIII.8)}$$

In the previous chapter, we studied several sample considering the binary and the non-binary populations altogether, but here both populations will be compared. In Figure 168, three different samples are plotted: the entire sample, the binary population, and the sample without the binary population. From Maxwellian fits to the rotational frequency distributions, the mean rotational periods are 8.66 h for the entire sample, 8.31 h for the sample without the binary population and, finally, 10.08 h for the binary population. On the other hand, the mean rotational periods are 9.17 h, 9.27 h, and 9.06 h for the entire sample, the sample without the binary population and the binary population, respectively.

Duffard et al. (2009) noted that the centaur population has a higher mean rotational period. In fact, as this population is more collisionally evolved, their rotational period might be affected. We removed them from our different samples and proposed two new Maxwellian distributions. In Figure 169, we plotted: the sample without the centaur population and the sample without the centaur and the binary populations. Based on the Maxwellian distribution fits, we computed a mean rotational period of 8.25 h, 7.90 h for the sample without the centaur population and for the sample without centaur and the binary populations, respectively. On the other hand, the mean rotational periods are 8.77 h, and 8.71 h for the sample without the centaur population and for the sample without the centaur and the binary populations, respectively.

In conclusion, based on the Maxwellian distribution fits, we found a mean rotational period for the sample without the binary and the centaur populations of 8.64 h, whereas the binary population seems to have a higher mean rotational period of 10.08 h. We must point out that the number of binary/multiple systems whose short-term variability has been studied is limited, but it is reasonable to expect that binary systems have longer rotational periodicities. In fact, several effects can slow down the primary rotational rate.

For example, collision can slow down the primary rotational rate. In fact, by means of N-body numerical simulations, Takeda and Ohtsuki (2009) concluded than, after a catastrophic collision,
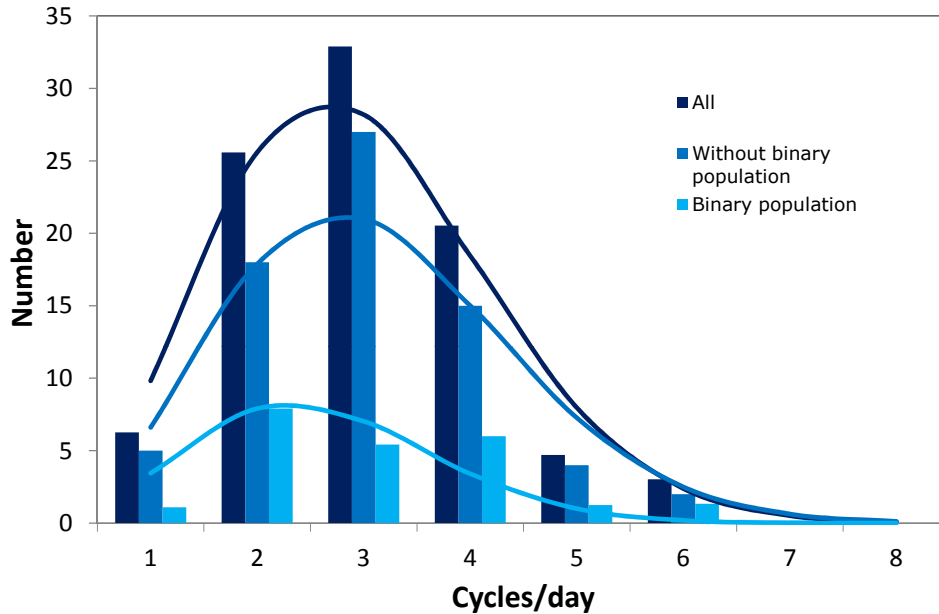
Figure 168: *Number of objects versus cycles/day:* I plotted three different samples: the entire sample, the binary population, and the sample without the binary population. A Maxwellian fit to the entire sample gives a mean rotational period of 8.04 h. The Maxwellian fit of the sample without binary objects and gives a mean rotational period of 7.76 h. Finally, the fit for the binary population gives a mean rotational period of 9.17 h.

the largest remaining fragment always rotates slower that before the collision. The second effect able to slow down the primary (and the secondary) rotational rate is the tidal effect. In fact, tidal effects can synchronize the spin rate of the primary/secondary to its orbital period, such as for the Pluto-Charon system.

VIII.2   Tidal effect

Part of this dissertation is dedicated to the short-term variability of TNOs, and we reported the short-term variability studies of several binary/multiple systems (see Chapter VI). In case of binary/multiple systems, one has to take into account the tidal effects between both components. To understand the tidal effects in a binary system, we will present the case of the Earth-Moon system.

    The long term effect of the tides is that energy is dissipated by friction in the oceans and the land and in the distortion of the Moon by the tidal pull of the Earth. This slows down the rotation rate of the Earth and moves the Moon further away from the Earth. The Earth loses rotational energy which is given to the Moon's orbit. The Earth's rotation rate will be slowed down so that it is the same as that of the orbital period of the Moon Hubbard (1984). The Earth will then always keep the same face towards the Moon in the same way that the Moon already keeps the same face towards the Earth. After that the system will slowly lose energy so that the Moon will come closer to the Earth again. Obviously, this is a very slow effect. The present rate of change is that the Earth's rotation rate is slowing by 16 seconds every million years and the distance of the Moon is
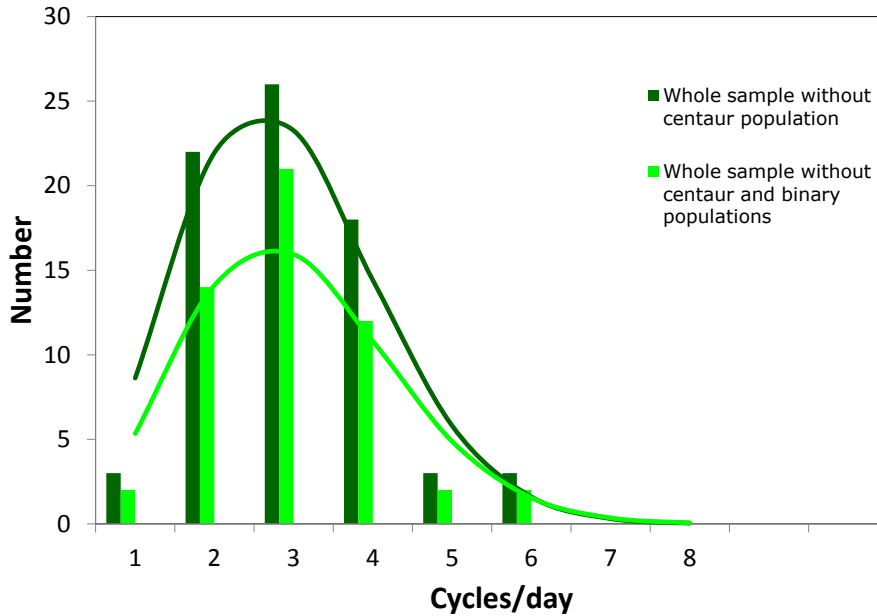
Figure 169: *Number of objects versus cycles/day:* I plotted two different samples: the sample without the centaur population, and the sample without the centaur and the binary populations. A Maxwellian fit to the first sample gives a mean rotational period of 8.25 h. The second Maxwellian fit of the sample without binaries and centaurs gives a mean rotational period of 7.90 h.

increasing by 120 cm each year Hubbard (1984).

In the same way the the tidal forces of the Earth on the Moon have caused it to rotate in synchronism with its orbital period, almost all of the satellites of the planets do the same. Such an effect must also to be considered for the BTNOs. None of the studied systems reported in this work are tidally locked, because we have evidences for rotational periods of several hours. However, it is interesting to check if we have to expect that such systems are tidally locked, so to confirm our observations, and we can estimate the time required for such systems to be tidally locked and get constraints on internal properties of the objects. On the other hand, tidal effect can circularize the satellite orbit, so we can deduce if the orbit is circular or not.

VIII.2.1 Circularization time

According to Goldreich and Soter (1966), the time needed to circularize an orbit is:

$$t_{circular} = \frac{4Q_{satellite}M_{satellite}}{63M_{primary}}\sqrt{\frac{a^3}{G(M_{primary}+M_{satellite})}}\left(\frac{a}{R_{satellite}}\right)^5 \quad \text{(Equation VIII.9)}$$

where G is the gravitational constant, $M_{satellite}$ and $M_{primary}$ are the satellite and primary masses (respectively), a is the orbital semimajor axis, $Q_{satellite}$ is the dissipation parameter of the satellite, and $R_{satellite}$ is the satellite radius.

The dissipation parameter depends on the body rigidity, the acceleration of gravity at the object surface, density, and size. According to Goldreich and Soter (1966), this parameter range is 10 to 6×10^4. We will test three different values of dissipation: i) Q=10, Q=100 (typical value used in the TNO case (Noll et al., 2008a)), and iii) Q=6×10^4.

In Table 16, all the BTNOs whose short-term variability has been studied in this work are reported, as well as the parameters needed to compute the circularization time.

In the following paragraphs, we will discuss the circularization time computed assuming a dissipation fo 100. In the case of Actaea, and the satellites of Huya and 2003 MW$_{12}$, the times required to circularize the orbit are "short" (compared to the age of the Solar System) and so, we expect nearly circular orbits. With an orbital eccentricity of 0.0084±0.0076 and 0.02±0.04 for Actaea and for the satellite of 2003 MW$_{12}$ (respectively), both orbits are nearly circular (Stansberry et al., 2012; Grundy et al., 2011c). The orbit of Huya's satellite is unknown, but we expect a nearly circular orbit.

The times required to circularize the orbit of Echidna, Vanth, and the satellites of 2007 UK$_{126}$ and 2002 UX$_{25}$ are long, and so we can expect non-circular orbits. With an orbital eccentricity of 0.526±0.015 for Echidna, its orbit is not circular (Grundy et al., 2008). The orbits of 2002 UX$_{25}$, and 2007 UK$_{126}$ satellites are unknown, but we have to expect non-circular orbits in both cases. The orbit of the satellite of 2007 TY$_{430}$ is far from circular and will require a long time to be circular. According to Sheppard, Ragozzine and Trujillo (2012), the orbital eccentricity is 0.1529±0.0028, this confirms the non-circular orbit. The orbits of Weywot, and of the satellites of 2001 QY$_{297}$ and 2003 AZ$_{84}$ will also require a long time to be circular. Fraser et al. (2013) derived an orbital eccentricity of ∼0.13-0.16 for Weywot, and Grundy et al. (2011c) estimated an orbital eccentricity of 0.4175±0.0023 for the satellite of 2001 QY$_{297}$. So, both orbits are not circular. The orbit of the satellite of 2003 AZ$_{84}$ is unknown but, we expect a non-circular orbit. Based on the "short" time required to circularize the orbit of Vanth, we can expect a non-circular orbit, which is in agreement with the upper limit of the eccentricity of 0.0036 estimated by Brown et al. (2010). But as pointed out in Ortiz et al. (2011) it is quite possible that Vanth has a much larger mass and size than originally estimated by Brown et al. (2010).

We also test value of 10 and 6×10^4 for the dissipation in order to have a range of circularization times.

Table 16: In this table, we summarize the system names, the dissipation parameter of the satellite, $Q_{satellite}$, the orbital semi-major axis (a), and the time required to circularize the orbit ($t_{circular}$). The orbital semi-major axes are available in the references listed in the last column. We must point that in the case of 2003 MW_{12}, 2007 UK_{126}, 2002 UX_{25}, and 2003 AZ_{84} systems, the orbital semi-major axes are from the circulars announcing the satellite discovery, and so such values are crude estimations.

System	$Q_{satellite}$	a [km]	$t_{circular}$ [years]	Ref.
Haumea-Namaka	10	25,657±91	$(2.50\text{-}2.61)\times10^7$	Ragozzine and Brown (2009)
Haumea-Namaka	100	...	$(2.50\text{-}2.61)\times10^8$	...
Haumea-Namaka	6×10^4	...	$(1.50\text{-}1.57)\times10^{11}$	...
Haumea-Hi'iaka	10	49,880±198	$(4.69\text{-}4.93)\times10^{10}$	Ragozzine and Brown (2009)
Haumea-Hi'iaka	100	...	$(4.69\text{-}4.93)\times10^{11}$	...
Haumea-Hi'iaka	6×10^4	...	$(2.82\text{-}2.96)\times10^{14}$	...
Orcus-Vanth[a]	10	8,980±23	$(7.81\text{-}8.97)\times10^4$	Brown et al. (2010)
Orcus-Vanth	100	...	$(7.81\text{-}8.97)\times10^5$	...
Orcus-Vanth	6×10^4	...	$(4.69\text{-}5.31)\times10^8$	...
Orcus-Vanth[b]	10	8,980±23	$(1.96\text{-}2.15)\times10^5$	Ortiz et al. (2011)
Orcus-Vanth	100	...	$(1.96\text{-}2.15)\times10^6$	...
Orcus-Vanth	6×10^4	...	$(1.29\text{-}1.18)\times10^9$	...
Salacia-Actaea	10	5,619±87	$(4.17\text{-}7.16)\times10^3$	Stansberry et al. (2012)
Salacia-Actaea	100	...	$(4.17\text{-}7.16)\times10^4$	...
Salacia-Actaea	6×10^4	...	$(2.07\text{-}4.30)\times10^7$	...
Huya	10	1,800	205	Noll et al. (2012)
Huya	100	...	2.05×10^3	...
Huya	6×10^4	...	1.23×10^6	...
2003 MW_{12}	10	4,200	994	Grundy et al. (2011b)
2003 MW_{12}	100	...	9.94×10^3	...
2003 MW_{12}	6×10^4	...	5.97×10^6	...
2007 UK_{126}	10	3,600	2.49×10^4	Grundy et al. (2011b)
2007 UK_{126}	100	...	2.49×10^5	...
2007 UK_{126}	6×10^4	...	1.50×10^8	...
2007 TY_{430}	10	21,000±160	$(1.87\text{-}2.07)\times10^{12}$	Sheppard, Ragozzine and Trujillo (2012)
2007 TY_{430}	100	...	$(1.87\text{-}2.07)\times10^{13}$	...
2007 TY_{430}	6×10^4	...	$(1.12\text{-}1.24)\times10^{16}$	...
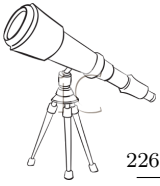
Table 16: continued.

System	$Q_{satellite}$	a [km]	$t_{circular}$ [years]	Ref.
Quaoar-Weywot	10	14,500±800	$(6.76\text{-}13.2)\times10^6$	Fraser and Brown (2010)
Quaoar-Weywot	100	...	$(6.76\text{-}13.2)\times10^7$	...
Quaoar-Weywot	6×10^4	...	$(4.05\text{-}7.94)\times10^{10}$	...
Typhon-Echidna	10	1,628±29	$(4.27\text{-}7.52)\times10^4$	Grundy et al. (2008)
Typhon-Echidna	100	...	$(4.27\text{-}7.52)\times10^5$	...
Typhon-Echidna	6×10^4	...	$(2.91\text{-}4.51)\times10^8$	...
2001 QY$_{297}$	10	9,960±31	$(2.73\text{-}2.84)\times10^6$	Grundy et al. (2011c)
2001 QY$_{297}$	100	...	$(2.73\text{-}2.84)\times10^7$	...
2001 QY$_{297}$	6×10^4	...	$(1.64\text{-}1.70)\times10^{10}$	...
2002 UX$_{25}$	10	5,000	1.51×10^4	Brown and Suer (2007)
2002 UX$_{25}$	100	...	1.51×10^5	...
2002 UX$_{25}$	6×10^4	...	9.09×10^7	...
2003 AZ$_{84}$	10	7,200	1.65×10^6	Brown and Suer (2007)
2003 AZ$_{84}$	100	...	1.65×10^7	...
2003 AZ$_{84}$	6×10^4	...	9.88×10^{10}	...

Notes:
[a]: Assuming a secondary-to-primary mass ratio of 0.03; [b]: Assuming a secondary-to-primary mass ratio of 0.09.

Previously, we have considered the tidal effects as main factor to circularize the orbit. However, the Kozai mechanism can also circularize the orbits (Kozai, 1962). Such a mechanism refers to the orbit of a satellite that is perturbed by another body orbiting farther out, such as the Sun in our case. Due to the perturbation, the orbit of the satellite experiences libration (oscillation) of its argument of pericenter. Porter and Grundy (2012) presented an exhaustive study about Kozai effect on BTNOs. They simulated a large set of synthetic BTNOs and confirmed that the Kozai effect can completely reshape the initial orbits of the systems. One result of Porter and Grundy (2012) simulations is that a large number of the simulated BTNOs finished with a very tight and circular orbits. In conclusion, we have to expect that most of the BTNOs have circular orbits. To date, only 18 objects have well-known orbits and 30 objects have ambiguous orbits, but it appears that several systems have near-circular orbits (Grundy et al., 2011b).

VIII.2.2   Synchronization time

Tidal effects can synchronize the satellite and primary spin rates to the orbital period. Several formula have been proposed in the literature to estimate the time needed to lock the primary/secondary rotational rates. Here, we will compute such a time using two equations: i) Hubbard (1984) formula that has been used to study the tidal effect in the system Moon/Earth, as well as the Earth's spin slowing down, and ii) the Gladman et al. (1996) formula which takes into account the body rigidity.

VIII.2.2.1   Hubbard formula

The time needed to lock the primary rotational rate to the mutual orbital period, according to Hubbard (1984), is:

$$t_{lock} = \frac{2\pi M_{primary} a^6}{3k_{primary}^s G M_{satellite}^2 R_{primary}^3 T_0 \delta} \qquad \text{(Equation VIII.10)}$$

where T_0 is the primary initial rotational rate, $R_{primary}$ and $M_{primary}$ are, respectively, the primary radius and mass, and $M_{satellite}$ is the satellite mass. The parameter δ is expressed as arctan $(1/Q)$ where Q is the dissipation. The parameter $k_{primary}$ is the secular Love number of the primary. Assuming bodies in hydrostatic equilibrium, limits for the secular Love number are $k_{primary}^s$=1.5 for a homogeneous body and $k_{primary}^0$=0 if the mass is condensed at the body center (Bursa, 1992).

In Table 17 are summarized parameters used to compute the time needed to tidally lock the primary. Assuming that both components have the same density is a good approximation in a first time, but we must keep in mind that not necessarily both components have the same density. So, to provide a complete study, we considered three cases for most of the binaries: i) the density of the satellite is the same as the density of the primary (i.e. the system density), ii) the density of the satellite is 1 g cm^{-3}, and iii) the density of the satellite is 0.5 g cm^{-3}.

Assuming a dissipation of Q=100, the times to tidally lock 2007 TY$_{430}$, Quaoar, and 2001 QY$_{297}$ are long (regarding to the age of the Solar System), and so we expect that none of these systems is tidally locked. We must point out that this fact is confirmed thanks to our short-term variability studies of these systems which show evidences for rotation periods of several hours (see Chapter VI). As the densities of 2007 TY$_{430}$, 2007 UK$_{126}$, 2001 QY$_{297}$, and Typhon are low, < 0.5 g cm^{-3}, we only considered satellites with the same density as the primary. Assuming a dissipation of Q=100, the times to tidally locked Salacia, Huya, 2003 MW$_{12}$, Typhon, Orcus, 2003 AZ$_{84}$, and 2002 UX$_{25}$ are short (regarding to the age of the Solar System). So, we expect that these systems are tidally locked. However, there are evidences for rotation periods of several hours in several of them so, primaries are not tidally locked (see Chapter VI).
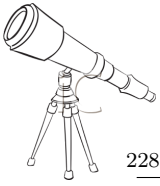
The parameter with the highest range of uncertainty in the Equation VIII.10 is the dissipation parameter (Goldreich and Soter, 1966). We can test the effect of the dissipation parameter.

Assuming that binary systems are primordial (Petit and Mousis, 2004), typically formed $\sim 10^9$ years ago, one can compute a lower limit of the dissipation parameter. For example, considering that Salacia and Actaea have the same density of 1.38 ± 0.27 g cm^{-3}, and taking into account that this system is primordial, the dissipation requires would be $2\text{-}3 \times 10^4$ (Table 17). If the satellite density is lower, the dissipation parameter is lower: if the satellite density is 0.5 g cm^{-3}, the lower limit of the dissipation is $3\text{-}4 \times 10^3$. The computed lower limits of the dissipation are high and there is no reason to expect such values in the Trans-Neptunian belt. We must point out that Equation VIII.10 does not take into account the body rigidity that might have an influence in the tidal locking time.
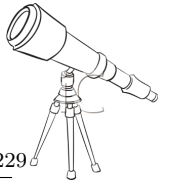
Table 17: In this table, we summarized primary and satellite names, the secular Love number of the primary ($k^s_{primary}$), primary and satellite densities ($\rho_{primary}$ and $\rho_{satellite}$, respectively), initial rotational rate of the primary (T_0), and the time needed to tidally locked the primary (τ_{lock}). We assume a density of 0.5-1 g cm^{-3} for the satellite, except in the case of 2007 TY$_{430}$ B, 2001 QY$_{297}$ B, 2007 UK$_{126}$ B, Echidna. The initial rotational period of the primary is the breakup rotation rate (upper limit) expressed as: $T_0 = (3\pi/G\rho_{primary})^{1/2}$. The Equation VIII.10 has been used.

Primary	Satellite	$k^s_{primary}$	$\rho_{primary}$ [g cm^{-3}]	$\rho_{satellite}$ [g cm^{-3}]	T_0 [h]	Q	τ_{lock} [years]
Salacia	Actaea	1.5	1.38±0.27	1.38±0.27	2.57-3.13	100	(4-5)×10^6
Salacia	Actaea	1.5	1.38±0.27	1.38±0.27	2.57-3.13	(2-3)×10^4	1×10^9
Salacia	Actaea	1.5	1.38±0.27	1.00	2.57-3.13	100	(7-9)×10^6
Salacia	Actaea	1.5	1.38±0.27	1.00	2.57-3.13	(1-2)×10^4	1×10^9
Salacia	Actaea	1.5	1.38±0.27	0.50	2.57-3.13	100	(3-4)×10^7
Salacia	Actaea	1.5	1.38±0.27	0.50	2.57-3.13	(3-4)×10^3	1×10^9
Huya	Huya B	1.5	1.43	1.43	2.76	100	3×10^6
Huya	Huya B	1.5	1.43	1.43	2.76	3×10^6	1×10^9
Huya	Huya B	1.5	1.43	1.00	2.76	100	7×10^4
Huya	Huya B	1.5	1.43	1.00	2.76	2×10^6	1×10^9
Huya	Huya B	1.5	1.43	0.50	2.76	100	3×10^5
Huya	Huya B	1.5	1.43	0.50	2.76	4×10^5	1×10^9
2003 MW$_{12}$	2003 MW$_{12}$ B	1.5	1.11	1.11	3.13	100	2×10^5
2003 MW$_{12}$	2003 MW$_{12}$ B	1.5	1.11	1.11	3.13	7×10^5	1×10^9
2003 MW$_{12}$	2003 MW$_{12}$ B	1.5	1.11	1.00	3.13	100	2×10^5
2003 MW$_{12}$	2003 MW$_{12}$ B	1.5	1.11	1.00	3.13	5×10^5	1×10^9
2003 MW$_{12}$	2003 MW$_{12}$ B	1.5	1.11	0.50	3.15	100	8×10^5
2003 MW$_{12}$	2003 MW$_{12}$ B	1.5	1.11	0.50	3.15	1×10^5	1×10^9
2007 UK$_{126}$	2007 UK$_{126}$ B	1.5	0.32	0.32	5.84	100	3×10^8
2007 UK$_{126}$	2007 UK$_{126}$ B	1.5	0.32	0.32	5.84	4×10^3	1×10^9
2007 TY$_{430}$	2007 TY$_{430}$ B	1.5	0.46	0.46	4.87	100	6×10^{13}
Typhon	Echidna	1.5	$0.36^{+0.08}_{-0.07}$	$0.36^{+0.08}_{-0.07}$	4.98-6.13	100	(4-7)×10^6
Typhon	Echidna	1.5	$0.36^{+0.08}_{-0.07}$	$0.36^{+0.08}_{-0.07}$	4.98-6.13	2×10^4	1×10^9
Quaoar	Weywot	1.5	1.99±0.46	1.99±0.46	2.11-2.67	100	2×10^{12}
Quaoar	Weywot	1.5	$2.18^{+0.43}_{-0.36}$	$2.18^{+0.43}_{-0.36}$	2.04-2.45	100	2×10^{12}
Quaoar	Weywot	1.5	2.7-5.0	2.7-5.0	1.48-2.01	100	(1-2)×10^{12}
Quaoar	Weywot	1.5	1.99±0.46	1.00	2.11-2.67	100	(0.5-1)×10^{13}

Quaoar	Weywot	1.5	1.99 ± 0.46	0.50	2.11-2.67	100	$(2\text{-}4)\times10^{13}$
Quaoar	Weywot	1.5	$2.18^{+0.43}_{-0.36}$	1.00	2.04-2.45	100	$(0.7\text{-}1)\times10^{13}$
Quaoar	Weywot	1.5	$2.18^{+0.43}_{-0.36}$	0.50	2.04-2.45	100	$(3\text{-}4)\times10^{13}$
Quaoar	Weywot	1.5	2.7-5.0	1.00	1.48-2.01	100	$(1\text{-}3)\times10^{13}$
Quaoar	Weywot	1.5	2.7-5.0	0.50	1.48-2.01	100	$(0.5\text{-}1)\times10^{14}$
Orcus	Vanth	1.5	$1.53^{+0.15}_{-0.13}$	$1.53^{+0.15}_{-0.13}$	2.55-2.79	100	$(0.6\text{-}1)\times10^{8}$
Orcus	Vanth	1.5	$1.53^{+0.15}_{-0.13}$	$1.53^{+0.15}_{-0.13}$	2.55-2.79	1×10^{4}	1×10^{9}
Orcus	Vanth	1.5	$1.53^{+0.15}_{-0.13}$	1.00	2.55-2.79	100	$(1\text{-}3)\times10^{8}$
Orcus	Vanth	1.5	$1.53^{+0.15}_{-0.13}$	1.00	2.55-2.79	9×10^{3}	1×10^{9}
Orcus	Vanth	1.5	$1.53^{+0.15}_{-0.13}$	0.50	2.55-2.79	100	$(6\text{-}11)\times10^{8}$
2001 QY$_{297}$	2001 QY$_{297}$ B	1.5	0.29	0.29	6.13	100	2×10^{9}
2003 AZ$_{84}$	2003 AZ$_{84}$ B	1.5	0.85	0.85	3.58	100	4×10^{8}
2003 AZ$_{84}$	2003 AZ$_{84}$ B	1.5	0.85	0.50	3.58	250	1×10^{9}
2002 UX$_{25}$	2002 UX$_{25}$ B	1.5	0.91	0.91	3.46	100	2×10^{7}
2002 UX$_{25}$	2002 UX$_{25}$ B	1.5	0.91	0.91	3.46	7×10^{3}	1×10^{9}
2002 UX$_{25}$	2002 UX$_{25}$ B	1.5	0.91	0.50	3.46	100	5×10^{7}
2002 UX$_{25}$	2002 UX$_{25}$ B	1.5	0.91	0.50	3.46	2×10^{3}	1×10^{9}

VIII.2.2.2   Gladman et al. formula

According to Gladman et al. (1996), the time needed (τ_{lock}) to tidally locked a primary is expressed as:

$$\tau_{lock} = \frac{\omega_{primary} a^6 I_{primary} Q}{3 G M^2_{satellite} k_{primary} R^5_{primary}} \qquad \text{(Equation VIII.11)}$$

where $\omega_{primary}$ is the initial rotational rate of the primary, a is the distance between the primary and the satellite, Q is the dissipation, G is the gravitational constant, $M_{satellite}$ and $R_{primary}$ are, respectively, the mass of the satellite and the radius of the primary, I is the moment of inertia of the primary (such as $I = 0.4 M_{primary} R^2_{primary}$), and $k_{primary}$ is the Love number of the primary.

The Love parameter is:

$$k_{primary} = \frac{1.5}{1 + 19 \mu_{primary}/(2 \rho_{primary} g_{primary} R_{primary})} \qquad \text{(Equation VIII.12)}$$

where $g_{primary} = GM_{primary}/R^2_{primary}$ is the surface gravity of the primary, $\rho_{primary}$ is the primary density, and $\mu_{primary}$ is the primary rigidity. The rigidity is estimated to 3×10^{10} N m^{-2} for rocky objects and 4×10^9 N m^{-2} for icy ones.

In Table 18 are summarized parameters used to compute the time needed to tidally locked the primary. As previously, we considered three cases: i) the density of the satellite is the same as the density of the primary (i.e. the system density), ii) the density of the satellite is 1 g cm^{-3}, and iii) the density of the satellite is 0.5 g cm^{-3}.

Assuming a dissipation of Q=100, and that both components have the same density, times to tidally lock most of the binaries presented here are long (compared to the age of the Solar System), and so we have to expect that none of these systems is tidally locked. We must point out that this fact is confirmed thanks to our short-term variability studies of these systems which show evidences for rotation periods of several hours (see Chapter VI).

However, the times to tidally lock Huya and 2003 MW$_{12}$ are short. And so, we can expect that such systems are tidally locked. However, there are evidences for rotation periods of several hours, and so, primaries are not tidally locked (see Chapter VI). By considering a satellite with a lower density (0.5 g cm^{-3}) and a rigidity for rocky bodies, we computed times to tidally lock the primary around 10^9 years.

Computed tidal locking times according to Gladman et al. (1996) seem in agreement with our observational results. Several formula can be used to compute the tidal locking time, but, as we can see here, results can vary a lot. In conclusion, studied systems in this work are not yet in the state of synchronous (or double synchronous). But, the tidal effects between the primary and the satellite might already have slowed down the primary rotational rate and might explain the rotational period distributions found.

On the other hand, we must point out that tidal circularization and tidal despinning are complex effects. For example, in the case of equal-sized objects, the secondary tidal effect cannot be ignorable. And, assumptions used to derived Equation VIII.9 are not valid for binaries with a moderate to high eccentricity. More studies about tidal effects, as well as estimations of the parameter Q are needed.

Table 18: In this table, we summarized the system names, the Love number of the primary ($k_{primary}$), primary and satellite densities ($\rho_{primary}$ and $\rho_{satellite}$, respectively), initial rotational rate of the primary (T_0), and the time needed to tidally locked the primary (τ_{lock}). We assume a density of 0.5-1 g cm^{-3} for the satellite, except in some cases (see Section VIII.2). The initial rotational period of the primary is the breakup rotation rate (upper limit) expressed as: $T_0 = (3\pi/G\rho_{primary})^{1/2}$. The Equation VIII.11 has been used to compute the time needed to tidally locked the primary.

System	$g_{primary}$ [m kg^{-1} s^{-2}]	μ [N m^{-2}]	$k_{primary}$	$\rho_{primary}$ [g cm^{-3}]	$\rho_{satellite}$ [g cm^{-3}]	T_0 [h]	Q	τ_{lock} [years]
Salacia-Actaea	$(1.33\text{-}1.97)\times10^{-1}$	4×10^9	$(2.5\text{-}5.5)\times10^{-3}$	1.38 ± 0.27	1.38 ± 0.27	2.57-3.13	100	$(0.4\text{-}1)\times10^9$
Salacia-Actaea	$(1.33\text{-}1.97)\times10^{-1}$	3×10^{10}	$(3.3\text{-}7.3)\times10^{-4}$	1.38 ± 0.27	1.38 ± 0.27	2.57-3.13	100	$(3\text{-}9)\times10^9$
Salacia-Actaea	$(1.33\text{-}1.97)\times10^{-1}$	4×10^9	$(2.5\text{-}5.5)\times10^{-3}$	1.38 ± 0.27	1.00	2.57-3.13	100	$(1.2\text{-}1.5)\times10^9$
Salacia-Actaea	$(1.33\text{-}1.97)\times10^{-1}$	4×10^9	$(2.5\text{-}5.5)\times10^{-3}$	1.38 ± 0.27	0.50	2.57-3.13	100	$(5\text{-}6)\times10^9$
Salacia-Actaea	$(1.33\text{-}1.97)\times10^{-1}$	3×10^{10}	$(3.3\text{-}7.3)\times10^{-4}$	1.38 ± 0.27	1.00	2.57-3.13	100	$(0.9\text{-}1.1)\times10^{10}$
Salacia-Actaea	$(1.33\text{-}1.97)\times10^{-1}$	3×10^{10}	$(3.3\text{-}7.3)\times10^{-4}$	1.38 ± 0.27	0.50	2.57-3.13	100	$(3.7\text{-}4.6)\times10^{10}$
Huya	7.78×10^{-2}	4×10^9	8.5×10^{-4}	1.43	1.43	2.76	100	2×10^7
Huya	7.78×10^{-2}	3×10^{10}	1.1×10^{-4}	1.43	1.43	2.76	100	1×10^8
Huya	7.78×10^{-2}	4×10^9	8.5×10^{-4}	1.43	1.00	2.76	100	5×10^7
Huya	7.78×10^{-2}	4×10^9	8.5×10^{-4}	1.43	0.50	2.76	100	2×10^8
Huya	7.78×10^{-2}	3×10^{10}	1.1×10^{-4}	1.43	1.00	2.76	100	4×10^8
Huya	7.78×10^{-2}	3×10^{10}	1.1×10^{-4}	1.43	0.50	2.76	100	1×10^9
2003 MW$_{12}$	1.14×10^{-1}	4×10^9	1.8×10^{-3}	1.11	1.11	3.13	100	5×10^7
2003 MW$_{12}$	1.14×10^{-1}	3×10^{10}	2.4×10^{-4}	1.11	1.11	3.13	100	4×10^8
2003 MW$_{12}$	1.14×10^{-1}	4×10^9	1.8×10^{-3}	1.11	1.00	3.13	100	6×10^7
2003 MW$_{12}$	1.14×10^{-1}	4×10^9	1.8×10^{-3}	1.11	0.50	3.13	100	3×10^8
2003 MW$_{12}$	1.14×10^{-1}	3×10^{10}	2.4×10^{-4}	1.11	1.00	3.13	100	5×10^8
2003 MW$_{12}$	1.14×10^{-1}	3×10^{10}	2.4×10^{-4}	1.11	0.50	3.13	100	2×10^9
2007 UK$_{126}$	2.64×10^{-2}	4×10^9	9.8×10^{-5}	0.32	0.32	5.84	100	2×10^{12}
2007 UK$_{126}$	2.64×10^{-2}	3×10^{10}	1.3×10^{-5}	0.32	0.32	5.84	100	1×10^{13}
2007 TY$_{430}$	7.46×10^{-3}	4×10^9	7.89×10^{-6}	0.46	0.46	4.87	100	4.6×10^{17}
2007 TY$_{430}$	7.46×10^{-3}	3×10^{10}	1.05×10^{-6}	0.46	0.46	4.87	100	3.5×10^{18}
Typhon-Echidna	$(6.57\text{-}9.96)\times10^{-3}$	4×10^9	$(0.6\text{-}1.4)\times10^{-5}$	$0.36^{+0.08}_{-0.07}$	$0.36^{+0.08}_{-0.07}$	4.98-6.13	100	$(2.3\text{-}6.5)\times10^{11}$
Typhon-Echidna	$(6.57\text{-}9.96)\times10^{-3}$	3×10^{10}	$(0.8\text{-}1.9)\times10^{-6}$	$0.36^{+0.08}_{-0.07}$	$0.36^{+0.08}_{-0.07}$	4.98-6.13	100	$(1.7\text{-}4.9)\times10^{12}$
Quaoar-Weywot	$(4.04\text{-}7.48)\times10^{-1}$	4×10^9	$(2.3\text{-}7.5)\times10^{-2}$	2.7-5.0	2.7-5.0	1.48-2.01	100	$(1.0\text{-}4.5)\times10^{13}$
Quaoar-Weywot	$(4.04\text{-}7.48)\times10^{-1}$	3×10^{10}	$(3.1\text{-}10.4)\times10^{-3}$	2.7-5.0	2.7-5.0	1.48-2.01	100	$(7.2\text{-}33.4)\times10^{13}$
Quaoar-Weywot	$(4.04\text{-}7.48)\times10^{-1}$	4×10^9	$(2.3\text{-}7.5)\times10^{-2}$	2.7-5.0	1.00	1.48-2.01	100	$(2.5\text{-}3.3)\times10^{14}$

Quaoar-Weywot	$(4.04\text{-}7.48)\times10^{-1}$	3×10^{10}	$(3.1\text{-}10.4)\times10^{-3}$	2.7-5.0	1.00	1.48-2.01	100	$(1.8\text{-}2.4)\times10^{15}$
Quaoar-Weywot	$(4.04\text{-}7.48)\times10^{-1}$	4×10^{9}	$(2.3\text{-}7.5)\times10^{-2}$	2.7-5.0	0.50	1.48-2.01	100	$(1.0\text{-}1.3)\times10^{15}$
Quaoar-Weywot	$(4.04\text{-}7.48)\times10^{-1}$	3×10^{10}	$(3.1\text{-}10.4)\times10^{-3}$	2.7-5.0	0.50	1.48-2.01	100	$(7.2\text{-}9.7)\times10^{15}$
Quaoar-Weywot	$(2.29\text{-}3.66)\times10^{-1}$	4×10^{9}	$(7.4\text{-}19)\times10^{-3}$	1.99 ± 0.46	1.99 ± 0.46	2.11-2.67	100	$(0.6\text{-}1.8)\times10^{14}$
Quaoar-Weywot	$(2.29\text{-}3.66)\times10^{-1}$	3×10^{10}	$(1\text{-}2.5)\times10^{-3}$	1.99 ± 0.46	1.99 ± 0.46	2.11-2.67	100	$(0.4\text{-}1.4)\times10^{15}$
Quaoar-Weywot	$(2.29\text{-}3.66)\times10^{-1}$	4×10^{9}	$(7.4\text{-}19)\times10^{-3}$	1.99 ± 0.46	1.00	2.11-2.67	100	$(3.4\text{-}4.3)\times10^{14}$
Quaoar-Weywot	$(2.29\text{-}3.66)\times10^{-1}$	3×10^{10}	$(1\text{-}2.5)\times10^{-3}$	1.99 ± 0.46	1.00	2.11-2.67	100	$(2.6\text{-}3.2)\times10^{15}$
Quaoar-Weywot	$(2.29\text{-}3.66)\times10^{-1}$	4×10^{9}	$(7.4\text{-}19)\times10^{-3}$	1.99 ± 0.46	0.50	2.11-2.67	100	$(1.4\text{-}1.7)\times10^{15}$
Quaoar-Weywot	$(2.29\text{-}3.66)\times10^{-1}$	3×10^{10}	$(1\text{-}2.5)\times10^{-3}$	1.99 ± 0.46	0.50	2.11-2.67	100	$(1.0\text{-}1.3)\times10^{16}$
Quaoar-Weywot	$(2.7\text{-}3.9)\times10^{-1}$	4×10^{9}	$(1.0\text{-}2.1)\times10^{-2}$	$2.18^{+0.43}_{-0.36}$	$2.18^{+0.43}_{-0.36}$	2.04-2.45	100	$(4.9\text{-}12)\times10^{13}$
Quaoar-Weywot	$(2.7\text{-}3.9)\times10^{-1}$	3×10^{10}	$(1.4\text{-}2.9)\times10^{-3}$	$2.18^{+0.43}_{-0.36}$	$2.18^{+0.43}_{-0.36}$	2.04-2.45	100	$(3.6\text{-}8.9)\times10^{14}$
Quaoar-Weywot	$(2.7\text{-}3.9)\times10^{-1}$	4×10^{9}	$(1.0\text{-}2.1)\times10^{-2}$	$2.18^{+0.43}_{-0.36}$	1.00	2.04-2.45	100	$(3.4\text{-}4.0)\times10^{14}$
Quaoar-Weywot	$(2.7\text{-}3.9)\times10^{-1}$	3×10^{10}	$(1.4\text{-}2.9)\times10^{-3}$	$2.18^{+0.43}_{-0.36}$	1.00	2.04-2.45	100	$(2.5\text{-}2.7)\times10^{15}$
Quaoar-Weywot	$(2.7\text{-}3.9)\times10^{-1}$	4×10^{9}	$(1.0\text{-}2.1)\times10^{-2}$	$2.18^{+0.43}_{-0.36}$	0.50	2.04-2.45	100	$(1.3\text{-}1.6)\times10^{15}$
Quaoar-Weywot	$(2.7\text{-}3.9)\times10^{-1}$	3×10^{10}	$(1.4\text{-}2.9)\times10^{-3}$	$2.18^{+0.43}_{-0.36}$	0.50	2.04-2.45	100	$(9.9\text{-}12)\times10^{15}$
Orcus-Vanth	$(1.85\text{-}2.21)\times10^{-1}$	4×10^{9}	$(4.8\text{-}6.9)\times10^{-3}$	$1.53^{+0.15}_{-0.13}$	$1.53^{+0.15}_{-0.13}$	2.55-2.79	100	$(4.9\text{-}7.7)\times10^{9}$
Orcus-Vanth	$(1.85\text{-}2.21)\times10^{-1}$	3×10^{10}	$(6.4\text{-}9.2)\times10^{-4}$	$1.53^{+0.15}_{-0.13}$	$1.53^{+0.15}_{-0.13}$	2.55-2.79	100	$(3.7\text{-}5.8)\times10^{10}$
Orcus-Vanth	$(1.85\text{-}2.21)\times10^{-1}$	4×10^{9}	$(4.8\text{-}6.9)\times10^{-3}$	$1.53^{+0.15}_{-0.13}$	1.00	2.55-2.79	100	$(1.4\text{-}1.5)\times10^{10}$
Orcus-Vanth	$(1.85\text{-}2.21)\times10^{-1}$	3×10^{10}	$(6.4\text{-}9.2)\times10^{-4}$	$1.53^{+0.15}_{-0.13}$	1.00	2.55-2.79	100	$(1.0\text{-}1.1)\times10^{11}$
Orcus-Vanth	$(1.85\text{-}2.21)\times10^{-1}$	4×10^{9}	$(4.8\text{-}6.9)\times10^{-3}$	$1.53^{+0.15}_{-0.13}$	0.50	2.55-2.79	100	$(5.6\text{-}6.1)\times10^{10}$
Orcus-Vanth	$(1.85\text{-}2.21)\times10^{-1}$	3×10^{10}	$(6.4\text{-}9.2)\times10^{-4}$	$1.53^{+0.15}_{-0.13}$	0.50	2.55-2.79	100	$(4.1\text{-}4.5)\times10^{11}$
2001 QY$_{297}$	1.13×10^{-2}	4×10^{9}	1.8×10^{-5}	0.29	0.29	6.13	100	5×10^{13}
2001 QY$_{297}$	1.13×10^{-2}	3×10^{10}	2.4×10^{-6}	0.29	0.29	6.13	100	4×10^{14}
2003 AZ$_{84}$	1.39×10^{-1}	4×10^{9}	2.7×10^{-3}	0.85	0.85	3.58	100	9×10^{10}
2003 AZ$_{84}$	1.39×10^{-1}	3×10^{10}	3.6×10^{-4}	0.85	0.85	3.58	100	7×10^{11}
2003 AZ$_{84}$	1.39×10^{-1}	4×10^{9}	2.7×10^{-3}	0.85	0.50	3.58	100	9×10^{10}
2003 AZ$_{84}$	1.39×10^{-1}	3×10^{10}	3.6×10^{-4}	0.85	0.50	3.58	100	2×10^{13}
2002 UX$_{25}$	8.45×10^{-2}	4×10^{9}	1.01×10^{-3}	0.91	0.91	3.46	100	9×10^{9}
2002 UX$_{25}$	8.45×10^{-2}	3×10^{10}	1.34×10^{-4}	0.91	0.91	3.46	100	7×10^{10}
2002 UX$_{25}$	8.45×10^{-2}	4×10^{9}	1.01×10^{-3}	0.91	0.50	3.46	100	3×10^{10}
2002 UX$_{25}$	8.45×10^{-2}	3×10^{10}	1.34×10^{-4}	0.91	0.50	3.46	100	2×10^{11}

VIII.3   Formation of binary/multiple systems

Various models have been proposed to explain the formation of binary/multiple systems. A complete review can be found in Noll et al. (2008a), here we will only introduce the formation models. They can be classified into three groups:

1. Capture models:

    (a) L^3 *mechanism:*

    Goldreich, Lithwick and Sari (2002) proposed a gravitational capture model with three bodies. If a body is strongly interacting with two others and are in the same Hill sphere, a capture might occur. The L^3 mechanism favors the formation of tight binaries. Both prograde and retrograde binaries are formed in roughly equal proportion (Schlichting and Sari, 2008a; Schlichting and Sari, 2008b).

    (b) L^2s *mechanism:*

    This model is inspired by the L^3 mechanism. The L^2s mechanism implies two objects which become bound due to the dynamical friction of a sea of small objects (Goldreich, Lithwick and Sari, 2002). This model is more efficient than the L^3 mechanism to form binaries by around an order of magnitude. Only retrograde binaries are form, and this mechanism fails in creating tight binaries (Schlichting and Sari, 2008a; Schlichting and Sari, 2008b).

    (c) *Chaos-assisted capture:*

    This model is similar to the L^3 mechanism. Astakhov, Lee and Farrelly (2005) considered that two bodies might become trapped in their mutual Hill spheres if a third body is dispersed by the first two bodies. This mechanism would create wide separation binaries with equal size and moderate eccentricity

2. Collisional model:

    (a) *Low velocity collision:*

    Durda et al. (2004) suggested that slow collisions between TNOs might form binary/multiple systems. The Pluto/Charon formation is well known and results from a collision (Canup, 2005; Stern et al., 2006)

3. Other models:

    (a) *Hybrid mechanism:*

    Weidenschilling (2002) suggested that equal-sized systems with a large separation between both components could be produced by a low velocity collision between two objects while in the Hill sphere of a third one.

    (b) *Gravitational collapse:*

    Nesvorný, Youdin and Richardson (2010) proposed the binary/multiple system formation from direct gravitational collapse. This model is able to reproduce a wide range of systems, such as equal-sized binaries, large eccentricities, wide systems. However, this mechanism has trouble producing the retrograde binaries.

(c) *Rotational fission:*

> Ortiz et al. (2012b) considered a rotational fission model to explain the formation of the Haumea system (see Chapter IX for more details). Such a model can also be tested with others and might explain the current configuration of Orcus and its satellite (Ortiz et al., 2011).

Both capture and collisional models require that the number of TNOs in the primordial Trans-Neptunian belt was at least a couple of orders of magnitude higher than currently and so, BTNOs are primordial systems (Petit and Mousis, 2004). Only the formation of few binary systems is well known, such as the Pluto/Charon formation. In fact, it is complicated to favor or discard any model, especially if the orbit is unknown. Currently, the binary formation via capture and/or collision as well as gravitational collapse are the most investigated and seem the most probable in the Trans-Neptunian belt. In fact, the rotational fission scenario is unlikely for most of the binaries, however, in some cases (see Chapter IX) it has to be considered.
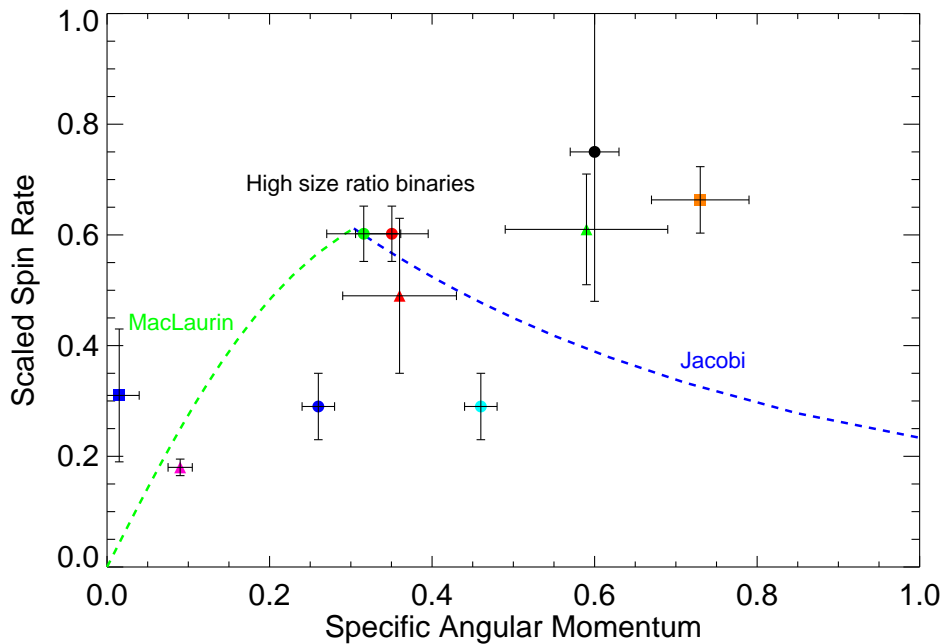
Figure 170: *Scaled Spin Rate versus specific Angular Momentum*: Scaled spin rate and Specific angular momenta computed as mentioned in the text. We indicated the MacLaurin and the Jacobi sequences. The "high size ratio binaries", as indicated in Descamps & Marchis (2008), is near the transition MacLaurin/Jacobi. The legend is as follow: red triangle for Salacia-Actaea, red circle for Haumea-Namaka, green circle for Haumea-Hi'iaka, green triangle for 2003 MW_{12} system, blue square for Quaoar-Weywot, blue circle for Orcus-Vanth assuming a secondary-to-primary mass ratio of 0.03, cyan circle for Orcus-Vanth assuming a secondary-to-primary mass ratio of 0.09, orange square for Typhon-Echidna, black circle for 1998 SM_{165} system, and pink triangle for Eris-Dysnomia. Several binaries are not plotted here (because we restricted the plot for a better visualization): 2007 TY_{430} system (see text), Teharonhiawako-Sawiskera with a specific angular momentum of 3.38±0.27 and a scaled spin rate of 0.51±0.15, and Ceto-Phorcys with a specific angular momentum of 1.11±0.10 and a scaled spin rate of 1.08±0.27. Error bars are approximative.

One argument in favor of a rotational fission scenario for some cases is the specific angular momentum of a binary/multiple system. The specific angular momentum (H), computed according to Descamps and Marchis (2008) is:

$$H = \frac{q}{(1+q)^{\frac{13}{6}}} \sqrt{\frac{a(1-e^2)}{R_{primary}}} + \frac{2}{5}\frac{\lambda_{primary}}{(1+q)^{\frac{5}{3}}}\Omega +$$
$$\frac{2}{5}\lambda_{satellite}\frac{q^{\frac{5}{3}}}{(1+q)^{\frac{7}{6}}}\left(\frac{R_{primary}}{a}\right)^{\frac{3}{2}} \quad \text{(Equation VIII.13)}$$

where q is the secondary-to-primary mass ratio, a is the semi-major axis, e is the eccentricity, and $R_{primary}$ is the primary radius. The Ω parameter is the normalized spin rate expressed as:

$$\Omega = \frac{\omega_{primary}}{\omega_{critical}} \quad \text{(Equation VIII.14)}$$

where $\omega_{primary}$ is the primary rotation rate and $\omega_{critical}$ the critical spin rate for a spherical body:

$$\omega_{critical} = \sqrt{\frac{GM_{system}}{R_{effective}^3}} \quad \text{(Equation VIII.15)}$$

G is the gravitational constant and M_{system} is the system mass and $R_{effective}$ the effective radius of the system (or equivalent radius).

Assuming triaxial objects with semi-axes as $a > b > c$, the λ shape parameter is

$$\lambda_{primary} = \frac{1 + \beta^2}{2(\alpha\beta)^{\frac{2}{3}}} \quad \text{(Equation VIII.16)}$$

where $\alpha = c/a$ and $\beta = b/a$. We considered the satellites as spherical bodies, so $\lambda_{satellite}$=1.

The Scaled Spin Rate (SSR), according to Chandrasekhar (1987) is expressed as:

$$SSR = \frac{\omega_{primary}}{\sqrt{\pi G \rho_{primary}}} \quad \text{(Equation VIII.17)}$$

where $\rho_{primary}$ is the density of the primary. We considered that both components have the same density which is the system density. Scaled spin rate and specific angular momentum are dimensionless values.

In Figure 170 are indicated the MacLaurin and Jacobi sequences (see Section V.1.2.1). Based on a binary asteroid population study, Descamps and Marchis (2008) concluded that binary systems near the MacLaurin/Jacobi transition are likely formed by rotational fission or mass shedding.

Table 19: In this table, we summarize the system names, the secondary-to-primary mass ratio (q), the semi-major axis (a), the eccentricity (e), the primary radius (R_p), the rotational period of the primary and its critical rotational period (respectively, P_p and P_c), the λ shape parameter of the primary (λ_p) and satellite. Here, we consider the satellites as spherical bodies, so $\lambda_s=1$. The specific angular momentum (H) and the scaled spin rate (SSR) are also reported.

System	q	a [km]	e	R_p [km]	λ_p	P_p [h]	P_c [h]	H	SSR	Ref.
Haumea–Namaka	0.001	25,657±91	0.249±0.015	709±50	1.49	3.92	2.09	0.32±0.05	0.61±0.05	R09, T10
Haumea–Hi'iaka	0.01	49,880±198	0.0513±0.0078	709±50	1.49	3.92	2.09	0.40±0.05	0.61±0.05	R09, T10
Orcus–Vanth	0.03	8,980±23	0.001±0.001	459±13	1.44	10.47	2.67±0.12	0.26±0.02	0.29±0.06	B10, T10
Orcus–Vanth	0.09	8,980±23	0.001±0.001	459±13	1.44	10.47	2.67±0.12	0.46±0.02	0.29±0.06	O11, T10
Salacia–Actaea	0.04	5,619±87	0.02±0.04	427±23	1.44	6.61	2.81±0.56	0.36±0.07	0.49±0.14	S12, T12
2003 MW$_{12}$ [a]	0.14	4,200	0.0084	399±46	1.43	5.91	3.13	0.59	0.61	G11b, T13, T12
2007 TY$_{430}$ [b]	>0.85	21,000±160	0.1529±0.0028	<58	1.47	9.28	4.87	4.33	0.61	Sh12, T12
Quaoar–Weywot	0.0004	14,500±800	~0.13–0.16	569^{+24}_{-17}	1.45	8.84	2.39±0.28	0.15±0.02	0.31±0.12	F10, T12
Typhon–Echidna	0.17	1,628±29	0.53±0.01	76^{+14}_{-16}	1.44	9.67	5.60±0.58	0.73±0.06	0.66±0.16	G08, T12
2001 QY$_{297}$	0.56	9,960±31	0.418±0.002	130±21	1.62	11.68	6.13±1.5	1.85±0.39	0.58±0.21	G11, T12
Eris–Dysnomia	0.001	37,600±300	0.017±0.007	1163±6	1.43	13.69	2.08±0.02	0.09±0.01	0.18±0.01	Si11, G11b
Ceto–Phorcys	0.45	1,850±40	0.008±0.009	112±5	1.44	4.43	4.13	1.11±0.10	1.08±0.37	G11b, D08, SS12
Teharonhiawako–Sawiskera	0.38	27,700±100	0.249±0.002	88±10	1.71	9.50	4.16±0.47	3.38±0.27	0.51±0.15	O03, V13
1998 SM$_{165}$	0.04	11,368±10	0.4732±0.0008	144±18	1.33	7.1	4.56±0.87	0.60±0.03	0.75±0.24	S06

Notes:

[a]. The orbit of 2003 MW$_{12}$ is unknown, and only values from the discovery circular are used here. Specific angular momentum and scaled spin rate computed using a lower limit to the density of 1.11 g cm^{-3}.

[b]. Specific angular momentum and scaled spin rate computed using a lower limit to the density of 0.46 g cm^{-3}, and upper limits to the component sizes.

O03: Osip, Kern and Elliot (2003); S06: Spencer et al. (2006); D08: Dotto et al. (2008); G08: Grundy et al. (2008); R09: Ragozzine and Brown (2009); B10: Brown et al. (2010); F10: Fraser and Brown (2010); T10: Thirouin et al. (2010); G11: Grundy et al. (2011c); G11b: Grundy et al. (2011b); S11: Sicardy et al. (2011); S12: Stansberry et al. (2012); T12: Thirouin et al. (2012); SS12: Santos-Sanz et al. (2012); Sh12: Sheppard, Ragozzine and Trujillo (2012); V13: Vilenius et al. (2013)
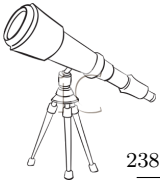
VIII.3.1   Salacia and Actaea

We computed a specific angular momentum of 0.36±0.07 and a scaled spin rate of 0.49±0.14 for this system. Such values allow us to discard a rotational fission scenario to explain the formation of this system (Figure 170). However, we must point out that several parameters used to compute the specific angular momentum and the scaled spin rate presents a high uncertainty, and considering the error bars, Salacia-Actaea may have suffered a rotational fission. For example, the Salacia-Actaea system density presents a high uncertainty: i) $1.16^{+0.59}_{-0.36}$ g cm^{-3} according to Stansberry et al. (2012), ii) 1.38±0.27 g cm^{-3} according to Vilenius et al. (2012), and iii) $1.29^{+0.29}_{-0.23}$ g cm^{-3} according to Fornasier et al. (2013).

The Salacia-Actaea lightcurve is flat, so, this object presents a homogeneous shape without or little deformation. For this reason and due to the size of the satellite, a collisional scenario is not favored to explain the Actaea formation (except a Pluto/Charon like formation). We suggest a capture or gravitational collapse model. A possible rotational fission scenario has to be confirmed.

VIII.3.2   2003 MW$_{12}$ system

We computed a specific angular momentum of 0.59 and a scaled spin rate of 0.61 (Figure 170). In the case of 2003 MW$_{12}$ system, we did not compute the error bars [2] of the specific angular momentum and the scaled spin rate, mainly because as no density estimation is available for this system, we had to use the lower limit of the density derived in this thesis which as already mentioned in only a very crude estimation.

The 2003 MW$_{12}$ system lightcurve is flat. This means that this object is probably a MacLaurin spheroid (or near) with limited shape deformation. So, we favor a capture scenario or gravitational collapse rather than a collisional scenario to explain the satellite formation. The second argument to discard a collisional scenario is the size of the satellite. In fact, the large size of 2003 MW$_{12}$ B suggests a non-collisional formation, except if it was created in a similar Pluto/Charon formation model. We must mention that a flat lightcurve can be due to a pole-on orientation. In such a case, the object may be deformed but we cannot detect it in the lightcurve variation.

However, we used the lower limit to the density to derive the specific angular momentum and the scaled spin rate, so we must keep in mind a possible rotational fission scenario to explain the formation of this system.

VIII.3.3   2007 TY$_{430}$ system

This wide binary system with a specific angular momentum around 4.33 and a scaled spin rate around 0.61 is not plotted in Figure 170 because it is out of the scale. To compute the specific angular momentum and the scaled spin rate of this system, we had to use the lower limit of the density derived in this thesis which as already mentioned in only a very crude estimation.

Sheppard, Ragozzine and Trujillo (2012) already proposed an exhaustive discussion about all possible (or not) formation models for this system. They considered two plausible scenarii: the L^3 mechanism based on gravitational capture proposed by Goldreich, Lithwick and Sari (2002) and the gravitational collapse mechanism studied by Nesvorný, Youdin and Richardson (2010).

VIII.3.4   2001 QY$_{297}$ system

The specific angular momentum of this binary is 1.85±0.39 and its scaled spin rate is 0.58±0.21, this is out of the scale in Figure 170. Those values seem to indicate that the 2001 QY$_{297}$ binary system

---

[2]In Figure 170, we use an error bar of ±0.1 for the specific angular momentum and the scaled spin rate as indication
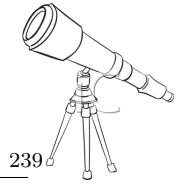
was not formed by rotational fission. In fact, the high value of the specific angular momentum and the scaled spin rate of this system do not fall into the "high size ratio binaries" region indicated in the Figure 170 of Descamps and Marchis (2008) and is far from the Jacobi or MacLaurin sequences. So, we can probably discard a possible rotational fission origin for this binary. We cannot favor any other formation scenario; this asynchronous binary could have been formed by capture and/or collision, or gravitational collapse.

VIII.3.5   Quaoar and Weywot

We computed a specific angular momentum of 0.15±0.02 and a scaled spin rate around 0.31±0.12. So, for this system, does not seem to come from a rotational fission scenario (Figure 170). The Quaoar-Weywot lightcurve has a moderate lightcurve amplitude. This means that this object is probably a MacLaurin spheroid (or near) with limited shape deformation. However, the satellite, Weywot has a small diameter of 81±11 km according to Fornasier et al. (2013) and so a collisional scenario seems the best option to explain the satellite formation.

VIII.3.6   Typhon and Echidna

We computed a specific angular momentum of 0.73±0.06 and a scaled spin rate of 0.66±0.16. This is not too far from the high mass ratio binaries that likely come from fissions. So we cannot discard a rotational fission to explain the system (Figure 170).

The rotational period of the Typhon-Echidna system is not secure but we can affirm that the lightcurve amplitude is low. This means that this object is probably a MacLaurin spheroid with limited shape deformation. And so, we favor a capture scenario or gravitational collapse rather than a collisional scenario to explain the satellite formation. We must mention that a flat lightcurve can be due to a pole-on orientation. In such case, the object may be deformed but we cannot detect it in the lightcurve variation.

VIII.3.7   Orcus and Vanth

We computed a specific angular momentum of 0.26±0.02 and a scaled spin rate of 0.29±0.06 considering a secondary-to-primary mass ratio of 0.09 (Brown et al., 2010) and a specific angular momentum of 0.46±0.02 and a scaled spin rate of 0.29±0.06 (Ortiz et al., 2011) considering a secondary-to-primary mass ratio of 0.03 (Figure 170).

Thanks to a mid-term photometric and astrometric study, Ortiz et al. (2011) suggested the rotational fission as possible formation of this binary system. In Ortiz et al. (2011) it has been shown that the satellite rotation is synchronous (rotational period of the satellite and orbital period are the same), and that the system is not double-synchronous because the primary is spining much faster than the orbital period (Thirouin et al., 2010). If we assume that the initial spin period of Orcus was around its critical value, the total angular momentum lost by the despun to 10 h (the current rotational period, see Chapter VI) would have been gained by the satellite, which would have reached exactly its current configuration if the mass ratio of the system is around 0.09 (the value obtained by assuming that Vanth's albedo is smaller than that of Orcus, which is likely the case according to their very different spectra (Carry et al., 2011)). This would give support to the idea that the satellite might be the result of a rotational fission (see Chapter IX for more details about rotational fission and the case of Orcus-Vanth).

VIII.3.8   2007 UK$_{126}$, Huya, 2002 WC$_{19}$, 2002 VT$_{130}$, 2002 UX$_{25}$, 2003 AZ$_{84}$ systems

We have not enough information about all these systems to compute their specific angular momenta, and scaled spin rates.
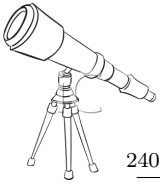
In the case of Huya, due to the satellite size and the flat lightcurve, we favor a capture scenario or a gravitational collapse.

In this work, we propose a very flat lightcurve for 2007 UK$_{126}$, which seems to discard the collisional scenario. However, the size of the satellite is compatible with a collisional formation. In conclusion, for this object, we cannot favor or discard any formation model based on our study.

Based on only few hours of observations, 2002 VT$_{130}$ seems to have a high lightcurve amplitude, and so a collisional scenario may be an option.

The system 2003 AZ$_{84}$ is composed by a large primary and a small satellite. Thus means that a collisional scenario seems the best option.

In the cases of 2002 WC$_{19}$ and 2002 UX$_{25}$ more information is needed to propose a possible formation models.

VIII.3.9   Eris-Dysnomia, Ceto-Phorcys, Teharonhiawako-Sawiskera, 1998 SM$_{165}$ systems

In Figure 170, and Table 19, we also report the cases of other binaries whose short-term variability has not been studied in this thesis, but is available in the literature. We derived the specific angular momentum and the scaled spin rate of each system.

In the case of Eris-Dysnomia, due to the satellite size and the flat lightcurve, we favor a capture scenario or a gravitational collapse.

In the case of 1998 SM$_{165}$ system, Ceto-Phorcys, Teharonhiawako-Sawiskera, due to the satellite size and the large lightcurve amplitude, we favor a collisional scenario.

VIII.4   Summary

We have analyzed short-term variability of several Binary Trans-Neptunian Objects (BTNOs). Two objects in our sample, 2007 TY$_{430}$, and 2001 QY$_{297}$, have a high amplitude lightcurve ($\Delta m > 0.15$ mag) and can be considered as Jacobi ellipsoids. Assuming that these systems are in hydrostatic equilibrium, we derived a lower limit to the density ($\rho > 0.46$ g cm^{-3}), a primary (secondary) radii of <58 (<55 km, respectively) and a geometric albedo of 0.12 for both components of the 2007 TY$_{430}$ system, whereas we obtained a lower limit to the density of >0.29 g cm^{-3} for 2001 QY$_{297}$, a primary (satellite) radii of <129 km (<107 km), and a geometric albedo of 0.08. Our albedo, size and density estimations are in agreement with Vilenius et al. (2013) who obtained the results from entirely different methods. Other BTNOs studied in this work showed small peak-to-peak amplitude variations, and so are oblate (MacLaurin spheroid). In such cases we can only derive mere academic guesses on density and geometric albedo. But we have shown that deriving several parameters from the lightcurves is a reliable method in the case of Jacobi ellipsoids.

An exhaustive study about short-term variability as well as derived properties from lightcurves allow us to draw some conclusions regarding the Trans-Neptunian belt binary population. Based on Maxwellian fit distributions, we suggested that the binary population is rotating slower than the non-binary one. Such slowing down can be attributed to tidal effects between the satellite and the primary, as expected. We showed that all systems in this work are not tidally locked, however the primary despinning process may have already affected the primary rate (as well as the satellite rotational rate). We computed the time required to circularize and tidally lock the systems studied in this work. We used the Gladman et al. (1996) formula to compute the time required to tidally lock the systems, but such a formula is based on several assumptions and approximations that do not always hold. Computed times are reasonable in most of the cases and confirm that none of

the systems studied here are tidally locked. However, more studies are necessary to understand the tidal effect between primary and satellite, and especially in the case of equal-sized systems.

We also summarized a large set of correlations and anti-correlations according to the dynamical classes, to the size, and to the binarity or not of our object sample. The binary population does not show any special feature and seems to present similar characteristics to the non binary population. We have shown that objects with a high lightcurve amplitude (deformed objects) are in circular orbits at low inclination, and are essentially small objects. Our search for correlations/anti-correlations between albedo and orbital parameters revealed different features according to the object size. In fact, small objects seem to have a low albedo whereas large objects have higher albedo. In various cases, the dynamically hot classical objects present two different features according to the object size. The dynamically cold classical objects seems to have similar characteristics as the dynamically hot classical small objects. However, the dynamically cold classical sample is still too limited to draw reliable features. Resonant and SDO/DO samples present several strong correlations/anti-correlations, unfortunately the samples are too limited.

Finally, by studying the specific angular momentum of the sample we proposed possible formation models for several BTNOs whose short-term variability have been studied in this work. In several cases, we do not have enough information about the systems to favor or discard a formation model.

Chapter IX

Presentation and formation of the Haumea family

$\mathcal{T}$his chapter is dedicated to the dwarf planet (136108) 2003 EL$_{61}$ Haumea. This object is probably one of the most interesting and intriguing Trans-Neptunian Objects (TNOs). In fact, from the short-term variability studies presented previously in this work, one can appreciate that Haumea is the fastest rotator known to date, close to a spin barrier suggesting that this object may have suffered a rotational fission. Haumea presents various atypical characteristics: it is large, bright, fast rotator, it has pure water ice on the surface, it has at least two satellites and there are more than ten TNOs with very similar orbital parameters and similar surface properties to Haumea. Haumea, its two moons and all bodies dynamically related with this TNO form a peculiar system in the Trans-Neptunian belt. However, the formation of such a family is not well understood yet. Various models have been proposed during the past few years. Unfortunately, all of them present severe limitations that we will point out. In this chapter, we will also propose a model in order to explain the creation of the Haumea family and system.

We participated on the elaboration of a new model able to explain the Haumea family genesis. After planning out the different steps of this model, we carried out more than 100 simulations in order to present a suitable study. The work dedicated to our new model is already published in Ortiz et al. (2012b) and it is thoroughly explained in this chapter.

A presentation of all possible formation models, proposed to date, and the likelihood of the proposed collisions is also the topic of another paper (Campo-Bagatin et al. (In prep)).

IX.1   Presentation of Haumea, Hi'iaka, and Namaka

IX.1.1   Haumea

Haumea (formerly (136108) 2003 EL$_{61}$) is in the 12:7 mean motion resonance with Neptune (Ragozzine and Brown, 2007). This object is a Jacobi ellipsoid with an elongated shape (Rabinowitz et al., 2006; Lellouch et al., 2010). Rabinowitz et al. (2006) estimated Haumea size as 980×759×498 km (semi-axes lengths), whereas Stansberry et al. (2008) and Lellouch et al. (2010) computed a Haumea mean radius of 575^{+125}_{-50} km and ∼650 km, respectively [1]
Haumea is a fast rotator with a double-peaked rotational period of 3.92 h (Rabinowitz et al.,

---

[1]We must emphasize that the radius obtained thank to *Spitzer Space Telescope* or *Herschel Space Observatory* are equivalent radius of the projected area, and not the "exact radius", so care has to be taken with this and as a consequence the derived density, for example, presents a high uncertainty. Assuming that the object is triaxial with semi-axes a>b>c, and viewed from its equator, the equivalent radius (R_{eq}) is:

$$R_{eq} = \sqrt{\frac{ca + cb}{2}} \approx 650 km \qquad \text{(Equation IX.1)}$$

2006; Lacerda, Jewitt and Peixinho, 2008; Thirouin et al., 2010). It also presents an asymmetric lightcurve and shows color variations due to a dark red spot on the surface according to Lacerda, Jewitt and Peixinho (2008). Haumea surface composition is dominated by water ice (Trujillo et al., 2007; Merlin et al., 2007; Tegler et al., 2007). This object has a high density of 2.5 to 3.3 g cm^{-3} (Rabinowitz et al., 2006) and a mass of $(4.006\pm0.040)\times10^{21}$ kg (Ragozzine and Brown, 2009). The V-band geometric albedo is p$_v\sim$0.70 - 0.75 (Lellouch et al., 2010).

From its high density, Haumea has to be mostly rocky, despite its high albedo and its surface of nearly pure water ice. This indicates that Haumea is probably a differentiated object with a rocky core and an icy mantle.
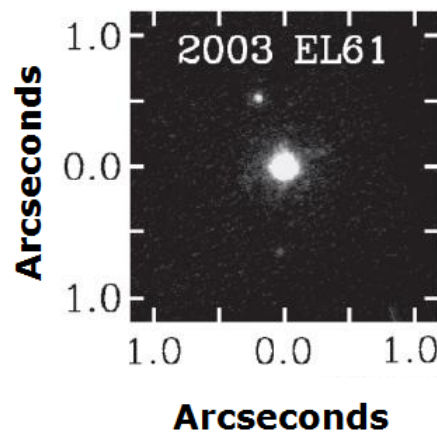
Figure 171: *Haumea, Hi'iaka, and Namaka*: Image obtained with the Keck Observatory Laser Guide Star Adaptive Optics system and extracted from Brown et al. (2006b). Haumea is in the center of the field. At the left, above Haumea is the brighter satellite, Hi'iaka, and directly below is Namaka.

IX.1.2   Hi'iaka and Namaka

In 2005, two satellites were discovered (Brown, 2005a; Brown, 2005b; Brown et al., 2006b) (Figure 171). The largest satellite, Hi'iaka has an apparent magnitude difference of 2.98±0.03 mag, whereas the smallest one, Namaka, is 4.6±0.5 mag fainter than Haumea (Brown, 2005a; Brown, 2005b) in the K' band. Hi'iaka mass is estimated to $(1.79\pm0.11)\times10^{19}$ kg (Ragozzine and Brown, 2009). This satellite is orbiting at 49880±198 km with an orbital period of 49.462±0.083 days (Ragozzine and Brown, 2009). Namaka mass is estimated to $(1.79\pm1.48)\times10^{18}$ kg (Ragozzine and Brown, 2009). This satellite is orbiting at 25657±91 km with an orbital period of 18.2783±0.0076 days (Ragozzine and Brown, 2009). Both satellites seem to present a similar water ice surface composition to that of Haumea (Barkume, Brown and Schaller, 2006).

Based on the lightcurve amplitude, and assuming that Haumea is in hydrostatic equilibrium, one can derivate that b/c=1.51 and a/c=1.96 (Chandrasekhar, 1987). Assuming the equivalent radius estimated by Lellouch et al. (2010), one can calculate the semi-axes: c=493.47 km, b=745.14 km, and a=967.21 km. Finally, the equivalent-volume radius can be expressed as:

$$R_{eq}^v = \sqrt[3]{abc} \approx 709 \; km \qquad \text{(Equation IX.2)}$$
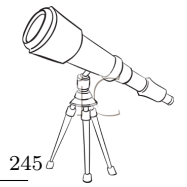
IX.2   The Haumea family

IX.2.1   The Haumea family members

Brown et al. (2007) identified a group of objects in relation with Haumea. Such objects present similar surface properties to Haumea (nearly pure water-ice) and present very similar proper orbital elements to Haumea. Brown et al. (2007) suggested that these objects, Haumea itself and its satellites formed a collisional family [2] as is the case for the families of the asteroid belt. Brown et al. (2007) proposed that the proto-Haumea [3] suffered a catastrophic impact that ejected a large fraction of its ice mantle, which formed the two satellites and the dynamical family [4]. Levison et al. (2008b) indicate that the Haumea family is probably the only collisional family in the Trans-Neptunian belt. However, Marcus et al. (2011) and Campo Bagatin and Benavidez (2012) expect more families in this region. In fact, Campo Bagatin and Benavidez (2012) suggest that a collision on a 400 km body would have produced a largest fragment not smaller than ∼300 km and fragments in the 50-100 km size range. So, most of the fragments would be very faint (23-24 mag) and their dynamical identification difficult.

The list of confirmed Haumea family members is still increasing:

- Brown et al. (2007) identified (24835) 1995 SM_{55}, (19308) 1996 TO_{66}, (55636) 2002 TX_{300}, (120178) 2003 OP_{32}, (145453) 2005 RR_{43}, (136108) Haumea, Namaka, and Hi'iaka.

- Ragozzine and Brown (2007) added (86047) 1999 OY_3, and 2003 UZ_{117}.

- Schaller and Brown (2008) added (308193) 2005 CB_{79}.

- Snodgrass et al. (2010) included 2003 SQ_{317}.

- Trujillo, Sheppard and Schaller (2011) confirmed the membership of 2009 YE_7.

- Recently, Volk and Malhotra (2012) suggested that (315530) 2008 AP_{129} belongs to a new class of rockier family members. 2008 AP_{129} has similar proper elements as the family but does not present a so strong water ice signature. Volk and Malhotra (2012) considered this object as a fragment from an inner part of the proto-Haumea, and so, the water feature is not so evident. On the other hand, Cook, Desch and Rubin (2011) based on Desch et al. (2009) work, suggested that the proto-Haumea was only partially differentiated. In fact, Desch et al. (2009) showed that TNOs with radii in the range 500-1000 km are only partially differentiated with a rocky core and an icy mantle surrounded by a thick crust of rock/ice mixture. Such a crust never reached temperatures high enough to melt or differentiate. In that case, the fragments forming the Haumea family are from the icy mantle and the crust, and so, one may expect icy and rocky members in the family.

Cook, Desch and Rubin (2011); Volk and Malhotra (2012) suggested a new kind of rockier family members, so, one is facing a problem in the "family" definition. There are two possible definitions: i) *the classical definition*: a family is composed by objects sharing similar proper orbital elements, and similar surface properties, and ii) *the enlarged definition*: a family is composed by objects sharing similar proper orbital elements, but not necessarily similar surface properties (Cook, Desch and Rubin, 2011; Volk and Malhotra, 2012) [5]. For the entire work presented here, we will use the classical definition of the term "family" because the membership of the rockier members is not confirmed yet.

---

[2]The term "family" has been imported from the study of asteroids where it refers to groups of objects very close in the proper elements space and comply clustering tests. In the Haumea case, the term "group" of objects is more appropriate, but, as the term "family" is always used in the literature, we will keep this terminology.

[3]The term "Proto-Haumea" is used to refer to the initial object (the object before any process capable to generate the family). The name "Haumea" is used to refer to the actual object.

[4]See Section IX.3.1 for more details.

[5]This is not the definition used for the asteroid families.

Table 20: In this table, we summarize the diameter, the mass, the albedo and the absolute magnitude for each confirmed family member. Absolute magnitudes (H) are from the Minor Planet Center database.

Object	H	Albedo[a]	Diameter [km]	Mass[b] $\times 10^{18}$ [kg]
(24835) 1995 SM$_{55}$	4.8	0.70	174	2.76
(19308) 1996 TO$_{66}$	4.5	0.70	200	4.19
(86047) 1999 OY$_3$	6.8	0.70	69	0.17
(86047) 2002 TX$_{300}$[c]	3.2	$0.88^{+0.15}_{-0.06}$	286±10	12.25
(136108) Haumea[d]	0.1	0.70 - 0.75	1150	4006±40
(120178) 2003 OP$_{32}$	3.6	0.70	303	14.57
2003 SQ$_{317}$	6.3	0.70	87	0.34
2003 UZ$_{117}$	5.3	0.70	138	1.38
Hi'iaka[e]	2.88	∼0.70	∼320	17.9±1.1
Namaka[e]	4.5	∼0.70	∼160	1.79±1.48
(308193) 2005 CB$_{79}$	4.7	0.70	182	3.16
(145453) 2005 RR$_{43}$	4.0	0.70	252	8.38
2009 YE$_7$	4.4	0.70	209	4.78

Notes:

[a]: Assuming an albedo of 0.70 for all objects, except for Haumea and 2002 TX$_{300}$ whose albedos are known.

[b]: Masses (except Haumea, Hi'iaka and Namaka masses) computed assuming a density of 1 g cm^{-3}.

[c]: Albedo and diameter extracted from Elliot et al. (2010).

[d]: Albedo and diameter extracted from Lellouch et al. (2010). Mass extracted from Ragozzine and Brown (2009).

[e]: Albedos, diameters, and masses extracted from Ragozzine and Brown (2009).

IX.2.2   The mass of the Haumea family

The mass of the entire family can be estimated as follows. First, we computed the diameter and the mass of each confirmed members (Table 20). The diameter (D) according to Chesley et al. (2002), can be estimated by:

$$D = \frac{1329}{\sqrt{p_\lambda}} 10^{-0.2H_\lambda} \qquad \text{(Equation IX.3)}$$

where p$_\lambda$ is the geometric albedo and H$_\lambda$ is the absolute magnitude in the λ band. Assuming that the family members are spherical, the mass M is:

$$M = \frac{4}{3}\pi\rho R^3 \qquad \text{(Equation IX.4)}$$

where ρ is the density and R is the radius of the object. By combining the previous equations, one can derive the mass, M, from:

$$M = \frac{\pi\rho}{6} \left(\frac{1329 \times 10^{-0.2H_\lambda}}{\sqrt{p_\lambda}} \right)^3 \qquad \text{(Equation IX.5)}$$

Based on the masses computed and reported in Table 20, we found a total mass of 4.08×10^{21} kg for the known family members (without Haumea, the total mass is 7.17×10^{19} kg ≈ 2%M$_{Haumea}$ where M$_{Haumea}$ is the mass of Haumea). We did not include 2008 AP$_{129}$ as member of the family because its membership is not confirmed yet (whose contribution would be very small, though). This mass estimation is obviously a lower limit because more small icy family members (and maybe rocky members) are expected to be found. On the other hand, as several members have no albedo

reported, the computed sizes reported in Table 20 are only estimations.

In Figure 172, from Carry et al. (2012), the cumulative size distribution of the Haumea family members and some candidates of this family is plotted. To estimate the mass of objects still to discover, Carry et al. (2012) compared the observed cumulative size distribution of the family members with some power laws, $N(>R) \propto R^{-q}$ (R is the object radius, and q is a constant). They used three different power laws [6]: i) distribution for collisional fragments with q=2.5 (Dohnanyi, 1969), ii) distribution for large TNOs with q=3.8 (Fraser and Kavelaars, 2009) and iii) distribution proposed by Leinhardt, Marcus and Stewart (2010) with q=4.5.

The first power law (with q=2.5) predicts that the largest object to be discovered has a diameter of ∼140 km. On the other hand, the second and third models suggest that the largest object to discover has a diameter between 220 and 250 km. In conclusion, in the case of a collisional size distribution, all large members are already known and missing members are small fragments not easily detectable with the current surveys. Extrapolating such models, a total mass of the family would be ∼2-7% of Haumea's mass. However, Carry et al. (2012) used collisional distributions to fit the cumulative size distribution of the Haumea family members, but the members of a family in the Trans-Neptunian population are unlikely collisionally evolved, due to small collisional probabilities after the LHB phase. Even in the case of asteroid families, Zappalà et al. (2002) showed that they are not following collisional distribution and they are rather represented by the characteristic distributions of fragment production after catastrophic collisions.

An empirical polynomial fit which is more appropriate from different points of view is shown in the red line of the Figure 172. The total mass inside this distribution is only slightly larger than 2% of the Haumea mass. Most of the mass is in the largest fragments, which are all known already.
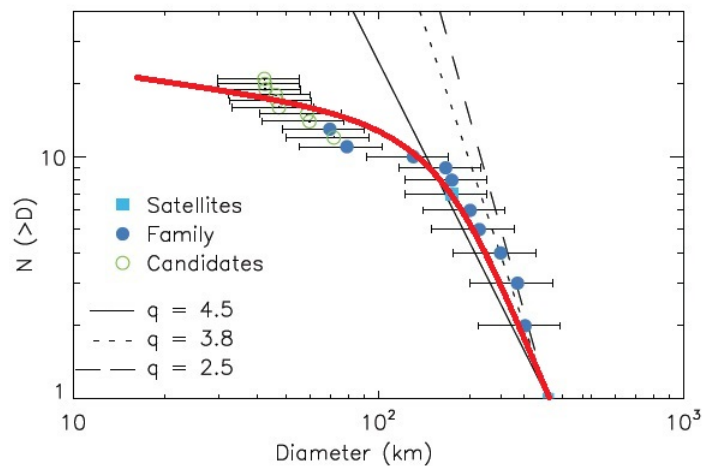
Figure 172: *Cumulative size distribution of the Haumea family*: Cumulative size distribution for confirmed and candidates objects compared with three power law models. Figure modified from Carry et al. (2012).

IX.2.3 The age of the Haumea family

Milani and Farinella (1994) developed a method to estimate the age of the Veritas asteroid family. They constrained the age based on the evolution in time of the shape of a collisional cloud by resonance diffusion. Ragozzine and Brown (2007) used the same method to constrain the Haumea family age. They concluded that a minimum of ∼1 Gyr is required to produce the current Haumea

---

[6]see Carry et al. (2012) for a complete explanation

position.

However, Rabinowitz et al. (2008) pointed out that the family members have a youthful appearance. In fact, the solar phase curves of the family members are flat and indicate that they have a high albedo which is confirmed by several studies (Elliot et al., 2010; Lellouch et al., 2010; Stansberry et al., 2013). Such a high albedo suggests a young surface of fresh ice in the last ∼100 Myr. After discarding possible resurfacing processes, they suggested that the family members must be depleted in carbon (confirmed by Pinilla-Alonso et al. (2009)) to avoid cosmic radiation to darken the surface. According to Pinilla-Alonso et al. (2009), due to the ratio of amorphous and crystalline water ice of the Haumea surface, the family should have more than 10^8 years.

IX.3   Formation models

The origin of the Haumea family is not well understood. During the past few years, various models have been proposed to explain the formation of such a family. Unfortunately, these models can only reproduce partially the known characteristics of this family. In the next sub-sections, we will introduce each model proposed to date and pin-point their limitations.

IX.3.1   Catastrophic collision

The Haumea family discovery as well as the first model to explain the family genesis have been reported by Brown et al. (2007).

Brown et al. (2007) announced the first six family members. All of them, as already mentioned, share a very similar surface composition with very deep absorption features characteristic of water ice. These objects are clustering in a small dynamical region of the Trans-Neptunian belt. Their proper orbital elements are mostly matching: i) semi-major axes vary by only 2.15 AU, ii) eccentricities differ by 0.08, iii) and inclinations differ by 1.4°. In Figure 173, from Carry et al. (2012), are plotted all the confirmed, to date, family members.

Brown et al. (2007) presented a catastrophic collision scenario as the origin of the family. They proposed that the proto-Haumea was a ∼830 km radius body with a density around 2 g cm^{-3}. They assumed that the collision occurred when the proto-Haumea crossed a higher-density portion of the Trans-Neptunian belt with an object of ∼ 60% of the radius of the proto-Haumea. Such collisions, with a typical velocity of 3 km s^{-1} would have removed around 20% of the initial proto-Haumea mass, principally the icy mantle. As the water ice was mostly taken away, the density increased to the current value (i.e. around 2.5 g cm^{-3}).

The velocity dispersion of the fragments ejected from the mantle after the collision is around 150 m s^{-1}. In Figure 173 are plotted the expected orbital elements for a dispersive velocity of 150 m s^{-1} and a dispersion centered on the average position of the fragments (except Haumea). However, it must be pointed out that Haumea itself requires a dispersion speed of 400 m s^{-1}, whereas the rest of the members of the family cluster around a dispersion speed of 150 m s^{-1}. Therefore, the fragments ejected from Haumea need an offset speed of around 300 to 500 m s^{-1} with respect to Haumea itself. Haumea is the only object not fitting the distribution, but, as Haumea belongs to a mean motion resonance with Neptune (Brown et al., 2007), it would be capable to raise its current eccentricity. However, only in 10% of the simulations such fact has been confirmed.

Brown et al. (2007) model presents various incoherences. Takeda and Ohtsuki (2009) demonstrated that a catastrophic collision, as proposed by Brown et al. (2007), generates a slow rotator and not a fast spinning one as suggested by Brown et al. (2007). Haumea is currently near its hydrostatic rotational instability, so a proto-Haumea rotating even faster is unlikely. Leinhardt, Marcus and Stewart (2010) simulated this scenario with exactly the same parameters proposed by Brown et al. (2007). The results of their simulations show that the largest remnant, with semi-axes of 1700×1500×1500 km, is bigger than the current Haumea (semi-axes of the current
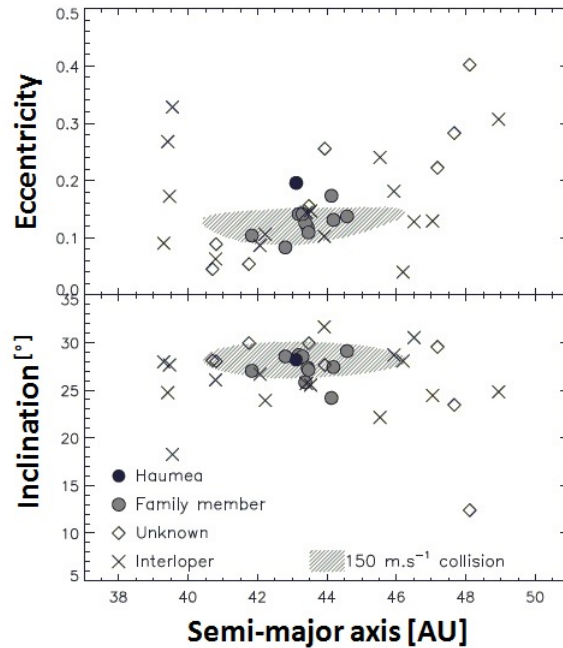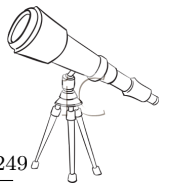
Figure 173: *Confirmed family members of the Haumea family*: Inclination and eccentricity of the Haumea family members. The dash area is plotted assuming a nominal collision with a velocity of 150 m s^{-1}. Objects belonging to this area are potential fragments of the proto-Haumea. Plots extracted from Carry et al. (2012).

Haumea are 1000×750×500 km) and, as expected, such collision produced a slow rotator with a rotational period of 28 h, far from the 4 h rotational period of the current Haumea. On the other hand, the current elongated shape of Humea is not explained in Brown's model, in fact, numerical simulations of catastrophic disruptions with enough resolution to resolve the shape of the largest remnant produce spherical remnants, not fast-spinning elongated remnants (Leinhardt, Richardson and Quinn, 2000; Leinhardt and Stewart, 2009). Finally, the estimated dispersion velocities are not consistent with the outcome of a catastrophic impact. The typical velocities for a catastrophic impact on objects of this size are 700 to 900 m s^{-1} (Leinhardt, Marcus and Stewart, 2010). These values are clearly larger than the dispersion velocity (150 m s^{-1}) of the family members.

A similar scenario is proposed by Levison et al. (2008b). They argue that a collision between two objects (typically, an object with a radius of $\sim$ 850 km and an impactor with a radius of $\sim$ 500 km) from the scattered disk on highly eccentric and unstable orbits could have generated enough orbital energy to put the family fragments on stable orbits. According to Levison et al. (2008b), the probability of such collision is high because the population of the scattered disk was much larger in the early Solar System.

Campo Bagatin and Benavidez (2012) developed the code Asteroid-LIke Collisional ANd Dynamical Evolution Package (hereinafter ALICANDEP). This package is a collisional evolution code that includes statistical elimination of objects according to the Nice Model by dynamical effects within the frame of a disk migrating and gradually dynamically exciting, as well as the dynamical migration of objects between regions. Campo-Bagatin et al. (In prep) used this model to compute the probability (or likelihood) of the collision needed in the Brown et al. (2007) model along the Solar System formation and evolution. They divided the Solar System formation and evolution into three stages: i) the pre-Late Heavy Bombardment (pre-LHB) at t< 700 Myr, ii) the Late Heavy Bombardment phase (LHB phase) between 700 and 800 Myr, and iii) the post-Late Heavy Bombardment (post-LHB) at t> 800 Myr. They found the following probabilities: i) less than 10^{-9} during the pre-LHB, ii) between 1.3×10^{-8} and 1.7×10^{-8} during the LHB phase, and iii)

1.5×10^{-6} during the post-LHB. So, the probability of the collision in the Brown et al. (2007) model is really low along the Solar System history. In other words, the creation of the Haumea collisional family as suggested by Brown et al. (2007) is unlikely along the Solar System history.

IX.3.2 Catastrophic collision, formation of a satellite and catastrophic collision on the satellite

This sub-section is dedicated to a Haumea family formation model proposed by Schlichting and Sari (2009).

This model can be divided into three steps (Figure 174):

- The proto-Haumea (with a diameter $\sim$800 km) suffered a large collision with an impactor around $\sim 60\%$ of the radius of the proto-Haumea at low velocity, around 1 km s^{-1}. This collision would accelerate the spinning of Haumea to $\sim$4 h. By accumulation, the material ejected during this collision formed a tightly bound satellite. The satellite has to be large enough to generate all the family (except Haumea) and the two current satellites around Haumea. Assuming a density of 1 g cm^{-3}, a satellite radius of $\sim$260 km would be able to produce the entire family (except Haumea). Hereafter, we will use the term "proto-satellite" to refer to this satellite created after the collision on the proto-Haumea.

- The tidal evolution increased the proto-satellite orbital separation from Haumea.

- The proto-satellite suffered a destructive collision with a TNO (radius estimated between 20 to 70 km for the impactor) which created the family. The typical dispersion velocity of the family would be around 190 m s^{-1}. Both satellites, Namaka and Hi'iaka, are also remnants of such collision but they did not escape as the rest of the family. However, during the first phase, various smallest satellites could have been formed. In such case, the two current moons are not remnants of the last collision, but were formed during the first step of this model.

The Schlichting and Sari (2009) model also presents some limitations. As already mentioned, a large collision could not produce a fast rotator (Takeda and Ohtsuki, 2009). The tidal dissipation between the primary and the satellite is also in disagreement with a fast rotator genesis. And finally, as pointed out by Schlichting and Sari (2009), the mutual inclination between Namaka and Hi'iaka is not explained by this model. The mutual inclination is around $13°$, it is too high if the satellites were formed during the first step of this model and too low if they were formed during the third step. However, the velocity dispersion computed by Schlichting and Sari (2009) after the collision on the proto-satellite is consistent with the observed dispersion velocity. Therefore, the collision on a proto-satellite idea is interesting.

Campo-Bagatin et al. (In prep) computed the probability of collisions in the Schlichting and Sari (2009) model during the three stages of the Solar System history (the three stages presented in the previous sub-section). For the first collision forming the tightly bound satellite, they found a probability of: 1.2×10^{-5} to 4×10^{-5} during the pre-LHB, 2.1×10^{-4} to 2.7×10^{-4} during the LHB, and 2.5×10^{-4} to 2.9×10^{-4} during the post-LHB. Campo-Bagatin et al. (In prep) estimated to 3% the probability of the second collision (collision on the proto-satellite) before the LHB phase. However, if the second collision and so the creation of the family, occurred before the LHB, the probability of the family survival during the LHB phase is very low. In fact, the family has to survive keeping exactly the same total mass, the same surface composition and similar proper orbital elements. If the proto-satellite is formed before the LHB and has to survive during the LHB phase, it has to be more massive than expected. It has been estimated that the proto-satellite had to be at least 100 times more massive in order to have enough mass to survive the dynamical instability phase and be observable at present Campo-Bagatin et al. (In prep). Finally, the probability of a collision on the proto-satellite during the post-LHB phase is low.
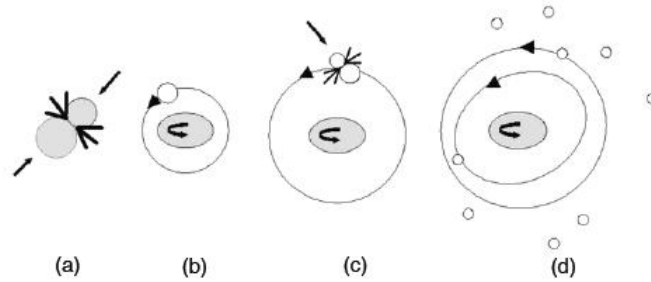
Figure 174: Schlichting and Sari (2009) model: Haumea suffered a giant impact (a). This collision gave rise to Haumea's fast, 4 hr spin period and ejected material that accumulated into a tightly bound proto-satellite around Haumea (b). The newly formed proto-satellite underwent tidal evolution that increased its orbital separation from Haumea. Haumea's proto-satellite suffered a destructive collision with an unbound TNO (c). This collision created and ejected the family and formed the two moons (d). (Figure from Schlichting and Sari (2009))

IX.3.3   Graze and merge giant impact

This sub-section is dedicated to the Leinhardt, Marcus and Stewart (2010) model based on a graze and merge giant impact between two similar sized bodies. They used the GADGET[7] code which is a smoothed particle hydrodynamics (SPH) code coupled with a N-body program (PKDGRAV).

Figure 175, from Leinhardt, Marcus and Stewart (2010), is a snapshot of one of their simulations [8]. They simulated two differentiated bodies (icy mantle and rocky core) with a radius of 650 km and a density around 2 g cm^{-3}, for both of them (frame a)). According to Leinhardt, Marcus and Stewart (2010) study, the best match between simulation and characteristic of the current Haumea is obtained with an impact velocity of 800 to 900 m s^{-1} and an impact parameter [9] between 0.6 and 0.65 (frame b)). During this collision (frames c) and d)), some material is exchanged between the two bodies. The majority of the exchanged material is from the icy mantles, whereas the cores remained intact. After the collision and the separation, both objects have similar sizes as previously (frames e) and f)). Due to their small separation and unstable orbits, both objects suffer a second collision (frame g)). This second collision has a lower impact velocity than the previous one, 260 m s^{-1}. After this impact, the rocky cores merge and form a unique differentiated body (frame h)). This new body spins so quickly that its icy mantle is ejected in small fragments (frames i) and j)). Part of the ejected mantle is gravitationally bound and part of it escapes (frame k)). In the last frame (frame l)), the largest remnant, Haumea, has an icy mantle which is a mix of the icy mantles from the two precursor bodies. The fragments ejected are principally from the icy mantles, but there are also some fragments from the rocky cores.

The rotational period of the largest remnant (lr) is 3.9 h which is in agreement with the current Haumea rotational period. Its mass (M_{lr}) and density are 4.2×10^{21} kg and 2.1 g cm^{-3} (respectively). The current mass and density of Haumea are 4.006×10^{21} kg (Ragozzine and Brown, 2009) and 2.6 to 3.3 g cm^{-3} (Rabinowitz et al., 2006). And so, the mass and the density are in agreement with the current values.

After two thousands spin orbits, there are around thirty-five objects gravitationally bound and in orbit around the primary (or largest remnant). The mass of ejected fragments is $\sim 0.07 M_{lr}$ as: i) $0.01 M_{lr}$ in orbit and, ii) $0.06 M_{lr}$ escaped. The masses of Namaka and Hi'iaka are respectively,

---

[7]A complete description of the GADGET code can be found at `http://www.mpa-garching.mpg.de/gadget/` or in Springel (2005).

[8]An animation of this simulation is available at `http://iopscience.iop.org/0004-637X/714/2/1789/fulltext/`

[9]See Section IX.4.2.4.1 for a definition of the impact parameter.
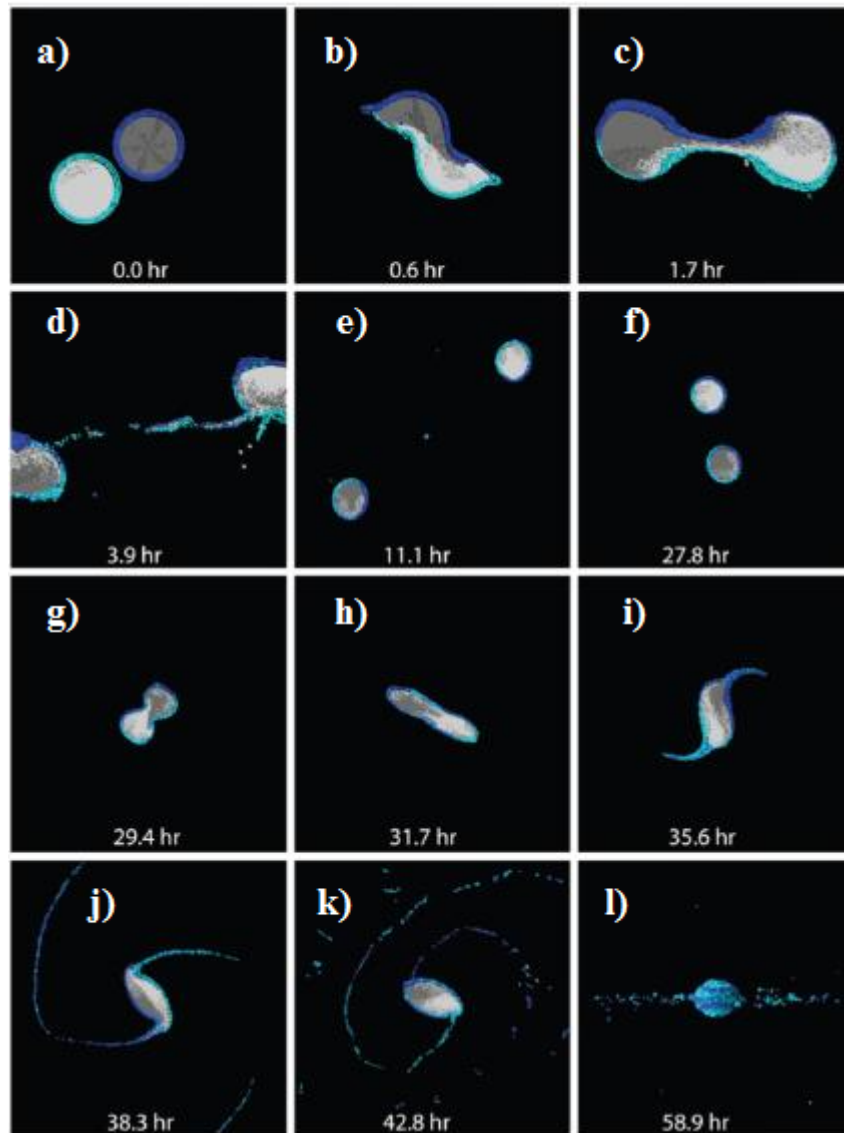
Figure 175: Leinhardt, Marcus and Stewart (2010) model: Time series of a graze and merge event: 650 km diameter bodies colliding at 900 m s^{-1} with an impact parameter of 0.6. Field of view is initially 5000×5000 km, increasing to 10000×10000 km at 11.1 h. The last frame shows the system edge on, whereas the other frames are cross-section views through the collision plane which is in the plane of the page. Color denotes the provenance of the materials: icy mantles (cyan and blue) and rocky cores (light and dark gray). Some material is exchanged during the first impact, each body remains largely intact after separation. The rocky cores merge after the second impact, forming a differentiated primary. The surface of the merged body has distinct patches of ice that originate from each of the precursor bodies. The fragments thrown from the merged body are primarily material from the icy mantles. (Figure adapted from Leinhardt, Marcus and Stewart (2010))

$(1.79\pm1.78)\times10^{18}$ kg and $(1.79\pm0.11)\times10^{19}$ kg. So, with an orbiting mass of $0.01\mathrm{M}_{lr}$, there is a mass excess in Leinhardt, Marcus and Stewart (2010) simulation. However, it is not expected that all ejected fragments survive to date. The escaped mass (mass of the family members) is also in excess. Obviously, as the total mass of the family is not known, and as probably some members of the family are still to discover, the excess of mass could be justified. Also, one can imagine that not all the ejected fragments survived. The ejection velocities of the fragments is low. Leinhardt, Marcus and Stewart (2010) proposed that the ejection velocities are not much greater than the escape velocity of the largest remnant. Some fragments are from the rocky cores of the

two progenitors, so one have to expect some family members with a different surface composition (Volk and Malhotra, 2012).

Campo-Bagatin et al. (In prep) computed a low probability for the impact in this model before the LHB ($<10^{-6}$). During the LHB phase, the probability is 7.8×10^{-5} to 1.1×10^{-4}. In the post-LHB phase, the probability is 8.2×10^{-5} to 1.2×10^{-4}. In summary, this model is unlikely in all stages of the Solar System history.

IX.4   A rotational fission model

IX.4.1   Clues on rotational fission playing a role

IX.4.1.1   Spin barrier and rotational frequency distribution

In Section VII.3, we mentioned the existence of a spin barrier around 4 h. In fact, no Trans-Neptunian Object (TNO) below this barrier has been found. This may indicate that the bodies with a rotational period below $\sim$4 h break up. Obviously, it is possible that such objects could not have been formed during the accretion phase, so they are not detected currently. However, some objects formed during the accretion phase may have undergone intense collisional histories that accelerated some of them and slowed down some others. Those TNOs that suffered spin-up to a significant degree would undergo significant mass loss if their critical rotation periods were reached. In fact, current models of the formation of the outer Solar System indicate that there was an intense collisional evolution in the early phases of the Trans-Neptunian belt so that spins were significantly altered. From this point of view, most of the rotational fissions would have taken place before or during the Late Heavy Bombardment (LHB) period, when collisions were more frequent.

According to Maxwellian distribution fits in Section VII.2.1 [10] one would expect some fast rotators (with a rotational period <4 h) in the current distribution. Duffard et al. (2009) showed that $\sim$ 15% of the objects cannot be equilibrium figures for a typical density of 1500 kg m^{-3}, whereas this percentage rises to 25% for a density of 1000 kg m^{-3}. In other words, under the assumption of hydrostatic equilibrium, around 20% of the objects would have fissioned due to their high rotation rates.

As Haumea is the fastest rotator to date, it seems the perfect candidate to explore the possibility of rotational fission in the Trans-Neptunian belt. On the other hand, we showed in Section VII.2.4 that the Haumea family members seem to rotate faster than other TNOs. Assuming that the proto-Haumea had initially a high angular momentum, one can expect that part of such a high angular momentum has been transferred to the current members of this system.

IX.4.1.2   Specific angular momentum

The specific angular momenta of the systems formed by Haumea-Namaka and Haumea-Hi'iaka were computed as in Descamps and Marchis (2008):

$$H = \frac{q}{(1+q)^{\frac{13}{6}}} \sqrt{\frac{a(1-e^2)}{R_{primary}}} + \frac{2}{5} \frac{\lambda_{primary}}{(1+q)^{\frac{5}{3}}} \Omega + \frac{2}{5} \lambda_{satellite} \frac{q^{\frac{5}{3}}}{(1+q)^{\frac{7}{6}}} \left(\frac{R_{primary}}{a} \right)^{\frac{3}{2}} \quad \text{(Equation IX.6)}$$

where q is the secondary-to-primary mass ratio, a the semi-major axis, e the eccentricity, and $R_{primary}$ the primary radius. Ω is the normalized spin rate expressed as:

$$\Omega = \frac{\omega_{primary}}{\omega_{critical}} \quad \text{(Equation IX.7)}$$

---

[10] Binzel et al. (1989) showed that the rotational frequency distribution for asteroids can be fitted by a Maxwellian distribution. In Section VII.2.1, we showed that Maxwellian distributions can also fit the TNOs frequency distribution.

where $\omega_{primary}$ is the primary rotation rate and $\omega_{critical}$ the critical spin rate for a spherical body:

$$\omega_{critical} = \sqrt{\frac{GM_{system}}{R_{effective}^3}} \qquad \text{(Equation IX.8)}$$

where G is the gravitational constant, $R_{effective}$ and M_{system} are the effective radius and the system mass (respectively). Assuming triaxial objects with semi-axes as $a > b > c$, λ parameter is:

$$\lambda = \frac{1 + \beta^2}{2(\alpha\beta)^{\frac{2}{3}}} \qquad \text{(Equation IX.9)}$$

where $\alpha = c/a$ and $\beta = b/a$. The λ parameter formula is the same for the primary and the satellite. In this work, satellites are considered as spherical so, $\lambda_{satellite}=1$.

The Scaled Spin Rate (SSR) was calculated as in Chandrasekhar (1987):

$$SSR = \frac{\omega_{primary}}{\sqrt{\pi G \rho_{primary}}} \qquad \text{(Equation IX.10)}$$

where $\omega_{primary}$ is the rotation rate of the primary and $\rho_{primary}$ is the primary density.

In Figure 176, both systems (Haumea-Namaka and Haumea-Hi'iaka) are represented in a Scaled Spin Rate versus Specific Angular Momentum plot. With specific angular momenta around 0.3 and a scaled spin rates around 0.6, both systems are falling into the "high size ratio binaries" area: based on an extensive study of binaries in the asteroid population, Descamps and Marchis (2008) concluded that systems in the "high size ratio binaries" area very likely formed by rotational fission or mass shedding. So, as Haumea systems (Haumea+Namaka and Haumea+Hi'iaka) are falling into this kind of binary, a possible formation by rotational fission or mass shedding has to be studied. Pravec et al. (2006) also showed that the specific angular momentum of most asynchronous binary systems in the near-Earth asteroids (NEA) population is similar (within 20% uncertainty) and close to the angular momentum of a sphere with the same total mass (and density) rotating at the breakup limit. This implies that those binaries were created by mechanisms related to rotation close to the critical limit for break up. Descamps and Marchis (2008) studied asteroid binary systems in particular, but the general analysis is scale independent on size and density. Once again, such arguments seem to indicate that Haumea would have experienced rotational fission or mass shedding. Toth and Lisse (2010) also suggested that Haumea was not stable against rotational breakup, in agreement with similar conclusions from Ortiz et al. (2006) in this regard.

IX.4.2   Numerical simulations

We decided to investigate the scenario numerically.

IX.4.2.1   PKDGRAV: a Parallel K-Dimensional tree GRAVity solver for N-body problems

All simulations presented here were performed with PKDGRAV. PKDGRAV is a parallel N-body tree code originally designed for cosmology simulations at the Astronomy Department of the University of Washington. This code has been improved by adding a collision treatment for dynamical simulations in the Solar System and modified for the gravitational aggregates study (Richardson et al., 2000; Stadel, 2001). A PKDGRAV description can be found in Appendix C.

IX.4.2.2   Creation of a proto-Haumea

The first step of our model is the creation of one possible proto-Haumea. By "possible" we mean that the exact characteristics of the proto-Haumea are unknown, so one can just extrapolate a possible object based on the characteristics of the current Haumea. Therefore, we decided to simulate
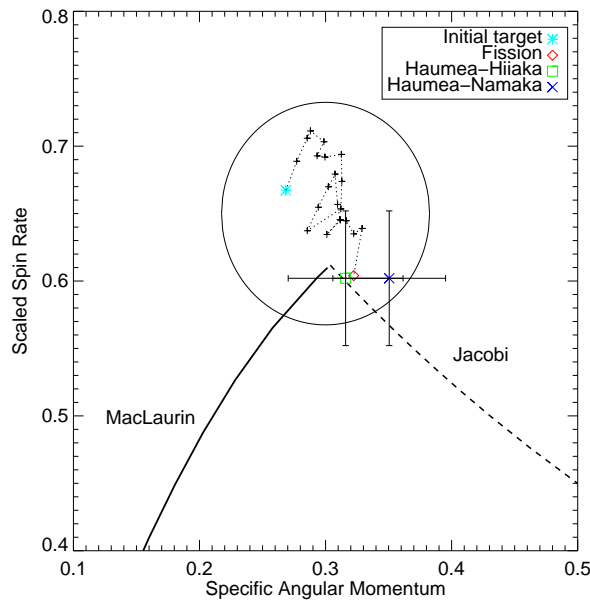
Figure 176: *Scaled spin rate versus specific angular momentum* for the Haumea-Namaka and Haumea-Hi'iaka systems. We plotted the MacLaurin and Jacobi sequences. Near the MacLaurin/Jacobi transition, Descamps and Marchis (2008) concluded that asteroid systems are likely form by rotational fission or mass shedding. The circle indicates the high-size-ratio binaries zone according to Descamps and Marchis (2008). In this figure, we also reported informations about simulation S1 that we will discuss in following sections. Each black cross represents a small increase of angular momentum described in Section IX.4.2.3.1. The blue asterisk is the initial target i.e, the proto-Haumea simulated in Section IX.4.2.2. The red diamond symbol indicates the point where the proto-Haumea underwent the rotational fission.

the proto-Haumea as follows:

- *Shape*: the current Haumea has an elongated shape. This shape was probably a primordial characteristic of the proto-Haumea.

- *Rotational period*: the current Haumea is a fast rotator. As catastrophic collisions are not viable to generate fast rotators (Takeda and Ohtsuki, 2009), the proto-Haumea was probably a fast rotator too.

- *Mass*: the current Haumea mass is 4.006×10^{21} kg (Ragozzine and Brown, 2009). At least the entire family, and the two current moons have to come out from the proto-Haumea as well. So, we estimated the proto-Haumea total mass between 5% and 10% larger than the current mass.

- *Density*: the current Haumea density is estimated between 2.5 and 3.3 g cm^{-3} (Rabinowitz et al., 2006), whereas Holsapple (2007) proposed a density between 1 and 3.0 g cm^{-3} considering tensile and cohesive strengths. The proto-Haumea density should be in the same range However, the object could be differentiated, with a rocky core (density around 3 g cm^{-3}) and an icy mantle (density around 1 g cm^{-3}). Therefore, we consider the proto-Haumea as a pre-shattered, non-differentiated body and we assume a density around 2 g cm^{-3}. The formation of a shattered body by groups of sub-catastrophic collisions is very likely in the early phases of the collisional evolution of TNOs. This is suggested by Housen (2009), who performed laboratory experiments in which he showed that N collisions –each with a fraction of the shattering threshold specific energy of the target, Q_S^*/N– cause the same amount of structural damage, into the target itself, as a single collision at Q_S^*. Therefore, N sub-catastrophic collisions can finally shatter a large target without ejecting mass

and producing a cohesionless structure that is similar in many respects to a gravitational aggregate. In the most conservative assumption, at least the whole crust would be easily fragmented.

The proto-Haumea is then generated by the gravitational collapse of a spinning cloud of particles as in Tanga et al. (2009). Figure 177 is an example of such a process. We simulated a rotating cloud of 1000 equal-sized particles. The cloud collapses and creates a gravitational aggregate. The final target is made of 866 particles, has a rotational period of 3.98 h, a density of 2.1 g cm^{-3} and a total mass of 4.48×10^{21} kg. Its shape is elongated with semi-axes of $1362\times744\times513$ km. The characteristics of the simulated target (hereafter Target 1) can be found in Table 21. Several proto-Haumeas were simulated for this work in the same way. We selected only proto-Haumeas in agreement with the criteria presented above.

The main purpose of using a cloud of particles collapsing gravitationally is to avoid "crystalline packings" of the particles forming the object and obtain random configurations of particles. The cloud has to be rotating because an elongated object has to be formed. If the cloud is not rotating, the gravitational collapse would form a spherical object. The number of particles was chosen according to two criteria: i) computing time: for a generic distribution of particles, a dependence of the integration time as a function of the particle number (N) has been empirically noticed being of NlogN, and ii) resolution: it was necessary to reproduce the current satellites to be larger than the size of each particle. Namely, at least 10 particles. If the satellite were represented by only one particle, the resolution would be have been way too poor and inadequate for a suitable study. In conclusion, about 1000 particles are a good compromise between computing time issues and need for resolution. The final object is obtained after a stabilization time. In fact, after the gravitational collapse, the object needs time to adjust itself to the corresponding rotational figure of equilibrium.
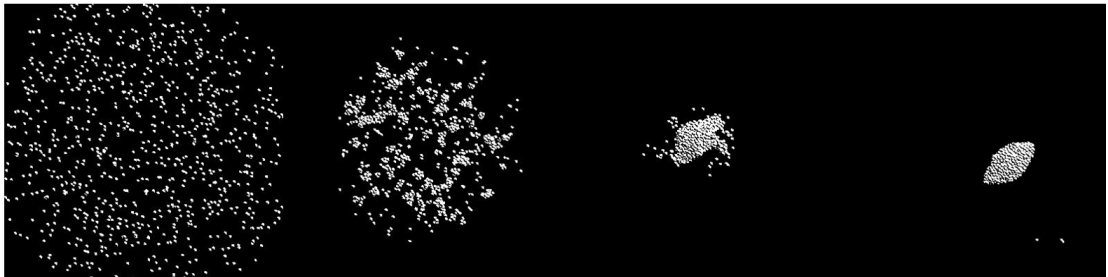
Figure 177: *Snapshot of the target formation simulation*: I simulated a rotating cloud of 1000 particles. The cloud of particles is collapsing in order to create a typical gravitational aggregate. The final target is composed by 866 particles, has a rotational period of 3.98 h, a density of 2.1 g cm^{-3} for a total mass of 4.48×10^{21} kg. The shape is elongated with semi-axes of, respectively, $1362\times744\times513$ km.

IX.4.2.3   First case: Rotational fission by increasing the angular momentum

IX.4.2.3.1   Simulation S1: pure rotational fission   The second step of our model is to test the feasibility of the rotational fission. In other words, it is necessary to test the object's disruption limit.

For this purpose, we increased the angular momentum of the synthetic object (Target 1) by twenty-one small increases of the angular momentum until the fission occurred. Such a simulation is in Figure 178. Each spin up corresponds to an increase of 1% of its angular momentum. After each increase, we allowed the object enough time to adjust itself to the corresponding rotational figure of equilibrium. All small increases are plotted in Figure 176 (plus symbols). The fission of the target occurred near the MacLaurin-Jacobi transition where, according to Descamps and Marchis (2008), binaries are mostly formed through rotational fission or mass shedding. One can conclude that forming a binary system through small increases of angular momentum is possible.
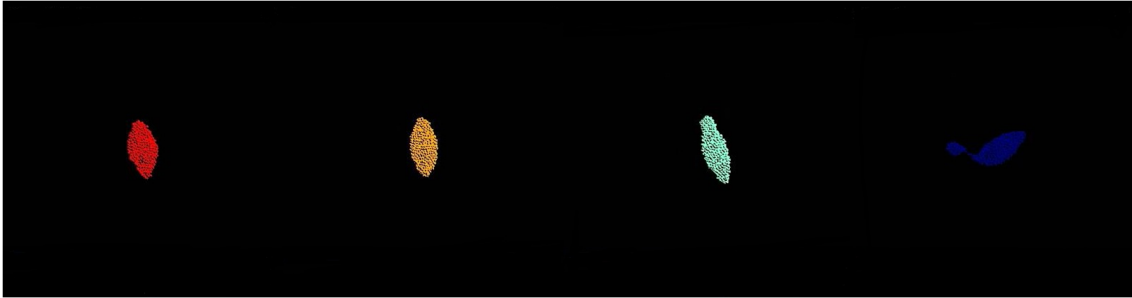
Figure 178: *Snapshot of the Simulation S1*: Different colors are used every time the object is spun-up (from left to right). The initial target (in red) suffered several increases of angular momentum. The target deformation is noted until its break up (in blue).

Dozens of simulations were performed and in all cases, binary systems were formed.

As already mentioned, simulation S1 was performed to test the feasibility of the rotational fission of a Haumea-like object, and it showed the formation of a binary system. The primary has similar mass as current Haumea and its rotational period is around 3.7 h, which is in agreement with the current rotational period. The formed proto-satellite would be big enough to generate the entire family members and the two current satellites. In Figure 179 the speed distribution of the ejected material in the simulation S1 is plotted. The fragments escaping the system immediately after rotational fission have average speeds of 0.3 km s^{-1}. However, the distribution of ejection speeds is very broad.

The ejected fragments in our simulations have a net predominant direction. Averaging the velocity vectors at infinity with respect to the center of mass of the system of all the ejected fragments generates a vector of components (13 m s^{-1}, 22 m s^{-1}, 0 m s^{-1}) with a modulus of 25.2 m s^{-1} and a standard deviation of 328 m s^{-1}.

IX.4.2.4   Second case: Rotational fission triggered by a sub-catastrophic collision

IX.4.2.4.1   Simulation S2: Rotational fission triggered by a low-speed collision   In the S1 set of simulation we have shown that rotational fission could be caused by a chain of small increases of angular momentum. Here, in the third step, we test that a small collision can provide enough increase of angular momentum to cause a final –induced– rotational fission.

First of all, we assume some initial conditions to test different possible collisions, schematically shown in Figure 180. We simulate a large set of collisions with different impact parameters, impact velocities and projectile sizes. We test the impact parameter between (0.1 and 0.8)$\times R_T$, where R_T is the target radius (i.e. the proto-Haumea radius expressed as R_T^3=a$\times$b$\times$c where a, and c are the three semi-axes) and impact velocity between 1 and 3 km s^{-1} (typical impact velocities in the Trans-Neptunian belt (Dell'Oro et al., 2001)). We simulated more than 100 cases of collisions, only the cases that match the current characteristics of the Haumea system/family are presented.

In simulation S2, we use as a target (hereafter Target 2) the body created after the 20th spin-up of simulation S1. The characteristics of Target 2 are reported in Table 21. We use this target because it was near rotational fission and the main idea is to check if one small collision can provoke the rotational fission. Figure 181 is an example. In this case, we perform a collision with a velocity of 1 km s^{-1} and an impact parameter of 0.3$\times R_T$. The projectile is spherical and has a typical density of TNOs (around 1 g cm^{-3}). The characteristics of the projectile are indicated in Table 21.

After the collision, one part of the projectile is encrusted on the target surface whereas the rest is ejected at high velocity. This feature may explain the dark spot reported on the current
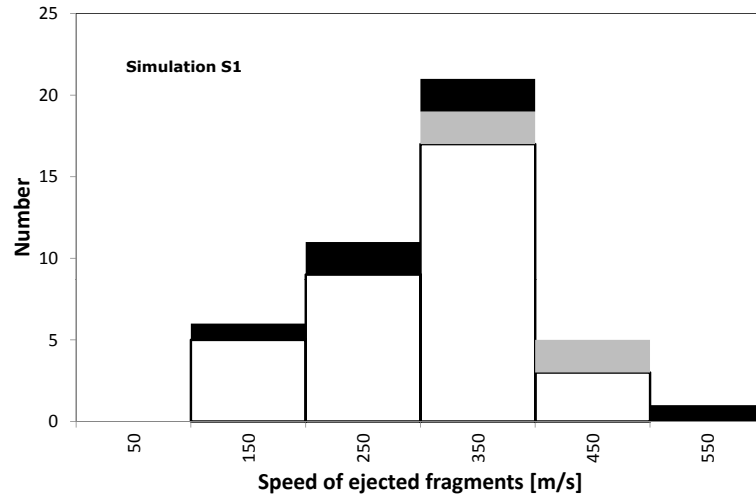
Figure 179: *Histogram of the speed distribution of the ejected fragments in the simulation S1*: Number is the number of fragments. The gray bars correspond to groups of two particles, the black bars correspond to ejected rubble piles composed by more than two particles, and white bars correspond to single particles ejected.
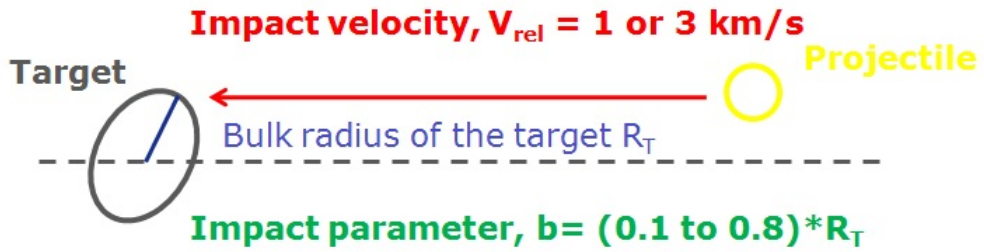
Figure 180: Schematic view of a collision as explained in the text.
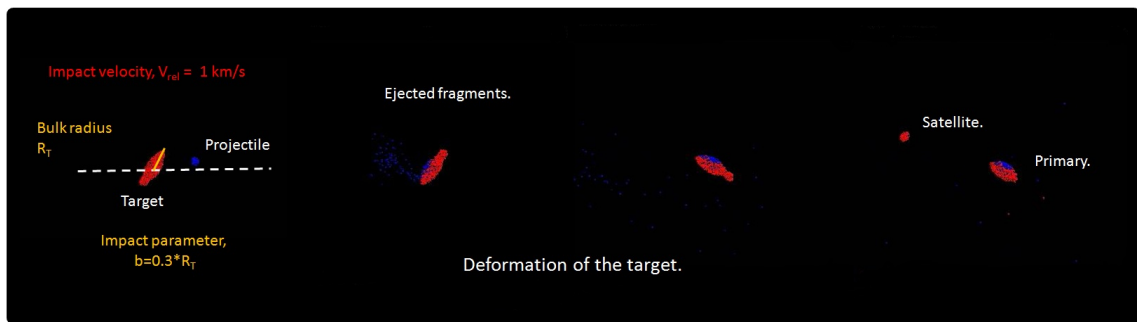
Figure 181: *Rotational fission triggered by a sub-catastrophic collision at low impact velocity*: Simulation S2 showing a collision at 1 km s^{-1}.

Haumea surface (Lacerda, Jewitt and Peixinho, 2008). We must point out that part of the target is also ejected during the collision. The quantity of target material ejected depends, basically, on the impact velocity. Due to its own rotation, the target becomes more and more deformed until it reaches a "skittle-form", known as Poincaré figure. Finally, due to its own rotation, the "head and the body of the skittle" are separated. The "head" becomes a satellite of the largest remnant.

In the set of simulations S2, we get rotational fission as triggered by a small collision, while in simulations S1, the main result is the formation of a binary system, the obtained primaries have rotational periods and a masses consistent with current values. In Figure 182, the speed distribution of the ejected material in the simulation S2 is plotted. The fragments escaping the system immediately after rotational fission have average speeds of 0.5 km s^{-1}. For simulation S2, the average velocity vector has components (-447 m s^{-1}, -189 m s^{-1}, -34.5 m s^{-1}) with a modulus of 487 m s^{-1} and a standard deviation of the speed around this direction of 314 m s^{-1}.
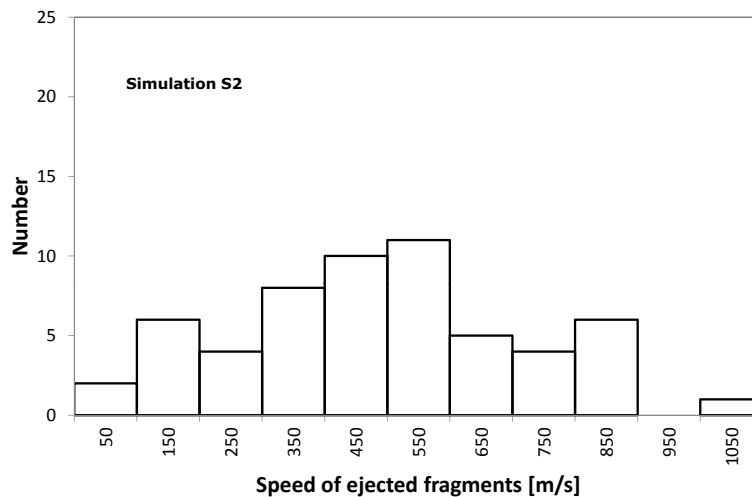
Figure 182: *Histogram of the speed distribution of the ejected fragments in the simulation S2*: Number is the number of fragments. White bars correspond to single particles ejected. This simulation did not produce groups with two or more particles.

IX.4.2.4.2 Simulation S3: Rotational fission triggered by a high-speed collision   As for the set of simulations S3 is concerned, we use the same target, the same projectile, and the same impact parameter as for simulations S2. But this time we choose a higher impact velocity, 3 km s^{-1} (Figure 183). The relative velocities that have been tested are close -or even above- the limit for sound speed in the target body. In a homogeneous body, hyper-velocity collisions should be handled in order to consider the damage produced by the propagation of the shock wave into the body structure, this may be handled by Smoothed-Particle Hydrodynamics (SPH) simulations. Nevertheless, these considerations do not flaw the validity of the used technique because we am dealing with bodies that have -at least- a crust of heavily fragmented material. In such environments, the shock wave is rapidly extinguished (Asphaug, 1999), the damage is limited to the collisional area where part of the energy is dissipated and the rest of the energy is available for dissipative collisions to occur between the fragments forming the outer structure of the body itself.

As in the previous simulations, the projectile is completely destroyed with part of it remaining on the target surface and part of it ejected. As expected, in this case, more material from the target is ejected than in case S2. The target is also deformed until it breaks up and part of the

target becomes a satellite.
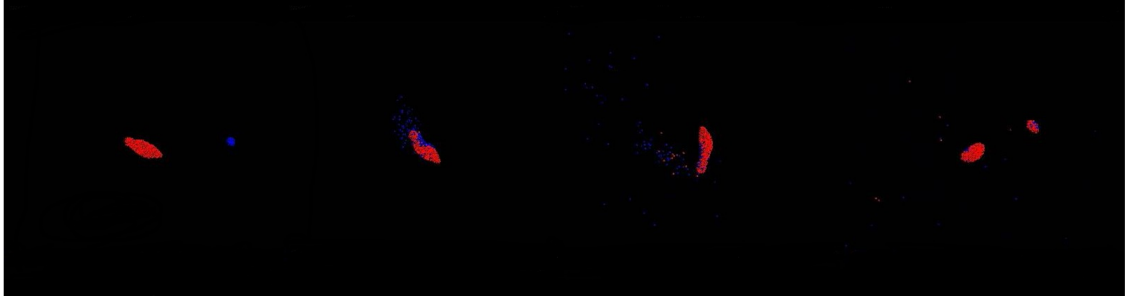
Figure 183: *Rotational fission triggered by a sub-catastrophic collision at high impact velocity*: Simulation S3 showing a collision at 3 km s^{-1}.

IX.4.2.5   Simulation S3

As for the simulations S1 and S2, the main result is again the formation of a binary system. The primary has a rotational period and a mass a little bit lower than the current values. The proto-satellite is bigger than in the previous two cases.

In Figure 184, the speed distribution of the ejected material in simulation S1 is plotted. The fragments escaping the system immediately after rotational fission have average speeds of 1.3 km s^{-1}. For simulation S3, the average velocity vector has components (-934 m s^{-1}, 442 m s^{-1}, 200 m s^{-1}) with a modulus of 1050 m s^{-1} and a standard deviation of the speed around this direction of 1250 m s^{-1}.
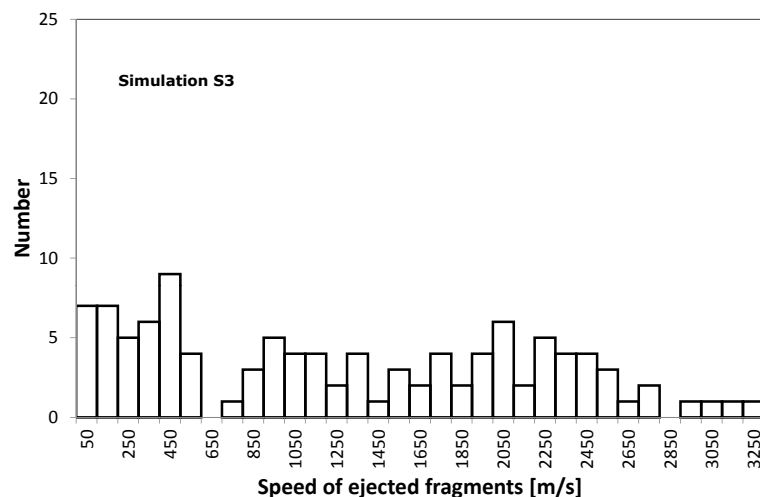
Figure 184: *Histogram of the speed distribution of the ejected fragments in the simulation S3*: Number is the number of fragments. White bars correspond to single particles ejected. This simulation did not produce groups with two or more particles.

Table 21: Physical characteristics of Target 1 (the proto-Haumea generated from the cloud). The Target 2 is the body created after the 20th spin-up of simulation S1. Target 2 is used in the collisionally induced rotational fission (simulations S2, S3). Target 3 is used for simulation S4. Also listed are the physical properties of the projectile used for the simulations S2, S3, and S4. Nb is the number of particles; a, b, and c are the semi-axes of the body; ρ_b is the initial bulk density; and P_0 is the initial rotation period.

Object	Nb	Mass $[\times 10^{21}$ kg]	a, b, c [km]	ρ_b [g cm^{-3}]	P_0 [h]
Target 1	866	4.48	$1362 \times 744 \times 513$	2.1	3.98
Target 2	797	4.12	$1620 \times 611 \times 483$	2.1	4.52
Target 3	846	4.38	$1355 \times 641 \times 506$	2.4	3.64
Projectile	183	0.192	$349 \times 338 \times 294$	1.3	No rotation

IX.4.2.6   Simulation S4

Nonetheless, we must point out that it is possible to create smaller satellites than those in Simulations S1 to S3. In fact, in simulation S4, we perform similar collisions as for simulations S3, but this time the target is slightly different. This new target, named target 3, is denser than the previous target and has an initial rotational period of 3.64 h. All characteristics of this new target can be found in Table 21. Once more, as happened for simulations S1 and S2, the main result is the formation of a binary system (Figure 185). The primary has a rotational period and a mass a little bit lower than current values and the satellite is smaller than in the previous two simulations (Table 22). Some fragments ejected with the correct dispersion velocities may have formed the family members and the satellites may have been formed during the impact.

In Figure 186, the speed distribution of the ejected material in simulation S4 is plotted. The fragments escaping the system immediately after rotational fission have average speeds of 1.9 km s^{-1}. For simulation S4, the average velocity vector of components is (-1730 m s^{-1}, 263 m s^{-1}, 11 m s^{-1}) with a modulus of 1750 m s^{-1} and a standard deviation of the speed around this direction of 1131 m s^{-1}.
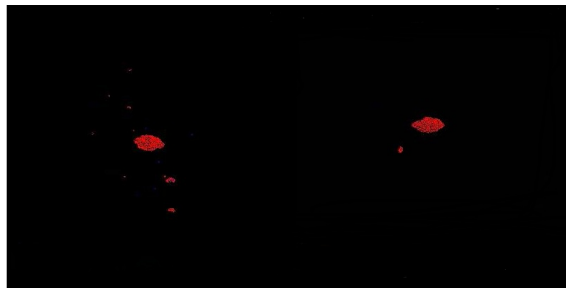
Figure 185: *Rotational fission triggered by a sub-catastrophic collision at high impact velocity*: Simulation S4 in which a lower-mass satellite is created compared to previous simulations.

In Table 22 some characteristics of the presented simulations are summarized. The results of each simulation are also discussed.

IX.4.3   Possible genesis of the Haumea family

IX.4.3.1   Ejected fragments

Haumea has an offset speed of 400 m s^{-1} with respect to the other members of the family (Brown et al., 2007). Such an offset is reproduced in our simulation S2, which seems the best approximation to explain the formation of the Haumea family. However, the mean velocity dispersion of the fragments is higher than the velocity dispersion of the family members ($\sim$140 m s^{-1}). In
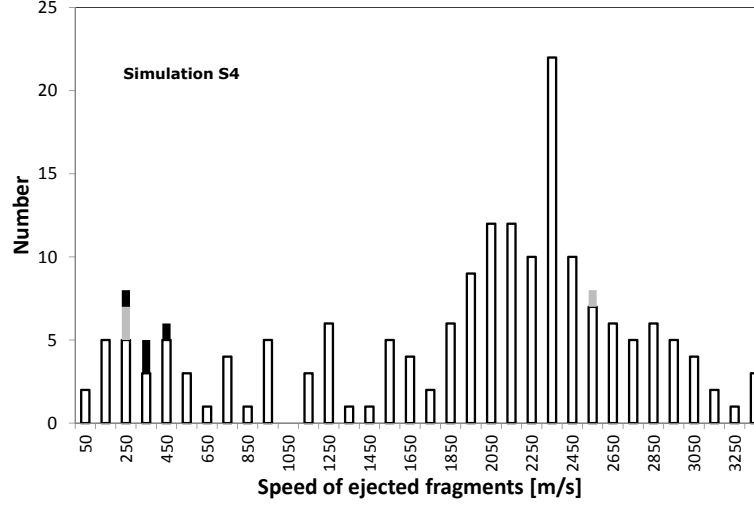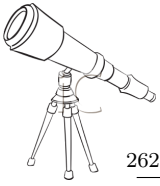
Figure 186: *Histogram of the speed distribution of the ejected fragments in the simulation S4*: Number is the number of fragments. The gray bars correspond to groups of two particles, the black bars correspond to ejected rubble piles composed by more than two particles, and white bars correspond to single particles.

Table 22: *Some results of the simulations.* M_p is the mass of the primary and M_e is the mass ejected from the system; M_s/M_p is the mass ratio of the binary system (mass of the satellite divided by mass of the primary); P is the rotation period of the primary; $<V_e>$ is the average speed of ejected free particles with respect to the center of mass, of ejected pairs of particles, and of ejected rubble piles, respectively.

Simulation	M_p $[\times10^{21}$ kg]	P [h]	M_s/M_p	M_e $[\times10^{20}$ kg]	$<V_e>$ [m/s]
S1	3.922	3.698	0.113	3.620	303, 429, 318
S2	4.302	3.823	0.113	1.327	490, 0*, 0*
S3	3.460	3.375	0.237	0.576	1296, 0*, 0*
S4	4.160	3.632	0.002	3.398	1912, 1009, 330

* In these simulations, no groups of two particles nor rubble-piles were ejected.

fact, the dispersion speed of 328 m s^{-1} of the fragments is still a factor of 2.3 higher than needed. But, as the velocity dispersion distribution is broad, some fragments ejected at lower velocity may have formed the family members. On the other hand, one should note that at least part of the 400 m s^{-1} offset of Haumea due to its displacement in eccentricity from the remainder of the family might be explained by Haumea's chaotic diffusion within the 12:7 mean-motion resonance with Neptune, which can change Haumea's eccentricity to its current value (Brown et al., 2007), but only with a 10% probability. In the presented model this eccentricity difference can be explained if the material was ejected in the orbital plane. In that case the orbits of the ejected fragments will have a very different eccentricity with respect to the progenitor, but not a significantly different inclination. If the spin axis of the proto-Haumea was nearly perpendicular to its orbital plane, the ejection of fragments would be close to the orbital plane, so one would expect a small spread in inclinations and a large separation in eccentricity with respect to the parent body. Thus there is no need to invoke chaotic resonance diffusion to explain the whole difference in eccentricity of Haumea with respect to the rest of the family members.

In conclusion, simulations S2 are qualitatively consistent with the observables and quantitatively very close to the exact values of the observables. However, we must point out that a slightly smaller impact speed below 1000 m s^{-1} might provide more precisely the offset speed and the
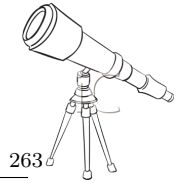
dispersion speed observed in the Haumea system. The offset (with respect to the family members) in Haumea's eccentricity, and not in inclination, is a consequence of the fission happening close to the orbital plane. The family members are part of the ejected components from the parent body. This circumstance is likely because large bodies in many cases have small obliquities.

Finally, we have to admit that, even if the model proposed is statistically more likely than others and does not need to invoke chaotic diffusion for the offset in eccentricity of Haumea with respect to family members, the formation of two satellites is never reproduced by any set of simulations. This is common to the rest of scenarios proposed in literature and is related to the fact that the range of parameter values is essentially infinite, while simulations can only cover a very limited part of them. Nevertheless, we consider that the essential features of the Haumea system are reproduced to a good extent.

IX.4.3.2   Collision on the proto-satellite

One can imagine alternative scenarios for the formation of the family. The first idea for a formation of the family members is inspired by Schlichting and Sari (2009) model. Schlichting and Sari (2009) proposed that an impact on the proto-satellite may have formed the entire family with the right dispersion velocity, and the current two moons. A catastrophic collision on a large proto-satellite formed after the rotational fission can be an alternative mechanism to generate the family with the observed dispersion speed. Such a collision could generate the family members as well as the two current moons. Such a collision on the proto-satellite would not require a large impactor nor a high impact velocity. This means that the probability of such a collision is not negligible. In fact, the size distribution of TNOs is steep in the size range [N(D, D±dD) dN $\propto$ D^{-b} dD, with b>4] and the probability of a shattering event on a 500-km sized proto-satellite, within an even rarefied classical disk is at least four orders of magnitude larger than that of having a catastrophic collision between two bodies of $\sim$1000 km in size each.

This scenario, as that proposed by Schlichting and Sari (2009) presents anyway several problems. In fact, the time span between the formation by fission and the required impact event may be enough to slow down Haumea's rotation through tidal interaction with the satellite. Currently, Haumea's rotation is still very fast, so, the scenario of a collision on a proto-satellite requires an impact shortly after the rotational fission event, which is unlikely.

We realized various collisional simulations on several proto-satellites, in order to test this eventuality. Simulations with different impact parameters and different impact velocities on the proto-satellites have been performed. We also performed collisions on the proto-satellite at different epochs along its orbit (i.e. collisions on the proto-satellite when it was both near and far from the primary), and for different kinds of evolution of the orbit (i.e. collisions on the proto-satellite when its orbits was circular or eccentric). Unfortunately, to date, none of these simulations allow to propose a match with the current characteristics of the family.

IX.4.3.3   Rotational fission of the proto-satellite

On a speculative basis, the second idea for a formation of the family members is based on Jacobson and Scheeres (2011) work about formation of binary/multiple asteroid systems. They proposed that low mass <0.2 ratio binary asteroids resulting from fission are generally unstable (Figure 187). However, stable cases arise when the satellite suffers spin-up through tidal interactions with the primary and finally undergoes a rotational fission itself, with dispersion of part of the system mass. The same mechanism might be applicable to TNOs and could explain the existence of a group of bodies with orbital elements related to those of Haumea (with small dispersion velocities). According to Jacobson and Scheeres (2011), the mechanism of rotational fission of the secondary is not rare, so one has to expect rotational fission families around other large TNOs. However, they pointed out that the spin up of the satellite and its fission can only take place in systems with satellite to primary mass ratios smaller than 0.2.

According to the lowest masses of the family members obtained in this chapter, one can show that the total mass of the family might be even smaller than a few per cent of that of Haumea. Then a satellite to primary mass ratio smaller than 0.2 would be enough to generate the entire family. Such simulations have not been performed in this work, mainly because of the long-term evolution required.
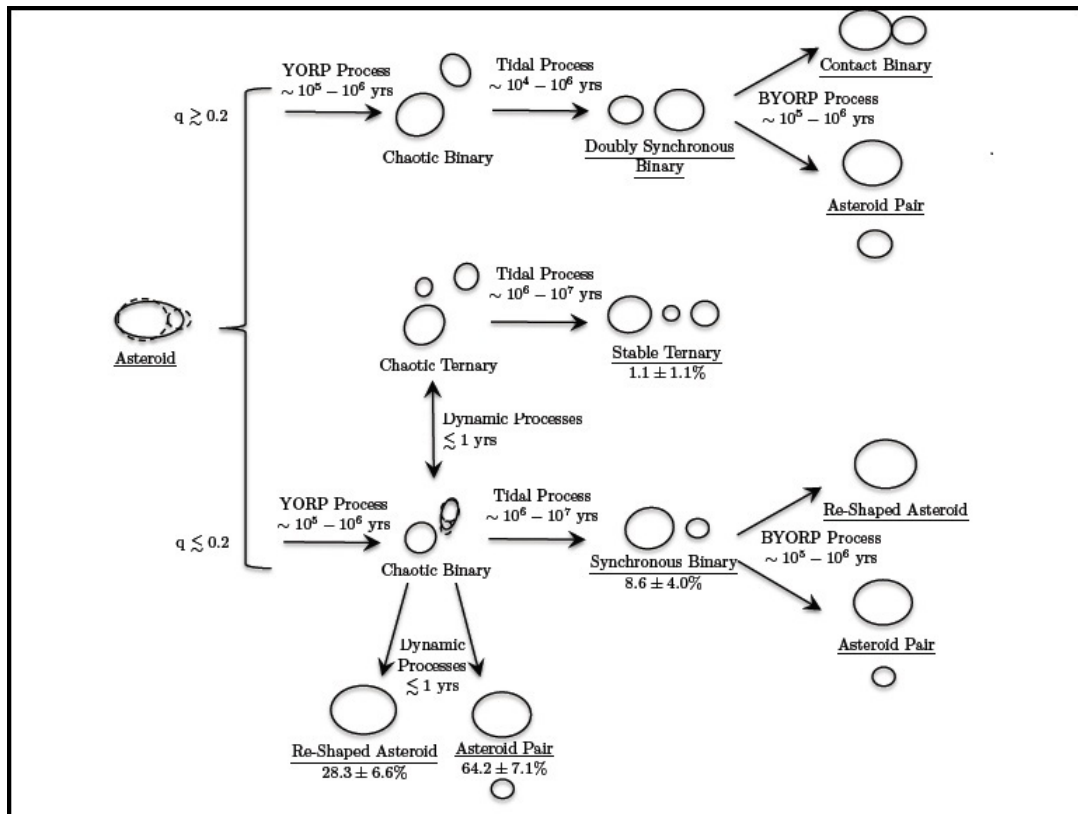
Figure 187: This figure represents the different mechanisms able to form binary/multiple asteroid systems and their evolution. The parameter "q" is the rotational fission component mass ratio (Satellite mass divided by primary mass). Arrows indicate the direction of evolution along with the process propelling the evolution and a typical timescale. Figure from Jacobson and Scheeres (2011).

IX.4.3.4   Formation of a pair and disruption of one of the members of the pair

Several pairs of asteroids have been found in the asteroid belt (Vokrouhlický and Nesvorný, 2008; Pravec et al., 2010), and perhaps in the Trans-Neptunian belt as well (Rabinowitz et al., 2011). Pairs of objects are formed by two objects with similar orbital parameters but that are not bound together (Vokrouhlický and Nesvorný, 2008). Backwards time integrations of such pairs show a common origin. Based on a model of near-Earth asteroid (NEA) rotational fission, Jacobson and Scheeres (2011) pointed out that systems with satellite to primary mass ratios larger than 0.2 always evolve to synchronous binaries, whereas asynchronous binaries, multiple systems and asteroid pairs can only form if their mass ratio is smaller than 0.2 (cf Figure 187). Based on an exhaustive asteroid study, Pravec et al. (2010) showed that asteroid pairs are formed by the rotational fission of a parent contact binary into a proto-binary which is then disrupted. This is found only for mass ratios smaller than 0.2, as expected from theory.

In several simulations run in this work, the proto-Haumea fission results in the formation of a TNO pair with a secondary size in the range 200 to 500 km. Two arguments seem to suggest that Haumea may be a suitable candidate for having featured a pair formation:

- *Lightcurve amplitude:* The primary objects of the asteroid pairs (i.e the biggest object of the pair) have larger lightcurve amplitudes than the primaries of binary asteroids with similar mass ratios. This indicates that primary elongated shapes can destabilize the system and eject the satellite (Pravec et al., 2010). Based on the current Haumea characteristics, one can envisage the feasibility of this scenario.

- *Rotational period:* According to Jacobson and Scheeres (2011), the time span in which a binary system ejects its satellite is usually very short, therefore the tidal interaction would
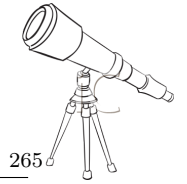
not slow down the primary significantly and it may still be observed in a high rotation state. The Haumea rotational period seems to indicate that tidal effects did not slow down the primary rotational rate.

After the pair formation, the secondary may then suffer a further rotational fission as proposed by Jacobson and Scheeres (2011) or a disruptive collision. After such an event, a group of bodies could be created and would share very similar orbital parameters to those of the primary. In other words, such a group of bodies formed from the secondary would look like a collisional family. The velocity dispersion of the fragments ejected in the collision would indeed be close to the typical escape velocities from a 500 km size body, as happens in the case of the Haumea family (140 m s^{-1}). According to our simulations of original or induced fissions, most of the fragments that escape shortly after have relative velocities with respect to the primary around 400-500 m s^{-1}, in the very range of the offset speed of Haumea with respect to the rest of the family members ($\sim$ 400 m s^{-1}).

A disruptive collision on the secondary of the pair is likely enough, so this scenario is plausible to explain a group of bodies with similar orbital parameters to that of the primary, as happens in the case of Haumea. Unfortunately, the probability of such a scenario is low, and requires a collision in a short time after the collision. On the other hand, this formation scenario would not explain the existence of the two current satellites. However, a multiple system might form soon after the rotational fission, so that the system ejected one of its satellites and retained the currently observed couple of Haumea's satellites. Jacobson and Scheeres (2011) pointed out that a fraction of low mass ratio proto-binaries can evolve to multiple systems that may eject one of its members. On the other hand, the interaction of a third body with the proto-binary formed in the fission process might also result in the ejection of the proto-satellite from the system at a small relative velocity with respect to Haumea. In this case, the mass ratio would not have to be smaller than 0.2. As explained above, if the ejected body underwent a catastrophic disruption, the generated fragments would likely share similar orbital parameters to Haumea's. The interactions of binaries with third bodies were studied by Petit and Mousis (2004) to estimate the stability and persistence of the primordial binaries. They found that these interactions were frequent in the early ages of the Solar System and a large fraction of binaries were destroyed. Therefore, such a mechanism might also have taken place in a young binary Haumea.

In conclusion, a mechanism that might account for all the observables would require that the proto-Haumea fissioned and formed a stable low mass ratio triple system (which is one of the outcomes of the evolution of rotational fission proto-binaries within the Jacobson and Scheeres (2011) formalism). That would explain the presence of the satellites Hi'iaka and Namaka. At the same time, part of the ejected mass should have the right dispersion velocity to form the observed family or be clustered into a single escaping body that should ultimately undergo a catastrophic disruption forming the family itself.

IX.5   Independent genesis of the satellite and the family

Finally an alternative model is considered in Campo-Bagatin et al. (In prep). They propose a scenario which implies independent geneses of Haumea and its satellites on, on one side, and of the family, on the other side. The formation of Haumea and the satellites would have occurred at some epoch and in some location in the trans-neptunian belt, and the formation of the family would have happened at a different epoch and at a different location. In fact, even if the current proper semimajor axes, eccentricities and inclinations are similar for the two groups, the information on the other orbital elements is quickly lost (longitude of the ascending node, argument of pericenter and initial epoch) so that any location for the original bodies is possible within the current range of values of the known orbital elements. They consider two distinct bodies: i) a proto-Haumea that generates both current moons and the current Haumea, and ii) a proto-family parent body with a diameter of $\sim$430 km that generates the observed family. Initially, both parent bodies may have had close orbital elements (a,e,i) but different orbital planes and orbital phases. Moreover, the respective collisions would have happened at different epochs. They propose a collisional event

triggering a rotational fission as origin of the satellites and the Haumea characteristics and a catastrophic collision as genesis of the family members at a completely independent epoch.

Campo-Bagatin et al. (In prep) compute a probability for this model of 1.5-2.5×10^{-2} over the Solar System age, which is an order of magnitude larger than some of the models proposed in the literature and summarized here.

Trujillo, Sheppard and Schaller (2011) showed, with a confidence level over $6\ \sigma$, that Haumea has less water absorption than the rest of the family. They found ratios of the J band to the H_2O 1.5 μm band (J-H_2O) of -0.85$\pm$0.04 for Haumea and J-H_2O = -1.50$\pm$0.1 for the Haumea family. This may potentially suggest a possible independent genesis.

However, the fact that the satellites, Haumea and the family share similar spectral feature indicates that both parent bodies originally have a similar composition of crystalline water ice. To date, water ice spectral features have been detected only on Haumea and associated objects. So, the main problem of this model is to suppose that crystalline water-rich bodies are -or were– more common than observed.

IX.6   Summary

In this chapter, we have presented evidences indicating that rotational fission has to be considered as possible origin of the Haumea family. In fact, based on several arguments as well as features of the current Haumea system, collisionally induced rotational fission seems to be suitable to explain the family formation. In fact, Campo-Bagatin et al. (In prep) computed the probabilities of the needed collisions. They are 7.7×10^{-4}-2.8×10^{-3} during the pre-LHB, of 8.4×10^{-3}-1.2×10^{-2} during the LHB, and 1.0-1.9×10^{-3} during the post-LHB. The probability of this rotational fission mechanism over the Solar System age is 1.2-1.4×10^{-2}, and to date, such a mechanism has the highest probability. The family members related to Haumea might derive from the ejected fragments after the fission. They could also be result of the proto-satellite evolution into a pair, or from the rotational fission of the proto-satellite as well as the proto-satellite disruption.

The rotational fission mechanism can also, by extension, explain the formation of some binary systems in the Trans-Neptunian belt as well as the formation of pairs.

The main problem of finding pairs of TNOs is the difficulty in determining orbital elements. In fact, the orbital elements of most TNOs are more uncertain than those of main belt asteroids. Therefore, searches for TNO pairs are more difficult. Moreover, there are only around 1500 known TNOs, too small a sample if compared to the around 500,000 known asteroids, among which only ~ 60 pairs were found (Vokrouhlický and Nesvorný, 2008). Besides, the small mass ratio implies that many TNO pairs may remain undetected because one of the members is too faint. Another difficulty resides in the fact that a large fraction of the pairs might have formed a few gigayears ago and therefore they would be more difficult to identify than in the asteroid belt, where pairs are much younger than 1 gigayear.

Ortiz et al. (2011) explored the rotational fission scenario as a possible formation of the binary system named Orcus-Vanth. Orcus is a plutino with a large moon called Vanth. Thanks to a midterm study, a high-precision relative astrometry and photometry of the Orcus system with respect to background stars has been realized. From the photometric study, it has been determined that Orcus' system has low variability (0.06$\pm$0.04 mag) and a period of 9.7$\pm$0.3 days. Such a period is consistent with the 9.53 days orbital period of Orcus' satellite estimated by Brown et al. (2010), and the variability found during the mid-term study is caused by the satellite. Therefore, at least the satellite rotation is synchronous. However, it has to be noticed that whether the rotation is synchronous or double synchronous is not known yet with no uncertainty, but there is considerable evidence that Orcus is spinning much faster than 9.5 days. The short-term variability of $\sim$0.04 mag
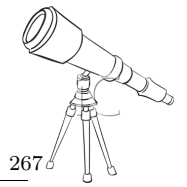
and period around 10.5 h reported by Ortiz et al. (2006); Thirouin et al. (2010) is a clear evidence in that sense. All that would indicate that Orcus has not been sufficiently tidally despun to reach a double synchronous state. If one assumes that the initial spin period of the Orcus parent body was around its critical value, the total angular momentum lost by the despun to 10 h (current Orcus' rotational period) would have been gained by the satellite, which would have reached exactly its current configuration if the mass ratio of the system were around 0.09 (the value obtained by assuming that Vanth's albedo is smaller than that of Orcus, which is likely the case according to their very different spectra). This would give support to the idea that the satellite might be the result of a rotational fission. In conclusion, several binary (multiple) systems have been probably formed through rotational fission in the trans-Neptunian belt and Haumea is the best candidate for such a process.

We must point out that in this chapter, which is dedicated to Haumea, we only report few simulations of more than 100 simulations realized. The results of several simulations were not matching our expectations to explain the formation of the Haumea family, then are not reported here. However, such simulations give us some ideas about future work. In fact, a large set of binary systems (as well as triple systems, pairs, and lots of small satellites around spherical (or nearly) primaries) with a large range of masses and sizes have been formed: systems with low mass ratios up to nearly equal size systems. We also obtained systems with a high range of separations between components. The simulations carried out for this work illustrate the transition to instability for Jacobi ellipsoids and will contribute to a future paper (Tanga et al, In prep.). Other interesting features of simulations are that a satellite can be formed directly due to rotational fission and that the accumulation of small fragments is also able to form satellites. On the other hand, not only equilibrium figures were formed, in some cases, the so-called Dumbbell sequence has been reproduced (Hachisu and Eriguchi, 1984): from a triaxial ellipsoid to a body with a more and more pronounced central narrowing which increases in size and eventually separates into two equal-sized and symmetric fragments.

Chapter X

Summary and Conclusions

$\mathcal{I}$ n this chapter, a summary and the general conclusions obtained during this work are presented.

- R-band and Clear-band photometric data for Trans-Neptunian Objects (TNOs) and Centaurs in order to increase the number of objects studied so far have been collected and analyzed. A homogeneous dataset composed of 54 TNOs and Centaurs is presented. Amplitudes as well as rotation periods have been derived for 45 of them with different degrees of reliability. For 9 objects, only an estimation of the amplitude and a very crude rotational period estimation are presented. A homogeneous data set from which some conclusions can be drawn has been presented. The percentage of low amplitude rotators is higher than previously thought. Only 7 of 45 objects ($\sim$16 per cent) in our sample show a lightcurve with an amplitude $\Delta m >$0.15 mag. The mean lightcurve amplitude is 0.12 mag for the TNOs and centaurs. There is not a dynamical group with a higher/smaller amplitude in our database.

- In the sample, around 84 per cent of the objects have a low variability (less than 0.15 mag) and corresponding lightcurves can be explained by albedo variations. Such bodies are probably oblate spheroids with a highly homogeneous surface. Only few objects present a large lightcurve amplitude and could be explained by the shape of triaxial ellipsoids. An estimation of 0.15 mag (based on Maxwellian fits and from other evidences) has been obtained that seems to be a good measure of the typical variability caused by albedo features. In other words, a lightcurve with a low amplitude is an albedo-dominated lightcurve whereas lightcurves with a large amplitude (larger than 0.15 mag) are shape-dominated lightcurves.

- The sample of targets in the literature is biased toward objects with a short rotational periods and large amplitudes. The best option to debias the sample is to carry out coordinated campaigns with two or three telescopes around the world. In this work, a first attempt of coordinated campaign for TNOs with two telescopes, one in Chile and one in the Canary Islands is reported.

- In the sample the rotation rates appear to be slightly higher (faster rotators) than previously suggested by Sheppard, Lacerda and Ortiz (2008). However, based on a larger sample that includes all the literature the mean rotational periods from the Maxwellian fits are 7.99 h for the entire sample (TNOs+centaurs), 8.97 h for the sample without the centaurs, and 7.95 h for the centaur population. Such mean rotational periods are slightly higher than previously reported by Duffard et al. (2009), but are consistent with the averages quoted in Sheppard, Lacerda and Ortiz (2008).

- A spin barrier has been reported at $\sim$4 h. This probably means that objects with a rotational period shorter than this limit get disrupted. Assuming this spin barrier as the critical rotational period, corresponding densities around 0.7 g cm^{-3} for spherical objects with no cohesion, and $\sim$0.8 g cm^{-3} for typical oblate objects with a semimajor axis of 100 km, a tensile strength of 0.01 MPa and an axis ratio of 0.8, which is more realistic, have been computed.

- The short-term variability of 6 members of the Haumea family which is composed by 13 members (to date) has been reported. The sample is still too limited to derive reliable conclusions. However, the Haumea family members seem to rotate faster than the other TNOs. Besides, there are two fast rotators in this family: Haumea and 2003 OP$_{32}$. It is also interesting to point out that these two fast rotators are also the members with the highest lightcurve amplitude. The rotational period distribution is not well fitted by a Maxwellian distribution which would mean that a catastrophic collision is not the origin of the family, but the data are too few to draw firm conclusions. On the other hand, not all the families even in the asteroid belt have Maxwellian distributions of their periods.

- Information about the TNOs and centaurs was derived such as: axis ratios (i.e. deformation of the objects), homogeneity or heterogeneity of the surface, density and cohesion:

  – Considering an equatorial viewing, the mean is 0.90 and 0.55 for the axes ratios a/b and c/a, respectively where a>b>c. The averages, assuming an observational angle of 60°, are lower with 0.79 for a/b and 0.51 for c/a.

  – Based on the assumption of hydrostatic equilibrium, and assuming that objects are Jacobi ellipsoids, lower limits to the density of several objects have been derived.

  – Based on the assumption of hydrostatic equilibrium, and assuming that objects are Jacobi ellipsoids, lower limits to the density of several objects have been derived. The biggest objects (diameter around 2000 km) have a mean density above 2 g cm^{-3} which implies a rock/water ice ratio of 70/30. The intermediate-size objects (diameter around 800 km) have densities above 1 g cm^{-3}. This suggests that these objects are essentially composed by ice with some denser rocky material. The smallest objects have low densities, less than 1 g cm^{-3} which indicates that they are porous (Jewitt and Sheppard, 2002), due to material composition or to internal structure.

  – Using Tancredi and Favre (2008) work, the condition for hydrostatic equilibrium in terms of absolute magnitude, density, albedo and material strength can be expressed. It is expected that the material in the interior of large TNOs can have tensile strengths of up to 1MPa but they can behave like fluids because the self-gravity overwhelms the material strength. However, for smaller bodies one can suspect that they are rubble piles (gravitational aggregates) so each fragment of the rubble pile can have its own internal cohesion, but as a whole, the body adopts the same figure of equilibrium as a fluid in response to rotation.

- From unresolved lightcurves for eleven binary systems and one triple system, information such as size and albedo of both components of the systems were derived:

  – Assuming that both components of the 2007 TY$_{430}$ system are in hydrostatic equilibrium a lower limit to their density (ρ>0.46 g cm^{-3}), a primary (secondary) radii of <58 km (<55 km, respectively) and a geometric albedo of >0.12 for both components have been obtained. A geometric albedo of >0.08 for the 2001 QY$_{297}$ system, a primary
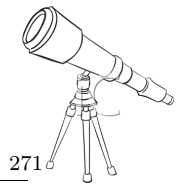
(secondary) radii of <129 km (<107 km), and a lower limit of the density of >0.29 g cm^{-3} have been derived. The study of this system is in agreement with Vilenius et al. (2013) based on *Herschel Space Observatory* data.

– Most of the lightcurves of binary systems studied in this thesis are more significantly affected by albedo effects than shape effects. In such cases, the objects are likely MacLaurin spheroids and direct constraints on sizes and albedos cannot be obtained.

– The majority of binary objects has a low lightcurve amplitude, <0.15 mag. Around 49% of the entire sample, 52% of the sample without the binary population and 56% of the binary sample have a low amplitude. There are hints that the lightcurve amplitudes of binary systems may be slightly larger than the non-binary population, but overall the distributions are similar and more studies about short-term variability of binary systems would be needed.

– Based on Maxwellian fits, the binary population is rotating slower than the non-binary one. Tidal effects between both components can slow down the rotational rates of the primary as well as of the secondary. None of the studied systems reported in this work are tidally locked, because there are evidences for rotational periods of several hours. Using the Gladman et al. (1996) approach to compute the synchronization time, values that are consistent with none of the binaries being tidally locked, for expected values of internal properties (rigidity and dissipation) are obtained.

– Several formation models for the binary systems studied in this work have been proposed.

• An exhaustive search for correlations/anti-correlations between physical and orbital parameters reveals several features depending on the dynamical classes and the object sizes. Nevertheless, the study of correlations/anti-correlations may reveal relations between parameters that come from observational biases in the sample, so caution is needed to interpret the results.

– A clear evidence of correlation with a very strong significance level is shown between the lightcurve amplitude and the absolute magnitude in most of the samples studied in this work. Such a correlation indicates that small objects have larger lightcurve amplitude than large ones. Small objects are probably more deformed than large ones. This seems in agreement with the collisional evolution scenario (Davis and Farinella, 1997).

– There are evidences of anti-correlation between lightcurve amplitude and inclination in several sub-groups, as well as between lightcurve amplitude and eccentricity. Such an anti-correlation indicates that objects with a small lightcurve amplitude (with less deformation) are in inclined orbits whereas objects with a high lightcurve amplitude (deformed objects) are in circular orbits at low inclination. Anti-correlation between lightcurve amplitude and eccentricity affects objects with an absolute magnitude (H) less than 5 (large objects). In the case of the classical population, all objects (independent on their sizes) follow such a tendency.

– There is an anti-correlation between albedos and inclinations in several samples, as well as between albedos and eccentricities. These anti-correlations indicate that objects with high albedos are at low inclinations and low eccentricities. Such an idea has been already noted by Brucker et al. (2009), in the case of dynamically cold classical objects. However, it must be pointed out that dynamically hot classical objects at high inclinations also present an anti-correlation between albedos and inclinations (based on a limited

sample of objects), although only for objects with H$\geq$5. The case of the sample without the centaur population is interesting and indicates different characteristics according to the object size. In fact, the sample limited to objects with H$<$5 presents a correlation, whereas the sample composed by objects with H$\geq$5 presents an anti-correlation.

– Several correlations and anti-correlations between rotational periods and ascending nodes, perihelion distances, and arguments of the perihelion are also listed. Reasons for such features are not obvious and may be attributed to observational biases. More observational information is required to confirm or discard such features. Several weak correlations/anti-correlations are obtained such as rotational period versus absolute magnitude in the dynamically cold classical and resonants groups, and rotational period versus eccentricity in the binary population. Unfortunately the samples are very small and more observations are needed to be conclusive.

– The binary population is not showing different features compared to the non-binary population regarding the correlations/anti-correlations. There are some hints that the binary population seems to have higher lightcurve amplitudes, however this may be due to observational biases as most of the BTNOs are dynamically cold classical objects that are known to have higher lightcurve amplitudes.

• Part of this work is dedicated to N-body numerical simulations of rotational fissions and collisionally induced rotational fissions.

– Simulations to reproduce the formation of Haumea have been made. Three main scenarios have been analyzed: i) rotational fission by increasing the angular momentum called pure rotational fission, ii) rotational fission triggered by a gentle collision, and iii) rotational fission triggered by a high-speed sub-catastrophic collision. In each set of simulations presented in this work, the creation of a satellite as well as a fast rotation for the primary is a common result.

– In the favorite scenario, the rotational fission induced by a small collision, the dispersion velocity of the fragments is a factor 2.3 higher than the current dispersion velocity of the family members. But as the velocity distribution is broad, some of the fragments ejected at lower velocity may have formed the current family.

– The family of bodies orbitally related to Haumea may directly come from fragments of the disruption but also be a result of the evolution of a proto-satellite in the proto-binary after the fission, or might arise from the disruption of an escaped fragment or an escaped satellite. In all these cases, Haumea speed with respect to the fragments is systematically different, as observed currently, and there is no need to invoke chaotic resonance diffusion (such process is inefficient, just 10%). In our preferred scenario, the required collision has a larger probability of occurring than other collisional scenarios that have been proposed in the literature to explain the existence of satellites and bodies orbitally related to Haumea. Also, angular momentum considerations about Haumea and its two satellites also indicate origin from rotational fission or mass shedding. Therefore this scenario is more plausible than catastrophic collision or other models in the literature.

– In the case of the rotational fission triggered by a sub-catastrophic collision, part of the projectile is encrusted on the target surface whereas the rest is ejected at high velocity. This feature may explain the dark spot reported on the current Haumea surface as noted by Lacerda, Jewitt and Peixinho (2008).

– It is expected that other binaries and even yet-to-be-found TNO pairs may have arisen by the mechanism, as it is the case in the asteroid belt (Vokrouhlický and Nesvorný,
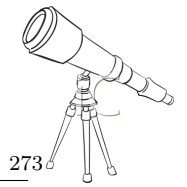
2008; Pravec et al., 2010). For instance, such a rotational fission may be the cause of the Orcus-Vanth system genesis (Ortiz et al., 2011).

- More short-term variability studies are required to confirm preliminary conclusions of this work for particular dynamical groups which have few member observed so far. Several groups, such as the centaurs and the small TNOs, in particular, need to be more thoroughly investigated.

$\mathcal{E}$ n este capítulo, se presentan un resumen y las conclusiones generales obtenidas durante esta tesis.

- Se han obtenido y analizado datos fotométricos en filtros R y Clear (sin filtro) de Objetos Trans-Neptunianos (TNOs) y Centauros para incrementar el número de objetos estudiados. Se presenta un conjunto homogéneo de datos compuesto por 54 TNOs y centauros. Las amplitudes y los períodos de rotación han sido derivados para 45 de ellos con diferentes grados de fiabilidad. Para 9 objetos, se ha propuesto solamente una estimación de la amplitud y una cruda estimación del período de rotación. Se ha presentado un conjunto homogéneo de datos de los cuales varias conclusiones se pueden apreciar. El porcentaje de objetos con una baja amplitud es mayor de lo que se pensaba. Solamente 7 de los 45 objetos ($\sim$16%) del conjunto de datos presentan una curva de luz con una amplitud $\Delta m >$0.15 mag. Se ha calculado una amplitud promedio de 0.12 mag para los TNOs y centauros. No se aprecia ningún grupo dinámico con mayor/menor amplitud en la base de datos.

- En la muestra, alrededor de 84% de los objetos tiene una variabilidad baja (menos de 0.15 mag) cuyas curvas de luz se pueden explicar por variaciones de albedo sobre la superficie del objeto. Dichos objetos son probablemente esferoides oblatos con una superficie muy homogénea. Sólo algunos objetos presentan una amplitud grande de curva de luz que puede deberse a la forma elongada de los objetos, llamados elipsoides triaxiales. Se ha estimado que 0.15 mag (basado en ajustes a Maxwelliana y debido a otras consideraciones) parece ser una buena medida de la variabilidad típica causada por variaciones de albedo. En otras palabras, una curva de luz con una amplitud baja es una curva de luz dominada por el albedo mientras que una curva de luz con una amplitud grande (superior a 0.15 mag) es dominada por la forma del objeto.

- La muestra de objetos estudiados en la literatura está sesgada hacia los objetos con un corto período de rotación y gran amplitud. La mejor opción para disminuir este sesgo es realizar campañas coordinadas con dos o tres telescopios alrededor del mundo. En este trabajo, se ha presentado la primera campaña coordinada para TNOs con dos telescopios, uno en Chile y uno en las Islas Canarias.

- En la muestra los períodos de rotación son ligeramente superiores (objetos más rápidos) a lo sugerido previamente por Sheppard, Lacerda and Ortiz (2008). Sin embargo, basándose en una muestra más grande que incluye toda la literatura los períodos de rotación medios de los ajustes a Maxwelliana son 7.99 h para toda la muestra (TNOs+centauros), 8.97 h para la muestra sin los centauros y 7.95 h para la población de los centauros. Tales valores son ligeramente más altos que los presentados por Duffard et al. (2009), pero son consistentes con el estudio de Sheppard, Lacerda and Ortiz (2008), si bien estos últimos no provienen de ajustes a Maxwellianas.

- Se ha notado una barrera de "spin" a $\sim$4 h. Esto probablemente significa que un objeto con un período de rotación más rápido que a límite se rompería. Considerando esta barerra de "spin" como un período crítico, se ha calculado una densidad correspondiente de $\sim$0.7 g cm^{-3} para objetos esféricos sin cohesión, de $\sim$0.8 g cm^{-3} para típicos objetos oblatos con un semieje de 100 km, una resistencia a la tracción de 0.01 MPa y una razón entre ejes de 0.8, lo que es más realista.

- Se han presentado estudios de fotometría relativa de series temporales para 6 de los 13 (hasta la fecha) miembros de la familia de Haumea. La muestra es todavía muy limitada para derivar conclusiones fiables. Sin embargo, parece que los miembros de la familia de Haumea giran más rápido que los demás TNOs. Además, hay que reseñar dos rotadores rápidos de esta

familia: Haumea y 2003 OP$_{32}$. También es de destacar que estos dos rotadores rápidos son los miembros con la mayor amplitud de curva de luz. La distribución de períodos de rotación no se ajusta bien a una distribución Maxwelliana, lo que podría significar que una colisión catastrófica no haya generado la familia, pero los datos son demasiado limitados para proponer conclusiones firmes. Por otro lado, no todas las familias del cinturón de asteroides tienen una distribución Maxwelliana de sus períodos de rotación.

- Se han derivado informaciones sobre los TNOs y los centauros, tales como: razones entre ejes (deformación de los objetos), homogeneidad o heterogeneidad de la superficie, densidad y cohesión:

  - Considerando una visión ecuatorial, se ha calculado una media de 0.90 y 0.55 para las razones entre ejes a/b y c/a, respectivamente donde a>b>c. Las medias, suponiendo un ángulo de observación de 60°, son inferiores a 0.79 para las razones a/b y 0.51 para c/a.

  - Considerando que los objetos están en equilibrio hydrostático, y que son ellipsoides de Jacobi, se ha derivado el límite inferior de la densidad de varios objetos.

  - Los objetos grandes (diámetro de unos 2000 km) tienen una densidad media por encima de 2 g cm^{-3} lo que implica una razón de hielo/roca de 70/30. Los objetos de tamaño intermedio (diámetro de unos 800 km) tienen densidades superiores a 1 g cm^{-3}. Esto sugiere que estos objetos están compuestos esencialmente por hielo con algún material rocoso más denso, mientras que los objetos más pequeños tienen densidades inferiores a 1 g cm^{-3}. De hecho, varios objetos tienen una densidad inferior a 1 g cm^{-3} lo que indica que estos objetos son porosos (Jewitt and Sheppard, 2002).

  - Basándose en el estudio de Tancredi and Favre (2008), se ha expresado la condición de equilibrio hidrostático en términos de magnitud absoluta, densidad, albedo y resistencia del material. Se espera que el material del interior de los TNOs grandes podría tener resistencia a la tracción hasta 1 MPa, pero pueden comportarse como fluidos porque la gravedad supera la resistencia del material. No obstante, para los objetos pequeños se sospecha que son montones de escombros (agregados gravitacionales) y cada fragmento de la pila de escombros puede tener su propia cohesión interna, pero en conjunto, el cuerpo adopta la misma figura de equilibrio que un fluido, en respuesta a su rotación.

- De las curvas de luz no-resueltas de once sistemas binarios y de un sistema triple, se han obtenido informaciones como el tamaño, y el albedo de cada componente del sistema:

  - Suponiendo que los dos componentes del sistema 2007 TY$_{430}$ están en equilibrio hidrostático, se ha derivado una densidad muy baja (ρ>0.46 g cm$^-$3), los radios del primario (secundario) son <58 km (<55 km, respectivamente) y un albedo geométrico de >0.12 para ambos componentes. Se ha estimado un albedo geométrico >0.08 para el sistema 2001 QY$_{297}$, los radios obtenidos son de <129 km (<107 km) para el primario (secundario) y se ha derivado un límite inferior a la densidad de >0.29 g cm$^-$3. Estos resultados sobre este sistema concuerdan con el estudio de Vilenius et al. (2013) basado en datos del *Herschel Space Observatory*.

  - La mayoría de las curvas de luz de los sistemas binarios estudiados en esta tesis están significativamente más afectadas por variaciones de albedo, que por efectos de forma. En tales casos, los objetos son probablemente esferoides de MacLaurin y no se puede derivar estimaciones directas de los tamaños y albedos.
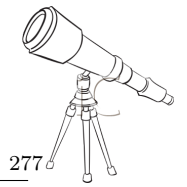
– La mayoría de los objetos tiene una amplitud de curva de luz muy baja, <0.15 mag. Alrededor de 49% de toda la muestra, 52% de la muestra sin la población binaria y 56% de la muestra de objetos binarios tienen una amplitud baja. Hay evidencias de que las amplitudes de curva de luz de los sistemas binarios/múltiples podrían ser ligeramente más grandes que los demás TNOs, pero en general las distribuciones son similares y más estudios sobre la fotometría relativa de series temporales de sistemas binarios/múltiples son necesarios.

– Basándose en ajustes a Maxwelliana, se ha notado que la población binaria está girando más lentamente que la población no binaria. Los efectos de mareas entre ambos componentes pueden ralentizar los períodos de rotación de los primarios, así como de los secundarios. Ninguno de los sistemas estudiados en este trabajo está sincronizado por efectos de mareas, porque hay evidencias de período de rotación de varias horas. Se ha utilizado el enfoque usado en Gladman et al. (1996) para calcular el tiempo de sincronización, y se han obtenido valores que concuerdan con que ninguno de los binarios de la muestra está sincronizado por efectos de mareas, para valores típicos de propiedades internas (rigidez y disipación).

– Se han propuesto modelos de formación para los sistemas binarios estudiados en este trabajo.

• Una búsqueda exhaustiva de correlaciones/anti-correlaciones entre parámetros físicos y orbitales revela varias características según las clases dinámicas y el tamaño del objeto. El estudio de las correlaciones/anti-correlaciones puede revelar relaciones entre los parámetros que provienen de sesgos observacionales de la muestra, así que hay que tener precaución a la hora de interpretar los resultados.

– Se ha obtenido una clara correlación con un nivel de significancia muy fuerte entre la amplitud de la curva de luz y la magnitud absoluta en la mayoría de las muestras estudiadas en este trabajo. Dicha correlación indica que los objetos pequeños tienen mayor amplitud de curva de luz que los grandes. Así, los objetos pequeños son probablemente más deformados que los grandes. Tal hecho parece de acuerdo con el escenario de evolución collisional de Davis and Farinella (1997).

– Existen evidencias de anti-correlación entre la amplitud de la curva de luz y la inclinación en varios subgrupos, así como entre la amplitud de la curva de luz y la excentricidad. Tal anti-correlacion indica que los objetos con una pequeña amplitud de curva de luz (es decir los objetos con menos deformación) están en órbitas inclinadas mientras que los objetos con una mayor amplitud de curva de luz (los objetos más deformados) se encuentran en órbitas circulares y con inclinación baja. La anti-correlación entre la amplitud de la curva de luz y la excentricidad afecta a los objetos con una magnitud absoluta (H) menos de 5 (objetos grandes). En el caso de la población clásica, todos los objetos (independientemente de su tamaño) siguen tal tendencia.

– Hay una anti-correlación entre el albedo y la inclinación en varias grupos, así como entre el albedo y la excentricidad. Estas anti-correlaciones indican que los objetos con un albedo elevado están a inclinación y excentricidad bajas. Tal tendencia ya ha sido señalada por Brucker et al. (2009), en el caso de los objetos clásicos dinámicamente fríos. Sin embargo, se debe de señalar que los objetos clásicos dinámicamente calientes con mayor inclinación, también presentan una anti-correlación entre el albedo y la inclinación (basado en una muestra limitada de objetos) pero sólo los objetos con H≥5. El caso del grupo sin la población de los centauros es interesante e indica características diferentes según el tamaño del objeto. La muestra limitada a los objetos con H<5 presenta

una correlación, mientras que la muestra compuesta por objetos con H≥5 favorece una anti-correlación.

– Se han pesentado varias correlaciones y anti-correlaciones entre el período de rotación y el nodo ascendente, la distancia del perihelio y el argumento del perihelio. Las razones de tales tendencias no son obvias y pueden ser atribuidas a sesgos observacionales. Solamente, más datos podrían confirmar o descartar tales características. Hay que destacar varias débiles correlaciones/anti-correlaciones entre el período de rotación y la magnitud absoluta en el grupo de objetos clásicos dinámicamente fríos y el grupo de resonantes y el período de rotación y la excentricidad en la población binaria. Por desgracia, las muestras son muy limitadas y más observaciones son necesarias para confirmar dichas tendencias.

– La población binaria no parece tener diferentes características a la población no binaria. Hay algunas evidencias de que la población binaria parece tener una mayor amplitud de curva de luz, sin embargo tal hecho puede ser debido a un sesgo observacional, ya que la mayoría de los BTNOs son dinámicament fríos que son conocidos por tener una mayor amplitud de curva de luz.

- Parte de esta tesis está dedicada a simulaciones numéricas de N-cuerpos sobre fisión por rotación y de fisión por rotación inducida por colisión.

  – Se han hecho simulaciones para reproducir la formación de Haumea. Tres escenarios principales han sido analizados: i) fisión por rotación debido a incrementos del momento angular, llamada fisión pura por rotación ii) fisión por rotación provocada por una colisión pequeña, y iii) fisión por rotación provocada por una colisión por alta velocidad. En cada simulación presentada en este trabajo, se han obtenido un satélite, así como una rápida rotación del primario.

  – En el escenario de la fisión rotacional inducida por una pequeña colisión, la velocidad de dispersión de los fragmentos es un factor 2.3 mayor que la actual velocidad de dispersión de los miembros de la familia. Pero, como la distribución de la velocidad es amplia, algunos de los fragmentos expulsados a baja velocidad pueden haber formado a los miembros de la familia.

  – La familia de objetos relacionados con Haumea puede provenir directamente de los fragmentos de la ruptura, pero también pueden ser el resultado de la evolución de un proto-satélite del sistema proto-binario después de la fisión, o pueden nacer de la ruptura de un fragmento escapado. En todos estos casos, la velocidad de Haumea con respecto a los fragmentos es sistemáticamente diferente, como se observa en la realidad, y no hay que invocar una difusión de resonancia caótica (que es poco eficiente, sólo un 10%). En este escenario, la colisión requerida tiene una mayor probabilidad de ocurrir que la de los otros escenarios que se han propuesto en la literatura para explicar la existencia de los satélites y cuerpos relacionados con Haumea. También, las consideraciones obtenidas del momento angular de Haumea y sus dos satélites indican una origen por fisión rotacional o expulsiones de masa. Por lo tanto se cree que este escenario es mucho más plausible que la colisión catastrófica y otros modelos de la literatura.

  – En el caso de la fisión por rotación provocada por una colisión sub-catastrófica, parte del proyectil se queda incrustado en la superficie del objeto. Esta característica puede explicar la mancha oscura sobre la superficie del Haumea actual, reportada por Lacerda, Jewitt and Peixinho (2008).
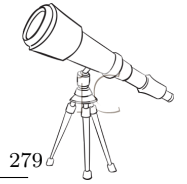
– Se piensa que otros binarios y pares de TNO todavía por descubrir pueden derivar de este mecanismo, como es el caso en del cinturón de asteroides (Vokrouhlický and Nesvorný, 2008; Pravec et al., 2010). Por otro lado, una fisión rotacional puede ser el origen del sistema Orcus-Vanth (Ortiz et al., 2011).

Más estudios de variabilidad a corto plazo se requerirían con objeto de confirmar varias conclusiones preliminares de este trabajo para determinados grupos dinámicos que tienen pocos miembros observados hasta la fecha. Varios grupos, como los centauros y los pequeños TNOs, en particular, deben ser investigados de forma más completa.

Appendix A

Short-term variability

In Chapter VI, we studied the short-term variability of 54 TNOs and centaurs. The final material of these 54 objects are long tables of photometry data per object, which cannot be reproduced here because of their sizes. An example of this material can be found in this Appendix. In the table, we report the name of the object, and for each image we specify the Julian date, the relative magnitude and the 1-σ error associated, the filter used during the observational run, the phase angle, the topocentric and heliocentric distances. The full table is available in .pdf or ascii format upon request.
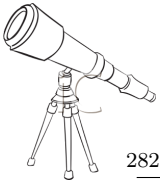
Table 23: The name of the object and for each image we specify the Julian date (not corrected for light time), the Relative magnitude [mag] and the 1-σ error associated (in magnitude), the filter used during observational runs, the phase angle (α, in degree), topocentric (r_h) and heliocentric (Δ) distances (both distances expressed in AU).

Object	Julian date	Relative magnitude [mag]	Error [mag]	Filter	α [°]	r_h [AU]	Δ [AU]
(38628) 2000 EB$_{173}$ Huya							
	2455355.38744	0.001	0.010	Clear	1.20	27.853	28.676
	2455355.39325	0.012	0.01 0	Clear	1.20	27.853	28.676
	2455355.39905	0.013	0.013	Clear	1.20	27.853	28.676
	2455355.40486	0.023	0.010	Clear	1.21	27.853	28.676
	2455355.41067	-0.017	0.012	Clear	1.21	27.853	28.676
	2455355.41647	0.013	0.012	Clear	1.21	27.853	28.676
	2455355.42228	0.006	0.013	Clear	1.21	27.853	28.676
	2455355.42809	0.007	0.011	Clear	1.21	27.854	28.676
	2455355.43389	-0.042	0.013	Clear	1.21	27.854	28.676
	2455355.43970	-0.004	0.013	Clear	1.21	27.854	28.676
	2455355.44551	-0.009	0.013	Clear	1.21	27.854	28.676
	2455355.45131	0.023	0.012	Clear	1.21	27.854	28.676
	2455355.45712	-0.028	0.014	Clear	1.21	27.854	28.676
	2455355.46293	0.003	0.013	Clear	1.21	27.854	28.676
	2455355.46873	-0.030	0.013	Clear	1.21	27.854	28.676
	2455355.47454	0.013	0.012	Clear	1.21	27.854	28.676
	2455355.48035	0.013	0.015	Clear	1.21	27.854	28.676
	2455355.48615	-0.016	0.012	Clear	1.21	27.854	28.676
	2455355.49221	0.006	0.015	Clear	1.21	27.854	28.676
	2455355.50596	-0.030	0.011	Clear	1.21	27.854	28.676
	2455355.51177	-0.008	0.010	Clear	1.21	27.854	28.676

Correlations of rotation paramaters with orbital and physical parameters

We searched for correlations between physical (albedo, rotational period, and lightcurve amplitude) and orbital parameters (perihelion distance, aphelion distance, absolute magnitude, argument of perihelion, longitude of the ascending node, inclination, orbital eccentricity, and semimajor axis). Only physical parameters derived from lighturves have been considered in this study. We used the Spearman rank correlation (Spearman, 1904) because this method is less sensitive to atypical/wrong values and do not assume any population probability distribution. We computed the strength of the correlations by calculated the Spearman coefficient ρ and the significance level (SL). For more details, see Section VII.7.

In Table 25, the orbital elements used for the correlations/anti-correlations search are listed. Orbital elements are from the Minor Planet Center database.

In Table 26, the albedos used for the correlations/anti-correlations search are listed. Rotational periods and lightcurve amplitudes can be found in Table 7.

Table 24: Some correlations/anti-correlations found using the lightcurve parameters and orbital/physical variables. We looked into 29 samples of data: the entire sample (All), just in the binary sample (Binary pop), in the sample without binaries (No binary pop), in a sample excluding the centaur population (No Cent pop), in a sample without the binary nor the centaur populations (No Centaur and no Binary) and according to the objects dynamical classes (Classical objects divided into two sub-groups: dynamically hot and dynamically cold classical objects, the resonants and the group composed of scattered disk objects (SDO) and detached objects (DO)) as well as respect to the object sizes. We indicate the Spearman rank correlation (ρ), the Significance Level (SL in percent), and the number of objects in each sample (Nb). All correlations/anti-correlations with a Spearman rank and Significance Level in agreement with our criterion (see Discussion) are in bold.

Correlated values	Sample	ρ	SL [%]	Nb
Amplitude versus eccentricity	All	-0.200	99.69	112
	All (H<5)	**-0.425**	**99.98**	**43**
	All (H≥5)	-0.218	98.89	69
	No binary pop	-0.122	95.06	85
	No binary pop (H<5)	**-0.508**	**99.92**	**30**
	No binary pop (H≥5)	-0.095	86.58	55
	Binary pop	**-0.406**	**99.49**	**27**
	Binary pop (H<5)	-0.284	96.98	13
	Binary pop (H≥5)	**-0.437**	**95.02**	**14**
	No centaur pop	-0.280	99.90	95
	No centaur pop (H<5)	**-0.425**	**99.98**	**43**
	No centaur pop (H≥5)	-0.263	97.88	52
	No Centaur and no Binary	-0.226	98.73	68
	No Centaur and no Binary (H<5)	**-0.508**	**99.91**	**30**
	No Centaur and no Binary (H≥5)	-0.160	85.13	38
	Classical	**-0.480**	**99.99**	**49**
	Classical (H<5)	**-0.482**	**99.86**	**24**
	Classical (H≥5)	**-0.427**	**97.05**	**25**
	Hot	-0.258	98.43	36
	Hot (H<5)	**-0.450**	**99.78**	**24**
	Hot (H≥5)	0.083	28.12	12
	Cold	-0.468	91.63	13
	Resonant	0.059	76.27	27
	Resonant (H<5)	-0.394	94.52	11
	Resonant (H≥5)	0.008	56.95	16
	SDO/DO	0.006	65.56	19
	SDO/DO (H<5)	-0.344	87.87	8
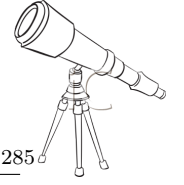
Correlated values	Sample	ρ	SL [%]	Nb
	SDO/DO (H≥5)	0.131	61.37	11
	Centaur	0.119	88.05	17
Amplitude versus inclination	**All**	**-0.322**	**100**	**112**
	All (H<5)	-0.082	92.28	43
	All (H≥5)	-0.174	96.94	69
	No binary pop	**-0.305**	**99.98**	**85**
	No binary pop (H<5)	-0.169	89.53	30
	No binary pop (H≥5)	-0.170	96.11	55
	Binary pop	**-0.398**	**99.47**	**27**
	Binary pop (H<5)	-0.099	95.81	13
	Binary pop (H≥5)	0.034	27.05	14
	No centaur pop	**-0.370**	**100**	**95**
	No centaur pop (H<5)	-0.082	92.28	43
	No centaur pop (H≥5)	-0.205	93.03	52
	No Centaur and no Binary	**-0.376**	**99.99**	**68**
	No Centaur and no Binary (H<5)	-0.169	89.53	30
	No Centaur and no Binary (H≥5)	-0.237	92.72	38
	Classical	**-0.431**	**99.96**	**49**
	Classical (H<5)	-0.149	90.08	24
	Classical (H≥5)	-0.230	80.37	25
	Hot	-0.172	94.29	36
	Hot (H<5)	-0.125	92.10	24
	Hot (H≥5)	-0.025	25.99	12
	Cold	-0.061	21.95	13
	Resonant	**-0.328**	**95.72**	**27**
	Resonant (H<5)	-0.180	62.94	11
	Resonant (H≥5)	-0.152	66.21	16
	SDO/DO	-0.185	86.24	19
	SDO/DO (H<5)	-0.004	80.94	8
	SDO/DO (H≥5)	-0.014	28.13	11
	Centaur	0.217	93.50	17
Amplitude versus absolute Magnitude	**All**	**0.410**	**100**	**112**
	All (H<5)	0.205	98.50	43
	All (H≥5)	0.110	90.67	69
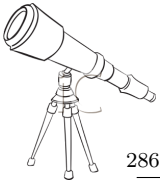
Correlated values	Sample	ρ	SL [%]	Nb
	No binary pop	**0.415**	**100**	**85**
	No binary pop (H<5)	**0.418**	**99.85**	**30**
	No binary pop (H≥5)	0.188	97.34	55
	Binary pop	**0.412**	**99.47**	**27**
	Binary pop (H<5)	-0.269	99.32	13
	Binary pop (H≥5)	-0.118	80.22	14
	No centaur pop	**0.476**	**100**	**95**
	No centaur pop (H<5)	0.206	98.50	43
	No centaur pop (H≥5)	0.259	98.31	52
	No Centaur and no Binary	**0.498**	**100**	**68**
	No Centaur and no Binary (H<5)	**0.418**	**99.85**	**30**
	No Centaur and no Binary (H≥5)	**0.368**	**99.37**	**38**
	Classical	**0.587**	**100**	**49**
	Classical (H<5)	0.282	98.60	24
	Classical (H≥5)	**0.470**	**98.81**	**25**
	Hot	**0.404**	**99.91**	**36**
	Hot (H<5)	0.263	98.66	24
	Hot (H≥5)	0.339	86.74	12
	Cold	0.354	79.96	13
	Resonant	0.285	97.46	27
	Resonant (H<5)	**-0.328**	**95.57**	**11**
	Resonant (H≥5)	0.030	60.21	16
	SDO/DO	**0.671**	**99.84**	**19**
	SDO/DO (H<5)	**0.709**	**98.70**	**8**
	SDO/DO (H≥5)	0.434	88.03	11
	Centaur	0.028	76.92	17
Amplitude versus ascending Node	All	-0.119	95.88	112
	All (H<5)	0.116	93.78	43
	All (H≥5)	-0.267	99.49	69
	No binary pop	-0.156	97.78	85
	No binary pop (H<5)	0.148	86.48	30
	No binary pop (H≥5)	**-0.300**	**99.68**	**55**
	Binary pop	-0.065	75.90	27
	Binary pop (H<5)	-0.023	92.69	13

Correlated values	Sample	ρ	SL [%]	Nb
	Binary pop (H≥5)	-0.266	78.07	14
	No centaur pop	-0.136	96.10	95
	No centaur pop (H<5)	0.116	93.78	43
	No centaur pop (H≥5)	**-0.371**	**99.70**	**52**
	No Centaur and no Binary	-0.183	97.75	68
	No Centaur and no Binary (H<5)	0.148	86.48	30
	No Centaur and no Binary (H≥5)	**-0.444**	**99.74**	**38**
	Classical	-0.236	97.64	49
	Classical (H<5)	-0.050	86.48	24
	Classical (H≥5)	-0.353	93.37	25
	Hot	-0.062	82.06	36
	Hot (H<5)	-0.064	87.34	24
	Hot (H≥5)	-0.171	55.67	12
	Cold	-0.157	49.03	13
	Resonant	-0.103	67.23	27
	Resonant (H<5)	**0.333**	**95.48**	**11**
	Resonant (H≥5)	-0.386	92.20	16
	SDO/DO	0.162	79.78	19
	SDO/DO (H<5)	0.321	89.34	8
	SDO/DO (H≥5)	-0.322	73.38	11
	Centaur	0.063	81.84	17
Amplitude versus perihelion distance	All	0.075	91.87	112
	All (H<5)	0.015	66.22	43
	All (H≥5)	0.275	99.84	69
	No binary pop	0.004	71.24	85
	No binary pop (H<5)	0.065	64.91	30
	No binary pop (H≥5)	0.195	98.88	55
	Binary pop	**0.362**	**99.07**	**27**
	Binary pop (H<5)	-0.088	87.43	13
	Binary pop (H≥5)	**0.482**	**97.64**	**14**
	No centaur pop	0.152	97.34	95
	No centaur pop (H<5)	0.014	66.22	43
	No centaur pop (H≥5)	0.290	99.42	52
	No Centaur and no Binary	0.086	82.07	68

Correlated values			
Sample	ρ	SL [%]	Nb
No Centaur and no Binary (H<5)	0.065	64.91	30
No Centaur and no Binary (H≥5)	0.024	48.06	38
Classical	**0.502**	**99.99**	**49**
Classical (H<5)	0.230	95.17	24
Classical (H≥5)	**0.593**	**99.80**	**25**
Hot	0.240	97.87	36
Hot (H<5)	0.214	95.17	24
Hot (H≥5)	0.299	80.68	12
Cold	**0.572**	**96.28**	**13**
Resonant	-0.082	77.30	27
Resonant (H<5)	-0.004	44.62	11
Resonant (H≥5)	-0.146	73.64	16
SDO/DO	**-0.447**	**96.87**	**19**
SDO/DO (H<5)	-0.532	90.66	8
SDO/DO (H≥5)	-0.100	37.65	11
Centaur	0.099	88.82	17
Amplitude versus aphelion distance			
All	-0.173	99.23	112
All (H<5)	**-0.368**	**99.94**	**43**
All (H≥5)	0.076	87.75	69
No binary pop	-0.137	97.62	85
No binary pop (H<5)	**-0.432**	**99.75**	**30**
No binary pop (H≥5)	0.142	96.78	55
Binary pop	**-0.328**	**98.39**	**27**
Binary pop (H<5)	-0.228	94.96	13
Binary pop (H≥5)	-0.413	90.62	14
No centaur pop	-0.199	98.72	95
No centaur pop (H<5)	**-0.368**	**99.94**	**43**
No centaur pop (H≥5)	-0.088	70.78	52
No Centaur and no Binary	-0.156	91.82	68
No Centaur and no Binary (H<5)	**-0.432**	**99.75**	**30**
No Centaur and no Binary (H≥5)	0.035	40.13	38
Classical	-0.293	98.80	49
Classical (H<5)	**-0.363**	**99.49**	**24**
Classical (H≥5)	-0.089	39.08	25

Correlated values	Sample	ρ	SL [%]	Nb
	Hot	-0.103	77.50	36
	Hot (H<5)	**-0.334**	**99.10**	**24**
	Hot (H≥5)	0.415	87.19	12
	Cold	-0.332	77.51	13
	Resonant	0.199	94.78	27
	Resonant (H<5)	-0.068	71.47	11
	Resonant (H≥5)	0.080	77.81	16
	SDO/DO	-0.148	74.18	19
	SDO/DO (H<5)	-0.364	90.67	8
	SDO/DO (H≥5)	0.310	79.62	11
	Centaur	0.234	96.76	17
Amplitude versus argument of perihelion	All	-0.202	99.83	112
	All (H<5)	-0.131	98.60	43
	All (H≥5)	-0.271	99.80	69
	No binary pop	-0.172	98.26	85
	No binary pop (H<5)	-0.137	87.29	30
	No binary pop (H≥5)	-0.216	98.89	55
	Binary pop	**-0.303**	**99.27**	**27**
	Binary pop (H<5)	-0.166	98.08	13
	Binary pop (H≥5)	-0.258	91.80	14
	No centaur pop	-0.265	99.96	95
	No centaur pop (H<5)	-0.131	98.60	43
	No centaur pop (H≥5)	**-0.393**	**99.92**	**52**
	No Centaur and no Binary	-0.253	99.10	68
	No Centaur and no Binary (H<5)	-0.137	87.29	30
	No Centaur and no Binary (H≥5)	**-0.384**	**99.52**	**38**
	Classical	-0.223	97.34	49
	Classical (H<5)	0.026	79.77	24
	Classical (H≥5)	-0.255	81.99	25
	Hot	-0.101	86.72	36
	Hot (H<5)	0.037	73.35	24
	Hot (H≥5)	-0.278	65.92	12
	Cold	-0.318	78.59	13
	Resonant	-0.163	96.03	27
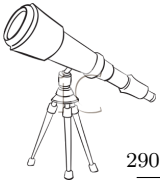
Sample	ρ	SL [%]	Nb
Correlated values			
Resonant (H<5)	0.091	73.82	11
Resonant (H≥5)	**-0.472**	**99.42**	**16**
SDO/DO	-0.069	60.12	19
SDO/DO (H<5)	-0.331	89.34	8
SDO/DO (H≥5)	-0.048	33.51	11
Centaur	0.193	96.65	17
Albedo versus eccentricity			
All	-0.149	96.67	102
All (H<5)	**0.319**	**98.29**	**33**
All (H≥5)	**-0.352**	**99.93**	**69**
No binary pop	-0.074	76.98	63
No binary pop (H<5)	0.322	93.66	21
No binary pop (H≥5)	0.012	55.82	42
Binary pop	-0.283	95.69	38
Binary pop (H<5)	0.345	84.20	11
Binary pop (H≥5)	**-0.404**	**96.50**	**27**
No centaur pop	-0.126	93.71	86
No centaur pop (H<5)	**0.328**	**98.17**	**31**
No centaur pop (H≥5)	**-0.382**	**99.90**	**55**
No Centaur and no Binary	0.117	88.21	51
No Centaur and no Binary (H<5)	0.322	93.66	21
No Centaur and no Binary (H≥5)	0.013	56.50	30
Classical	-0.212	93.00	44
Classical (H<5)	-0.047	56.31	14
Classical (H≥5)	-0.233	86.86	30
Hot	-0.177	89.57	20
Hot (H<5)	-0.031	53.11	13
Hot (H≥5)	-0.146	71.05	7
Cold	0.130	61.06	24
Resonant	-0.248	92.25	25
Resonant (H<5)	**-0.785**	**99.16**	**10**
Resonant (H≥5)	0.019	35.04	15
SDO/DO	0.026	32.66	18
SDO/DO (H<5)	0.571	86.94	8
SDO/DO (H≥5)	-0.173	55.63	10

Correlated values	Sample	ρ	SL [%]	Nb
	Centaur	0.278	70.81	14
Albedo versus inclination	All	-0.189	98.52	102
	All (H<5)	0.291	96.11	33
	All (H≥5)	**-0.495**	**100**	**69**
	No binary pop	-0.026	52.71	63
	No binary pop (H<5)	0.171	75.83	21
	No binary pop (H≥5)	-0.166	85.48	42
	Binary pop	**-0.359**	**98.93**	**38**
	Binary pop (H<5)	0.423	89.26	11
	Binary pop (H≥5)	**-0.708**	**99.98**	**27**
	No centaur pop	-0.190	97.93	86
	No centaur pop (H<5)	**0.313**	**97.26**	**31**
	No centaur pop (H≥5)	**-0.550**	**100**	**55**
	No Centaur and no Binary	-0.018	45.38	51
	No Centaur and no Binary (H<5)	0.171	75.83	21
	No Centaur and no Binary (H≥5)	-0.215	86.47	30
	Classical	**-0.502**	**99.98**	**44**
	Classical (H<5)	0.084	63.79	14
	Classical (H≥5)	**-0.708**	**99.99**	**30**
	Hot	0.057	54.94	20
	Hot (H<5)	0.047	51.87	13
	Hot (H≥5)	-0.543	94.23	7
	Cold	**-0.360**	**95.04**	**24**
	Resonant	-0.142	79.39	25
	Resonant (H<5)	0.080	32.42	10
	Resonant (H≥5)	-0.385	91.76	15
	SDO/DO	0.111	48.81	18
	SDO/DO (H<5)	0.476	79.23	8
	SDO/DO (H≥5)	0.096	45.27	10
	Centaur	-0.273	71.53	14
Albedo versus absolute magnitude	All	-0.142	96.32	102
	All (H<5)	**-0.646**	**100**	**33**
	All (H≥5)	0.022	63.22	69
	No binary pop	-0.225	98.64	63
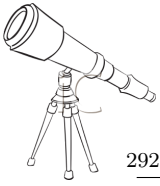
Correlated values	Sample	ρ	SL [%]	Nb
	No binary pop (H<5)	**-0.533**	**99.79**	**21**
	No binary pop (H≥5)	0.019	67.09	42
	Binary pop	0.035	44.10	38
	Binary pop (H<5)	**-0.866**	**99.66**	**11**
	Binary pop (H≥5)	0.190	75.57	27
	No centaur pop	-0.062	75.52	86
	No centaur pop (H<5)	**-0.674**	**100**	**31**
	No centaur pop (H≥5)	0.219	97.59	55
	No Centaur and no Binary	-0.177	95.99	51
	No Centaur and no Binary (H<5)	**-0.532**	**99.79**	**21**
	No Centaur and no Binary (H≥5)	0.211	94.12	30
	Classical	**0.341**	**99.37**	**44**
	Classical (H<5)	**-0.304**	**97.35**	**14**
	Classical (H≥5)	**0.404**	**98.99**	**30**
	Hot	**-0.507**	**99.74**	**20**
	Hot (H<5)	**-0.344**	**96.90**	**13**
	Hot (H≥5)	-0.379	90.94	7
	Cold	**0.389**	**97.45**	**24**
	Resonant	0.016	49.31	25
	Resonant (H<5)	**-0.701**	**96.91**	**10**
	Resonant (H≥5)	0.437	93.84	15
	SDO/DO	**-0.759**	**99.91**	**18**
	SDO/DO (H<5)	-0.643	91.10	8
	SDO/DO (H≥5)	-0.433	89.15	10
	Centaur	0.004	37.12	14
Albedo versus ascending Node	All	-0.074	83.66	102
	All (H<5)	-0.077	80.25	33
	All (H≥5)	-0.113	85.86	69
	No binary pop	0.131	93.13	63
	No binary pop (H<5)	0.129	69.88	21
	No binary pop (H≥5)	0.066	71.45	42
	Binary pop	**-0.420**	**99.59**	**38**
	Binary pop (H<5)	-0.339	81.40	11
	Binary pop (H≥5)	**-0.432**	**97.80**	**27**

Correlated values	Sample	ρ	SL [%]	Nb
	No centaur pop	-0.046	68.85	86
	No centaur pop (H<5)	-0.063	68.87	31
	No centaur pop (H≥5)	**-0.382**	**99.90**	**55**
	No Centaur and no Binary	0.229	98.18	51
	No Centaur and no Binary (H<5)	0.130	69.88	21
	No Centaur and no Binary (H≥5)	0.230	95.00	30
	Classical	-0.298	98.76	44
	Classical (H<5)	-0.198	86.58	14
	Classical (H≥5)	-0.233	87.84	30
	Hot	0.020	56.67	20
	Hot (H<5)	-0.225	84.10	13
	Hot (H≥5)	0.158	69.00	7
	Cold	-0.309	91.28	24
	Resonant	**0.421**	**99.42**	**25**
	Resonant (H<5)	0.264	73.26	10
	Resonant (H≥5)	**0.571**	**99.41**	**15**
	SDO/DO	-0.072	38.76	18
	SDO/DO (H<5)	-0.524	83.42	8
	SDO/DO (H≥5)	0.457	86.52	10
	Centaur	-0.385	85.73	14
Albedo versus argument of perihelion	All	-0.024	45.37	102
	All (H<5)	0.028	62.13	33
	All (H≥5)	-0.103	76.11	69
	No binary pop	0.171	92.95	63
	No binary pop (H<5)	0.186	86.76	21
	No binary pop (H≥5)	0.066	55.60	42
	Binary pop	-0.287	94.76	38
	Binary pop (H<5)	-0.206	64.24	11
	Binary pop (H≥5)	**-0.378**	**95.01**	**27**
	No centaur pop	0.006	41.19	86
	No centaur pop (H<5)	0.028	61.34	31
	No centaur pop (H≥5)	-0.080	63.87	55
	No Centaur and no Binary	0.234	96.82	51
	No Centaur and no Binary (H<5)	0.186	86.76	21
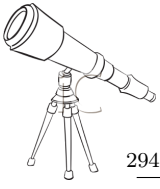
Correlated values	Sample	ρ	SL [%]	Nb
	No Centaur and no Binary (H≥5)	0.159	75.27	30
	Classical	-0.113	74.41	44
	Classical (H<5)	0.024	57.65	14
	Classical (H≥5)	-0.125	53.51	30
	Hot	0.022	53.75	20
	Hot (H<5)	-0.031	40.59	13
	Hot (H≥5)	-0.167	46.34	7
	Cold	0.021	15.08	24
	Resonant	0.008	48.71	25
	Resonant (H<5)	-0.284	73.26	10
	Resonant (H≥5)	0.128	60.84	15
	SDO/DO	0.159	61.49	18
	SDO/DO (H<5)	-0.024	5.02	8
	SDO/DO (H≥5)	-0.032	45.27	10
	Centaur	0.024	16.94	14
Albedo versus perihelion distance	**All**	**0.301**	**99.97**	**102**
	All (H<5)	-0.119	76.42	33
	All (H≥5)	**0.390**	**99.97**	**69**
	No binary pop	0.154	94.62	63
	No binary pop (H<5)	-0.173	78.39	21
	No binary pop (H≥5)	0.125	83.17	42
	Binary pop	**0.331**	**97.83**	**38**
	Binary pop (H<5)	0.131	71.25	11
	Binary pop (H≥5)	**0.383**	**95.36**	**27**
	No centaur pop	0.245	99.66	86
	No centaur pop (H<5)	-0.127	78.47	31
	No centaur pop (H≥5)	**0.369**	**99.87**	**55**
	No Centaur and no Binary	0.044	73.28	51
	No Centaur and no Binary (H<5)	-0.173	78.39	21
	No Centaur and no Binary (H≥5)	0.002	48.95	30
	Classical	0.235	95.12	44
	Classical (H<5)	-0.024	76.23	14
	Classical (H≥5)	0.188	76.46	30
	Hot	-0.023	69.83	20

Correlated values	Sample	ρ	SL [%]	Nb
	Hot (H<5)	-0.032	69.60	13
	Hot (H≥5)	0.351	92.96	7
	Cold	0.135	61.31	24
	Resonant	**-0.301**	**96.08**	**25**
	Resonant (H<5)	**-0.494**	**96.24**	**10**
	Resonant (H≥5)	-0.216	73.35	15
	SDO/DO	**0.613**	**99.43**	**18**
	SDO/DO (H<5)	0.000	0.00	8
	SDO/DO (H≥5)	0.483	92.90	10
	Centaur	0.349	87.77	14
Albedo versus aphelion distance	All	0.107	88.97	102
	All (H<5)	**0.314**	**98.16**	**33**
	All (H≥5)	0.017	47.61	69
	No binary pop	0.192	95.50	63
	No binary pop (H<5)	0.298	92.50	21
	No binary pop (H≥5)	0.141	83.96	42
	Binary pop	-0.144	76.32	38
	Binary pop (H<5)	0.359	87.94	11
	Binary pop (H≥5)	-0.289	87.41	27
	No centaur pop	-0.008	49.30	86
	No centaur pop (H<5)	**0.327**	**97.99**	**31**
	No centaur pop (H≥5)	-0.212	96.32	55
	No Centaur and no Binary	0.108	80.47	51
	No Centaur and no Binary (H<5)	0.295	92.50	21
	No Centaur and no Binary (H≥5)	0.005	38.79	30
	Classical	-0.051	60.86	44
	Classical (H<5)	-0.029	39.35	14
	Classical (H≥5)	-0.148	72.31	30
	Hot	-0.100	83.27	20
	Hot (H<5)	-0.063	40.59	13
	Hot (H≥5)	0.122	84.22	7
	Cold	0.308	89.76	24
	Resonant	-0.315	94.86	25
	Resonant (H<5)	**-0.589**	**95.25**	**10**
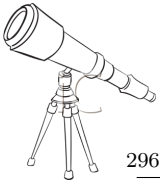
Correlated values	Sample	ρ	SL [%]	Nb
	Resonant (H≥5)	-0.121	60.80	15
	SDO/DO	0.295	87.88	18
	SDO/DO (H<5)	0.190	38.57	8
	SDO/DO (H≥5)	0.100	53.43	10
	Centaur	**0.505**	**96.56**	**14**
Rot. period versus eccentricity	All	0.118	96.08	108
	All (H<5)	0.138	86.09	39
	All (H≥5)	0.054	80.52	69
	No binary pop	0.222	99.48	83
	No binary pop (H<5)	0.156	81.39	28
	No binary pop (H≥5)	0.208	97.02	55
	Binary pop	-0.130	84.82	25
	Binary pop (H<5)	0.215	76.25	11
	Binary pop (H≥5)	-0.329	94.15	14
	No centaur pop	0.085	90.48	91
	No centaur pop (H<5)	0.137	85.54	39
	No centaur pop (H≥5)	0.018	68.42	52
	No Centaur and no Binary	0.190	97.90	66
	No Centaur and no Binary (H<5)	0.156	81.39	28
	No Centaur and no Binary (H≥5)	0.188	93.16	38
	Classical	-0.021	65.14	47
	Classical (H<5)	0.003	68.29	22
	Classical (H≥5)	-0.018	56.72	25
	Hot	0.131	83.48	34
	Hot (H<5)	0.003	68.29	22
	Hot (H≥5)	0.066	30.66	12
	Cold	-0.127	57.23	13
	Resonant	-0.071	49.55	25
	Resonant (H<5)	0.015	18.63	9
	Resonant (H≥5)	-0.202	71.90	16
	SDO/DO	0.124	70.26	19
	SDO/DO (H<5)	-0.707	94.92	8
	SDO/DO (H≥5)	0.331	89.87	11
	Centaur	0.364	90.64	17

Correlated values	Sample	ρ	SL [%]	Nb
Rot. period Vs. Inclination	All	-0.099	95.19	108
	All (H<5)	-0.049	65.55	39
	All (H≥5)	-0.024	63.17	69
	No binary pop	-0.091	88.86	83
	No binary pop (H<5)	-0.177	87.68	28
	No binary pop (H≥5)	0.045	73.51	55
	Binary pop	-0.151	87.57	25
	Binary pop (H<5)	0.093	61.16	11
	Binary pop (H≥5)	-0.117	70.60	14
	No centaur pop	-0.075	88.73	91
	No centaur pop (H<5)	-0.048	66.40	39
	No centaur pop (H≥5)	0.078	84.00	52
	No Centaur and no Binary	-0.063	78.51	66
	No Centaur and no Binary (H<5)	-0.177	87.68	28
	No Centaur and no Binary (H≥5)	0.181	92.18	38
	Classical	-0.022	67.04	47
	Classical (H<5)	0.053	82.53	22
	Classical (H≥5)	0.281	95.51	25
	Hot	0.001	65.32	34
	Hot (H<5)	0.053	82.35	22
	Hot (H≥5)	0.162	69.34	12
	Cold	-0.387	90.50	13
	Resonant	-0.121	63.64	25
	Resonant (H<5)	-0.006	3.76	9
	Resonant (H≥5)	0.090	63.22	16
	SDO/DO	-0.157	87.66	19
	SDO/DO (H<5)	-0.178	55.03	8
	SDO/DO (H≥5)	**-0.430**	**96.89**	**11**
	Centaur	-0.156	71.48	17
Rot. period Vs. Absolute Magnitude	All	0.080	95.24	108
	All (H<5)	-0.088	79.26	39
	All (H≥5)	-0.105	93.10	69
	No binary pop	0.102	95.87	83
	No binary pop (H<5)	0.110	82.35	28
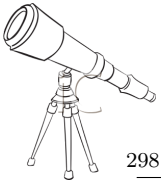
Correlated values			
Sample	ρ	SL [%]	Nb
No binary pop (H≥5)	-0.117	94.54	55
Binary pop	0.114	73.74	25
Binary pop (H<5)	-0.250	79.10	11
Binary pop (H≥5)	0.120	61.82	14
No centaur pop	0.069	86.45	91
No centaur pop (H<5)	-0.090	79.93	39
No centaur pop (H≥5)	-0.161	96.30	52
No Centaur and no Binary	0.091	85.45	66
No Centaur and no Binary (H<5)	0.110	82.35	28
No Centaur and no Binary (H≥5)	-0.206	97.29	38
Classical	0.095	86.82	47
Classical (H<5)	0.009	80.24	22
Classical (H≥5)	-0.235	90.51	25
Hot	0.138	92.66	34
Hot (H<5)	0.009	80.24	22
Hot (H≥5)	-0.067	39.89	12
Cold	-0.396	92.21	13
Resonant	0.180	81.62	25
Resonant (H<5)	-0.135	34.71	9
Resonant (H≥5)	-0.327	95.19	16
SDO/DO	-0.120	78.06	19
SDO/DO (H<5)	-0.037	19.89	8
SDO/DO (H≥5)	0.247	87.94	11
Centaur	0.204	92.56	17
Rot. period versus ascending node			
All	-0.022	78.09	108
All (H<5)	0.023	72.35	39
All (H≥5)	-0.016	71.35	69
No binary pop	-0.032	75.29	83
No binary pop (H<5)	0.015	75.01	28
No binary pop (H≥5)	-0.024	63.65	55
Binary pop	-0.014	65.60	25
Binary pop (H<5)	0.062	45.40	11
Binary pop (H≥5)	-0.034	67.92	14
No centaur pop	-0.014	71.93	91

Correlated values	Sample	ρ	SL [%]	Nb
	No centaur pop (H<5)	0.023	76.33	39
	No centaur pop (H≥5)	-0.015	79.93	52
	No Centaur and no Binary	-0.025	72.90	66
	No Centaur and no Binary (H<5)	0.016	75.01	28
	No Centaur and no Binary (H≥5)	-0.018	59.73	38
	Classical	0.104	94.79	47
	Classical (H<5)	0.252	98.43	22
	Classical (H≥5)	0.061	75.14	25
	Hot	0.154	97.22	34
	Hot (H<5)	0.253	98.43	22
	Hot (H≥5)	-0.010	51.34	12
	Cold	0.052	50.25	13
	Resonant	0.072	53.99	25
	Resonant (H<5)	0.345	67.78	9
	Resonant (H≥5)	-0.178	70.34	16
	SDO/DO	**-0382**	**99.14**	**19**
	SDO/DO (H<5)	-0.164	42.92	8
	SDO/DO (H≥5)	0.039	86.51	11
	Centaur	0.044	35.50	17
Rot. period versus perihelion distance	All	-0.038	86.66	108
	All (H<5)	0.094	79.66	39
	All (H≥5)	-0.015	76.82	69
	No binary pop	-0.148	99.15	83
	No binary pop (H<5)	0.028	52.47	28
	No binary pop (H≥5)	-0.114	95.52	55
	Binary pop	0.291	97.46	25
	Binary pop (H<5)	0.198	82.34	11
	Binary pop (H≥5)	**0.325**	**96.05**	**14**
	No centaur pop	-0.008	64.26	91
	No centaur pop (H<5)	0.095	80.47	39
	No centaur pop (H≥5)	-0.029	71.34	52
	No Centaur and no Binary	-0.144	94.28	66
	No Centaur and no Binary (H<5)	0.028	52.47	28
	No Centaur and no Binary (H≥5)	-0.189	95.44	38
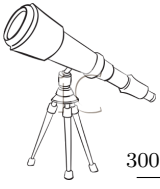
Correlated values	Sample	ρ	SL [%]	Nb
	Classical	-0.077	80.83	47
	Classical (H<5)	-0.162	91.48	22
	Classical (H≥5)	-0.103	71.48	25
	Hot	-0.264	97.84	34
	Hot (H<5)	-0.162	91.48	22
	Hot (H≥5)	-0.315	80.60	12
	Cold	0.206	77.14	13
	Resonant	-0.068	61.92	25
	Resonant (H<5)	-0.460	85.61	9
	Resonant (H≥5)	0.146	67.90	16
	SDO/DO	0.228	93.62	19
	SDO/DO (H<5)	0.523	85.26	8
	SDO/DO (H≥5)	-0.170	87.24	11
	Centaur	-0.115	87.62	17
Rot. period versus aphelion distance	All	0.001	73.50	108
	All (H<5)	0.168	91.16	39
	All (H≥5)	0.004	78.98	69
	No binary pop	0.031	71.94	83
	No binary pop (H<5)	0.191	89.57	28
	No binary pop (H≥5)	0.066	81.47	55
	Binary pop	-0.103	78.73	25
	Binary pop (H<5)	0.137	72.54	11
	Binary pop (H≥5)	-0.368	92.51	14
	No centaur pop	0.028	68.78	91
	No centaur pop (H<5)	0.169	92.92	39
	No centaur pop (H≥5)	-0.051	80.22	52
	No Centaur and no Binary	0.096	90.08	66
	No Centaur and no Binary (H<5)	0.191	89.57	28
	No Centaur and no Binary (H≥5)	0.076	78.13	38
	Classical	-0.114	91.86	47
	Classical (H<5)	-0.036	81.04	22
	Classical (H≥5)	-0.146	83.36	25
	Hot	-0.027	68.08	34
	Hot (H<5)	-0.036	81.04	22

Correlated values	Sample	ρ	SL [%]	Nb
	Hot (H≥5)	-0.061	30.66	12
	Cold	-0.108	60.50	13
	Resonant	-0.046	40.37	25
	Resonant (H<5)	-0.474	84.27	9
	Resonant (H≥5)	-0.040	35.14	16
	SDO/DO	0.205	92.35	19
	SDO/DO (H<5)	-0.532	85.26	8
	SDO/DO (H≥5)	0.112	74.98	11
	Centaur	0.131	68.74	17
Rot. period versus argument of perihelion	All	0.109	95.41	108
	All (H<5)	**0.322**	**99.59**	**39**
	All (H≥5)	0.014	71.06	69
	No binary pop	0.200	99.16	83
	No binary pop (H<5)	**0.437**	**99.74**	**28**
	No binary pop (H≥5)	0.084	86.97	55
	Binary pop	-0.156	83.00	25
	Binary pop (H<5)	-0.009	35.45	11
	Binary pop (H≥5)	-0.203	84.49	14
	No centaur pop	0.095	91.16	91
	No centaur pop (H<5)	**0.321**	**99.40**	**39**
	No centaur pop (H≥5)	-0.051	75.64	52
	No Centaur and no Binary	0.197	97.58	66
	No Centaur and no Binary (H<5)	**0.437**	**99.74**	**28**
	No Centaur and no Binary (H≥5)	0.032	57.21	38
	Classical	0.079	86.69	47
	Classical (H<5)	**0.446**	**99.88**	**22**
	Classical (H≥5)	-0.176	85.80	25
	Hot	0.134	93.12	34
	Hot (H<5)	**0.446**	**99.88**	**22**
	Hot (H≥5)	-0.288	82.14	12
	Cold	-0.141	59.69	13
	Resonant	0.228	81.73	25
	Resonant (H<5)	-0.095	22.27	9
	Resonant (H≥5)	0.203	73.12	16
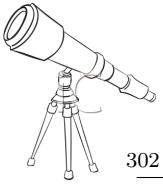
Correlated values

Sample	ρ	SL [%]	Nb
SDO/DO	-0.299	92.67	19
SDO/DO (H$<$5)	-0.608	89.85	8
SDO/DO (H$\geq$5)	-0.224	78.36	11
Centaur	0.282	93.61	17

Table 25: Orbital elements of the TNOs and centaurs for the correlations/anti-correlations search: in this table are reported the object name, the perihelion distance (q in AU), the aphelion distance (Q in AU), the absolute magnitude (H), the argument of perihelion (M in °), longitude of the ascending node (Node in °), the inclination (Incli in °), the orbital eccentricity (e), and the semimajor axis (a in AU). Orbital elements extracted from the Minor Planet Center (MPC) database.

Object	q	Q	H	M	Peri.	Node	Incli.	e	a
Pluto	29.666	49.119	-0.7	32.8	113.7	110.3	17.2	0.247	39.393
Charon	29.666	49.119	0.9	32.8	113.7	110.3	17.2	0.247	39.393
1977 UB	8.486	18.854	6.2	114.9	339.5	209.4	6.9	0.379	13.670
1992 AD	8.653	31.914	7.1	80.7	354.7	119.3	24.7	0.573	20.283
1993 HA$_2$	11.832	37.215	9.6	59.7	170.4	31.4	15.6	0.518	24.524
1993 SC	32.344	47.200	7.0	58.1	318.8	354.6	5.2	0.187	39.772
1994 TB	26.976	52.673	7.3	350.3	98.7	317.4	12.1	0.323	39.825
1994 VK$_8$	41.699	44.341	7.0	267.6	107.0	72.4	1.5	0.031	43.020
1995 DW$_2$	18.849	31.075	8.6	49.0	5.6	178.3	4.1	0.245	24.962
1995 GO	6.879	29.321	9.1	45.0	290.7	6.0	17.6	0.620	18.100
1995 QY$_9$	29.224	50.690	8.0	8.0	25.6	342.1	4.8	0.269	39.957
1995 SM$_{55}$	37.483	46.662	4.8	325.5	69.2	21.0	27.0	0.109	42.073
1996 TL$_{66}$	35.037	135.000	5.4	4.9	184.8	217.7	23.9	0.587	84.828
1996 TO$_{66}$	38.502	48.460	4.5	129.9	241.6	355.2	27.4	0.115	43.481
1996 TP$_{66}$	26.379	53.093	6.9	16.8	75.7	316.8	5.7	0.336	39.736
1997 CS$_{29}$	43.450	44.429	5.3	334.8	214.4	304.3	2.2	0.011	43.939
1997 CU$_{26}$	13.059	18.411	6.6	47.7	241.5	300.4	23.4	0.170	15.735
1997 CV$_{29}$	40.218	44.130	7.3	7.2	29.9	121.2	8.0	0.046	42.174
1998 BU$_{48}$	20.463	46.128	7.2	64.5	282.4	132.8	14.2	0.385	33.296
1998 SG$_{35}$	5.785	10.888	10.9	62.0	337.5	173.1	15.7	0.306	8.337
1998 SM$_{165}$	30.114	65.900	5.8	40.1	131.9	183.1	13.5	0.373	48.007
1998 SN$_{165}$	36.354	39.809	5.6	287.0	258.7	192.1	4.6	0.045	38.081
1998 TF$_{35}$	16.303	36.281	9.4	59.8	301.7	51.9	12.6	0.380	26.292
1998 WH$_{24}$	41.052	51.010	4.8	335.5	55.5	49.9	12.0	0.108	46.031
1998 WW$_{31}$	41.183	48.631	6.1	128.4	55.0	237.1	6.8	0.083	44.907
1999 DE$_9$	32.205	78.521	5.1	22.9	159.1	323.0	7.6	0.418	55.363
1999 DF$_9$	39.749	52.932	6.1	15.3	176.2	334.9	9.8	0.142	46.341
1999 KR$_{16}$	33.931	63.203	5.8	340.6	59.1	205.7	24.9	0.301	48.567
1999 OJ$_4$	37.057	39.177	7.1	281.8	288.1	127.5	4.0	0.028	38.117
1999 OX$_3$	17.593	47.272	7.4	336.9	144.1	259.3	2.6	0.458	32.433
1999 RZ$_{253}$	40.046	47.808	5.9	50.5	200.1	84.5	0.6	0.088	43.927
1999 TC$_{36}$	30.559	48.860	4.9	355.4	295.0	97.2	8.4	0.230	39.710
1999 TD$_{10}$	12.320	186.000	8.7	4.5	172.9	184.6	6.0	0.876	99.386
1999 UG$_5$	7.267	16.309	10.1	121.5	281.9	87.0	5.2	0.384	11.788
2000 CF$_{105}$	42.207	45.639	6.9	26.3	51.8	56.8	0.5	0.039	43.923
2000 CN$_{105}$	40.075	48.933	5.0	114.7	9.2	28.8	3.4	0.100	44.504
2000 EB$_{173}$	28.526	50.795	4.7	350.2	68.0	169.4	15.5	0.281	39.660
2000 EC$_{98}$	5.816	15.609	9.3	328.1	162.9	173.4	4.3	0.457	10.712
2000 FV$_{53}$	32.769	45.319	8.2	24.0	349.9	207.6	17.4	0.161	39.044
2000 GN$_{171}$	28.283	50.122	6.0	3.2	195.0	26.1	10.8	0.279	39.203
2000 OJ$_{67}$	42.132	43.765	6.1	79.6	157.0	96.8	1.1	0.019	42.948
2000 OK$_{67}$	40.019	53.445	5.9	347.7	359.5	4.4	4.9	0.144	46.732
2000 QB$_{243}$	15.315	54.655	8.3	34.6	284.8	330.1	6.8	0.562	34.985
2000 QC$_{243}$	13.240	19.887	7.5	276.0	151.8	337.8	20.7	0.201	16.564
2000 QL$_{251}$	37.512	58.573	6.6	29.1	100.1	223.4	3.7	0.219	48.042
2000 WR$_{106}$	40.731	45.471	3.6	99.2	271.4	97.3	17.2	0.055	43.101
2000 YW$_{134}$	41.083	75.065	4.9	27.1	316.0	127.0	19.8	0.293	58.074
2001 CZ$_{31}$	39.851	50.558	5.8	333.7	46.2	136.2	10.2	0.118	45.205
2001 FP$_{185}$	34.237	392.000	6.0	1.0	6.7	179.4	30.8	0.839	213.000

Table 25: continued.

Object	q	Q	H	M	Peri.	Node	Incli.	e	a
2001 KA$_{77}$	42.776	51.799	5.0	265.6	125.8	239.2	11.9	0.095	47.288
2001 KD$_{77}$	35.041	43.828	5.8	32.4	89.1	139.2	2.3	0.111	39.434
2001 KG$_{77}$	33.950	88.913	8.1	359.5	15.7	250.5	15.5	0.447	61.431
2001 KJ$_{76}$	40.108	46.966	6.8	302.2	274.1	47.7	6.7	0.079	43.537
2001 KU$_{76}$	37.675	51.948	6.6	348.9	205.6	45.0	10.7	0.159	44.812
2001 KX$_{76}$	29.732	49.109	3.3	274.8	300.3	71.0	19.7	0.246	39.421
2001 PT$_{13}$	8.580	12.760	9.0	134.8	87.4	205.2	20.3	0.196	10.670
2001 QC$_{298}$	40.583	52.089	6.3	11.8	4.7	334.8	30.6	0.124	46.336
2001 QD$_{298}$	40.280	44.921	5.7	61.5	197.9	70.8	5.0	0.054	42.601
2001 QF$_{298}$	35.278	43.722	5.1	148.0	42.2	164.2	22.3	0.107	39.500
2001 QG$_{298}$	31.763	47.470	7.2	1.6	209.7	162.5	6.5	0.198	39.616
2001 QT$_{297}$	43.056	45.205	5.8	154.5	236.0	304.8	2.6	0.024	44.131
2001 QW$_{322}$	43.046	45.040	7.8	116.6	75.5	124.7	4.8	0.023	44.043
2001 QY$_{297}$	40.334	47.431	5.6	76.7	127.0	108.7	1.5	0.081	43.882
2001 RZ$_{143}$	41.263	47.428	6.4	353.5	32.3	8.3	2.1	0.070	44.345
2001 UQ$_{18}$	41.865	47.141	5.7	112.6	304.6	1.8	5.2	0.059	44.503
2001 UR$_{163}$	37.218	66.525	4.2	71.9	344.0	302.2	0.8	0.282	51.871
2001 XR$_{254}$	41.845	44.342	5.7	219.1	76.7	179.6	1.2	0.029	43.094
2001 YH$_{140}$	36.368	48.582	5.5	16.0	354.7	108.8	11.1	0.144	42.475
2002 AW$_{197}$	41.221	53.181	3.4	286.9	295.6	297.4	24.4	0.127	47.201
2002 CR$_{46}$	17.512	58.000	7.5	9.1	158.8	351.9	2.4	0.536	37.756
2002 GB$_{10}$	15.177	34.724	7.8	26.5	238.9	315.5	13.3	0.392	24.951
2002 GO$_9$	14.042	24.694	8.8	41.5	92.7	117.4	12.8	0.275	19.368
2002 GP$_{32}$	32.016	78.182	6.9	5.0	110.6	124.0	1.6	0.419	55.099
2002 GV$_{31}$	40.027	47.879	6.0	343.3	129.6	59.1	2.2	0.089	43.953
2002 GZ$_{32}$	17.998	27.987	7.0	335.7	155.6	107.3	15.0	0.217	22.993
2002 KW$_{14}$	37.212	55.750	5.0	45.1	122.1	59.9	9.8	0.199	46.481
2002 KX$_{14}$	36.877	40.463	4.4	250.7	77.1	286.6	0.4	0.046	38.670
2002 LM$_{60}$	41.583	44.858	2.6	276.4	161.7	189.0	8.0	0.038	43.220
2002 MS$_4$	35.517	47.825	3.7	212.6	214.3	216.2	17.7	0.148	41.671
2002 PN$_{34}$	13.373	48.865	8.6	21.3	358.7	299.2	16.6	0.570	31.119
2002 TC$_{302}$	39.172	72.272	3.9	319.9	85.8	23.8	35.0	0.297	55.722
2002 TX$_{300}$	38.121	48.890	3.2	65.0	343.0	324.6	25.9	0.124	43.506
2002 UX$_{25}$	36.771	49.116	3.7	292.5	275.2	204.6	19.4	0.144	42.944
2002 VE$_{95}$	27.985	51.244	5.6	14.9	207.4	199.7	16.3	0.294	39.614
2002 VR$_{128}$	29.170	50.146	5.6	66.1	289.6	23.0	14.0	0.264	39.658
2002 VU$_{130}$	31.202	47.476	6.1	267.4	279.4	268.0	1.4	0.207	39.339
2002 WC$_{19}$	35.495	60.797	5.1	312.5	43.2	109.7	9.2	0.263	48.146
2002 XU$_{93}$	20.984	113.000	8.0	2.3	27.8	90.3	77.9	0.686	66.796
2002 XV$_{93}$	34.633	44.368	5.0	277.3	162.5	19.0	13.3	0.123	39.501
2002 XW$_{93}$	28.419	46.927	5.5	132.6	248.8	46.7	14.3	0.246	37.673
2003 AZ$_{84}$	32.609	46.505	3.6	222.0	15.3	251.9	13.5	0.176	39.557
2003 BF$_{91}$	42.137	43.361	11.7	360.0	102.3	110.1	1.5	0.014	42.749
2003 BG$_{91}$	39.108	47.764	10.7	320.8	83.3	176.2	2.5	0.100	43.436
2003 BH$_{91}$	42.555	45.382	11.9	360.0	131.8	80.5	2.0	0.032	43.969
2003 CO$_1$	10.913	30.439	8.9	21.2	116.1	78.5	19.8	0.472	20.676
2003 EL$_{61}$	34.502	51.477	0.2	205.2	240.6	121.9	28.2	0.197	42.990
2003 FE$_{128}$	35.846	59.574	6.5	2.4	53.7	169.3	3.4	0.249	47.710
2003 FM$_{127}$	40.925	46.284	7.1	90.0	74.1	52.4	4.3	0.061	43.604
2003 FX$_{128}$	17.756	182.000	6.3	8.1	319.4	172.0	22.3	0.823	100.000
2003 FY$_{128}$	36.982	61.530	4.9	25.6	173.8	341.8	11.8	0.249	49.256
2003 MW$_{12}$	39.030	52.208	3.4	261.5	184.1	184.2	21.5	0.144	45.619
2003 OP$_{32}$	38.732	47.763	3.6	64.4	69.9	183.1	27.1	0.104	43.247
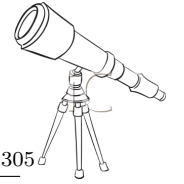
Table 25: continued.

Object	q	Q	H	M	Peri.	Node	Incli.	e	a
2003 QW$_{90}$	40.578	47.415	5.4	276.8	83.4	17.8	10.3	0.078	43.997
2003 QY$_{90}$	40.691	45.003	6.4	194.2	37.2	104.2	3.8	0.050	42.847
2003 SQ$_{317}$	39.239	46.468	6.3	357.9	194.1	176.3	28.5	0.084	42.853
2003 TJ$_{58}$	40.559	48.787	8.0	28.2	12.6	37.2	1.0	0.092	44.673
2003 UB$_{313}$	38.464	97.631	-1.2	202.2	150.9	36.1	43.8	0.435	68.048
2003 UN$_{284}$	42.485	43.266	7.4	15.1	13.6	36.0	3.1	0.009	42.876
2003 UR$_{292}$	26.768	38.365	7.3	359.3	248.5	146.4	2.7	0.178	32.567
2003 UT$_{292}$	27.727	51.391	6.9	340.7	255.2	210.9	17.5	0.299	39.559
2003 UZ$_{413}$	30.750	48.124	4.2	101.4	146.7	136.0	12.0	0.220	39.437
2003 VB$_{12}$	76.313	1009.000	1.6	358.2	310.9	144.4	11.9	0.859	542.000
2003 VS$_2$	36.433	42.910	4.1	11.0	113.0	302.8	14.8	0.082	39.672
2003 WL$_7$	14.954	25.576	8.6	3.6	70.6	4.7	11.2	0.262	20.265
2004 DW	30.469	48.087	2.3	168.1	73.6	268.5	20.5	0.224	39.278
2004 EW$_{95}$	26.969	51.535	6.7	351.2	204.6	25.7	29.3	0.313	39.252
2004 GV$_9$	40.945	46.309	7.4	71.3	302.1	176.9	0.6	0.061	43.627
2004 NT$_{33}$	36.964	50.053	4.4	33.6	38.8	241.1	31.2	0.150	43.509
2004 PB$_{108}$	40.216	50.370	6.6	303.2	272.0	147.4	20.2	0.112	45.293
2004 PF$_{115}$	36.515	41.573	4.4	161.1	83.1	84.7	13.4	0.065	39.044
2004 PT$_{107}$	38.187	42.877	6.0	347.1	21.8	321.0	26.2	0.058	40.532
2004 SB$_{60}$	37.842	46.543	4.2	113.7	311.1	280.2	23.9	0.103	42.193
2004 TY$_{364}$	36.540	41.617	4.5	266.7	353.2	140.5	24.8	0.065	39.079
2004 UX$_{10}$	37.611	40.855	4.5	80.2	161.0	147.9	9.5	0.041	39.233
2004 XA$_{192}$	35.485	59.374	4.0	352.8	131.7	328.6	38.1	0.252	47.430
2005 CB$_{79}$	37.252	49.447	4.7	313.6	91.0	112.8	28.6	0.141	43.350
2005 EF$_{298}$	40.100	47.869	6.1	331.6	75.4	118.0	2.9	0.088	43.985
2005 EO$_{304}$	42.524	48.428	6.3	320.1	150.5	93.8	3.4	0.065	45.476
2005 FY$_9$	38.051	52.822	-0.4	153.9	296.5	79.3	29.0	0.163	45.436
2005 GE$_{187}$	26.533	51.883	7.1	330.8	86.2	205.5	18.3	0.323	39.208
2005 QU$_{182}$	37.016	188.000	3.5	12.4	224.3	78.5	14.0	0.671	113.000
2005 RM$_{43}$	35.112	149.000	4.4	3.0	318.4	84.7	28.7	0.620	92.283
2005 RN$_{43}$	40.550	42.677	3.9	333.6	174.6	187.1	19.2	0.026	41.613
2005 RR$_{43}$	37.289	49.735	4.0	37.1	281.0	85.9	28.5	0.143	43.512
2005 TB$_{190}$	46.193	106.000	4.7	357.3	171.8	180.5	26.4	0.394	76.185
2005 UJ$_{438}$	8.259	27.136	10.7	8.2	208.1	262.9	3.8	0.533	17.698
2005 UQ$_{513}$	37.313	49.766	3.4	221.0	220.0	307.8	25.7	0.143	43.539
2006 BR$_{284}$	42.057	45.733	6.9	15.5	101.0	15.2	1.2	0.042	43.895
2006 CH$_{69}$	44.071	47.524	6.6	32.1	66.2	40.9	1.8	0.038	45.798
2006 HJ$_{123}$	27.433	51.183	5.7	302.5	102.8	222.6	12.5	0.302	39.308
2006 JZ$_{81}$	41.101	47.962	6.7	3.8	181.5	36.4	3.6	0.077	44.531
2007 JF$_{43}$	32.047	46.391	5.6	286.7	123.7	207.5	15.1	0.183	39.219
2007 JJ$_{43}$	40.307	55.247	3.9	332.8	8.7	272.5	12.1	0.156	47.777
2007 OC$_{10}$	35.484	64.015	5.7	4.3	53.1	258.3	21.7	0.287	49.749
2007 OR$_{10}$	33.440	101.000	2.0	102.1	206.9	336.8	30.8	0.501	67.027
2007 RW$_{10}$	21.243	39.462	6.6	57.6	96.9	187.0	36.1	0.300	30.353
2007 TY$_{430}$	28.845	50.190	6.8	353.3	205.4	196.7	11.3	0.270	39.518
2007 UK$_{126}$	37.600	111.000	3.4	341.6	345.9	131.3	23.3	0.494	74.377
2007 UL$_{126}$	8.628	16.611	9.5	22.5	99.8	245.4	19.5	0.316	12.620
2010 EK$_{139}$	32.495	105.000	3.8	343.5	284.8	346.2	29.5	0.528	68.910
2010 EL$_{139}$	36.666	41.858	5.1	30.3	201.6	331.1	23.0	0.066	39.262
2010 EP$_{65}$	33.056	61.949	5.5	357.4	351.8	205.0	18.9	0.304	47.503
2010 ET$_{65}$	39.624	84.762	5.2	359.5	353.7	189.6	30.6	0.363	62.193
2010 FX$_{86}$	43.856	49.433	4.3	279.0	356.5	310.9	25.2	0.060	46.644
2010 HE$_{79}$	31.849	45.821	5.2	56.8	281.1	238.7	15.8	0.180	38.835
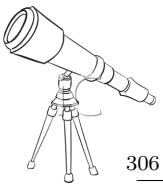
Table 25: continued.

Object	q	Q	H	M	Peri.	Node	Incli.	e	a
2010 PU$_{75}$	35.893	133.000	5.6	353.1	256.4	78.4	8.9	0.576	84.683
2010 VK$_{201}$	38.745	48.114	4.5	160.7	90.4	156.5	28.8	0.108	43.429

Table 26: In this table are listed the object name, and the albedos (Alb) used for the correlations/anti-correlations search. The albedo can be estimated from the direct imaging (imaging), lightcurve (lightcurve), thermal modeling (thermal), from occultation, and estimated from the determined from mutual orbit of binary components (dynamical).

Object	Alb imaging	Alb lightcurve	Alb thermal	Alb occultation	Alb dynamical	Ref.
1977 UB	-	-	$0.13^{+0.04}_{-0.03}$, $0.0757^{+0.0103}_{-0.0087}$	-	-	A95, S08
1992 AD	-	-	0.044 ± 0.013, 0.043 ± 0.02, $0.08^{+0.07}_{-0.03}$	-	-	D93, D96, S08
1993 HA$_2$	-	-	$0.065^{+0.053}_{-0.025}$	-	-	S08
1995 DW$_2$	-	-	$0.062^{+0.05}_{-0.03}$	-	-	S08
1995 GO	-	-	0.095 ± 0.015, $0.5460^{+0.0127}_{-0.0080}$	-	-	S05, S08
1996 TL$_{66}$	-	-	$0.035^{+0.020}_{-0.010}$, $0.110^{+0.015}_{-0.015}$	-	-	S08, SS12
1996 TP$_{66}$	-	-	0.03 ± 0.01, $0.074^{+0.07}_{-0.03}$; $0.074^{+0.063}_{-0.031}$	-	-	S05, S08, M12
1997 CS$_{29}$	-	-	0.06 ± 0.02, $0.095^{+0.033}_{-0.020}$, $0.086^{+0.026}_{-0.017}$	-	-	M10, V12, G12
1997 CU$_{26}$	-	-	0.055 ± 0.008, 0.1 ± 0.02, $0.0573^{+0.0049}_{-0.0042}$	-	-	A01, S05, S08
1998 SG$_{35}$	-	-	0.03 ± 0.005, $0.0249^{+0.0081}_{-0.0055}$	-	-	S05, S08
1998 SM$_{165}$	-	-	0.07 ± 0.02, $0.0633^{+0.0153}_{-0.0116}$	-	-	Sp06, S08
1998 SN$_{165}$	-	-	$0.043^{+0.018}_{-0.012}$	-	-	S08
1998 TF$_{35}$	-	-	$0.115^{+0.09}_{-0.05}$	-	-	S08
1998 WH$_{24}$	-	-	$0.050^{+0.030}_{-0.016}$	-	0.16 ± 0.07	V12
1998 WW$_{31}$	-	-	-	-	-	G11
1999 DE$_9$	-	-	$0.0685^{+0.0158}_{-0.0119}$	-	-	S08
1999 KR$_{16}$	-	-	$0.204^{+0.070}_{-0.050}$	-	-	SS12
1999 OJ$_4$	-	-	-	-	0.225 ± 0.095	G11
1999 RZ$_{253}$	-	-	-	-	0.175 ± 0.075	G11
1999 TC$_{36}$	-	-	0.15 ± 0.04, $0.079^{+0.031}_{-0.021}$, $0.0718^{+0.0153}_{-0.0117}$, $0.079^{+0.013}_{-0.011}$	-	-	S05, S06, S08, M12
1999 UG$_5$	-	-	$0.1^{+0.04}_{-0.03}$	-	-	S08
2000 CF$_{105}$	-	-	-	-	$0.30^{+0.04}_{-0.03}$	P11
2000 CN$_{105}$	-	-	-	-	$0.043^{+0.030}_{-0.010}$	K06
2000 EB$_{173}$	-	-	0.11 ± 0.02, $0.0504^{+0.0050}_{-0.0041}$, 0.081 ± 0.011	-	-	S05, S08, M12
2000 EC$_{98}$	-	-	0.125 ± 0.045, $0.0383^{+0.0189}_{-0.0108}$	-	-	S05, S08
2000 GN$_{171}$	-	-	$0.0568^{+0.0254}_{-0.0159}$, $0.215^{+0.093}_{-0.070}$	-	-	S08, M12

Table 26: continued.

Object	Alb imaging	Alb lightcurve	Alb thermal	Alb occultation	Alb dynamical	Ref.
2000 OJ$_{67}$	-	-	-	-	0.16 ± 0.07	G11
2000 OK$_{67}$	-	-	>0.16, $0.20^{+0.21}_{-0.08}$	-	-	B09, V12
2000 QC$_{243}$	-	-	0.055 ± 0.015, $0.0344^{+0.0127}_{-0.0082}$	-	-	S05, S08
2000 QL$_{251}$	-	-	-	-	0.07 ± 0.03	G11
2000 WR$_{106}$	-	-	$0.038^{+0.022}_{-0.010}$, 0.21 ± 0.09, $0.16^{+0.10}_{-0.08}$, $0.088^{+0.042}_{-0.031}$	-	-	L02, S05, S08, B09
2000 YW$_{134}$	-	-	>0.08	-	-	M10
2001 FP$_{185}$	-	-	0.046 ± 0.007	-	-	SS12
2001 KA$_{77}$	-	-	$0.025^{+0.0095}_{-0.008}$, $0.099^{+0.052}_{-0.056}$	-	-	B09, V12
2001 KD$_{77}$	-	-	$0.089^{+0.044}_{-0.027}$	-	-	M12
2001 KX$_{76}$	-	-	0.375 ± 0.125, $0.12^{+0.14}_{-0.06}$	-	-	S05, S08
2001 QD$_{298}$	-	-	$0.18^{+0.17}_{-0.08}$	-	-	B09
2001 QF$_{298}$	-	-	$0.071^{+0.020}_{-0.014}$	-	-	M12
2001 QT$_{297}$	-	-	$0.129^{+0.062}_{-0.036}$	-	-	V12
2001 QW$_{322}$	-	-	-	-	$0.093^{+0.010}_{-0.006}$	P11
2001 QY$_{297}$	-	-	$0.104^{+0.094}_{-0.050}$	-	-	V12
2001 RZ$_{143}$	-	-	$0.191^{+0.066}_{-0.045}$	-	-	V12
2001 UQ$_{18}$	-	-	$0.071^{+0.049}_{-0.021}$	-	-	V12
2001 UR$_{163}$	-	-	-	-	$0.062^{+0.038}_{-0.014}$	K06
2001 XR$_{254}$	-	-	-	-	-	V12
2002 AW$_{197}$	-	-	$0.17^{+0.19}_{-0.05}$, $0.1177^{+0.0442}_{-0.0300}$, $0.115^{+0.041}_{-0.025}$	-	-	S05, S08, B09
2002 CR$_{46}$	-	>0.09	0.10 ± 0.02, $0.051^{+0.013}_{-0.009}$, 0.08 ± 0.01, 0.044 ± 0.003	-	-	S05, S08, M10, SS12, TW
2002 GB$_{10}$	-	-	$0.1796^{+0.0777}_{-0.0470}$	-	-	S08
2002 GO$_{9}$	-	-	$0.11^{+0.07}_{-0.04}$	-	-	S08
2002 GV$_{31}$	-	-	>0.22	-	-	V12
2002 KW$_{14}$	-	-	>0.05, $0.09^{+0.14}_{-0.05}$	-	-	B09, V12
2002 KX$_{14}$	-	>0.06	$0.60^{+0.36}_{-0.23}$, $0.097^{+0.014}_{-0.013}$	-	-	B09, V12
2002 LM$_{60}$	$0.0965^{+0.0390}_{-0.0240}$	-	$0.199^{+0.132}_{-0.070}$, $0.172^{+0.055}_{-0.036}$	0.109 ± 0.007	-	B04, S08, B09, B13, TW
2002 MS$_{4}$	-	-	$0.0841^{+0.0378}_{-0.0226}$, $0.073^{+0.058}_{-0.032}$, $0.051^{+0.036}_{-0.022}$	-	-	S08, B09, V12

Table 26: continued.

Object	Alb imaging	Alb lightcurve	Alb thermal	Alb occultation	Alb dynamical	Ref.
2002 PN$_{34}$	-	-	$0.0425^{+0.0083}_{-0.0065}$, 0.049 ± 0.006	-	-	S08, SS12
2002 UX$_{25}$	-	-	$0.1150^{+0.0509}_{-0.0309}$, $0.111^{+0.049}_{-0.030}$	-	-	S08, B09
2002 VE$_{95}$	-	-	$0.149^{+0.019}_{-0.016}$	-	-	M12
2002 TC$_{302}$	-	-	$0.031^{+0.012}_{-0.029}$	-	-	S08
2002 VR$_{128}$	-	-	$0.052^{+0.027}_{-0.018}$	-	-	M12
2002 VU$_{130}$	-	-	$0.179^{+0.202}_{-0.103}$	-	-	M12
2002 WC$_{19}$	-	-	-	-	$0.043^{+0.030}_{-0.010}$	K06
2002 XU$_{93}$	-	-	0.038 ± 0.004	-	-	SS12
2002 XV$_{93}$	-	-	$0.040^{+0.020}_{-0.015}$	-	-	M12
2002 XW$_{93}$	-	-	$0.050^{+0.030}_{-0.016}$	-	-	V12
2003 AZ$_{84}$	-	-	$0.1232^{+0.0431}_{-0.0291}$, 0.07 ± 0.02, $0.107^{+0.023}_{-0.016}$	-	-	S08, M10, M12
2003 CO$_{1}$	-	-	$0.0574^{+0.0149}_{-0.0109}$	-	-	S08
2003 EL$_{61}$	-	0.665 ± 0.065	$0.84^{+0.1}_{-0.2}$, 0.698 ± 0.189	-	-	R06, S08, Le10
2003 FX$_{128}$	-	-	$0.0767^{+0.0138}_{-0.0110}$, 0.056 ± 0.006	-	-	S08, SS12
2003 FY$_{128}$	-	-	0079 ± 0.010	-	-	SS12
2003 MW$_{12}$	-	>0.09	-	-	-	T13
2003 QW$_{90}$	-	-	-	-	$0.054^{+0.035}_{-0.012}$	K06
2003 QY$_{90}$	-	-	-	-	0.31 ± 0.13	G11
2003 TJ$_{58}$	-	-	-	-	0.295 ± 0.125	G11
2003 UB$_{313}$	0.86 ± 0.07	-	$0.70^{+0.15}_{-0.20}$, 0.845 ± 0.088	$0.96^{+0.09}_{-0.04}$	-	B06, S08, Si11, SS12
2003 UN$_{284}$	-	-	-	-	$0.09^{+0.03}_{-0.01}$	P11
2003 UR$_{292}$	-	-	$0.16^{+0.19}_{-0.08}$	-	-	V12
2003 UT$_{292}$	-	-	$0.069^{+0.068}_{-0.034}$	-	-	M12
2003 VB12	-	-	>0.16, 0.32 ± 0.06	-	-	S08, P12
2003 VS$_{2}$	-	-	$0.147^{+0.063}_{-0.043}$	-	-	M12
2004 DW	-	>0.09	$0.1972^{+0.0340}_{-0.0276}$, $0.27^{+0.07}_{-0.05}$	-	-	S08, L10, TW
2004 EW$_{95}$	-	-	$0.044^{+0.021}_{-0.015}$	-	-	M12
2004 GV$_{9}$	-	-	$0.0805^{+0.0194}_{-0.0146}$, $0.073^{+0.049}_{-0.029}$, $0.0770^{+0.0084}_{-0.0077}$	-	-	S08, B09, V12

Table 26: continued.

Object	Alb imaging	Alb lightcurve	Alb thermal	Alb occultation	Alb dynamical	Ref.
2004 PB$_{108}$	-	-	-	-	0.035±0.015	G11
2004 PF$_{115}$	-	-	$0.123^{+0.043}_{-0.033}$	-	-	M12
2004 SB$_{60}$	-	>0.03	$0.0357^{+0.0072}_{-0.0056}$, 0.0439±0.0044	-	-	S12, V12, T13
2004 UX$_{10}$	-	-	$0.141^{+0.044}_{-0.031}$	-	-	M12
2005 EF$_{298}$	-	-	$0.16^{+0.13}_{-0.07}$	-	-	V12
2005 EO$_{304}$	-	-	-	-	0.15±0.01	P11
2005 FY$_9$	-	-	$0.8^{+0.1}_{-0.2}$, 0.8±0.1	0.70±0.03	-	S08, L10, O12
2005 QU$_{182}$	-	-	$0.328^{+0.160}_{-0.109}$	-	-	SS12
2005 RN$_{43}$	-	-	$0.107^{+0.029}_{-0.018}$	-	-	V12
2005 TB$_{190}$	-	-	0.19±0.05, $0.148^{+0.051}_{-0.036}$	-	-	M10, SS12
2006 BR$_{284}$	-	-	-	-	0.22±0.01	P11
2006 CH$_{69}$	-	-	-	-	$0.23^{+0.09}_{-0.06}$	P11
2006 HJ$_{123}$	-	-	$0.281^{+0.259}_{-0.152}$	-	-	M12
2006 JZ$_{81}$	-	-	-	-	0.17±0.07	P11
2007 OC$_{10}$	-	-	$0.127^{+0.040}_{-0.028}$	-	-	SS12
2007 OR$_{10}$	-	-	$0.185^{+0.076}_{-0.052}$	-	-	SS12
2007 RW$_{10}$	-	-	$0.083^{+0.068}_{-0.039}$	-	-	SS12
2007 TY$_{430}$	-	>0.12	-	-	-	T13
2007 UK$_{126}$	-	-	$0.167^{+0.058}_{-0.038}$	-	-	SS12
2010 EK$_{139}$	-	-	$0.25^{+0.02}_{-0.05}$	-	-	P12

References:

D93: Davies et al. (1993); A95: Altenhoff and Stumpff (1995); D96: Davies, Tholen and Ballantyne (1996); A01: Altenhoff, Menten and Bertoldi (2001); L02: Lellouch et al. (2002); B04: Brown and Trujillo (2004); S05: Stansberry et al. (2005); B06: Brown et al. (2006a); K06: Kern (2006); R06: Rabinowitz et al. (2006); Sp06: Spencer et al. (2006); S08: Stansberry et al. (2008); B09: Brucker et al. (2009); L10: Lim et al. (2010); Le10: Lellouch et al. (2010); M10: Müller et al. (2010); G11: Grundy et al. (2011c); P11: Parker et al. (2011); Si11: Sicardy et al. (2011); G12: Grundy et al. (2012); M12: Mommert et al. (2012); O12: Ortiz et al. (2012b); P12: Pál et al. (2012); V12: Vilenius et al. (2012); S12: Stansberry et al. (2012); SS12: Santos-Sanz et al. (2012); B13: Braga-Ribas et al. (2013); T13: Thirouin et al. (2013b); TW: this work (results unpublished).

Parallel K-D tree GRAVity solver for N-body problems

All simulations presented in this dissertation were performed with a Parallel K-D tree GRAVity code (PKDGRAV). PKDGRAV is a N-body code originally designed for cosmology simulations at the Astronomy Department of the University of Washington. This code has been improved by adding a collision treatment for dynamical simulations in the Solar System and modified for the gravitational aggregates study (Richardson et al., 2000; Stadel, 2001).

Here, we will introduce the most relevant parameters used during this work as well as some basics about this program. A complete introduction to PKDGRAV can be found in (Richardson et al., 2000; Stadel, 2001)

C.1   The k-D Tree Structure

Time is a critical factor in N-body simulations. In fact, at each step, a N-body interaction simulation must determine N^2 interaction forces, then the computation time increases rapidly. To palliate this problem, the tree code proposed by Barnes and Hut (1986) has been implemented for the calculation of the forces. The main purpose of the tree code is to limit to a precise computation only the nearby particles interactions, while for far particles it only considers the effects of a truncated multipole expansion.

The tree code consists in the subdivision of the space in cubic bins. An example of tree code cells is shown in Figure 188. The Barnes and Hut (1986) algorithm works by grouping particles using a hierarchy of cubes arranged in oct-tree structure i.e. each node in the tree has 8 siblings. The system is first surrounded by a single cube or cell encompassing all of the particles. This main cell is subdivided into 8 sub-cells, each containing their own subset of particles. The tree structure continues down in scale until cells contain only 1 particle. For each cell or node in the tree, the total mass, center of mass and higher order multipole moments (typically only up to quadrupole order) is calculated. Such handling also allows a lower time of integration. In fact, the integration time varies as a function of the particle number (N) has been empirically noticed being of NlogN instead of N^2. This tree structure can be built very rapidly making it feasible to rebuild it at each time step.

C.2   Calculating Gravity

Gravitational forces on a single particle do not arise from all other particles in the system. Instead, a process is applied whereby particles that are further away and thus have less effect are grouped together as a single entity around the center of mass and the gravitational effect from this single
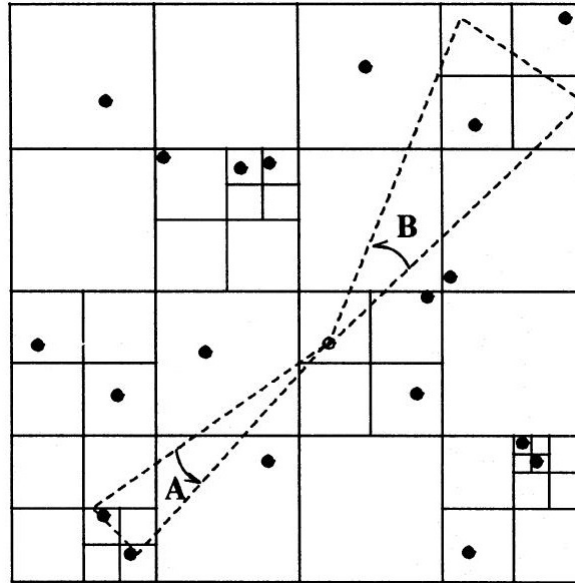
Figure 188: *Example of tree code cells:* Two possible expansions are shown for one particle (open circle): in the case A, the angle is small enough for a multipole expansion, whereas in the case B, the angle is too large and so the force contribution of the two particles in the upper right would be added individually. Figure from Richardson (1993)

mass is considered. This is a fast multipole expansion algorithm, of which PKDGRAV can calculate up to hexadecapole expansions. Starting at the top layer of the tree, PKDGRAV determines the effect of a cell on a bucket by defining an opening radius:

$$r_{open} = \frac{2B_{max}}{\sqrt{3}\theta} + B_{center} \qquad \text{(Equation III.1)}$$

where B_{max} is the maximum distance particle to center of mass, B_{center} is the maximum distance particle to center of cell, θ is the opening angle.

C.3   Integrator

Time integrations occurs by discrete and constant time steps (see Section C.4) whose length is selectable by the parameter τ.

The integration is performed using a 2nd order Leapfrog Method which consists in the alternated integration of position and velocity. In fact, the velocity and position are updated via a staggered time step; i.e. the position may be calculated at full time steps, and the velocity at half integer time steps. Every step can be decomposed into three parts: i) the stored velocities of the particles are linearly updated for a time $\tau/2$ with a constant acceleration equal to the simple ratio between the total force acting on the particle and the particle's mass, ii) the integration of the positions is performed at constant velocity for a time τ, iii) velocities are updated by integrating them for another $\tau/2$ interval. At the end of each step, the tree is then rebuild with the new particles positions.

C.4   Time step

The time needed (t_{step}) for a cloud of particles to collapse under its own gravity is:

$$t_{step} = \frac{\pi R^3}{\sqrt{2GM}} \qquad \text{(Equation III.2)}$$
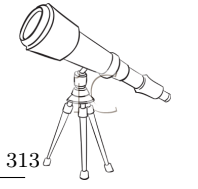
where R is the cloud radius, M its mass, and G is the gravitational constant. The cloud density, ρ, is:

$$\rho = \frac{M}{V} = \frac{M}{\frac{4}{3}\pi R^3} \qquad \text{(Equation III.3)}$$

where V is the cloud volume. By using the previous equation, one can expressed the Equation III.2 as:

$$t_{step} = \sqrt{\frac{3\pi}{8G\rho}} \qquad \text{(Equation III.4)}$$

In the simulations presented in this thesis, the time step has been chosen following Richardson, Elankumaran and Sanderson (2005). Each simulation uses a time step of around 1% of the "dynamical time", $t_{dyn} \approx 3/\sqrt{G\rho}$ where G is the gravitational constant and ρ is the density.

C.5   Collision detection

When updating the positions of particles, the possibility for two particles to come in contact must be taken into account. To anticipate a possible collision during any given time step, it is necessary to determine, for every particle pair, if they are approaching or not. This means the following relation has to be checked:

$$\mathbf{v} \cdot \mathbf{r} < 0 \qquad \text{(Equation III.5)}$$

$\mathbf{r}$ is the relative position of the objects and $\mathbf{v}$ is their relative velocity.

Collisions are predicted at the beginning of each time step. PKDGRAV uses a linear transformation that computes the time necessary for them to collide (t_{coll}), given by:

$$t_{coll} = -\frac{\mathbf{v} \cdot \mathbf{r}}{v^2}\left(1 \pm \sqrt{1 - \left(\frac{r^2 - (R_1 + R_2)^2}{(r \cdot v)^2}\right)v^2}\right) \qquad \text{(Equation III.6)}$$

where R_1 and R_2 are the physical radii of the objects. The ambiguity on sign is resolved by choosing the smallest positive value of t_{coll}.

For any particle, N_b particles are considered in the collision detection, N_b is usually between 8 and 32. The "neighbour finding" algorithm uses a balanced K-D tree to search the particles in N_b log(N) operations.

If t_{colli} is shorter than the drift step, a collision occurs. If more than one pair of particles are found to collide, they collide in order of increasing t_{coll}. Therefore the collisions are performed in the correct order.

If a collision has been detected to occur, the program proceeds as follow:

- The smallest t_{coll} is looked first: the corresponding collision is done first.

- Integration of positions up to the time t_{coll}.

- The post-collisional velocities of the particles are computed and used to update the pre-collision positions.

- Revision of all the possible future collisions involving these two particles.

- The possible following collision is determined by comparison of the new set of t_{coll} values.

C.6   Collision Resolution

If a collision is detected to happen, we have to determine the parameters (such as velocities of the particles) after the impact.

Considering two particles (1 and 2) with masses M_1, and M_2, with radii $\mathbf{R}_1$, and $\mathbf{R}_2$, with the velocities $\mathbf{v}_1$, and $\mathbf{v}_2$, at the positions $\mathbf{r}_1$, and $\mathbf{r}_2$, and the spins as $\vec{\omega_1}$, and $\vec{\omega_2}$ before the impact. One can define:

$$\mathbf{r} = \mathbf{r_2} - \mathbf{r_1} \qquad \text{(Equation III.7)}$$
$$\mathbf{v} = \mathbf{v_2} - \mathbf{v_1} \qquad \text{(Equation III.8)}$$
$$\mathbf{R_1} = R_1\hat{n} \qquad \text{(Equation III.9)}$$
$$\mathbf{R_2} = -R_2\hat{n} \qquad \text{(Equation III.10)}$$
$$\sigma_\mathbf{i} = \omega_\mathbf{i} \times R_i \qquad \text{(Equation III.11)}$$
$$\sigma = \sigma_\mathbf{2} - \sigma_\mathbf{1} \qquad \text{(Equation III.12)}$$
$$\mathbf{u} = \mathbf{v} + \sigma \qquad \text{(Equation III.13)}$$
$$\mathbf{u_n} = \hat{\mathbf{n}}(\mathbf{u}\cdot)\hat{\mathbf{n}} \qquad \text{(Equation III.14)}$$
$$\mathbf{u_t} = \mathbf{u} - \mathbf{u_n} \qquad \text{(Equation III.15)}$$
$$M = M_1 + M_2 \qquad \text{(Equation III.16)}$$
$$I = \frac{2}{5}m_i R_i^2 \qquad \text{(Equation III.17)}$$

where $\hat{n}$ is the unit vector such as $\hat{n}=\mathbf{r}/\mathrm{r}$.

After the impact, one can express the momentum conservation, such as:

$$M_1(\mathbf{v_1^{after}} - \mathbf{v_1}) = -M_2(\mathbf{v_2^{after}} - \mathbf{v_2}) \qquad \text{(Equation III.18)}$$

where $\mathbf{v}_i^{after}$ is the velocity after the impact. Each of the particles will apply a torque on the other modifying their rotational states, as:

$$I_i(\omega_\mathbf{i}^{after} - \omega_\mathbf{i}) = M_i\mathbf{R_i} \times (\mathbf{v_i^{after}} - \mathbf{v_i}) \qquad \text{(Equation III.19)}$$

We also have to consider the dissipative forces between the two particles:

$$\mathbf{u^{after}} = -\epsilon_n\mathbf{u_n} + \epsilon_t\mathbf{u_t} \qquad \text{(Equation III.20)}$$

where ϵ_n and ϵ_t are, respectively, the normal and tangential coefficients of elastic restitution [1]. Previous equations give us the after-impact parameters.

C.7   Inelastic collapse

When two particles collide with a low relative speed, this can create a problem. In fact, because of the speed loss in the collision between two particles, such particles might collide again after a small interval and so, reducing the collision interval more and more and blocking the program.

To avoid such problem, PKDGRAV uses the *dCollapseLimit* parameter. This parameter is a speed threshold and so any collision happening at lower speed is considered as elastic impact (i.e. ignoring the values selected for the parameters: ϵ_t and ϵ_n). The *dCollapseLimit* parameter is expressed as a fraction of the mutual escape velocity of the two particles given by:

$$v_{escape} = \sqrt{\frac{2G(M_1 + M_2)}{R_1 + R_2}} \qquad \text{(Equation III.21)}$$

Generally, this parameter is set at a low value in order to avoid any too visible effect at large scale.

C.8   Case of overlapping

In some cases, and especially for dense systems like gravitational aggregates, two (or more) particles may be found overlapping. In such case, PKDGRAV offers four possibilities:

- *backstep*: the particles are integrated back in time to a position just before the overlapping occurs, and the collision is resolved at that time.

---

[1] If $\epsilon_t= \epsilon_n=1$: elastic, no friction case, whereas if $\epsilon_t= \epsilon_n=0$: inelastic case.
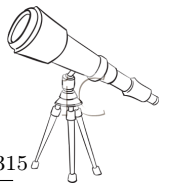
- *adjpos*: the particles are moved away along the line connecting the centers for the smallest possible non-overlapping distance.

- *repel*: the particles are allowed to overlap, but the mutual gravity is substituted by a repulsive force.

- *merge*: the particles are removed from the simulation and replaced by a new one with the same total mass and angular momentum.

Only the *backstep* and the *repel* settings have been considered in this work. Both options are associated to:

- *dBackstepLimit*: the maximum backstep time.

- *dRepelFactor*: the value of the repulsive force, as a fraction of mutual gravity.

C.9   Few relevant parameters

PKDGRAV needs several input parameters. Here, we will present some parameters used during this work:

- *dDelta* is the time step discussed above (expressed in year$/2\pi$).

- *nSteps* is the number of steps in interval of dDelta.

- *nSmooth* is the number of nearest neighbours checked for collision with each particles each step.

- *dEpsN* is the normal restitution coefficient. Normally, we set it between 0.3 and 0.5.

- *dEpsT* is the tangential restitution coefficient. Normally, we set it at 0.8.

- *dCollapseLimit* is the inelastic collapse detection limit. Normally, we set it at 10^{-6}

- *iOverlapOption* is the parameter used in case of overlapping between particles.

C.10   The Rubble Pile Analyzer

The Rubble Pile Analyzer (hereinafter rpa) is used to extract statistical data from simulations. One can obtain the mass, radius, position, velocity and spin vectors for each particle (or groups of particles), as well as simulation time, the mass accreting onto the largest rubble pile, the mass orbiting or escaping the largest rubble pile, the velocity dispersion magnitude of free particles, of particles pairs, and of rubble piles, mass of the free particles, of free particle pairs, and of rubble piles, largest rubble pile bulk density, the three components of the largest rubble pile semi-axis lengths, the largest rubble pile kinetic energy, the largest rubble pile angular momentum, the largest rubble pile effective spin, the three components of the largest rubble pile spin vector, the magnitude of the largest rubble pile velocity vector, the mass of the largest rubble pile found, the magnitude of the system spin vector, the magnitude of the system center-of-mass velocity vector, the magnitude of the system center-of-mass position vector, and, the radius of minimum enclosing sphere of the entire system.

C.10.1   Identification of aggregates

The programme rpa uses a recursive test to determine and isolate aggregates. Initially, rpa considers every particle as a separate aggregate and then follows the next steps:

- Analysis of one aggregate at a time and check for the nearest aggregate(s).

- For each neighbour found, rpa determines if the spheres centered in the two mass centers overlap at least partially.

- If the previous test is positive, rpa determines if the two aggregates are both single particles, in which case the overall test is considered as positive, and the two particles are a single aggregate.

- In case of multi-particles aggregates, rpa checks if: i) the two spheres centered on the mass centers overlap or ii) the center of one of the two aggregates is found.

- Finally, if at least a pair of aggregates has been merged into one, another cycles of analyses is performed.

C.10.2   Dimensions of the aggregate

If an aggregate is found, rpa will try to estimate its dimensions assuming that it is an ellipsoid. The first step is to determine the center of mass and then the direction of the axes by computing the inertia tensor. Then, the semi-axes lengths are computed from the center of mass to the farthest particles in the three directions.

C.10.3   Angular velocity of the aggregates

The angular velocity, Ω, depends on the angular momentum (L) with respect to the center of mass, as:

$$L = I \cdot \Omega \qquad \text{(Equation III.22)}$$

where I is the moment of inertia. The angular momentum is calculated from the particles' positions and velocities.

Bibliography

Agnor, C. B. and **D. P. Hamilton:** Neptune's capture of its moon Triton in a binary-planet gravitational encounter. Nature, vol. 441, May 2006, pp. 192–194.

Alard, C.: Image subtraction using a space-varying kernel. Astronomy and Astrophysics, vol. 144, June 2000, pp. 363–370.

Alard, C. and **R. Lupton:** ISIS: A method for optimal image subtraction. September 1999, Astrophysics Source Code Library

Allen, R. L., **G. M. Bernstein** and **R. Malhotra:** Observational Limits on a Distant Cold Kuiper Belt. The Astronomical Journal, vol. 124, November 2002, pp. 2949–2954.

Altenhoff, W. J., **K. M. Menten** and **F. Bertoldi:** Size determination of the Centaur Chariklo from millimeter-wavelength bolometer observations. Astronomy and Astrophysics, vol. 366, February 2001, L9–L12.

Altenhoff, W. J. and **P. Stumpff:** Size estimate of "asteroid" 2060 chiron from 250GHz measurements. Astronomy and Astrophysics, vol. 293, January 1995, L41–L42.

Asphaug, E.: Survival of the weakest. Nature, vol. 402, November 1999, pp. 127–128.

Astakhov, S. A., **E. A. Lee** and **D. Farrelly:** Formation of Kuiper-belt binaries through multiple chaotic scattering encounters with low-mass intruders. Monthly Notices of the Royal Astronomical Society, vol. 360, June 2005, pp. 401–415.

Barkume, K. M., **M. E. Brown** and **E. L. Schaller:** Water Ice on the Satellite of Kuiper Belt Object 2003 EL_{61}. The Astrophysical Journal, vol. 640, March 2006, L87–L89.

Barnes, J. and **P. Hut:** A hierarchical O(N log N) force-calculation algorithm. Nature, vol. 324, December 1986, pp. 446–449.

Barucci, M. A. et al.: New insights on ices in Centaur and Transneptunian populations. Icarus, vol. 214, July 2011, pp. 297–307.

Batygin, K., **M. E. Brown** and **W. C. Fraser:** Retention of a Primordial Cold Classical Kuiper Belt in an Instability-Driven Model of Solar System Formation. The Astrophysical Journal, vol. 738, September 2011, 13.

Bauer, J. M. et al.: Observations of the Centaur 1999 UG5: Evidence of a Unique Outer Solar System Surface. Publications of the Astronomical Society of the Pacific, vol. 114, December 2002, pp. 1309–1321.

Bauer, J. M. et al.: Physical survey of 24 Centaurs with visible photometry. Icarus, vol. 166, November 2003, pp. 195–211.

Belskaya, I. N., **A. M. Barucci** and **Y. G. Shkuratov:** Opposition Effect of Kuiper Belt Objects: preliminary estimations. Earth Moon and Planets, vol. 92, June 2003, pp. 201–206.

**Belskaya, I. N. et al.:** Low phase angle effects in photometry of trans-neptunian objects: 20000 Varuna and 19308 (1996 TO$_{66}$). Icarus, vol. 184, September 2006, pp. 277–284.

Benecchi, S. D. et al.: The correlated colors of transneptunian binaries. Icarus, vol. 200, March 2009, pp. 292–303.

Benecchi, S. D. et al.: (47171) 1999 TC$_{36}$, A transneptunian triple. Icarus, vol. 207, June 2010, pp. 978–991.

Benecchi, S. D. and **S. S. Sheppard:** Light Curves of 32 Large Transneptunian Objects. The Astronomical Journal, vol. 145, May 2013, pp. 124.

Bernstein, G. M. et al.: The Size Distribution of Trans-Neptunian Bodies. The Astronomical Journal, vol. 128, September 2004, pp. 1364–1390.

Bertoldi, F. et al.: The transneptunian object UB$_{313}$ is larger than Pluto. Nature, vol. 439, February 2006, pp. 563–564.

Bessell, M. S.: UBVRI passbands. Astronomical Society of the Pacific, vol. 102, October 1990, pp. 1181–1199.

Bessell, M. S.: Standard Photometric Systems. Annual Review of Astronomy and Astrophysics, vol. 43, September 2005, pp. 293–336.

Bevington, P. R. and **D. K. Robinson:** Data reduction and error analysis for the physical sciences. 2003

Binzel, R. P. et al.: Asteroid rotation rates Distributions, statistics. 1989, pp. 416–441.

Binzel, R. P. and **W. B. Hubbard; Stern, S. A.** and **D. J. Tholen, editors:** Mutual Events and Stellar Occultations. 1997, pp. 85.

Boyle, W. and **G.E. Smith:** Charge-couples semiconductor devices. Bell Systems Technical Journal, vol. 49, April 1970, pp. 587–593.

Braga-Ribas, F et al.: Size, shape, albedo, density and atmospheric limit of transneptunian object (50000) Quaoar from multi-chord stellar occultations. The Astrophysical Journal, 2013, Submitted

Brown, M. E.: The Inclination Distribution of the Kuiper Belt. The Astronomical Journal, vol. 121, May 2001, pp. 2804–2814.

Brown, M. E.: S/2005 (2003 EL_61) 1. IAU Circular, vol. 8577, July 2005a, pp. 1.

Brown, M. E.: S/2005 (2003 EL_61) 2. IAU Circular, vol. 8636, December 2005b, pp. 1.

Brown, M. E. et al.: A collisional family of icy objects in the Kuiper belt. Nature, vol. 446, March 2007, pp. 294–296.

Brown, M. E., **A. J. Burgasser** and **W. C. Fraser:** The Surface Composition of Large Kuiper Belt Object 2007 OR10. The Astrophysical Journal Letters, vol. 738, September 2011, L26.

Brown, M. E. et al.: The Size, Density, and Formation of the Orcus-Vanth System in the Kuiper Belt. The Astronomical Journal, vol. 139, June 2010, pp. 2700–2705.

Brown, M. E. et al.: Direct Measurement of the Size of 2003 UB313 from the Hubble Space Telescope. The Astrophysical Journal, vol. 643, May 2006a, L61–L63.

Brown, M. E. and **T.A. Suer:** Satellites of 2003 AZ84, (50000), (55637), and (90482). IAU Circular, vol. 8812, February 2007, pp. 1.

Brown, M. E., **C. Trujillo** and **D. Rabinowitz:** Discovery of a Candidate Inner Oort Cloud Planetoid. The Astrophysical Journal, vol. 617, December 2004, pp. 645–649.
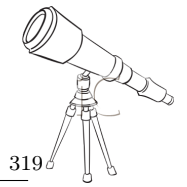
Brown, M. E. and **C. A. Trujillo:** (26308) 1998 SM165. IAU Circular, vol. 7807, January 2002, pp. 1.

Brown, M. E. and **C. A. Trujillo:** Direct Measurement of the Size of the Large Kuiper Belt Object (50000) Quaoar. Astronomical Journal, vol. 127, April 2004, pp. 2413–2417.

Brown, M. E. et al.: Satellites of the Largest Kuiper Belt Objects. The Astrophysical Journal, vol. 639, March 2006b, L43–L46.

Brucker, M. J. et al.: High albedos of low inclination Classical Kuiper belt objects. Icarus, vol. 201, May 2009, pp. 284–294.

Brunini, A. and **M. D. Melita:** The Existence of a Planet beyond 50 AU and the Orbital Distribution of the Classical Edgeworth-Kuiper-Belt Objects. Icarus, vol. 160, November 2002, pp. 32–43.

Buie, M. W. and **S. J. Bus:** Physical observations of (5145) Pholus. Icarus, vol. 100, December 1992, pp. 288–294.

Buie, M. W. et al.: Orbits and Photometry of Pluto's Satellites: Charon, S/2005 P1, and S/2005 P2. The Astronomical Journal, vol. 132, July 2006, pp. 290–298.

Buie, M. W. et al.: Pluto and Charon with the Hubble Space Telescope. II. Resolving Changes on Pluto's Surface and a Map for Charon. The Astronomical Journal, vol. 139, March 2010, pp. 1128–1143.

Buie, M. W. and **D. J. Tholen:** The surface albedo distribution of Pluto. Icarus, vol. 79, May 1989, pp. 23–37.

Buie, M. W., **D. J. Tholen** and **L. H. Wasserman:** Separate Lightcurves of Pluto, Charon. Icarus, vol. 125, February 1997, pp. 233–244.

Buratti, B. J. et al.: Photometry of pluto in the last decade and before: evidence for volatile transport? Icarus, vol. 162, March 2003, pp. 171–182.

Burns, J. A. and **V. S. Safronov:** Asteroid nutation angles. Monthly Notices of the Royal Astronomical Society, vol. 165, 1973, pp. 403.

Bursa, M.: Secular Love numbers of the major planets. Earth Moon and Planets, vol. 59, December 1992, pp. 239–244.

Bus, S. J. et al.: 2060 Chiron CCD, electronographic photometry. Icarus, vol. 77, February 1989, pp. 223–238.

Campo Bagatin, A. and **P. G. Benavidez:** Collisional evolution of trans-Neptunian object populations in a Nice model environment. Monthly Notices of the Royal Astronomical Society, vol. 423, June 2012, pp. 1254–1266.

Canup, R. M.: A Giant Impact Origin of Pluto-Charon. Science, vol. 307, January 2005, pp. 546–550.

Carry, B. et al.: Integral-field spectroscopy of (90482) Orcus-Vanth. Astronomy and Astrophysics, vol. 534, October 2011, A115.

Carry, B. et al.: Characterisation of candidate members of (136108) Haumea's family. II. Follow-up observations. Astronomy and Astrophysics, vol. 544, August 2012, A137.

Chandrasekhar, S.: Ellipsoidal figures of equilibrium. New York : Dover, 1987., 1987

Chesley, S. R. et al.: Quantifying the Risk Posed by Potential Earth Impacts. Icarus, vol. 159, October 2002, pp. 423–432.

Chiang, E. I. and **M. E. Brown:** Keck Pencil-Beam Survey for Faint Kuiper Belt Objects. The Astronomical Journal, vol. 118, September 1999, pp. 1411–1422.

Chiang, E. I. and **A. B. Jordan:** On the Plutinos and Twotinos of the Kuiper Belt. The Astronomical Journal, vol. 124, December 2002, pp. 3430–3444.

Choi, Y. J., **N. Brosch** and **D. Prialnik:** Rotation and cometary activity of KBO (29981) 1999 TD$_{10}$. Icarus, vol. 165, September 2003, pp. 101–111.

Choi, Y.-J. and **P. Weissman:** Discovery of Cometary Activity for Centaur 174P/Echeclus (60558). vol. 38, September 2006, pp. 551.

Chorney, N. and **J. J. Kavelaars:** A rotational light curve for the Kuiper belt object 1997 CV29. Icarus, vol. 167, January 2004, pp. 220–224.

Cole, G. H. A.: A planet is a cold body - II. Journal of the British Astronomical Association, vol. 94, April 1984, pp. 113–117.

Collander-Brown, S. J. et al.: Light curves of the trans-Neptunian objects 1996 TP66 and 1994 VK8. Monthly Notices of the Royal Astronomical Society, vol. 308, September 1999, pp. 588–592.

Collander-Brown, S. J. et al.: The scattered transNeptunian object 1998 XY95. Monthly Notices of the Royal Astronomical Society, vol. 325, August 2001, pp. 972–978.

Consolmagno, G. J. et al.: Size, Shape, Rotation,, Color of the Outer Solar System Object 1999 TD10. vol. 32, October 2000, pp. 1032.

Cook, J. C., **S. J. Desch** and **M. Rubin:** The Black Sheep of Haumea's Collisional Family. vol. 42, March 2011, 2503

Cousins, A. W. J.: Revised zero points and UBV photometry of stars in the Harvard E and F regions. Mem. R. Astron. Soc, vol. 77, 1973, pp. 223–236.

Davidsson, B. J. R.: Tidal Splitting, Rotational Breakup of Solid Spheres. Icarus, Vol. 142, December 1999, pp. 525–535.

Davidsson, B. J. R.: Tidal Splitting, Rotational Breakup of Solid Biaxial Ellipsoids. Icarus, vol. 149, February 2001, pp. 375–383.

Davies, J. et al.: (5145) Pholus. IAU Circular, vol. 5698, January 1993, pp. 2.

Davies, J. K. et al.: Visible, Infrared Photometry of Six Centaurs. Icarus, vol. 134, August 1998, pp. 213–227.

Davies, J. K., **D. J. Tholen** and **D. R. Ballantyne:** Infrared Observations of Distant Asteroids. vol. 107, 1996, pp. 97–105.

Davis, D. R. and **P. Farinella:** Collisional Evolution of Edgeworth-Kuiper Belt Objects. Icarus, vol. 125, January 1997, pp.50–60.

Dell'Oro, A. et al.: Updated collisional probabilities of minor body populations. Astronomy and Astrophysics, vol. 366, February 2001, pp. 1053–1060.

Descamps, P. and **F. Marchis:** Angular momentum of binary asteroids: Implications for their possible origin. Icarus, vol. 193, January 2008, pp. 74–84.

Descamps, P. et al.: Figure of the double Asteroid 90 Antiope from adaptive optics and lightcurve observations. Icarus, vol. 187, April 2007, pp. 482–499.

Desch, S. J. et al.: Thermal evolution of Kuiper belt objects, with implications for cryovolcanism. Icarus, vol. 202, August 2009, pp. 694–714.

Dohnanyi, J. S.: Collisional Model of Asteroids and Their Debris. Journal of Geophysical Research, vol. 74, May 1969, pp. 2531.
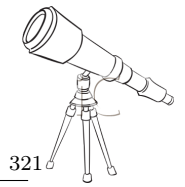
Doressoundiram, A. et al.: The Color Distribution in the Edgeworth-Kuiper Belt. The Astronomical Journal, vol. 124, October 2002, pp. 2279–2296.

Dotto, E. et al.: Rotational properties of Centaurs, TransNeptunian Objects. Lightcurves, densities. Astronomy and Astrophysics, vol. 490, November 2008, pp. 829–833.

Duffard, R. et al.: A study of photometric variations on the dwarf planet (136199) Eris. Astronomy and Astrophysics, vol. 479, March 2008, pp. 877–881.

Duffard, R. et al.: Transneptunian objects, Centaurs from light curves. Astronomy and Astrophysics, vol. 505, October 2009, pp. 1283–1295.

Duncan, M. J. and **H. F. Levison:** A scattered comet disk and the origin of Jupiter family comets. Science, vol. 276 1997, pp. 1670–1672.

Durda, D. D. et al.: The formation of asteroid satellites in large impacts: results from numerical simulations. Icarus, vol. 170, July 2004, pp. 243–257.

Edgeworth, K. E.: The evolution of our planetary system. Journal of the British Astronomical Association, vol. 53, 1943, pp. 181–188.

Edgeworth, K. E.: The origin and evolution of the Solar System. Monthly Notices of the Royal Astronomical Society, vol. 109, 1949, pp. 600–609.

Elliot, J. L. et al.: The Deep Ecliptic Survey: A Search for Kuiper Belt Objects and Centaurs. II. Dynamical Classification, the Kuiper Belt Plane, and the Core Population. The Astronomical Journal, vol. 129, February 2005, pp. 1117–1162.

Elliot, J. L. et al.: Size and albedo of Kuiper belt object 55636 from a stellar occultation. Nature, vol. 465, June 2010, pp. 897–900.

Farnham, T. L.: Rotation and Color Studies of Centaurs, KBOs and Comets. vol. 33, November 2001, pp. 1047.

Farnham, T. L.: The Rotation Axis of the Centaur 5145 Pholus. Icarus, vol. 152, August 2001a, pp. 238–245.

Farnham, T. L. and **J. K. Davies:** The rotational, physical properties of the Centaur (32532) 2001 PT13. Icarus, vol. 164, August 2003, pp. 418–427.

Fernandez, J. A.: On the existence of a comet belt beyond Neptune. Monthly Notices of the Royal Astronomical Society, vol. 192, August 1980, pp. 481–491.

Fernandez, J. A. and **W.-H. Ip:** Some dynamical aspects of the accretion of Uranus and Neptune - The exchange of orbital angular momentum with planetesimals. Icarus, vol. 58, April 1984, pp. 109–120.

Fornasier, S. et al.: TNOs are Cool: A survey of the trans-Neptunian region. VIII. Combined Herschel PACS and SPIRE observations of 9 bright targets at 70–500 micron. ArXiv e-prints May 2013

Foster, G.: The cleanest Fourier spectrum. Astronomical Journal, vol. 109, April 1995, pp. 1889–1902.

Fraser, W. C. et al.: The mass, orbit, and tidal evolution of the Quaoar-Weywot system. Icarus, vol. 222, January 2013, pp. 357–363.

Fraser, W. C. and **M. E. Brown:** Quaoar: A Rock in the Kuiper Belt. Astrophysical Journal, vol. 714, May 2010, pp. 1547–1550.

Fraser, W. C. and **J. J. Kavelaars:** A derivation of the luminosity function of the Kuiper belt from a broken power-law size distribution. Icarus, vol. 198, December 2008, pp. 452–458.

Fraser, W. C. and **J. J. Kavelaars:** The Size Distribution of Kuiper Belt Objects for D gsim 10 km. The Astronomical Journal, vol. 137, January 2009, pp. 72–82.

Fraser, W. C. et al.: The Kuiper belt luminosity function from m=21 to 26. Icarus, vol. 195, June 2008, pp. 827–843.

Fuentes, C. I. and **M. J. Holman:** A SUBARU Archival Search for Faint Trans-Neptunian Objects. The Astronomical Journal, vol. 136, July 2008, pp. 83–97.

Gaudi, B. S. et al.: On the Rotation Period of (90377) Sedna. Astrophysical Journal, vol. 629, August 2005, L49–L52

Gehrels, T.: Minor planets. I. The rotation of Vesta. The Astronomical Journal, vol. 72, October 1967, pp. 929.

Gladman, B. et al.: Synchronous Locking of Tidally Evolving Satellites. Icarus, vol. 122, July 1996, pp. 166–192.

Gladman, B. et al.: Evidence for an Extended Scattered Disk. Icarus, vol. 157, June 2002, pp. 269–279.

Gladman, B. et al.: The Structure of the Kuiper Belt: Size Distribution and Radial Extent. The Astronomical Journal, vol. 122, August 2001, pp. 1051–1066.

Gladman, B. et al.: The Resonant Trans-Neptunian Populations. The Astronomical Journal, vol. 144, July 2012, pp. 23.

Gladman, B., **B. G. Marsden** and **C. Vanlaerhoven; Barucci, M. A., Boehnhardt, H., Cruikshank, D. P., Morbidelli, A., & Dotson, R., editor:** Nomenclature in the Outer Solar System. 2008, pp. 43–57.

Goldreich, P., **Y. Lithwick** and **R. Sari:** Formation of Kuiper-belt binaries by dynamical friction and three-body encounters. Nature, vol. 420, December 2002, pp. 643–646.

Goldreich, P. and **S. Soter:** Q in the Solar System. Icarus, vol. 5, 1966, pp. 375–389.

Gomes, R. et al.: Origin of the cataclysmic Late Heavy Bombardment period of the terrestrial planets. Nature, vol. 435, May 2005, pp. 466–469.

Gomes, R. S.: Planetary Migration and Plutino Orbital Inclinations. The Astronomical Journal, vol. 120, November 2000, pp. 2695–2707.

Gomes, R. S.: The origin of the Kuiper Belt high-inclination population. Icarus, vol. 161, February 2003, pp. 404–418.

Gomes, R. S.: The origin of TNO 2004 XR_{190} as a primordial scattered object. Icarus, vol. 215, October 2011, pp. 661–668.

Gomes, R. S. et al.; Barucci, M. A. et al., editors: The Scattered Disk: Origins, Dynamics, and End States. 2008, pp. 259–273.

Grav, T., **M. J. Holman** and **W. C. Fraser:** Photometry of Irregular Satellites of Uranus and Neptune. The Astrophysical Journal, vol. 613, September 2004, L77–L80.

Grav, T. et al.: Photometric survey of the irregular satellites. Icarus, vol. 166, November 2003, pp. 33–45.

Grundy, W. M. et al.: A New NOAO Survey Program: Mutual Orbits and Masses of Kuiper Belt Binaries. October 2011a, pp. 1078.

Grundy, W. M. et al.: A New NOAO Survey Program: Mutual Orbits and Masses of Kuiper Belt Binaries. October 2011b, pp. 1078
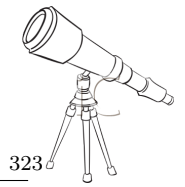
Grundy, W. M. et al.: Mutual events in the Cold Classical transneptunian binary system Sila and Nunam. Icarus, vol. 220, July 2012, pp. 74–83.

Grundy, W. M. et al.: Five new and three improved mutual orbits of transneptunian binaries. Icarus, vol. 213, June 2011c, pp. 678–692.

Grundy, W. M. et al.: (42355) Typhon Echidna: Scheduling observations for binary orbit determination. Icarus, vol. 197, September 2008, pp. 260–268.

Gutiérrez, P. J. et al.: Short term variability of Centaur 1999 UG5. Astronomy and Astrophysics, vol. 371, June 2001, L1–L4.

Hachisu, I. and **Y. Eriguchi:** Fission sequence and equilibrium models of rigidity rotating polytropes. International Astronomical Union, vol. 99, February 1984, pp. 71–74.

Hahn, G. and **M. E. Bailey:** Rapid dynamical evolution of giant Comet Chiron. Nature, vol. 348, November 1990, pp. 132–136.

Hahn, J. M. and **R. Malhotra:** Orbital Evolution of Planets Embedded in a Planetesimal Disk. The Astronomical Journal, vol. 117, June 1999, pp. 3041–3053.

Hainaut, O. R., **H. Boehnhardt** and **S. Protopapa:** Colours of minor bodies in the outer solar system. II. A statistical analysis revisited. Astronomy and Astrophysics, vol. 546, October 2012, pp. A115.

Hainaut, O. R. et al.: Physical properties of TNO 1996 TO66. Lightcurves, possible cometary activity. Astronomy and Astrophysics, vol. 356, April 2000, pp. 1076–1088.

Hainaut, O. R. and **A. C. Delsanti:** Colors of Minor Bodies in the Outer Solar System. A statistical analysis. Astronomy and Astrophysics, vol. 389, july 2002, pp. 641–664.

Harris, A. W.: A Thermal Model for Near-Earth Asteroids. Icarus, vol. 131, February 1998, pp. 291–301.

Harris, A. W. et al.: Photoelectric observations of asteroids 3, 24, 60, 261, 863. Icarus, vol. 77, January 1989, pp. 171–186.

Heinze, A. N. and **D. de Lahunta:** The Rotation Period and LightCurve Amplitude of Kuiper Belt Dwarf Planet 136472 Makemake (2005 FY9). The Astronomical Journal, vol. 138, August 2009, pp. 428–438.

Heppenheimer, T. A. and **C. Porco:** New contributions to the problem of capture. Icarus, vol. 30, February 1977, pp. 385–401.

Hicks, M. D., **D. P. Simonelli** and **B. J. Buratti:** Photometric behavior of 20000 Varuna at very small solar phase angles. Icarus, vol. 176, August 2005, pp. 492–498.

Hoffmann, M. and **et al.:** Photometric, spectroscopic observations of 5145 1992 AD. vol. 30, 1992, pp. 203.

Högbom, J. A.: Aperture Synthesis with a Non-Regular Distribution of Interferometer Baselines. Astronomy and Astrophysics Supplement, Vol. 15, June 1974, pp. 417.

Holsapple, K. A.: Equilibrium Configurations of Solid Cohesionless Bodies. Icarus, vol. 154, December 2001, pp. 432–448.

Holsapple, K. A.: Equilibrium figures of spinning bodies with selfgravity. Icarus, vol. 172, November 2004, pp. 272–303.

Holsapple, K. A.: Spin limits of Solar System bodies: From the small fast-rotators to 2003 EL61. Icarus, vol. 187, April 2007, pp. 500–509.

Housen, K.: Cumulative damage in strength-dominated collisions of rocky asteroids: Rubble piles and brick piles. Planetary and Space Science, vol. 57, February 2009, pp. 142–153.

Howell, S. B.: Two-dimensional aperture photometry - Signal-to-noise ratio of point-source observations and optimal data-extraction techniques. Astronomical Society of the Pacific Publications, vol. 101, June 1989, pp. 616–622.

Howell, S. B.: Book Review: Handbook of CCD astronomy / Cambridge University Press Cambridge, 164 pp., 2000, ISBN 0-521-64834-3 (paperback), ISBN 0-521-64058-X (hard cover). Ciel et Terre, 117, June 2001, pp. 112.

Hubbard, W. B.: Planetary interiors. 1984

Ida, S., **J. Larwood** and **A. Burkert:** Evidence for Early Stellar Encounters in the Orbital Distribution of Edgeworth-Kuiper Belt Objects. The Astrophysical Journal, vol. 528, January 2000, pp. 351–356.

Jacobson, S. A. and **D. J. Scheeres:** Dynamics of rotationally fissioned asteroids: Source of observed small asteroid systems. Icarus, vol. 214, July 2011, pp. 161–178.

Jewitt, D.: The Active Centaurs. The Astronomical Journal 1 May 2009

Jewitt, D. and **J. Luu:** Discovery of the candidate Kuiper belt object 1992 QB1. Nature, vol. 362, April 1993, pp. 730–732.

Jewitt, D., **J. Luu** and **C. Trujillo:** Large Kuiper Belt Objects: The Mauna Kea 8K CCD Survey. The Astronomical Journal, vol. 115, May 1998, pp. 2125–2135.

Jewitt, D. C. and **J. X. Luu:** The solar system beyond Neptune. The Astronomical Journal, vol. 109, April 1995, pp. 1867–1876.

Jewitt, D. C., **S. Sheppard** and **C. Porco; Bagenal, F.**,**T. E. Dowling** and **W. B. McKinnon, editors:** Jupiter's outer satellites and Trojans. 2004, pp. 263–280.

Jewitt, D. C. and **S. S. Sheppard:** Physical Properties of TransNeptunian Object (20000) Varuna. Astronomical Journal, vol. 123, April 2002, pp. 2110–2120.

Johnson, H. L. and **W. W. Morgan:** Fundamental stellar photometry for standards of spectral type on the revised system of the Yerkes spectral atlas. The Astrophysical Journal, vol. 117, May 1953, pp. 313.

Johnson, T. V. and **J. I. Lunine:** Saturn's moon Phoebe as a captured body from the outer Solar System. Nature, vol. 435, May 2005, pp. 69–71.

Johnson, T. V. and **T. R. McGetchin:** Topography on satellite surfaces and the shape of asteroids. Icarus, vol. 18, April 1973, pp. 612–620.

Jones, R. L. et al.: The CFEPS Kuiper Belt Survey: Strategy and presurvey results. Icarus, vol. 185, December 2006, pp. 508–522.

Kaasalainen, M. and **J. Torppa:** Optimization Methods for Asteroid Lightcurve Inversion. I. Shape Determination. Icarus, vol. 153, September 2001, pp. 24–36.

Kaasalainen, M., **J. Torppa** and **K. Muinonen:** Optimization Methods for Asteroid Lightcurve Inversion. II. The Complete Inverse Problem. Icarus, vol. 153, September 2001, pp. 37–51.

Kavelaars, J. J. et al.: The Canada-France Ecliptic Plane Survey-L3 Data Release: The Orbital Structure of the Kuiper Belt. The Astronomical Journal, vol. 137, June 2009, pp. 4917–4935.

Kenyon, S. J. and **R. A. Windhorst:** The Kuiper Belt and Olbers's Paradox. The Astrophysical Journal, vol. 547, January 2001, L69–L73.

Kern, S. D.: A study of binary Kuiper belt objects. Ph. D thesis, Massachusetts Institute of Technology, 2006
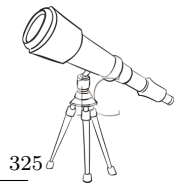
Kern, S. D. and **J. L. Elliot:** 2005 EO 304. IAU circular, vol. 8526 May 2005, pp. 2.

Kern, S. D. and **J. L. Elliot:** Discovery, characteristics of the Kuiper belt binary 2003 QY90. Icarus, vol. 183, July 2006a, pp. 179–185.

Kern, S. D. and **J. L. Elliot:** The Frequency of Binary Kuiper Belt Objects. The Astrophysical Journal, vol. 643, May 2006b, L57–L60.

Kern, S. D. et al.: Compositional Variation on the Surface of Centaur 8405 Asbolus. Astrophysical Journal, vol. 542, October 2000, L155–L159.

Kowal, C. T.: A solar system survey. Icarus, vol. 77, January 1989, pp. 118–123.

Kowal, C. T., **W. Liller** and **L. J. Chaisson:** 1977 UB. IAU Circular, vol. 3147, December 1977, pp. 1.

Kozai, Y.: Secular perturbations of asteroids with high inclination and eccentricity. The Astronomical Journal, vol. 67, November 1962, pp. 591.

Kuiper, G. P.: On the Origin of the Solar System. Proceedings of the National Academy of Science, vol. 37, January 1951, pp. 1–14.

Lacerda, P.: A Change in the Light Curve of Kuiper Belt Contact Binary (139775) 2001 QG$_{298}$. The Astronomical Journal, vol. 142, September 2011, pp. 90.

Lacerda, P., **D. Jewitt** and **N. Peixinho:** High-Precision Photometry of Extreme KBO 2003 EL$_{61}$. The Astronomical Journal, vol. 135, May 2008, pp. 1749–1756.

Lacerda, P. and **J. Luu:** On the detectability of lightcurves of Kuiper belt objects. Icarus, vol. 161, January 2003, pp. 174–180.

Lacerda, P. and **J. Luu:** Analysis of the Rotational Properties of Kuiper Belt Objects. Astronomical Journal, vol. 131, April 2006, pp. 2314–2326.

Lagerkvist, C.I., **P. Magnusson** and **H. Rickman:** Asteroids, comets, meteors III. Abstracts. Uppsala Astronomical Observatory Reports vol. 48, February 1989

Landolt, A. U.: UBVRI photometric standard stars in the magnitude range 11.5-16.0 around the celestial equator. Astronomical Journal, vol. 104, July 1992, pp. 340–371.

Larsen, J. A. et al.: The Spacewatch Wide-Area Survey for Bright Centaurs and Trans-Neptunian Objects. The Astronomical Journal, vol. 121, January 2001, pp. 562–579.

Leinhardt, Z. M., **R. A. Marcus** and **S. T. Stewart:** The Formation of the Collisional Family Around the Dwarf Planet Haumea. The Astrophysical Journal, vol. 714, May 2010, pp. 1789–1799..

Leinhardt, Z. M., **D. C. Richardson** and **T. Quinn:** Direct N-body Simulations of Rubble Pile Collisions. Icarus, vol. 146, July 2000, pp. 133–151.

Leinhardt, Z. M. and **S. T. Stewart:** Full numerical simulations of catastrophic small body collisions. Icarus, vol. 199, February 2009, pp. 542–559.

Lellouch, E. et al.: "TNOs are cool": A survey of the transNeptunian region. II. The thermal lightcurve of (136108) Haumea. Astronomy and Astrophysics, vol. 518, July 2010, L147.

Lellouch, E. et al.: Coordinated thermal and optical observations of Trans-Neptunian object (20 000)Varuna from Sierra Nevada. Astronomy and Astrophysics, vol. 391, September 2002, pp. 1133–1139.

Leonard, F. C.: The New Planet Pluto. Leaflet of the Astronomical Society of the Pacific, vol. 1, 1930, pp. 121.

Leone, G. et al.: Equilibrium models of binary asteroids. Astronomy and Astrophysics, vol. 140, November 1984, pp. 265–272.

Levison, H. F. and **M. J. Duncan:** From the Kuiper Belt to Jupiter-Family Comets: The Spatial Distribution of Ecliptic Comets. Icarus, vol. 127, May 1997, pp. 13–32.

Levison, H. F. and **A. Morbidelli:** The formation of the Kuiper belt by the outward transport of bodies during Neptune's migration. Nature, vol. 426, November 2003, pp. 419–421.

Levison, H. F. et al.: Origin of the structure of the Kuiper belt during a dynamical instability in the orbits of Uranus and Neptune. Icarus, vol. 196, July 2008a, pp. 258–273.

Levison, H. F. et al.: On a Scattered-Disk Origin for the 2003 EL_{61} Collisional Family-An Example of the Importance of Collisions on the Dynamics of Small Bodies. The Astronomical Journal, vol. 136, September 2008b, pp. 1079–1088.

Levison, H. F. and **S. A. Stern:** On the Size Dependence of the Inclination Distribution of the Main Kuiper Belt. The Astronomical Journal, vol. 121, March 2001, pp. 1730–1735.

Licandro, J. et al.: Trans-neptunian object (55636) 2002 TX_{300}, a fresh icy surface in the outer solar system. Astronomy and Astrophysics, vol. 457, October 2006a, pp. 329–333.

Licandro, J. et al.: Visible spectroscopy of 2003 UB313: evidence for N2 ice on the surface of the largest TNO? Astronomy and Astrophysics, vol. 458, October 2006b, L5–L8.

Licandro, J. et al.: The methane ice rich surface of large TNO 2005 FY_9: a Pluto-twin in the trans-neptunian belt? Astronomy and Astrophysics, vol. 445, January 2006c, L35–L38.

Lim, T. L. et al.: "TNOs are Cool": A survey of the transNeptunian region . III. Thermophysical properties of 90482 Orcus and 136472 Makemake. Astronomy and Astrophysics, vol. 518, July 2010, L148.

Lin, H.-W. et al.: On the Detection of Two New Trans-Neptunian Binaries from the CFEPS Kuiper Belt Survey. PASP, vol. 122, September 2010, pp. 1030–1034.

Lin, H.W., **Y.L. Wu** and **W.H. Ip:** Observations of dwarf planet (136199) Eris, other large TNOs on Lulin Observatory. Advances in Space Research, vol. 40, 2007, pp. 238–243.

Lomb, N. R.: Leastsquares frequency analysis of unequally spaced data. Astrophysics and Space Science, vol. 39, February 1976, pp. 447–462.

Lupo, M. J. and **J. S. Lewis:** Mass-radius relationships in icy satellites. Icarus, vol. 40, November 1979, pp. 157–170.

Luu, J. X. and **D. C. Jewitt:** Optical and Infrared Reflectance Spectrum of Kuiper Belt Object 1996 TL 66. Astrophysical Journal Letter, vol. 494, February 1998, L117.

Luu, J. X. and **D. C. Jewitt:** Kuiper Belt Objects: Relics from the Accretion Disk of the Sun. Annual Review of Astronomy and Astrophysics, vol. 40, 2002, pp. 63–101.

Lykawka, P. S. and **T. Mukai:** An Outer Planet Beyond Pluto and the Origin of the Trans-Neptunian Belt Architecture. The Astronomical Journal, vol. 135, April 2008, pp. 1161–1200.

Magnusson, P.: Distribution of spin axes and senses of rotation for 20 large asteroids. Icarus, vol. 68, October 1986, pp. 1–39.

Magnusson, P. and **C.-I. Lagerkvist:** Physical studies of asteroids. XXII - Photometric photometry of the asteroids 34, 98, 115, 174, 270, 389, 419 and 804. Astronomy and Astrophysics Supplement Series, vol. 87, February 1991, pp. 269–275.

Malhotra, R.: The origin of Pluto's peculiar orbit. Nature, vol. 365, October 1993, pp. 819–821.

Malhotra, R.: The Origin of Pluto's Orbit: Implications for the Solar System Beyond Neptune. Astronomical Journal, vol. 110, July 1995, pp. 420.
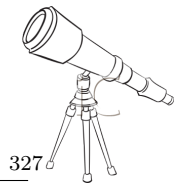
Marcus, R. A. et al.: Identifying Collisional Families in the Kuiper Belt. The Astrophysical Journal, vol. 733, May 2011, 40.

Meech, K. J. and **M. J. S. Belton:** (2060) Chiron. IAU Circular, vol. 4770, April 1989, pp. 1.

Merlin, F. et al.: Properties of the icy surface of the TNO 136108 (2003 EL61). Astronomy and Astrophysics, vol. 466, May 2007, pp. 1185–1188.

Milani, A. and **P. Farinella:** The age of the Veritas asteroid family deduced by chaotic chronology. Nature, vol. 370, July 1994, pp. 40–42.

Millis, R. L. et al.: The Deep Ecliptic Survey: A Search for Kuiper Belt Objects and Centaurs. I. Description of Methods and Initial Results. The Astronomical Journal, vol. 123, April 2002, pp. 2083–2109.

Mommert, M. et al.: TNOs are cool: A survey of the transNeptunian region. V. Physical characterization of 18 Plutinos using HerschelPACS observations. Astronomy and Astrophysics, vol. 541, May 2012, A93.

Morbidelli, A. and **H. F. Levison:** Planetary science:Kuiper-belt interlopers. Nature, vol. 422, March 2003, pp. 30–31.

Morbidelli, A. and **H. F. Levison:** Scenarios for the Origin of the Orbits of the Trans-Neptunian Objects 2000 CR$_{105}$ and 2003 VB$_{12}$ (Sedna). The Astronomical Journal, vol. 128, November 2004, pp. 2564–2576.

Morbidelli, A. et al.: Chaotic capture of Jupiter's Trojan asteroids in the early Solar System. Nature, vol. 435, May 2005, pp. 462–465.

Morbidelli, A. and **G. B. Valsecchi:** NOTE: Neptune Scattered Planetesimals Could Have Sculpted the Primordial Edgeworth-Kuiper Belt. Icarus, vol. 128, August 1997, pp. 464–468.

Mueller, B. E. A. et al.: Simultaneous visible, nearinfrared time resolved observations of the outer Solar System object (29981) 1999 TD10. Icarus, vol. 171, October 2004, pp. 506–515.

Müller, T. G. et al.: TNOs are Cool: A Survey of the Transneptunian Region. Earth Moon and Planets, vol. 105, September 2009, pp. 209–219.

Müller, T. G. et al.: "TNOs are Cool": A survey of the trans-Neptunian region. I. Results from the Herschel science demonstration phase (SDP). Astronomy and Astrophysics, vol. 518, July 2010, L146.

Nesvorný, D., **A. N. Youdin** and **D. C. Richardson:** Formation of Kuiper Belt Binaries by Gravitational Collapse. The Astronomical Journal, vol. 140, September 2010, pp. 785–793.

Noll, K. S., **S. D. Benecchi** and **W. M. Grundy:** 2002 VF130. IAU Circular, vol. 9040, May 2009, pp. 1.

Noll, K. S. et al.: 2002 XH91. IAU Circular, vol. 9046, May 2009a, pp. 1.

Noll, K. S. et al.: 1999 XY143, 1999 RY214, and 2002 VT130. IAU Circular, vol. 9075, September 2009b, pp. 2.

Noll, K. S. et al.: 2000 WT169 and 2003 YU179. IAU Circular, vol. 9076, September 2009c, pp. 2.

Noll, K. S. et al.; Barucci, M. A., Boehnhardt, H., Cruikshank, D. P., Morbidelli, A., & Dotson, R., editor: Binaries in the Kuiper Belt. 2008a, pp. 345–363.

Noll, K. S. et al.: (119979) 2002 WC19. IAU Circular, vol. 8814, February 2007a, pp. 1.

**Noll, K. S. et al.:** 2002 GZ31. IAU Circular, vol. 8815, February 2007b, pp. 1.

Noll, K. S. et al.: 2004 PB108 and (60621) 2000 FE8. IAU Circular, vol. 8816, March 2007c, pp. 1.

Noll, K. S. et al.: 2001 QQ322 and 2005 PR21. IAU Circular, vol. 8925, March 2008b, pp. 2.

Noll, K. S. et al.: 1999 RT214. IAU Circular, vol. 8756, September 2006a, pp. 2.

Noll, K. S. et al.: (60458) 2000 CM114. IAU Circular, vol. 8689, March 2006b, pp. 2.

Noll, K. S. et al.: (38628) Huya. IAU Circular, vol. 9253 July 2012, pp. 2.

Noll, K. S. et al.: 2003 QW111. IAU Circular, vol. 8745, September 2006c, pp. 1.

Noll, K. S. et al.: (42355) 2002 CR 46. Minor Planet Electronic Circular, 2006d, vol. 8689,

Noll, K. S. et al.: 2006 SF369. IAU Circular, vol. 8922, February 2008c, pp. 1.

Noll, K. S. et al.: (160256) 2002 PD149. IAU Circular, vol. 8866, September 2007d, pp. 3.

Noll, K. S. et al.: (120347) 2004 SB 60. IAU Circular, vol. 8751, September 2006e, pp. 1.

Noll, K. S. et al.: 2000 QL251. IAU Circular, vol. 8746, September 2006f, pp. 1.

Noll, K. S. et al.: (123509) 2000 WK183. IAU Circular, vol. 8811, February 2007e, pp. 1.

Ortiz, J. L. et al.: A mid-term astrometric and photometric study of transNeptunian object (90482) Orcus. Astronomy and Astrophysics, vol. 525, January 2011, A31.

Ortiz, J. L. et al.: A study of short term rotational variability in TNOs, Centaurs from Sierra Nevada Observatory. Astronomy and Astrophysics, vol. 407, September 2003a, pp. 1149–1155.

Ortiz, J. L. et al.: Short-term rotational variability of eight KBOs from Sierra Nevada Observatory. Astronomy and Astrophysics, vol. 447, March 2006, pp. 1131–1144.

Ortiz, J. L. et al.: Rotational brightness variations in TransNeptunian Object 50000 Quaoar. Astronomy and Astrophysics, vol. 409, October 2003b, L13–L16

Ortiz, J. L. et al.: Possible patterns in the distribution of planetary formation regions. Monthly Notices of the Royal Astronomical Society, vol. 379, August 2007a, pp. 1222–1226.

Ortiz, J. L. et al.: Short-term rotational variability in the large TNO 2005 FY9. Astronomy and Astrophysics, vol. 468, June 2007b, L13–L16

Ortiz, J. L. et al.: Albedo and atmospheric constraints of dwarf planet Makemake from a stellar occultation. Nature, vol. 491, November 2012a, pp. 566–569.

Ortiz, J. L. et al.: A study of TransNeptunian object 55636 (2002 TX300). Astronomy and Astrophysics, vol. 420, June 2004, pp. 383–388.

Ortiz, J. L. et al.: Rotational fission of transNeptunian objects: the case of Haumea. Monthly Notices of the Royal Astronomical Society, vol. 419, January 2012b, pp. 2315–2324.

Osip, D. J., **S. D. Kern** and **J. L. Elliot:** Physical Characterization of the Binary Edgeworth-Kuiper Belt Object 2001 QT_{297}. Earth Moon and Planets, vol. 92, June 2003, pp. 409–421.

Osip, D. J. et al.: First-generation instruments for the Magellan telescopes: characteristics, operation, and performance. 5492 2004

Pál, A. et al.: "TNOs are Cool": A survey of the trans-Neptunian region. VII. Size and surface characteristics of (90377) Sedna and 2010 EK_{139}. Astronomy and Astrophysics, vol. 541, May 2012, L6.

Paolicchi, P., **J. A. Burns** and **S. J. Weidenschilling:** Side Effects of Collisions: Spin Rate Changes, Tumbling Rotation States, and Binary Asteroids. Asteroids III, 2002, pp. 517–526.
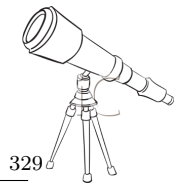
Parker, A. H. and **J. J. Kavelaars:** Collisional Evolution of Ultra-wide Trans-Neptunian Binaries. The Astrophysical Journal, vol. 744, January 2012, 139.

Parker, A. H. et al.: Characterization of Seven Ultrawide Trans-Neptunian Binaries. The Astronomical Journal, vol. 743, December 2011, 1.

Peixinho, N. et al.: The bimodal colors of Centaurs and small Kuiper belt objects. Astronomy and Astrophysics, vol. 546, October 2012, A86.

Peixinho, N. et al.: Reopening the TNOs color controversy: Centaurs bimodality and TNOs unimodality. Astronomy and Astrophysics, vol. 410, October 2003, L29–L32.

Peixinho, N., **A. Doressoundiram** and **J. Romon-Martin:** Visible IR colors and lightcurve analysis of two bright TNOs: 1999 TC36 and 1998 SN165. New Astronomy, vol. 7, September 2002, pp. 359–367.

Peixinho, N., **P. Lacerda** and **D. Jewitt:** Color-Inclination Relation of the Classical Kuiper Belt Objects. The Astronomical Journal, vol. 136, November 2008, pp. 1837–1845.

Perna, D. et al.: Rotations and densities of transNeptunian objects. Astronomy and Astrophysics, vol. 508, December 2009, pp. 451–455.

Petit, J.-M. et al.: The Kuiper Belt luminosity function from m_R= 22 to 25. Monthly Notices of the Royal Astronomical Society, vol. 365, January 2006, pp. 429–438.

Petit, J.-M. et al.: The Canada-France Ecliptic Plane Survey-Full Data Release: The Orbital Structure of the Kuiper Belt. The Astronomical Journal, vol. 142, October 2011, pp. 131.

Petit, J.-M. et al.: The Extreme Kuiper Belt Binary 2001 QW_{322}. Science, vol. 322, October 2008, pp. 432.

Petit, J.-M., **A. Morbidelli** and **G. B. Valsecchi:** Large Scattered Planetesimals and the Excitation of the Small Body Belts. Icarus, vol. 141, October 1999, pp. 367–387.

Petit, J.-M. and **O. Mousis:** KBO binaries: how numerous were they? Icarus, vol. 168, April 2004, pp. 409–419.

Petrovic, J. J.: Review mechanical properties of ice and snow. Journal of materials science, vol. 38, 2003, pp. 1–6.

Pinilla-Alonso, N. et al.: The surface of (136108) Haumea (2003 EL{61}), the largest carbon-depleted object in the trans-Neptunian belt. Astronomy and Astrophysics, vol. 496, March 2009, pp. 547–556.

Pollack, J. B., **J. A. Burns** and **M. E. Tauber:** Gas drag in primordial circumplanetary envelopes - A mechanism for satellite capture. Icarus, vol. 37, March 1979, pp. 587–611.

Porter, S. B. and **W. M. Grundy:** KCTF evolution of trans-neptunian binaries: Connecting formation to observation. Icarus, vol. 220, August 2012, pp. 947–957.

Pravec, P. and **A. W. Harris:** Fast and Slow Rotation of Asteroids. Icarus, vol. 148, November 2000, pp. 12–20.

Pravec, P., **L. Sarounova** and **M. Wolf:** Lightcurves of 7 Near-Earth Asteroids. Icarus, vol. 124, December 1996, pp. 471–482.

Pravec, P. et al.: Photometric survey of binary near-Earth asteroids. Icarus, vol. 181, March 2006, pp. 63–93.

Pravec, P. et al.: Formation of asteroid pairs by rotational fission. Nature, vol. 466, August 2010, pp. 1085–1088.

Press, W. H. et al.: Numerical recipes in FORTRAN. The art of scientific computing. Cambridge: University Press, 1992, 2nd ed., 1992

Rabinowitz, D. et al.: A Tale of Two TNOs. October 2011, pp. 1642.

Rabinowitz, D. et al.: The La Silla-QUEST Kuiper Belt Survey. The Astronomical Journal, vol. 144, November 2012, pp. 140.

Rabinowitz, D. et al.: The Peculiar Photometric Properties of 2010 WG9: A Slowly-Rotating Trans-Neptunian Object from the Oort Cloud. ArXiv e-prints May 2013

Rabinowitz, D. L. et al.: Photometric Observations Constraining the Size, Shape, Albedo of 2003 EL61, a Rapidly Rotating, Plutosized Object in the Kuiper Belt. Astrophysicall Journal, vol. 639, March 2006, pp. 1238–1251.

Rabinowitz, D. L. et al.: The Youthful Appearance of the 2003 EL61 Collisional Family. Astronomical Journal, vol. 136, October 2008, pp. 1502–1509.

Rabinowitz, D. L., **B. E. Schaefer** and **S. W. Tourtellotte:** The Diverse Solar Phase Curves of Distant Icy Bodies. I. Photometric Observations of 18 TransNeptunian Objects, 7 Centaurs,, Nereid. Astronomical Journal, vol. 133, January 2007, pp. 26–43.

Ragozzine, D. and **M. E. Brown:** Candidate Members and Age Estimate of the Family of Kuiper Belt Object 2003 EL61. The Astronomical Journal, vol. 134, December 2007, pp. 2160–2167.

Ragozzine, D. and **M. E. Brown:** Orbits and Masses of the Satellites of the Dwarf Planet Haumea (2003 EL61). The Astronomical Journal, vol. 137, June 2009, pp. 4766–4776.

Ragozzine, D. and **M. E. Brown:** Hubble Space Telescope Observations of Haumea during a Predicted Mutual Event. vol. 42, October 2010, pp. 993.

Richardson, D. C.: A new tree code method for simulation of planetesimal dynamics. Monthly Notices of the Royal Astronomical Society, vol. 261, March 1993, pp. 396–414.

Richardson, D. C., **P. Elankumaran** and **R. E. Sanderson:** Numerical experiments with rubble piles: equilibrium shapes and spins. Icarus, vol. 173, February 2005, pp.349–361.

Richardson, D. C. et al.: Direct Large-Scale N-Body Simulations of Planetesimal Dynamics. Icarus, vol. 143, January 2000, pp. 45–59.

Roberts, D. H., **J. Lehar** and **J. W. Dreher:** Time Series Analysis with Clean - Part One - Derivation of a Spectrum. Astronomical Journal, vol. 93, April 1987, pp. 968.

Roe, H. G., **R. E. Pike** and **M. E. Brown:** Tentative detection of the rotation of Eris. Icarus, vol. 198, December 2008, pp. 459–464.

Romanishin, W. and **S. C. Tegler:** Rotation rates of Kuiper belt objects from their light curves. Nature, vol. 398, March 1999, pp. 129–132.

Romanishin, W. et al.: 1998 SM165: A large Kuiper belt object with an irregular shape. Proceedings of the National Academy of Science, vol. 98, 2001, pp. 11863–11866.

Rousselot, P. et al.: Polarimetric, Photometric Phase Effects Observed on Transneptunian Object (29981) 1999 TD10. Earth Moon, Planets, vol. 97, December 2005a, pp. 353–364.

Rousselot, P. and **J. Petit:** Photometric Study Of 28978 Ixion At Small Phase Angle. vol. 42, October 2010, pp. 40.19.

Rousselot, P. et al.: Photometric study of Centaur (60558) 2000 EC98, (55637) 2002 UX25 at different phase angles. Icarus, vol. 176, August 2005b, pp. 478–491.

Rousselot, P. et al.: Photometry of the Kuiper Belt object 1999 TD10 at different phase angles. Astronomy and Astrophysics, vol. 407, September 2003, pp. 1139–1147.

Russell, H. N.: On the Albedo of the Planets and Their Satellites. The Astrophysical Journal, vol. 43, April 1916, pp. 173.
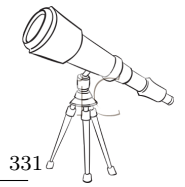
Santos-Sanz, P. et al.: "TNOs are Cool": A survey of the transNeptunian region. IV. Size/albedo characterization of 15 scattered disk and detached objects observed with HerschelPACS. Astronomy and Astrophysics, vol. 541, May 2012, A92.

Santos-Sanz, P. et al.: New BVRI photometry results on Kuiper Belt Objects from the ESO VLT. Astronomy and Astrophysics, vol. 494, February 2009, pp. 693–706.

Scargle, J. D.: Studies in astronomical time series analysis. II - Statistical aspects of spectral analysis of unevenly spaced data. The Astrophysical Journal, vol. 263, December 1982, pp. 835–853.

Schaefer, B. E. and **D. L. Rabinowitz:** Photometric Light Curve for the Kuiper Belt Object 2000 EB173 on 78 Nights. Icarus, vol. 160, November 2002, pp. 52–58.

Schaller, E. L. and **M. E. Brown:** A Deep Keck Search for Binary Kuiper Belt Objects. vol. 35, May 2003, pp. 993.

Schaller, E. L. and **M. E. Brown:** Detection of Additional Members of the 2003 EL61 Collisional Family via Near-Infrared Spectroscopy. The Astrophysical Journal, vol. 684, September 2008, L107–L109.

Schlichting, H. E. and **R. Sari:** Formation of Kuiper Belt Binaries. The Astrophysical Journal, vol. 673, February 2008a, pp. 1218–1224.

Schlichting, H. E. and **R. Sari:** The Ratio of Retrograde to Prograde Orbits: A Test for Kuiper Belt Binary Formation Theories. The Astrophysical Journal, vol. 686, October 2008b, pp. 741–747.

Schlichting, H. E. and **R. Sari:** The Creation of Haumea's Collisional Family. The Astrophysical Journal, vol. 700, August 2009, pp. 1242–1246.

Shankman, C. et al.: A Divot in the Size Distribution of the Kuiper Belt's Scattering Objects. ArXiv e-prints October 2012

Sheppard, S. S.: Small bodies in the outer solar system: From Kuiper Belt objects to Centaurs to satellites. Ph. D thesis, UNIVERSITY OF HAWAI'I, 2004

Sheppard, S. S.: Light Curves of Dwarf Plutonian Planets, other Large Kuiper Belt Objects: Their Rotations, Phase Functions, Absolute Magnitudes. Astronomical Journal, vol. 134, August 2007, pp. 787–798.

Sheppard, S. S. and **D. Jewitt:** Extreme Kuiper Belt Object 2001 QG298, the Fraction of Contact Binaries. Astronomical Journal, vol. 127, May 2004, pp. 3023–3033.

Sheppard, S. S. and **D. C. Jewitt:** Time-resolved Photometry of Kuiper Belt Objects: Rotations, Shapes, and Phase Functions. The Astronomical Journal, vol. 124, September 2002, pp. 1757–1775.

Sheppard, S. S. and **D. C. Jewitt:** Hawaii Kuiper Belt Variability Project: An Update. Earth Moon, Planets, vol. 92, June 2003, pp. 207–219.

Sheppard, S. S. et al.: A Wide-Field CCD Survey for Centaurs and Kuiper Belt Objects. The Astronomical Journal, vol. 120, November 2000, pp. 2687–2694.

Sheppard, S. S., **P. Lacerda** and **J. L. Ortiz:** Photometric Lightcurves of Transneptunian Objects, Centaurs: Rotations, Shapes, Densities. The Solar System Beyond Neptune, 2008, pp. 129–142.

Sheppard, S. S., **D. Ragozzine** and **C. Trujillo:** 2007 TY430: A Cold Classical Kuiper Belt Type Binary in the Plutino Population. The Astronomical Journal, vol. 143, March 2012, 58.

Sheppard, S. S. and **C. A. Trujillo:** A Thick Cloud of Neptune Trojans and Their Colors. Science, vol. 313, July 2006, pp. 511–514.

Sheppard, S. S. and **C. A. Trujillo:** 2007 TY_430. Minor Planet Electronic Circular, vol. 8962, August 2008, pp. 2.

Sheppard, S. S. et al.: A Southern Sky and Galactic Plane Survey for Bright Kuiper Belt Objects. The Astronomical Journal, vol. 142, October 2011, 98.

Sicardy, B. et al.: A Pluto-like radius and a high albedo for the dwarf planet Eris from an occultation. Nature, vol. 478, October 2011, pp. 493–496.

Slyuta, E. N. and **S. A. Voropaev:** Gravitational Deformation in Shaping Asteroids and Small Satellites. Icarus, vol. 129, October 1997, pp. 401–414.

Smith, B. A.: Astronomical imaging applications for CCDs. 1976, pp. 135–138.

Snodgrass, C. et al.: Characterisation of candidate members of (136108) Haumea's family. Astronomy and Astrophysics, vol. 511, February 2010, A72.

Sonnett, S., **K. J. Meech** and **G. Sarid:** Bi-Color Light Curves of Eight Neutral Trans-Neptunian Objects. LPI Contributions, vol. 1667, May 2012, 6429.

Spearman, C.: The proof and measurement of association between two things. The American Journal of Psychology, vol. 15, January 1904, pp. 72–101.

Spencer, J. R. et al.: A Low Density for Binary Kuiper Belt Object (26308) 1998 SM165. vol. 38, September 2006, pp. 546.

Springel, V.: The cosmological simulation code GADGET-2. Monthly Notices of the Royal Astronomical Society, vol. 364, December 2005, pp. 1105–1134.

Stadel, J. G.: Cosmological N-body simulations and their analysis. Ph. D thesis, UNIVERSITY OF WASHINGTON, 2001

Stansberry, J. et al.; Barucci, M. A., Boehnhardt, H., Cruikshank, D. P., Morbidelli, A., & Dotson, R., editor: Physical Properties of Kuiper Belt and Centaur Objects: Constraints from the Spitzer Space Telescope. 2008, pp. 161–179.

Stansberry, J. A. et al.: Albedos, Diameters (and a Density) of Kuiper Belt and Centaur Objects. vol. 37, August 2005, pp. 737.

Stansberry, J. A. et al.: Physical properties of transneptunian binaries (120347) Salacia Actaea and (42355) Typhon Echidna. Icarus, vol. 219, June 2012, pp. 676–688.

Stansberry, J. A. et al.: TNOs are Cool: A survey of the Trans-Neptunian region. The Haumea Family. Astronomy and Astrophysics 2013

Stellingwerf, R. F.: Period determination using phase dispersion minimization. Astrophysical Journal, vol. 224, September 1978, pp. 953–960.

Stephens, D. C. and **K. S. Noll:** Detection of Six TransNeptunian Binaries with NICMOS: A High Fraction of Binaries in the Cold Classical Disk. The Astronomical Journal, vol. 131, February 2006, pp. 1142–1148.

Stephens, D. C. et al.: HST Photometry of trans-Neptunian Objects. Earth Moon and Planets, vol. 92, June 2003, pp. 251–260.

Stern, S. A.: On the Collisional Environment, Accretion Time Scales, and Architecture of the Massive, Primordial Kuiper Belt. The Astronomical Journal, vol. 112, September 1996, pp. 1203.

Stern, S. A. et al.: A giant impact origin for Pluto's small moons and satellite multiplicity in the Kuiper belt. Nature, vol. 439, February 2006, pp. 946–948.

Stetson, P. B.: DAOPHOT - A computer program for crowded-field stellar photometry. Astronomical Society of the Pacific Publications, vol. 99, March 1987, pp. 191–222.
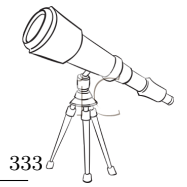
Stetson, P. B.: On the growth-curve method for calibrating stellar photometry with CCDs. Astronomical Society of the Pacific Publications, vol. 102, August 1990, pp. 932–948.

Takeda, T. and **K. Ohtsuki:** Mass dispersal and angular momentum transfer during collisions between rubble-pile asteroids. II. Effects of initial rotation and spin-down through disruptive collisions. Icarus, vol. 202, August 2009, pp. 514–524.

Tancredi, G. and **S. Favre:** Which are the dwarfs in the Solar System? Icarus, vol. 195, June 2008, pp. 851–862.

Tanga, P. et al.: Rubble-Pile Reshaping Reproduces Overall Asteroid Shapes. The Astrophysical Journal, vol. 706, November 2009, L197–L202.

Tegler, S. C. et al.: Optical Spectroscopy of the Large Kuiper Belt Objects 136472 (2005 FY9) and 136108 (2003 EL61). The Astronomical Journal, vol. 133, February 2007, pp. 526–530.

Tegler, S. C. and **W. Romanishin:** Resolution of the kuiper belt object color controversy: two distinct color populations. Icarus, vol. 161, January 2003, pp. 181–191.

Tegler, S. C. et al.: The period of rotation, shape, density, homogeneous surface color of the Centaur 5145 Pholus. Icarus, vol. 175, June 2005, pp. 390–396.

Tegler, S. C. et al.: Photometry of the transneptunian object 1993 SC. Astronomical Journal, vol. 114, September 1997, pp. 1230–1233.

Thébault, P. and **A. Doressoundiram:** Colors and collision rates within the Kuiper belt: problems with the collisional resurfacing scenario. Icarus, vol. 162, March 2003, pp. 27–37.

Thirouin, A. et al.: Short-term variability of Kuiper Belt Objects, In preparation. 2013a

Thirouin, A. et al.: Physical Characterization of Binary Trans-Neptunian Objects. Monthly Notices of the Royal Astronomical Society, 2013b, Submitted

Thirouin, A. et al.: Short-term variability of 10 trans-Neptunian objects. Monthly Notices of the Royal Astronomical Society, vol. 424, August 2012, pp. 3156–3177.

Thirouin, A. et al.: Short-term variability of a sample of 29 transNeptunian objects and Centaurs. Astronomy and Astrophysics, vol. 522, November 2010, A93.

Thomas, P. C.: The shapes of small satellites. Icarus, vol. 77, February 1989, pp. 248–274.

Toth, I. and **C. M. Lisse:** Effect of the tensile strength on the stability against rotational breakup of icy bodies. vol. 263, 2010, pp. 131–140.

Trilling, D. E. and **G. M. Bernstein:** Light Curves of 20-100 km Kuiper Belt Objects Using the Hubble Space Telescope. Astronomical Journal, vol. 131, February 2006, pp. 1149–1162.

Trujillo, C. A. and **M. E. Brown:** 1999 TC36. Minor Planet Electronic Circular, vol. 7787, January 2002a, pp. 1.

Trujillo, C. A. and **M. E. Brown:** A Correlation between Inclination and Color in the Classical Kuiper Belt. The Astrophysical Journal, 566, February 2002b, L125–L128

Trujillo, C. A. et al.: The Surface of 2003 EL_{61} in the Near-Infrared. The Astrophysical Journal, 655, February 2007, pp. 1172–1178.

Trujillo, C. A. et al.: Near-Infrared Surface Properties of the Two Intrinsically Brightest Minor Planets: (90377) Sedna and (90482) Orcus. The Astrophysical Journal, vol. 627, July 2005, pp. 1057–1065.

Trujillo, C. A., **D. C. Jewitt** and **J. X. Luu:** Properties of the Trans-Neptunian Belt: Statistics from the Canada-France-Hawaii Telescope Survey. The Astronomical Journal, vol. 122, July 2001, pp. 457–473.

Trujillo, C. A., **S. S. Sheppard** and **E. L. Schaller:** A Photometric System for Detection of Water and Methane Ices on Kuiper Belt Objects. The Astrophysical Journal, vol. 730, April 2011, 105.

Tsiganis, K. et al.: Origin of the orbital architecture of the giant planets of the Solar System. Nature, vol. 435, May 2005, pp. 459–461.

Vachier, F., **J. Berthier** and **F. Marchis:** Determination of binary asteroid orbits with a genetic-based algorithm. Astronomy and Astrophysics, vol. 543, July 2012, A68.

Veillet, C. et al.: The binary Kuiper belt object 1998 WW31. Nature, vol. 416, April 2002, pp. 711–713.

Vilenius, E. et al.: "TNOs are Cool": A survey of the transNeptunian region. VI. Herschel/PACS observations and thermal modeling of 19 classical Kuiper belt objects. Astronomy and Astrophysics, vol. 541, May 2012, A94.

Vilenius, E. et al.: "TNOs are Cool": A survey of the trans-Neptunian region. IX. Analysis of classical Kuiper belt objects from Herschel and Spitzer observations. Astronomy and Astrophysics 2013

Vokrouhlický, D. and **D. Nesvorný:** Pairs of Asteroids Probably of a Common Origin. The Astronomical Journal, vol. 136, July 2008, pp. 280–290.

Volk, K. and **R. Malhotra:** The effect of orbital evolution on the Haumea (2003 EL_{61}) collisional family. Icarus, vol. 221, September 2012, pp. 106–115.

Weidenschilling, S. J.: On the Origin of Binary Transneptunian Objects. Icarus, vol. 160, November 2002, pp. 212–215.

Whipple, F. L.: Evidence for a Comet Belt beyond Neptune. Proceedings of the National Academy of Science, vol. 51, May 1964, pp. 711–718.

Yu, Q. and **S. Tremaine:** The Dynamics of Plutinos. The Astronomical Journal, vol. 118, October 1999, pp. 1873–1881.

Yuan, F. and **C. W. Akerlof:** Astronomical Image Subtraction by Cross-Convolution. The Astrophysical Journal, vol. 677, April 2008, pp. 808–812.

Zappala, V.: A semi-analytic method for pole determination of asteroids. Moon and Planets, vol. 24, May 1981, pp. 319–325.

Zappalà, V. et al.: Physical and Dynamical Properties of Asteroid Families. Asteroids III, 2002, pp. 619–631.